Lecture Notes in Electrical Engineering 442

Avinash Konkani
Rabindranath Bera
Samrat Paul
Editors

Advances in Systems, Control and Automation

ETAEERE-2016

Springer

Lecture Notes in Electrical Engineering

Volume 442

About this Series

"Lecture Notes in Electrical Engineering (LNEE)" is a book series which reports the latest research and developments in Electrical Engineering, namely:

- Communication, Networks, and Information Theory
- Computer Engineering
- Signal, Image, Speech and Information Processing
- Circuits and Systems
- Bioengineering

LNEE publishes authored monographs and contributed volumes which present cutting edge research information as well as new perspectives on classical fields, while maintaining Springer's high standards of academic excellence. Also considered for publication are lecture materials, proceedings, and other related materials of exceptionally high quality and interest. The subject matter should be original and timely, reporting the latest research and developments in all areas of electrical engineering.

The audience for the books in LNEE consists of advanced level students, researchers, and industry professionals working at the forefront of their fields. Much like Springer's other Lecture Notes series, LNEE will be distributed through Springer's print and electronic publishing channels.

More information about this series at http://www.springer.com/series/7818

Avinash Konkani · Rabindranath Bera
Samrat Paul
Editors

Advances in Systems, Control and Automation

ETAEERE-2016

Springer

Editors
Avinash Konkani
Clinical Engineering
University of Virginia Health System
Charlottesville, VA
USA

Samrat Paul
Department of Energy Engineering
North-Eastern Hill University
Shillong, Megalaya
India

Rabindranath Bera
Department of Electronics and
Communication Engineering
Sikkim Manipal Institute of Technology
(SMIT)
Rangpo, Sikkim
India

ISSN 1876-1100 ISSN 1876-1119 (electronic)
Lecture Notes in Electrical Engineering
ISBN 978-981-10-4761-9 ISBN 978-981-10-4762-6 (eBook)
https://doi.org/ 10.1007/978-981-10-4762-6

Library of Congress Control Number: 2017939623

Printed on acid-free paper

This Springer imprint is published by Springer Nature
The registered company is Springer Nature Singapore Pte Ltd.
The registered company address is: 152 Beach Road, #21-01/04 Gateway East, Singapore 189721, Singapore

Preface

Advances in Systems, Control and Automation is a collection of research articles and critical review articles presented in the International Conference on 'Emerging Trends and Advances in Electrical Engineering and Renewable Energy ETAEERE-2016,' organized by the Department of Electrical and Electronics Engineering (EEE) of Sikkim Manipal Institute of Technology (SMIT), Majhitar, Sikkim, India, during December 17–18, 2016. This was a very unique conference which combined renewable energy, electronics, computing, communication, systems, controls and automations under one roof. Moreover, it is a matter of honor for SMIT to learn that Springer was associated with ETAEERE-2016 as a major publication sponsor for the event. The proceedings of this conference come out with four different book volumes titled under Lecture Notes in Electrical Engineering (LNEE). The chapters cover the problems of multivariable control systems and provide the necessary background for performing research in the fields of control and automation. Aimed at helping readers understand the classical and modern design of different intelligent automated systems, this book presents coverage on the control of linear and nonlinear systems, intelligent systems, stochastic control, knowledge-based systems applications, fault diagnosis and tolerant control, real-time control applications, etc.

Eminent speakers like former Vice-Chancellor Prof. A Chakrabarti of Jadavpur University; Prof. A Rajaraman of IIT Chennai; Prof. Gyoo-Shee Chae of Baekshok University, South Korea; Prof. Avinash Konkani of University of Virginia, USA; Prof. Kamani KK (the global economic advisor of Karnataka); Prof. Manjesh of Bangalore University and Dr. Amitanshu Patnaik of DRDO Delhi shared their knowledge and experience. The conference attended and presented by participants from institutes such as IISc; IITs; NITs; NEHU; BIT; VIT; MIT Manipal; IIEST Kolkata and abroad deliberated on their research works. In addition the paper presentations were accompanied by six keynote addresses from leading academic and industry researchers around the globe. The paper presentations took place in 3 different tracks with 18 parallel sessions. Through the platform of ETAEERE-2016, we got the opportunity to promote the national campaign "Make In India."

The review committee has done an excellent job in reviewing the articles and approving the high quality research articles to be published in the conference proceedings. The editors are thankful to all of the faculty and students of these various committees for their dedication in making this a very successful conference and also to the editing and printing support staff of Springer for making the compilation possible. We sincerely hope that this volume will inspire researchers.

Majhitar, Sikkim, India

Karma Sonam Sherpa
Akash Kumar Bhoi
Mohammed Nasir Ansari
Amit Kumar Singh

Editorial Board

Dr. Ashok Kumar Pradhan, IIT Kharagpur
Dr. Bhim Singh, IIT Delhi
Dr. Ganapati Panda, IIT Bhubaneswar
Dr. Debashish Jena, NITK, India
Dr. N.P. Padhy, IIT Roorkee
Dr. C. Subramani, IIT Roorkee
Dr. Patnaik S.K., Anna University
Dr. G. Uma, Anna University
Dr. Avik Bhattacharya, IIT Roorkee
Dr. Smarajit Ghosh, Thapar University
Dr. Sandeep Chakravorty, Baddi University
Dr. Krishnendu Chakraborty, KGEC
Dr. Urmila Kar, NITTTR, Kolkata
Dr. Abhijit Chakrabarti, IIEST, Shibpur
Er. Kunal Munshi, Managing Partner at Sunrator Technologies LLP
Er. Bikash Rai, Assistant Engineering, Power & Energy Department, Government of Sikkim

Reviewer Committee
Dr. Ahmed Faheem Zobaa, Department of ECE, BU, UK
Dr. Avinash Konkani, AHFP, Clinical Engineer, University of Virginia Health System, USA
Dr. Atilla Elci, Chairman, EEE, Aksaray University, Turkey
Dr. Kamran Morovati, CS, University of New Brunswick, Canada
Dr. Karma Sonam Sherpa, HOD EEE, SMIT
Dr. Chandrashekar Bhuiyan, CE, SMIT
Dr. Seshadev Sahoo, ME, Purdue University, USA
Dr. Akhtar Kalam, Leader–Smart Energy Research Unit, VU, Australia
Dr. Richard Blanchard, Renewable Energy, LBU, UK
Dr. Utpal Deka, Physics, SMIT
Dr. Nitai Paitya, ECE, SMIT
Dr. N.K. Bhattacharyya, Chemistry, SMIT
Dr. A. Senthil Kumar, EEE, VEC, Chennai
Dr. Samarjeet Borah, Department of CA, SMIT

Organizing Committee

(Sikkim Manipal Institute of Technology)

Overall Incharge
Prof. Karma Sonam Sherpa, Convenor
Prof. Akash Kumar Bhoi, Secretary
Prof. Mohammed Nasir Ansari, Convenor
Prof. Amit Kumar Singh, Convenor

Publicity
Prof. Pradeep Kumar Mallick
Prof. Himangshu Pal

Hall and Stage Arrangements
Prof. Shabbiruddin
Prof. Sandip Kumar Gupta

Caterings and Refreshment
Prof. Sunam Saha
Prof. Roshan Pradhan

Transport
Prof. Arunava Tikader
Prof. Arijit Ghosh

Help Desk and Registration
Prof. Chitrangada Roy
Prof. Dibyadeep Bhattacharya

Sponsorship
Prof. Saikat Chatterjee
Prof. Anirban Sengupta

Guest Hospitality
Prof. Moumi Pandit
Prof. Bijay Rai
Prof. Rahul Kumar

Printing
Prof. Pratik Pradhan
Prof. Rajiv Pradhan

Student Organizing Committee

(Sikkim Manipal Institute of Technology)

Yupphung Keimba Limbu
Kunglho Lepcha
Sagar Pradhan
Avinash Gupta
Avinash Pradhan
Tshering Sangmo Sherpa
Sisir Chettri
Deepika Chettri
Suyog Pradhan

Contents

About the Editors

Dr. Avinash Konkani is a Healthcare Technology Management (HTM) professional, researcher, and an author with strong educational, research, and work experience in Biomedical, Clinical, Human Factors, and Systems Engineering. He is Board of Certification in Professional Ergonomics (BCPE) certified Associate Human Factors Professional (AHFP) with more than 10 years of combined work experience as an assistant professor, research scholar, and a clinical engineer. He received his Ph.D. in Systems Engineering from the Department of Industrial and Systems Engineering at Oakland University, Rochester, Michigan, USA. He obtained his Master's in Biomedical Ergonomic Engineering from Wright State University, Dayton, Ohio, USA, and Bachelor's degree in Biomedical Engineering from Karnatak University, Dharwad, India.

Prof. (Dr.) Rabindranath Bera received his B.Tech., M.Tech., and Ph.D. degrees from the Institute of Radio Physics and Electronics, University of Calcutta, in 1982, 1985, and 1997, respectively. He has been working as a Professor and Dean, Head of the Department of Electronics and Communication Engineering, Sikkim Manipal University, since 2004. In 34 years of dedicated service, he has completed major projects for the MIT, All India Council for Technical Education (AICTE), Defence Research and Development Organisation (DRDO), Tata Iron and Steel Company (TISCO), Department of Science and Technology (DST), and others. He has published more than 150 journal articles and 85 conference papers. His areas of specialization include microwave/millimeter wave-based broadband communication including 4G mobile, remote sensing using radar and radiometer, and advanced digital signal processing.

Dr. Samrat Paul received his Ph.D. in Energy (2012) and M.Tech. in Energy Technology (2007) from Tezpur University, Assam. He is currently an Assistant Professor at the Department of Energy Engineering, North-Eastern Hill University (NEHU), Shillong. Before joining the NEHU, he served as an Assistant Professor at the Central University of Jharkhand's Centre for Energy Engineering. His research areas include the synthesis of nanomaterials for energy applications including catalytic biodiesel, biodiesel storage, etc. Dr. Paul received the Young Scientist Award from the Indian Science Congress Association (ISCA) and the Swarna Jayanti Puraskar Award from the National Academy of Sciences, India (NASI) (both in 2012).

Evaluation of Harmonics and THD in Five-Phase Inverter Constructed with High-Pass Filter by MATLAB Simulation

Manjesh, A.S. Ananda, Akash Kumar Bhoi and K.S. Sherpa

Abstract This chapter proposes and evaluates the feasible method to minimize the harmonic and its distortion. Many modern power systems incorporate different techniques to eradicate the harmonics, and filters are widespread methods used all over the world. Multi/polyphase power systems are trending because of improved performance of the system by their inherent advantages over traditional single and three-phase techniques [1]. The five-phase inverter is designed and studied with low-pass LC filter to evaluate and eradicate the behavior of harmonics in the five-phase inverter. Harmonics and THD comparison of the five-phase normal configuration with high-pass filter configuration are analyzed practically, and the results are presented in this chapter.

Keywords Five phase · Harmonics · Inverter · THD · Filters
High-pass filter

1 Introduction

Power quality improvement has been the motto for many researchers while designing the power systems. Higher phase order (HPO) systems have gained the attention in worldwide, and it is the specially designed power system which is better than the active

Manjesh (✉) · A.S. Ananda
Department of Electronic Science, Bangalore University, Bengaluru, India
e-mail: manjesh1972@gmail.com

A.S. Ananda
e-mail: a.sanand@yahoo.com

A.K. Bhoi · K.S. Sherpa
Department of Electrical & Engineering, Research Electronics Engineering, Research & development Section, Sikkim Manipal Institute of Technology, Sikkim Manipal University, Majitar, Sikkim, India
e-mail: akash730@gmail.com

K.S. Sherpa
e-mail: karmasherpa23@gmail.com

A. Konkani et al. (eds.), *Advances in Systems, Control and Automation*,
Lecture Notes in Electrical Engineering 442, https://doi.org/10.1007/978-981-10-4762-6_1

three-phase power electronic scheme. Polyphase power electronic system has broad applications in industries and aircraft applications because of its high torque and low maintenance. Induction motor efficiency deteriorates and causes voltage imbalance in the windings of the induction motor which in turn generates dv/dt and ripple voltages at converter and inverter output power electronic systems. Multi/poly phase system is implemented in the applications of marines, powered vehicles (PVs) and hybrid powered vehicles (HPVs), aviation, traction, and very high-voltage and current etc. Polyphase power system has many advantages such as current reduction, reliable during its fault operations, and also ripple current reduction at the output of the converter system.

Many methods are reported in the prior research study for the injection of harmonics, and the one among them is nonlinear load in the inverter. Eradication of harmonics is considered as top priority in power quality improvement. Harmonics appear at resonance in any power systems, both in parallel and in series forms. Parallel resonance will effect in the amplification of the output line voltage distortions and series resonance will effect in obnoxious maximum harmonic load current. Nonlinear loads such as power switches in the inverter switching ON/OFF at high speed will generate harmonics and EMIs. These harmonics are superimposed on the fundamental pure sine wave, cause adverse effect on the power system performance by degrading the quality of the fundamental sine wave.

Power quality is optimized by suppressing the harmonics and to remove from the power electronic system the harmonics filter technique is feasible and also effective in power systems [12]. Passive and active are the two types of filters that can remove the harmonics and THD. In the five-phase systems, present harmonic orders are 3, 7, 9, 11, 13, 17, etc., and fifth and every multiple of fifth harmonic order are absent. The third harmonic order is the leading harmonic order which degrades the performance. To remove the third harmonic order, a high-pass filter is connected at the load stage of the inverter.

2 High-Pass Filter

There are three types of high-pass filter such as first order, second order, and third order. In the first order, capacitor and resistor are used and the power losses are more due to the presence of resistor. The second order is preferred by many designers to remove the higher-order harmonics. The second-order high-pass filter includes inductor, capacitor, and resistor, and a low resistor value leads to low power dissipation. High-pass filter is designed to remove the third harmonic order. The filter is designed to 15 Hz, and the capacitor (C), inductor (L), and resistor (R) are calculated as follows:

$$Q = R/(L2\pi f\mathrm{r})$$

where

$$Q = \text{quality factor}$$
$$f_r = \text{resonant frequency}.$$

3 Five-Phase Inverter

Inverter is constructed using ten power switches S_1–S_{10}, and MOSFET or IGBT can be used as switches. Gating signals are programmed by pulse generators and connected to the input gate of the IGBT's as shown in Fig. 1. All the ten switches are turned ON for the conduction period of 180° mode and having 72° out of phase with each other. Ten switching modes are programmed using pulse generator as depicted in Fig. 2. At Mode-1, switches $S_1S_3S_5S_7S_9$ will conduct; similarly, at Mode-2, $S_6S_8S_{10}S_2S_4$ will conduct.

Five-phase inverter drive is constructed with high-pass filter to eliminate the harmonics as shown in Fig. 2.

The calculated values of inductors L_1–L_5, capacitors C_1–C_5, and resistors R_1–R_5 in high-pass filter are shown in Table 1.

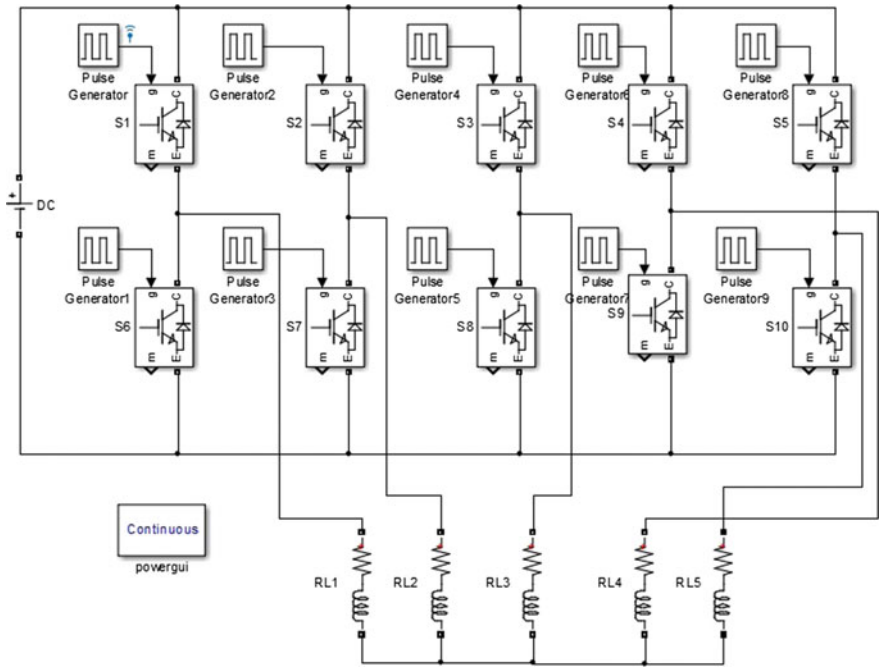

Fig. 1 5-phase inverter drive with RL load

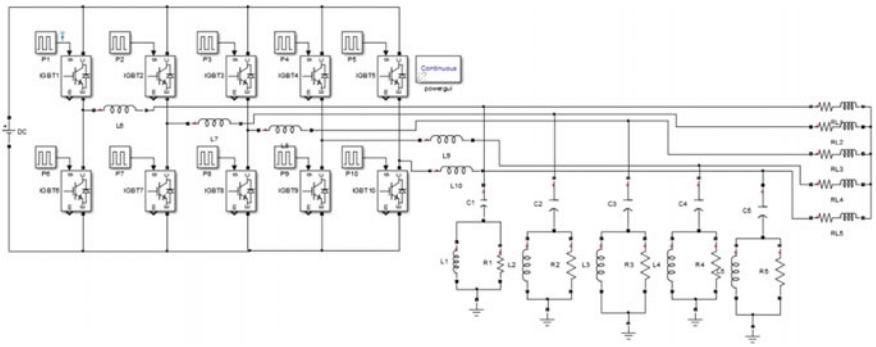

Fig. 2 Circuit diagram of five-phase inverter with high-pass filter

Table 1 Calculated values of parameters in high-pass filter for 15 Hz

R1–R5	90 Ω
C1–C5	1000 µF
L1–L5	129 mH

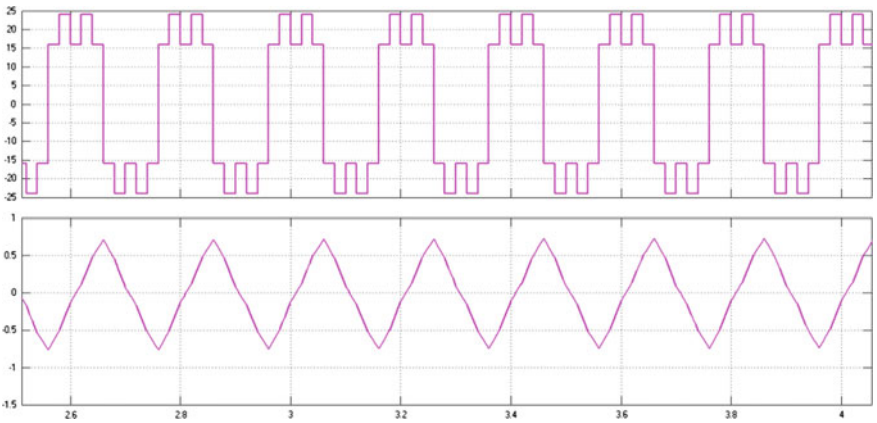

Fig. 3 Voltage and current of an individual phase in five-phase inverter

4 Simulation Results

Simulation has been done for the input frequency of 5 Hz and simulated with RL load for $R = 1.7\ \Omega$ and $L = 1.3$ mH which is employed to study the harmonic analysis of five-phase inverter drive. THD is also measured for both the inverters, voltage and current of an individual phase in five-phase inverter, without filter and using filter at the output of the inverter as shown in Figs. 3 and 4.

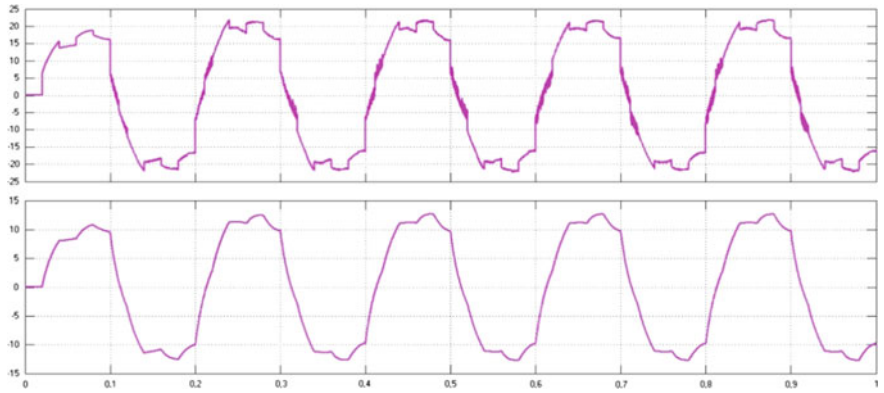

Fig. 4 Voltage and current of an individual phase in five-phase inverter with high-pass filter

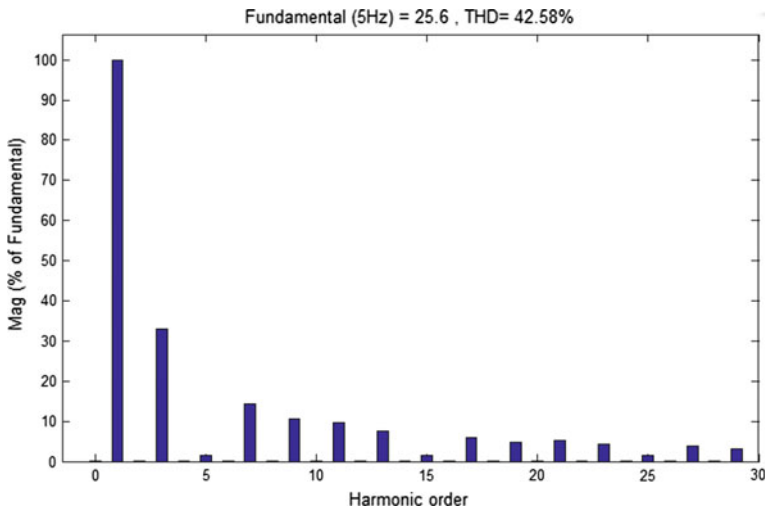

Fig. 5 Analysis of FFT in five-phase inverter

FFT analysis is used to measure the THD and harmonics at the load side of the five-phase inverter without filter and with high-pass filter as shown in Figs. 5 and 6, respectively. Table 2 shows overall total harmonic distortion of five-phase inverter without and with high-pass filter.

Table 3 shows the individual voltages of harmonic order of five-phase inverter without and with high-pass filter.

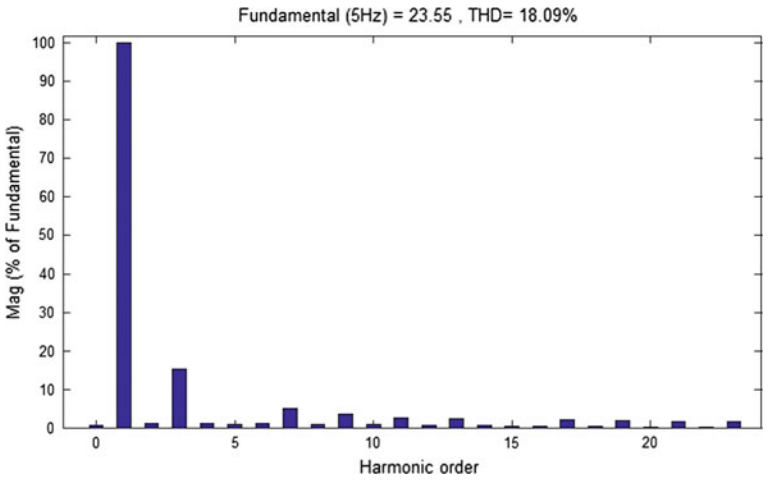

Fig. 6 Analysis of FFT of five-phase inverter with high-pass filter

Table 2 Overall THD of five-phase inverter without and with filter

Modes	THD in %
Five-phase inverter without filter	42.7
Five-phase inverter with series passive filter	20.07

Table 3 Individual voltage of harmonic order of five-phase inverter without and with high-pass filter

Harmonic order	Individual voltage of five-phase inverter without filter (normal) (V)	Individual voltage of five-phase inverter with high-pass filter (V)
1	25.46	23.51
3	8.48	3.55
5	0	0
7	3.63	1.42
9	2.82	1.03
11	2.31	0.81
13	1.95	0.66
15	0	0
17	1.49	0.49
19	1.34	0.43

5 Conclusion

The analysis of harmonics and total harmonic distortion of five-phase PWM inverter drive has been constructed and studied using MATLAB software. The circuit is simulated for the frequency $f = 15$ Hz for an input frequency of the

inverter to eliminate the third harmonic order, which is the dominant harmonic in magnitude, that simply super imposed on the fundamental harmonic, it might be adverse effect on the performance of the five-phase inverter and also the harmonic reduction with THD has been analyzed and obtained the results. The comparison of harmonics and total harmonic distortion has been presented with normal five-phase PWM inverter and five-phase inverter using high-pass filter. It is found that the harmonics and THD are found to be less using high-pass filter. This work is used to study the stator heat analysis of five-phase asynchronous motor in future.

References

1. Levi, E., Bojoi, R., Profumo, F., Toliyat, H.A., Williamson, S.: Multiphase induction motor drives—a technology status review. IET Elect. Power Appl. **1**(4), 489–516 (2007)
2. Ahmed, S.M., Abu-Rub, H., Iqbal, A., Rizwan Khan, M., Payami, S.: A three-to-five-phase matrix converter based five-phase induction motor drive system. Int. J. Recent Trends Eng. Technol. **8**(2) (2013)
3. Kim, N.H., Kim, M.H.: Modified direct torque control system of five phase induction motor. J. Electr. Eng. Technol. **4**(2), 266–271 (2009)
4. Levi, E., Jones, M., Vukosavic, S.N., Toliyat, H.A.: A five-phase two-machine vector controlled induction motor drive supplied from a single inverter. EPE J. **14**(3), 38–48 (2004)
5. Jones, M., Levi, E.: A literature survey of state-of-the-art in multiphase AC drives. In: Proceedings of 37th International UPEC, Stafford, U.K., pp. 505–510 (2002)
6. Levi, E.: Multi-phase machines for variable speed applications. EEE Trans. Ind. Electron. **55** (5), 1893–1909 (2008)
7. Ananda, A.S., Manjesh, Analysis of harmonics in a five phase PWM inverter with LR load and mitigation of harmonics by π filter. In: IEEE 2016 Biennial International Conference on Power and Energy Systems: Towards Sustainable Energy (PESTSE)
8. Dr Manjesh, Ananda, A.S.: Analysis and study of total harmonic distortion in five phase PWM inverter using LC filter with neutral point DC link capacitor voltage balancing scheme. In: IEEE International Conference on Magnetics, Machines and Drives (2014)
9. Prasad Rao, K.P., Krishna Veni, B., Ravithej, D.: FIVE-LEG INVERTER for FIVE-PHASE SUPPLY. Int. J. Eng. Trends Technol. **3**(2) (2012)
10. Tawfeeq, O.T.: THD reduction of a current source rectifier-DC motor drive using single tuned filters. Int. J. Inventive Eng. Sci. (IJIES), **1**(12). ISSN: 2319-9598, November 2013
11. Memon, Z.A., Uquaili, M.A., Unar, M.A.: Harmonics mitigation of industrial power system using passive filters. Mehran Univ. Res. J. Eng. Technol. **31**(2) (2012)
12. Kanwar, S., Mahela, O.P., Mittal, D.: Power quality improvement in faulty conditions using tuned harmonic filters. IOSR J. Electr. Electron. Eng. (IOSR-JEEE) **6**(5), 2278-1676. ISSN: 2320-3331 (2013)

Theoretical Analysis of the Electrical and Optical Properties of ZnS

Amruta Pattnaik, Monika Tomar, Pradeep Kumar Jha, Akash Kumar Bhoi, Vinay Gupta and Basudev Prasad

Abstract This chapter deals with the electrical and optical properties of ZnS by using the first principle plane-wave pseudopotential technique [ab initio *Technique*]. The obtained results show that the bandgap of ZnS system becomes narrow under the transition state condition, and also it changes the conductivity of ZnS from semiconductor to metal behavior. Zinc sulfide is a direct bandgap-type non-toxic semiconductor material. Moreover, it is used as an optical device. The above-mentioned properties show that the ZnS is a favorable candidate for luminous materials as well as solar photovoltaic cell. Doping of rare earth element and transition element in ZnS is used as a good phosphor material.

Keywords CASTEP · Bandgap · Dielectric · Reflectivity · IR spectrum Raman spectra

A. Pattnaik (✉) · B. Prasad
Department of Energy & Environment, TERI University,
Vasant Kunj, New Delhi 110070, Delhi, India
e-mail: amruta.pattnaik@students.teriuniversity.ac.in

V. Gupta
Department of Physics & Astrophysics, University of Delhi,
New Delhi 110007, Delhi, India

M. Tomar
Departments of Physics, Miranda House College, University of Delhi,
New Delhi 110007, Delhi, India

P.K. Jha
Dindayal Upadhyay College, University of Delhi, New Delhi 110078, Delhi, India

A.K. Bhoi
Department of Electrical & Electronics Engineering, Research & Development Section,
Sikkim Manipal Institute of Technology, Sikkim Manipal University, Majitar, India
e-mail: akash730@gmail.com

A. Konkani et al. (eds.), *Advances in Systems, Control and Automation*,
Lecture Notes in Electrical Engineering 442, https://doi.org/10.1007/978-981-10-4762-6_2

1 Introduction

The non-toxic and wide bandgap semiconductor materials of the II–VI group such as zinc sulfide, zinc selenide, cadmium selenide, and cadmium sulfide are used as photo and electroluminescence materials. Zinc sulfide has a direct and wide bandgap semiconductor material (3.73 eV) along with the large band energy of exciton (37 meV). The above-mentioned properties signify that zinc sulfide is a favorable material for optical devices like ultraviolet LEDs [1–3], flat-panel displays [4, 5], solar photovoltaic cells [6], and sensor devices [7]. Zinc sulfide is an inorganic material which is in the form of sphalerite (cubic form) or zinc blende and wurtzite (hexagonal form). The material is an intrinsic semiconductor with a wide bandgap of about 3.54 eV for a cubic form of ZnS and 3.91 eV for hexagonal form. Such types of semiconductors are suitable for the analysis of discrete energy level states in the bandgap [2, 8, 9].

The optical, electrical, and electronic properties of semiconductors are likely to be characterized by the help of reflectivity, absorption spectra, and vibrational spectroscopy. The above optical constants depend upon photosensitive bandgap of the material.

In this work, the band structure, the density of states (DOS), dielectric functions, refractive index, absorption spectra, reflectivity, optical conductivity, and vibrational spectroscopy of ZnS are studied by the help of plane-wave pseudopotential method using density functional theory (DFT).

2 Computational Study by CASTEP

The computational study of zinc sulfide is performed by using the software code CASTEP [10] in the frame of density functional theory (DFT) with generalized gradient approximation (GGA) and the Perdew–Burke–Ernzerhof (PBE) as exchange functional [11–14]. The collaborations between ion and electron are represented by norm-conserving pseudopotentials for Zn and S atoms [15]. All the computing properties of ZnS used 380 eV as plane wave basis set cut-off energy, and k-point is $1 \times 1 \times 1$ Monkhorst–Pack [16] grid for the selection of the Brillouin zone. Geometrical optimization is conducted that 5×10^{-6} eV atom^{-1}: convergence thresholds for the total energy, 0.01 eV Å^{-1}: the maximum force, 0.02 Gpa: maximum stress and 5×10^{-4} Å: maximum displacement under the transition state method for DFT-D connections. BFGS method is used in a geometric optimization of ZnS [17, 18]. The space group number of sphalerite ZnS is F-43 M (216) [19, 20].

Generally in the study of the interface between light and matter, adiabatic and only electron approximation is used. The effect of phonon interaction in the transition process whether the intraband and interband is ignored since the transition frequency $\geq$ phonon frequency. According to the transition probabilities and

Kramers–Kronig dispersion process, it can analyze the different optical properties like absorption spectra, dielectric functions, reflectivity, refractive index, and vibrational spectroscopy.

The optical response of the semiconductor can be defined by the complex dielectric function $\varepsilon(\omega) = \varepsilon(\omega)_{\text{real}} \pm \varepsilon(\omega)_{\text{imaginary}}$ where $\varepsilon 1(\omega) = \varepsilon(\omega)_{\text{real}}$ and $\varepsilon 2(\omega) = \varepsilon(\omega)_{\text{imaginary}}$ are given below Eqs. (1) and (2) [21].

$$\varepsilon 2(\omega) = \left(\frac{\pi}{\varepsilon 0}\right) * \left(\frac{e}{m\omega}\right)^2 * \sum_{v,c} \left\{ \int_{BZ} \left[2dK/(2\Pi)^2\right) |a * Mv, c|^2 * \delta[Ec(K) - Ev(K) - \hbar\omega] \right\} \tag{1}$$

$$\varepsilon 1(\omega) = 1 + \left(\frac{2e}{\varepsilon 0 m^2}\right) * \sum_{v,c} \int 2dK |a * Mv, c(K)|^2 / (2\pi)^2 \frac{[Ec(K) - Ev(K)]}{\hbar} * \frac{1}{\frac{[Ec(K) - Ev(K)]^2}{\hbar^2 - \omega^2}} \tag{2}$$

In the above equation, K: the electron wave vector, $\varepsilon 0$: the vacuum dielectric constant, c and v: the conduction and valance band, respectively, BZ: the first Brillouin zone, ω: the angular frequency, and $E_c(K)$ and $E_v(K)$: the intrinsic energy level of conduction and valence band, respectively. Equations (1) and (2) are used to analyze the band structure and optical effects of material [13, 21].

3 Computational Results and Analysis

3.1 Band Structure and Electronic Density of States

In Fig. 1, the Brillouin zone path is used to compute the bandgap of ZnS. The line at zero signifies the fermi level. From the figure of band structure, it can be seen that the ZnS has formed the crystalline of pure zinc blende or sphalerite. It is observed that ZnS has a direct bandgap-type semiconductor at G point of Brillouin zone. The calculated E_g [Band Gap Energy], 1.317 eV, which is lower than the experimental E_g [Band Gap Energy] value 3.68 eV. The above-mentioned difference in values due to DFT uses the ground state, whereas the energy gap lies in the excited state. The difference in calculation does not affect the computational study of ZnS [16].

From Fig. 1, it is known that the valence band of ZnS consists of lower valance band, i.e., −5.5 to −7.4 eV and higher valence band, i.e., −4.4 to 0 eV. The DOS sharp peak is obtained at −6.4 eV of valance band side.

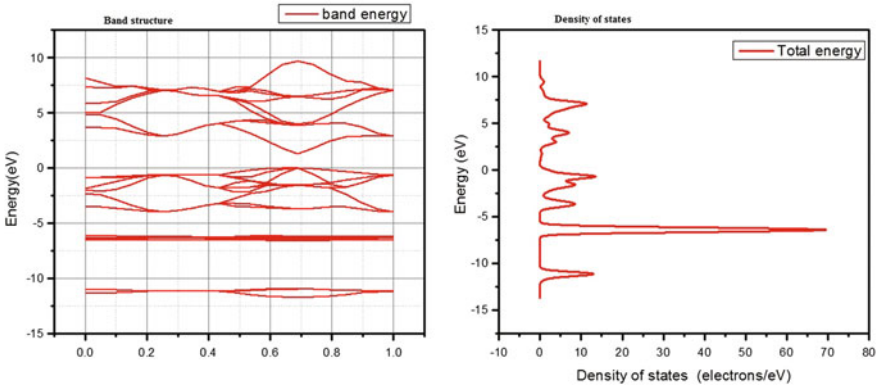

Fig. 1 Band structure and DOS of ZnS

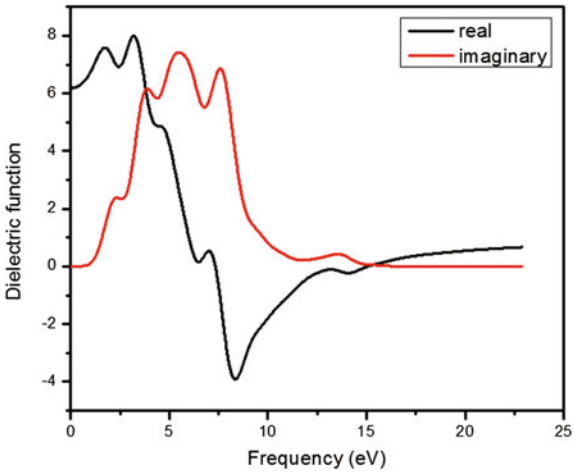

Fig. 2 Dielectric function of ZnS

3.2 Complex Dielectric Function

The dielectric function (ε) is a complex quantity which is divided into two parts, i.e., real and imaginary, which is known as the complex dielectric function $\left[\varepsilon(\omega) = \varepsilon(\omega)_{\text{real}} \pm \varepsilon(\omega)_{\text{imaginary}}\right]$. Where, $\varepsilon(\omega)_{\text{real}}$ signifies that the material becomes polarized under the electric field, and $\varepsilon(\omega)_{\text{imaginary}}$ represents the absorption in a semiconductor material. In Fig. 2, the energy is in the range of 0.8–15 eV. In a metal, the induced dipole oscillations are likely to be large as well as it can absorb the energy from the applied field. $E(\omega)_{\text{imaginary}}$ becomes important at the time of absorption as well as it must be nonzero under absorption. It is important that the

shape of $\varepsilon(\omega)_{\text{real}}$ is responsible for the changes in the shape of $\varepsilon(\omega)_{\text{imaginary}}$ and vice versa. This is called as the Kramers–Kronig relation for complex dielectric function. The dielectric function and refractive index are associated with the material by the equation $\varepsilon = n^2 = n \pm j\,k$. Figure (2) shows that the photon energy is responsible for the change of n [real] and k [imaginary] of the complex dielectric function. It can be seen that the n of the dielectric constant increases with photon energy. It touches its maximum point at 3.2 eV and after that it decreases continuously with the energy rise of photon varies in between 4.2 and 7.4 eV.

3.3 Absorption Spectrum

The absorption coefficient [α] defines an attenuation of light strength in percentage per units of distance traveling through the medium. The absorption spectrum of ZnS is given via the Eq. (3) [2, 8, 9, 22] as follows:

$$\alpha \equiv \frac{2\omega K}{c} = \frac{4\pi K}{\lambda_0} \tag{3}$$

Figure 3 displays that the absorption becomes zero at the energy ≤ 1.2 eV and ≥ 19.6 eV. When the energy of photon ≥ 1.2 eV, then the absorption coefficient [α] is increasing up to the maximum peak intensity on 300,000 cm^{-1} at 8.2 eV. Subsequently, it drops to zero with the rise of photon energy ≥ 8.2 eV. It can be concluded from Fig. 3 that ZnS has an absorption coefficient in the range 10^5 cm^{-1} along with a very actuate cutoff response in the spectrum of UV.

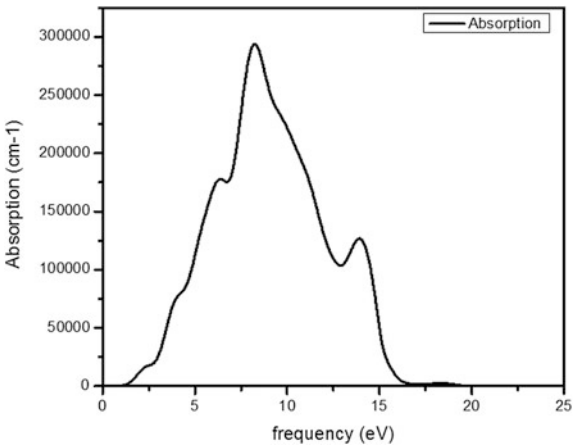

Fig. 3 Absorption spectra of ZnS

3.4 Refractive Index

The link between refractive index and dielectric function mentioned in below equations [11, 15–17, 21, 23, 24]. Those are as follows:

$$\varepsilon(\omega) = \varepsilon(\omega)_{\text{real}} \pm \varepsilon(\omega)_{\text{imaginary}} \tag{4}$$

$$N(\omega) = n(\omega) \pm j(\omega) \tag{5}$$

$$\varepsilon(\omega)_{\text{real}} = n^2 - k^2 \tag{6}$$

$$\varepsilon(\omega)_{\text{imaginary}} = 2nk \tag{7}$$

[Note: 'n' is the refractive index and 'k' is the extinction coefficient].

The refractive index of ZnS is shown in Fig. 4. The maximum peak lies at 3.2 eV. It is seen that the maximum peak changed with the increase and decrease of photon energy. $\varepsilon 1(\omega)$ and $\varepsilon 2(\omega)$ show its peaks lie at 3 and 8.5 eV, respectively. It intersects the real axis at 7.2 and 15.0 eV. 7.2 eV is called as resonance frequency (indicated as ω_0), whereas 15.0 eV is a plasma frequency (indicated as ω_p).

3.5 Reflective Spectra

The correlation of the reflectivity $R(\omega)$ and complex refractive index can be obtained from the below Eq. (8) [13, 14, 21]

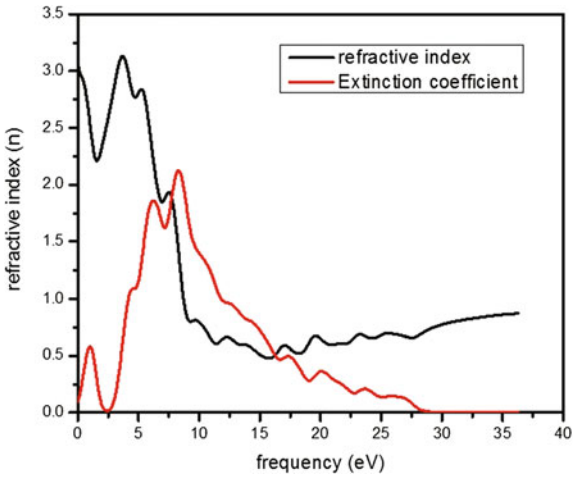

Fig. 4 Refractive index spectra of ZnS

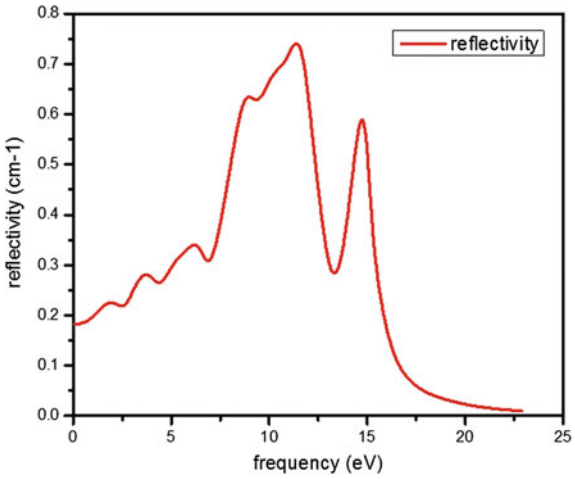

Fig. 5 Reflectivity spectra of ZnS

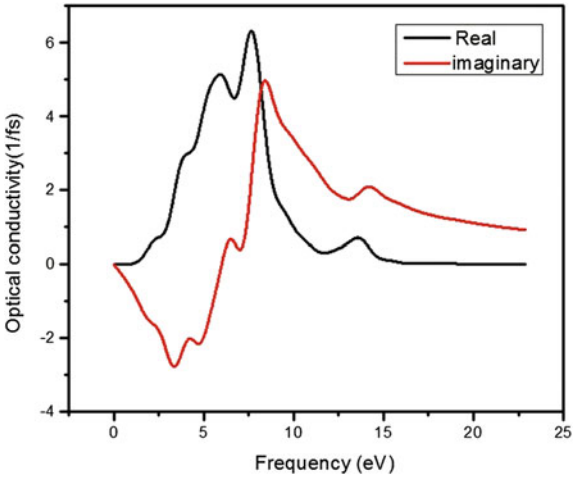

Fig. 6 Optical conductivity spectra of ZnS

$$R(\omega) = \frac{(n-1)^2 + k^2}{(n+1)^2 + k^2} \tag{8}$$

[Note: 'n' is the refractive index and 'k' is the extinction coefficient].

Figure 5 represents the reflectivity spectrum of ZnS. It is seen that the reflective spectra are very strong in the range of 7–16 eV. From Fig. 5, it can be concluded that ZnS shows metal reflective properties.

3.6 Optical Conductivity

Optical conductivity is the ratio of the current density to the electric field of a material, and it results due to the increase and decrease of illumination [2]. The complex optical conductivity [$\sigma(\omega) = \sigma 1(\omega) \pm j\sigma 2(\omega)$] is shown in Fig. 6. The real part [$\sigma 1\ (\omega)$] of optical conductivity becomes zero when it lies at ≤ 1.5 eV and ≥ 16 eV. Its maximum peak lies at 7.5 eV. The imaginary part becomes negative at the beginning, and it intersects at 8 eV.

3.7 Energy Loss Function

The energy loss function defines the loss which is occurred by energy when the electron cross through a homogenous dielectric field. It can be calculated from Eq. (9) [10, 11, 15–17, 21, 23, 24].

$$L(\omega) = im\left(\frac{-1}{\varepsilon(\omega)}\right) = \frac{\varepsilon 2(\omega)}{[\varepsilon 1^2(\omega) + \varepsilon 2^2(\omega)]} \tag{9}$$

The energy loss function peak signifies its characteristic along with the oscillation of plasma frequency. Figure 7 shows the spectra of ZnS energy loss function. It can be noticed that the highest peak lies at 15.0 eV which is the plasma energy of ZnS.

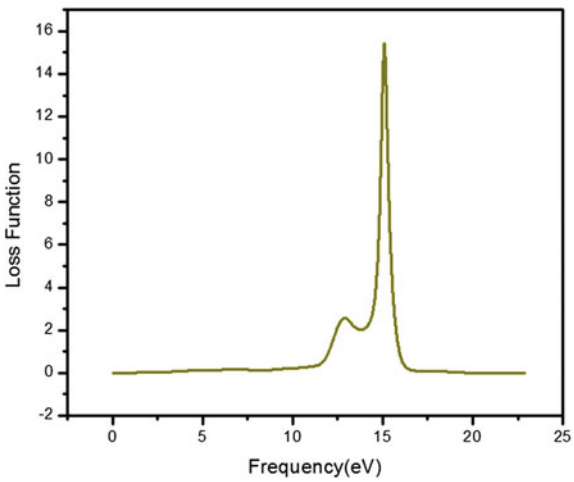

Fig. 7 Loss function spectra of ZnS

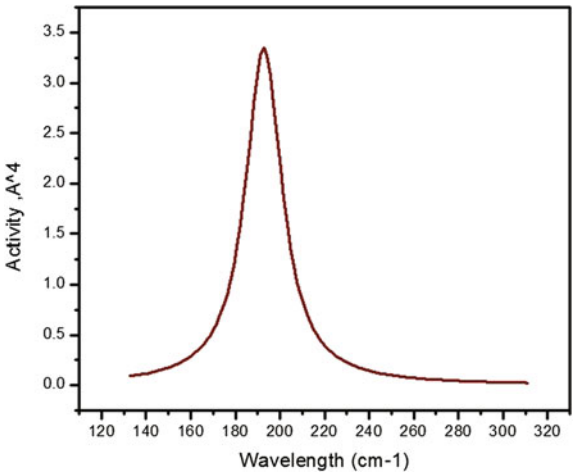

Fig. 8 Raman spectra of ZnS

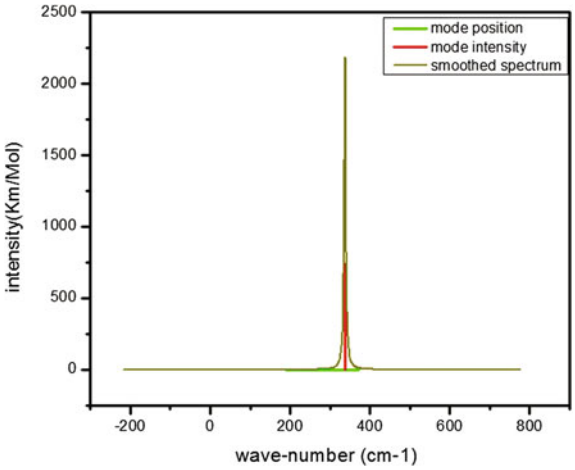

Fig. 9 IR spectrum of ZnS

3.8 Vibrational Spectroscopy

Raman and infrared (IR) spectroscopies are known as vibrational spectroscopy, and it is used for analysis and characterization of the spectrum within the region of 0.3–5 THz. The requirement of vibrational spectroscopy is to calculate the phonon frequencies, phonon displacement patterns as well as intensities of Raman and IR spectra [25].

Molecular crystals can be analyzed by Raman spectrum. Here in Fig. 8, the highest active mode lies at 194 cm^{-1} whose maximum activity is 3.4 A^4.

There are many ways to get the information regarding the functional group of inorganic crystals. IR spectroscopy is one of the vibrational spectroscopies which can provide the functional group or to measure the vibration of phonons. In Fig. 9, we got the peak of 2192 km/Mole at 338 cm^{-1} frequency. In Fig. 9, it shows that ZnS has far-infrared spectrum, where its wave number lies in between −500 to 500 cm^{-1}.

4 Conclusion

The bandgap, DOS, and optical characteristics consisting of the absorption coefficient, reflectivity, conductivity, energy loss, vibrational spectroscopy, and refractive index of ZnS are measured which are based upon a plane-wave pseudopotential method. The outcomes show that ZnS is a wide bandgap-type material. So it can be concluded that the computational results of ZnS have a structure of cubic, and the bandgap of ZnS becomes narrow under the specified condition as compared to theoretical one.

References

1. Clark, S.J., et al.: First principles methods using CASTEP. Z. Kristallogr. **220**, 567–570 (2005)
2. Segall, M.D., Lindan, P.J.D., Probert, M.J., Pickard, C.J., Hasnip, P.J., Clark, S.J., Payne, M. C.: First-principles simulation: ideas, illustrations and the CASTEP code. J. Phys.: Condens. Matter **14**, 2717–2744 (2002)
3. Chen, J., Fu, L., Yang, H.: Parallel efficiency and parametric optimization in CASTEP (2011)
4. Shi, L.B., Xu, C.Y., Yuan, H.K.: A CASTEP: study on magnetic properties of C-doped ZnO crystal. Physica B **406**, 3187–3191 (2011)
5. Hernanndez-Paredes, J., Glossman-Mitnik, D., Esparza-Ponce, H.E., Alvarez-Ramos, M.E., Duarte-Moller, A.: Band structure, optical properties and infrared spectrum of glycine-sodium nitrate crystal. J. Mol. Struct. **875**, 295–301 (2008)
6. Duan, C.J., et al.: Preparation, electronic structure, and photoluminescence properties of Eu^{2+} and Ce^{3+}/Li^{+} activated alkaline earth silicon nitride MSiN2 (M = Sr, Ba). Chem. Mater **20**, 1597–1605 (2008)
7. Sun, J., Wang, H.T., He, J., Tian, Y.: Ab initio investigations of optical properties of the high-pressure phases of ZnO. Phys. Rev. B - Condens. Matter Mater. Phys. **71**, 1–5 (2005)
8. Samantaray, C.B., Sim, H., Hwang, H.: The electronic structures and optical properties of $BaTiO_3$ and $SrTiO_3$ using first-principles calculations. Microelectr. J. **36**, 725–728 (2005)
9. Shwetha, G., Kanchana, V., Valsakumar, M.C.: Excitonic effects in oxyhalide scintillating host compounds. J. Appl. Phys. **116** (2014)
10. Perdew, J.P., Zunger, A.: Self-interaction correction to density-functional approximations for many-electron systems. Phys. Rev. B **23**, 5048–5079 (1981)
11. Perdew, J.P., Burke, K., Ernzerhof, M.: Generalized gradient approximation made simple. Phys. Rev. Lett. **77**, 3865–3868 (1996)

12. Li, L., Wang, W., et al.: First principles calculation of electronic band structure and optical properties of Cr doped ZnO. J. Phys. Chem. C **113**, (2009)
13. Zhang, X.D., et al.: First principle study of electronic and optical properties in Wurtzite $Zn_{1-x}Cd_XO$
14. Zhang, F.P., et al.: Electronic structure and thermal properties of doped $CaMnO_3$ systems. J. Alloy. Compd. **509**, 4171–4175 (2011)
15. Pickett, W.E., et al.: Pseudo potential methods in condensed matter applications. Comput. Phys. Rep. **9**, 115–198 (1989)
16. Monkhorst, H.J., Pack, J.D.: Special points for Brillouin-zone integrations. Phys. Rev. B **13**, 5188–5192 (1976)
17. Chen, Q., Xie, Q., Yan, W.J.: First principles study of $MgSi_2$ electronic and optical properties. Sci. China (Ser. G) **38**(7), 825–833 (2008)
18. Stampfl, C., Van de Walle, C.G.: Density-functional calculations for III–V nitrides using the local-density approximation and the generalized gradient approximation. Phys. Rev. B **59**, 5521–5534 (1999)
19. Xie, H.-Q., Chen, Y., Huang, W.-Q., Huang, G.-F., Peng, P., Peng, L., Wang, T.-H., Zeng, Y.: Optical characteristics of La-doped ZnS thin films prepared by chemical bath deposition. Chin. Phys. Lett. **28**(2), 27806 (2011)
20. Xie, H., Zeng, Y., Huang, W., Peng, L., Peng, P., Wang, T.: First-principles study on electronic and optical properties of La-doped ZnS. Int. J. Phys. Sci. **5**(17), 2672–2678 (2010)
21. Du, Y., et al.: Optik Electronic structure and optical properties of zinc-blende GaN. Opt. Int. J. Light Electron Opt. **123**, 2208–2212 (2012)
22. Brik, M.G.: First-principles calculations of electronic, optical and elastic properties of $ZnAl_2S_4$ and $ZnGa_2O_4$. J. Phys. Chem. Solids **71**, 1435–1442 (2010)
23. Fang, R.C.: Spectroscopy of Solid, pp. 71–75. University of Science and Technology Press, Hefei (2001)
24. Sheng, X.J.: The Spectrum and Optical Property of Semiconductor, pp. 76–94. Science Press, Beijing (2002)
25. Milman, V., et al.: Electron and vibrational spectroscopies using DFT, plane waves, and pseudopotentials: CASTEP implementation. J. Mol. Struct. THEOCHEM **954**, 22–35 (2010)

Hybrid Fuzzy Recommendation System for Enhanced E-learning

Padmaja Appalla, Rajalakshmi Selvaraj, Venu Madhav Kuthadi and Tshilidzi Marwala

Abstract The heterogeneous e-learning materials are generated in the progress of online e-learning technique. The system of e-learning is providing huge opportunities for learning online for learners with enhanced and efficient practices of learning. The system of e-learning needs to cater for the individual learner requirements including learner's profile and activities of learning in the form of tree structure. There are several issues of pedagogical learning. In case of learning phenomenon, this is too difficult for any learner or user to select their suitable learning resources without having exact background knowledge. To address these issues, this research is proposing two enhanced techniques called as Hybrid Fuzzy-based Matching Recommendation Algorithm and Collaborative Sequential Map Filtering Algorithm. This proposed approach recommends a new method to assist users on their individual as well as collaborative learning methods for accessing learning resources.

Keywords Fuzzy tree matching · Knowledge-based recommendation Sequential map · Collaborative filter · Personalize

1 Introduction

The development in communication and Web-based information technologies has indeed popularized e-learning system among educational institutions. The acceptance of e-learning system has altered the conventional learning procedures of learners (students) and offers a new condition to them, which greatly enhances and supports online learning. In the advent of different learning methodologies (element of

Padmaja Appalla (✉) · V.M. Kuthadi · T. Marwala
University of Johannesburg, Johannesburg, South Africa
e-mail: Padmaja_app@yahoo.com

Rajalakshmi Selvaraj
Department of Information Systems, BIUST, Gaborone, Botswana
e-mail: selvarajr@biust.ac.bw

A. Konkani et al. (eds.), *Advances in Systems, Control and Automation*,
Lecture Notes in Electrical Engineering 442, https://doi.org/10.1007/978-981-10-4762-6_3

understanding [1], such as learning resources, subjects, and other relevant content) in the online learning platform, students are finding it difficult to choose appropriate learning activity that better suits their needs. In this era of big data, problem due to overloading of information has been increasingly acute. It is necessary that e-learning platform should generate tailor-made suggestions with minimal manual intervention to help learners' activities [2], and as suggested by Lu [3], an "E-Learning Recommender System" should ideally generate personalized recommendations. This paper strives to develop an approach to help learners to select the most perfect learning method in online learning system. The paper proposes Collaborative Sequential Map Filtering Algorithm and Hybrid Fuzzy-based Matching Recommendation Algorithm. The former uses the benefits of collaborative filtering and knowledge-based suggestion methods. Let us learn the similarities exist between learners for both collaborative filtering and sequential mapping learning methods [4]. While analyzing the similarities of collaborative filtering, instead of using the common learning activities, the grades of matched learning actions are taken into consideration. A learner's need is usually mentioned as "very important or highly required." Techniques such as fuzzy sets can handle such category data which are uncertain. Fuzzy logic [5] is ideal for making decisions relied on fuzzy classification. The aim is to provide a tailor-made e-learning method with the help of techniques known as sequential mapping and collaborative filtering. The integrated filtering method [6] has been followed.

2 Related Work

Several researches have been undertaken in the e-learning field. In one such research undertaken to understand a better way of learning, [7] proposed that e-learning can be enhanced using two features: one that focused on learner interest, and two that focused on background knowledge. When hybrid and content-based approaches were compared, [7] found the hybrid collaborative filtering method not only outperformed Web-based educational systems in adaption and personalization, but it also lowered computational costs. Baylari and Montazer [8] proposed the development of a multiple e-learning platform that could include adopting tests runs on IRT (item response theory), and ANN (artificial neural networks). Another method by [9] sought to include two modules that incorporated content-based and collaborative filtering approaches so that learners could access automatically recommendations based on their recent activities without seeking feedbacks online. For this, an offline module containing the names of learners and their content is compared with online modules to suggest what kind of content satisfies a learner's needs or goals. In any form of learning, recommendations and feedbacks are necessary, and it is the same with online learning as well. Keeping this in mind, [10] introduced Comtella-D wherein, a learner's history of learning could be retrieved to design an appropriate strategy for him or her based on their input data. In one such experiment, it assessed that collaborative filtering techniques could indeed be successful when tested on discussion forums. Garcia et al. [11] went a step further and designed a data mining apparatus to assist non-expert educators to improve their online teaching methods by

sharing and studying their outcomes with other non-expert educators. However, considering that there would be dynamic interests, multi-preferences, and varied interests among these non-expert educators, [12] proposed the sequencing of data using algorithms such as "Apriori" and "Prefix Span" to identify latent patterns to access learning content. However, [13] wanted a simpler and unified approach to understanding a learner's learning preference and sought to introduce a CT (compact tree) approach. Salehi and Nakhai Kamalabadi's [13] method outperformed the earlier algorithmic calculations in terms of its accuracy, recalls, and listings.

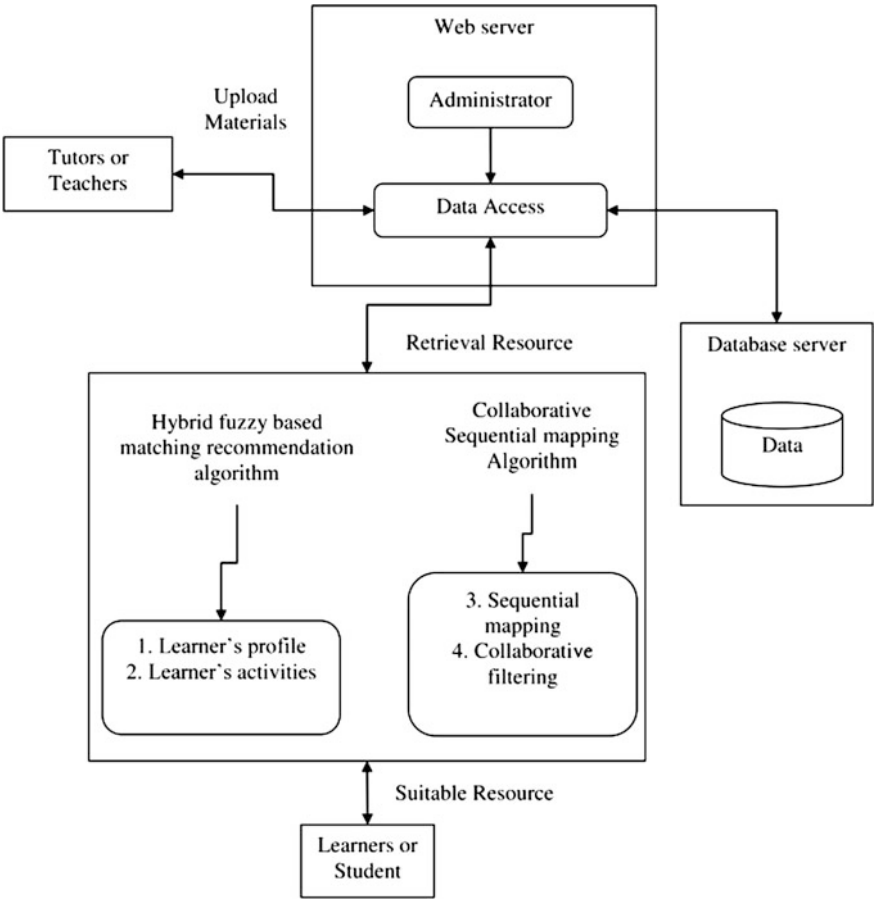

Fig. 1 Hybrid fuzzy tree matching recommendation

3 Hybrid Fuzzy Tree Matching Recommendation

By introducing a suitable learning mechanism, students will be able to learn more effectively online. This work is proposing the idea of data uploading in cloud server side, while learners are trying to access the data. By giving query to e-learning system, the learner can retrieve the similar data by using sequential mapping process. It is classifying the data from cloud server and then classified data filtered by collaborative filter based on similarity. The relevance data are recommended to user with the help of hybrid fuzzy tree matching (Fig. 1).

Learners' profiles are stored in the system administrator, and it can be filtered using a password. It is a user's profile that determines his or her learning preferences. Similarly, a learner's profile can be used to retrieve details of other learners with similar interests, otherwise called as the learner's neighborhood.

The activities of learners are an activity of periodical learning performing a complied proposed subject or the request of instructor likewise: group discussion on specific topic, chat on specific topic, online video for any specific topic, etc., producing the resources of e-learning within several different types of supports.

The matching approach of fuzzy system has been proposed for evaluating the concept similarity. As per the requirement of students and material information of learning system seen over the concept, the approach of fuzzy matching is completely suitable to find out the learning material recommendation based on the requirement of students. The given component, requirement set R_i of a particular student x_i implies association rule to form R_i L_i, (calculate L_i on the basis of R_i), where the learning material L_i is set of learning material taxonomy subject. The component task is for finding the set of material for e-learning $L_i = (l_{i1}, l_{i2}, \ldots, l_{ik})$ for student x_i, the functionality l_{im} could be either one or one class for material of learning at similar level that is matching with the fuzzy technique function R_i.

3.1 Matching Algorithm

Using the matching rule of fuzzy system for discovering the association relation between students and their requirements, the component would be generating a recommendation material of personalized learning list for (N materials) for every student. This proposed component is addressing that how to determine the value of "N" for the top-N e-learning recommendation material and recommendation format.

3.2 Collaborative Sequential Mapping Algorithm

3.2.1 Collaborative Filtering

Collaborative filtering is an important strategy in the recommender system. The technique of collaborative filtering for e-learning is based on grouping of common interests of learners. The approaches are broadly divided into three categories. They are: i) learner's activities such as material, ii) materials uploaded by tutor, and iii) collaborative material. Collaborative e-learning platforms are fast growing, making them an irreplaceable provider of learning materials. The user preferences are collected and are propagated aggressively through word-of-mouth recommendations.

3.2.2 Efficient Collaborative Filter Algorithm

The proposed algorithm, efficient collaborative filtering, is to filter the profile of learner and the activity of learner through cloud database.

Input: Profile of Learner
Output: The node set is being recommended for respective strength and the value of w

1. Recommended Nodes set $\leftarrow \Phi$;
2. Strength Set $\leftarrow \Phi$;
3. Every node v is being registered on the Table pattern DO
4. IF Dist(w, p) $\leq \rho_d$, where ρ is the pattern of v, THEN
5. Recommended Nodes set $\leftarrow$ Uv;
6. FOR each node $v \in$ Recommended Nodes set DO
7. Set of Strength $\leftarrow$ U $U = \frac{\text{Conf}_{(v,\omega)}}{\Sigma_i \text{Conf}_{(v_i,\omega)}}$ where $v_i \in$ Set Of Recommended Nodes;
8. Recommended Nodes Output set and Strength Set

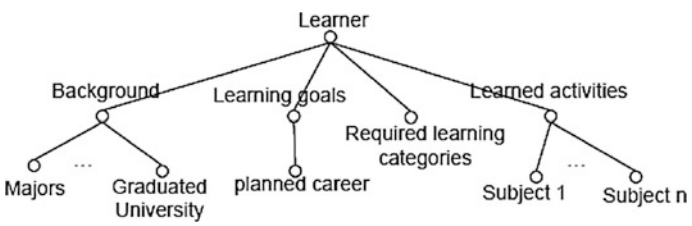

Fig. 2 Fuzzy tree structure

3.2.3 Sequential Mapping

Several factors are considered by the learner when he selects a learning activity such as his background, goals, and choice of learning categories. These factors are comprised of several sub-factors, which eventually takes a tree structure. Learners most likely express their requirements with linguistic terms in real-time applications. This may include phrases like "Highly Required." A fuzzy set technique might be suitable in handling the linguistic terms.

3.3 Personal Recommendation System

In this system, information such as learner's demographics and previous education, goals, and choice of learning categories are recorded during the registration and learning process. Most importantly, the planned careers of the learners are noted from the predefined career list (Fig. 2).

3.4 Cloud Database Storage

The cloud database stores all information about learning objects and user. The layer of database includes the knowledge library of current user's or learner's, the object of learning resources, the assessment score of learner's, and rules mining through the algorithm of sequential mapping. The knowledge library of current users or learners is having the behavior of each and every learner's and other all relevant properties including knowledge ID of current learning, learning time, and learning level.

3.5 Hybrid Fuzzy-Based Matching Recommendation Algorithm

The proposed rule of fuzzy matching is being used to find out the materials of learning that matches to learner's requirement. The taxonomy of learning material is being represented as structure of tree classifying the low-level set of learning material into high-level set of learning material. The tree leaves are denoting instances of learning material, and non-leaf nodes are denoting the material of learning obtained through the combination of lower level nodes within one parent node.

Input: two trees $T_u[j]$, $T_i[k]$ and the mapping set M
Output: the conceptual similarity between $T_u[j]$ and $T_i[k]$

1: mapping set $M_1 \leftarrow \{(t_u[j], t_i[k])\}$
2: if $F_u[j] = \phi, F_i[k] = \phi$

3: $sc_{T1} \leftarrow sc(a(t_u[j]), a(t_i[k]))$
4: else if $F_u[j] = \phi, F_i[k] \neq \phi$
5: $sc_{T1} \leftarrow \alpha \cdot sc(a(t_u[j]), a(t_i[k])) + (1-\alpha) \cdot \sum_{t=1}^{n_k} w_{k_t} \cdot sc_T(T_u[j], T_i[k_t], \phi)$
6: else if $F_u[j] \neq \phi, F_i[k] = \phi$
7: $sc_{T1} \leftarrow \alpha \cdot sc(a(t_u[j]), a(t_i[k])) + (1-\alpha) \cdot \sum_{t=1}^{n_j} w_{j_t} \cdot sc_T(T_u[j_t], T_i[k], \phi)$
8: else if $F_u[j] \neq \phi, F_i[k] \neq \phi$
9: $V_j \leftarrow \{t_u[j_1], t_u[j_2], \ldots t_u[j_{n_j}]\}$
10: $V_k \leftarrow \{t_i[k_1], t_i[k_2], \ldots t_i[k_{n_k}]\}$
11: for s = 1 to n_j
12: for t = 1 to n_k
13: new mapping set $M_{s,t}$
14: $ew_{s,t} \leftarrow sc_T(T_u[j_s], T_i[k_t], M_{s,t})$
15: $m \leftarrow$ *Compute Matching* ($V_j \cup V_k$, *ew*)
16: for each $(t_u[j_s], t_i[j_t]) \in m$,
17: $M_1 \leftarrow M_1 \cup M_{s,t}$
18: $sc_{T1} \leftarrow \alpha \cdot sc(a(t_u[j]), a(t_i[k])) + (1-\alpha) \cdot \sum_{(t_u[j_s], t_i[j_t]) \in m} w_{s,t} \cdot ew_{s,t}$
19: $sc_{T2} \leftarrow 0$, mapping set $M_2 \leftarrow \phi$
20: for t = 1 to n_k
21: new mapping set $M_{j,t}$
22: $sc_t \leftarrow w_t \cdot sc_T(T_u[j], T_i[k_t], M_{j,t})$
23: if $sc_{T2} < sc_t$
24: $sc_{T2} \leftarrow sc_t$, $M_2 \leftarrow M_{j,t}$
25: $sc_{T3} \leftarrow 0$, mapping set $M_3 \leftarrow \phi$
26: for t = 1 to n_j
27: new mapping set $M_{t,k}$
28: $sc_t \leftarrow w_t \cdot sc_T(T_u[j_t], T_i[k], M_{t,k})$
29: if $sc_{T3} < sc_t$
30: $sc_{T3} \leftarrow sc_t$, $M_3 \leftarrow M_{t,k}$
31: for p = 1, 2, 3
32: if $sc_{Tp} = \max\{sc_{T1}, sc_{T2}, sc_{T3}\}$

Table 1 Learner with subjects

Subjects	L1	L2	L3	L4	L5
S1: Business intelligence		4	4	5	
S2: ECE subjects	3		2		
S3: CS and engineering		3	3		
S4: RDBMS and DBMS	3	4			
S5: Program languages	4		3		
S6: EEE subjects	5			2	
S7: Mach materials		2		4	
S8: Information technology					

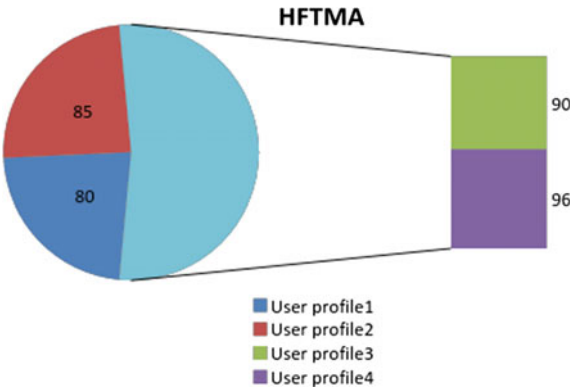

Fig. 3 Fuzzy system user profile-based recommendation results

33: $M \leftarrow M \cup M_p$
34: return $\max\{sc_{T1}, sc_{T2}, sc_{T3}\}$

3.6 Result and Discussion

For carrying experimentation of the proposed approach, a system consisting of Windows 7 or XP operating system with i3 processor with 2-GB RAM and 500-GB hard disk drive with Java for implementation of recommendations using hybrid fuzzy tree matching is needed.

In Table 1, a new registered user is shown as Learner 5 and a subject, and study material design is shown as S8. The subjects recommended by the system for Learners 4 and 5 will be generated in the paper. Alternative subjects for Learners 4 and 5 are also calculated.

The recommendations alternatives are selected for Learners 4 and 5 based on the SMCF similarity degrees calculated between learners.

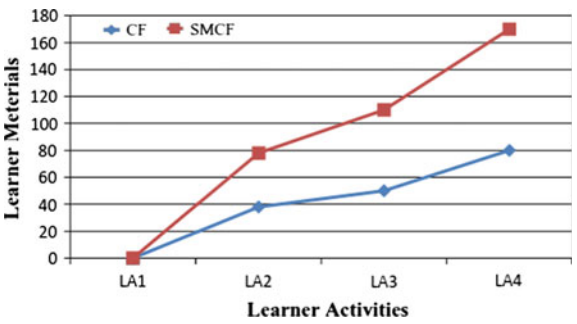

Fig. 4 Collaborative filtering process results

Table 2 Comparison between the proposed new system and the background E-learning recommender system

E-learning recommender system	Tree-structured data	Fuzzy learning activity	Learner profiles similarity	Fuzzy learner requirement	Pedagogical constraint	Matching knowledge	Sequential mapping and CF similarity	Semantic and CF similarity
Proposed system: TeLRS	✓	✓	✓	✓	✓	✓	✓	
Dianshuang Wu, Jie Lu, and Guangquan Zhang	✓	✓	✓	✓	✓	✓		✓
Sibel Somyurek; Julio Guerra Roya Hosseini	✓			✓	✓	✓		

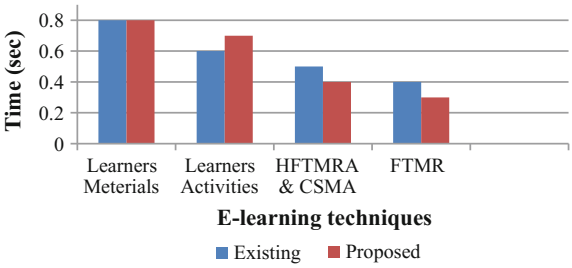

Fig. 5 Result-based learner time frame

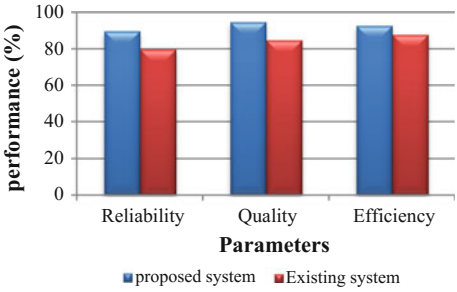

Fig. 6 Parameters performance

Figure 3 shows number of user profile; User activities and user preferences are also used by the proposed work based on HFTMA algorithm. This proposed algorithm is HFTMA; it is compared with background fuzzy tree structure algorithm. Finally, result is showing new proposed system (96) better than existing system (90).

The results shown in Fig. 4 indicate that the proposed new system is more efficient than the existing one due to the use of collaborative filtering sequential mapping process for finding similarities of activities.

Table 2 shows comparison between the proposed system with the existing system where "*v*" represents recommended system. It is seen from Table 2, the developed HFTMA will be able to handle more complex data in comparison with background e-learning recommender system.

Figure 5 shows the process of existing and proposed system. When compared to existing system, the proposed system, hybrid fuzzy tree matching recommendation, is high based on time between learners' materials and learners' activities. The technical processes of existing and proposed systems are shown in Fig. 5, while parameter performances are shown in Fig. 6. On comparison, it is seen that the proposed system has high reliability, quality, and efficiency.

4 Conclusion

Based on user's or learner's profile and activities, the proposed technique of Hybrid Fuzzy-based Matching Recommendation Algorithm and Collaborative Sequential Map Filtering Algorithm gives an accurate e-learning recommendation compared to knowledge-based recommendation. This is due to the tree-structured fuzzy-based learning activity model in the proposed system within learner's profile model which is responsible for the improved recommendation system. The fuzzy system proposes a similarity model within collaborative sequential filtering. This model makes evaluation of similarity measurements in respect of learning activity and learner's profile. It is seen that the proposed system is very fast and gives an accurate results of user's query and requirement. In addition, the proposed approach is compatible with different types of data such as text, audio, video, pdf, and images.

References

1. Drachsler, H., Hummel, H.G.K., Koper, R.: Personal recommender systems for learners in lifelong learning networks: the requirements, techniques and model. Int. J. Learn. Technol. **3**, 404–423 (2008)
2. Zaıane, O.R., Luo, J.: Web usage mining for a better web-based learning environment. In: Proceedings of Conference on Advanced Technology for Education, pp. 60–64 (2001)
3. Lu, J.: Personalized e-learning material recommender system. In: Proceedings of the 2nd International Conference on Information Technology for Application (Icita 2004), pp. 374–379 (2004)
4. Vaishali, F., Archana, G., Monika, G., Vidya, G., Sanap, M.: E-learning recommendation system using fuzzy logic and ontology. Int. J. Adv. Res. Comput. Eng. Technol. (Ijarcet) **5**(1), 165 (2016). ISSN: 2278–1323
5. Drachsler, H., Hummel, H.G.K., Koper, R.: Personal recommender systems for learners in lifelong learning networks: the requirements, techniques and model. Int. J. Learn. Technol. **3** (4), 404–423 (2008)
6. Polson, M.C., Richardson, J.J.: Foundations of Intelligent Tutoring Systems. Psychology Press (2013)
7. Tang, T.Y., Mccalla, G.I.: Smart recommendation for an evolving e-learning system: architecture and experiment. Int. J. E-Learn. **4**(1), 105–129 (2005)
8. Baylari, A., Montazer, G.A.: Design a personalized e-learning system based on item response theory and artificial neural network approach. Expert Syst. Appl. **36**(4), 8013–8021 (2009)
9. Khribi, M.K., Jemni, M., Nasraoui, O.: Automatic recommendations for e-learning personalization based on web usage mining techniques and information retrieval. In: 8th Ieee International Conference on Advanced Learning Technologies (Icalt 2008), Santander, Cantabria, 1–5 July, Ieee Computer Society: California (2008)
10. Abel, F., Bittencourt, I.I., Costa, E., Henze, N., Krause, D., Vassileva, J.: Recommendations in online discussion forums for e-learning systems. IEEE Trans. Learn. Technol. **3**(2), 165–176 (2010)
11. Garcia, E., Romero, C., Ventura, S., Castro, C.D.A.: Collaborative educational association rule mining tool. Internet High. Educ. **14**(2), 77–88 (2011)

12. Salehi, M., Kamalabadi, N., Ghaznavi Ghoushchi, M.B.: Personalized recommendation of learning material using sequential pattern mining and attribute based collaborative filtering. Educ. Inform. Technol. **17**(4), 1–23 (2012)
13. Salehi, M., Nakhai Kamalabadi, I.: Hybrid recommendation approach for learning material based on sequential pattern of the accessed material and the learner's preference tree. Knowl.-Based Syst. **48**, 57–69 (2013)

Tension Controllers for a Strip Tension Levelling Line

Daniel Magura, Viliam Fedák, Padmanaban Sanjeevikumar and Karol Kyslan

Abstract Strip material processed in continuous production lines causes a mechanical coupling among tension rolls driven by a multi-motor drive system. Thus, the drives are mutually mechanically coupled and influenced in their operation. One of the key techniques, to guarantee the output product quality in the fibre, paper, plastic and metal plating industries, consists in controlling the strip tension on a preset value that should be set differently for each section of the line. This paper describes two newly developed types of tension controllers: a tension controller with the ramp and a stepper tension controller, which are suitable for the line sections with high and low level of the tension, respectively. The proposed controllers were verified experimentally on a real tension levelling line.

Keywords Tension controller · Stepper controller · Ramp generator

D. Magura
BWG k.s., Prešov, Slovakia
e-mail: daniel.magura@gmail.com

V. Fedák · K. Kyslan
Department of Electrical Engineering and Mechatronics,
Technical University of Košice, Košice, Slovak Republic
e-mail: viliam.fedak@tuke.sk

K. Kyslan
e-mail: karol.kyslan@tuke.sk

P. Sanjeevikumar (✉)
Department of Electrical and Electronics Engineering,
University of Johannesburg, Auckland Park, Johannesburg, South Africa
e-mail: sanjeevi_12@yahoo.co.in

P. Sanjeevikumar
Research and Development, Ohm Technologies, Chennai, India

A. Konkani et al. (eds.), *Advances in Systems, Control and Automation*,
Lecture Notes in Electrical Engineering 442, https://doi.org/10.1007/978-981-10-4762-6_4

1 Introduction

During technological process in strip processing lines, the processed material changes its mechanical properties. Strip causes mechanical coupling of motors, and thus, they are mutually influenced in their operation. In manufacture and processing of continuous strips such as paper products, plastic films, metal foils and rubber profiles, it is important to maintain the tension and the speed of the strip at the set point values between consecutive pairs of driving rolls. In order to achieve required quality of the outgoing strip, the tension in the strip and its elongation in each line section should be kept within specified, preset boundaries. Unprecise tension control may result in deterioration of the material quality, strip deformation or even in a strip breaking.

From the technological point of view, the tension in the strip should be kept at constant, preset value, regardless variations of the strip speed. Several control methods to keep the constant tension are known, [1–6]. The authors in [1] present the tension control using PI controller, where variable parameters of the controller are calculated according to the diameter of the rolls, inertia and strip speed. In [2], a strip tension controller based on feedback information about the position difference between two rollers is proposed. The tension controller is implemented in parallel with the speed controller and improves dynamic reaction to changes in the strip tension.

Complex systems usually require the involvement of fuzzy tension controllers, but for users it is troublesome to modify the table of the fuzzy controller, [3]. The authors [4] have published a methodology for a self-tuning fuzzy controller, in which the control parameters can be changed so that the whole system has sufficient stability and performance in the presence of variable system parameters or structure uncertainty. Some methods, based on implementation of observer techniques replacing tension transducers, were published in [5, 6]. Such solution is suitable for low-cost applications. The authors [7] have realized a control algorithm for continuous line designed on the basis of the II. Lyapunov method in laboratory environment.

One of the key problems in processing the strips is to get flat-rolled products of high flatness quality. Strip shape equipment—flatteners or levellers—generally presents the heart of most manufacturer's or service centre's coil processing lines [8]. The quality of unflattened strips can be improved in strip tension levelling lines, the main part of which is a tension leveller [9].

The goal of this paper consists in presenting two developed tension controllers, which can be used in various applications of the direct strip tension control: for the line sections with high tension, a tension controller with the ramp was developed, and for the line sections with low tensions, a stepper tension controller is introduced. The operation of both controllers has been verified practically at experimentation on a strip tension levelling line for aluminium sheets.

2 Description of the Strip Levelling Line

A tension levelling line is divided by material storages into three parts (Fig. 1) containing the following machines:

- Entry section:
  - Uncoiler(s),
  - Side trimmer,
  - Strip connecting station (joiner).
- Strip processing section:
  - Annealing section (oven),
  - Tension leveller—Levelflex,
  - Cleaning section.
- Exit section:
  - Inspection table,
  - Drum shear,
  - Recoiler(s).

Arrangement of the machines in the line (arrangement of working and transport rolls) depends on application and customer requirements: some machine changes directly mechanical properties of the strip material (e.g. at annealing, or in rolling mills), the other ones deal with the surface treatment (cleaning—pickling, galvanization, zincification, coating, straightening, etc.), or serve for manipulation of the processed strip—its transport, loading the strip into the line, accumulation/storage of the strip, connecting its endings, cutting the strips, etc.

The rolls and the working machines are mutually bounded by the processed strip. From the technology of strip processing, it follows that a different tension in the strip is required in each from the line sections.

In the analysed line, the block "Technological Process" in Fig. 1 contains a part of the line with an annealing oven because during cold rolling (prior entering the

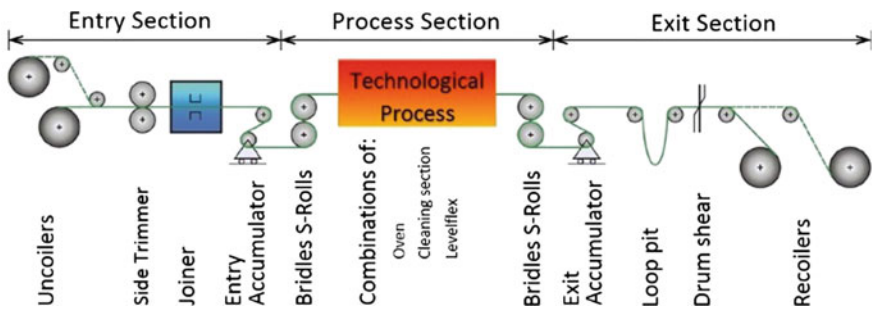

Fig. 1 Diagram of a continuous strip levelling line

strip into the analysed line), the aluminium strip solidifies, has residual stress and must be annealed to regain its formability for further processing.

From the point of view of tension levelling technology description, it follows that there are two types of the line sections: high strip tension and low strip tension. For each from these categories, we have developed a special tension controller:

(1) The sections in which tensions in the strip reach the highest values (high tensions) which are necessary for getting the strip with the high flatness. Such sections usually occur in the entry and output sections of the line (in case of aluminium strip having the tensions of σ = 5–10 MPa) and in levelling section (with very high tensions of σ = 15–70 MPa) consisting of a roller levelling device and bridles (tension rolls). The designed tension controller is described in the Sect. 3.2.
(2) The sections with low-level tensions (low tensions) what is the case of a technological section inside (in our case an annealing oven with a long length section—about 100 m, where the strip is supported by hot compressed air and the tension reaches values round σ = 1 MPa). The designed tension controller is described in the Sect. 3.3.

Proposed structures of these tension controllers were successfully implemented for the control of tensions in the line sections of a strip levelling line produced by company BWG.

3 Tension Control

The basic formula used for calculation of a required strip tension is based on the relationship between the tension F_p acting on the roll on the motor torque M_T [8]:

$$M_T = F_p \cdot R \tag{1}$$

where R is radius of the tensional roll.

Except of the torque M_T causing the tension in the strip, the total motor torque consists also from the acceleration component $\left(J\frac{\mathrm{d}\omega}{\mathrm{d}t}\right)$ and friction component (M_{Tr}).

When considering the gear ratio j for creating the required tension F, the motor must develop the torque:

$$M_M = \frac{1}{j}M_T + \frac{1}{j^2}J\frac{\mathrm{d}\omega}{\mathrm{d}t} + M_{Tr} \tag{2}$$

Having to disposal measured mechanical losses and moment of inertia of each drive in the line then, in an ideal case, the actual value of the tension should correspond to the required value of the tension in the section between the working rolls [10].

Of course, in the praxis it is impossible to measure nor to obtain mechanical losses (depending also on the strip speed) within the whole speed range and simultaneously also to consider the temperature of the motors and the environment, material friction nor friction in the bearings. For this reason, to control the strip tension, the tension controllers are used.

3.1 PI Tension Controller

At first, let us consider dynamical properties of a classical PI tension controller presenting the simplest controller that is often used in the tension control circuit. Its advantage consists in its easy implementation—it is usually implemented in the library of each digital control system, and thus, one does not need to program it. The controller can be set up and tuned directly on place at commissioning of the line. Its tuning does not require any extra burden but sometimes it is necessary to modify or adapt the controller parameters according to variable speed of the strip and/or for various materials of different quality and cross sections.

Another problem the PI controller meets presents an oscillating value of the tension signal on its input, which is measured or estimated from other process variables. This also causes oscillations of the PI controller output value which gives rise to undesirable oscillations that are led into the motor torque limiter. In praxis, we try to avoid using a classic PI controller with constant parameters for the control of the strip tension. It is more advantageous to use developed simple tension controllers, as presented in this paper.

3.2 Tension Controller with Ramp Generator

We use this kind of controller for controlling the high tensions in the strip. These occur in the straightening section of the line in Fig. 2.

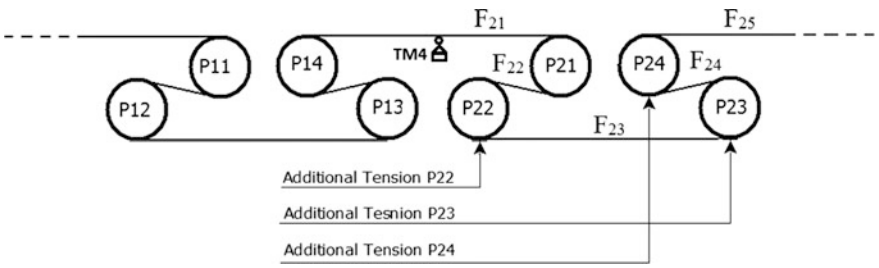

Fig. 2 Scheme of arrangement of the drives in central part of the analysed continuous strip processing line

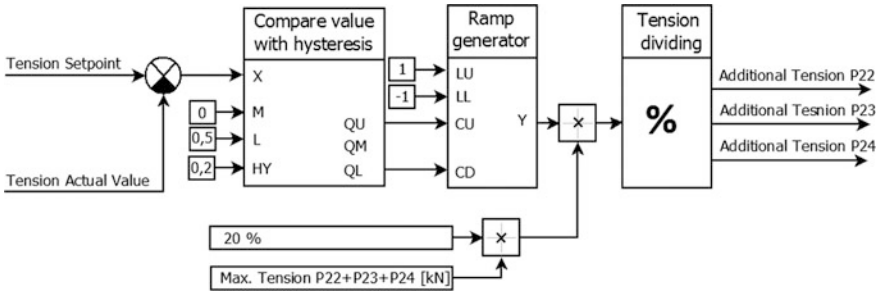

Fig. 3 Tension controller equipped by a ramp generator

Fig. 4 Comparator principle

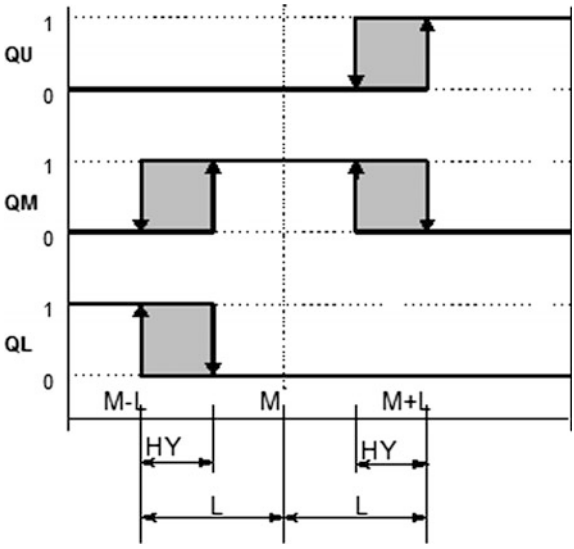

The notation P11, P12 … P31 presents drive bridles (the tension rolls). The tensions in the strip between these drives reach high values. Satisfactory control results can be obtained with a controller that gradually changes the required value of the tension in the line section (smoothly or by slow changes) in time instants, when the actual value tension reaches the set point value within a band of hysteresis (set up by the programmer). The smoothly changed value is generated by a ramp generator. In our tension levelling line, it is allowed that the preset tension can vary within the boundaries of $\pm 1\%$, what means that a controller having a constant control deviation can be also used.

The controller scheme is shown in Fig. 3. We have named the presented structure as a tension controller with ramp. The control deviation X is compared to the value M which is set to zero in order to keep the control deviation at zero value.

Figure 4 shows the function of the block comparing the value with hysteresis.

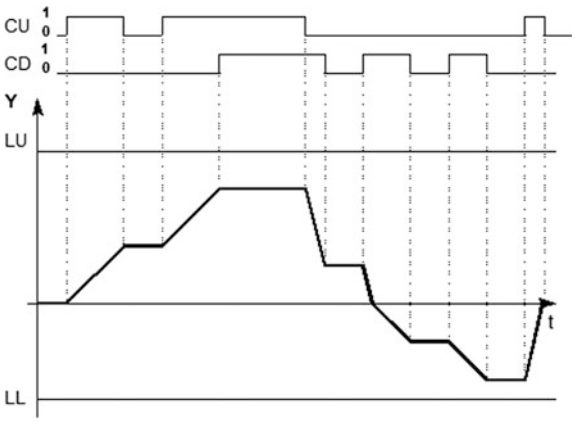

Fig. 5 Ramp generator principle

The ramp generator principle of operation is shown in Fig. 5. If the signal CU = 1, the output of ramp generator is raised; if CU = 0 and CD = 0, the output of the ramp generator does not change.

The ramp generator output is multiplied by the tension, and the signal is divided among the drives to compensate arose control deviation. In our control system, the output from the ramp generator is multiplied by a constant presenting 20% of the sum of all maximal possible tensions for the drives P22, P23 and P24. This constant corresponds to the maximum actuating controller intervention. It also depends on precise measurement of mechanical loses in the line equipment and correct estimation of the inertia of rotating parts. The value of 20% has been estimated empirically for the given line having certain parameters.

The entire controller structure is designed for a four-drive system, as shown in Fig. 2. One of the drives works as a lead one—the master drive (drive P21 in Fig. 2). It is a speed-controlled drive without torque limitation, i.e. the torque limiter is set to maximum. Its function is to keep strip elongation on a required value according to the preset speed value.

The signal from the tension controller presents an additional tension signal for the drives P22, P23 and P24. The block *Tension dividing* divides the actuating intervention of the controller among the adjacent drives.

Based on the production technology, partition of the tension among the drives can be done by operator/programmer himself in time of commissioning the line. Two conditions to be considered are to take in the consideration the power rating of the drives and to ensure that the tensions in the line satisfy the condition (3):

$$F_{21} > F_{22} > F_{23} > F_{24} \tag{3}$$

i.e. the master drive should develop the highest tension, and thus, it has the highest torque.

The experimental results from a real line are shown in Fig. 6. It can be observed that the initial transport speed of the strip $v = 5$ m/min was changed by the operator

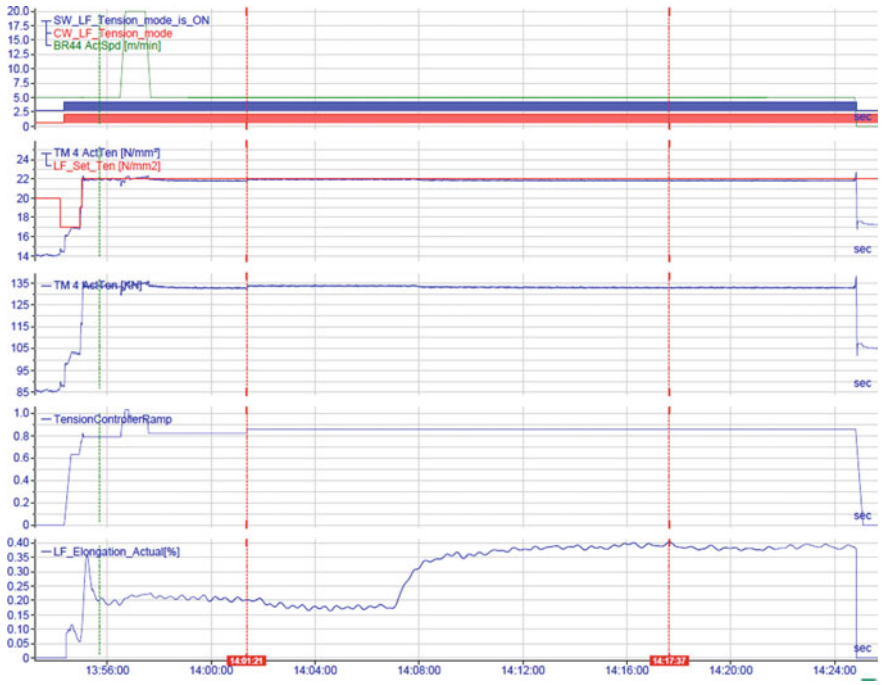

Fig. 6 Time responses of the variables in line with the ramp tension controller (for the labeling of the curves see Table 1).

to the value of $v = 20$ m/min within a short-time interval. In the time instant, when the tension mode was switched on, the output signal from the controller has increased (the trace *Tension Controller Ramp*). The reference value of the tension was set to the value of $\sigma = 22$ N/mm^2 by the superimposed control loop. During the tension mode, the tension in the line was kept on approximately constant value (the trace *TM4 ActTen*).

During the first measurement on the real line, the deviation from the set value was $\Delta\sigma = 0.24$ N/mm^2 and during the second measurement it was $\Delta\sigma = 0.18$ N/mm^2. Note that the relative elongation during a run at the constant speed is not constant. We suppose this is caused by changes of the material properties.

3.3 Stepper Tension Controller

In case a low tension in the strip is required, we have designed another solution. As an example for such a case, an annealing oven for the aluminium strips serves here. The length of the strip in the oven is 100 m. The mechanical arrangement of the

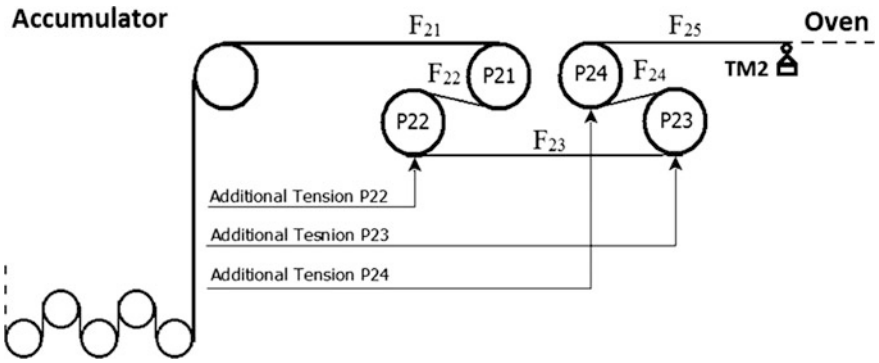

Fig. 7 Scheme of arrangement of drives in the oven section

Table 1 Labelling of the curves in Fig. 6

BR44_ActSpd (m/min)	Actual speed one of the drives in Levelflex
SW_LF_Tension_mode_is_on	Tension mode is on if value is log 1
CW_LF_Tension_mode_is_on	Tension mode is active if value is log 1
LF_Set_Ten (N/mm^2)	Set value of tension in Levelflex
TM4 ActTen (N/mm^2)	Actual value of tension in Levelflex
Tension Controller Ramp	Tension controller output
LF_Elongation_Actual (%)	Elongation actual value

drives in the input part of the oven is shown in Fig. 7. The tension in the strip coming out from the accumulator is high, and it is decreased by a tension section consisting of four drives working in the generator mode.

The value of the tension F_{25} in the oven is as follows:

$$F_{25} = F_{21} - T_{21} - T_{22} - T_{23} - T_{24} \tag{4}$$

where the variable T_{ij} presents a tension corresponding to the developed torque by the drive P_{ij}. It consists of two components: the calculated contribution of the torque (a portion of the total required torque for four drives) and signal corresponding to the additional tension from the tension controller. The variable F_{21} presents the strip tension in the output from the accumulator.

For such an arrangement of the section, *a stepper tension controller* was developed as shown in Fig. 8. Its operation is based on increasing or decreasing of the set tension value in steps: the controller works until the control deviation is lower than the preset range. If any difference between the set and actual number of impulses occurs, the controller increases or decreases its output. The output from the counter is multiplied by the tension, and then, it is divided among the drives which control the arisen control deviation.

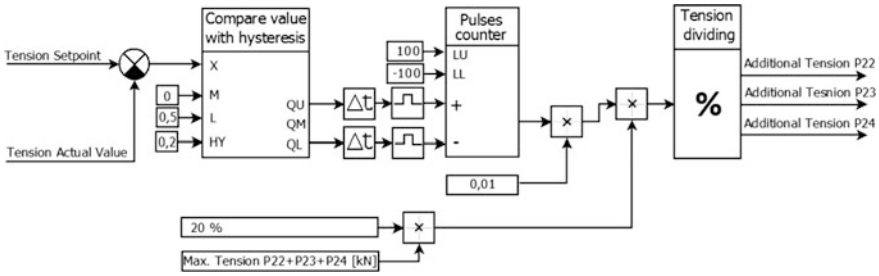

Fig. 8 Internal structure of the stepper tension controller (for the line sections with low level of the tension)

Fig. 9 Time courses of tensions in the strip in annealing oven with the stepper tension controller

The described low-tension controller was applied in the control system of the drives in the annealing oven, and the main variables were recorded in Fig. 9, where labeling of the curves is listed in Table 2. During measurement, the set value of tension in the strip was adjusted to the value 1 N/mm^2 and the tension was controlled with the maximum control deviation of ±0.1 N/mm^2.

It can be observed in Fig. 9 that the control deviation between reference tension *FU_Set_Ten* and the actual tension in the oven *TM2_ActTen* really does not exceed value of ±0.1 N/mm^2. The step value of the tension controller output is led into

Table 2 Labelling of the curves in Fig. 9

BR21_ActSpd[m/min]	Actual speed of the drive in front of furnace
TM 2_ActTen[N/mm^2]	Actual tension in furnace
TM 2_ActTen[kN]	Actual tension in furnace
FU_Set_Ten[N/mm^2]	Set value of tension in furnace
FU_Set_Ten[kN]	Set value of tension in furnace
FurnanceControllerCounter	Output from controller
BR24_SetTrq[Nm]	Set torque for drive BR24
BR23_SetTrq[Nm]	Set torque for drive BR23
BR22_SetTrq[Nm]	Set torque for drive BR22
BR21_SetTrq[Nm]	Set torque for drive BR21

control circuits of the drives changing the motor torques, and thus, the tension in the strip is also changed.

It is advantageous to use the described stepper controller in cases when operational intervention of the controller allows a slow change of the controlled variable or when the time of the system response is not known or when this time depends on various other parameters (temperature in the oven, the strip speed, strip cross section).

4 Conclusion

This paper deals with the design and description of two developed tension controllers for a continuous strip straightening section of the strip processing line. Two special tension controllers were developed based on practical experiences. The first one is a tension controller with ramp, which is advisable to use for the control of high tensions. The second controller is a stepper controller, which can be advantageously used for the control of low tensions in a very long section. The controllers were successfully applied during commissioning of a continuous levelling line for aluminium strips and they work reliable. They consist of basic programming blocks that are involved in the basic libraries of digital control systems.

Acknowledgements The research was supported by the project of the Slovak Grant Agency VEGA No 1/0464/15 titled “Research of New Principles and Methods for Design of Electrotechnical Systems”.

References

1. Dechuan, C., Hao, Z., Meifang, W.: An intelligent tension control system in strip unwinding process. In: IEEE International Conference on Control and Automation, ICCA’07, pp. 342–345 (2007)

2. Nevaranta, N., Niemelä, M., Pyrhönen, J., Pyrhönen, O., Lindh, T.: Indirect tension control method for an intermittent strip transport system. In: International Power Electronics and Motion Control Conference, ECCE-EPE-PEMC'12, Novi Sad, Serbia, pp. DS2a.2 1–6 (2012)
3. He, F., Wang, Q.: Compensation and fuzzy control of tension in strip winding control system. In: IEEE International Conference Industrial Electronics and Applications, IEEE-ICIEA'12, Singapore (2012)
4. Sakamoto, T., Izumihara, Y.: Decentralized control strategies for strip tension control system. In: IEEE International Symposium on Industrial Electronics, pp. 1086–1089 (1997)
5. Valenzuela, M., Bentley, J., Lorenz, R.: Sensorless tension control in paper machines. IEEE Trans. Ind. Appl. **39**, 294–304 (2002)
6. Lynch, A.F., Bortoff, S., Röbenack, K.: Nonlinear tension observers for strip machines. Automatica **40**, 1517–1524 (2004)
7. Perduková, D., Fedor, P., Timko, J.: The multi-motor drive model for teaching in the motion and process control engineering. Acta Electrotechnica et Informatica. Košice, Elfa, pp. 19–25 (2002)
8. Theis, E.: Levelling in detail. Everything you need to know about flatteners and levellers for coil processing, Parts 1–4. Available online: http://apdesign.co.za/levelling.html
9. Tension Leveler: Printmetal Technologies Japan, Lt. Available online: http://www.primetals.co.jp/products/pro3_4_1.html
10. Magura, D., Fedák, V., Kyslan, K.: Modeling and analysis of multi-motor drive properties in a strip processing continuous line. Modelling of Mechanical and Mechatronic Systems—MMaMS'14. The High Tatras, Elsevier, pp. 281–288 (2014)

Linear Synchronous Reluctance Motor—A Comprehensive Review

N.C. Lenin, P. Sanjeevikumar, Atif Iqbal and Charles Mbohwa

Abstract Linear synchronous reluctance motors (LSRELMs) are becoming an attractive alternative for linear induction motors (LIMs), linear synchronous motors (LSMs), and linear switched reluctance motors (LSRMs). This paper reviews the scientific status, development, and future scope of the LSRELMs. These include analysis techniques, design prospects, control aspects, optimization techniques, and parameter identifications.

Keywords Analysis · Design · Optimization · Control
Linear synchronous reluctance motor

1 Introduction

Over the past two decades, researchers have been inspired by linear synchronous reluctance motor drives. The key advantages of this motor are the following: absence of windings in the translator, easy of field weakening, possibility of

N.C. Lenin
School of Electrical Engineering, Vellore Institute of Technology (VIT), Chennai, India
e-mail: lenin.nc@vit.ac.in

P. Sanjeevikumar (✉) · C. Mbohwa
Department of Electrical and Electronics Engineering, University of Johannesburg, Auckland Park, Johannesburg, South Africa
e-mail: sanjeevikumarp@uj.ac.za

C. Mbohwa
e-mail: cmbohwa@uj.ac.za

A. Iqbal
Department of Electrical Engineering, Qatar University, Doha, Qatar
e-mail: atif.iqbal@qu.edu.qa

A. Konkani et al. (eds.), *Advances in Systems, Control and Automation*,
Lecture Notes in Electrical Engineering 442, https://doi.org/10.1007/978-981-10-4762-6_5

high-speed operation, and low cost (absence of permanent magnets). This work makes an attempt to afford a comprehensive review on both longitudinal flux and transverse flux LSRELMs.

2 Introduction to Linear Motors

Linear electric motors can drive a linear motion load without intermediate gears, screws, or crank shafts [1]. Different linear motor topologies are presented in Fig. 1. In practice, linear motion can be produced by four different ways. They are electrostatic, electromagnetic, piezoelectric, and magnetostrictive. The electromagnetic-type linear motors are again broadly classified into three groups: (i) DC motors (ii) induction motors, and (iii) synchronous motors. The main difference between them is the excitation approach. Figure 2 shows the classification of linear motors [2].

3 Introduction to Linear Synchronous Reluctance Motors

Although linear synchronous reluctance motors (LSRELMs) are not commonly spread in industrial applications, they are not utterly unfamiliar. The motor technology was dated back to 1975. Linear reluctance motor (LRM) having segmented secondary has been studied in [3–6]. A semi-analytical theory for segmental-rotor LRM having larger air gaps was developed and correlated with the experimental results in [7]. Expressions for a goodness factor, efficiency, and power factor are derived. LRM for urban transport vehicle application was designed and tested in [8]. Figure 3 shows the equivalent circuit of the LRM.

A test rig was constructed in which the solid-steel rotor segments speeds of up to 5 m/s. The normal force of a toothed LRM had been analyzed using the permeance

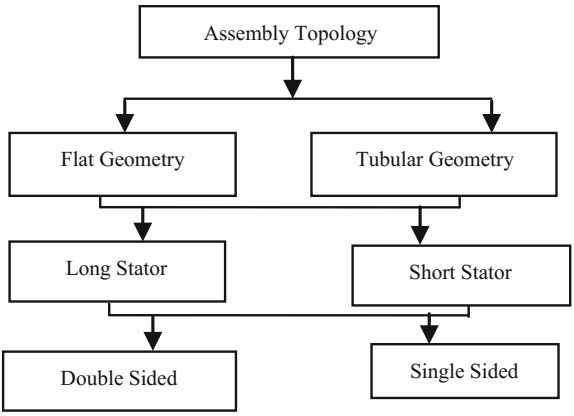

Fig. 1 Linear motor topologies

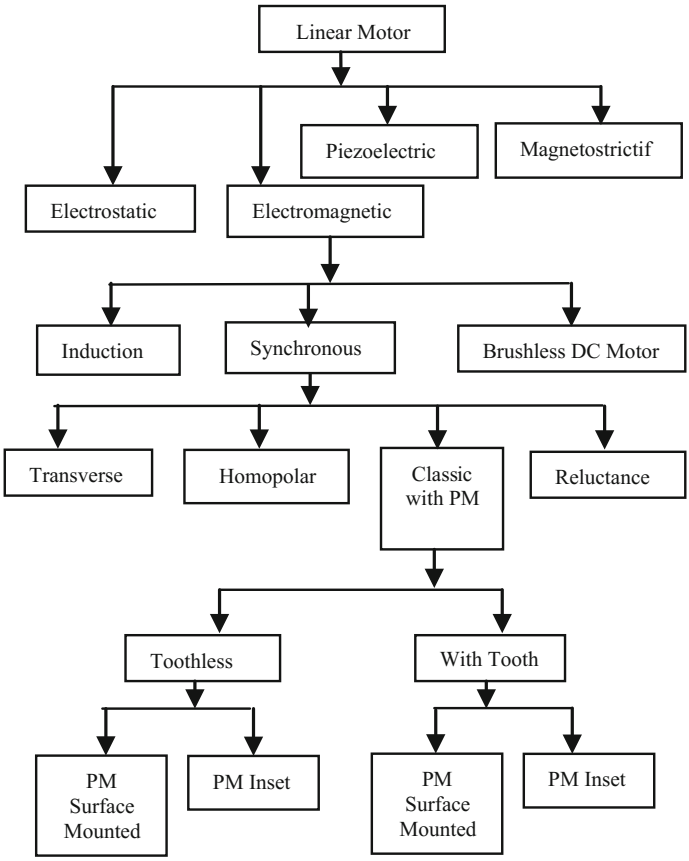

Fig. 2 Classification of linear motors. Note: *PM* permanent magnet

Fig. 3 Equivalent circuit for LRM

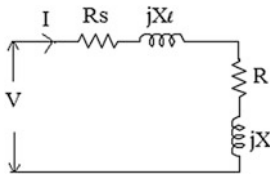

function approach [9]. Figure 4 shows the two-phase toothed LRM. The advantage of the toothed linear motor is that, no mechanical linkage is positioned between the motor and the device. LRM with short secondary has been described in [10, 11]. Figure 5a, b shows the tractive and normal forces for the studied LRM, respectively (Fig. 6)..

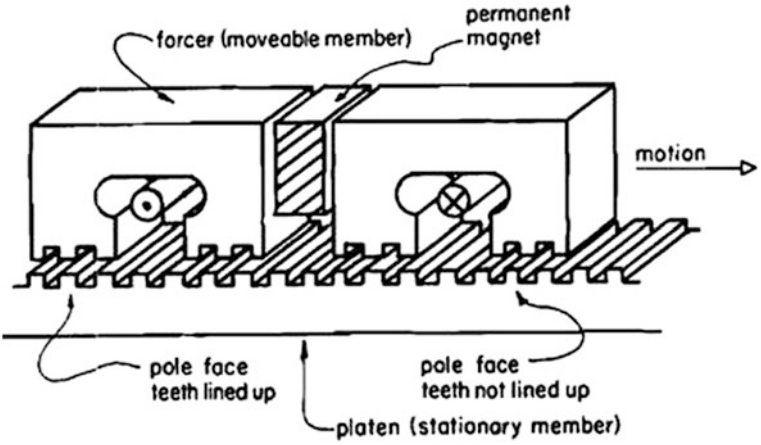

Fig. 4 Two-phase toothed LRM

Fig. 5 **a** Tractive force. **b** Normal force

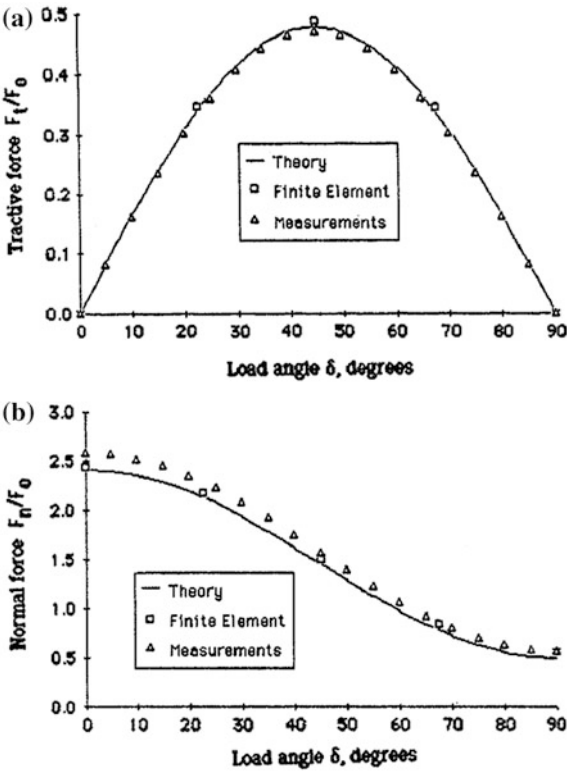

4 Modeling and Analysis of LSRELM

4.1 Nonlinear Two-Axis Analysis [12]

A two-axis dynamic model in *d-q* reference frame was developed to analyze the various parameters of LSRELM. The voltage balances in both the axes are described by (1)

$$\begin{bmatrix} V_d \\ V_q \end{bmatrix} = R\begin{bmatrix} i_d \\ i_q \end{bmatrix} + \frac{\mathrm{d}}{\mathrm{d}t}\begin{bmatrix} \Psi_d \\ \Psi_q \end{bmatrix} + \frac{\pi}{\tau_p}\frac{\mathrm{d}x}{\mathrm{d}t}\begin{bmatrix} -\Psi_q \\ \Psi_d \end{bmatrix} \tag{1}$$

The motor thrust force, F_e, is given by (2)

$$F_e = \frac{\pi}{\tau_p}\left(\Psi_d i_q - \Psi_q i_d\right) \tag{2}$$

where V, I, Ψ, and τ_p represent voltage, current, flux linkage, and pole pitch, respectively. The subscripts d and q stand for direct and quadrature axis components. The trajectories of the thrust force, friction force, and flux linkages are shown in Fig. 7.

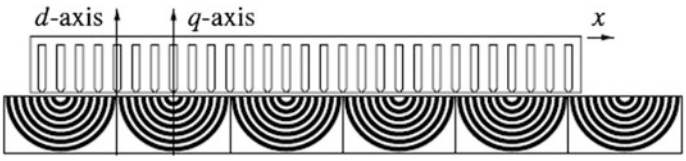

Fig. 6 Schematic of LSRELM

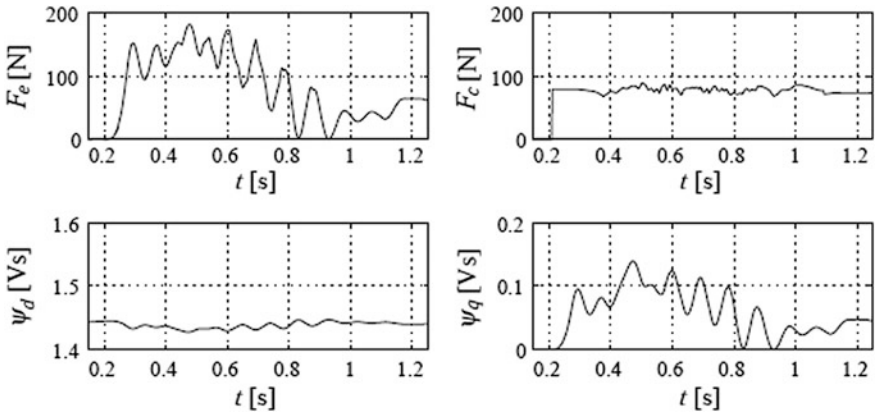

Fig. 7 Motor thrust, Coulomb friction, and flux linkages

4.2 Analysis of cross-magnetization effect using finite element method [13]

The effects of cross-magnetization and saturation on the inductances under load conditions are described using a modified two-axis dynamic model. The magnetic conditions in the motor were computed by two-dimensional (2-D) FEM using (3).

$$\mathrm{rot}(\gamma \mathrm{rot}(A)) = J \tag{3}$$

where

γ reluctivity
A magnetic vector potential
J current density

Figure 8 shows the magnetic field distribution of LSRELM using FEM. In the presented results, the direct axis is collinear with the magnetic axis of the phase winding.

4.3 Analysis of Cross-Saturation Effects [14–16]

A magnetically nonlinear two-axis dynamic model was developed to identify the cross-saturation effect and their characteristics. Experimental setup used for determining current-dependent characteristics of flux linkages is schematically shown in Fig. 9. The measured and the calculated q-axis currents and voltages are depicted in Figs. 13 and 14.

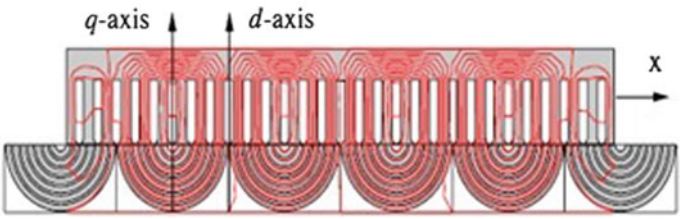

Fig. 8 Magnetic field distribution using FEM

5 Design Prospects of LSRELM

5.1 Basic design [17]

A three-phase, four-pole, two-layer LSRELM has been designed and optimized using FEA. The secondary parameters such as teeth width and teeth height are designed initially as 32.27 and 25.12 mm, respectively. Figure 10 shows the flowchart for thrust analysis using finite element analysis.

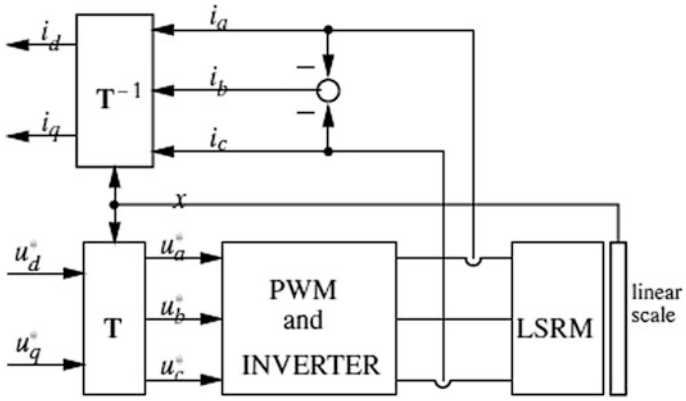

Fig. 9 Experimental setup

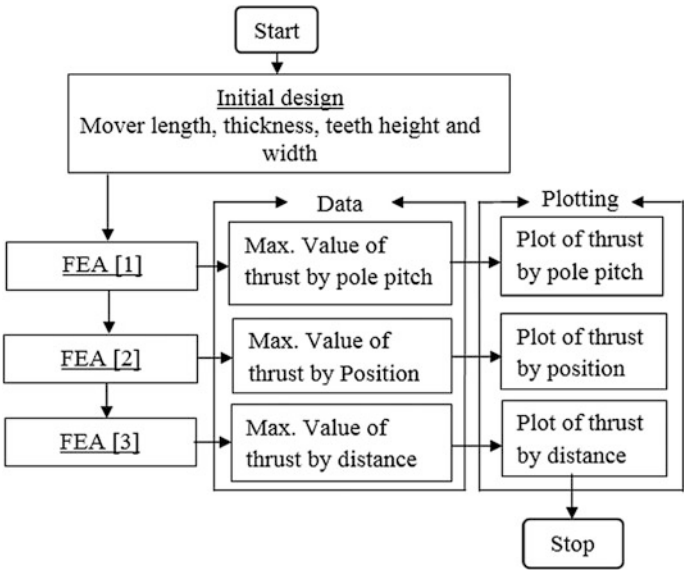

Fig. 10 Flowchart of design process

5.2 *LSRELM with Multi-flux Barrier [18, 19]*

A reluctance equalization structure was designed in such a way that the reluctances of all iron layers were equal with respect to the conventional equal-width structure.

5.2.1 Slotless Stator

The primary side is regarded as slotless, and the excitation current is treated as a distributed current on the stator surface. It is evident from Fig. 11 that, forming a reluctance equalization structure increases the thrust and is more effective under operating conditions at which the iron layer will cause magnetic saturation.

5.2.2 Stator with Slots

Figure 12 shows the stator designed with slots. Three slot shapes are studied: (i) open slots (ii) semi-closed slots, and (iii) fully closed slots. On the other hand, two different mover slot shapes are considered: (i) angular and (ii) circular shapes. Both the mover structures are shown in Fig. 13.

5.2.3 Double-Sided LSRELM [20–22]

The schematic model of LSRELM with double-sided stator is shown in Fig. 14. In this configuration, the thrust ripple ratio is 92% and the attractive force ripple ratio is 21.5%.

To avoid these ripples, the mover was divided into a few segments as shown in Fig. 15. The thrust ripple ratio of Type-B is 26.1% and Type-C is 19.0%. The attractive force ripple ratio of Type-B is 5.8% and Type-C is 2.3%. These are improved of the Type-A. The thrust of the Type-B is only decreased by 0.3%. As the thrust of the Type-C is decreased by 17.1% from the Type-A, the Type-C mover is unfavorable for carrier systems.

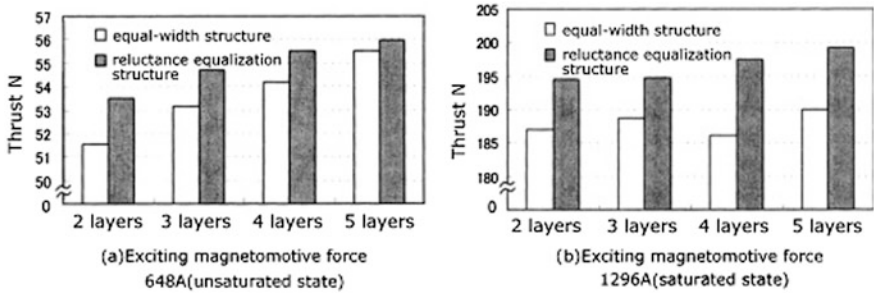

Fig. 11 Comparison of maximum thrust

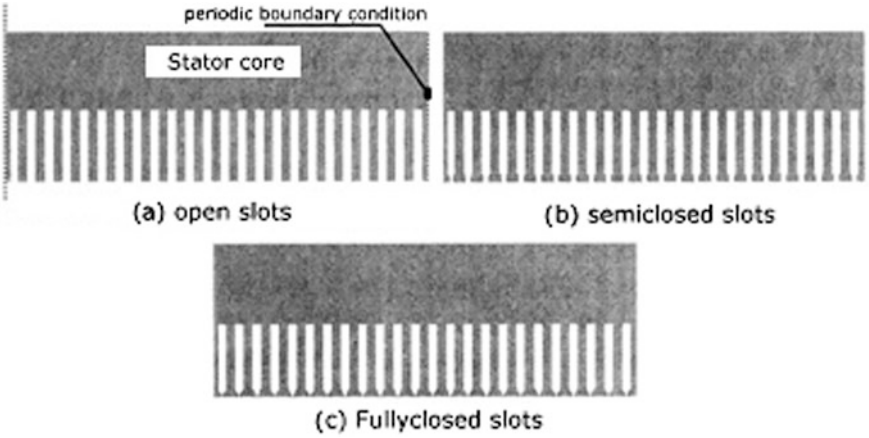

Fig. 12 Analytical models of stator

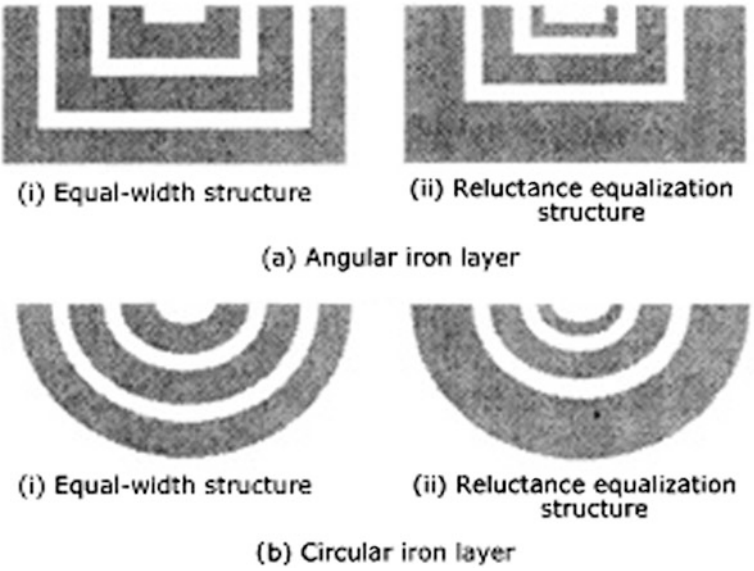

Fig. 13 Analytical models of mover

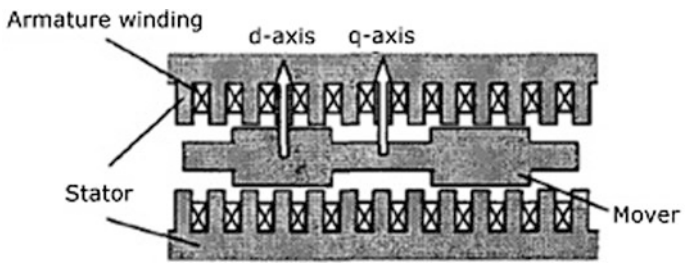

Fig. 14 LSRELM with double-sided stator

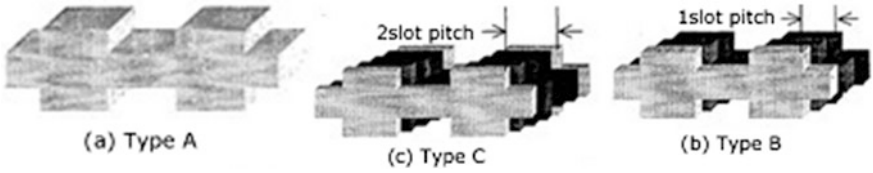

Fig. 15 Mover structures

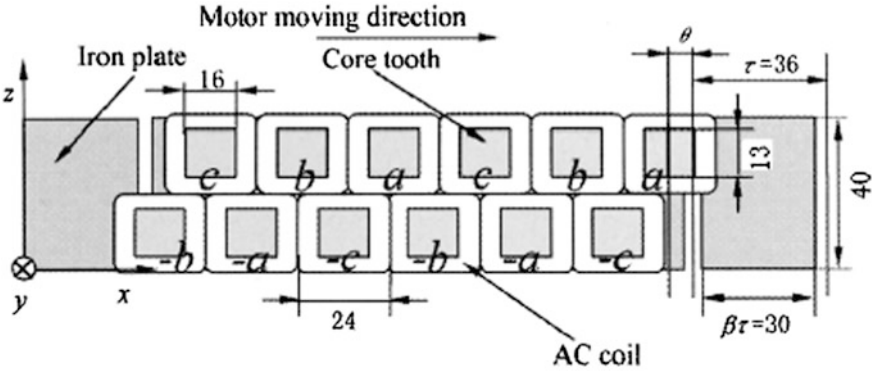

Fig. 16 Double-sided LRM with novel structure

5.2.4 Permanent Magnet Double-Sided LRM [23–27]

Three-dimensional (3-D) analyses on a double-sided LRM with and without permanent magnets, by applying three-dimensional boundary integral equation to a short-primary motor (without magnet), are shown in Fig. 16. Six kinds of different secondary geometries (refer Fig. 17) are calculated, and their characteristics are discussed.

In addition, analyses are made on both single-sided and coreless permanent magnet linear reluctance motor (PMLRM). The load angle characteristics for secondary iron plates of different configurations are analyzed.

5.2.5 Four-Pole Double-Sided PMLRM

A four-pole double-sided test PMLRM is shown in Fig. 18. This test machine employs rare-earth magnets with a thickness of 7 mm, a pitch of 24 mm, and a width of 20 mm, and the is air-cored to avoid magnetic attraction. The load angle characteristics of the test PMLRM at effective primary current values of 2 and 3 A are explained.

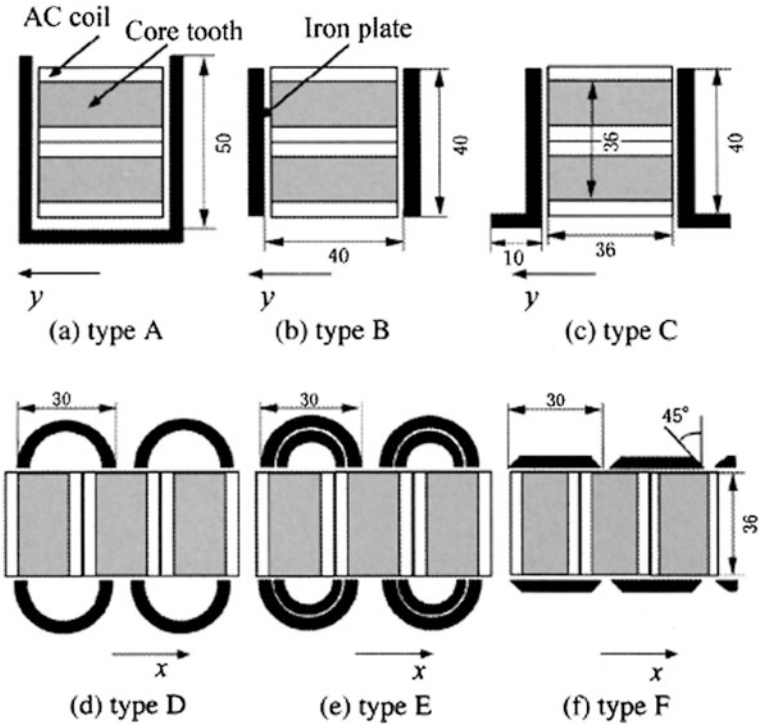

Fig. 17 Geometries of secondary iron plates

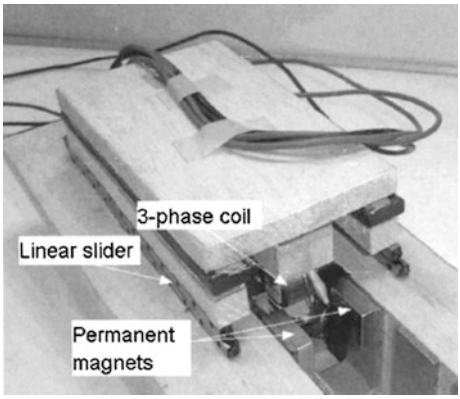

Fig. 18 Four-pole double-sided PMLRM

5.2.6 Design of Optimal Secondary Segment Shapes Using Stochastic Searching [28]

For the optimal design of secondary segment, stochastic search method was used to change the shape of the secondary segments. In the initial shape of the segments, two lamellas per primary slot pitch are considered (Fig. 19), which causes force oscillations. The optimized shape obtained using FEM is depicted in Fig. 20. The force oscillations occurring during the shift of the primary for one pole pitch were analyzed.

5.2.7 LSRELM for Electromagnetic Aircraft Launch System [29, 30]

LSRELM with the maximum-output thrust force and optimum power factor was designed for electromagnetic aircraft launch system. In this model, a long primary and a short secondary with a solid or laminated are evaluated. Figure 21 shows the cross-sectional view of the designed motor.

The pole pitch was 150 mm for a 20-pole machine. Two type of winding arrangement for stators in a blade system were considered; one N–N and another N–S. The key results are shown in Figs. 22, 23, and 24, respectively. With the Patterson model, the linear machine output force is not achievable. To overcome this problem, a new machine configuration was proposed with modified secondary shown in Fig. 25. Results such as thrust force, flux density variation, and harmonic spectrum are shown in Figs. 26, 27, and 28, respectively, for model MM.

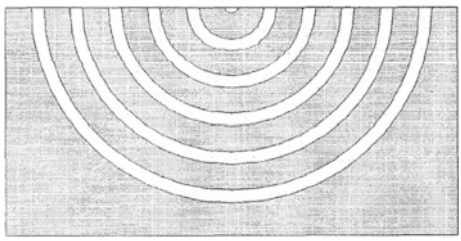

Fig. 19 Initial shape

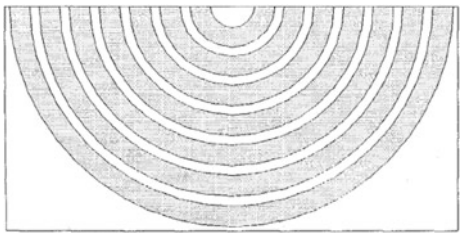

Fig. 20 Final shape

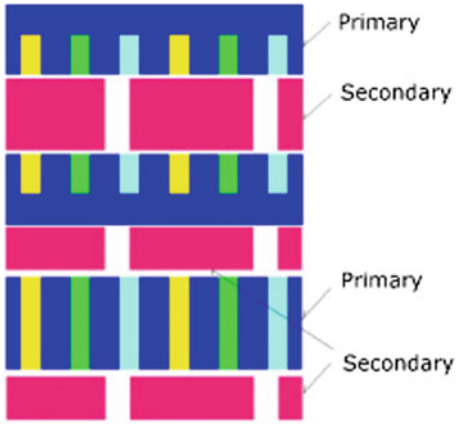

Fig. 21 Designed linear motor—model M

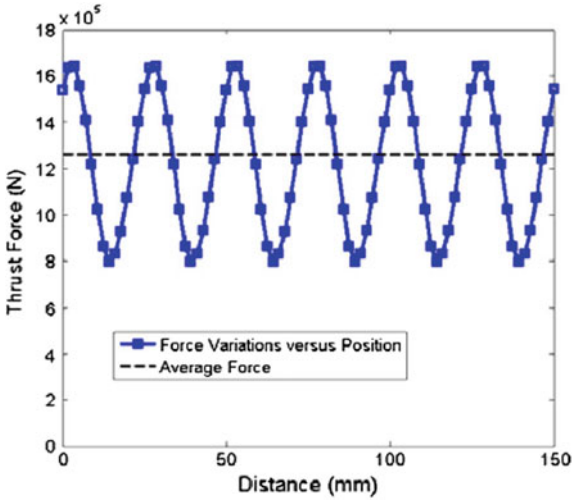

Fig. 22 Force variation

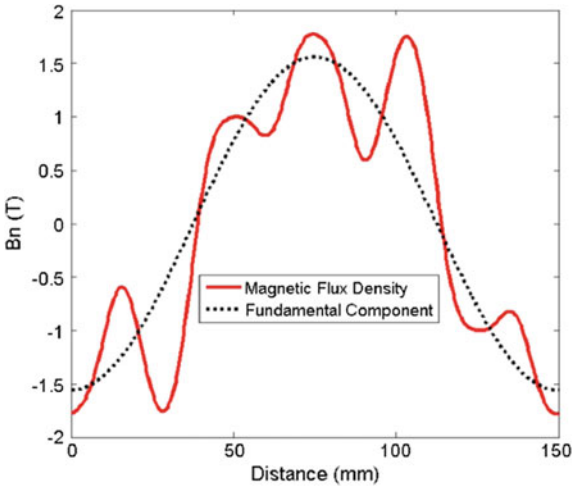

Fig. 23 Magnetic flux density variations

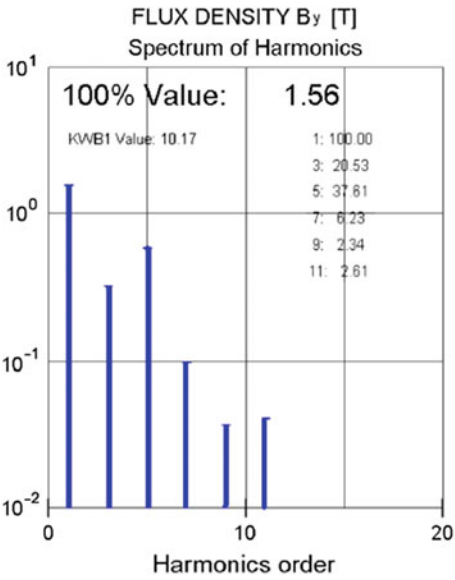

Fig. 24 Harmonic spectrum

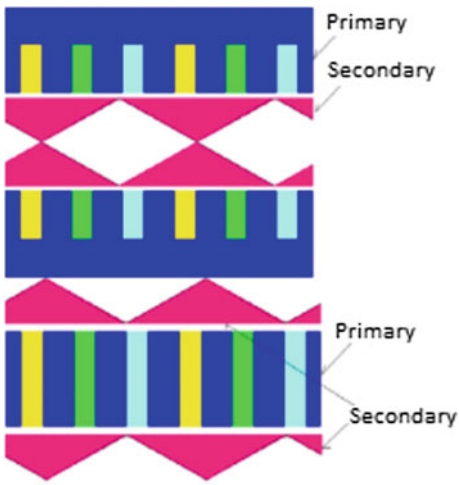

Fig. 25 Modified secondary —model MM

5.2.8 Vertical-Type Double-Sided HTS LRM [31]

A high-temperature superconducting (HTS) bulk double-sided vertical-type LRM was designed for elevator application, shown in Fig. 29. The *x*-axis and *z*-axis denoted the direction of propulsion and guidance. The cage frame is made of

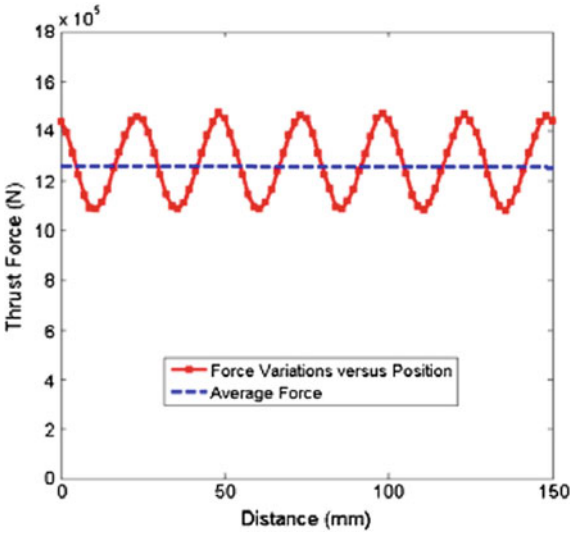

Fig. 26 Force variation

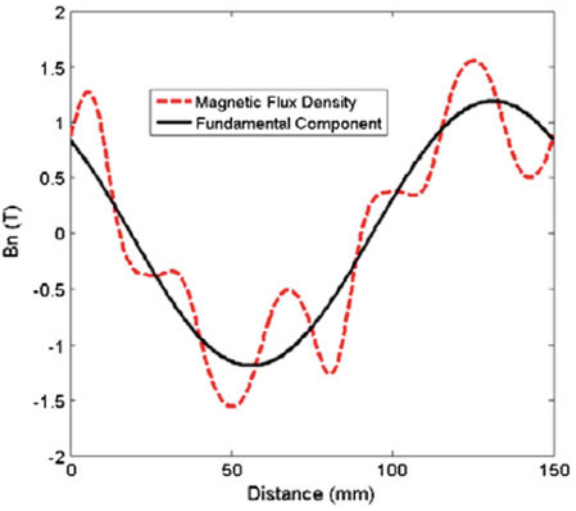

Fig. 27 Magnetic flux density variations

aluminum. The cage has two pieces of HTS bulk on a side of the armature. The shape of the bulk is a rectangular parallelepiped. Figure 30 shows width dependence of thrust and guidance forces on each length of the parameter. The larger the thrust force increases, the thinner the thickness of the bulk. Figure 31 shows the relation between HTS bulk volume and thrust force/HTS bulk volume (F_x/V_{HTS}).

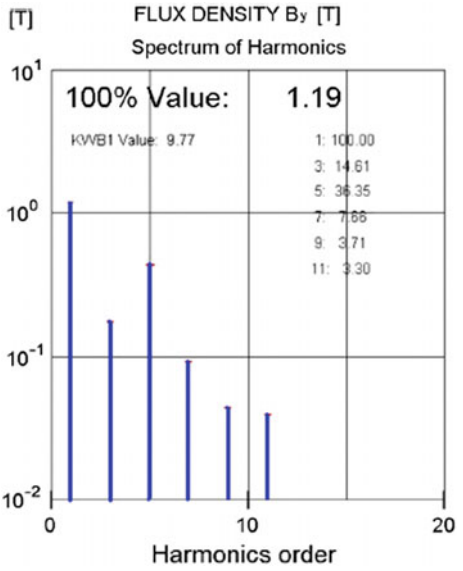

Fig. 28 Harmonic spectrum

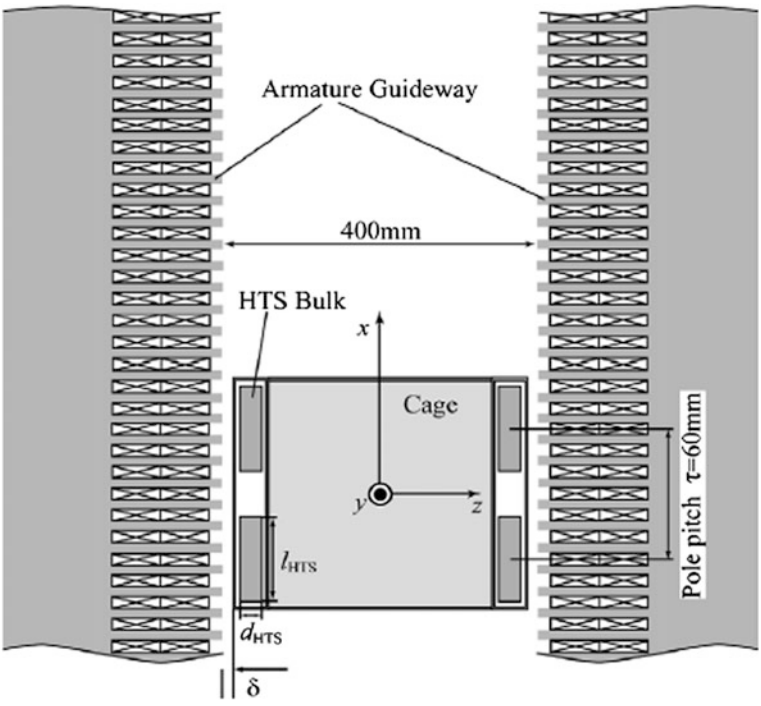

Fig. 29 HTS bulk LRM model

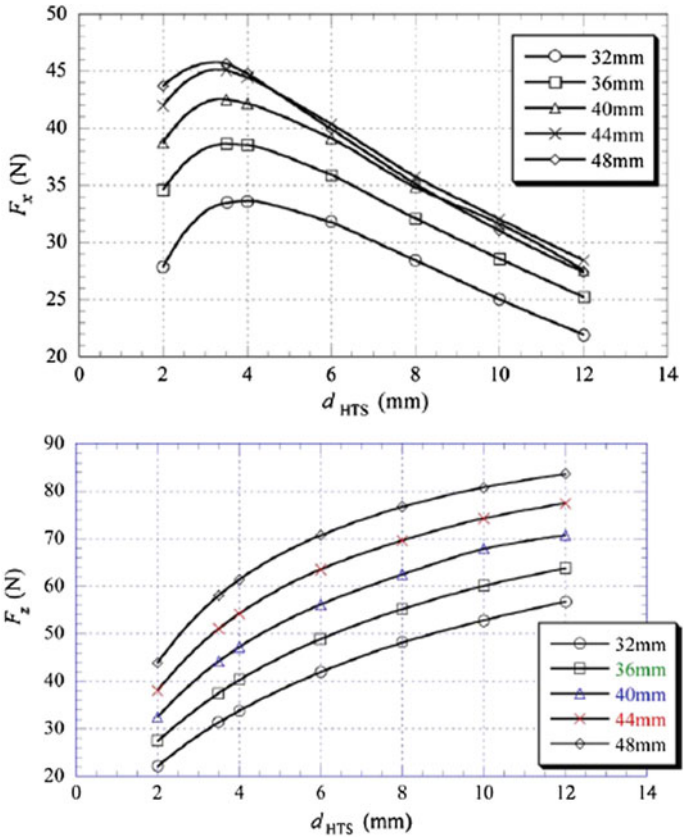

Fig. 30 Thrust and guidance force

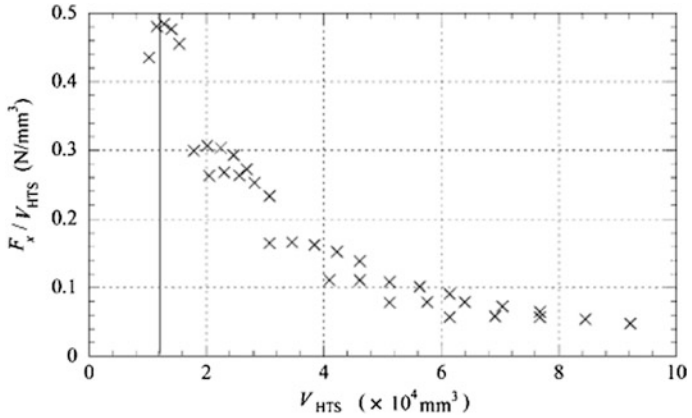

Fig. 31 Relation of HTS bulk volume

6 Control Aspects of LSRELM

6.1 Parameters Identification in LSRELM [32, 33]

The experimental methods used for determining the aforementioned characteristics are based on the closed-loop current control of the LSRELM supplied by a voltage source inverter. The responded currents and the reference voltages, measured during the experiment, are shown in Fig. 32.

Figure 33 shows the calculated flux linkages, and their partial derivatives. The trajectories of calculated thrust, Coulomb friction force, and flux linkages are calculated based on the control algorithms.

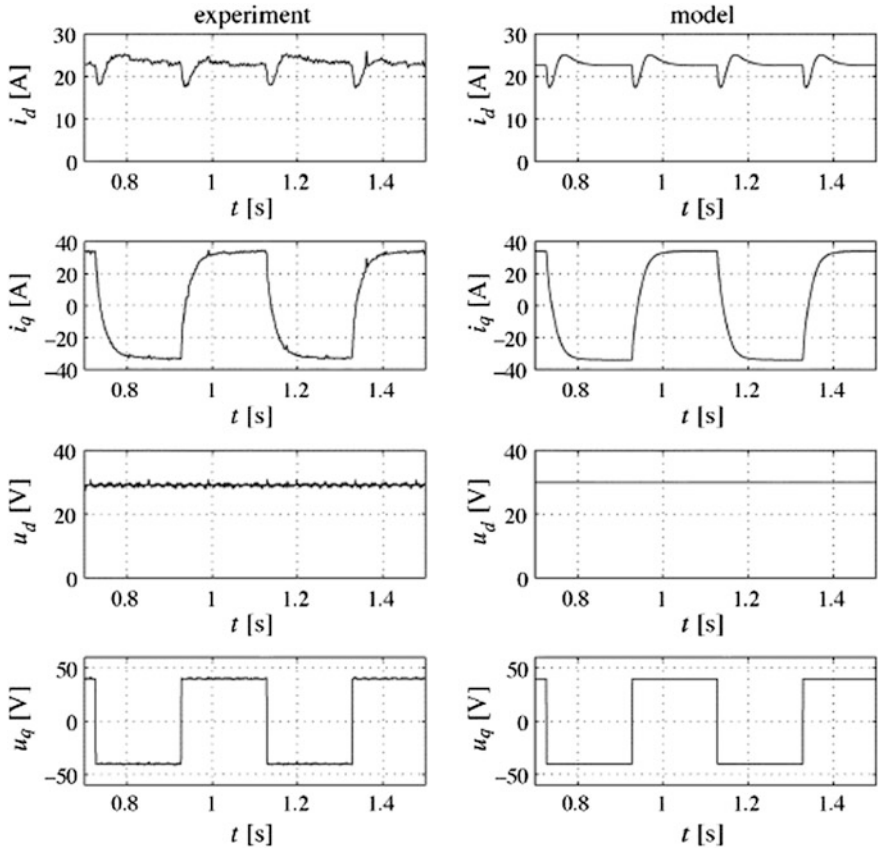

Fig. 32 Responded currents and reference voltages

6.2 High-Performance Position Tracking [34–39]

Input–output linearizing control combined with the tracking controllers provides good tracking performances and high disturbance rejection of a servo drive. The translation range of the tested LSRELM is limited; therefore, the position, speed, and acceleration trajectories are calculated from the kinematic model. The block diagram of the input–output linearized system and its equivalent circuit is shown in Fig. 34. Here, '*M*' denotes the motor model. The system in Fig. 34 is linearized, decoupled, and unstable. The simulated and experimental results are shown in Figs. 35 and 36, respectively.

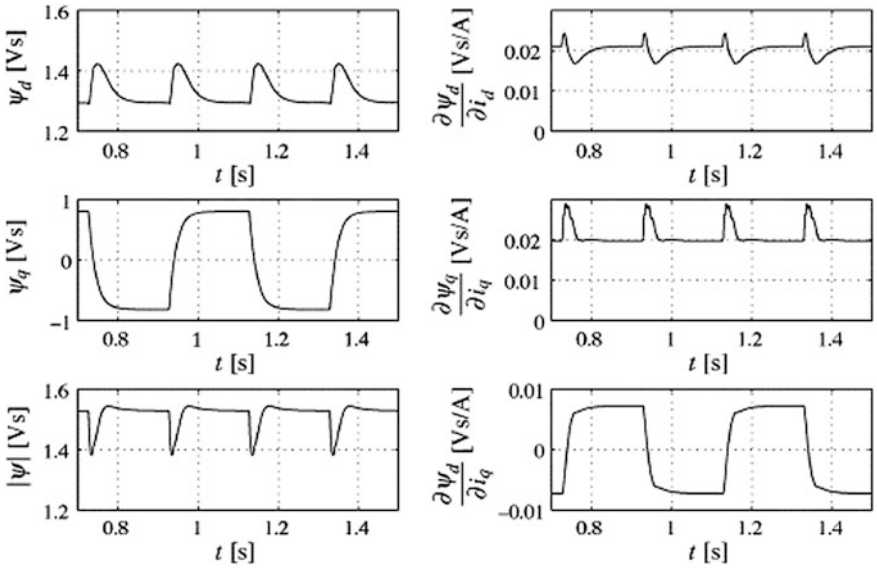

Fig. 33 Flux linkages and partial derivatives

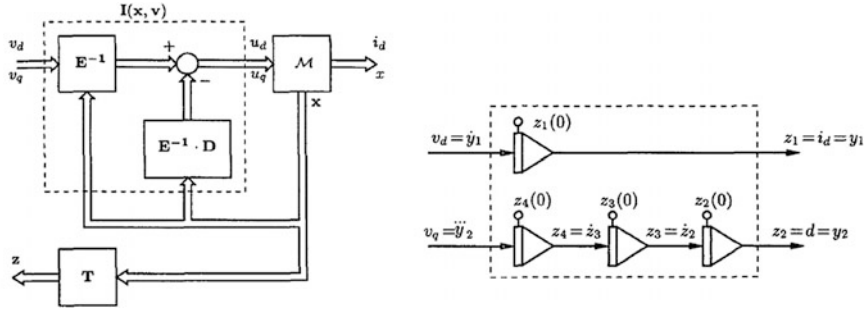

Fig. 34 Input–output linearized system and its equivalent representation

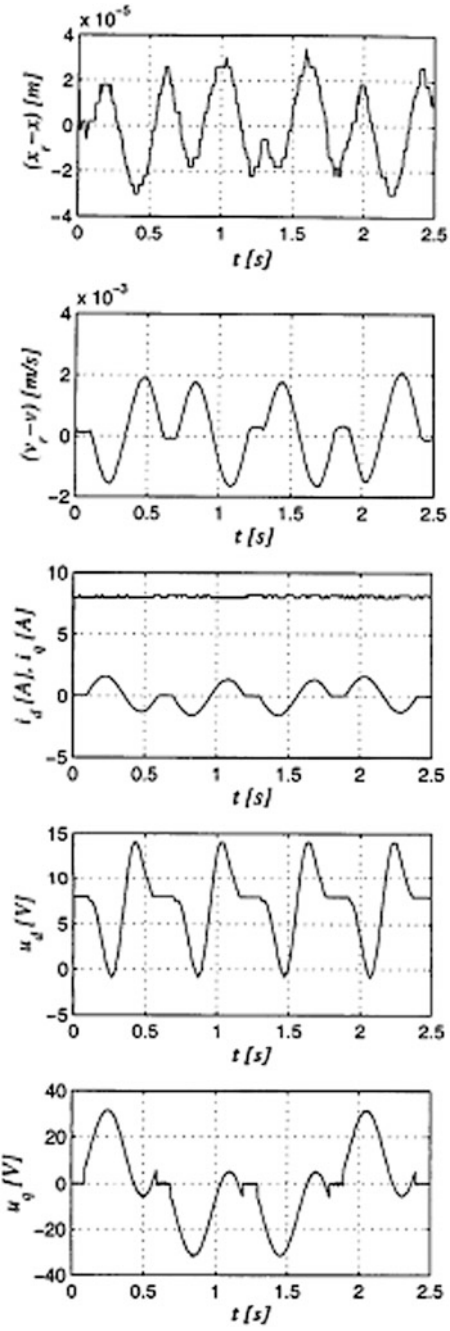

Fig. 35 Simulated result

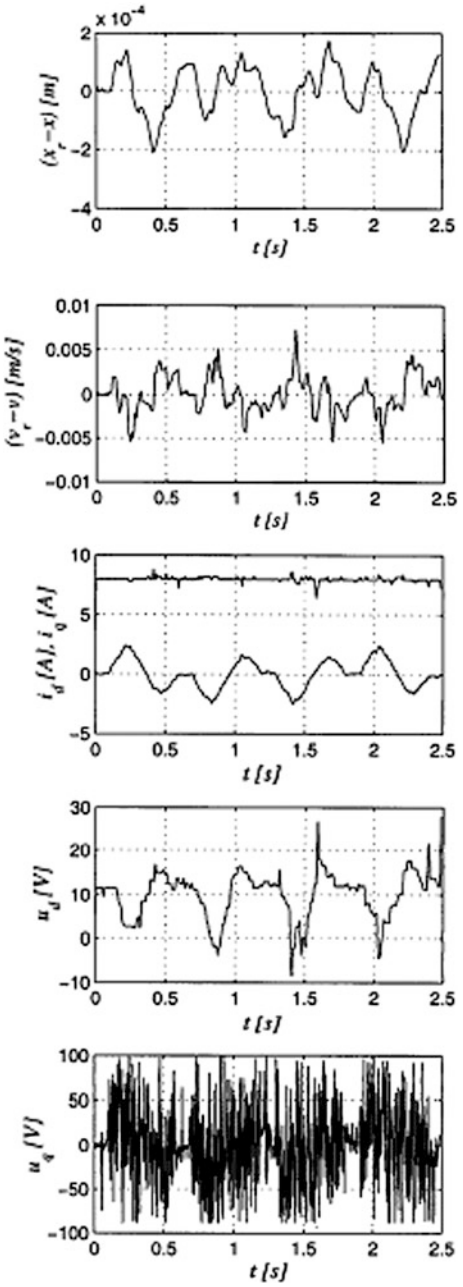

Fig. 36 Experimental result

6.3 Transverse Flux LSRELM [40–46]

A static test machine, which has a transverse flux coil arrangement and a thin ferromagnetic reaction plate, has been manufactured and shown in Fig. 37. Two types of rail systems are designed and implemented: (i) Segment-type reaction rail and (ii) reluctance-type reaction rail.

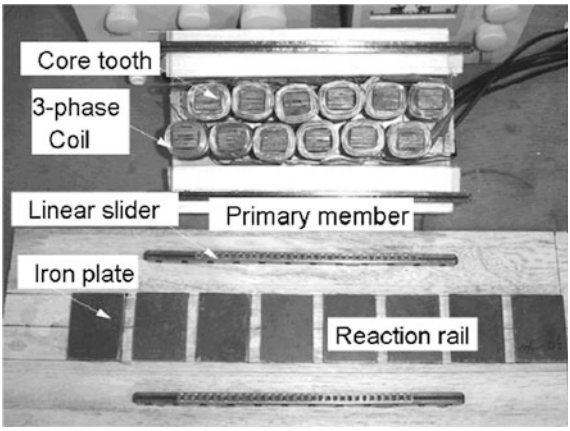

Fig. 37 Four-pole static test machine

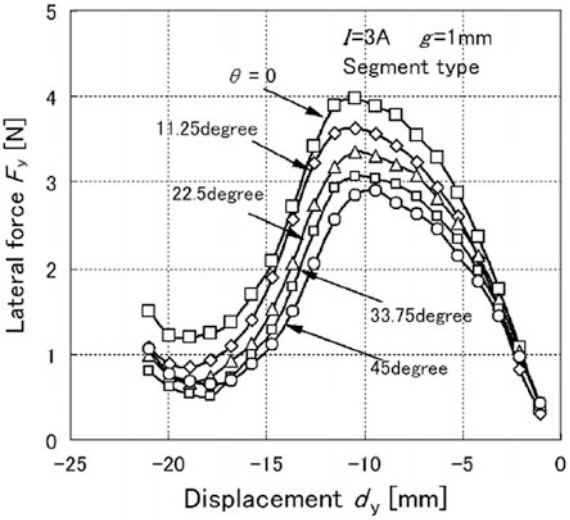

Fig. 38 Lateral force versus displacement

6.4 Lateral Force in Segment-Type Reaction Rail

In this type of motor (refer Fig. 37 for reaction rail), the lateral force works to pull back a primary member to the center of a reaction rail if a vehicle displaces in a transverse direction. Figure 38 indicates the change of the lateral force for different displacements as a parameter of load angle. When the load angle varies, the lateral force decreases by 27, 36, and 26% for the air gap length of 1, 1.5, and 2 mm, respectively.

7 Application and Future Scope

The applications of LSRELMs have been increased exponentially for the past one decade. Some of the noted applications of LSRELMs are as follows:

1. High-speed trains
2. Elevators
3. High precision industrial servo drives
4. Electromagnetic aircraft launch system
5. Machining applications
6. Material handling systems, etc.

Although LSRELMs have many advantages, such as direct drive, more freedom for structure design, and easy recycling, it suffers from poor power factor. Design of magnetic structures with increased direct axis inductance, make use of advance control aspects, and optimal converter configuration are few possible solutions to increase the power factor as well as performance of the machine, which the authors consider as the future scope of this linear drive system.

8 Conclusions

This paper comprehensively reviewed the modeling, analysis, design concepts, control aspects, optimization techniques, different classifications, and recent trends in linear synchronous reluctance motors. Experimental and simulation results taken from an assortment of publications of eminent authors are illustrated throughout the paper. First, the paper concentrates on the analyses and modeling techniques. Secondly, design techniques for single-sided and double-sided machines with optimization process have been reviewed. Control aspects are explored in the next section. Finally, transverse flux machines with different types of rail systems were discussed.

References

1. Jacek Gieras, F., Zbigniew Piech, J., Bronislaw, T.: Linear Synchronous Motors: Transportation and Automation Systems. CRC Press (2011)
2. Boldea, I., Nasar, S.A.: Linear Electric Actuators and Generators. Cambridge University Press (1997)
3. Boldea, I., Nasar, S.A.: Thrust and normal forces in a segmented secondary linear reluctance motor. Proc. IEE **122**(9), 922–924 (1975)
4. Zavgorodny, V.D., Arthur Wagner, J., Nasar, S.A.: Segmented secondary linear reluctance motor: analytical and experimental results. Int. J. Electr. Mach. Power Syst. **1**(2), 163–174 (1977)
5. Arthur Wagner, J., Zavgorodny, V.D., Nasar, S.A.: Segmented secondary linear reluctance motor: a parametric study. Int. J. Electr. Mach. Power Syst. **2**(1), 1–24 (1977)
6. Arthur Wagner, J., Zavgorodny, V.D., Nasar, S.A.: Tangential force distribution and force pulsation in a linear reluctance motor. Int. J. Electr. Mach. Power Syst. **2**(4), 341–355 (1978)
7. Edwards, J.D., El-Antably, A.M.: Segmental rotor linear reluctance motors with large airgaps. Proc. IEE **125**(3), 209–214 (1978)
8. El-Antably, A.M., Edwards, J.D., Williams, G., Lindon, P., Luke, P.D.: Steady state performance characteristics of linear reluctance motor. IEEE Trans. Magn. **15**(6), 1440–1442 (1979)
9. Arthur, Wagner J., Cornwall, W.J.: A study of normal force in a toothed linear reluctance motor. Int. J. Electr. Mach. Power Syst. **7**(2), 143–153 (1982)
10. Edwards, J.D., Williams, G., Preston, M.A.: Forces in short secondary linear reluctance motor. IEEE Trans. Magn. **23**(5), 2829–2831 (1987)
11. Edwards, J.D., Preston, M.A.: Forces in screened-secondary linear reluctance motor. IEEE Trans. Magn. **24**(6), 2913–2915 (1988)
12. Stumberger, G., Stumberger, B., Dolinar, D.: Position and current dependent flux linkages, thrust and friction force of linear synchronous reluctance motor. In: Proceedings of 36th IAS Annual Meeting Industry Applications Conference, vol. 4, Chicago, IL, USA, pp. 2310–2317 (2011)
13. Stumberger, G., Stumberger, B., Dolinar, D., Hamler, A.: Cross magnetization effect on inductances of linear synchronous reluctance motor under load conditions. IEEE Trans. Magn. **37**(5) (2001)
14. Stumberger, G., Stumberger, B., Dolinar, D.: Analysis of cross–saturation effects in a linear synchronous reluctance motor performed by finite elements method and measurements. In: Proceedings of EPE-PEMC, Portoroz, Slovenia, pp. 1907–1912 (2006)
15. Stumberger, G., Stumberger, B., Dolinar, D.: Two–axis dynamic model of linear synchronous reluctance motor with magnetically nonlinear and anisotropic iron core. In: Proceedings of EUROCON'03, Ljubljana (Slovenia), pp. 225–229 (2003)
16. Damiano, A., Marongiu, I., Delpizzo, A., Perfetto, A.: Modeling improvement of a high anisotropy linear reluctance motor. In: Proceedings of Ist International Symposium on Linear Drives for Industry Applications, Ioujima-Nagasaki (Japan), pp. 179–182 (1995)
17. Jang, S.M., Park, J.H., Kwon, J.K., Choi, J.Y., Cho, H.W., Jang, W.B.: Design and experimental verification of linear synchronous reluctance motor. In: Proceedings of INTERMAG Asia Magnetics Conference, Nagoya (Japan), pp. 1427–1428 (2005)
18. Sanada, M., Mori, H., Morimoto, S., Takeda, Y.: Improvement of characteristics of linear SynRM with reluctance equalization. IEE Trans. **6**, 804–805 (1998)
19. Sanada, M., Asano, M., Morimoto, S., Takeda, Y.: Mover design and performance analysis of linear synchronous reluctance motor. J. Electr. Eng. (Japan) **138**(4), 61–69 (2002)
20. Sai, S., Sanada, M., Morimoto, S., Takeda, Y.: Fundamental investigation of LSynRM with magnetic suspension using armature winding for propulsion. In: Proceedings of National Convention Record, IEE (Japan), pp. 5–84 (2001)

21. Sai, S., Sanada, M., Morimoto, S., Takeda, Y.: Fundamental investigation of LSynRM with magnetic suspension using armature winding for propulsion. In: Proceedings of Power Conversion Conference, PCC-Osaka, vol. 1, pp. 48–53 (2002)
22. Sanada, M., Morimoto, S., Takeda, Y.: Speed control method of LSynRM with magnetic suspension using armature winding for propulsation. In: Proceedings of 4th International Symposium on Linear Drives for Industrial Applications, Birmingham (UK), pp. 109–112 (2003)
23. Ogawa, K.: 3-D numerical analysis of a short primary linear reluctance motor. In: Proceedings of 16th International Conference on Electrical Machines (2004)
24. Ogawa, K.: Static thrust of a short primary linear reluctance motor with simple secondary structure. In: Proceedings of 18th International Conference on Magnetically Levitated Systems and Linear Drives, Shanghai (China), pp. 905–910 (2004)
25. Ogawa, K., Higuchi, T.: D numerical analysis and test result of a short primary linear reluctance motor. J. Electr. Eng. (Japan) **125-D**(8), 786–792 (2005)
26. Ogawa, K., Higuchi, T.: 3D numerical analysis and test results of a short-primary linear reluctance motor. J. Electr. Eng. (Japan) **161**(1), 58–65 (2007)
27. Ueno, Y., Tahara, S., Ogawa, K.: 3D numerical analysis and test results of a short-primary linear reluctance motor. In: Proceedings of International Conference on Electrical Machines and Systems (2007)
28. Hamler, A., Trlep, M., Hribernik, B.: Optimal secondary segment shapes of linear reluctance motors using stochastic searching. IEEE Trans. Magn. **34**(5), 3519–3521 (1998)
29. Mirzaei, M., Abdollahi, S.E., Vahedi, A.: Design optimization of reluctance synchronous linear machines for electromagnetic aircraft launch system. In: Proceedings of 14th Symposium on Electromagnetic Launch Technology, Victoria, BC, pp. 1–6 (2008)
30. Mirzaei, M., Abdollahi, S.E.: Design optimization of reluctance synchronous linear machines for electromagnetic aircraft launch system. IEEE Trans. Magn. **45**(1), 389–395 (2009)
31. Yoshida, K., Matsumoto, H., Eguchi, M.: Optimal design of thrust force in vertical-type HTS bulk LRM. J. Physica C 839–847 (2005)
32. Stumberger, G., Stumberger, B., Dolinar, D.: Identification of linear synchronous reluctance motor parameters. In: Proceedings of Conference Record of Industry Applications Conference, vol. 1, Rome, pp. 7–14 (2000)
33. Stumberger, G., Stumberger, B., Dolinar, D.: Identification of linear synchronous reluctance motor parameters. IEEE Trans. Ind. Appl. **40**(5), 1317–1324 (2004)
34. Dolinar, D., Stumberger, G., Grcar, B.: Input-output linearizing control of linear synchronous reluctance motor. In: Proceedings of PES, Marbella (Spain) (2000)
35. Dolinar, D., Stumberger, G., Hameyer, K., Grcar, B., Zagradisnik, I.: Exact tracking of linear synchronous reluctance servo drive. In: Proceedings of International Conference on Electrical Machines, vol. 1, pp. 227–234 (2000)
36. Dolinar, D., Stumberger, G.: High performance tracking of linear synchronous reluctance servo drive. In: Proceedings of 7th International Workshop on Advanced Motion Control, Slovenia, pp. 182–187 (2002)
37. Dolinar, D., Stumberger, G., Milanovic, M.: Position tracking control of saturated LSRM. ISA Trans. Instrum. Syst. Autom. Soc. **43**, 527–538 (2004)
38. Dolinar, D., Stumberger, G., Milanovic, M.: Tracking improvement of LSRM at low-speed operation. Eur. Trans. Electr. Power **15**, 257–270 (2005)
39. Dolinar, D., Stumberger, G.: Low speed tracking control improvement of linear synchronous reluctance machines. In: Proceedings of 25th IASTED International Conference on Modelling, Identification and Control, Canary Islands (Spain), pp. 97–102 (2006)
40. Ogawa, K.: Performance of a linear reluctance motor with novel structure. In: Proceedings of International Symposium on Linear Drives for Industry Applications, Birmingham (UK), pp. 57–60 (2003)
41. Ogawa, K., Matsuo, T.: A new construction of a short primary linear reluctance motor. In: Proceedings Japan-France congress on Mechatronics and Asia-Europe Congress on Mechatronics, pp. 53–540 (2003)

42. Ogawa, K.: Secondary geometry of a short primary linear reluctance motor. In: Proceedings of International Conference on Mechatronics and Information Technology, Jecheon (Korea), pp. 474–479 (2003)
43. Ogawa, K., Okada, H., Higuchi, T.: Thrust and lateral force in a linear reluctance motors with novel structure. J. Jpn. Soc. Appl. Electromagnet. Mech. **12**(3), 232–238 (2004)
44. Ogawa, K.: Lateral force of a linear synchronous reluctance motor. In: Proceedings of International Symposium on Linear Drives for Industry Applications, pp. 84–87 (2005)
45. Ueno, Y., Suehiro, S., Tahara, S., Ogawa, K.: Flux density distribution of a linear synchronous reluctance motor with transverse flux structure. In: Proceedings of International Conference on Electrical Machines and Systems, DS1E2-03 (2006)
46. Ueno, Y., Tahara, S., Ogawa, K.: Thrust and lateral force of a linear synchronous reluctance motor using by 3-D boundary integral equation method. In: Proceedings of International Conference on Electrical Machines and Systems, Seoul (Korea), pp. 8–11 (2007)

Mitigation of Circulating Current in Diode clamped MLI fed Induction Motor Drive Using Carrier Shifting PWM Techniques

C. Bharatiraja, P. Sanjeevikumar, J.L. Munda, Lars Norum and S. Raghu

Abstract Reduction in circulating current is one of the major considerations in inverter-fed electrical drives. Diode-clamped MLI (DC-MLI) enables higher output current per phase, thereby rating of the drive gets increased effectiveness. Various methods of triggering in the inverter legs create a better voltage profile and lead to the enabling of circulating current in the drive system. The induced circulating current (CC) flows through the apparatus neutral (N), and supply ground (G) is caused by the existence of parasitic capacitance. This circulating current may cause potential danger, especially when parasitic capacitance poses large. In the past, different modulation techniques and conversion topologies have been introduced to minimize the flow of circulating current. However, these techniques lead to complexity, high cost, low voltage profile, and efficiency due to lower modulation parameters. This paper proposes PS, POD, PD carrier shifting PWM algorithms for DC-MLI to tumbling the CC. The performances of the proposed algorithm, in terms

C. Bharatiraja
Department of Electrical & Electronics Engineering, SRM University, Chennai, India
e-mail: bharatiraja@gmail.com

P. Sanjeevikumar (✉)
Department of Electrical & Electronics Engineering, University of Johannesburg, Auckland Park, Johannesburg, South Africa
e-mail: sanjeevi_12@yahoo.co.in

J.L. Munda
The Centre for Energy and Electric Power (CEEP), Tshwane University of Technology, Tshwane, South Africa
e-mail: ljmunda@gmail.com

L. Norum
Department of Electric Power Engineering, Norwegian University of Science and Technology, Trondheim, Norway
e-mail: norum@ntnu.no

S. Raghu
Department of Water Resources Development & Management, Indian Institute of Technology, Roorkee, India
e-mail: raghu.selvaraj89@gmail.com

A. Konkani et al. (eds.), *Advances in Systems, Control and Automation*,
Lecture Notes in Electrical Engineering 442, https://doi.org/10.1007/978-981-10-4762-6_6

of CC, THD, losses, and efficiencies are analyzed theoretically and are validated via simulation and experimental results.

Keywords Diode-clamped MLI · Circulating current · Carrier shifting PWM

1 Introduction

Voltage source inverters (VSIs) are widely applied in different industrial needs for conditioning the power in adjustable speed drives and renewable energy system because of its ability to generate the desired output profile [1, 2]. Multilevel topologies are employed mainly to reduce the total harmonics distraction (THD) in the inverter voltage and current output waveforms and to reach the required voltage rating of the power switches and equipments. MLIs are eye-catching, more widespread because of its power rating, reduced harmonics, and EMI. The multilevel inverter contains three topologies, namely diode-clamped (DC-MLI), cascaded inverters (H-bridge-MLI), and capacitor-clamped inverters (FC-MLI) [3, 4]. The inverters have various types of modulation strategies to control the performance. Space vector modulation (SVM) is one of the most popular PWM techniques. The carrier-based PWM strategy can be segregated into two types: single carrier and multicarrier PWM. The diode-clamped multilevel inverters are having some good advance features such as stair case waveform and minimized harmonics, and it is having an advantage of controlling the medium voltage drives [5]. In DC-MLIs, modulation schemes like, phase disposition (PD), phase opposition disposition (POD), alternative phase opposition disposition (APOD), PS (phase shift) gives best results in terms of constant carrier frequency not synchronized with the stator terminal frequency [6, 7]. For diode-clamped inverters, POD modulation strategy is widely used, however it offers a high harmonic performance [8]. Out of the modulation strategies, the space vector PWM gives a greater fundamental output voltage and improved harmonic performance of the inverter. The analysis of circulating current is more important in the AC motor drives application. It produces between neutral point (N) of the motor and supply ground (G). The existence of shaft voltage, bearing damage, etc., is some of the major effect of circulating current. The concurrent switching of the series connected switches creates high dv/dt across the load terminals of the inverter. The increase in circulating current affects the motor insulation and also the cables. In drive applications, it may cause the electromagnetic interference (EMI), and this noise causes to trip the inverter drive [9]. It is very essential to limit the CC to certain boundary. A MLI can reduce the CC. The output voltage of multilevel inverter will vary in small increments because of the number of switching states [10], and it allows to mitigate the low-frequency harmonics, thereby the switching loss will be reduced. Furthermore, the CC can be reduced by reducing the dv/dt [11]. The cascaded inverter is widely implemented in the industrial applications in the literature [12, 13]; however, the main drawback of this type of configuration is it requires isolation transformers on

the AC side and a number of DC sources. Among all the configurations present in multilevel inverter, the analysis of circulating current is derived from the DC-MLI, which is the more frequent topology of the three-level inverters. For medium- and high-voltage AC drives, this topology can be connected directly to the power system utility.

The effect of shaft voltage and its resulting current was studied by Alger in the 1920s [14]. Various mechanical modifications in the system had been presented in the literature to eliminate the negative effects of the circulating current over motor bearing, such as cable type, passive filters, and the type of the bearing. There are two types of cables available: shielded type and unshielded type; the unshielded type of cable has no impact on the circulating currents, and the shielded type of cable has no impact on small rating motors and on higher rated motors; the magnitude of CC is inversely relative to the motor speed. Pairodamonchai [15] has given the procedure for designing and complications while designing passive filters. There are four types of filters available to mitigate the CC: dv/dt filters, reactors [16], sinusoidal filters [17], and common-mode (CM) chokes [18]. The elimination of bearing current is 30–90% [16, 19] based on the type of the filter on large rating motors, and there is no impact [20] in small rating motors. Moreover, the passive filters have more size and weight penalties. There are two types of bearings available: insulated bearing [21, 22] and hybrid bearing. Insulated bearing eliminates 40–60% of the circulating current on small rating motors and 60–80% [23] on large rating motors. Hybrid bearings give complete suppression of bearing currents in small motors not suitable for the large motor applications [24], [25], [26].

The different PWM technique provides different values of circulating current in the inverter. In this paper, the circulating current suppression is proposed with the different modulation strategies. A three-level DC-MLI is designed to drive 400-V, three-phase induction motor. Sinusoidal PWM, PD, POD, PS techniques are implemented using a MATLAB-2013b for the modulating index, ma = 0.9 and switching frequency of 1050 Hz. The partial elimination of circulating current implemented using SPARTEN III family FPGA processor. The simulation and experimental results are provided to validate the CC in three-level DC-MLI.

2 Effect of High Circulating Currents

The circulating current can be defined as the current that exists between the application neutral and ground.

$$I_{NG} = \frac{I_{AN} + I_{BN} + I_{CN}}{3} \tag{1}$$

The motor shaft voltage on the rotor side is induced due to the common mode voltage (CMV) with higher voltage and frequency in modern PWM inverter[27]. If the breakdown voltage of lubricant in the bearing of the motor is lesser than the

induced shaft voltage, circulating current in larger value will be flowing through the apparatus neutral (N) and supply ground (G) [21].

$$i_c = C_b \frac{\mathrm{d}V_b}{\mathrm{d}t} \tag{2}$$

$$i_c = \mathrm{BVR} \cdot C_b \frac{\mathrm{d}V_{\mathrm{NG}}}{\mathrm{d}t} \tag{3}$$

where BVR is the bearing voltage ratio.

This circulating current causes the malfunctioning of the sensitive electronic equipment such as in control systems, false tripping of the ground fault relays. In rotating electrical machines, this current damages the bearing which in turn damages the machine and also causes electromagnetic interference. The instantaneous current sum is called as the circulating current. The generation of circulating current can be observed from Fig. 1.

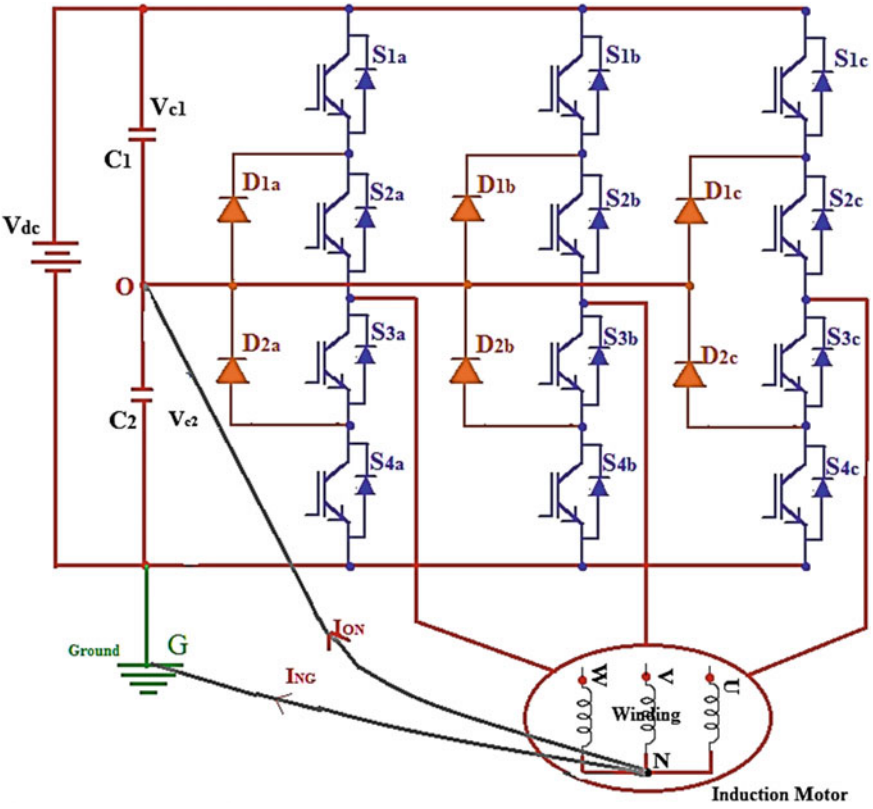

Fig. 1 Three-level DC-MLI/NPC-fed induction motor drive with marking of circulating current

3 Carrier Shifting Algorithms

To generate the required PWM signal on the carrier-based pulse width modulation, the triangular carrier wave is compared with the reference sine wave.

A. ***Single carrier pulse width modulation (PWM)***

The SPWM is one of the top modulation methods in the control of VSI. In SPWM, single triangular carrier wave is related to the single sine wave reference in order to generate firing signals for switching of the power electronic switches. In the medium-voltage applications, power dissipation is one of the most common problems. The open-loop SPWM control method of fundamental frequency is to minimize the switching losses.

B. ***Multicarrier PWM***

The multicarrier PWM (MC-PWM) technique is employed only for the MLIs. This practice is used to increase the efficiency of the inverter output. In this PWM technique, the carrier waves are in two ways: horizontal and vertical. The vertical carrier distribution techniques are classified into two configurations: PD and POD, where the horizontal distribution arrangement is only one type and that is PS control technique.

C. ***Phase disposition (PD)***

The phase disposition is one of the techniques in the MC-PWM. In this type of technique, the number of carriers depends upon the number of levels in the VSI. The formula for knowing the number of carriers is $(m - 1)$. Here, m is number of levels. All carriers should be in phase disposition (PD, the PD-PWM is best suited for the NPC). We can observe this technique from Fig. 2.

D. ***Phase opposition disposition (POD)***

The number of carriers is $(m - 1)$, and all these carriers are in phase with zero reference. Here, the carriers are arranged above the zero reference and below the

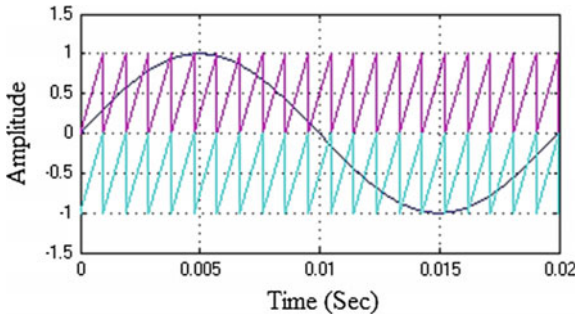

Fig. 2 Phase disposition (PD) PWM technique

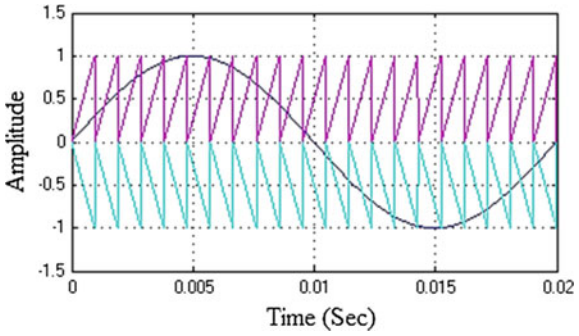

Fig. 3 Phase opposition disposition (POD) PWM technique

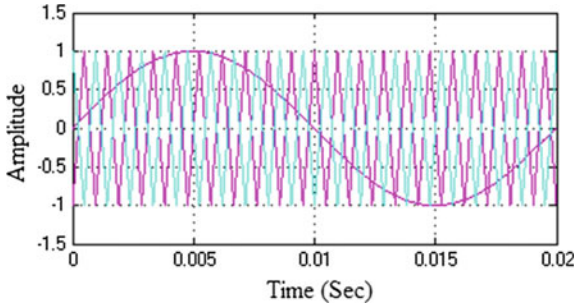

Fig. 4 Phase shift PWM technique

zero reference in phase and phase opposition, respectively. Fig. 3 represents the POD technique.

E. ***Phase shift (PS) PWM***

The number of carriers is $(m - 1)$, and each carrier is shifted by an angle of 90° accordingly. Figure 4 represents the phase shift technique.

4 Analysis of Circulating Current Depends on Switching States

The circulating currents have been discussed for the different switching states available in the below sections. The circulating current can be stated as the current between the applied N and the G points of the inverter. Magnitude of circulating current depends on the amount of the inverter input current. In the balanced star-connected load, the sum of phase currents is zero. The three-level NPC inverter produces different combinations of the phase current depends on the switching states. There are 27 possible different switching states available, and each switching state has different amount of circulating current. The state 1 produces the phase

current of $+I_{dc}/2$, state 0 produces 0 and −1 state produces $-I_{dc}/2$. All over 12 switching states produce $\pm I_{dc}/6$, 7 states produce zero circulating current, six states produce $\pm I_{dc}/3$, and two states produce $\pm I_{dc}/2$. Some sample different switching states and their circulating current shown in Fig. 5.

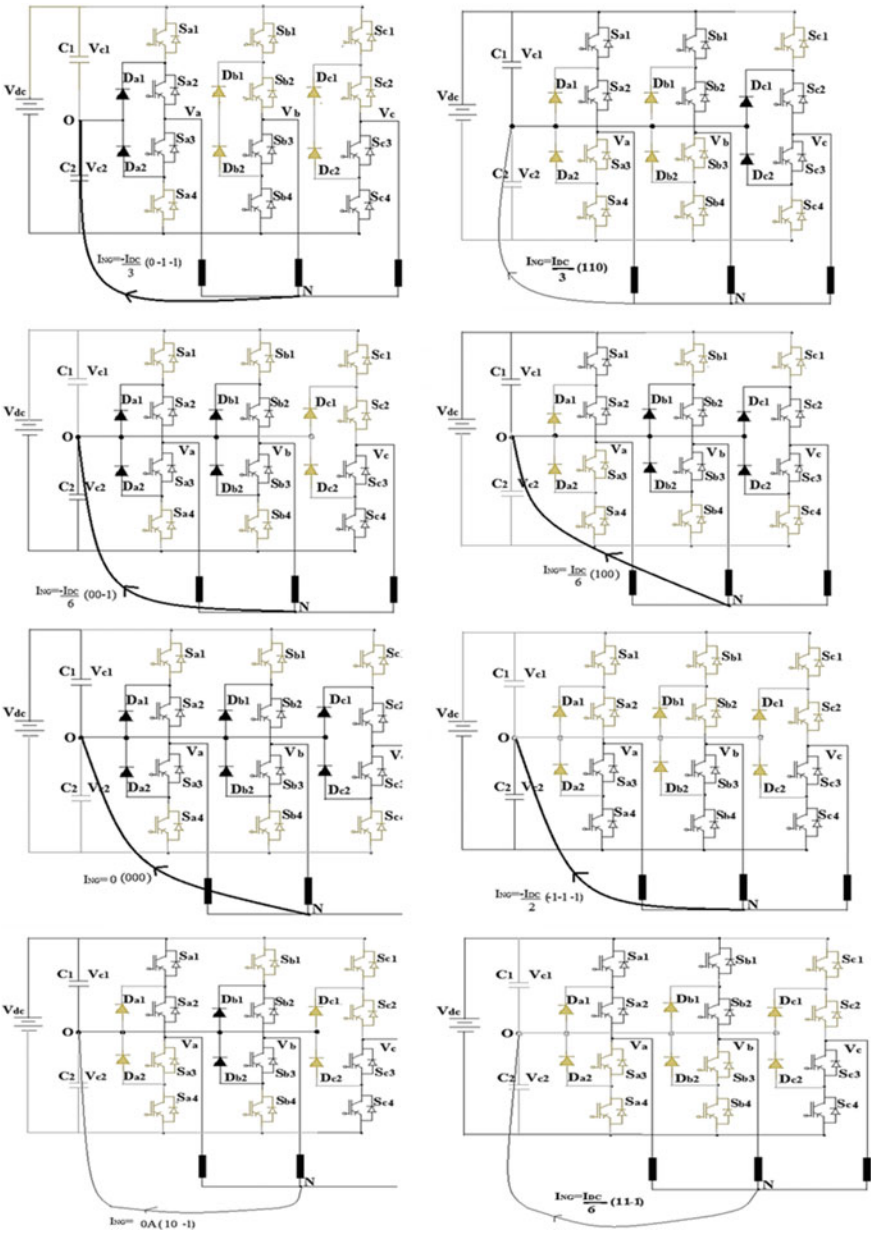

Fig. 5 Different switching states and its circulating current

5 Circulating Current Reduction

The circulating current minimization can be done by avoiding the abnormal switching of the inverter. The PWM techniques such as PD, POD, and PS can control the circulating current to such an extent, though the controlling of switching operation is not possible. The above chapter gives the detailed analysis of the available switching states and corresponding circulating current. From that analysis, selecting the proper switching states the circulating current can be minimized. In the partial reduction of circulating current can be eliminated up to $I_{dc}/3(n-1)$ for n-level inverter. In the partial elimination, the three-level inverter allows the circulating current magnitude of $\pm I_{dc}/6$. Harmonics are inversely proportional to the common mode voltage. This shows that the reduction in harmonics can be achieved by eliminating the common mode voltage. Similarly, the circulating current is directly proportional to the harmonics. The amount of harmonics will decrease with the reduction in the circulating current. Different PWM techniques such as PS, PD, and POD will reduce the circulating current to such an extent. The PS PWM technique eliminates only till the level of $\pm I_{dc}/2$. The PD technique will reduce the circulating current till $\pm I_{dc}/6$.

The necessity to reduce the CC is more with the aim of protecting the device from the failures. Finally, the POD algorithm will reduce the circulating current till $\pm I_{dc}/3$. By comparing all the above results, the best algorithm to reduce the CC is PD algorithm type. As we know already, the circulating current is directly proportional to the harmonics. So the harmonic level in the PD technique is comparatively low compared to all different algorithms.

6 Simulation Results

The circulating current reduction in PD, POD, and PS for three-phase three-level NPC-NLI has been simulated using MATLAB/Simulink software to supply the drive system with 2.2 kW, 1440 RPM induction motor. The machine parameters are rated voltage, VT = 380 V, rated current, I_s = 5 A, stator resistance, R_s = 2.9 Ω, rotor resistance, R_r = 2.2 Ω, stator leakage induction, L_s = 12 mH, rotor leakage induction, L_r = 12 mH, and mutual induction, L_m = 290 mH. An open-loop *v/f* speed control method is used to control the speed of the motor, and a DC link sets at 440 V. Both the simulation and experimental results are carried out for 1050 Hz switching frequency and modulation index of 0.86 at 50 Hz. The MATLAB simulation and experimental results for the partial elimination of CC at neutral are shown in Fig. 6. In the following figures, the observation that can be made is what is the amount of current is present and what is the amount of the

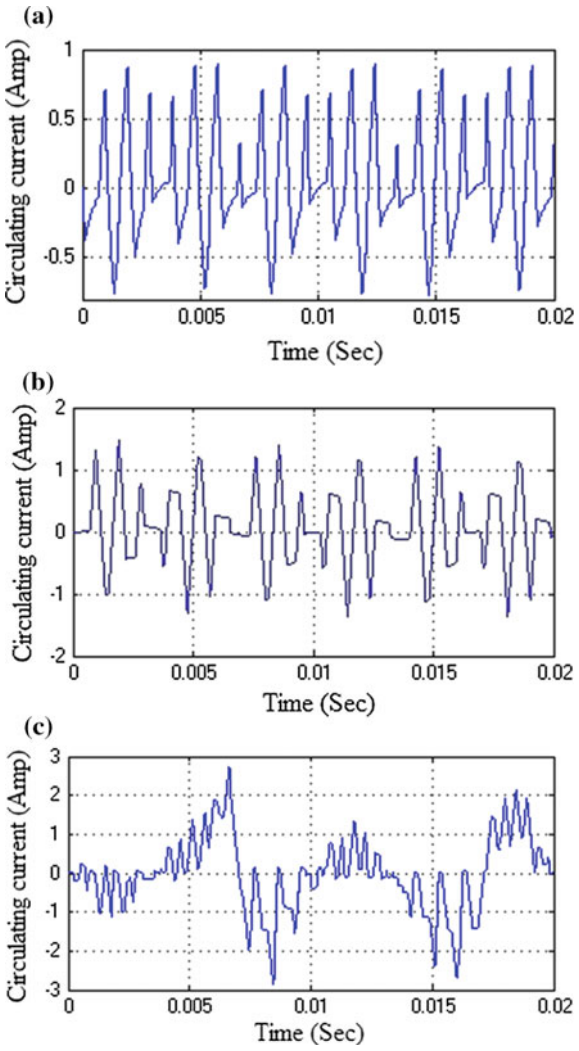

Fig. 6 Simulation results **a** three-level DC-MLI using PD ($I_{dc}/6$), **b** three-level DC-MLI is using POD ($I_{dc}/3$), **c** three-level DC-MLI is using PS ($I_{dc}/2$)

circulating current eliminated. When related to the three different PWM techniques, the PD technique provides good results in terms of the circulating current and harmonics. This is the partial elimination technique of the circulating current. The complete elimination is not possible while using POD. The simulation, provided in Fig. 6, which is exactly matches with the experimental results.

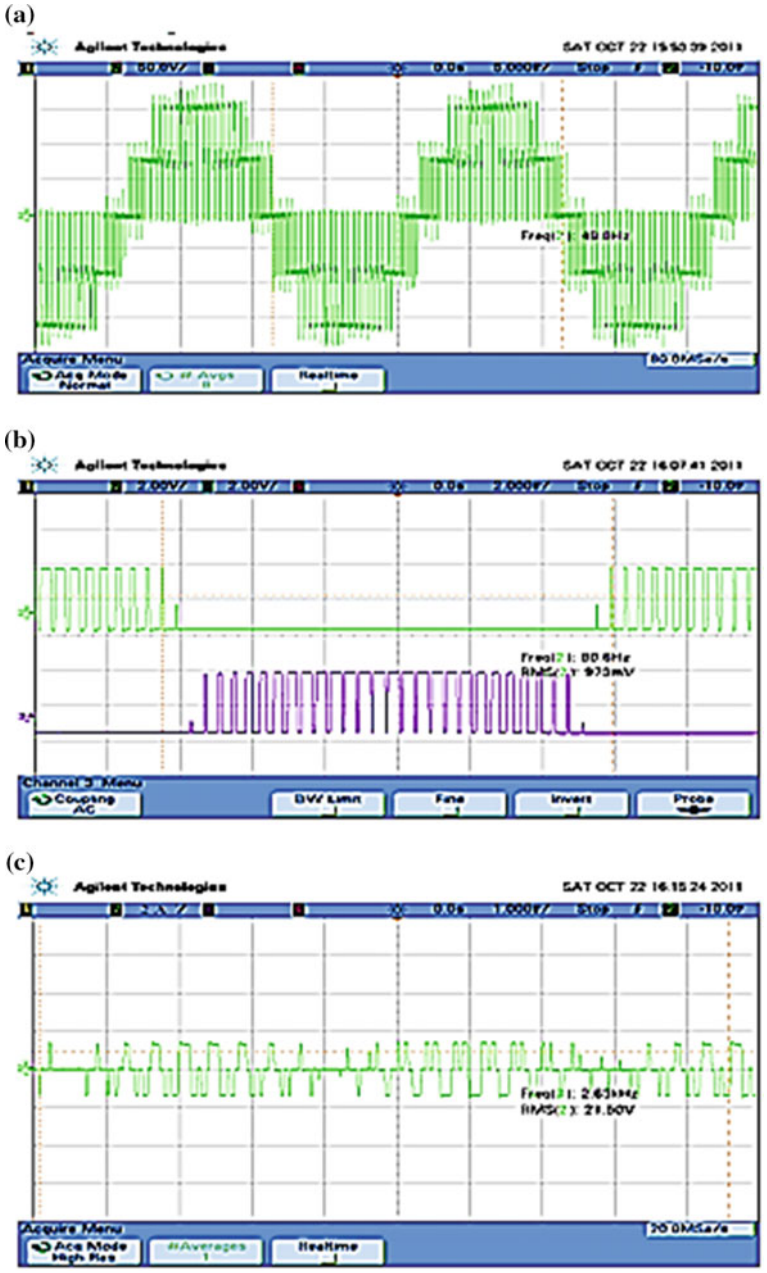

Fig. 7 Experimental results for PD technique. **a** Output voltage (50 V/div), **b** pulse generation (2A/div), **c** circulating current (2A/div)

Table 1 Result comparison

PWM technique	THD	Circulating current
PD	51.36	$+I_{dc}/6$
POD	59.82	$+I_{dc}/3$
PS	89.48	$+I_{dc}/2$

7 Experimental Results

In this section, theoretical and simulation results for a 1 kW load system are shown. All waveforms shown in this section are captured from FPGA SPARTAN-III-3AN-XC3S400. The simulated MATLAB code connected with the FPGA board through system generated tool ensures the less computational complexity environment [28, 29]. Three-phase three-level IGBT-based NPC MLI was used for to experimentation of the proposed PD PWM. The Fig. 7 shows the experimental results of PD PWM. Where in Fig. 7a shows the output voltage, Fig. 7b shows the pulse generation, and Fig. 7c shows the circulating current. The following waveforms represent the voltage output, pulse generation and circulating current, respectively. The IGBT used here is IRG4BC20FD with a fundamental frequency of 50 Hz and switching frequency of 1 kHz. The input DC bus voltage is 150 V. 1 kW motor with 50 mH inductance and 15 nF capacitance is used here. The circulating current mitigated using the PD technique is $\pm I_{dc}/6$ and that can be observed from the following diagram, and the performance of the system is improved in terms of harmonics (Table 1).

8 Conclusions

Premature failure of the bearings in the conventional two-level inverter is due to the induced circulating current in it. MLIs have their intrinsic ability to lessen the circulating current. Simulation and experimental results prove that the magnitude of the circulating current minimized to $\pm I_{dc}/6$, and that has a minimum THD in the line voltage and current. The proposed three different PWM techniques will also decrease the cost of reduction. Thus, when compared to the two-level inverter, the multilevel inverters have lots of advantages in terms of leakage current and harmonics.

References

1. Bose, B.K.: Modern Power Electronics and AC Drives. Prentice Hall PTR (2002). ISBN: 0130167436
2. Rashid, M.H.: Power Electronics: Circuits, Devices and Applications. Prentice Hall, New Jersey (2001)

3. Rodriguez, J., Lai, J.S., Peng, F.Z.: Multilevel inverters: a survey of topologies, controls, and applications. IEEE Trans. Ind. Electron. **49**, 724–738 (2002)
4. Colak, Ilhami, Kabalci, Ersan, Bayindira, Ramazan: Review of multilevel voltage source inverter topologies and control Schemes. Proc. Elsevier Energy Convers. Manage. **52**, 1114–1128 (2011)
5. Nabae, A., Takahashi, I., Akagi, H.: A new neutral-point clamped PWM inverter. IEEE Trans. Appl. **IA-17**(5), 518–523 (1981)
6. Renge, M.M., Suryawanshi, H.M.: Five-level diode clamped inverter to eliminate common mode voltage and reduce dv/dt in medium voltage rating induction motor drives. IEEE Trans. Power Electron. **23**(4), 1598–1607 (2008)
7. McGrath, B.P., Holmes, D.G.: Multicarrier PWM strategies for multilevel inverters. IEEE Trans. Ind. Electron. **49**(4), 858–867 (2002)
8. Renge, M.M., Suryawanshi, Hiralal M.: Multilevel inverter to reduce common mode voltage in AC motor drives using SPWM technique. J. Power Electron. **11**(1), 143–152 (2011)
9. Akagi, H., Tamura, S.: A passive EMI filter for eliminating both bearing current and ground leakage current from an inverter-driven motor. IEEE Trans. Power Electron. **21**(5), 982–989 (2006)
10. Sanjeevikumar, P., Siano, P., Ertas, A.H., Rajasekar, S., Pandav, K.M.: Single-phase seven-level stack multicell converter using level shifting SPWM technique. In: Conference of Proceedings of 16 IEEE International Conferrence on Environment and Electrical Engineering. Florence (Italy), pp. 7–10 (2016)
11. Julian, A.L., Oriti, G., Lipo, T.A.: Elimination of common-mode voltage in three-phase sinusoidal power converters. IEEE Trans. Power Electron. **14**(5), 982–989 (1999)
12. Gupta, A.K., Khambadkone, A.M.: A space vector modulation scheme to reduce common mode voltage for cascaded multilevel inverters. IEEE Trans. Ind. Electron. vol. **22**(5), 1672–1681 (2007)
13. Loh, P.C., Holmes, D.G., Fukuta, Y., Lipo, T.A.: Reduced common-mode modulation strategies for cascaded multilevel inverters. IEEE Trans. Ind. Appl. **39**(5), 1386–1395 (2003)
14. Alger, P., Samson, H.: Shaft currents in electric machines. In: A.I.R.E. Conference (1924)
15. Sanjeevikumar, P., Blaabjerg, F., Wheeler, P., Khanna, R., Mahajan, S.B., Dwivedi, S.: Optimized carrier based five-level generated modified dual three-phase open-winding inverter for medium power application. In: Conference Prof. of IEEE International Transportation Electrification Conference and Expo, Asia-Pacific, (IEEE-ITEC'16), Busan (Korea), pp. 40–45 (2016)
16. von Jouanne, A., Enjeti, P.: Design considerations for an inverter output filter to mitigate the effects of long motor leads in ASD applications. IEEE Trans. Ind. Appl. **33**(5), 1138–1145 (1997)
17. Pairodamonchai, P., Suwankawin, S., Sangwongwanich, S.: Design and implementation of a hybrid output EMI filter for high-frequency commonmode voltage compensation in PWM inverters. IEEE Trans. Ind. Appl. **45**(5), 1647–1659 (2009)
18. Ogasawara, S., Akagi, H.: Modeling and damping of high-frequency leakage currents in PWM inverter-fed AC motor drive systems. IEEE Trans. Ind. Appl. **32**(5), 1105–1114 (1996)
19. Moreira, A., Santos, P., Lipo, T., Venkataramanan, G.: Filter networks for long cable drives and their influence on motor voltage distribution and common-mode currents. IEEE Trans. Ind. Electron. **52**(2), 515–522 (2005)
20. Graovac, D., Hoffmann, T., Haltmair, A.: A transfer function approach to a common mode filter optimization in the PWM inverter supplied motor drives. IEEE Trans. Energy Convers. **26**(1), 93–101 (2011)
21. Bharatiraja, C., Raghu, S.: Comparative analysis of different PWM techniques to reduce the common mode voltage in three-level neutral-point-clamped inverters for variable speed induction drives. Int. J. Power Electron. Drive Syst. **3**(1), 105–155 (2013)
22. Cavalcanti, M., de Oliveira, K., de Farias, A., Neves, F., Azevedo, G., Camboim, F.: Modulation techniques to eliminate leakage currents in transformerless three-phase photovoltaic systems. IEEE Trans. Ind. Electron. **57**(4), 1360–1368 (2010)

23. Bell, S., Cookson, T., Cope, S., Epperly, R., Fischer, A., Schlegel, D., Skibinski, G.: Experience with variable-frequency drives and motor bearing reliability. IEEE Trans. Ind. Appl. **37**(5), 1438–1446 (2001)
24. Busse, D., Erdman, J., Kerkman, R., Schlegel, D., Skibinski, G.: An evaluation of the electrostatic shielded induction motor: a solution for rotor shaft voltage buildup and bearing current. IEEE Trans. Ind. Appl. **33**(6), 1563–1570 (1997)
25. Bharatiraja, C., Jeevananthan, S., Latha, R., Mohan, V.: Vector selection approach-based hexagonal hysteresis space vector current controller for a three-phase diode clamped MLI with capacitor voltage balancing. IET Power Electron. **9**(7), 1350–1361 (2016)
26. Bharatiraja, C., Latha, R., Jeevananthan, S., Raghu, S., Dash, S.S.: Design and validation of simple space vector PWM scheme for three-level NPC—MLI with Investigation of DC link imbalance using FPGA IP core. J. Electr. Eng. 13(1), 54–63 (2013)
27. Bharatiraja, C., Jeevananthan, S., Munda, J.L., Latha, R.: Improved SVPWM vector selection approaches in OVM region to reduce common-mode voltage for three-level neutral point clamped inverter. Int. J. Electr. Power Energy Syst. **79**, 285–297 (2016)
28. Bharati Raja, C., Jeevananthan, S., Dash, S.S.: A vector selection approach based on control degree of freedom to provide DC-link voltage balancing in diode clamped multilevel inverter. Int. Rev. Electr. Eng. **8**(1), 39–51 (2013)
29. Bharatiraja, C., Jeevananthan, S., Latha, R.: FPGA based practical implementation of NPC-MLI with SVPWM for an autonomous operation PV system with capacitor balancing. Int. J. Electr. Power Energy Syst. **61**, 489–509 (2014)

Suppression of Harmonics and THD Using Three-Level Inverter with C-Type Filter at the Output of the Inverter Using Simulink/MATLAB

Manjesh and B. Rajesh

Abstract The inverters and converters are introducing harmonics due to its properties. The most commonly used load for a three-phase line is a motor for industrial applications. The major problem of linear and nonlinear loads like motors are heats up due to harmonics introduced in the line voltage. The analysis of total harmonic distortion and magnitude of harmonics at the output of the three-phase inverter drive is carried out in this work. The simulation is obtained using MATLAB/Simulink. A traditional three-level inverter and three-level inverter with C-type filter are constructed and simulated. The circuits are built using IGBTs as switches and pulse generators are used to provide the gating signal to the switches. A three-phase asynchronous machine is provided with the same parameter of actual motor. An FFT analysis is done to obtain magnitudes of harmonics at the inverter output voltage, and the obtained results are compared.

Keywords Three-phase inverter · Diode-clamped inverter · Three-level inverter Multilevel inverter · Harmonics · THD · Total harmonic distortion · Filters C-type filter · PWM

1 Introduction

Many researchers have done their studies on intelligent power modules to construct inverter and converters for high-power electronic system. Different methods are used to control various electric machines, and most of these machines are nonlinear loads. The voltage and current harmonics produced by these nonlinear loads causes damage to the power grid, and quality of the power supplied by the grid is reduced. The important parameter in power quality is the power system harmonics, the most

Manjesh (✉) · B. Rajesh
Department of Electronic Science, Bangalore University, Bangalore, India
e-mail: manjesh1972@gmail.com

B. Rajesh
e-mail: rajeshb0201@gmail.com

A. Konkani et al. (eds.), *Advances in Systems, Control and Automation*,
Lecture Notes in Electrical Engineering 442, https://doi.org/10.1007/978-981-10-4762-6_7

conventional method of reducing these harmonics is to use filters and multilevel inverters. The power electronic system has their own limits on the magnitude of voltage and/or current harmonics in electrical machine. The variable speed applications in industries are induction motors and synchronous motors, and the pulse-width modulation (PWM) inverters are used to achieve motor's speed variation. The various techniques of PWM inverters are used to drive the induction motor. To control the speed of the induction motor, a voltage/frequency method is employed, and the major drawback of the inverter is it produces odd harmonics [1–4]. Percentage of total harmonic distortion is obtained using FFT analysis, and in this work a three-level inverter is used to vary the speed of induction motor. For high-power applications in industry a three-level inverter is widely used, and the inverter constructed with multilevels synthesizes the output voltage approximately sinusoidal than the normal two-level inverter. The three-level inverter approximately improves magnitude of harmonics four times the normal inverter drive. Many researchers use the PWM multilevel inverters to minimize the harmonics, and in addition to multilevel inverters, filters can also be used to eliminate the harmonics completely at the output of the inverter. There are many types of filters for PWM inverter drives to limit the harmonics. The output of multilevel inverter provides an output voltage with more and more sinusoidal. The PWM inverter output is added with additional odd harmonics such as 5th, 7th, 11th, 13th. The fifth harmonic magnitude is equal to 20% of the nonlinear load current, and similarly seventh harmonic is 14.30%. The suppression of inverter output harmonics is an added advantage, and the nominal power (P_1) is given by Eq. 1 where P_1 is nominal power, V_1 is line-to-line voltage across load, and R is the resistance of the load. The elements used in this experimental work are a resistor and an inductor. The reactance X_1 is calculated using Eq. 2. The reactive power (Q_1) is given by Eq. 3, where V is line-to-line voltage across load [4–9].

$$P_1 = V_1^2 * R \tag{1}$$

$$X_1 = \omega L \text{ or } X_1 = 2\pi fL \tag{2}$$

$$Q_1 = V_1^2 * X_1 \tag{3}$$

2 Traditional or Two-Level Inverter (TID)

The traditional or two-level inverter circuit has six IGBTs. Figure 1 depicts the circuit diagram of a three-phase two-level inverter. Three phases in the inverter are 120° out of phase with each other, and pulse generators are used to provide the gating signal to the switches. The switch S_{b1} is turned on with a phase shift of 120°, and the switch S_{a1} and switch S_{c1} will be turned on for the next phase shift of 120° with respect to S_{b1}. All the IGBTs used in the circuit can be divided into upper and

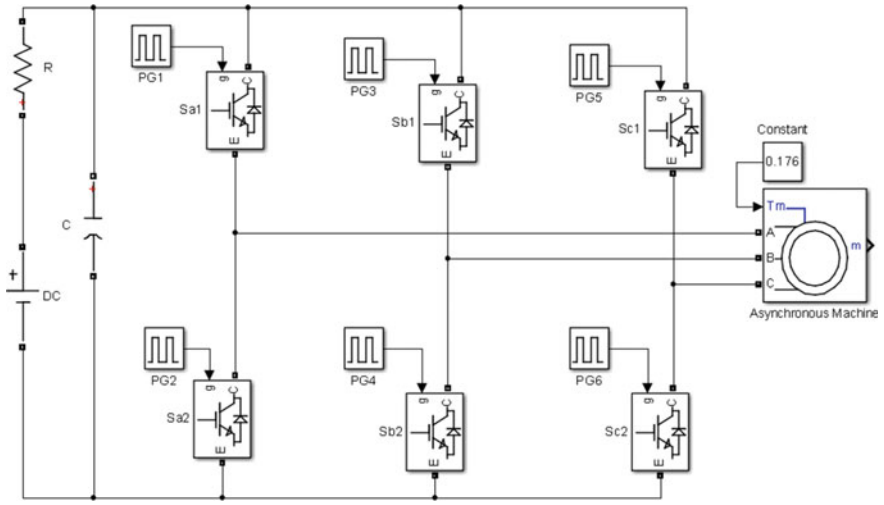

Fig. 1 Traditional inverter drive with three-phase induction machine as a load

lower IGBTs. The IGBT's S_{a1}, S_{b1}, and S_{c1} are +ve group of switches, and also S_{a2}, $S_{b2,}$ and S_{c2} are −ve group switches. The −ve group switches—S_{a2}, $S_{b2,}$ and S_{c2} are compliment signals with respect to their upper switches—S_{a1}, $S_{b1,}$ and S_{c1}. Both +ve and −ve group switches in the same leg should never turned on together. The pattern in which the switches are turned on can be analyzed, if two switches from +ve group are ON, and one switch from −ve group is ON or two switches from −ve group are ON, and one switch from +ve group is ON. The combination of these control signals produce a three-phase output voltage which is connected to drive the three-phase induction motor.

3 Diode-Clamped Multilevel Inverter (DCMI)

The three-level PWM inverter is constructed with 12 IGBTs. Figure 2 shows the construction of three-level inverter. Control signals are generated by pulse generators. All the three-phase signals have 120° phase shift with each other. The $IGBT_5$ is switched on for a phase shift of 120° with reference to $IGBT_1$, and also $IGBT_9$ will be turned on with a phase shift of 120° with reference to $IGBT_5$. The $IGBT_2$, $IGBT_{6,}$ and $IGBT_{10}$ are switched on with a phase shift of 10° with respect to IGBT1, $IGBT_{5,}$ and $IGBT_9$ are ON for the period of 160°. $IGBT_1$, $IGBT_2$ $IGBT_5$, $IGBT_6$, $IGBT_{9,}$ and $IGBT_{10}$ are the +group switches, and $IGBT_3$, $IGBT_4$ $IGBT_7$, $IGBT_8$, $IGBT_{11,}$ and $IGBT_{12}$ are the −ve group switches. The −ve group switches are the compliments of +ve group switches. $IGBT_3$, $IGBT_4$ $IGBT_7$, $IGBT_8$, $IGBT_{11,}$ and $IGBT_{12}$ are the compliments of $IGBT_1$, $IGBT_2$ $IGBT_5$, $IGBT_6$, $IGBT_{9,}$ and $IGBT_{10}$, respectively.

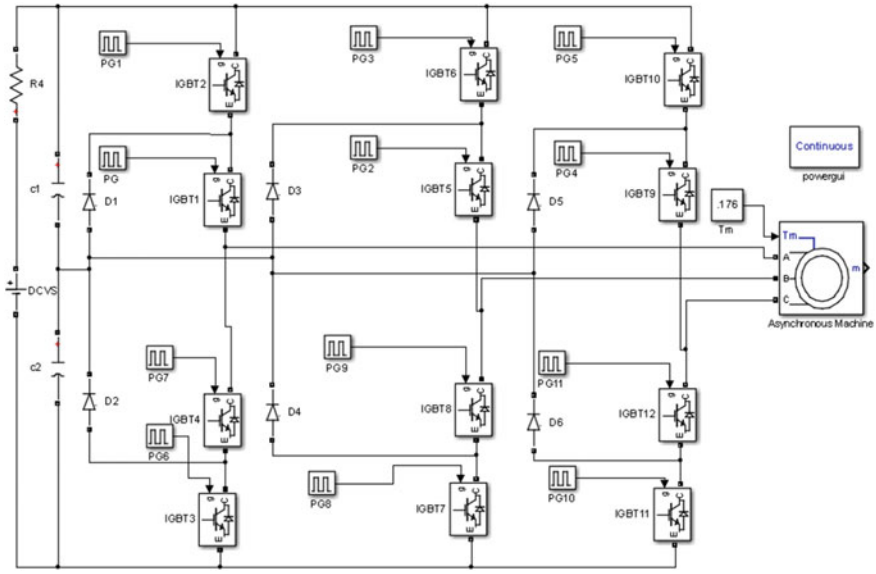

Fig. 2 Diode-clamped inverter drive with three-phase induction motor as a load

4 Diode-Clamped Multilevel Inverter (DCMI) with C-Type Filter

The C-type filter is introduced at the output of the inverter along with a line inductor; the circuit is as shown in Fig. 3. The line inductor used in this work is $L = 47$ mH. The filter parameters R, L, and C are determined by trial-and-error procedure for harmonics. The input parameters for filter are nominal voltage and frequency, employed to obtain the output voltage of the inverter.

5 Results

The total harmonic distortion (THD) and harmonics are measured at two-level traditional inverter output and three-level DCMI inverter drive, and the work is extended for construction of three-level DCMI with C-type filter. The induction machine is run with a frequency of 8 Hz. The circuits have been simulated in MATLAB/Simulink, in this work the harmonic analysis and THD are studied, and the results are obtained after repetitive trials with variable elements. The output voltage of traditional inverter, DCMI, and DCMI with filter is obtained and presented in Figs. 4, 5, and 6. The harmonic graph of line-to-ground voltage for traditional inverter drive (TID) and DCMI is presented in Fig. 7. Figure 8 shows voltage harmonics and current harmonics for TID. Figure 9 shows harmonic plot of current with DCMI and DCMI with filter (Table 1).

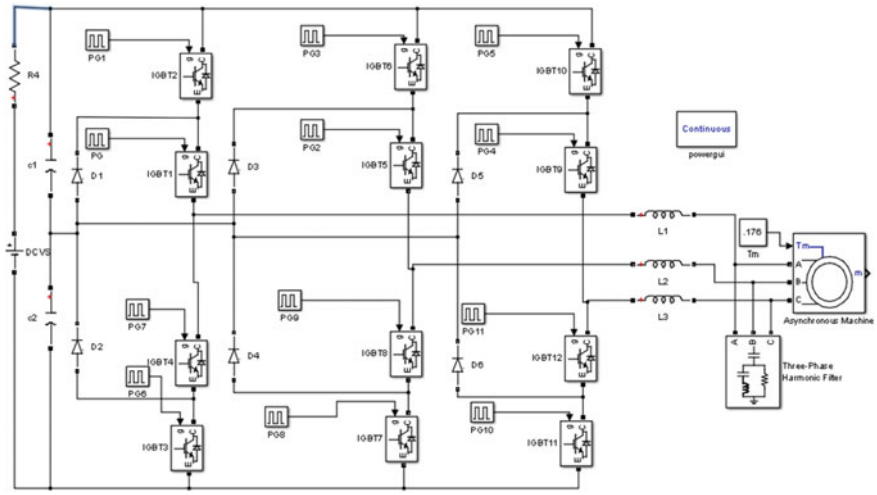

Fig. 3 Diode-clamped inverter drive with C-type filter for three-phase induction machine as a load

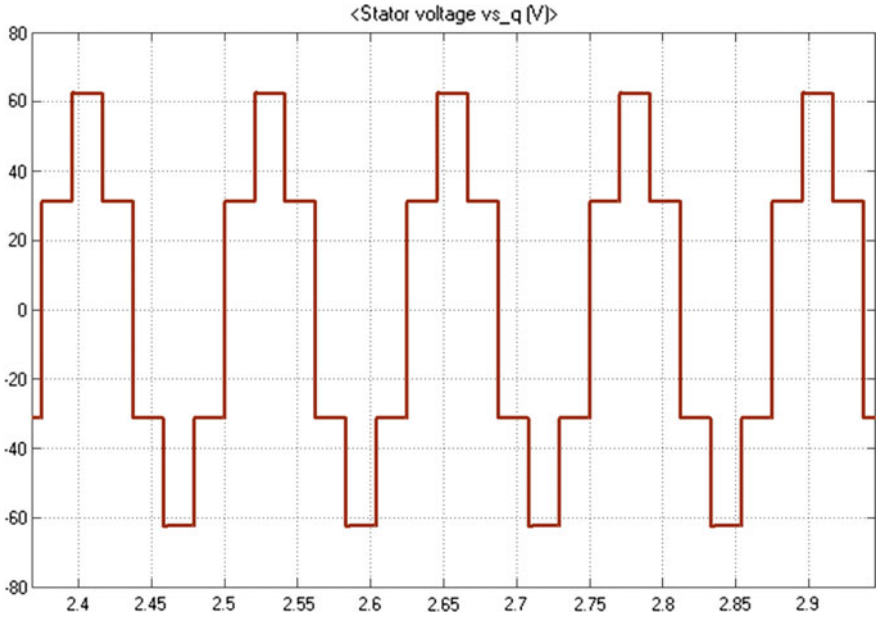

Fig. 4 Phase A of Three-phase out voltage of normal inverter

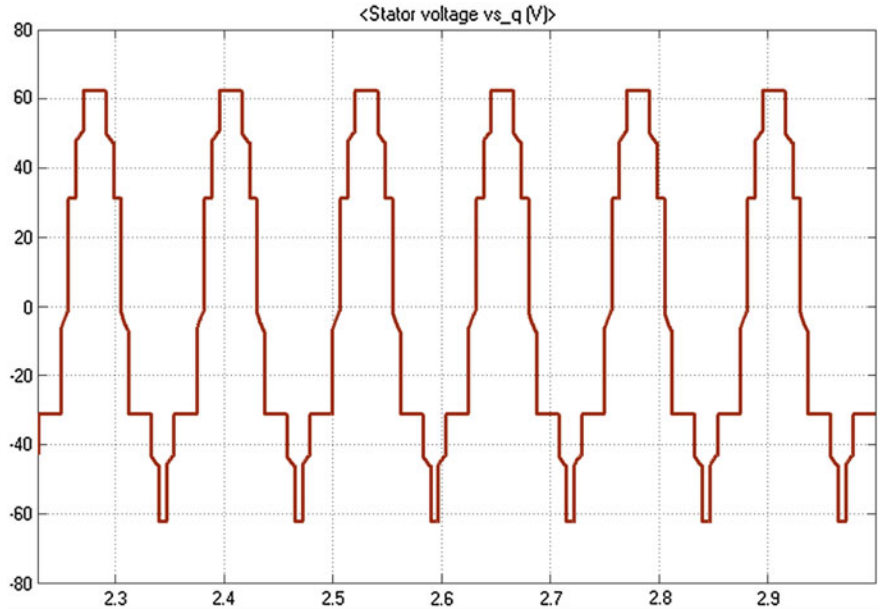

Fig. 5 The output voltage of three-level diode-clamped inverter with induction machine

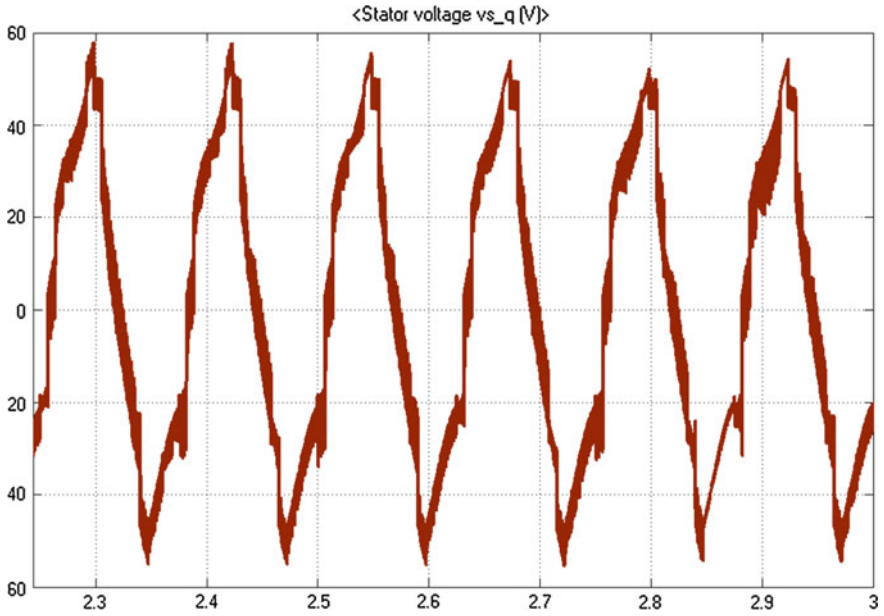

Fig. 6 The output voltage of three-level diode-clamped inverter with C-type filter for induction machine

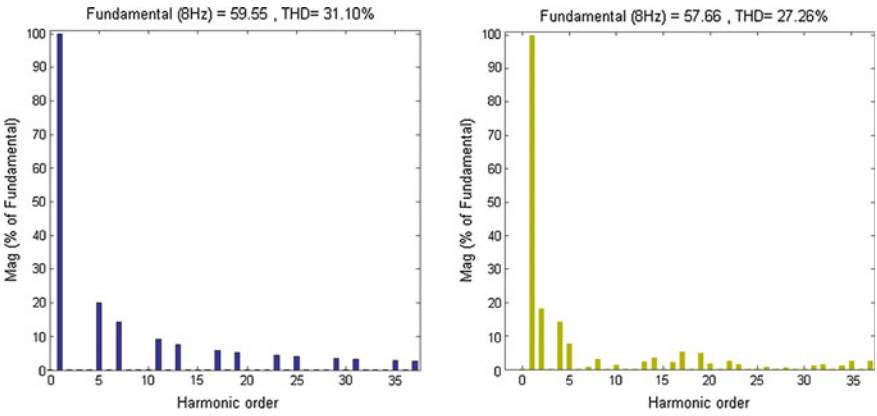

Fig. 7 Harmonic plot of L-N voltage for TID and DCMI

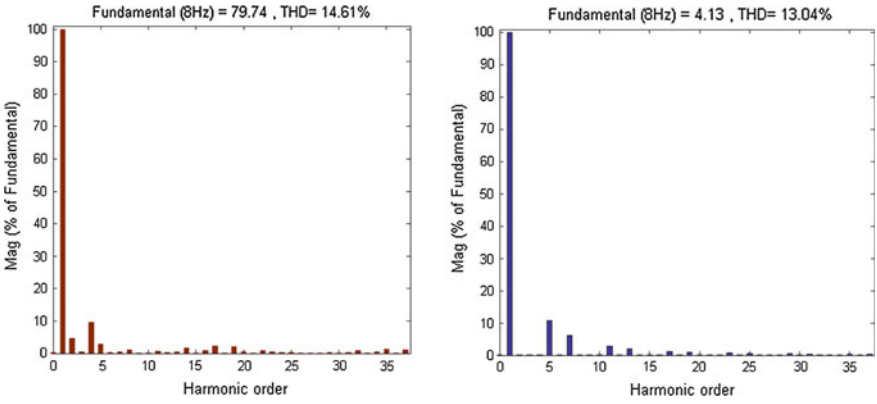

Fig. 8 Harmonic plot of line-to-neutral voltage for DCMI with filter and line current for TID

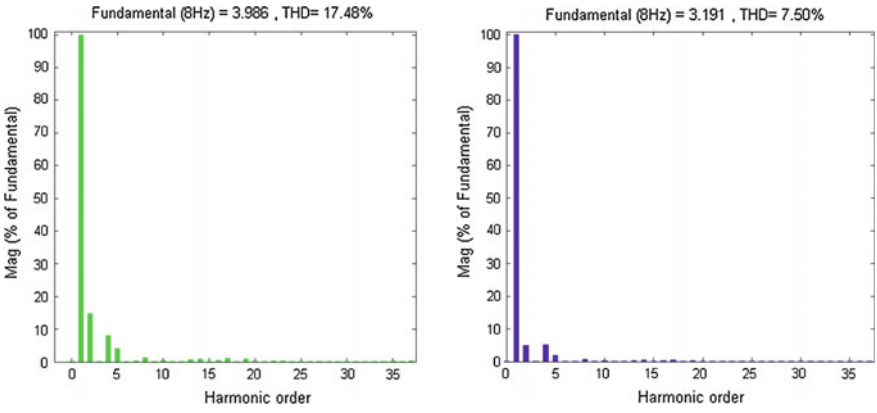

Fig. 9 Harmonic plot of line current for DCMI and DCMI with filter

Table 1 Total harmonic distortion in percentage for both the inverters and with filter

THD of	Normal inverter drive (%)	DCMI (%)	DCMI with filter (%)
Voltage	31.1	27.26	14.61
Current	13.04	17.49	7.6

6 Conclusion

The traditional inverter, three-level diode-clamped multilevel inverter, and DCMI with filter have been constructed using MATLAB/Simulink. A C-type filter is connected at the output of inverter to study the effects of harmonics; the results obtained with and without C-type filter have been simulated and compared. The analysis shows that the inverter output is nearly sinusoidal output; the individual harmonics at the PWM inverter are also reduced. The total harmonic distortion is also found to be less. It is concluded that using C-type filter at the output of the inverter has made significant improvements to the harmonic suppression. The results can be extended to carry out temperature analysis of three-phase asynchronous motor in future.

References

1. Mangroliya, D.G., Rupapara, V.J., Akabari, R.P., Vaghela, N.M.: An advanced three phase VSI with 1500 conduction mode using pic16f72. J. Inform. Knowl. Res. Electr. Eng. **02**(02), 352 (2013)
2. Chaturvedi, P., Jain, S., Agrawal, P.: Modelling, simulation and analysis of three-level neutral point clamped inverter using Matlab/Simulink/Power System Blockset. In: Proceedings of the 8th International Conference on Electrical Machines and Systems 2005, Nanjing, China, Vol. 2, 27–29 September 2005, pp. 1223–1227 (2005)
3. Latif, M.A., Alam, M.J., Rashid, M.A., Karim, A., Ramly, N.H., Daut, I.: Microcontroller based PWM inverter for speed control of a three phase induction motor. Int. J. Eng. Technol. **5** (2), 624–630 (2013)
4. Peng, F.Z.,: A generalized multilevel inverter topology with self voltage balancing. In: IEEE industry applications conference 2000, Rome, Italy, Vol. 3, 8–12 October 2000, pp. 2024–2203 (2000)
5. Dendavey, E.S., Barve, E.A.: Design of renewable energy source based inverter with 1200, 1500 and 1800 mode of conduction with and without filter. Int. J. Sci. Eng. Technol. Res. **2**(3) (2013)
6. Prathiba, T., Renuga, P.: A comparative study of total harmonic distortion in multi level inverter topologies. J. Inform. Eng. Appl. **2**(3), 26–36 (2012)
7. Memon, Z.A., Uquaili, M.A. and Unar, M.A.: Harmonics mitigation of industrial power system using passive filters. Mehran Univ. Res. J. Eng. Technol. **31**(2) (2012)
8. Tawfeeq, O.T.: THD reduction of a current source rectifier-DC motor drive using single tuned filters. Int. J. Inventive Eng. Sci. **1**(12) (2013)
9. Purushothaman, S.K.: A quantitative approach to minimize harmonics elimination using filter design. Int. J. Adv. Res. Comput. Sci. Softw. Eng. **3**(12) (2013)

Computation of Actuation Voltage and Stress Made of Hafnium Oxide Materials Used in Radio Frequency Micro-electromechanical System Switch

Ankur Saxena

Abstract When radio frequency micro-electromechanical switch is closed position, it provides very small insertion loss, and in opened position, it provides superior isolation. RF MEMS switch is presented for low actuation voltage and stress computation. The flexures and multiple perforation is used to reduce actuation voltages due to this the spring constant is also reduces. The stress is calculated by simulating slender micro-membrane which is made up of hafnium oxide material. The RF MEMS switch is designed with supporting of various types of flexures which provides different displacement and capacitance. The RF MEMS switch is designed Fixed Fixed beam with supported of various types of meanders or flexures.

Keywords Fixed-fixed beam · Electrostatic actuation · Flexures Dielectric · Perforation · Stiction

1 Introduction

From last few years the Radio frequency Micro-electromechanical system (MEMS) based devices or switches have created more revolution in industry or in Electronics markets [1]. RF MEMS switch is fabricated with semiconductor technology for communication application due to their small size and good performance [2]. Pin diode requires a power to operate at high frequency. RF micro-electromechanical switch consumes low power for operation [2]. MEMS switch has drawback of high pull in voltage against the current which is useless in micro-system. The drawback is removing by using electrostatic mechanism which is to control the pull in voltage of switch. To reduce the pull in voltage, the researchers employed reducing the stiffness constant by increasing the length or decreasing the width of switch, reducing the air gap between electrodes and increasing the actuation area [3].

A. Saxena (✉)
Jagannath University, Jaipur, India
e-mail: ankur_saxena6481@yahoo.com

A. Konkani et al. (eds.), *Advances in Systems, Control and Automation*,
Lecture Notes in Electrical Engineering 442, https://doi.org/10.1007/978-981-10-4762-6_8

The stiffness constant concept is depend on spring constant of beam. As decreasing in spring constant of beam with increasing the length of beam or reducing the width of beam but it should be ensures that beam have doesn't any stiction with surface. As stiction problems created, the losses of restoring force increases due to this it could not decrement in pull in voltage [3]. MEMS switches are classified in two parts: capacitive and direct. Direct contact Microelectronic mechanical switch is generally used for gigahertz operated application while for high frequency application used capacitive switches. MEMS switch has two stable states, ON state and OFF state, which is applied through mechanism of electrostatic, magentostatic, or thermally induced forces. Radio frequency micro-electromechanical system switch is widely used for electrostatic actuation due to little insertion loss, small power consumption, highly reliable for higher frequency, and short switching time. Electrostatic MEMS switches entail an excessive actuation voltage to operate the movable component. In the wireless communication application, RF MEMS switch requires low pull in voltage [4].

2 Material

The material plays a vital role in RF MEMS switch. The material which has a higher constant is being considered with a thin layer providing same performance.

Hafnium oxide dielectric materials have been latterly focused for their reliable performance. As some dielectric materials contain very low crystallizing temperature, it is very major task to integrate them into CMOS. The hafnium oxide dielectric material has advantages over other dielectric material as it has good insulation and capacitance interpretation. It prevents diffusion of dopants such as boron and phosphorus and protects from breakdown performance. It also has good thermal stability, sound interface, and high recrystallization temperature qualities [5].

3 Electrostatic Actuation

The electrostatic actuation technique is a popular technique for capacitive switch.

The actuation process is also achieved by thermal, magnetic, and piezoelectric techniques. In electrostatic actuation method, a DC voltage is given between the two electrodes or bridge and the base of electrode. The square of electric field E is proportional to the downward force of beam. The spring force is proportional to the deflection of the beam due to which beam will be moved towards ground electrode. The applied voltage is given by Vin, gap between two electrodes is given by g, and area is defined by A. The spring constant of the beam depends on geometry dimension of the beam. The beam spring constant will be varying with change in Young's modulus, Poisson's ratio, and material. The variation in geometrical of beam changed the pull down voltage and also changed displacement between

ground and electrode. As applied voltage is apply on beam due to this downward force on beam is increases fastly in the compare of upward force and beam found to deflect [6]. The high electrostatic actuation voltages give conflicting effect on reliability of switch. As the electric field changes, it will change the gap and actuation voltage E [6].

4 Surface Contact Analysis

RF MEMS shunt switch executes vital role in examination of surface contact. The radio frequency signal flow through a pathway lies between opened transmission lines and switch beam. The system loss and insertion loss on the transmission line path will be determined during the process. When electrostatic actuation voltage is applied to electrodes, the beam changes its position and its move downward in z-direction. In Fixed-Fixed beam the middle tip will be touch the ground electrode due to this the RF signal transmit through the switch [7].

5 Stress Analysis

In multiphysics, software computes the von Mises stress of the fixed-fixed beam membrane at fixed height [8]. The hafnium oxide material is introduced in membrane which provides maximum stress of 20.84 MPa for Switch A and 45.55 MPa for Switch B. The two switches are designed with different flexures of support It provides distinct stress analysis. The switch B is provides maximum stress so it has good quality to hold higher switching with maximum stress.

6 Flexures

In this research aim design the RF MEMS switch with reduced spring constant value and minimized actuation voltage. The flexures or meanders are added in the beam to provide supported beam [9]. These flexures pull down the value of spring constant [9]. As more flexures are added, it significantly reduced the spring constant without extremely increasing the required space. As smallness is essential for a device to be fixed in RF MEMS application, Eqs. 1 and 2 are as follows

$$k = \frac{48\mathrm{GJ}}{la^2\left[\frac{J}{EIx}I_a + I_b\right]n^3} \tag{1}$$

$$J = \frac{1}{3}t^3 w\left(1 - \frac{192}{\pi^3}\frac{t}{w}\sum_{i=1,i\text{odd}}^{\infty}\frac{1}{i^5}\tanh\left(\frac{i\pi w}{2t}\right)\right) \quad (2)$$

where

n	number of meanders in the serpentine flexure,
$G = E/2(1 + v)$	the torsion modulus,
Ix = wt3	the moment of inertia.

The torsion constant is given for $la >> lb$, and the spring constant of the serpentine flexure becomes $k \approx 4Ew\ (t/(nl\text{a})3$ [5].

7 Geometry and Simulation of RF MEMS Shunt Switch

The sacrificial layer is removed by adding perforation beam plates during the fabrication process. The perforated beam or switch advance changes in capacitance ratio of switch and switching time [10]. The shunt RF MEMS switch is a switch in which both ends are fixed at both sides above free gap. The dielectric material HfO_2 with high dielectric constant value and good thermal stability is used in RF MEMS switch. The beam is supported at both ends with flexures or meanders which provides greater flexibility. Here, two types of meanders are connected to the beam, and due to this, it provides various properties of switch. The design and simulation of RF MEMS switch done bys using Comsol multiphysics software. The software calculated the pull in voltage, capacitance and stress. As in Fig. 1, Switch A and Switch B simulated are shown which represent the maximum displacement in z-direction at pull in voltage. Both switches also compute stress due electrostatic force.

8 Result and Discussion

The amount of rectangular perforation is used in RF MEMS switch which is approximately same in both switches. Figure 1 shows the simulation Switch A 22.1 V at the maximum displacement −0.308 μm. The Switch B provides maximum displacement −0.418 μm at 22.1 V. The concept of switches is designed for low power consumption and reduces squeeze film damping, residual stress, and high switching speed. The fringing fields and air resistance of switch can be reduced by adding perforation. The graph is between applied voltage and displacement for Switch A and Switch B for various voltages. As air gaps reduce, the value of down capacitance continuously increases. The Switch A capacitance is 26.8 fF, and Switch B capacitance is 27.6 fF.

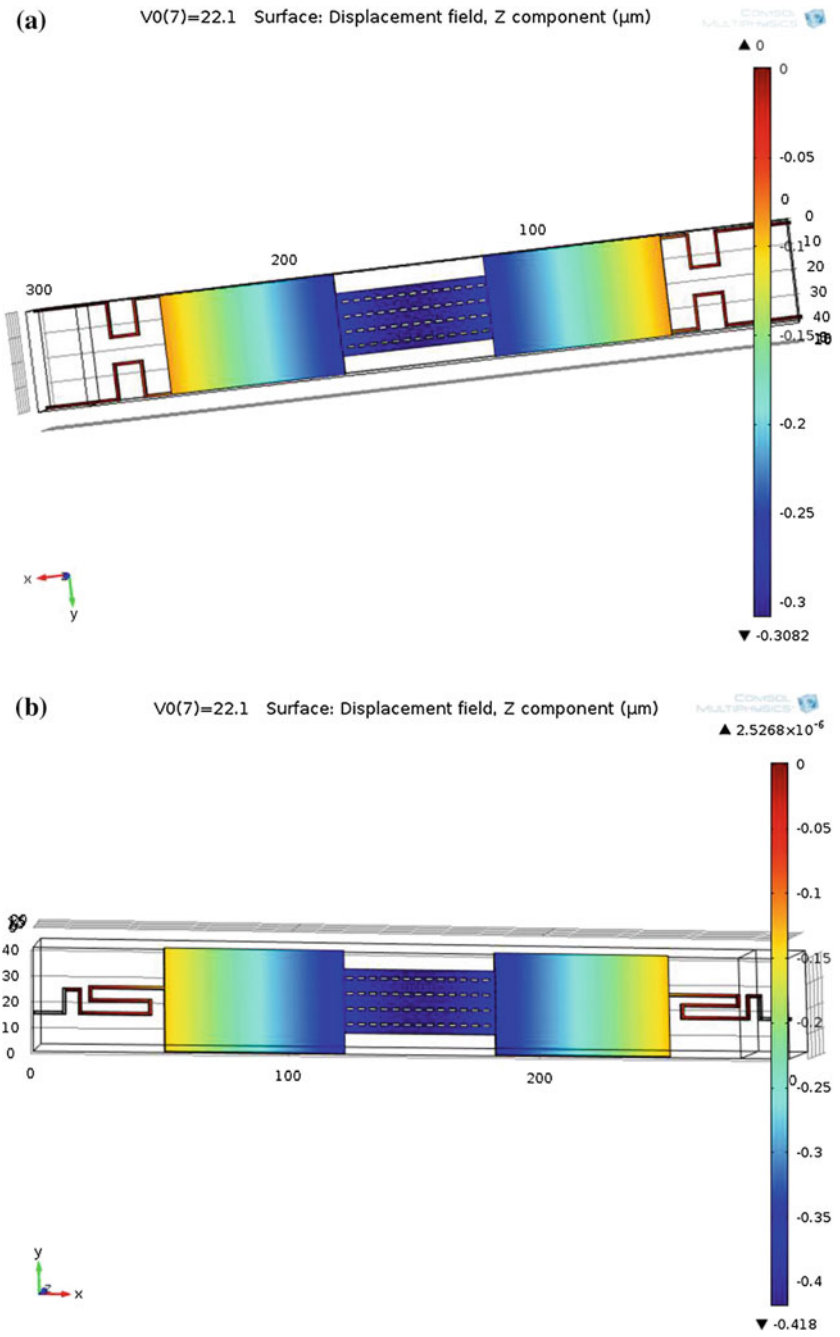

Fig. 1 **a** Simulated Switch A at 22.1 V. **b** Simulated Switch B at 22.1 V. **c** Graph between applied voltage and displacement of Switch A. **d** Graph between applied voltage and displacement of Switch B. **e** Graph between capacitance and applied voltage of Switch A. **f** Graph between capacitance and applied voltage of Switch B

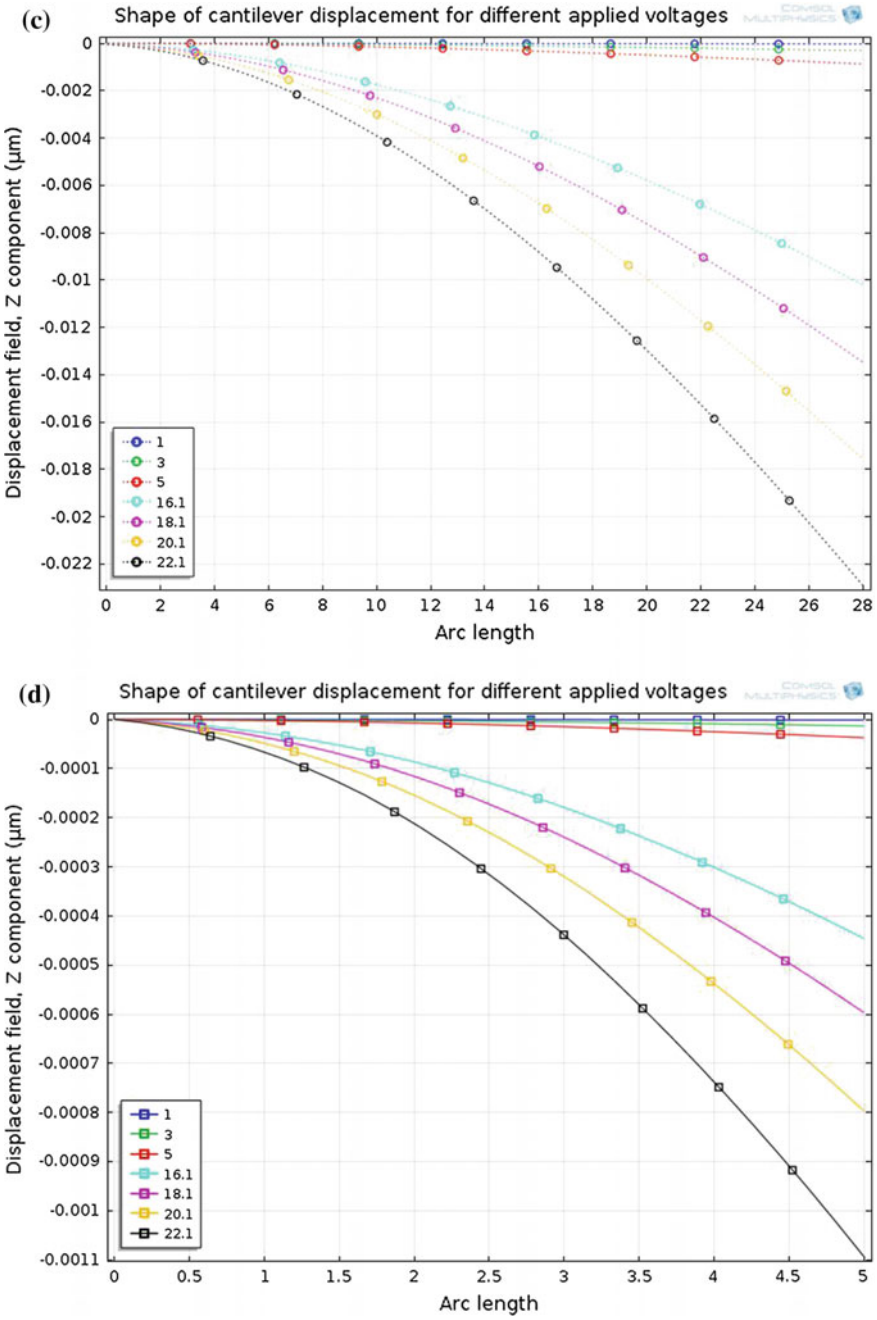

Fig. 1 (continued)

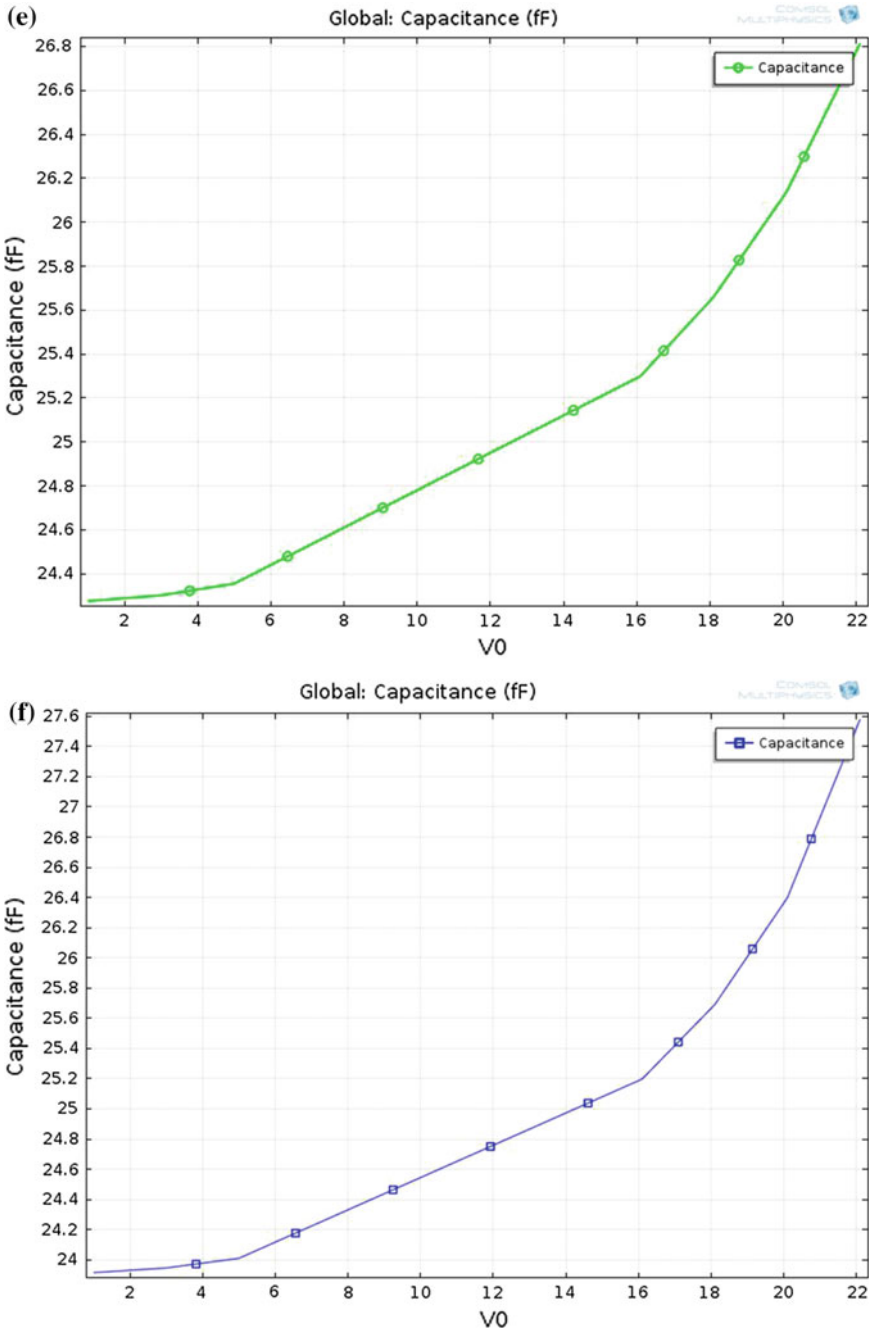

Fig. 1 (continued)

9 Conclusion

As result conclude structure of flexures reduced the pull in voltaage and provide maximum displacement. If switch required low actuation voltage and high switching speed, then the Switch B is used for better reliability. The hafnium oxide material with high dielectric constant value provides high switching speed and lower mass and reduces squeeze film damping at low actuation voltage. The capacitance of Switch B provides greater displacement compared to Switch A.

References

1. Singh, T.: Computation of beam stress and RF performance of a thin film based Q-band optimized RF MEMS switch. Trans. Electr. Electron. Mater. **16**(4), 173–178 (2015)
2. Mercado, L., Kuo, S.M., Lee, T.Y.T., Liu, L.: A mechanical approach to overcome RF MEMS switch stiction problem. In: Electronic Components and Technology Conference, pp. 377–384 (2003)
3. Manivannan, M., Joseph Daniel, R., Sumangala, K.: Low actuation voltage RF MEMS switch using varying section composite fixed-fixed beam. Int. J. Microwave Sci. Technol. **2014** (862649), 12 (2014)
4. Attaran, A., Rashidzadeh, R.: Ultra low actuation voltage RF MEMS switch. Micro Nano Syst. Lett. (2015)
5. Huang, A.P., Yang, Z.C., Chu, P.K.: Hafnium-based high-k gate dielectrics. Adv. Solid State Circ. Techno., pp. 446 (2010). ISBN: 978-953-307-086-5
6. Newman, H.S.: RF MEMS switches and applications. In: Annual International Reliability Physics Symposium, IEEE 02CH37320.40R, Dallas, Texas (2002)
7. Jaafa, H., Nan, F.L., Yunus, N.A.M.: Design and simulation of high performance RF MEMS series switch. In: RSM2011 Proceedings, Kota Kinabalu, Malaysia (2011)
8. Singh, T., Khaira, N.K., Sengar, J.S.: Stress analysis using finite element modeling of a novel RF microelectromechanical system shunt switch designed on quartz substrate for low-voltage applications. Trans. Electr. Electron. Mater. **14**(5), 225–230 (2013)
9. Jaafar, H., Sidek, O., Miskam, A., Korakkottil, S.: Design and simulation of microelectromechanical system capacitive shunt switches. Am. J. Eng. Appl. Sci. **2**(4), 655–660 (2009)
10. Guha, K., Kumar, M., Agarwal, S., Baishya, S.: A modified capacitance model of RF MEMS shunt switch incorporating fringing field effects of perforated beam. Solid-State Electron. **114**, 35–42 (2015)

Optimal Design Configuration Using HOMER

Prashant Kumar and Sanjay Deokar

Abstract The aim of this chapter was to present an idea of using free sources of energy for designing stand-alone hybrid renewable energy system. This stand-alone hybrid system is used for powering the Electrical Engineering Department of AMGOI, located at latitude and longitude 16.8347 and 74.3148, respectively, of Peth Vadgaon Kolhapur, Maharashtra. The target of designing this system is to find the optimal net present cost (NPC), cost of energy, emissions, and monthly electricity production. The motive of this paper is to give optimal solution to the problems of energy crisis in the globe. In current scenario, the non-renewable sources are available in plenty amount to fulfill our increasing demand. Considering the above information, we have made an effort to analyze advantage of distributed generation. If we use only solar power or wind power, it can fluctuate and is not a reliable source of energy. The combination of solar and wind energy sources with diesel generator provides a reliable generation and a constant source of energy flow for the designed system. The main task of this research work is to analyze the possibility of solar–wind–diesel hybrid power system by maximizing the use of non-conventional generation system while minimizing the total system cost.

Keywords Distributed generation · HOMER software · Optimal cost Renewable energy

1 Introduction

In recent era, there is a great scope for advancement in power generation considering environment-friendly technology such as renewable energy technology which is technically viable and environment friendly. All over the world, effort is being made to study the feasibility of renewable energy incorporated within hybrid system which will prove to be the best alternative of diesel generator. In village, hybrid

P. Kumar (✉) · S. Deokar
Zeal College of Engineering and Research, Pune, India
e-mail: Prashant2685@gmail.com

A. Konkani et al. (eds.), *Advances in Systems, Control and Automation*,
Lecture Notes in Electrical Engineering 442, https://doi.org/10.1007/978-981-10-4762-6_9

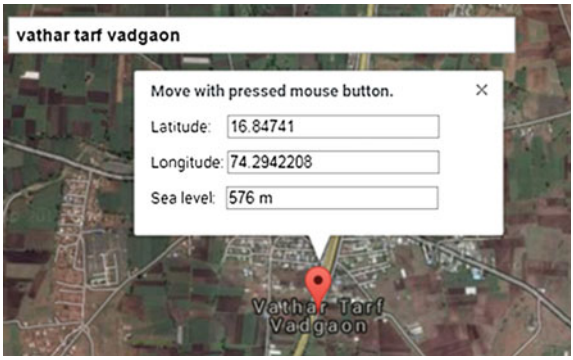

Fig. 1 Coordinates location, AMGOI, Vathar

energy system offers an attractive and practical solution to meet electrical power demand in rural communities around the globe [1–3].

Main drawbacks of the stand-alone system are irregular delivery of power due to fluctuations of energy as provided by free source of energy. This can be a bottleneck in different areas, such as agriculture and factory, where reliable and continuous supply are required. Such types of problems can be solved by using stand-alone hybrid systems. A hybrid power system usually consists of more than two energy sources to increase the efficiency and reliability. In comparison with conventional sources, hybrid system uses the better features of individual energy resource. The electricity generated by hybrid system has quality as par with conventional ones, with a wide power range.

The major advantage of a hybrid system is that it is continuous and reliable. At any time of the day, one of the power sources will be usually at higher level, even if other is running at lower level. Solar panel is less effective on cloudy and windy days so it will produce lower energy levels, while wind generator may be producing a lot of energy. Similarly, for wind generation, the main issue is location of the site, where the flow of wind is irregular. The major use of non-conventional energy is that the long-term energy prices are reduced, and diesel generator combination is used as backup in emergency such as high loads or low renewable power availability.

This case study is done on the Electrical Engineering Department of AMGOI, Kolhapur, one of the remote areas where grid connectivity/extension is difficult; in our case study, Vathar and Kolhapur areas are considered whose latitude is 17° 53′ 0″ North and longitude is 74° 9′ 0″ East (Fig. 1).

1.1 Advantages of Distributed Generation

The basic tangible benefits of distributed generation are as follows:

- Using prefabricated standardized components helps in easy and faster installation.
- For long distance, high-voltage transmission is economical.

- Eco-friendly means reduction in emission using non-conventional energy sources.
- Using non-conventional sources, the running cost remains constant over a period of time.
- Less complexity encourages possibility of user-operator participation.

1.2 HOMER Software

HOMER is the acronym for Hybrid Optimization Model for Electric Renewable. It is the most widely used software and developed in 1993 [1]. HOMER does both optimization and sensitivity analysis. With the help of HOMER, system performs the energy balance calculation considering several numbers and sizes of component. A sorted list of configuration result based on the total net present cost (TNPC) has been displayed on the software. Sensitivity analysis determines varying factors such as wind speed and fuel cost. HOMER displays simulation results in a tabular and graphical form on the basis of possible configurations. These results assist in comparison with different configurations and evaluation based on their economic merits [3–5].

2 Methodology

In this paper, the proposed simulated hybrid renewable energy system consists of wind turbine, photovoltaic (PV) array with power converter, battery, and diesel generator. In case of an emergency, battery is used as a backup unit for the considered system that acts as a storage medium. The considered system is designed specifically for an off-grid continuous power supply (24/7) to ATM machine. The data required for solar and wind resources for the automatic teller machine site were taken from online data of NASAs Meteorological department. The survey has been made to plot a graph between daily load profile and energy consumption of ATM. Simulations, optimization, and sensitivity analysis are the key tasks of HOMER software that plays an important role in determination of optimized solution [6]. These main tasks of the HOMER software are discussed below.

2.1 HOMER: Simulation

The proposed system is designed on the basis of the selection of components by design engineer. Here, the considered components are PV array, wind turbine, diesel generator with battery, and converter for the purpose of analysis [4, 5]. After simulation, it determines the best optimal system configuration which is suitable to

provide the energy demand. HOMER will simulate the designed system based on the estimation of NPC [3, 4].

2.2 HOMER: Optimization

The best optimal possible system configuration has been obtained by performing search operation after simulation process. A list of configuration result displayed in a sorted form considers total net present cost (TNPC). HOMER analyzes the different possible configurations of system according to TNPC. However, the sensitivity variable selected by the designer can impact the system configuration which is based on TNPC.

2.3 HOMER: Sensitivity Analysis

For a sensitive analysis, software shows that how the outputs of the problem is related with inputs. The HOMER software will perform the iterations to get optimal result for each. Various system configurations of designed hybrid renewable energy will be presented in a tabular form considering cost-wise analysis in an ascending order of TNPC. The designed energy system having lowest TNPC will be considered as an optimal solution [2, 4, 5].

3 Simulation MODEL

3.1 Load

The load profile is based on our EE department load of AMGOI, Vathar. Load calculation is done on day where maximum load occurs as compared to other days in week. Figure 2 illustrates load profile. In the mentioned case study, the majority of the load occurs between 10 am and 5 pm. For the rest of the day, there is a small base load of 0.2 kW (Figs. 3, 4, 5, 6 and 7).

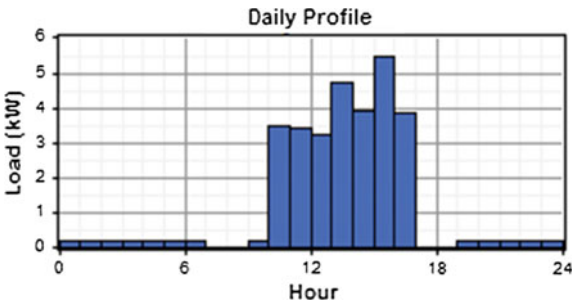

Fig. 2 Illustrated by HOMER

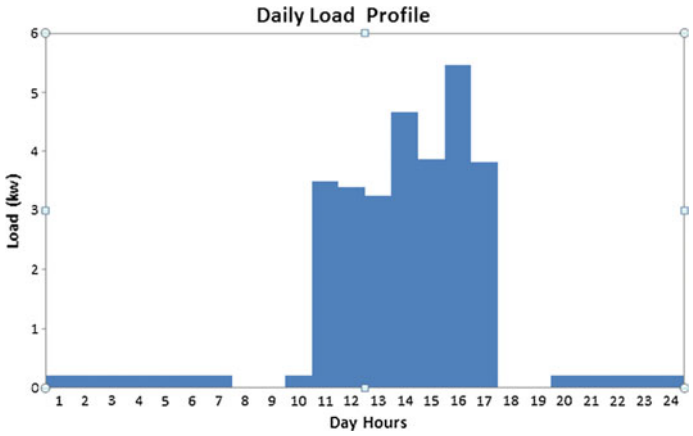

Fig. 3 Hourly load profile

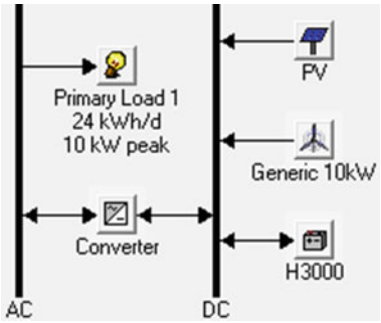

Fig. 4 SLD of solar–wind hybrid system

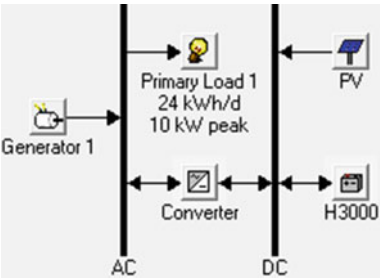

Fig. 5 SLD of solar–diesel generation system

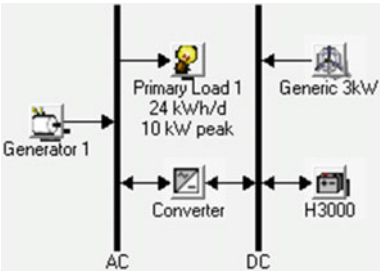

Fig. 6 SLD of wind–diesel generation system

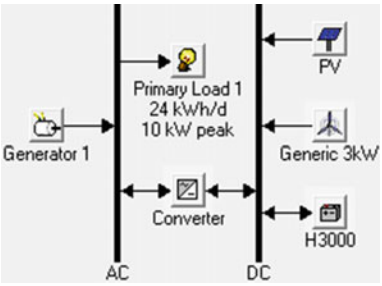

Fig. 7 SLD of solar–wind–diesel system

4 Optimization Result

In the hybrid renewable energy system, for every selected sensitivity variable, the optimization process will be repeated by the HOMER software.

Various optimization results with different configurations are shown below.

From the optimization result there are two best optimal system designed solutions but best solution in which components are solar, generator, converter, and battery as shown in the form of categorized optimal result of solar–wind–diesel system (Table 1).

5 Conclusion

In this work, we designed four hybrid systems: solar–wind, solar–diesel, wind–diesel, and solar–wind–diesel. According to the NPC, ranks are given to all optimization systems used in the case study. Economic values are calculated for the purpose of electrifying Electrical Engineering Department of AMGOI and finding the optimal net present cost (NPC), cost of energy, emissions, and monthly electricity production. Based on these values and comparisons, the optimal system is solar–wind power system. The cost of energy and the net present cost of the solar–wind hybrid system are lesser than other systems because operating and

Table 1 Comparisons of hybrid systems

PV (kW)	G3	Label (kW)	H3000	Conv. (kW)	Initial Capital	Operating Cost ($/yr)	Total NPC	COE ($/kWh)	Ren. Frac.	Diesel (L)	Label (hrs)
10		6	2	8	$ 25,864	960	$ 38,135	0.339	0.92	492	347
10		6	2	12	$ 26,196	954	$ 38,386	0.341	0.93	484	338
10		6	2	15	$ 26,445	960	$ 38,720	0.344	0.93	484	338
12		6	2	8	$ 30,056	767	$ 39,866	0.355	0.95	389	275
12		6	2	12	$ 30,388	763	$ 40,138	0.357	0.95	382	267
10		4	8	8	$ 33,584	528	$ 40,334	0.359	0.95	289	228
12		6	2	15	$ 30,637	769	$ 40,472	0.360	0.95	382	267
10		8	2	8	$ 26,364	1,112	$ 40,585	0.361	0.92	546	333
10		4	8	12	$ 33,916	524	$ 40,617	0.361	0.95	283	218
10		6	8	8	$ 34,084	519	$ 40,724	0.362	0.95	285	153
10	2	6	2	8	$ 29,254	905	$ 40,821	0.363	0.95	385	286
10		8	2	12	$ 26,696	1,106	$ 40,837	0.363	0.92	537	326
10		6	8	12	$ 34,416	507	$ 40,901	0.364	0.95	276	142
10		4	8	15	$ 34,165	531	$ 40,951	0.364	0.95	283	218
10	2	6	2	12	$ 29,586	904	$ 41,144	0.366	0.95	379	280
10		8	2	15	$ 26,945	1,113	$ 41,171	0.366	0.92	537	326
10		6	8	15	$ 34,665	514	$ 41,235	0.367	0.95	276	142
10		8	8	12	$ 34,916	508	$ 41,414	0.368	0.95	277	111
10		8	8	8	$ 34,584	536	$ 41,433	0.368	0.95	296	124
10	2	6	2	15	$ 29,835	911	$ 41,478	0.369	0.95	379	280
10		8	8	15	$ 35,165	515	$ 41,748	0.371	0.95	277	111
10	3	6	2	8	$ 30,949	903	$ 42,492	0.378	0.95	347	260
10	3	6	2	12	$ 31,281	902	$ 42,812	0.381	0.96	340	254
12		8	2	12	$ 30,888	934	$ 42,825	0.381	0.95	445	279
12		8	2	8	$ 30,556	961	$ 42,837	0.381	0.95	462	294

PV (kW)	G3	Label (kW)	H3000	Conv. (kW)	Initial Capital	Operating Cost ($/yr)	Total NPC	COE ($/kWh)	Ren. Frac.	Diesel (L)	Label (hrs)
10		6	2	8	$ 25,864	960	$ 38,135	0.339	0.92	492	347
10	2	6	2	8	$ 29,254	905	$ 40,821	0.363	0.95	385	286
12	4	6		8	$ 34,096	9,796	$ 159,324	1.417	0.72	4,508	4,776
12		8		8	$ 27,816	14,349	$ 211,247	1.879	0.59	6,774	5,415

S. No.	Parameters	Solar-wind	Solar-diesel	Wind-diesel	Solar-wind-diesel
1	Net present cost ($)	28,111	35,817	72,572	40,821
2	Cost of energy ($/Kwh)	0.250	0.319	0.646	0.363
3	Capital cost ($)	25,199	24,035	18,214	29,254
4	Electricity Production (kWh/yr)	18,179	14,118	13,664	18,620
5	Excess electricity production (kWh/yr)	8,036	3,897	3,773	8,649
6	Production of emission	No	Yes	Yes	Yes

1$ is equal to 66.33 Rupees

maintenance costs are less and fuel is not required. Hence, solar–wind system is best optimal solution than solar–diesel hybrid system.

The results obtained from the HOMER in our case study give the optimized initial capital cost, 25,199$; net present cost, 28,111$; and cost of energy, 0.250$.

References

1. Kumar, P.: Optimal design configuration using HOMER. Elsevier Procedia Technol. **24**, 499–504 (2016)
2. Kumar, P., Bade, A., Patil, D., Jadhav, A., Patil, S.: Optimal design solution for distributed power generation using HOME. In: 3rd International Conference on Electronics and Communication System, pp. 1048–1051 (2016)
3. Kumar, P.: Analysis of hybrid systems: software tools. In: International Conference on Advances in Electrical, Electronics, Information, Communication and Bio-Informatics (AEEICB16), pp. 329–332 (2016)
4. Zoulias, E.I., Lymberopoulos, N.: Techno-economic analysis of the integration of hydrogen energy technologies in renewable energy-based stand-alone power systems. Renew. Energy **32** (4), 680–696 (2007)
5. Ellabban, O., Abu-Rub, H., Blaabjerg, F.: Renewable energy resources current status, future prospects and their enabling technology. Renew. Sustain. Energy Rev. **39**, 748–764 (2014)
6. Markvart, Tomas: Sizing of hybrid PV-wind energy system. Sol. Energy **57**(4), 227–281 (1996)
7. Elhadidy, M.A., Shaahid, S.M.: Parametric study of hybrid (wind + solar + diesel) power generating systems. J. Renew. Energy **21**, 129–139 (2000)

Designing of a Half-Bridge Converter for Lead-Acid Battery Charger

Jitendra Singh Tamang, Rachit Saxena, Snigdha Kalita and Akash Kumar Bhoi

Abstract In our daily life, power electronic circuits such as inverters, UPS, and SMPS comprise of AC–DC converters and DC–DC converters are widely used. The chapter, however, makes an effort to present a charging circuit comprising of transistors, control circuit, and rectifiers for a discharged battery to make it chargeable which can be used in electric vehicle and mobile applications. In this chapter, we have tried designing a converter using different softwares viz OrCAD, MATLAB, and PROTEUS and tried calculating the different parameters related to each design. Further based on the obtained results, we have done the hardware implementation of the converter. Almost all the designing methods encourage the implementation of different types of SMPS converters because of higher efficiency and greater transformer utilization factor (TUF). Among these converters, half-bridge and full-bridge converters have enormous and important role in the field of power electronics and industry application. The converters can be designed and implemented in different ways depending on the area of application.

Keywords AC–DC converters · DC–DC converters · Battery charging Half-bridge converters · Power electronic circuits

J.S. Tamang (✉) · R. Saxena (✉) · S. Kalita (✉)
Department of E&C Engineering, Sikkim Manipal Institute of Technology (SMIT), Majitar, India
e-mail: js.tamang@gmail.com

R. Saxena
e-mail: rachitsaxena93@yahoo.co.in

S. Kalita
e-mail: snigdhakalita08@gmail.com

A.K. Bhoi (✉)
Department of E&E Engineering, Sikkim Manipal University, Sikkim Manipal Institute of Technology (SMIT), Majitar, India
e-mail: akash730@gmail.com

A. Konkani et al. (eds.), *Advances in Systems, Control and Automation*,
Lecture Notes in Electrical Engineering 442, https://doi.org/10.1007/978-981-10-4762-6_10

1 Introduction

The converters always play a vital role especially in the field of industry and automation. However, only few converters make their significance known based on their different factors like form factors, ripple factors, power conversion efficiency [1, 2]. The major part of electronic and automation applications are its batteries and filter circuits. Therefore, the rectifying and charging circuit for a particular electronic device is very essential for any electrical and electronic system. For charging purposes in the area of power electronics, isolated DC–DC converters [3, 4] are used. The DC–DC converters or DC–AC converters or AC–DC converters are chosen in such a way that their conversion percentage makes them more efficient to use for different technology.

The different types of converters mainly are a kind of SMPS. Starting from half-bridge converters [2, 5] to push–pull converters and then to full-bridge converters, each has its own power consumption and efficiency. However, among them half-bridge converter topology is extremely used in power electronics and basic electronic applications. The converter is capable enough to provide an output power utilization of more than 450 W.

In recent times, apart from designing a simple half-bridge converter, a particular concept of switching characteristics of a transistor is also taken into consideration. More emphasis is given on their designing and electrical properties rather than implementing them in charging and rectifying circuits. Apart from amplification, switching purpose is also being highlighted if one designs a converter. The only possibility is switching characteristics of a power semiconductor device can be controlled and thus maintaining a proper efficiency. Though the charging circuit proposed by us follows constant current principle, the another method of charging a discharged battery is by using a bidirectional converter [6, 7]. The main objective of the project is to study the purpose of isolated DC–DC converters and design and implement a battery charging circuit using different formulae [1].

2 Methods

2.1 Proposed Block Diagram

Before going into the methods of how we have tried designing and making a prototype of the battery charger, at first we should know why the half-bridge converters are preferred among other converters viz flyback, forward, and full-bridge converters. The reasons behind choosing such converter are as follows:

1. The circuits of half-bridge converters are simpler.
2. It is more cost-effective (low cost).
3. Due to the presence of capacitors, the output in the on time of the transistors increases efficiency to 90% range.

4. Physical size of the circuit is small.
5. Power density is more.
6. Square wave frequency is twice that of other converters (e.g., forward converters).
7. For low- and medium-power applications, half-bridge converters provide a better solution than full-bridge converters which are generally used for high-power applications ranging from several hundred to thousand kilowatts (kWs).

The simplest block diagram for the proposed half-bridge converter is given in Fig. 1.

2.2 *Simulation of the Proposed Block Diagram Using Different Software Tools*

The designing and calculation of different parameters of the half-bridge converter was being done using software tools like OrCAD, PROTEUS, and MATLAB. The proposed block diagram was being tested using PROTEUS software tool as given in Fig. 2.

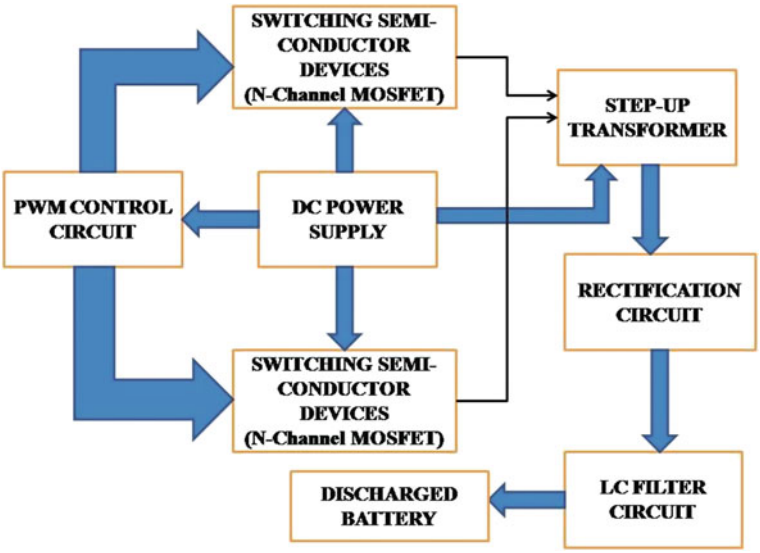

Fig. 1 Proposed block diagram

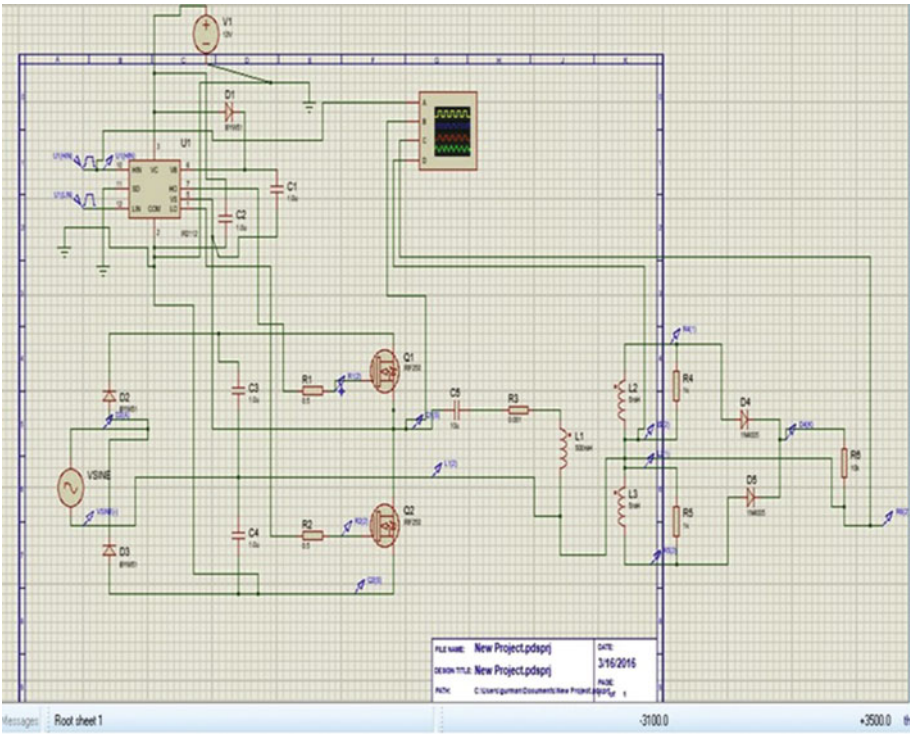

Fig. 2 Simulated proposed model

3 Results and Discussions

3.1 Using Proteus Software Tool

The output of the simulated model taking the PROTEUS software tool is shown in Fig. 3.

Here, the yellow-lined pulse denotes the pulse generated by the PWM IC. Blue output waveform denotes the wave generated by the transistor Q_1. Pink line denotes the current generated across the inductor that is the inductor current. And green line denotes the output waveform across the load which a straight line that means we can see that the output is a regulated DC pulse.

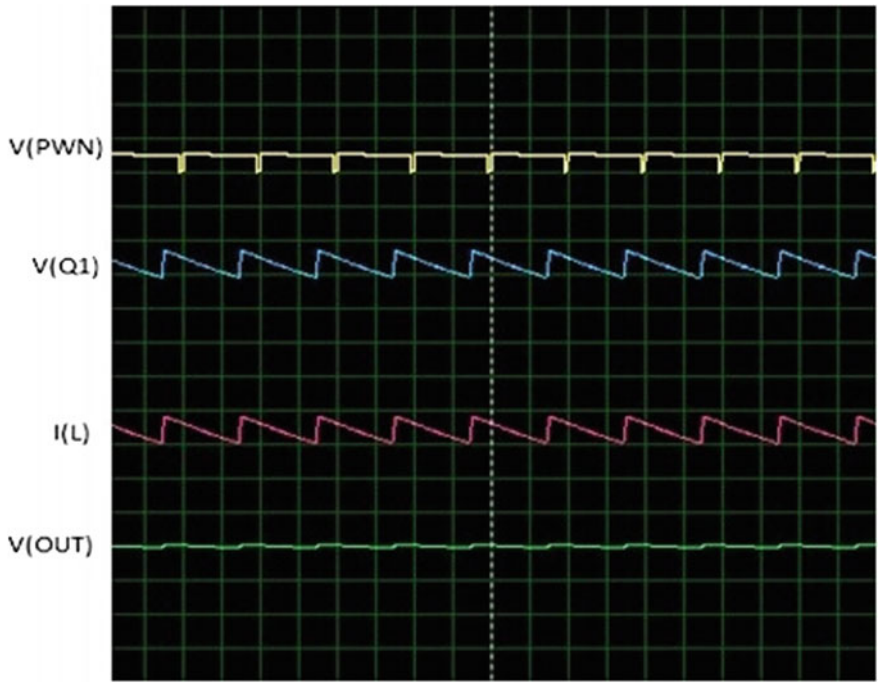

Fig. 3 Output waveforms of the simulated model

Table 1 Calculated values of different parameters in different software tools

Sl. No.	Parameters defined	Software tools used		
		OrCAD	MATLAB	PROTEUS
1	Time period (T)	0.04 ms	0.1 µs	2 ms
2	On-time period (t_{ON})	0.018 ms	0.042 µs	1.9 ms
3	No. of N_P and N_S	N_P = 31 turns N_S = 23 turns	N_P = 102 turns N_S = 87 turns	N_P = 2142 turns N_S = 1071 turns
4	Resonant frequency (f_r)	237.25 Hz	67581.85 Hz	71.17 Hz

3.2 *Calculation of Different Parameters Using Different Software Tools*

Based on the software tools used viz OrCAD, PROTEUS, MATLAB and taking the help of the proposed block diagram, the parameters like time period (T), on-time period (t_{ON}), no. of turns in the primary (N_P), secondary side (N_S), and resonant frequency (f_r) are being calculated, and a comparison is being drawn among all the calculated parameters [1].

Table 1 shows the comparison of the above-mentioned parameters being calculated using different software tools.

From the values of the above table, we can notice that each and every parameter values play a significant role for designing a half-bridge converter. The OrCAD software has a very less time period and less no. of turns required in the primary side and secondary side of the transformer but has more resonant frequency than the one calculated in the PROTEUS software tool. The maximum resonant frequency which we calculated is in MATLAB software tool, but the drawback lies in the less time period and on-time period as compared with the other software tools. Therefore, we can notice that for different software tools, we get different parametric values which will be helpful enough for us to design different kinds of half-bridge converters. Based on the calculated values and taking the help of the proposed block diagram, we were being able to have a hardware implementation of the half-bridge DC–DC converter which can be used as a lead-acid battery charger.

4 Conclusion

The closed loop hardware implementation and simulation using various software of the half-bridge converter with calculations and different ratings was done. The development of a converter for charging a discharged battery taking the concept of half-bridge converter with several parameters was completed. The assistance of a discharged battery was taken wherein it was being charged to around 15 V to understand the importance of half-bridge converter. Also, apart from charging a discharged battery, the half-bridge converter also has a rectifier circuit to minimize and remove any ripples present after conversion. This feature makes it idle to be utilized in automation and electronic fields.

Throughout the implementation of the converter, we gained the knowledge of how different simulating software tools help us to get the desired values. Henceforth, the proposed block was implemented in PROTEUS and expected outputs were obtained, and later the same was modified to achieve desired results for the hardware implementation. Apart from UPS, the SMPS also operates like half-bridge converters and full-bridge converters. Hard switching SMPS also finds its role in the power switches in order to have higher power efficiency. To achieve high-efficiency circuit configuration, zero voltage switching (ZVS) and zero current switching (ZCS) are being implemented making the half-bridge converter just as an alternative option. Therefore, to achieve higher power output, one concentrates mainly on full-bridge converters as it is used for high-power applications ranging from several hundred to thousand kWs even though it is complex and not user-friendly.

References

1. McLyman, C.W.T.: Designing A Half Bridge Converter Using A Core Master E2000Q Core. http://www.coremaster.com/appnotes/an108.pdf
2. Ou, S.Y., Li, J.C., Lu, J.K.: Small signal analysis and controller design of a half-bridge single stage power converter, PEDS, pp. 284–287 (2009)
3. Agarwal, V., Sundarsingh, V.P., Bontemps, S., Grafham, D.: A smart power converter module for buck applications operating at high input power factor. IEEE Trans. Power Electron. **5**(4), 1202–1207 (2002)
4. Sivaprasad, A., Deepa, K., Mathew, K.: Half bridge converter for battery charging application, Int. J. Eng. Res. Appl. **2**(4), 994–999 (2012)
5. Ou, S.Y., Hsiao H.P., Tien, C.H.: Analysis and design of a prototype single-stage half-bridge power converter. In: 5th IEEE Conference on Industrial Electronics and Applications, pp. 1168–1173 (2010)
6. Jain, M., Daniele, M., Jain, P.K.: A bidirectional DC–DC converter topology for low power application. IEEE Trans. Power Electron. **15**(4), 595–606 (2000)
7. Odelu, P., Vinay Kumar, K., Kumaraswamy, D.: A novel control technique for buck-boost controller for battery application. Trans Power Control IOJETR Trans. Power. Eng. **18**, 327–343 (2014)

A Comparative Analysis of Determination of Design Parameters of Boost and Buck–Boost Converters Using Artificial Intelligence

Ipsita Das and Moumi Pandit

Abstract Conventionally, mathematical calculations based on formulas are required to model and design any converter for software or hardware implementation. However, in this chapter, an alternative method has been suggested to replace the conventional method of formula-based mathematical calculations by developing a hybrid model known as adaptive neuro-fuzzy inference system (ANFIS). It is a hybrid system which combines two most important methodologies of soft computation namely artificial neural network and fuzzy logic. It has been used as the tool in MATLAB platform to determine the design parameters of Boost and Buck–Boost converters. The alternative suggested in this chapter also focuses on reduction of computational time and susceptibility toward human error in mathematical calculation.

Keywords ANFIS · Buck · Buck–Boost · Hybrid · MATLAB

1 Introduction

To understand and analyze any system, proper designing and modeling is very important. Modeling and designing also helps to anticipate the behavior and nature of the system in the future. Various soft computing methods based on artificial intelligence have emerged as effective tool to simplify the process of modeling and designing of complex systems. One such efficient hybrid method which integrates neural network and fuzzy logic is ANFIS. Fuzzy logic helps to deal with uncertainties and imprecision with the help of linguistic variables which are the fuzzy if-then rules while neural network presents the ability of learning capability and self

Ipsita Das · Moumi Pandit (✉)
Department of Electrical and Electronics Engineering,
Sikkim Manipal Institute of Technology, Sikkim Manipal University, Majitar, India
e-mail: moumi_pandit@yahoo.co.in

Ipsita Das
e-mail: das.ipsita28@gmail.com

A. Konkani et al. (eds.), *Advances in Systems, Control and Automation*,
Lecture Notes in Electrical Engineering 442, https://doi.org/10.1007/978-981-10-4762-6_11

adaptability. A Takagi–Sugeno-type ANFIS model has been considered in this chapter. The ANFIS model is an adaptive network consisting of nodes which are interlinked with each other. Parameters are associated with each node, and they change in accordance with the membership function associated with them throughout the learning process. Various artificial models have been developed using soft computation techniques to implement them as controllers in various converters [1, 2], but in this proposed work, these artificial models have been successfully implemented for designing converters. With the increase in demand of regulated power supply, DC–DC power converters have emerged as an important trend in power electronics. Boost and Buck–Boost converters have been considered for modeling and designing in this chapter. Both the converters convert unregulated DC input voltage to regulated output DC voltage. Boost converter produces regulated output voltage which is greater than the input voltage [3, 4], whereas the Buck–Boost converter produces either increased or decreased output voltage magnitude for a given input voltage [5].

2 Design of Converter Models

The circuit diagram of the boost converter is shown in Fig. 1. The percentage of conversion ratio of output voltage (V_o) to input voltage (V_{in}) also called duty cycle (D) of Boost converter can be varied from 0 to 100% and is given by the relation as $V_o = V_{in}/(1 - D)$.

The circuit arrangement of the Buck–Boost converter is shown in Fig. 2. This converter inverts the polarity of the output voltage, and therefore, it is also

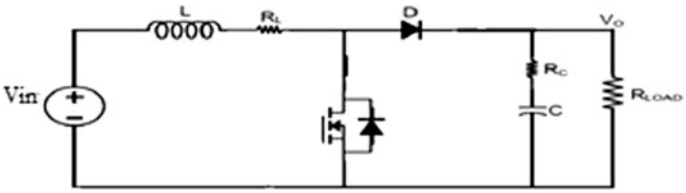

Fig. 1 Circuit diagram of boost converter

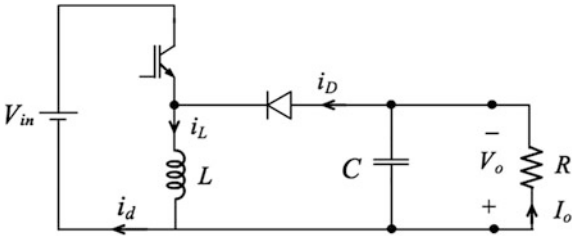

Fig. 2 Circuit diagram of Buck–Boost converter

considered as inverting converter. The conversion ratio of output voltage (V_o) to input voltage (V_{in}) of Buck–Boost converter is given by the relation:

$$V_o = V_{in}\,[-D/(1-D)]$$

When the duty cycle is less than 50%, the converter works in Buck mode, and when the duty cycle is between 50 and 100%, the converter works in boost mode. At 50% duty cycle, the converter gives an output which is equal to the input voltage.

2.1 Simulation of Boost and Buck–Boost Converters

The parameters listed in Table 1 have been used to simulate the open-looped DC–DC boost converter and open-looped Buck–Boost converter in MATLAB platform. The PWM block provides the pulse to the gate of the MOSFET switch. The PWM block used for both the converters has been simulated as shown in Fig. 3, and the simulated model of boost and Buck–Boost converters has been shown in Figs. 4 and 5, respectively.

Table 1 Values of parameters of the Simulink model of Boost and Buck–Boost converters

Parameters	Value
Inductor (L)	161.95 µH
Parasitic inductive resistance (R_l)	80 mΩ
Capacitor (C)	220 µF
Parasitic capacitive resistance (R_c)	5 mΩ
Load (R)	10 Ω
Switching frequency (F_s)	100 kHz
Duty cycle (D)	50%
Input voltage	24 V

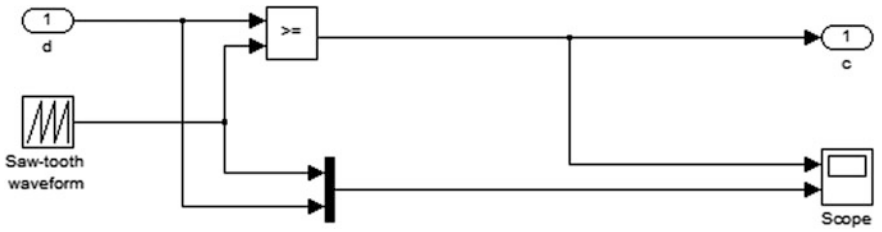

Fig. 3 PWM block of Boost and Buck–Boost converters

3 Development of the ANFIS Model

For the purpose of design and development of the ANFIS model, the most important steps are collection of data, loading of data, and training the data sets. The steps are discussed in details as follows:

- Collection of data: The Simulink model of the open-loop boost and Buck–Boost converters as shown in Figs. 4 and 5, respectively, has been used to collect the required data of output voltage. A total of 646 sets of simulated output data of Boost and Buck–Boost converters have been obtained by varying one of the input design parameters keeping the rest constant. The input design parameters and their range of variations of values for both the converters have been listed in Table 2.

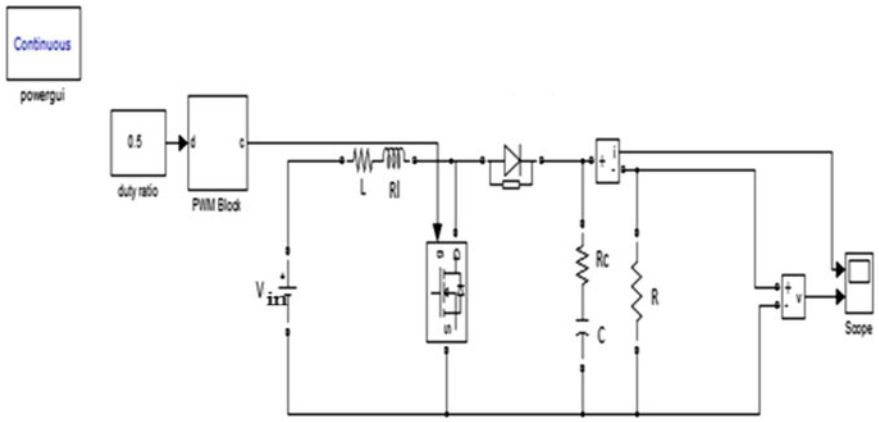

Fig. 4 Simulink model of Boost converter

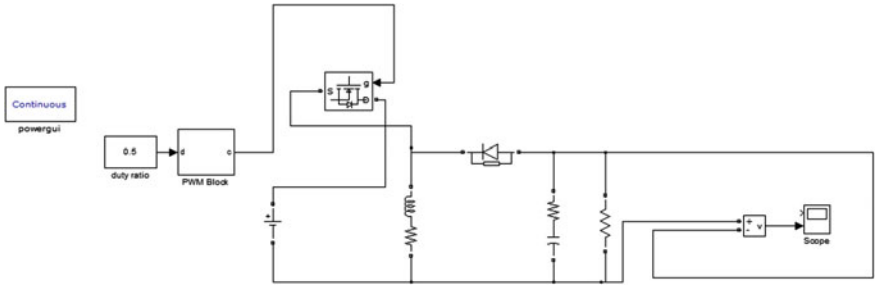

Fig. 5 Simulink model of Buck–Boost converter

Table 2 Circuit parameters with the range of variation of their rating

Parameters	Range
Inductance (L)	1000.95–1 μH
Capacitance (C)	300–0.1 μF
Duty ratio (D)	0.1–1
Switching frequency (F_s)	150–1 kHz

Table 3 Particulars of ANFIS structure

Name of particulars	Value
No. of nodes	36
Total number of parameters	40
Training data pair	646
Fuzzy rule	8

- Loading of data: In this chapter, the input and output data sets obtained by simulating the converter models have been arranged in the form of matrix where the output data set occupied the last row in the matrix.
- Training of data sets: For the training process of the ANFIS model of the two converters, the adaptive networks have been provided with input pattern which is simulated output voltage value (V_o) and an output pattern which consists of seven parameters, i.e., input voltage (V_{in}), inductance (L), parasitic inductive resistance (R_l), capacitance (C), parasitic capacitive resistance (R_c), switching frequency (F_s), and duty ratio (D). To evaluate the variation between the targeted voltage (V_o) and the actual output voltage given by the ANFIS model, hybrid learning algorithm consisting of least square method and back propagation technique was implemented [4, 6–10]. The learning process continued till the accuracy of the ANFIS output was maximum. The number of epoch for the training process was kept as 50. The training particulars of the developed ANFIS models for the two converters in this chapter have been listed in Table 3.

3.1 Algorithm for the Development of ANFIS Structure

MATLAB software was used to develop the ANFIS model. The algorithm for the developed program has been mentioned below:

Step 1. The data pairs consisting of input voltage (V_{in}), inductance (L), parasitic inductive resistance (R_l), capacitance (C), parasitic capacitive resistance (R_c), switching frequency (F_s), duty ratio (D), and load (R) along with the corresponding output voltage data pair (V_o) have been loaded.

Step 2. Command ‘genfis1’ has been used to generate the Sugeno-type FIS structure with default input and output membership functions.

Step 3. Generalized bell membership function (gbellmf) has been chosen to characterize the input parameter fuzzy sets.

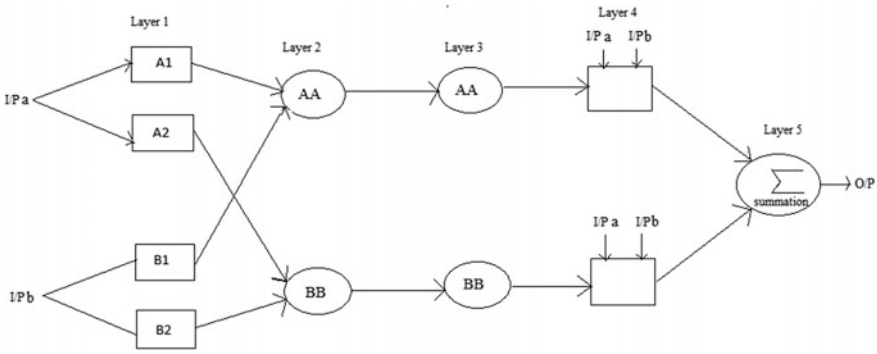

Fig. 6 Generalized structure of ANFIS

Step 4. The total number of membership functions and the number of epoch have been set as 50.
Step 5. To train the developed FIS structure, command 'trndata' has been used.
Step 6. To obtain the required output, the designed parameters corresponding to its output voltage have been computed using command 'evalfis' which performs the fuzzy inference calculations.

During the training process, the parameters related to the MFs changed throughout the learning process till the error percentage is negligible. After the FIS structure has been generated and trained using the appropriate training data. A five-layer generalized ANFIS structure has been developed, where a hybrid learning algorithm combining the least square technique and back propagation technique has been implemented. The general ANFIS model is shown in Fig. 6. Five layers have been represented, namely the fuzzy layer, the product layer, the normalized layer, the defuzzy layer, and the output layer in the ANFIS structure [11–16].

4 Result and Analysis

To validate the developed ANFIS model in this chapter, any desired input voltage different training data set has been provided to the ANFIS model, and corresponding values of 8 design parameters were collected as output. The design parameters obtained from the ANFIS model for the corresponding user inputs were then used to simulate the Simulink model shown in Figs. 4 and 5 accordingly, and its corresponding output for both Boost and Buck–Boost converters was recorded which has been mentioned in Tables 4 and 5, respectively.

Table 4 ANFIS-generated design parameters for boost converter with their ratings for the corresponding user input voltage

Input voltage (V)	ANFIS-generated parameters						
	L (μH)	C (μF)	R_l (mΩ)	R_c (mΩ)	F_s (kHz)	D	V_{in} (V)
26.2424	161.0316	220.6357	80.0009	5.0001	99.7908	0.1615	24.0003
30.0001	156.1214	213.7146	80.0011	5.0001	99.1820	0.2138	24.0003
31.5179	161.7497	224.0157	80.0014	5.0001	99.9231	0.2608	24.0004
32.2103	165.9603	228.5439	80.0006	5	100.5059	0.2860	24.0002
33.8876	168.4860	227.5748	79.9992	5	100.7918	0.3303	23.9998
34.5421	166.9057	224.3051	79.9991	4.9999	100.5515	0.3447	23.9997
35.7589	162.5734	217.2525	79.9992	4.9999	99.9566	0.3730	23.9997
36.4961	159.7027	212.9682	79.9993	5	99.5924	0.3916	23.9998
42.5770	179.0383	264.7260	80.0009	5.0001	103.5514	0.4783	24.0003
43.8115	198.2968	286.6351	80.0004	5	104.8138	0.4963	24.0001
44.5579	203.5351	283.8720	80.0001	5	104.0423	0.5070	24
45.1234	203.3826	274.1546	80	5	102.7631	0.5133	24
46.8799	185.5831	218.4532	79.9999	5	96.5358	0.5255	24
47.3390	181.7893	212.3038	80	5	96.8371	0.5299	24
48.0240	178.2253	199.5241	80	5	93.8697	0.5302	24

Table 5 ANFIS-generated design parameters for Buck–Boost converter with their ratings for the corresponding user input voltage

Input (V)	ANFIS-generated parameters						
	L (μH)	C (μF)	R_l (mΩ)	R_c (mΩ)	F_s (kHz)	D	V_{in} (V)
26.2424	160.0326	218.5327	80	5	99.8909	0.5093	24
30.0001	156.1214	211.4136	80	5	99.9982	0.5238	24
31.5179	159.5949	223.5187	80	5	100.2241	0.5274	24
32.2103	165.9603	226.4711	80	5	100.5091	0.5299	24
33.8876	169.6820	228.3172	80	5	100.6591	0.5373	24
36.4961	159.7027	213.6162	80	5	99.7934	0.5661	24
42.5770	180.2481	265.7061	80	5	104.4764	0.6412	24.0001
43.8115	196.7998	287.1352	80	5	105.8834	0.6755	24
45.1234	205.6816	275.5013	80	5	101.0988	0.6933	24
46.8799	183.6841	217.1158	80	5	96.0057	0.6956	24
47.3390	181.7798	210.5381	80	5	96.9923	0.7099	24
48.0240	179.8765	195.4152	80	5	95.7644	0.7288	24

The percentage error between the output obtained using ANFIS-generated parameters and the user input of the Boost and Buck–Boost converters has been shown in Tables 6 and 7, respectively, where the percentage error is calculated as:

Percentage error = [(Simulated value − value obtained using ANFIS-generated parameters)/Simulated value] * 100.

Table 6 Percentage error in simulated output voltage using ANFIS-generated parameters corresponding to the user input voltage for boost converter

User input voltage (V)	Simulated output voltage using ANFIS-generated parameters (V)	Percentage error (%)
26.2424	27.4513	4.40
30.0001	29.2543	2.55
31.5179	31.0730	1.43
32.2103	32.1385	0.22
33.8876	34.1873	0.87
36.4961	37.4599	2.57
42.5770	43.1912	1.42
43.8115	44.5831	1.73
45.1234	45.9793	1.86
46.8799	47.0418	2.1184
47.3390	47.2903	0.1029
48.0240	47.3387	1.4476

Table 7 Percentage error in simulated output voltage using ANFIS-generated parameters corresponding to the user input voltage for Buck–Boost converter

User input voltage (V)	Simulated output voltage using ANFIS-generated parameters (V)	Percentage error (%)
26.2424	27.3367	4.17
30.0001	30.6782	2.26
31.5179	30.9225	1.87
32.2103	31.6534	1.72
33.8876	34.3354	1.32
36.4961	37.4599	2.64
42.5770	43.6754	2.58
43.8115	43.2831	1.20
45.1234	45.2354	0.24
46.8799	46.9067	0.06
47.3390	47.9865	1.36
48.0240	50.0021	4.11

5 Conclusion

The ANFIS model developed in this chapter can be established as an effective alternative which eliminates the real-world problem of hard computation and formula-oriented time-consuming mathematical computations to determine the design parameters of any converter. For every new desired output voltage of a specific range of the converters, one single model of the developed ANFIS structure can compute all the necessary design parameters within a very short time and without having to go through long mathematical calculations repeatedly. Also with

numerous number of soft computation methods like genetic algorithm and artificial intelligence, ANFIS holds an edge over them as the complexity of evaluation, learning, and defuzzification in ANFIS is simpler. The output of the developed ANFIS model also holds advantage over other soft computation method as it implements hybrid algorithm which results in optimized, less error-prone output.

References

1. Jafari, M., Imanieh, M., Malekjamshidi, Z.: Design, simulation and implementation of a full bridge series-parallel resonant DC–DC converter using ANN controller. In: Control and Communications, International Siberian Conference on Control and Communications SIBCON. pp. 97–103 (2011)
2. Rajarajeswari, N., Thanushkodi, K.: Design of an intelligent bidirectional DC–DC Converter with half bridge topology. Eur. J. Sci. Res. **22**, 90–95 (2008)
3. Bhat, S., Nagaraja, H.N.: Effect of parasitic elements on the performance of buck-boost converter for PV systems. Int. J. Electr. Comput. Eng. **4** (2014)
4. Jeong, G.J., Kim, I.H., Son, Y.I.: Design of an adaptive output feedback controller for a DC/DC boost converter subject to load variations. Int. J. Innov. Comput Inf. Control. **7**, 791–803 (2011)
5. Lozano, C.A.: State variable model for considering the parasitic inductor resistance on the open loop performance of DC–DC converter. J. Comput. Commun. **2**, 41–48 (2014)
6. Sathya, P., Natarajan, R.: Design and implementation of 12 V/24 V closed loop boost converter for solar powered LED lightning system. Int. J. Eng. Technol. **5**, 254–264 (2013)
7. Jang, J.S.R.: ANFIS: adaptive-network-based fuzzy inference system. IEEE Trans. Syst. Man Cybern. **23**, 665–685 (1993)
8. Al-Hmouz, A., Shen, J., Al-Hmouz, R., Yan, J.: Modeling and simulation of an adaptive neuro-fuzzy inference system (ANFIS) for mobile learning. IEEE Trans. Learn. Technol. **05** (3), 226–237 (2012)
9. Roy, S.S.: Design of adaptive neuro fuzzy inference system for predicting surface roughness in turning operation. J. Sci. Ind. Res. **64**, 653–659 (2005)
10. Sarikaya, N., Guney, K., Yildiz, C.: Adaptive neuro fuzzy inference system for the computation of the characteristic impedance and the effective permittivity of the micro-coplanar strip line. Prog Electromagnet. Res. B **6**, 225–237 (2008)
11. Pathak, S.S., Sood, H., Sharma, S., Khitoliya, R.K.: Prediction of compressive strength of self compacting concrete with flyash and rice husk ash using adaptive neuro fuzzy inference system. Int. J. Adv. Comput. Sci. Appl. **3**, 119 (2012)
12. Mohdeb, N., Hacib, T.: A new application of an adaptive neuro fuzzy inference system for the shape optimal design of electromagnetic devices. Int. J. Intell. Syst. Appl. **6**, 11–19 (2012)
13. Martinek, R., Kelnar, M., Vanys, J., Bilik, P., Zidek, J.: A robust approach for acoustic noise suppression in speech using adaptive neuro fuzzy inference system. J. Electr. Eng. **66**, 301–310 (2015)
14. Yeh, J.-P., Yang, R.-P.: Application of the adaptive neuro fuzzy inference system for optimal design of reinforced concrete beams. J. Intell. Learn. Syst. Appl. **6**, 162–175 (2014)
15. Kharb, R.K., Fahim Ansari, M.D., Shimi, S.L.: Design and implementation of ANFIS based MPPT scheme with open loop boost converter for solar PV module. Int. J. Adv. Res. Electr. Electron. Instrum. Eng. **3** (2014)
16. Walia, N., Singh, H.: ANFIS: adaptive neuro fuzzy inference system, a survey. Int. J. Comput. Appl. **123** (2015)

Optimization of Induction Motor Using Genetic Algorithm and GUI of Optimal Induction Motor Design in MATLAB

Rakeshkumar Chaudhary, Rajesh Sanghavi and Sanjay Mahagaokar

Abstract In this paper, an optimal design of induction motor using genetic algorithm is discussed and the results obtained are compared with a conventionally designed induction motor. Graphical user interface (GUI)-based user simplified interface is prepared in MATLAB to achieve an optimal design of different power-rated three-phase squirrel cage induction motors. Full-load efficiency and active material cost are chosen as an objective function to be optimized, and based on that, the concept of dual optimization is explained. To achieve the best suitable design, different variables are chosen and different constraints are imposed on the design of induction motor.

Keywords Optimization · Induction motor · Optimal design
Graphical user interface

1 Introduction

Increasing power demand is being a crucial issue in power sector from last some years. Efforts are made to reach power demand and decrease demand generation gap. So to solve this issue of demand generation gap, a new concept of optimization is suggested [1].

A MATLAB-based program is developed for designing a three-phase squirrel cage induction motor. "Full-load efficiency" and "active material cost" are taken as an objective function. A 50 kW, 440 V, 50 Hz, 1000 RPM induction motor is

R. Chaudhary (✉) · R. Sanghavi
G. H. Patel College of Engineering, Anand 388001, India
e-mail: rakeshdchaudhary@gmail.com

R. Sanghavi
e-mail: rajeshsanghvi@gcet.ac.in

S. Mahagaokar
Rotomotive Power Drives India Ltd., Anand, India
e-mail: s.mahagaokar@rotomotive.com

A. Konkani et al. (eds.), *Advances in Systems, Control and Automation*,
Lecture Notes in Electrical Engineering 442, https://doi.org/10.1007/978-981-10-4762-6_12

chosen for designing, and then, genetic algorithm is implemented on this motor for efficiency and cost improvement in a way to increase efficiency and decrease cost. Results of optimized design of induction motor are compared with the conventionally designed induction motor to check for performance parameters and real-time implementation. Graphical user interface in MATLAB gives the user a flexibility and easiness to user program for problem-solving in a much easier way. So a generalized program is developed to design any kW motor and optimize that design using genetic algorithm and then GUI of the same generalized program is done for development of user-friendly environment.

2 Design Optimization of Induction Motor

The process of optimization of induction motor is expressed as follows:

Find Z (Z_1, Z_2, Z_n), so that $F(Z)$ is minimum [1], where $F(Z)$ is an objective function.

Satisfying; All desired constraints and all design variables within specified limits are satisfied [2].

A. Design Variables

Design variables are basic parameters used in designing induction motor, and they are made free to take any value within its limits to achieve best suitable design. For proposed work, all these variable parameters are adjusted, so that for high efficiency and low cost, an optimal or best design can be achieved (Table 1).

B. List of Constraints

Constraints are imposed on an optimal design of induction so that it satisfies certain requirements. Main performance parameters are chosen as constraints. So while running genetic algorithm, no constraint is violated and satisfactory design can be achieved with all constraints to be satisfied (Table 2).

Table 1 List of design variables

Design variables	Lower limit	Upper limit
Specific magnetic loading (Tesla)	0.35	0.53
Specific electric loading (Ac/m)	25,000	50,000
Stator winding current density (A/mm^2)	3	5
Flux density in the rotor bar (Tesla)	1.2	1.4
Current density of rotor bar (A/mm^2)	4	7
Depth of rotor bar (mm)	5	8
Current density for end ring (A/mm^2)	4	10
Flux density in the rotor bar (Tesla)	1.35	1.70

Table 2 List of constraints

S. No.	Inequality constraints	Violation limit
1	Temperature rise	≤ 50 °C
2	Starting torque	≥ 1.2 * full-load torque
3	Full-load slip	$\leq 3.5\%$
4	kg per kW	≤ 6.5

C. Objective Function

Objective functions are main performance parameter or main goal of whole design. In this paper, proposed scheme of optimization is implemented choosing two different objective functions.

(1) full-load efficiency and
(2) active material cost

where

Full-load efficiency is defined as follows:

$$\text{Efficiency} = \text{kW}/(\text{kW} + P_{\text{total}}/1000) * 100;$$

Active material cost is defined as follows:

$$C_{\text{material}} = C_{\text{iron}} + C_{\text{copper}};$$

Two different designs are prepared for two different objective functions. In design 1, efficiency is chosen as an objective function so a feasible designed is achieved in such a way that highest efficiency can be achieved satisfying all the constraints. In design 2, active material cost is chosen as an objective function so a feasible designed is achieved in such a way that low active material cost can be achieved by satisfying all the constraints and also maintaining good efficiency but not the highest.

3 Results and Discussion

I. Single-Objective Optimization

Efficiency and cost are chosen as two separate objective functions, and GA is implemented as optimization technique. Comparison between conventionally designed motor and optimally designed motor is made in a way to clearly understand performance improvement and comparison.

A 50 kW, 50 Hz, 440 V, 1000 RPM induction motor is chosen. Two different designs are prepared for two different objective functions:

Design 1: full-load efficiency as an objective function and
Design 2: active material cost as an objective function.

From the above results, it is shown that very good value of efficiency can be obtained when efficiency is taken as an objective function and optimization is done using genetic algorithm. But active material cost of the motor is higher compared to Design 2.

Design 2 is prepared to choose active material cost as an objective function; optimization is done; and a visible decrease in active material cost is achieved with little compromise on efficiency.

II. Multiobjective Optimization Technique/Dual Optimization

Results presented in Table 3 shows that Design 1, in which efficiency is taken as objective function, gives higher efficiency at higher cost compared to Design 2. In Design 2, active material cost is taken as an objective function where cost definitely decreases and efficiency also decreases. So we have to choose the best value of efficiency or cost to compromise in another value of objective function. To solve this problem, a method of "dual optimization" can be implemented with two

Table 3 Result comparison of different methods

S. No.	Variable/Parameters	Design 1 (efficiency)	Design 2 (active material cost)
1	Specific magnetic loading (Tesla)	0.3832	0.3879
2	Specific electric loading (Ac/m)	32511	39046
3	Stator winding current density (A/mm^2)	4.93	3.2
4	Flux density in the rotor bar (Tesla)	1.2	1.39
5	Current density of rotor bar (A/mm^2)	4.85	6.59
6	Depth of rotor bar (mm)	7.76	5
7	Current density for end ring (A/mm^2)	4.02	4.11
8	Flux density in the rotor bar (Tesla)	1.70	1.70
9	Efficiency	**92.21**	90.73
10	Full-load slip	**1.88**	2.72
11	Starting torque	**1.88 * FL Tq**	2.72 * FL Tq
12	Temperature rise (°C)	**38.43**	47.32
13	Total weight (kg)	267.62	**234.63**
14	kg required per kW (kg)	5.35	**4.69**
15	Cost of active material (Rs.)	4375 Rs.	**3769.0 Rs.**

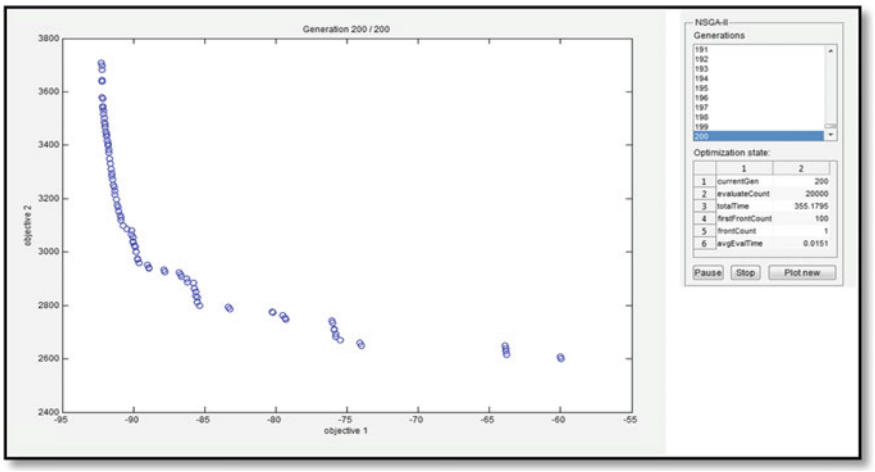

Fig. 1 Results of NSGA-II program in MATLAB for efficiency and cost as objective function

objective functions together. A NSGA-II program in MATLAB [3, 4] is used for dual optimization with efficiency and active material cost as an objective function (Fig. 1).

Above Graph shows the relation between two objective functions. This is obtained using NSGA-II Program in MATLAB. A number of generations selected are 200 and 50 populations for each generation. Average time taken for each Generation is 0.0111 s. From above graph shows that with the higher efficiency, cost of the motor is higher and it decreases with decrease in efficiency. So a proper motor can be designed as per requirement from results obtained using NSGA-II program using the concept of dual optimization.

III. Graphical User Interface (GUI)

As shown in Fig. 2, a MATLAB-based GUI is prepared for designing of induction motor with single-objective function. In Fig. 2 a, demonstration is shown with efficiency as an objective function. GUI gives the user a flexibility to use program easily and shows results in very user-friendly way. In the proposed GUI, certain input parameters are to be fed and interface is made to run, which will give optimized design of induction motor.

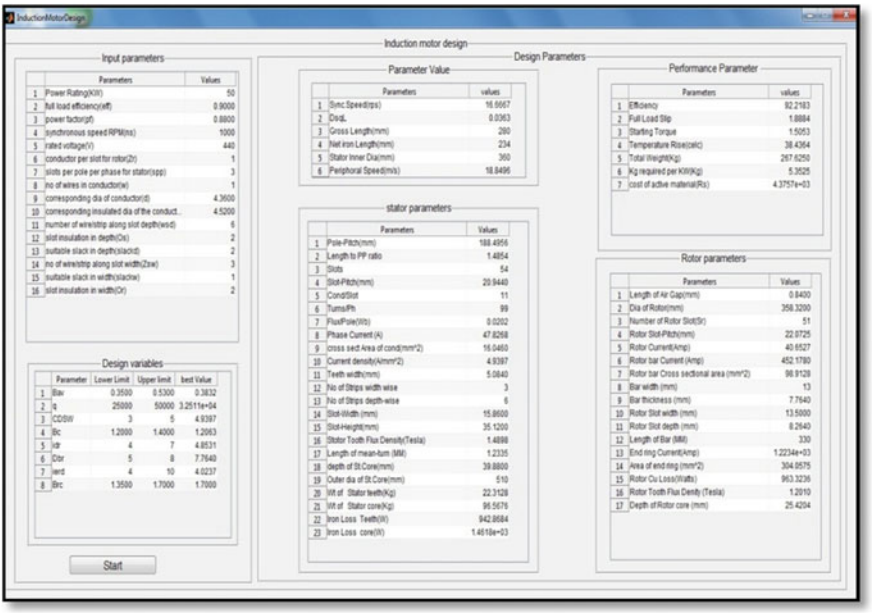

Fig. 2 MATLAB GUI for optimal induction motor design

4 Conclusion

Design optimization of three-phase squirrel cage induction motor is presented in this paper. Results show that when efficiency is considered as an objective function and GA is implemented for optimization, efficiency increases to 2.12%; and when active material cost is considered as an objective function and GA is implemented for optimization, active material cost decreases to 19.15% compared to the conventionally designed induction motor. Dual optimization can be successfully used for two objective functions together, and motor can be designed as per the desired performance requirement.

References

1. Sakthivel, V.P., Bhuvaneswari, R., Subramanian, S.: Economic design of three-phase induction motor by particle swarm optimization. J. Electromagn. Anal. Appl. 301–310 (2010)
2. Chaudhary, R.K., Patel, A.S., Patel, S.: Design optimization of three phase induction motor: a technological review. Trends Electr. Eng. **6**(1), 1–9 (2016)
3. Deb, K., Pratap, A., Agrawal, S.: A fast and elitist multiobjective genetic algorithm Nsga-II. Evol. Comput. **6**(2), 182–197 (2002)
4. Deb, K., Sundar, J.: Reference point based multi-objective optimization using evolutionary algorithms. Int. J. Comput. Intell. Res. **2**(3), 273–286 (2006)

High Response Photon-Counting for Phase Fraction Measurement Using Compact-RIO with FPGA

Merina Mathew, N. Ramesh Babu, M. Suresh and P. Sanjeevikumar

Abstract This paper presents the measurement of phase fraction of multiphase using LabVIEW/FPGA&RT. Phase fraction measurement is done by high-frequency gamma ray photons attenuation from multiple scintillation detectors without dead time between dwell intervals. This phase fraction measurement method is based on the differences in the linear or mass attenuation coefficient of components of each phase to light. The electromagnetic wave attenuation based on Beer-Lambert's law gives the width of individual phases. Even though this method requires shielding, it has the advantages of penetrating through steel. Other phase fraction methods include differences in the permittivity of the components of phases. The voltage across the two electrodes kept opposite to each other determines the phase fraction. But, it has the disadvantages of requirements of special shielding for low capacitance and stray capacitance. Besides, the differences in the conductivity can measure the path resistance. This conductivity change gives phase fraction. Among the above volume—percentage measurement methods, former method is more accurate for industrial applications.

Keywords LabVIEW/FPGA&RT · Phase fraction · Compact-RIO
Gamma ray photons · Industrial application

M. Mathew · N. Ramesh Babu (✉)
School of Electrical Engineering, VIT University, Vellore, Tamil Nadu, India
e-mail: nrameshbabu@vit.ac.in

M. Mathew
e-mail: merina.mathew1922@gmail.com

M. Suresh
Fluid Control Research Institute, Palghat, Kerala, India
e-mail: ms.here@gmail.com

P. Sanjeevikumar
Department of Electrical and Electronics Engineering, University of Johannesburg, Auckland Park, Johannesburg, South Africa
e-mail: sanjeevi_12@yahoo.co.in

A. Konkani et al. (eds.), *Advances in Systems, Control and Automation*,
Lecture Notes in Electrical Engineering 442, https://doi.org/10.1007/978-981-10-4762-6_13

1 Introduction

In industrial applications such as petroleum industry and thermal power plants, the phase fraction measurement should be accurate since a minute change in the volume may cause a disaster. There are different methods such as void phase fraction, capacitive measurements to measure the area of phases in a given cross section. The disadvantages of these methods are that it produces dead time and lose data in some intervals of time. This will be resulting in a big loss to the industry. In such conditions, an accurate device is needed to measure the phase fraction at every instant. In such a pondering, phase fraction measurement without dead time came into existence.

Three gamma rays are passed through the water–gas mixture containing pipeline. Since the angle of fall of rays on the pipeline varies, the area of cross section that the rays passing through will be different. Each ray captured at scintillation counter varies, because of the quantity of fluid that absorbs the rays is different. The intensity of gamma rays is decayed after passing through the water–gas mixture pipeline. The analog values—pressure of water, flow of water, temperature of water, differential pressure of air, pressure of air, temperature of air, air–water mixture differential pressure, air–water mixture pressure, air–water mixture temperature—are measured online and values for each microsecond is recoded.

2 Multiphase Flow

Multiphase describes multiple fluid components in a flowing stream. Difficult multiphase [1] measurement usually involves liquid–gas mixture such as water–air mixture. The measurement difficulty comes into existence since the gas has the tendency to separate [2] from liquid creating a heterogeneous fluid. Fluids that can emulsify easily can be mixed and measured accurately. To measure the multiphase flow, the count measurement of gas and liquid is taken separately.

The homogenization of two phases [3] and measure of the count for fictitious single phase are difficult processes in industry for different flow patterns [4]. But, homogenization method is widely used in chemical engineering applications and nuclear industry. The principle of the multiphase flow is based on the bulk flow or mass flow rate of the fluid which gives the information about the phase fraction of individual phases considering the slip between each phase is nil. Measurement of multiphase flow is very difficult since it is characterized by extreme changes in the flow properties such as viscosity, density, and surface tension. Figure 1 shows the block diagram representation of the detector scheme for phase fraction measurement.

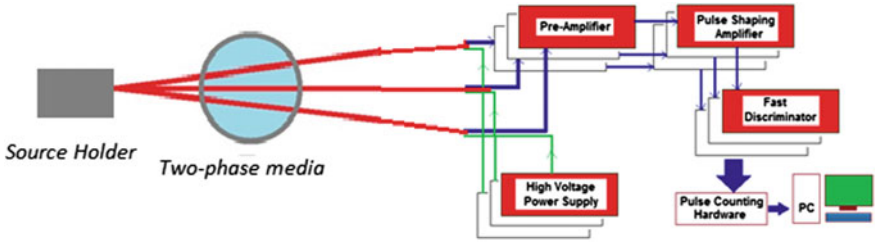

Fig. 1 Schematic for the detector instrumentation for phase fraction measurement

High-frequency gamma [5] rays are passed through the pipeline containing water or gas (air) or water–air mixture. The attenuated rays are captured at scintillation detector kept after the pipeline. The attenuation is due to the linear absorption of gamma rays by steel, with which the pipe is made, and the medium.

In scintillators, the ionizing radiations are converted into light pulses. The light output of scintillator [5] is directly proportional to the energy deposited in the radiation source. The photons, which are the output of the scintillation counter, are converted into electrical signals by photomultiplier tube (PMT). The amplified output from the PMT is further amplified by preamplifier circuitry. Preamplifier produces pulse outputs whose amplitudes are proportional to the energy of incident gamma photons. The radiation source used in this project is cesium 137. These pulse outputs are fed through a chain of pulse processing circuitries consisting mainly of pulse shaping spectroscopy amplifier, energy discriminator, and finally pulse counting interface hardware for computer.

The dwell time is the average time spent by a particle in a given region of space. The duration of time in minutes is also added in the front panel. The less time among total dwell time and total time in minutes will be selected, and up to that time the count will be taken. These time settings should be presetted.

The basic clocking frequency of FPGA 9024 is 40 MHz. The frequency can be multiplied or divided in accordance with the need. In this project, the frequency is multiplied by two and made it 80 MHz. Since the count is to be taken in each milliseconds and all the rising edge or all the falling edge should be noted, 80 MHz is required. The fetching speed of the data in FPGA should be high in order not to miss any pulses. The fetching speed of data by FPGA should be greater than the storage speed in FIFO. The gamma ray frequency is of the order of maximum 10 MHz. Before started taking readings, initial values are resettled. Since same values of time and count are shown in the excel sheet after taking readings, the multiple same values are weeded out through a subprogram.

3 Design Requirements

Compact-RIO (C-RIO) with FPGA is used for receiving the instantaneous values of analog signals, which are gamma rays [6]. C-RIO-embedded real-time controller is programmed in LabVIEW. This depicted program can be converted into C program by FPGA modules. In a particular dwell [7, 8] off time and dwell on time, the signals from the radiation source are taken in FPGA and shifted to FIFO of host. Cesium 137 is used as the gamma ray source and is shown in Fig. 2.

All compact-RIO will be having reconfigurable FPGA module. FPGA is used for fetching of high-speed values. Since the FPGA has very low memory, the captured values cannot be stored in it. The values in each microsecond are captured by FPGA and shifted to the host computer. It is done with First In First Out

Fig. 2 Gamma ray source holder

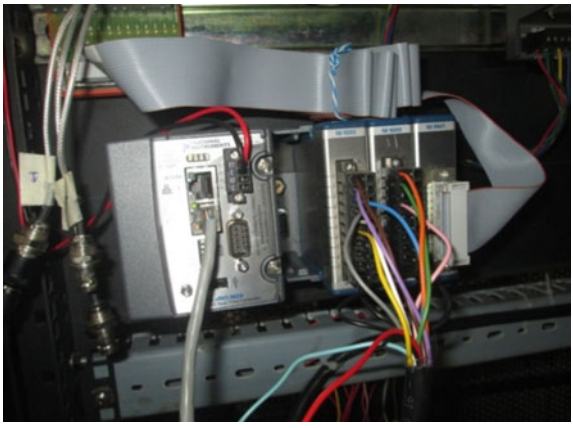

Fig. 3 C-RIO 9024 with modules

memory. The data will be stored in the host as an excel sheet. The data includes the time (in seconds), number of signals, and eight analog values. In FPGA program, the dwell time and the number of dwell intervals can be set manually. In Fig. 3, C-RIO 9024 with two analog modules and one output digital module is shown. Two analog modules 9203 are kept in the case as well as one digital module 9401 to convert the counts in digital format.

4 Conclusion

In this paper, phase flow measurement using high-frequency gamma ray emission method for multiphase flow measurement has been carried out. The method is implemented using Labview/C-RIO hardware setup in the laboratory and validated the results. Among multiphase flow measurement using different methods done, gamma ray emission is found to be the accurate method for multiphase flow measurement.

References

1. Wu, H., Tan, C., Dong, F.: A simulation experimental system of multiphase pipe flow. In: Proceedings of Chinese Control and Decision Conference (CCDC), pp. 3962–3966 (2012)
2. Wylie, S.R., Shaw, A., Al-Shamma'a, A.I.: RF sensor for multiphase flow measurement through an oil pipeline. Meas. Sci. Technol. **17**, 2141 (2006)
3. Xie, C.G.: Measurement of multiphase flow water fraction and water-cut. AIP Conf. Proc. **914**, 232–239 (2007)
4. Sharaf, S., Meulen, P.V.D., Agunlejika, E.O., Azzopardi, B.J.: Structures in gas–liquid churn flow in a large diameter vertical pipe. Int. J. Multiph. Flow **78**, 88–103 (2016)
5. Kraft, S., Maddox, E., Buis, E.J., Owens, A., Quarati, F.G.A., Dorenbos, P., Drozdowski, W., Bos, A.J.J., de Haas, J.T.M., Brouwer, H., Dathy, C., Ouspenski, V., Brandenburg, S., Ostendorf, R.: Development and characterization of large La-Halide gamma-ray scintillators for future planetary missions. IEEE Trans. Nucl. Sci. **54**, 873–878 (2007)
6. Varma, R., Bhusarapu, S., O'sullivan, J.A., Al-Dahhan, M.H.: A comparison of alternating minimization and expectation maximization algorithms for single source gamma ray tomography. Meas. Sci. Technol. **19**, 015506 (2007)
7. Kelkar, N.G.: Three-body dwell time. Phys. Rev. **1**, 062109 (2010)
8. Yang, W., Li, Y., Wu, Z., Tsamakis, D., Learmonth, D., Xie, C.G., Huang, S., Lenn, C., Cutler, A.: Multiphase flow measurement by electrical capacitance tomography. In: Proceeding of IEEE International Conference on Imaging System Technique, pp. 108–111 (2011)

Numerical Stress Analysis of Artificial Femur Bone

Sujoy Kumar Dey, Vikash Mainali, B.B. Pradhan and Sutanu Samanta

Abstract Femur bone is one of the strongest bones of the human body, and it bears a maximum weight of the body with the different types of daily life activities. In the present study, we are trying to use semi-crystalline polymer such as polyetheretherketone (PEEK) and its composites such as hydroxyapatite-polyetheretherketone (HA–PEEK) as a substitute for bone implant. First a solid cylinder was designed of human bone, PEEK, and HA–PEEK, and the effect of compressive loading was analyzed using directional deformation and Von-mises stress, respectively, in the ANSYS. In the second analysis, a human femur bone was designed using software and analysis was made using ANSYS for the compressive loading. From the analysis, it can be seen that both PEEK and HA–PEEK have shown nearer Von-mises stress and directional deformation as compared to that of a natural bone. HA–PEEK had more close value as compared to the pure PEEK.

Keywords Femur bone · HA–PEEK · PEEK · ANSYS

S.K. Dey (✉) · V. Mainali (✉) · B.B. Pradhan
Department of Mechanical Engineering, Sikkim Manipal Institute of Technology, Majitar, Sikkim, India
e-mail: Dey.sujoykumar@gmail.com

V. Mainali
e-mail: Vikashmainali91@gmail.com

B.B. Pradhan
e-mail: bbpradhan1@rediffmail.com

S. Samanta
Department of Mechanical Engineering, NERIST, Nirjuli, Arunachal Pradesh, India
e-mail: suta_sama@yahoo.co.in

A. Konkani et al. (eds.), *Advances in Systems, Control and Automation*,
Lecture Notes in Electrical Engineering 442, https://doi.org/10.1007/978-981-10-4762-6_14

1 Introduction

In this modern era, lot of research has been going on in the field of orthopedic implants and lots of materials have been tried as a bone replacement. But none of materials behaved like natural bone. Once the material have been implanted, there are always chances of revision surgery, and this is due to the *stress shielding* which makes the bone weaker and has to be replaced in due course of time. Revision surgery at an old age is quite risky, and serious problem may occur during surgery. Stress shielding occurs mainly in the metal implants [1].

$$\text{Stress Shielding} = \frac{\{\text{SE (treated)} - \text{SE (reference)}\}}{\text{SE (reference)}} \tag{1}$$

where

$$\text{Strain Energy (SE)} = \frac{\text{Strain Energy Density}}{\text{Apparent Density}}$$

The mentioned Eq. (1) was given by Weinans et al. [2].

To reduce the chances of revision surgery and stress shielding problem, we are trying to find out the polymer which have directional deformation and equivalent stress (Von-mises) closer or nearer to the natural human bone. In this paper, we have taken two polymer materials: one is PEEK, and the other is HA–PEEK. PEEK is a semi-crystalline polymer having excellent mechanical properties and chemically inert to most organic and inorganic chemicals. PEEK is a thermoplastic material which is wear resistant having stability at high temperature [3]. It has a glass transition temperature of 143 °C and a melting point of 335 °C. Some researchers have also described the potential of PEEK in medical applications [4], and it can serve as a replacement of the metal implants in orthopedic surgery [5]. PEEK also remained stable during the process of sterilization process [6] and is biocompatible in both the cases of in vivo and in vitro [7, 8]. It can be modified to increase its bioactivity by surface modification or incorporation of fiber into PEEK matrix [9, 10]. Previously, static analysis has also been done on the artificial femur bone using different materials such as Ti–Al—4 V and structural steel [11]. Analysis has been done for different loading conditions such as walking, standing, running, and jumping [12]. Such analysis helps to know about the stress distribution and from where the facture will occur due to loading.

2 Manufacturing

PEEK can be manufactured easily from injection molding, extrusion, conventional plastic processing techniques [13, 14]. HA is the one common material that has been used to increase the bioactivity of the PEEK. Various methods can be used to

make a HA–PEEK composite, such as plasma spraying, cold spraying, and spin coating. Plasma spraying method can be used to deposit metallic or nonmetallic material in a molten or semi-molten state onto a different material [15]. High-quality HA coatings can be made using gas plasma sprays [16]. Cold spraying has also been used by some researchers to coat PEEK with the HA. In cold spraying, the particles are accelerated to a very high velocity toward a substrate. The particles to be sprayed are kept below the melting point [17]. Spin coating has also been done for coating HA over PEEK polymer. Zhang et al. [18] have manufactured the HA–PEEK by selective laser sintering process and done the evaluation of the cell attachment. Scaffold development of PEEK and HA has also been done using the laser sintering process [19].

3 Modeling and Material Properties

(a) Modeling of Solid Cylinder

1. A circle of diameter 8 mm was drawn using a sketch tool.
2. The circle was extruded to 100 mm length along the normal direction (Figs. 1 and 2).

(b) Model of the Human Femur Bone

The material properties of PEEK [20], PEEK and HA in the ratio of 70:30 [21], and human femur bone [22] are given in Table 1.

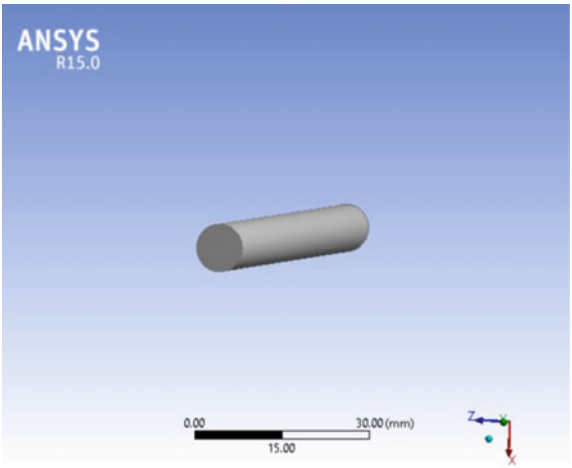

Fig. 1 Model of solid cylinder

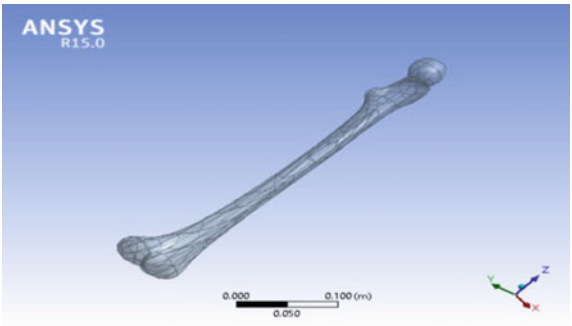

Fig. 2 Model of human femur bone

Table 1 Properties of human bone PEEK and PEEK composite

Properties	Human bone	PEEK	HA–PEEK
Density (g/cm^3)	2	1.291	1.851
Poisson ratio	0.3	0.42	0.38
Young's modulus (Gpa)	2.13	3.2	6.8

The density of the HA–PEEK is calculated using the formula of density of composite, given by

$$\rho_c = \rho_f v_f + \rho_m v_m$$

where ρ_c, ρ_f, ρ_m is density of the composite, fiber, and matrix, respectively, and v_m, v_f are the volume fraction of the matrix and the fiber.

4 Analysis

4.1 Analysis of the Solid Cylinder

Static analysis of the cylinder has been done considering the material to be isotropic and homogenous. Material properties are assigned as given in Table 1.

Step 1: Meshing
Meshing was done all over the volume of the cylinder, with 66,722 nodes and 15,496 elements using a mesh tool. Figure 3 shows the meshed model.
Step 2: Condition for Analysis
One end of the cylinder has been fixed, and a compressive load of 750 pa [5], which is consider to be a weight of 75 kg person, is applied on the other end of the cylinder. We have taken compressive load as during walking or standing the nature of the load is compressive on the human femur bone. Figures 4 and 5 show the end conditions.

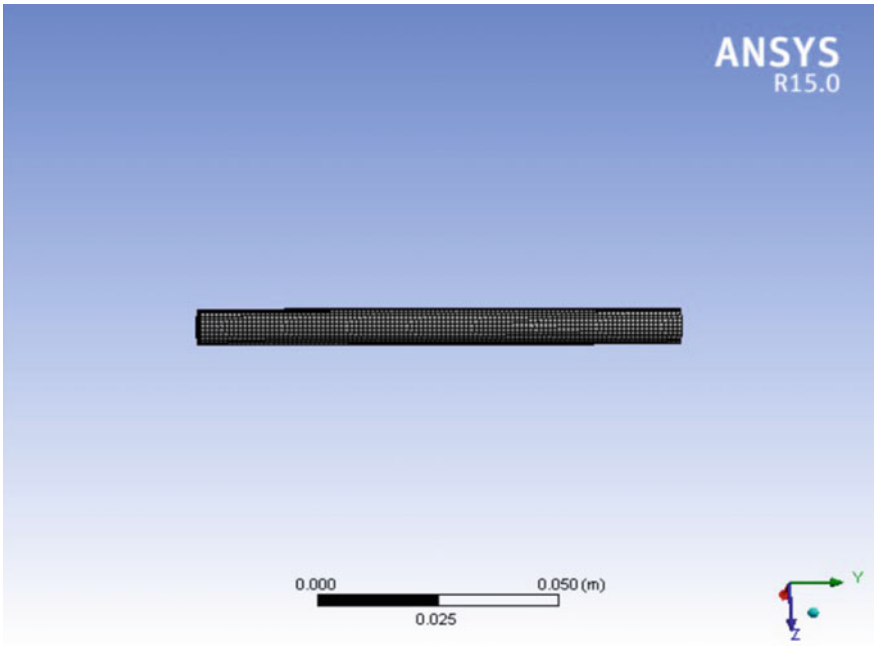

Fig. 3 Meshed model

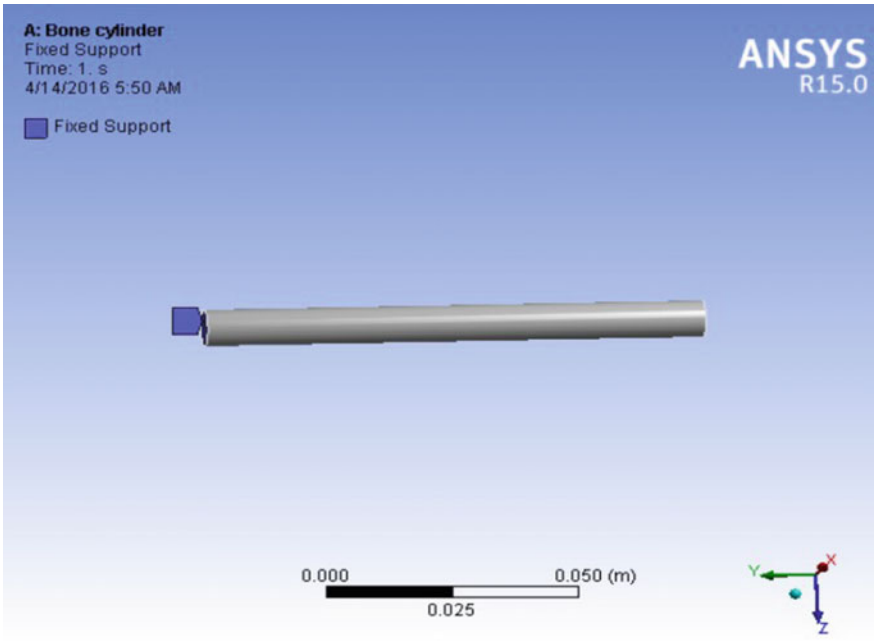

Fig. 4 Fixed support

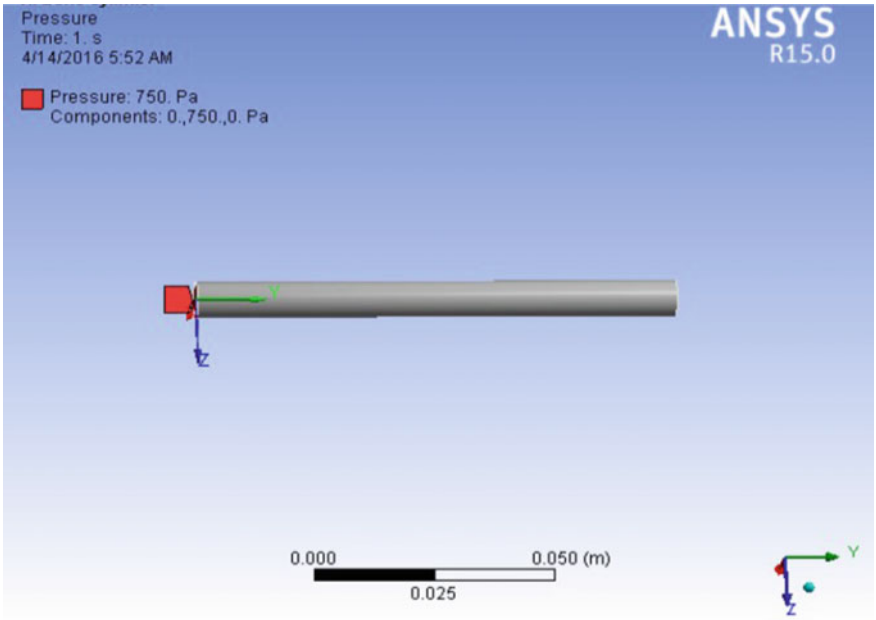

Fig. 5 Load application

Step 3: Results and Discussion

On the basis of the static structural analysis done in the ANSYS and considering the results based on the Von-mises stress and directional deformation, Figs. 6 and 7 show the directional deformation and equivalent stress in all the three materials: bone, PEEK, and HA–PEEK.

As per the static analysis of the natural bone, we find the value of the directional deformation is 3.513×10^{-8} m and the stress is equal to 1026.9 pa (maximum) and 373.87 pa (minimum) (Figs. 8 and 9).

As per the static analysis of the PEEK cylinder, we find the value of the directional deformation is 2.332×10^{-8} m and the stress is equal to 1175.1 pa (maximum) and 179.38 pa (minimum) (Figs. 10 and 11).

As per the static analysis of the HA–PEEK cylinder, we find the value of the directional deformation is 1.099×10^{-8} m and the stress is equal to 1120.4 pa (maximum) and 250.12 pa (minimum).

The above results are given in Table 2 for the comparison of the directional deformation and equivalent stress.

From the analysis, it can been seen that HA–PEEK has closer properties as compared to the natural bone and even its directional deformation is less than both the bone and PEEK, so it can act as a substitute in orthopedic implants.

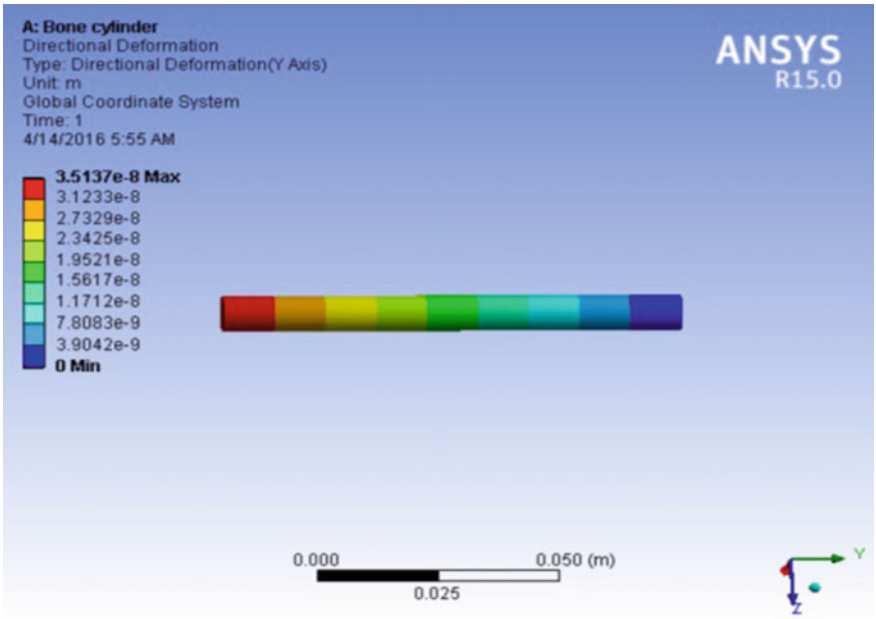

Fig. 6 Directional deformation of bone cylinder

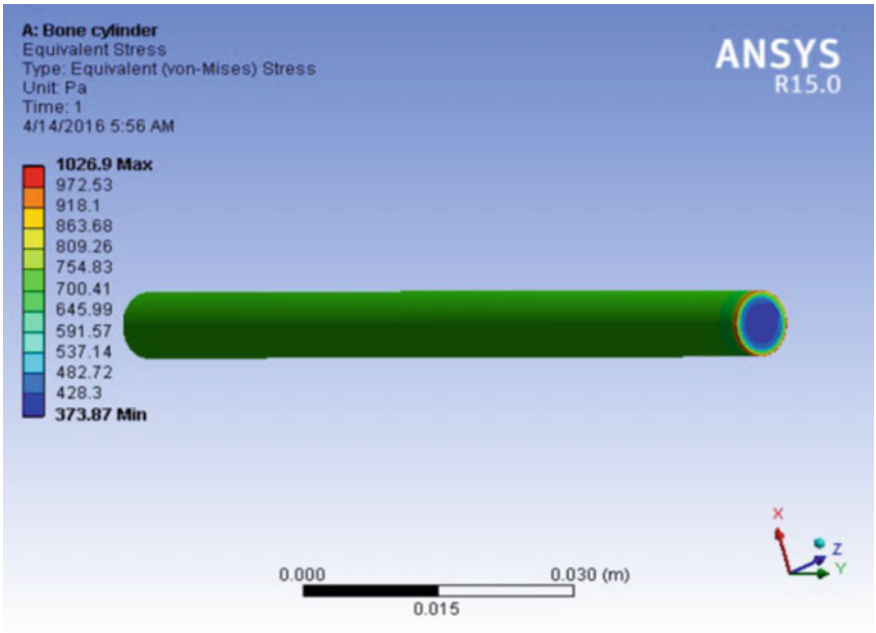

Fig. 7 Equivalent stress in bone cylinder

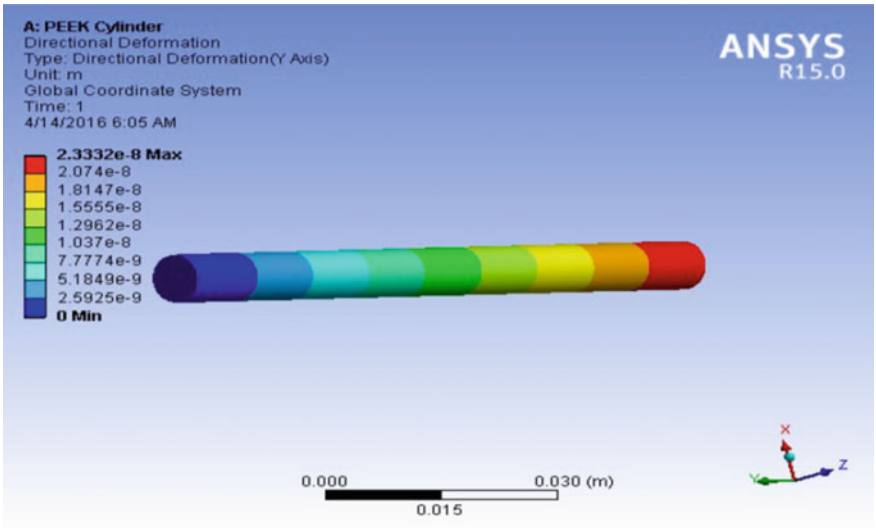

Fig. 8 Directional deformation of PEEK cylinder

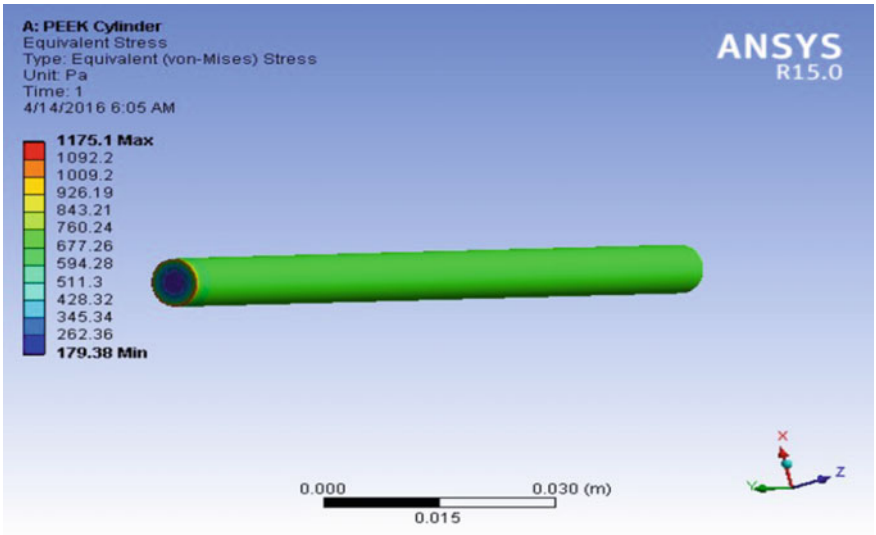

Fig. 9 Equivalent stress in PEEK cylinder

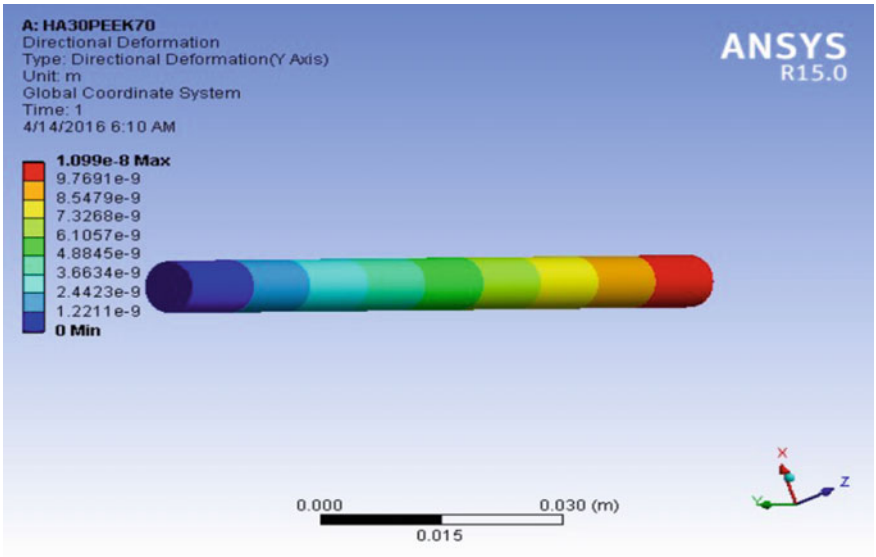

Fig. 10 Directional deformation in the HA–PEEK cylinder

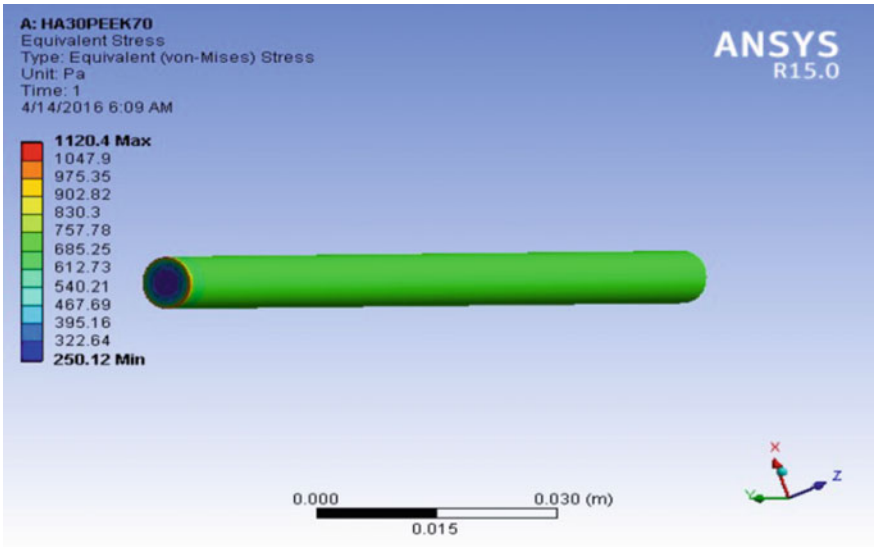

Fig. 11 Equivalent stress in HA–PEEK cylinder

Table 2 Results of the analysis

	Bone	PEEK	HA–PEEK
Directional deformation (m)	3.513×10^{-8}	2.332×10^{-8}	1.099×10^{-8}
Equivalent stress (Pa) max.	1026.9	1175.1	1120.4
Equivalent stress (Pa) min.	373.87	179.38	250.12

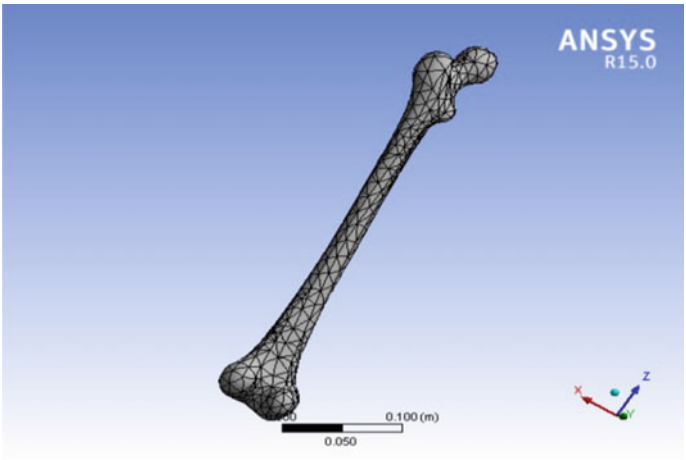

Fig. 12 Meshed geometry

4.2 Analysis of Human Femur Bone

The static analysis has been on the model considering it to the isotropic and homogenous material though the human femur bone is heterogeneous. Material properties have been assigned as given in Table 1.

Step 1: Meshing
The geometry is meshed using a meshing tool into 34,362 nodes and 23,531 elements. Figure 12 shows the meshed geometry of human femur bone.

Step 2: Analysis Conditions
Human bone is inflexible so we had fixed lower end of the femur bone. A compressive load of 750 Pa [22] which is considered to be a weight of 75 kg person is applied on the upper end. The changes in the equivalent stress and directional deformation have been compared between natural bone and bone made of PEEK, HA–PEEK. Figures 13 and 14 show the fixed and compressive loading conditions in human bone.

Step 3: Results and Discussion
On the analysis made on the ANSYS workbench using static structural following results were produced (Figs. 15 and 16).

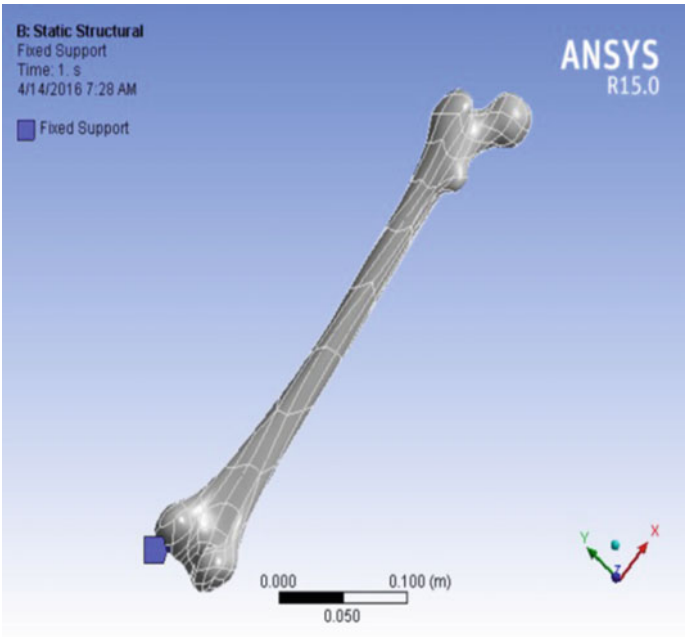

Fig. 13 Fixed condition

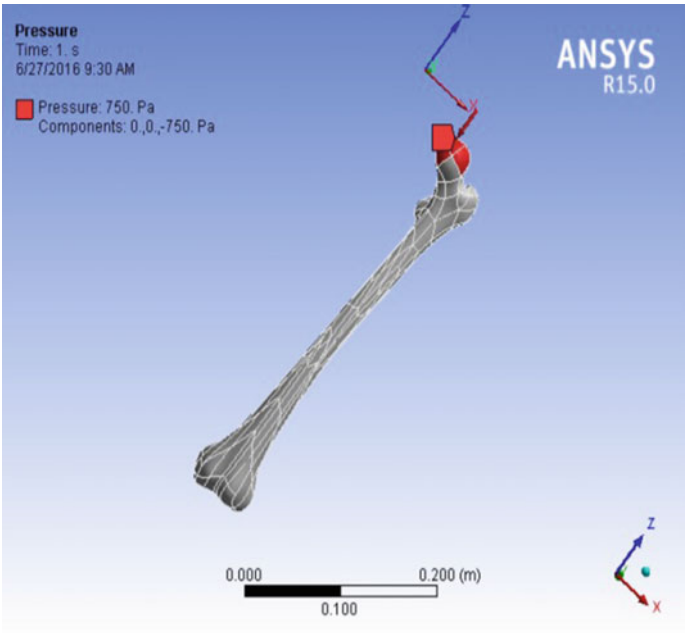

Fig. 14 Compresssive loading

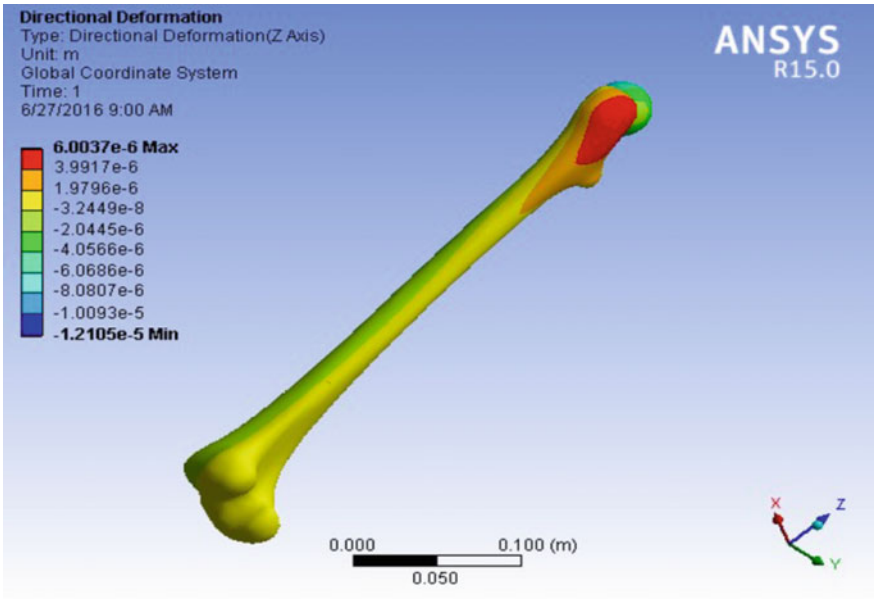

Fig. 15 Directional deformation of the femur bone

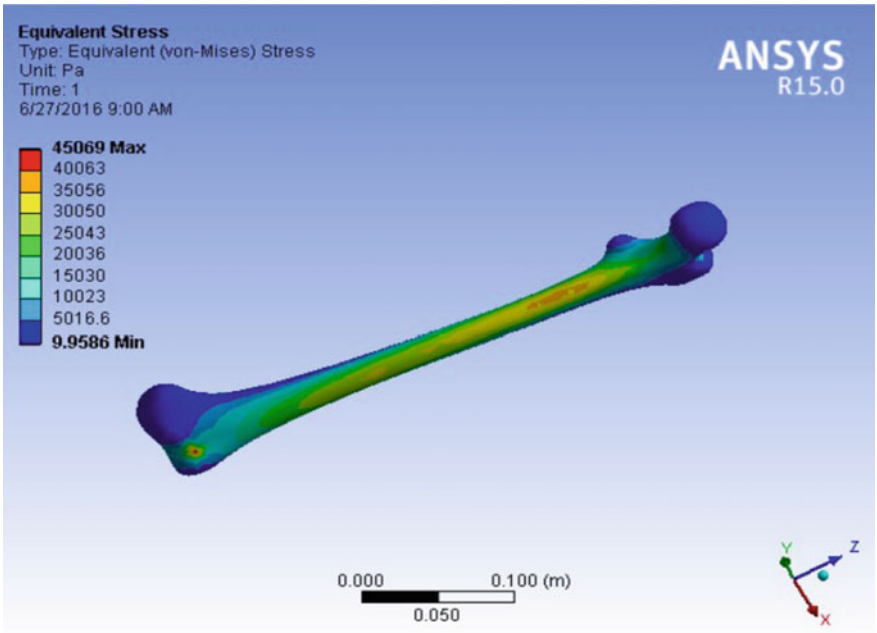

Fig. 16 Equivalent stress of the femur bone

As per the static analysis, we find the value of the directional deformation is 4.046×10^{-5} m and the stress is equal to 45,069 Pa (maximum) and 9.9586 Pa (minimum) in the case of bone (Figs. 17 and 18).

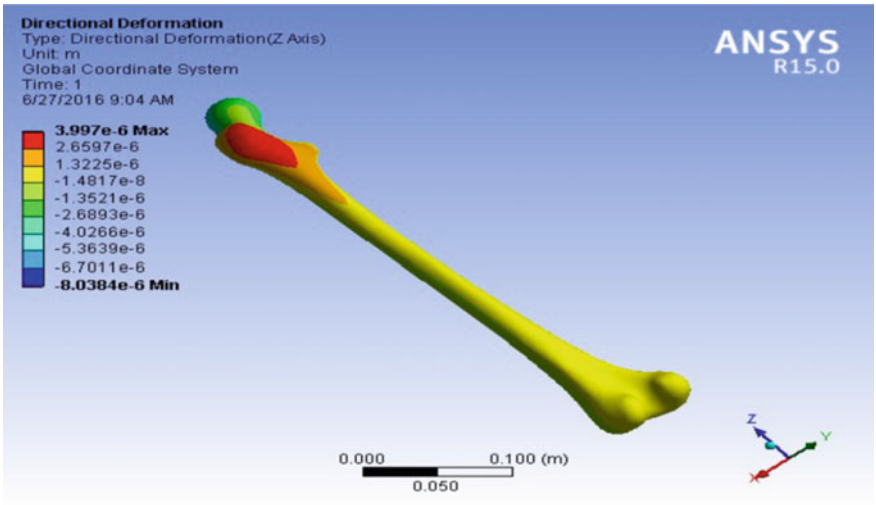

Fig. 17 Directional deformation of PEEK femur bone

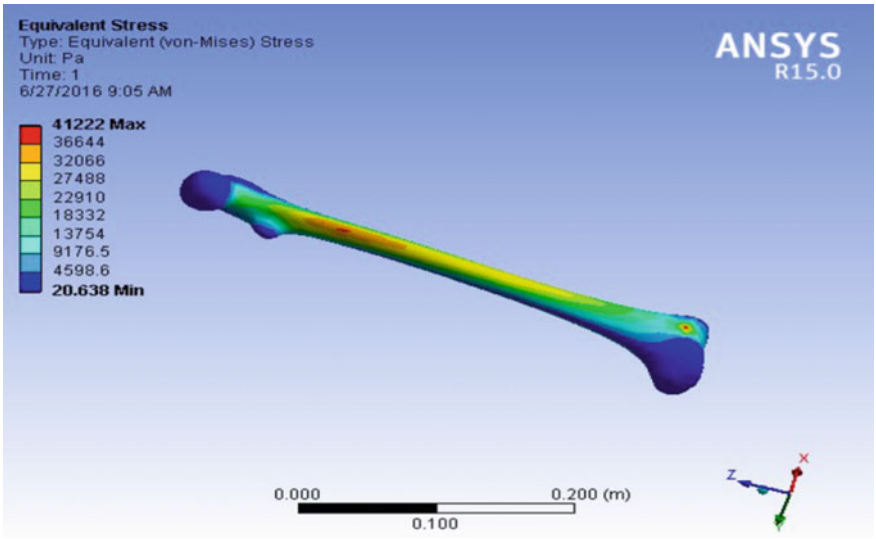

Fig. 18 Equivalent stress of PEEK femur bone

As per the static analysis, we find the value of the directional deformation is 3.997×10^{-6} m and the stress is equal to 41,222 Pa (maximum) and 20.638 Pa (minimum) in the case of PEEK femur bone (Figs. 19 and 20).

As per the static analysis, we find the value of the directional deformation is 1.8804×10^{-6} m and the stress is equal to 42,769 Pa (maximum) and 16.083 Pa (minimum) in the case of HA–PEEK femur bone.

Comparative results are given in Table 3.

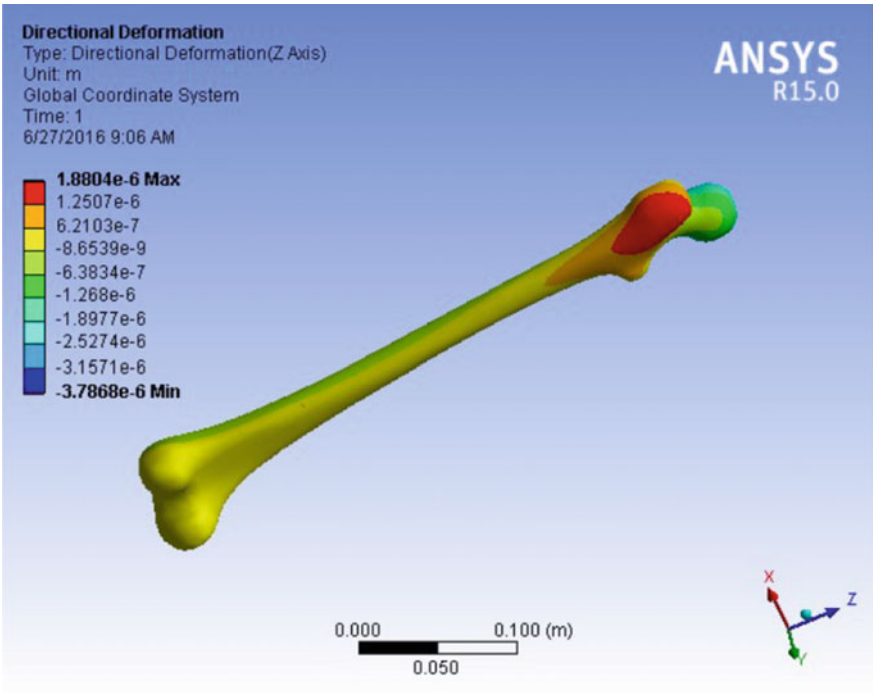

Fig. 19 Directional deformation of HA–PEEK femur bone

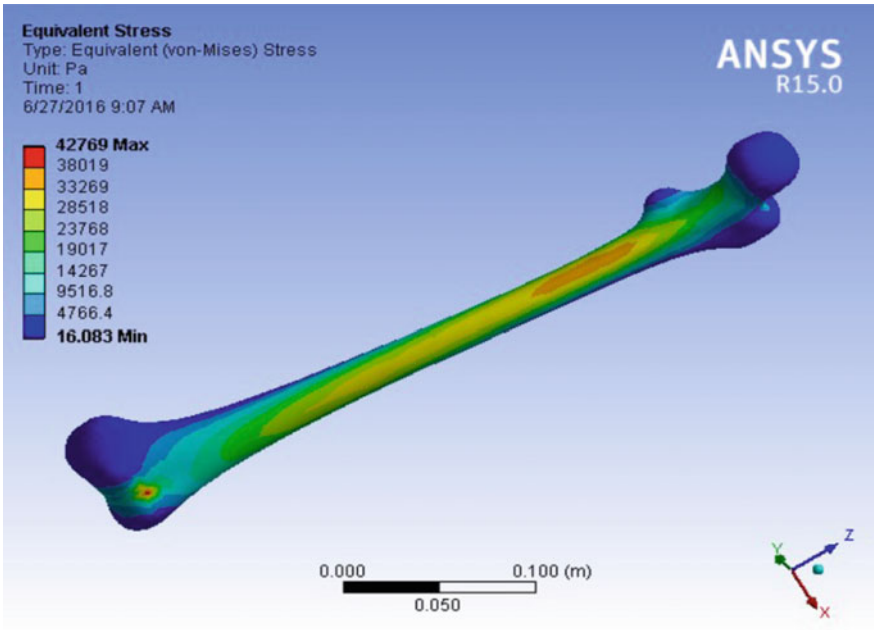

Fig. 20 Equivalent stress in HA–PEEK femur bone

Table 3 Results of analysis

	Human bone	PEEK	HA–PEEK
Directional deformation (m)	4.046×10^{-5}	3.997×10^{-6}	1.8804×10^{-6}
Equivalent stress max (Pa)	45,069	41,222	42,769
Equivalent stress min (Pa)	9.9586	20.638	16.083

5 Conclusion

- Comparison was done between natural bone, the artificial PEEK, and HA–PEEK bone.
- PEEK and HA–PEEK showed closer properties with natural bone and can act as a material for bone implants.
- HA–PEEK showed closer as results compared to PEEK.

References

1. Ridzwan, M.I.Z., Shuib, S., Hassan, A.Y., Shokri, A.A., Ibrahin, M.N.M.: Problem of stress shielding and improvement of the hip implant design. J. Med. Sci. **7**(3), 460–467 (2007)
2. Weinans, H., Sunner, D.R., Igloria, R., Natrajan, R.N.: Sensitivity of periprosthetic stress shielding to load and the bone density-modulus relationship in subject-specific finite element models. J. Biomechanics **33**, 809–817 (2000)
3. Eschbach, L.: Nonresorbable polymers in bone surgery. Injury **31**, 22–27 (2000)
4. Williams, D.F., McNamar, A., Turner, R.M.: Potentials of PEEK and carbon reinforced PEEK in medical applications. J. Mat. Sci. Lett. **6**, 188–190 (1997)
5. Kurtz, S.M., Devine, J.N.: PEEK biomaterials in trauma, orthopedic, and spinal implants. Biomaterials **28**, 4845–4869 (2007)
6. Godara, A., Raabe, D., Green, S.: The influence of sterilization processes on the micromechanical properties of carbon fiber-reinforced PEEK composites for bone implant applications. Acta Biomater. **3**, 209–220 (2007)
7. Wenz, L.M., Merritt, K., Brown, S.A., Moet, A., Steffee, A.D.: In vitro biocompatibility of polyetheretherketone and polysulfone composites. J. Biomed. Mater. Res. **24**, 207–215 (1990)
8. Rivard, C.H., Coillard, C., Rhalmi, S.: In vivo biocompatibility testing of peek polymer for a spinal implant system: a study in rabbits. J. Biomed. Mater. Res. **62**, 488–498 (2002)
9. Du, Y.W., Zhang, L.N., Hou, Z.T.: Physical modification of polyetheretherketone for orthopedic implants. Front. Mat. Sci. (2014)
10. Ma, R., Tang, T.: Current strategies to improve the bioactivity of PEEK. Int. J. Mol. Sci. **15**, 5426–5445 (2014)
11. Shireesha, Y., Ramana, S.V., Rao, P.G.: Modelling and static analysis of femur bone by using different implants materials. IOSR J. Mech. Civil Eng. **7**(4), 82–91 (2013)
12. Kumar, K.C.N., Tandon, T., Silori, P., Shaikh, A.: Biomechanical stress analysis of a human Femur bone using ANSYS. Mat. Today Proc. **2**, 2115–2120 (2015)
13. Lustiger, A., Uralil, F.S., Newaz, G.M.: Processing and structural optimization of PEEK composites. Polym. Compos **11**, 65 (1990)
14. Sarasua, J.R., Remiro, P.M.: The mechanical behaviour of PEEK short fibre composites. J. Mat. Sci. **30**, 3501 (1995)
15. Yang, C.Y., Chen, C.R., Chang, E., Lee, T.M.: Characteristics of Hydroxyapatite Coated Titanium Porous Coatings on Ti-6Al—4 V Substrates by Plasma Sprayed Method. Wiley Interscience (2007)
16. Wu, G.M., Hsiao, W.D., Kung, S.F.: Investigation of hydroxyapatite coated polyether ether ketone composites by gas plasma sprays. Surf. Coat. Technol. **203**, 2755–2758 (200)
17. Lee, J.H., Jang, H.L., Lee, M.K., Baek, H.R., Jin, K., Hong, K.S., Noh, J.H., Lee, H.K.: Invitro and In vivo evaluation of the bioactivity of hydroxyapatite-coated polyetheretherketone biocomposites created by cold spray technology. Acta Biomaterialia **9**, 6177–6187 (2013)
18. Zhang, Y., Hao, L., Savalani, M.M., Harris, R.A., di Silvio, L., Tanner, K.E.: In vitro biocompatibility of hydroxyapatite-reinforced polymeric composites manufactured by selective laser sintering. J. Biomed. Mater. Res. A **91**, 1018–1027 (2009)
19. Tana, K.H., Chua, C.K., Leong, K.F., Cheah, C.M., Cheang, P., Bakar, M.S.A., Cha, S.W.: Scaffold development using selective laser sintering of polyetheretherketone–hydroxyapatite biocomposite blends. Biomaterials **24**, 3115–3123 (2003)
20. Fan, J.P., Tsui, C.P., Tang, C.Y.: Modeling of the mechanical behavior of HA/PEEK biocomposite under quasi static tensile load. Mat. Sci. Eng. A **328**, 341–350 (2004)

21. Bakar, M.S.A., Cheng, M.H.W., Tang, S.M., Yu, S.C., Liao, K., Tan, C.T., Khor, K.A., Cheang, P.: Tensile properties, tension-tension fatigue and biological response of PEEK-HA composites for load bearing orthopedic implants. Biomaterials **24**, 2245–2250 (2003)
22. Maharaj, P.S.R.S., Maheswaran, R., Vasanthanathana, A.: Numerical analysis of fractured femur bone with prosthetic bone plate (International Conference on Design and Manufacturing, IConDM 2013). Procedia Eng. **64**, 1242–1251 (2013)

Performance Metrics of Three-Phase Shunt APF Using Hybrid Control-Based Instantaneous Vector Control Theory

P. Karthigeyan, T. Murugesh Vasan, R.S. Abilash, R. Elavarasu and M. Senthil Raja

Abstract This chapter presents about one of the power quality improvement issues such a current harmonic compensation in a shunt active power filter as power quality issues distort the system. The control theory employed here is PI–hysteresis controller-based instantaneous PQ current theory. Simulation is done in MATLAB for a three-phase shunt active power filter, and the results of load current, filter current, and source current have been verified before and after compensation. An FFT analysis is done to evaluate the total harmonic distortion.

Keywords Active power filter · PI · Hysteresis controller
Instantaneous active and reactive current · Direct quadrature
Vector control theory · Fast Fourier transform · Total harmonic distortion

1 Introduction

Active power filter is used to cancel the harmonics and ripple-free currents [1]. Harmonics are generated by nonlinear loads. Harmonics originate from rectifiers and cycloconverters (Figs. 5 and 7). Harmonics lead to overheating, malfunction, and distortion. Control scheme is based on current modulation and harmonic

P. Karthigeyan (✉)
I.I.T Madras, Chennai 600036, India
e-mail: karthigeyan.iitm@gmail.com

T. Murugesh Vasan
MET Engineering College, Kanyakumari 629304, Tamil Nadu, India

R.S. Abilash
College of Engineering, Vadakara 629304, India

R. Elavarasu
Rajalakshmi Institute of Technology, Chennai 600124, India

M. Senthil Raja
Vi Institute of Technology, Chennai 603108, India

A. Konkani et al. (eds.), *Advances in Systems, Control and Automation*,
Lecture Notes in Electrical Engineering 442, https://doi.org/10.1007/978-981-10-4762-6_15

extraction. Harmonic extraction deals with extracting reference currents [2] using active and reactive current theory and direct quadrature theory because of their accurate results. Current modulator provides gate pulse to the converter.

2 Shunt Active Power Filter

Active power filters are divided into shunt and series that are connected in parallel and series with the loads. As shunt APF cancels the distorted currents, series active filter compensates the voltages as shown in Fig. 6. The control technique is incorporated to obtain filtered currents, as shown in Fig. 8. APF consists of a voltage source converter with a dc link capacitor with an energy storage device [3, 4] (Fig. 1).

3 Instantaneous Vector Control Method

The active filter currents are produced using the above method. The transformations used here are Parke and Clarke transformations. The transformations are applied to load currents with respect to synchronous rotating frame of reference (Parke

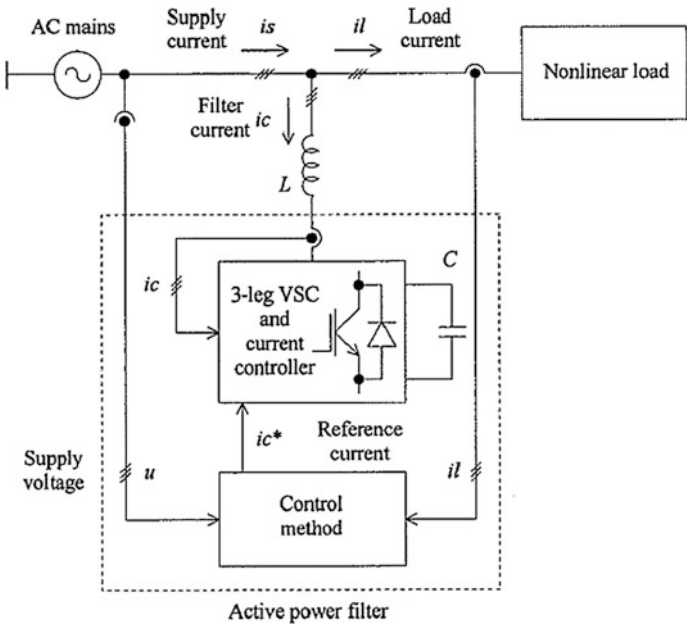

Fig. 1 General structure of active power filter

transformation) and arbitrary frame of reference (Clarke transformation) fed back to the source to get the reference currents Fig. 8.

$$\begin{pmatrix} ild \\ ilq \end{pmatrix} = \begin{pmatrix} \cos\theta & \sin\theta \\ \sin\theta & \cos\theta \end{pmatrix} \begin{pmatrix} il\alpha \\ il\beta \end{pmatrix}$$

where

$$\theta = \tan^{-1}\left(\frac{u\beta}{u\alpha}\right)$$

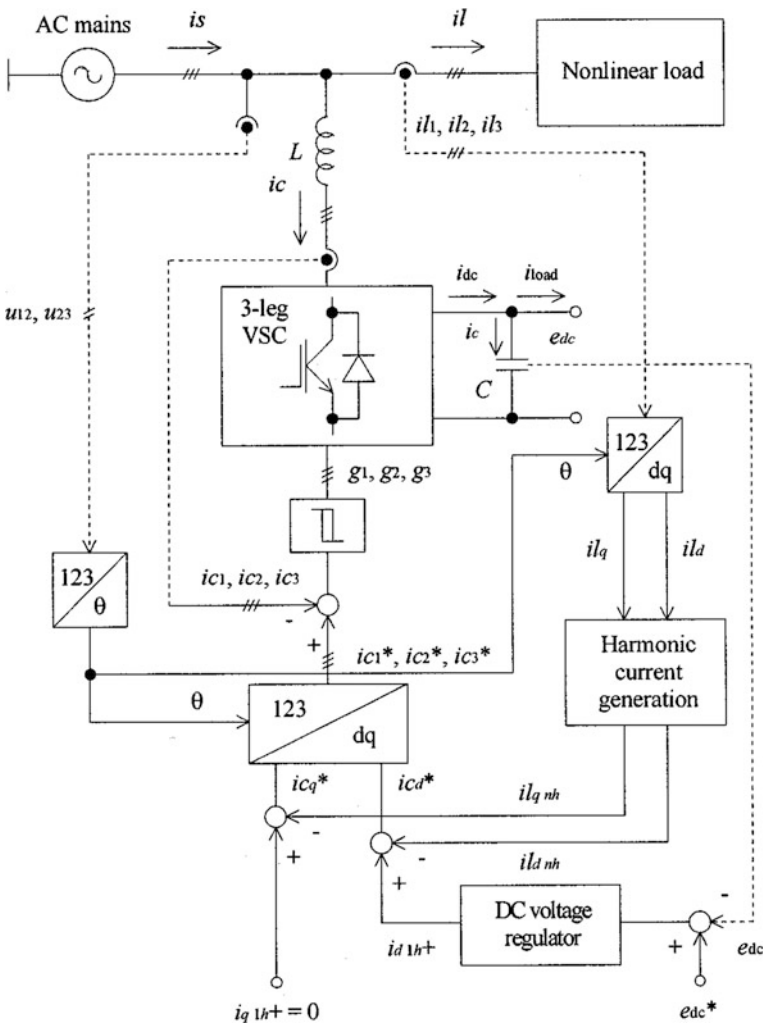

Fig. 2 Instantaneous active and reactive current control

$$\begin{pmatrix} ild \\ ilq \end{pmatrix} = \frac{1}{\sqrt{u\alpha^2 + u\beta^2}} \begin{pmatrix} u\alpha & u\beta \\ -u\beta & u\alpha \end{pmatrix} \begin{pmatrix} il\alpha \\ il\beta \end{pmatrix}$$

Instantaneous *ild* and *ilq* can be split into

$$ild = \sim ild + Ild \quad \text{and} \quad ilq = \sim ilq + Ilq$$

The positive sequence of the first harmonic currents is transformed into dc quantities, $ild1h^+$, $ilq1h^+$. These components contain the average current components. Hence, the filtered currents are given by (Fig. 2):

$$\begin{pmatrix} ic\alpha \\ ic\beta \end{pmatrix} = 1/\sqrt{u\alpha^2 + \mathrm{u}\beta^2} \begin{pmatrix} u\alpha & -u\beta \\ u\beta & u\alpha \end{pmatrix} \begin{pmatrix} icd \\ icq \end{pmatrix}$$

4 PI Controller and Hysteresis Current Controller

The actual and the reference currents are compared, and the error is fed back to a PI controller to track the reference current [5, 6]. The three-phase reference and actual currents are fed back to hysteresis band which chooses the converter switches [7, 8]. As the current switches, the lower switch of that phase has to be switched ON, and as the current decreases, the upper switch has to be switched ON which is in turn feedback as gate pulse to the converter [9, 10] (Fig. 3).

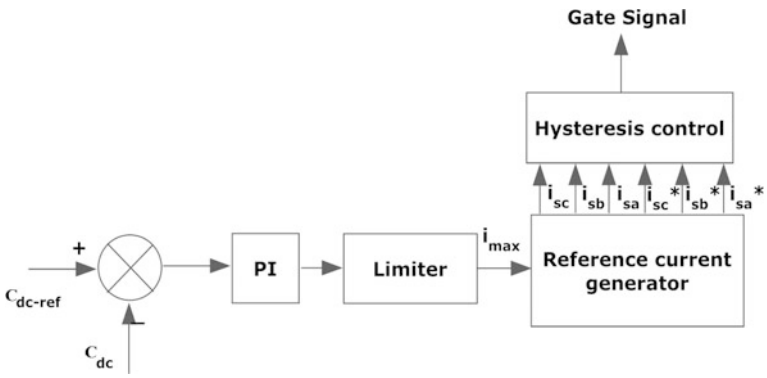

Fig. 3 Hysteresis–PI controller

5 Results and Simulation

The active power filter is simulated using the system parameters with voltage sources—220 V, frequency—50 Hz, inductance—0.1 mH, and resistance—15 Ω (Figs. 4, 5, 6, 7, and 8).

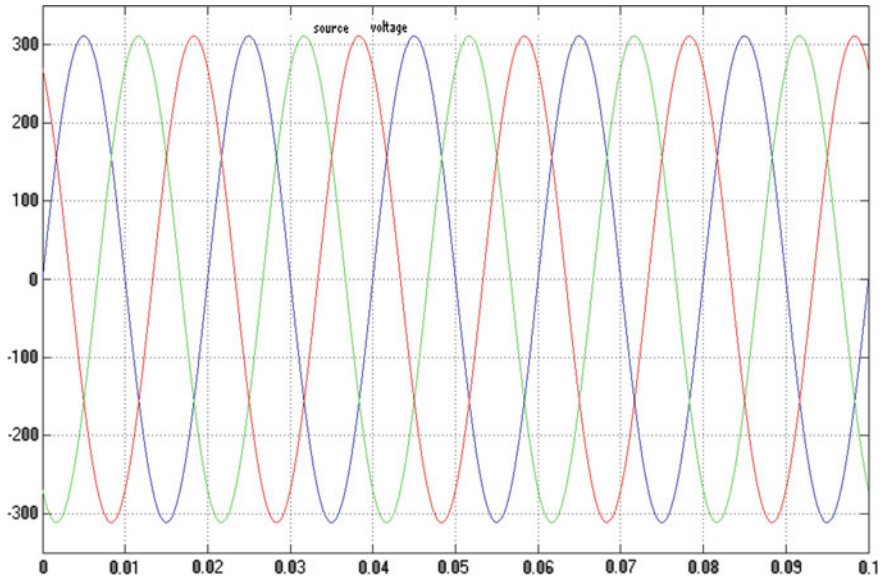

Fig. 4 Source voltage

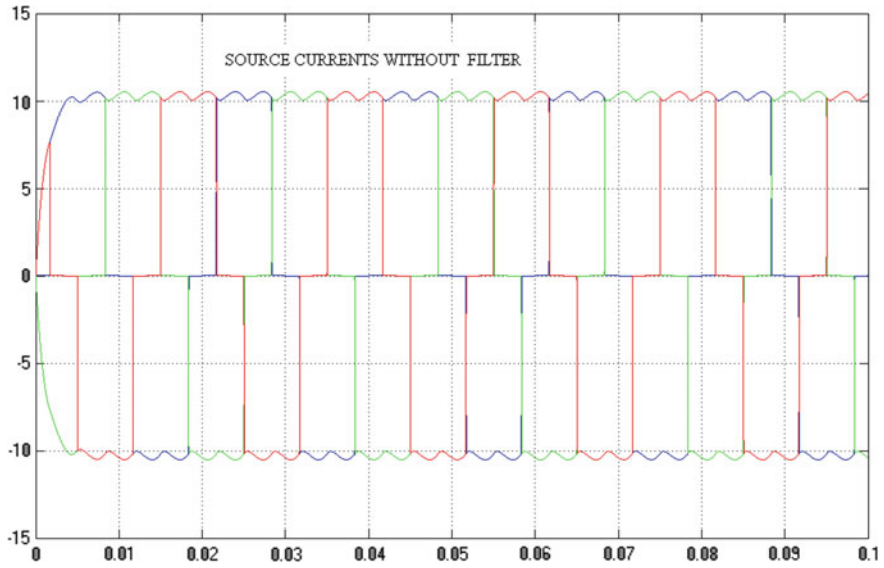

Fig. 5 Source currents without filter

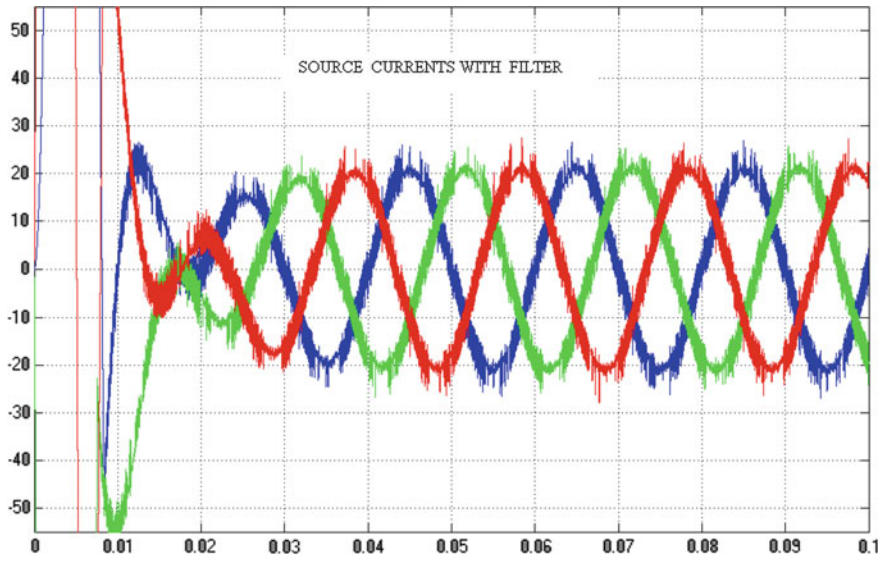

Fig. 6 Source currents with filter

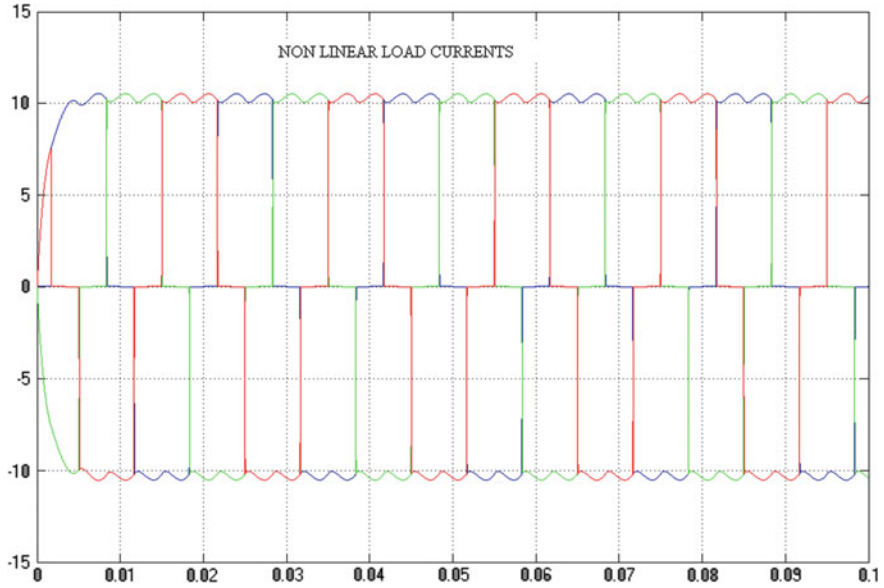

Fig. 7 Load currents

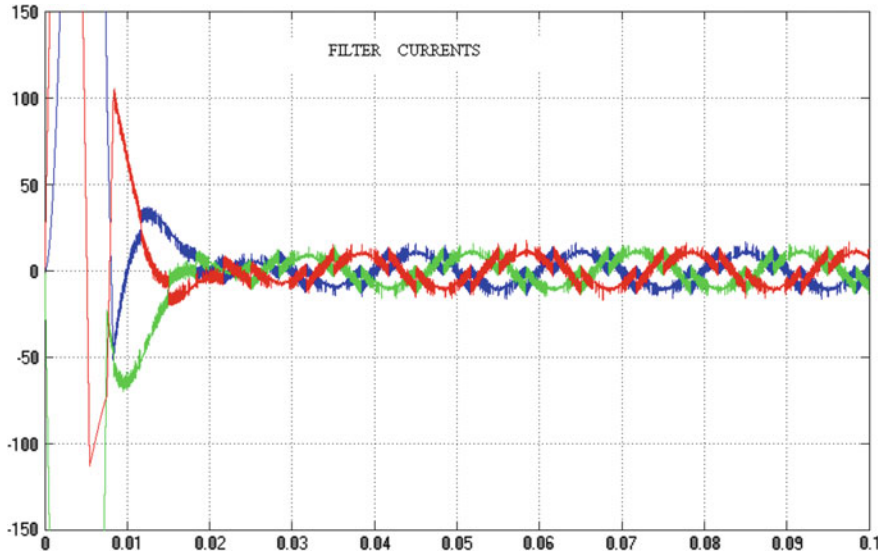

Fig. 8 Filter currents

6 Table

The results tabulated below are the source currents and the load currents before and after compensation, and its THD is calculated using FFT analysis.

6.1 Source Currents

Harmonic order	Without filter	With filter	Total harmonic distortion
3rd	1.15	52.4	29.2%
5th	20.0	18.5	
7th	14.75	15.70	
9th	1.20	14.9	

6.2 Filter Currents

Harmonic order	Without filter	With filter	Total harmonic distortion
3rd	1.15	25.2	3.75%
5th	20.00	7.8	
7th	14.75	9.4	
9th	1.20	8.6	

7 Conclusion

Thus, the power quality issues in the said system say positive sequence and negative sequence current harmonics were compensated using shunt active power-filtered instantaneous vector control theory. The instantaneous theory holds the advantage of operation of active power filter under varying frequency conditions, overall providing stability to the system.

References

1. Trinh, Q.-N., Lee, H.-H.: An advanced current control strategy for three-phase shunt active power filters. IEEE Trans. Ind. Electron. **60**(12), 5400–5410 (2013)
2. Hamad, M., Masoud, M., Ahmed, K., Williams, B.W.: A shunt active power filter for a medium-voltage twelve-pulse current source converter using open loop control compensation. IEEE Trans. Ind. Electron. **61**(11), 5840–5850 (2014)
3. Angulo, M., Lago, J., Ruiz-Caballero, D., Mussa, S., Heldwein, M.: Active power filter control strategy with implicit closed loop current control and resonant controller. IEEE Trans. Ind. Electron. **60**(7), 2721–2730 (2013)
4. Qasim, M., Kanjiya, P., Khadkikar, V.: Artificial neural network based phase locking scheme for active power filters. IEEE Trans. Ind. Electron. **61**(8), 3857–3866 (2014)
5. Biricik, S., Redif, S., Ozerdem, O.C., Khadem, S.K., Ba, M.: Real-time control of shunt active power filter under distorted grid voltage and unbalanced load condition using self-tuning filter. IET Power Electron. **7**(7), 1895–1905 (2014)
6. Uyyuru, K.R., Mishra, M.K., Ghosh, A.: An optimization-based algorithm for shunt active filter under distorted supply voltages. IEEE Trans. Power Electron. **24**(5), 1223–1232 (2009)
7. Kanjiya, P., Khadkikar, V., Zeineldin, H.: A noniterative optimized algorithm for shunt active power filter under distorted and unbalanced supply voltages. IEEE Trans. Ind. Electron. **60** (12), 5376–5390 (2013)
8. Chang, G.W., Yeh, C.-M., Chen, W.-C.: Meeting IEEE-519 current harmonics and power factor constraints with a three-phase three-wire active power filter under distorted source voltages. IEEE Trans. Power Del. **21**(3), 1648–1654 (2006)
9. Chang, G.W.: A new approach for optimal shunt active power filter control considering alternative performance indices. IEEE Trans. Power Del. **21**(1), 406–413 (2006)
10. George, S., Agarwal, V.: Optimum control of selective and total harmonic distortion in current and voltage under nonsinusoidal conditions. IEEE Trans. Power Del. **23**(2), 937–944 (2008)

Energy-Efficient Illumination Control Using Image Parameters in a Machine Vision Environment for Optimum Surface Texture Identification

R. Manish and S. Denis Ashok

Abstract Synergy of optimum illumination and image processing techniques is a very important aspect which needs to be incorporated in a machine vision environment to improve the durability of the lighting unit and also to conserve power requirements. This research work presents a novel way to optimize lighting requirements in a machine vision system using image feature analysis and image processing algorithms for texture identification. The practical implementation could be considered for automated machine vision environment for object surface inspection and quality monitoring.

Keywords Illumination control · Image processing · Canny algorithm
Surface texture · Fourier transform · Harris corner points · Intensity maps

1 Introduction

Nowadays, in many of the automated manufacturing and packaging industries, machine vision-based applications have a vital role in defining the product quality and finish. The need for a vision-based equipment in any manufacturing and inspection process is a necessity due to the fact that human visual system has limitations considering the environment conditions, robustness of deciphering an image, ability to focus only on the ROI, pixel level object identification, etc. All these issues can be clearly addressed as per the user requirements, by using a right combination of lens, camera, lighting equipment, corresponding data acquisition hardware, and image processing software. With the advancement of automation technology, production and inspection process in manufacturing companies have become simplified using online visual inspection methods where in the scope of

R. Manish (✉) · S. Denis Ashok
Department of Design and Automation, VIT University, Vellore, India
e-mail: manishraj.vit9@gmail.com

S. Denis Ashok
e-mail: denisashok@vit.ac.in

A. Konkani et al. (eds.), *Advances in Systems, Control and Automation*,
Lecture Notes in Electrical Engineering 442, https://doi.org/10.1007/978-981-10-4762-6_16

human involvement all the stages are minimized. The production cycle, i.e., from part production to inspection and packaging, is completely controlled and monitored by a central server zone. Many researchers have contributed to the varied fields consisting of machine vision applications. Chan et al. [1] have presented the scope of machine vision applications in industries. Kumar [2] researched upon the fabric defect detection applications in textile industry. Ke et al. [3] researched upon the online surface inspection in steel industries. Yu et al. [4] researched upon the micro-tool wear measurements using machine vision. Duan et al. [5] researched, developed, and successfully implemented a prototype which can detect bottle defects using machine vision application. Zhao et al. [6] researched and have presented work for identifying wooden sample species identification based upon the shape and texture of the wooden surfaces. Jin-Cong et al. [7] have investigated upon the wooden surface feature defect detection based upon texture features using image processing parameters. Li et al. [8] have done in-depth study regarding tool wear monitoring implementing image texture and segmentation analysis.

Taking inspiration from the above research works, this present research work aims at addressing unmanned and quick visual inspections of engravings/texture features on metallic surface objects in an automated industrial inspection environment.

2 Experimental Setup

The image capturing is done in a static environment (Fig. 1) where the object of interest which is a cylindrical aluminum (AISI 304 Grade) shaft specimen of circular cross section manufactured using facing operation, 14 mm in diameter, 50 mm in length, is kept stationary against an ideal background. The camera

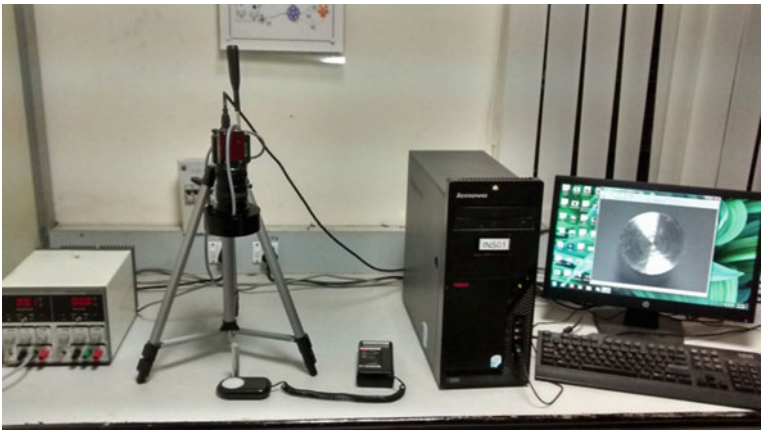

Fig. 1 Imaging and illumination control environment

distance from the object is also fixed at 33 cm (setup followed resembles that of an industrial product inspection environment). The camera and object are aligned vertically in-line. Front lighting arrangement using LED ring lighting module is opted for providing the required illumination upon the surface of the object.

2.1 Image Acquisition Environment

The ring lighting is mounted on the lens of the camera, and the illumination conditions are controlled by tuning the LED ring lighting intensity which is controlled by a voltage regulator to the desired luminance. The luminance is captured by using a lux meter from time to time to get a measure of the increasing brightness or darkness in the object environment.

The digital images are captured by the CMOS Marlin AVT grayscale camera which is connected to a PC by the means of a corresponding hardware. The captured grayscale images are processed using corresponding image processing software. The sequence of lighting conditions (Figs. 2 and 3) which is shown above gives an overall understanding of the image capturing process and the functioning of the entire experimental setup. The images are captured in 8-bit grayscale format. The image resolution is 800 × 600 (Width × Height). Each image thereby consists of 480,000 pixels. The intensity of the pixels ranges from 0 to 255 (gray level values). The proposed work to understand lighting condition and surface feature/texture detection is explained in Fig. 4.

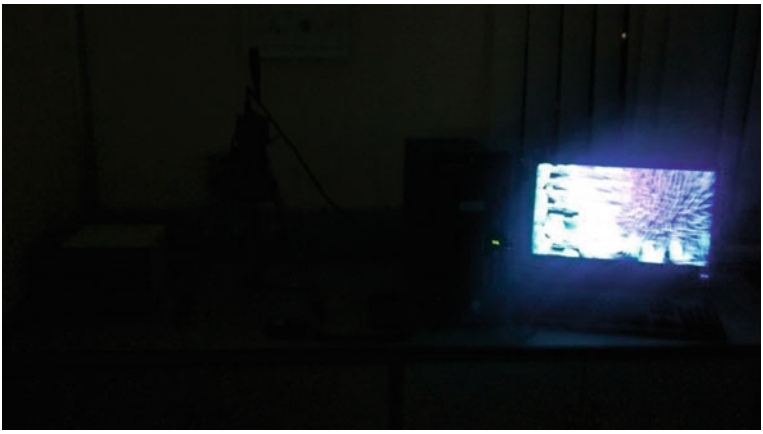

Fig. 2 Dark illumination condition

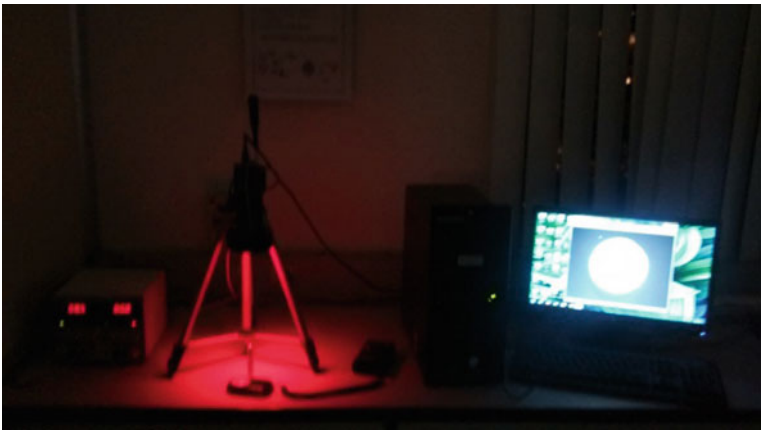

Fig. 3 Controlled illumination condition

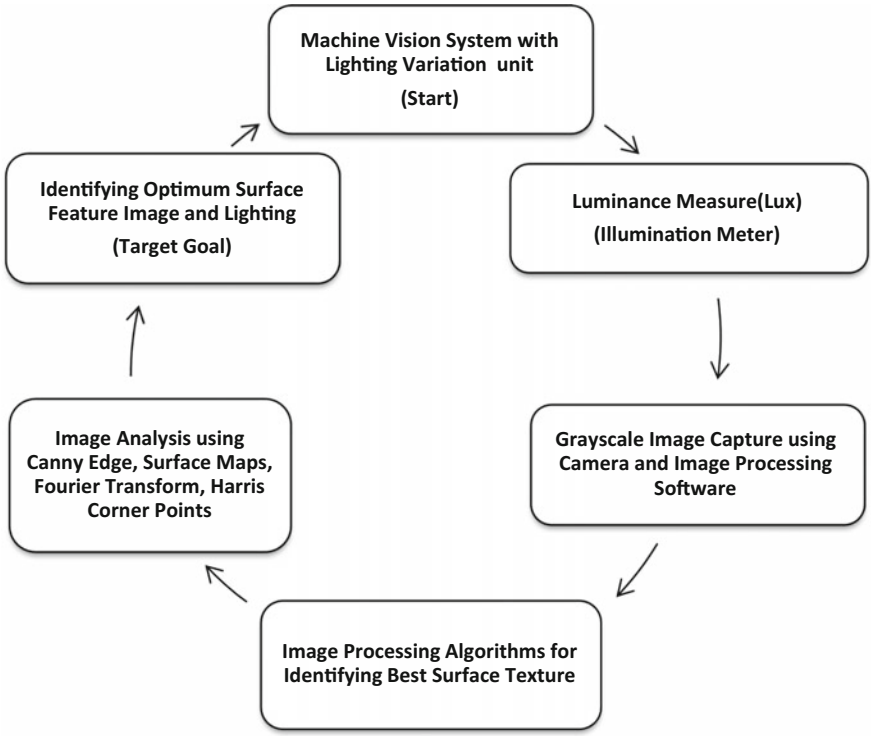

Fig. 4 Proposed methodology

3 Surface Pixel Intensities at Varying Lighting Conditions

Surface Image Maps: It is observed from the intensity maps that when there is a change in the lighting intensity, surface texture has a corresponding pixel intensity change. Shown in Figs. 5, 6, 7, 8, 9, 10, 11, and 12 are the surface images (left) and corresponding grayscale images (right) at various illumination conditions. The color in the intensity maps corresponds to grayscale intensity, where the color scale from blue to red corresponds to gray values from 0 (blue) to 255 (red).

Observations: It can be seen that the surface features tend to appear in a distinct manner at an illumination intensity of 19.96 lx in Fig. 8. In further sections of this paper, the supporting criteria which make Fig. 8 an optimum image are verified by the results of maximum feature edges detected by Canny algorithm in Fig. 17 and maximum Harris corner points distributed on the object surface as observed in Fig. 23. Also, the image is shown in Fig. 8. Has the maximum Fourier magnitude as compared to other images indicating an optimum edgier texture among the other image sets. There by, suggesting that illumination can be optimized using Image Parameters.

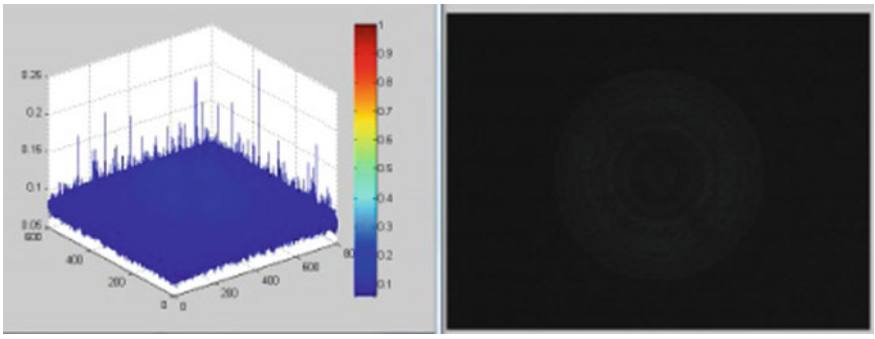

Fig. 5 Surface map 3.5 lx

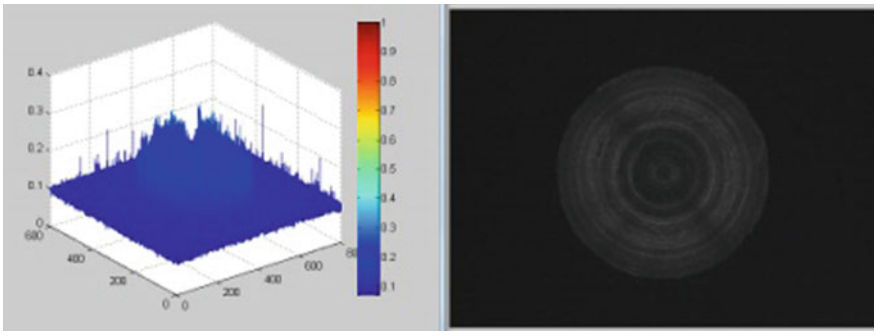

Fig. 6 Surface map 5.66 lx

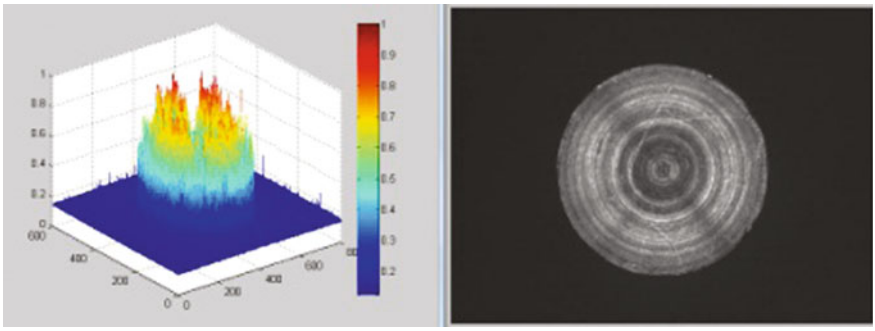

Fig. 7 Surface map 10.10 lx

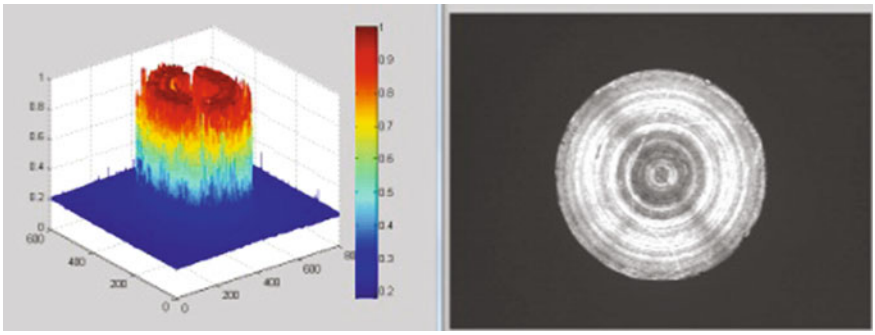

Fig. 8 Surface map 19.96 lx

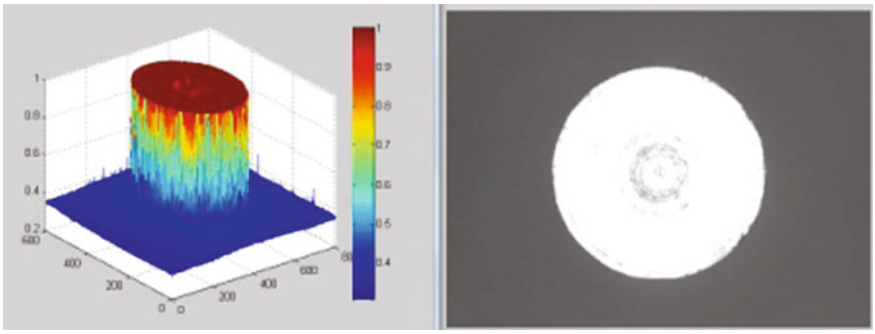

Fig. 9 Surface map 34.43 lx

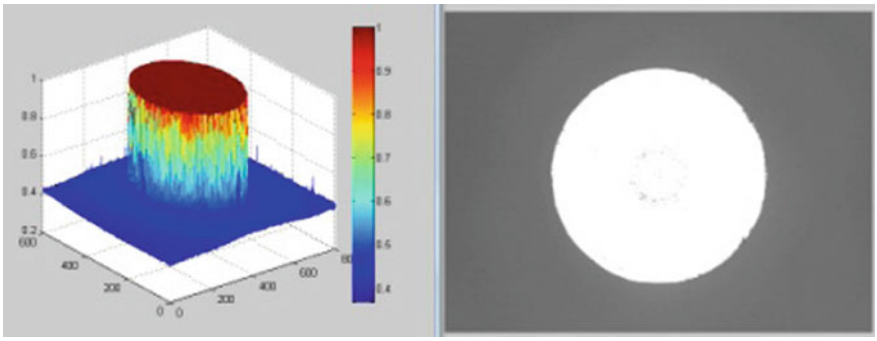

Fig. 10 Surface map 50.80 lx

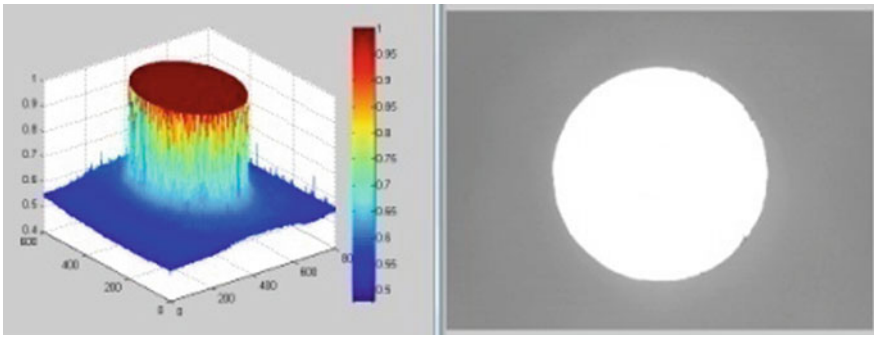

Fig. 11 Surface map 65.03 lx

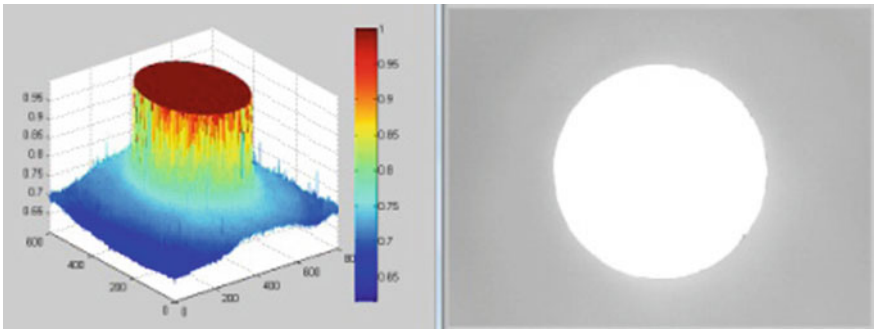

Fig. 12 Surface map 76.20 lx

4 Image Processing and Canny Edge Detection

4.1 Grayscale Image Representation

A 2D grayscale image $f(x, y)$ can be represented as a matrix consisting of gray level values ranging from 0 (black) to 255 (white). This can be mathematically represented as:

$$f(x,y) = \begin{bmatrix} f(1,1) & f(1,2) & f(1,3) \\ \cdots & \cdots & \cdots \\ f(n,1) & \cdots & f(n,n) \end{bmatrix}$$

The row and column elements in the above matrix represent the gray intensity of the image pixel at that particular point on the 2D image plane represented by $I(x, y)$.

4.2 Canny Edge Criteria and Algorithm

John Canny proposed the Canny edge algorithm [9] and had come up with three important criteria for optimum edge detection. It involves the following:

(a) SNR Value: True edges cannot be missed, and filtration of spurious edges is necessary. A high SNR (Eq. 1) means true edge is properly detected.

$$\text{SNR} = \frac{\left|\int_{-w}^{+w} E(-x)f(x)\mathrm{d}x\right|}{\delta\sqrt{\int_{-w}^{+w} f^2(x)\mathrm{d}x}} \tag{1}$$

Filter impulse response of edge $[-w, w]$ is $f(x)$, RMS of Gaussian noise is δ, and $E(x)$ is edge function.

(b) Accurate Edge Localization: This implies a minimal distance criteria between actual edge and located edge. The located edge should be at sub-pixel vicinity of the actual edge. Localization (Eq. 2) value should be high for detecting true edges.

$$\text{EdgeLoc} = \frac{\left|\int_{-w}^{+w} E'(-x)f'(x)\mathrm{d}x\right|}{\delta\sqrt{\int_{-w}^{+w} (f'(x))^2\mathrm{d}x}} \tag{2}$$

(c) Single Response Criteria: Multi-responses (non-maxima) to a single edge is minimized. Single edge response (Eq. 3) is obtained. $X_{\max}(f)$ is the pixel distance between the adjacent maxima in the response noise to f.

$$X_{\max}(f) = 2x_{zc}(f) = 2\pi \left[\frac{\int_{-\infty}^{\infty} (f'(x))^2 \mathrm{d}x}{\int_{-\infty}^{\infty} (f''(x))\mathrm{d}x} \right]^{1/2} \tag{3}$$

4.3 Canny Algorithm

The algorithm is represented in Fig. 13. It is a multistage edge detector yielding an optimum edge image with the appropriate threshold value inputs.

Step 1: *Gaussian Filter Smoothing*: Image is made noise free in this stage using Gaussian function (Eq. 4) over the image $F(x, y)$.

$$G(x,y) = \frac{1}{2\pi\sigma^2} e^{\left[\frac{-(x^2+y^2)}{2\sigma^2}\right]} \tag{4}$$

The gradient vector is given by: $\nabla G = \left[\frac{\mathrm{d}G}{\mathrm{d}x} / \frac{\mathrm{d}G}{\mathrm{d}y}\right]$.

Here, σ is the width of the Gaussian filter, which is the frequency band, and large σ implies a wide frequency band. σ value can be varied as per requirement.

Step 2: *Gradient and Magnitude Calculation*: Using first-order differential operator, the gradient and magnitude are calculated of the smoothed image obtained above. Gradient is calculated as represented by Eqs. (5) and (6) below.

$$P_x(i,j) = [I(i,j+1) - I(i,j) + I(i+1,j+1) - I(i+1,j)]/2 \tag{5}$$

$$P_y(i,j) = [I(i,j) - I(i+1,j) + I(i,j+1) - I(i+1,j+1)]/2 \tag{6}$$

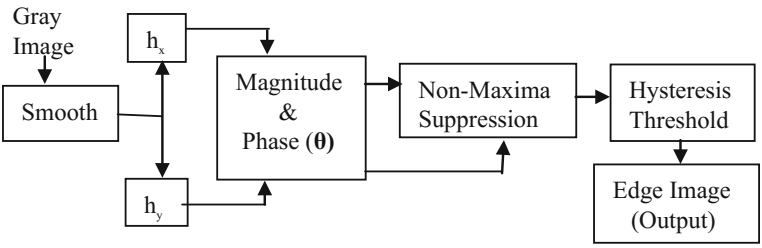

Fig. 13 Canny edge algorithm

Magnitude (Eq. 7) and direction (Eq. 8) of pixel point $P(i, j)$ are given by:

$$\text{Magnitude} = M(i,j) = \sqrt{\left(P_x^2(i,j)\right) + \left(P_y^2(i,j)\right)} \tag{7}$$

$$\text{Direction} = \theta(i,j) = \text{arcTan}\left[\frac{P_x(x,y)}{P_y(x,y)}\right] \tag{8}$$

Step 3: *Non-Maxima Suppression*: Only the local maxima magnitude is retained, and pseudo-edges are suppressed to get a refined true edges.

Step 4: *Hysteresis Thresholding*: Higher and lower thresholds (T_H and T_L) are set, and edges are marked based upon the gradient magnitude $M(i, j)$ being linked in the threshold range.

- If $M(i, j) > T_L$ implies, the point is an edge.
- If $T_L < M(i, j) < T_H$ implies, the point is an edge, provided the adjacent pixels are edge points, otherwise it is not an edge.
- If $M(i, j) > T_H$ implies, the point is an edge.

5 Canny Edge Images Under Varying Illumination Conditions

Edge detection for obtaining surface features for the experimental setup is shown below. Grayscale images (right) and Canny edge images (left) are presented in Figs. 14, 15, 16, 17, 18, 19, 20, and 21. Using minimum pixel intensity averaging, the thresholds were fixed at $T_l = 50$ and $T_h = 100$ (1:2) ratio for optimum edge.

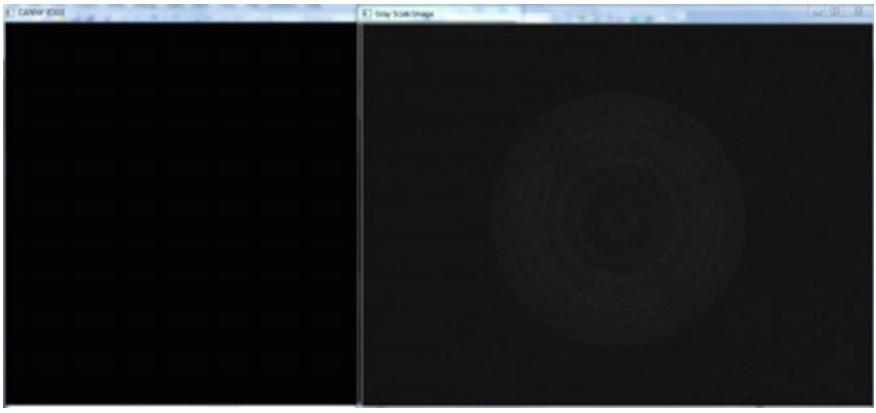

Fig. 14 Canny edge image at 3.5 lx

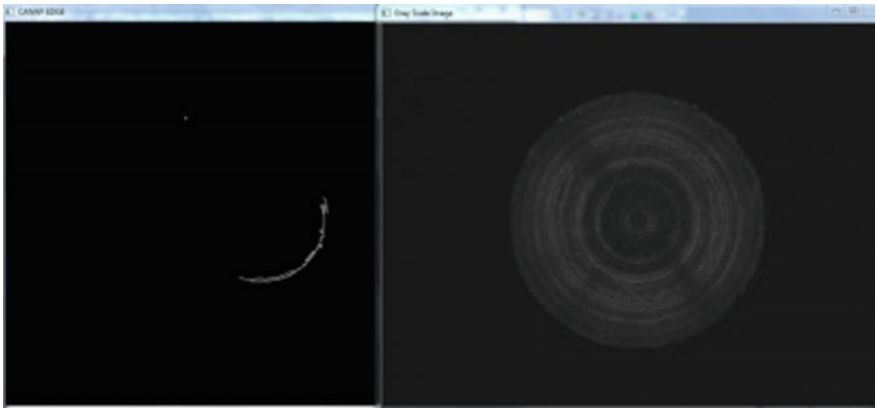

Fig. 15 Canny edge image at 5.66 lx

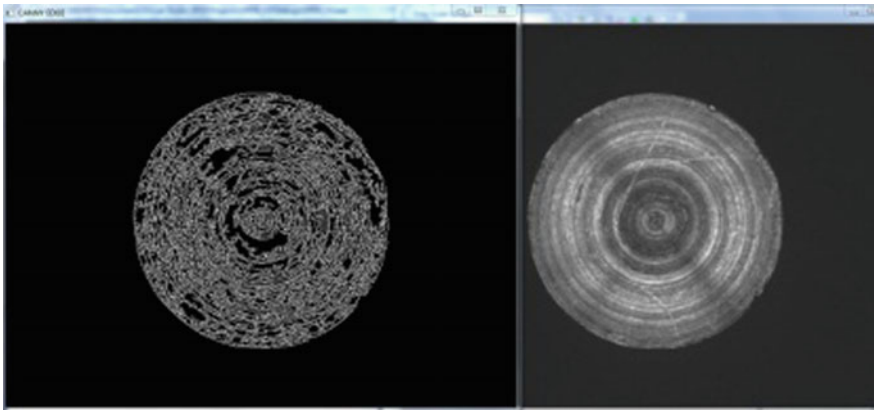

Fig. 16 Canny edge image at 10.1 lx

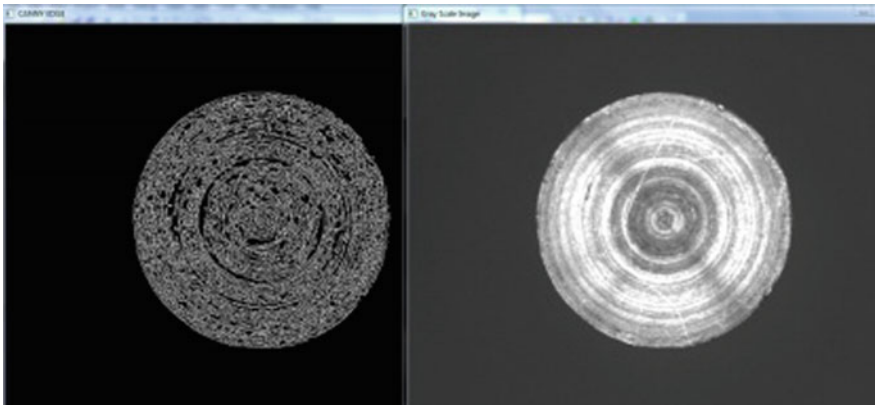

Fig. 17 Canny edge image at 19.9 lx

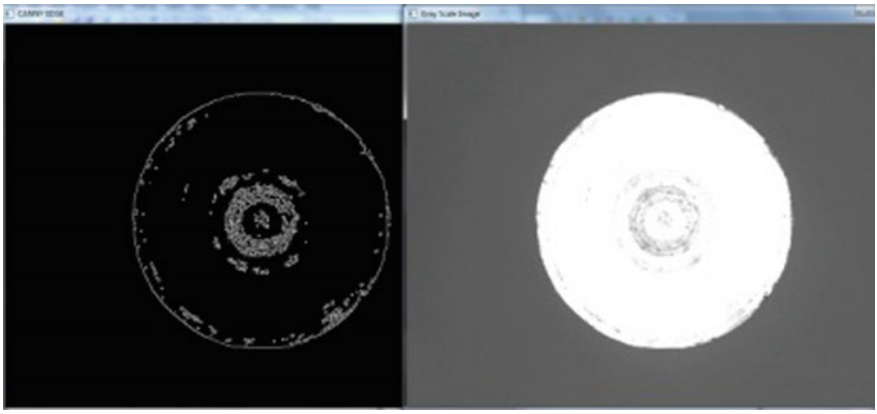

Fig. 18 Canny edge image at 34.4 lx

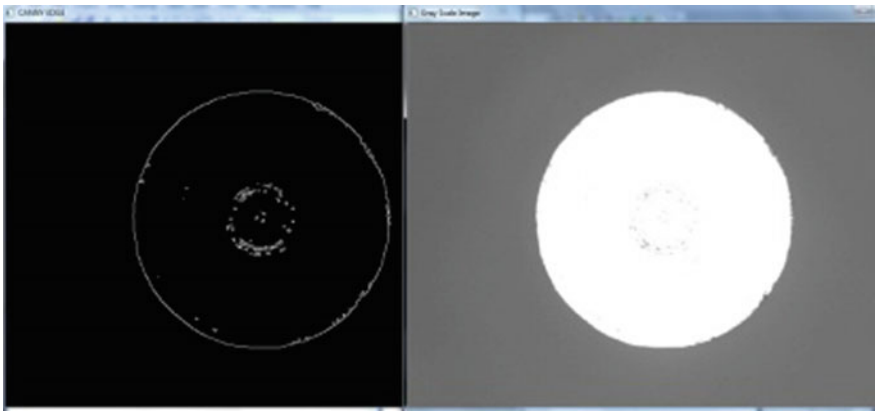

Fig. 19 Canny edge image at 50.8 lx

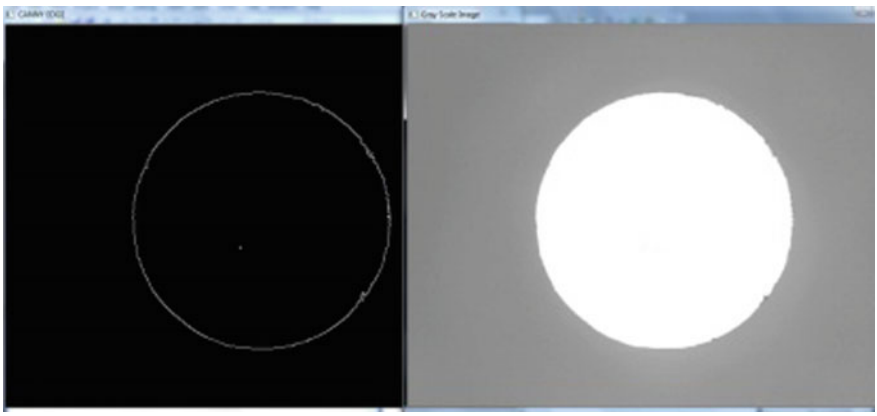

Fig. 20 Canny edge image at 65.0 lx

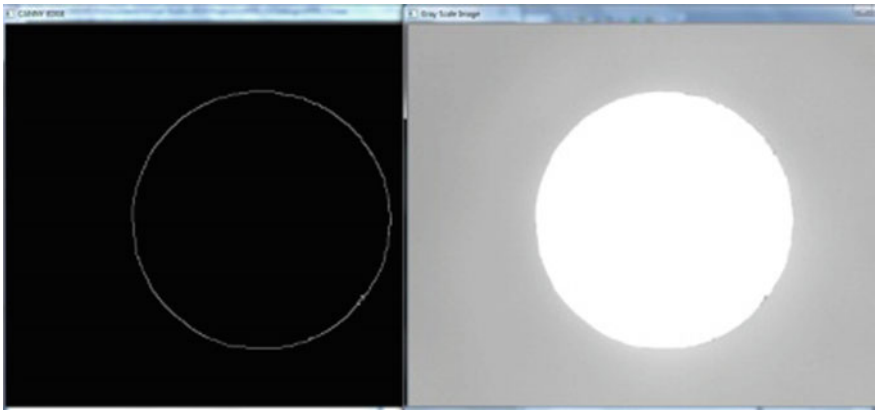

Fig. 21 Canny edge image at 76.2 lx

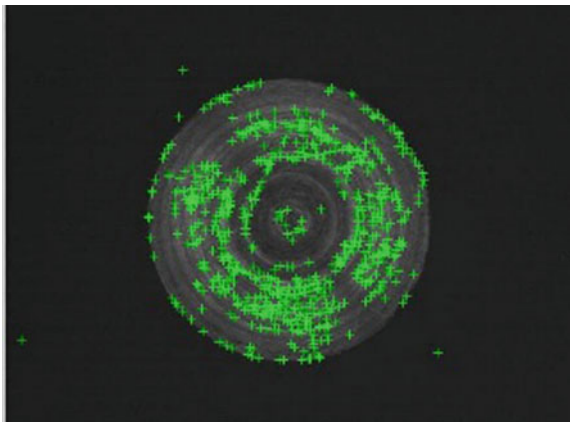

Fig. 22 HC points at 5.66 lx (low illumination)

6 Harris Corner Points and FFT for the Image Sets

Harris Corner Points: Harris corner [10] (HC) points are pixel locations which correspond to a region in the image where there is a significant change in the pixel intensity values surrounding the pivot pixel $P(i, j)$. The detected corners are the local maxima of an 8-pixel neighborhood for a pivot pixel P. Implementing the Harris corner algorithm in MATLAB yielded the following results.

Observations: It is seen that at low illumination (Fig. 22), the detected Harris corner points are 657 in number, and at optimum illumination (Fig. 23), there are maximum Harris corner points detected (1035), indicating a wide range of texture variations on the object surface, while at high illumination condition (Fig. 24), the detected points are 392 in number, thereby indicating that the surface features are not detected in an optimum manner at both high and low illumination conditions.

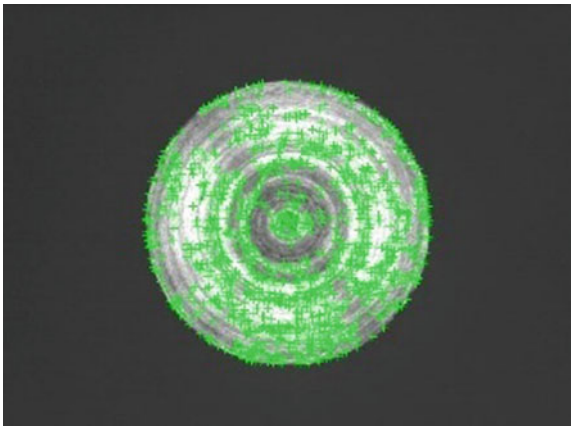

Fig. 23 HC points at 19.96 lx (optimum illumination)

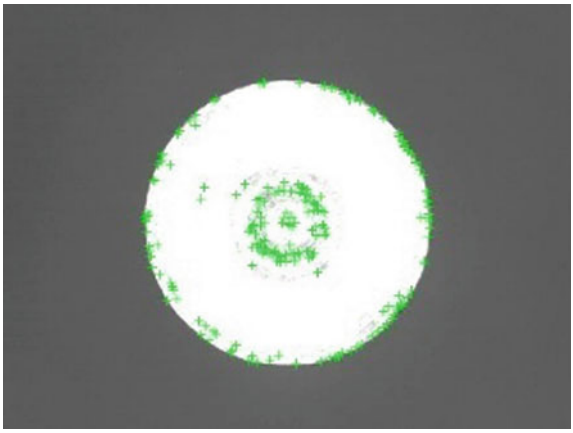

Fig. 24 HC points at 50.80 lx (high illumination)

Fast Fourier Transform: Converting the image into a frequency domain signal helps in understanding the edge features in a profound manner. To understand briefly, "higher magnitude response for an image using Fourier transform indicates edgier image texture." Implementing Fourier transform for the image sets, it has been observed that at an illumination of 19.96 lx, the maximum Fourier magnitude was obtained which indicates that the image with the optimum edge features and best surface texture is obtained at the corresponding illumination condition.

Inference: In this experimental work, it is seen that illumination conditions above 19.96 lx are not needed for optimum surface feature inspection. Voltage requirements and corresponding power for the LED lighting unit can be optimized by utilizing only the required luminance from the lighting unit, which can be calibrated and set using image parameters and their values.

7 Conclusion

From this research work, it can be concluded that for identifying optimum surface texture, image parameters such as edges, corner points, Fourier magnitude, and surface maps have been found highly useful for validation, and accordingly, the illumination conditions can be modulated for obtaining the best surface features based upon the image parameters, giving a synergy between lighting control and image processing in a machine vision environment.

Acknowledgements The authors would like to thank VIT University, Vellore, India; Department of Science and Technology (DST), Science and Engineering Research Board (SERB), New Delhi, India, for having provided the necessary research funding. Reference No. SB/FTP/ETA-276/2012, under fast track young scientists scheme, to develop and establish the Machine Vision Lab Environment for Industrial Application Research Work.

References

1. Chan, J.P., Palmer, G.S.: Machine vision-applications in industry. In: IEE Colloquium on Application of Machine Vision, p. 1. IET (1995)
2. Kumar, A.: Computer-vision-based fabric defect detection: a survey. IEEE Trans. Ind. Electron. **55**(1), 348–363 (2008)
3. Ke, X., Chaolin, Y.: On-line defect detection algorithms for surface inspection of hot rolled strips. In: 2010 International Conference on Mechanic Automation and Control Engineering (MACE), pp. 2350–2353. IEEE (2010)
4. Yu, H., Zhang, L., Xu, J., Yu, Z.: Detection method for tool wear of small lathe. J. Changchun Univ. Sci. Technol (Natural Science Edition) **2**, 001 (2014)
5. Duan, F., Wang, Y.N., Liu, H.J., Tan, W.: Empty bottle inspector based on machine vision. In: Proceedings of 2004 International Conference on Machine Learning and Cybernetics 2004, vol. 6, pp. 3845–3850. IEEE (2004)
6. Zhao, P., Dou, G., Chen, G.S.: Wood species identification using improved active shape model. Optik-Int. J. Light Electron Opt. **125**(18), 5212–5217 (2014)
7. YongHua, X., Jin-Cong, W.: Study on the identification of the wood surface defects based on texture features. Optik-Int. J. Light Electron Opt. **126**(19), 2231–2235 (2015)
8. Li, L., An, Q.: An in-depth study of tool wear monitoring technique based on image segmentation and texture analysis. Measurement **79**, 44–52 (2016)
9. Canny, J.: A computational approach to edge detection. IEEE Trans. Pattern Anal. Mach. Intell. **6**, 679–698 (1986)
10. Harris, C., Stephens, M.: A combined corner and edge detector. In: Alvey Vision Conference, vol. 15, p. 50 (1988)

Accuracy Analysis of Machine Vision for Detection of Malignant Melanoma Using Pixel Intensity Matrix Parameters

Punal M. Arabi, Gayatri Joshi, Surekha Nigudgi and N. Vamsha Deepa

Abstract Malignant melanoma is a life threatening disease which develops in the skin cells and has the potential to spread the other parts of the body. Early detection and treatment not only increase the survival rate but also reduce the cost of treatment. Sun exposure/ultraviolet exposure, free radicals and history of melanoma in first degree relative are important few factors of the many factors which cause malignant melanoma. Image processing and image analyzing techniques can be intelligently employed for computer aided diagnosis of malignant melanoma. Every year 132,000 people are affected by skin cancer worldwide. This paper proposes a method for the computer aided diagnosis of malignant melanoma using pixel intensity matrix parameters; the accuracy of the proposed method is also found. The results obtained show that the proposed method may be useful for developing an automated diagnosis system for malignant melanoma.

Keywords Accuracy analysis · Machine vision · Color component
Pixel intensity matrix parameters

1 Introduction

Skin cancer, a life threatening disease is the most common one of all types of cancers. It is caused by the uncontrolled growth of abnormal cells in the skin. Malignant melanoma is curable if it is diagnosed at early stages and the cost of

P.M. Arabi (✉) · Gayatri Joshi · Surekha Nigudgi · N. Vamsha Deepa
Department of Biomedical Engineering, ACSCE, Bangalore, India
e-mail: arabi.punal@gmail.com

Gayatri Joshi
e-mail: gayitrijoshi@gmail.com

Surekha Nigudgi
e-mail: sursanju@gmail.com

N. Vamsha Deepa
e-mail: vamshi.deepa@gmail.com

A. Konkani et al. (eds.), *Advances in Systems, Control and Automation*,
Lecture Notes in Electrical Engineering 442, https://doi.org/10.1007/978-981-10-4762-6_17

treatment is also reduced [1]. Main factors that cause melanoma are over exposure to sunlight and genetic factors [2]. Skin cancer can be reduced by limiting or avoiding over exposure to the UV (ultraviolet) radiation. Early detection of melanoma is given by the mnemonic "ABCDE": Asymmetry; Borders (irregular); Color; Diameter (greater than 6 mm (0.24 in.) Evolving over time.

Sadeghi et al. [3] proposed a method for melanoma diagnosis by identifying the presence or absence of streaks in skin lesions, analyzing and classifying the detected streaks in pigmented skin lesions.

Sirakov et al. [4], proposed two automatic skin lesion classification systems to identify the malignant and benign based on the shape, texture and color features. Ali et al. [5], developed a computer aided diagnosis system to assist dermatologists to detect the lesion boundary with highest diagnostic accuracy. Sáez et al. [6], described a method using local and global patterns to detect melanocytic lesions. Abdul Jaleel et al. [7], proposed the artificial neural network and image processing techniques for diagnosing skin cancer instead of going for biopsy test. Li et al. [8], developed a new approach using a spectroscopic device to extract the features of the image based on statistical measurements. Jose Luis García Arroyo et al. [9], developed an algorithm for the detection of reticular pattern over dermoscopic images to diagnose malignant melanoma.

The diagnosis of malignant melanoma by ABCDE parameters is a popular method. Out of these parameters color variation in a mole gives a notable clue about the nature of the mole i.e. whether it is normal or abnormal. This paper proposes a novel method for diagnosis of malignant melanoma using pixel intensity matrix parameters and computer vision.

2 Methodology

In the proposed method as shown in Fig. 1, pre-processing is done on acquired images and here the color variation of the mole is taken for experimentation and the proposed method attempts to develop a pilot computer aided diagnosis system for the detection of malignant melanoma by the pixel intensity matrix parameters; the proposed method involves two stages as

(1) Image enhancement
(2) Filtering by low pass filter.

For this work a set of 30 images of cancerous and normal moles are taken for analysis. The acquired images are RGB images and hence converted into gray images. ROI from the gray images of 400–600 pixel size are then identified. Pixel intensity matrix from these ROI's are found from which co-variance, standard deviation and maximum intensity level of pixels are calculated and tabulated.

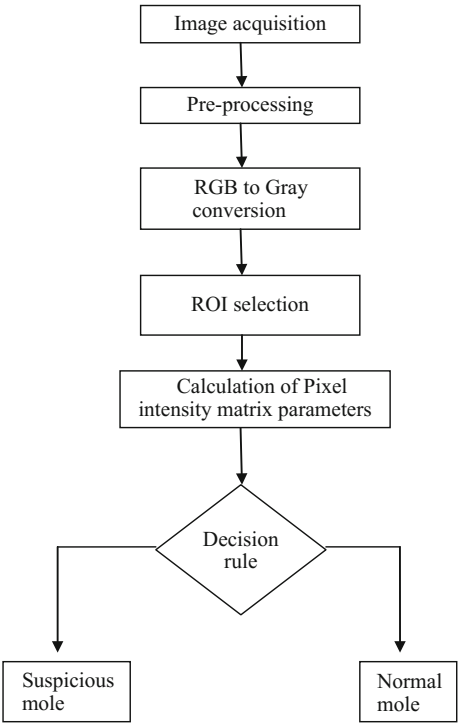

Fig. 1 Block diagram of CAD

2.1 Pixel Intensity Matrix Analysis

The pixel intensity matrix of the gray image is found for which the covariance, standard deviation, mean *fv* (maximum intensity pixel) are calculated.

$$\text{Covariance: } C(x,y) = E[\{x - E[x]\}\{y - E[y]\}] \tag{1}$$

where

x Row intensity value,
Y Column intensity value,
E Mathematical Expectation

$$\text{Standard deviation: } S = \sqrt{\frac{1}{n-1}\sum_{i=1}^{n}(x - x^{\wedge})^2} \tag{2}$$

where n = Total number of pixels in the selected region, $x^{\wedge}$ = Mean.

3 Decision Rule

If the values of the pixel intensity parameters of the image of concern are greater than the threshold values, the image is a suspicious one, may be a malignant mole. If the values are lesser than the respective threshold values, the image of interest may be a normal one. The threshold values are calculated by two methods as explained below.

Method-1: Average values of pixel intensity parameters of normal images are fixed as threshold values.

Method-2: The average values of all parameters of the normal images are found and is denoted as x. The values greater than the average values are found; a data set is created of these values and is represented as X. Using the following relation the reference values (threshold values) are arrived at as:

$$\text{Reference value } R = x + \sum (X - x)/N \tag{3}$$

where

R Reference value
x average values of pixel intensity parameters
X values > average values of the parameters $[X_1, X_2, \ldots X_n]$
N no. of values that are > average values

Sample calculation:

$$x = \frac{(538.23 + 730.8 + 323.7 + 1378 + 731.71 + 1065 + 1001 + 679.6 + 504.5 + 969.045)}{10}$$

$$\mathbf{x = 792.27}$$

$$\sum (X - x)/N$$

where

$$(X - x) = [X_1 - x, X_2 - x, \ldots X_n - x]$$

$$\sum (X - x)/N = \sum (X_1 - x, + X_2 - x, + \cdots + X_n - x)/N$$

$$X_1 = 1378; \quad X_2 = 1065; \quad X_3 = 1001; \quad X_4 = 969.04$$

$$\sum (X - x) = [(1378 - 792.27) + (1065 - 792.27) + (1001 - 792.27) + (969.04 - 92.27)]$$
$$= 1243.96$$

$$\sum (X - x)/N = (1243.96)/4 = 310.99$$

$$R = 310.99 + 792 = 1102$$

Note: For sample calculation the parameter covariance from Table 2 is considered. Table 2 shows that there are four values greater than the average pixel intensity value i.e., **x = 792.27** which are taken as $X_1 = 1378$, $X_2 = 1065$, $X_3 = 1001$, $X_4 = 969.04$ for the above calculation.

4 Results

Figure 2 shows set of normal mole images and Fig. 3 shows the set of abnormal mole of images. Tables 1 and 2 show the pixel intensity matrix parameter values for abnormal and normal moles. Table 3 shows the accuracy analysis of Method-1 and Method-2.

Fig. 2 Set of normal mole images

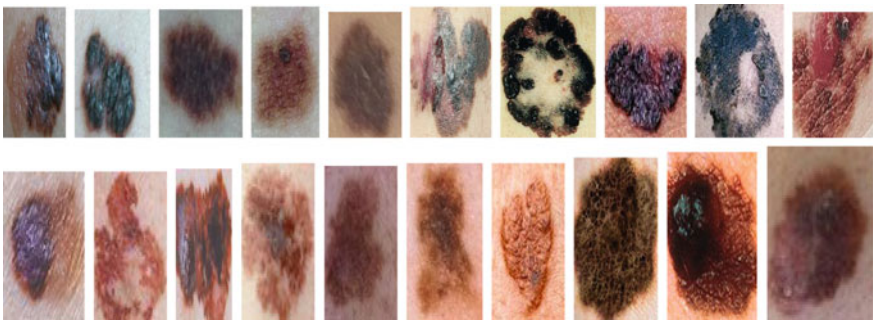

Fig. 3 Set of abnormal mole images

Table 1 Pixel intensity matrix parameters for abnormal mole images

Images	Covariance	Standard deviation	Δfv (mode)
1	1250	35.3559	87
2	2612	51.1139	146
3	1352	36.7752	98
4	1036	32.1908	116
5	826.46	28.7482	130
6	2141.3	46.2745	134
7	6474.7	80.4656	94
8	3079.9	55.4971	183
9	3816.3	61.7762	251
10	2099.8	45.8232	202
11	4676.6	68.3855	252
12	1373.6	37.0627	207
13	1325.5	36.4076	221
14	1839.1	42.8843	205
15	2022.7	44.9743	129
16	929.69	30.4910	154
17	1798.2	42.4051	213
18	1669.3	40.8574	244
19	4155.9	64.4666	117
20	3392.4	58.2445	134

Table 2 Pixel intensity matrix parameters for normal mole images

Images	Covariance	Standard deviation	Δfv (mode)
1	538.2395	23.20	60
2	730.8888	27.0349	24
3	323.7036	17.99	66
4	1378	37.12	82
5	731.7138	27.052	18
6	1065	32.63	20
7	1001.8	31.65	42
8	679.658	26.07	33
9	504.5856	22.46	23
10	969.0458	31.12	68
Average	792.25	27.63	43.6

5 Discussion

Malignant melanoma is diagnosed using A, B, C, D, E Parameters. Out of these parameters, color variation in moles is taken for experimentation. Twenty images of abnormal moles and ten images of normal moles are taken here for the experimentation.

Table 3 % Accuracy of I and II methods

Methods	% Accuracy					
	Normal mole images			Abnormal mole images		
	Covariance	Standard deviation	Mode	Covariance	Standard deviation	Mode
Method-1	60	60	60	100	100	100
Method-2	90	90	90	90	85	100

The pixel intensity matrices of these moles are obtained. The average values of the parameters namely co-variance, standard deviation, Δfv (mode) are found. To find Δfv (mode), every image is divided into 4 quadrants and this would lead to $4fv$ (Maximum pixel intensity values) values for every image. Out of these values maximum and minimum values are found from which Δfv (mode) is calculated as Δfv = [maximum fv − minimum fv]. Table 2 shows the parameters with average values. Using these average values the accuracy analysis of machine vision method for diagnosis malignant melanoma is carried out by two methods as described in the decision rule section. In method-1, the average values are taken as threshold values or reference values. By method-1, abnormal moles are found out very accurately where as normal moles are not accurately classified; 40% of false positive results are found in our experiment (i.e. the normal moles are classified as abnormal moles). To reduce the false positives, an empirical relation is proposed in method-2 as $R = x + \sum(X - x)/N$. In this method the reference value R is calculated using the above relation. The accuracy obtained by this method reduces false positives. Though it introduces few false negatives (i.e. abnormal moles are classified as normal moles), the overall efficiency obtained by this method is much greater compared to method-1.

6 Conclusion

The diagnosis of malignant melanoma by ABCDE parameters is a popular method. Out of these parameters color variation in a mole gives a notable clue about the nature of the mole i.e. whether it is normal or abnormal. This paper proposes a novel method for diagnosis of malignant melanoma using pixel intensity matrix parameters and computer vision.

If the value of pixel intensity parameters of the image of concern are greater than the threshold values, the image is a suspicious one, may be a malignant mole. If the values are lesser than the respective threshold values, the image of interest may be a normal mole. The results obtained show that the proposed method is of considerable accuracy that this will throw light on developing a computer aided diagnosis system for malignant melanoma. However the accuracy of the method can be confirmed only after experimenting with many more images and after clinical studies.

Acknowledgements The authors thank the Management and Principal of ACS College of engineering, Mysore road, Bangalore for permitting and supporting to carry out the research work.

References

1. Barbara Gilchrest, A.: Sun exposure and vitamin D sufficiency 1,2,3,4. Am. J. Clin. Nutr. **88**, 570S–577S (2008)
2. Han, J., Colditz, G.A., Liu, J.S., Hunter, D.J.: Genetic variation in XPD, sun exposure and risk of skin cancer. Cancer Epidemiol. Biomarkers Prev. **14**, 1539–1544 (2005)
3. Sadeghi, M., Lee, T.K., McLean, D., Lui, H., Stella Atkins, M.: Detection and analysis of irregular streaks in dermoscopic images of skin lesions. IEEE Trans. Med. Imaging **32**, 849–861 (2013)
4. Sirakov, N.M., Mete, M., Selvaggi, R., Luong, M.: New accurate automated melanoma diagnosing systems. Int. Conf. Healthcare Inf. 374–379 (2015)
5. Ali, A.R.A., Deserno, T.M.: A systematic review of automated melanoma detection in dermatoscopic images and its ground truth data. In: Proceedings of SPIE, vol. 8318, pp. 83181I-1–83181I-11 (2012)
6. Saez, A., Acha, B., Serrano, C.: Pattern Analysis in Dermoscopic Images, Computer Vision Techniques for the Diagnosis 23 of Skin Cancer, Series in BioEngineering, pp. 23–48. Springer, Berlin (2014)
7. Abdul Jaleel, J., Salim, S., Aswin, R.B.: An optimized, economical and painless artificial intelligence technique to diagnose Melanoma. Int. J. Soft Comput. Softw. Eng. (JSCSE) **3**. e-ISSN: 2251-7545 (2013)
8. Li, L., Zhang, Q., Ding, Y., Jiang, H., Thiers, B.H., Wang, J.Z.: Automatic diagnosis of melanoma using machine learning methods on a spectroscopic system. BMC Med. Imaging Res. 1–12 (2014)
9. Arroyo, J.L.G., Zapirain, B.G.: Detection of pigment network in dermoscopy images using supervised machine learning and structural analysis. Comput. Biol. Med. **44**, 144–157. Elsivier (2014)

Investigation of Perylene as a Converter Material for Fast Neutron Detection and Spectroscopy Using GEANT4 Monte Carlo Simulations

Shivang Tripathi, Chandrakant Upadhyay, C.P. Nagaraj, A. Venkatesan, K. Devan and K. Madhusoodanan

Abstract Monte Carlo simulations have been performed to investigate the perylene ($C_{20}H_{12}$) as a converter layer for fast neutron detection and spectroscopy. Perylene is an organic semiconductor material having high hydrogen content which could be utilized as a medium of elastic scattering for fast neutrons to produce recoil protons such as in proton recoil detector. This charged recoil proton would further liberate e-hole pairs while traversing through the material which will induce the detector's response in the associated electronics with appropriate applied reverse voltage. Perylene is used as a neutron converter layer on top of the wide band-gap semiconductor material such as silicon carbide (SiC) which can maintain its typical characteristics even in the harsh radiation environment. SiC would help in efficient charge collection resulting from recoil proton. The thickness of perylene as a converter layer was optimized and found to be $\sim$500 μm for wide energy range of fast neutrons. This work would further aid in the comparative study of different converter material for SiC-based fast neutron detector.

Keywords Monte Carlo · GEANT4 · Semiconductor detectors · Perylene
Proton recoil method · Fast neutron · Silicon carbide
Wide band-gap semiconductor

1 Introduction

Neutron detectors are employed for nuclear applications such as monitoring of nuclear reactor core, fuel reprocessing plant [1], special nuclear material detection, and high-energy physics experiments, and for fast neutron radiation therapy [2]. Gas-filled neutron detectors are currently being used for nuclear applications that

S. Tripathi (✉)
Homi Bhabha National Institute, Anushaktinagar, Mumbai 400094, India
e-mail: shivang@igcar.gov.in

S. Tripathi · C. Upadhyay · C.P. Nagaraj · A. Venkatesan · K. Devan · K. Madhusoodanan
Indira Gandhi Centre for Atomic Research, Kalpakkam 603102, India

A. Konkani et al. (eds.), *Advances in Systems, Control and Automation*,
Lecture Notes in Electrical Engineering 442, https://doi.org/10.1007/978-981-10-4762-6_18

could not provide the energy spectrum which is a major drawback along with other shortcomings such as gas purity, space charge effect, wall effect, high voltage supply requirement, bulky structure [3]. These gas-filled detectors have high radiation hardness in comparison to semiconductor detectors. Si-based semiconductor detectors are very much prone to radiation induce defects [4]. Recent research in the area of wide band-gap semiconductors has revealed a new era of semiconductor detectors which are unsusceptible to radiation-induced damages. Wide band-gap semiconductors such as silicon carbide (SiC), boron nitride (BN), aluminum nitride (AlN), gallium arsenide (GaAs), and gallium nitride (GaN) are extensively being researched for the development of radiation hard detectors [5–12]. SiC, with wide bang-gap of $\sim$3.25 eV and displacement threshold energy of 21.8 eV [5, 13], has shown a great potential to become a future material of choice for harsh environment radiation detectors. SiC can detect neutron directly and indirectly. Silicon and carbon atoms in SiC can directly undergo elastic and inelastic scattering reaction upon interaction with fast neutrons [14–16]. A layer of neutron converter material would further enhance the detection efficiency [15, 17]. A low-Z hydrogenous material is preferred for neutron converter since it has a higher cross section for elastic scattering with fast neutrons [3]. We have optimized the thickness of hydrogenous converter layer *polyethylene* in our previous work [18]. Recoil proton generated in converter would lose part of its energy in converter itself which could not be collected, thus resulting in a continuum of energy spectrum. A. Kargar et al. have reported a fast neutron detector based on organic semiconductor, i.e., *perylene* [19]. Perylene has good optical properties and thermal stability, and it is generally used for blue-emitting dopant material in OLEDs [20]. Since the mobility of electrons and holes in perylene is low, i.e., 5.5 and 87.4 cm^2/V s at 60 K, respectively, [21] which could hinder the efficient charge collection process.

Therefore, to increase the charge collection efficiency (CCE), we have presented perylene as a hydrogenous neutron converter material in this work. Perylene upon interaction with fast neutrons would generate recoil proton which will further liberate e-hole pairs in SiC detector active region. This method of fast neutron detection is primarily known as proton recoil method [3]. It must be noted that as we increase the thickness of converter, more number of neutrons will interact resulting in a large number of recoils [18]. But these recoils will have a certain range in a particular material. If the thickness of converter is more than the range of energetic recoil, most of the recoils will die out in converter itself, or it may enter detector active area with very less energy which can be considered as a background. Thus, Monte Carlo-based GEANT4 [22] simulations have been performed to optimize the thickness of perylene for the wide energy range of neutron detection.

2 GEANT4 Simulation Methodology

GEANT4, stands for GEometry ANd Tracking, is a simulation toolkit for particle transport through matter. It has a complete range of functionality including tracking, geometry, physics models, and processes [23]. It is capable of tracking down the secondary particles generated due to the primary reaction. It provides a vast set of well-defined physics models including hadronic, electromagnetic, and optical process from low energy to very high energy range [24]. It has been developed with software engineering and object-oriented technology and implemented in C++ programming language. The neutron transport class library described in GEANT4 simulates the interactions of neutrons with kinetic energies from thermal energies up to 20 meV.

2.1 Model Description

GEANT4.10.01 version is used to build the detector model. The planar detector geometry has been constructed using GEANT4 geometry category class as shown in Fig. 1. It consists of a converter layer of perylene (density 1.28 g/cc) with 1 cm^2 front face (*XY*-plane), and thickness (*Z*-axis) is varied from one micrometer to few millimeters using GEANT4 macro file to optimize the thickness of converter. Here, optimized thickness represents the thickness at which the detector efficiency is maximum [25]. In other words, the thickness at which, maximum number of recoil protons will stretch out of the converter layer into the SiC semiconductor to generate a detectable signal. Adjacent to the converter is a detector layer made up of SiC with similar *XY*-plane, and thickness is kept at 500 µm as shown in Fig. 1. General Particle Source Class of particle category has been used to generate neutron of various energies and spectrum of ^{241}Am-Be neutron source. ROOT, a data analysis framework [26], is integrated to generate various histograms. In order to optimize the converter thickness, 10^8 neutrons have been simulated 5 times at different converter thickness for different energy neutron sources.

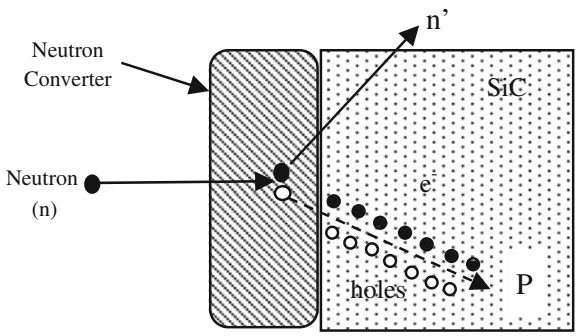

Fig. 1 Demonstration of SiC-based planar neutron detector

3 Results and Discussion

3.1 SiC as a Neutron Detector

SiC exists in about 250 crystalline forms [27], and similar crystalline structures are termed as polytypes. Major polytypes are 3C–SiC, 4H–SiC, and 6H–SiC. 4H–SiC polytype is a popular choice for radiation detectors due to its substantially higher electron transport properties and higher band-gap compared to other polytypes [28]. SiC can be used directly to detect fast neutron. Silicon and carbon atoms in SiC will undergo elastic to generate ^{28}Si or ^{12}C recoils, respectively, and inelastic scatterings to produce alpha, protons, or other charged particles as per their reaction cross section [29]. Energy deposition in SiC due to neutron interaction is demonstrated in Fig. 2. Most probable reaction, i.e., elastic scattering will produce Si and C recoils. We have generated ^{241}Am–Be neutron source with 10^7 events for demonstration purpose. Table 1 listed out the major particles produced in SiC detector. A layer of neutron converter layer to increase the efficiency is discussed in next section.

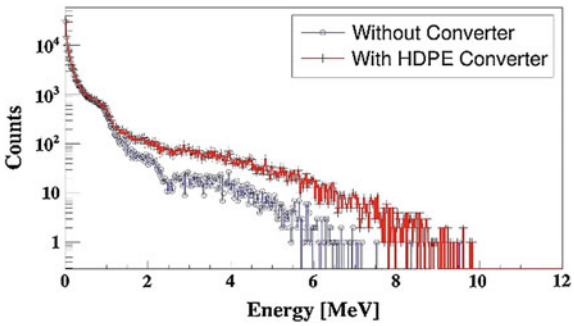

Fig. 2 Comparison of energy deposition in SiC detector with and without converter

Table 1 List of particles generated in SiC

Generated particles	Number	Mean K.E.	Range of K.E.
Al^{28}	1324	369.57 keV	17.661 keV → 1.098 meV
Be^{9}	378	1.2535 meV	17.818 keV → 3.2302 meV
C^{12}	45,277	380.6 keV	3.2477 eV → 2.8088 meV
C^{13}	499	377.55 keV	672.02 eV → 1.9826 meV
Mg^{25}	674	902.31 keV	52.417 keV → 2.3485 meV
Si^{28}	57,921	135.98 keV	3.86 eV → 1.3867 meV
Si^{29}	2716	145.4 keV	13.78 eV → 1.231 meV
Si^{30}	1843	139.76 keV	71.395 eV → 1.1567 meV
Alpha	1093	3.3006 meV	335.52 keV → 9.5139 meV
Proton	1359	3.1518 meV	421.08 keV → 7.0983 meV

3.2 SiC Detector with Neutron Converter Layer

A layer of hydrogenous converter layer would significantly increase the detection efficiency of SiC-based detectors [15]. High-density polyethylene (HDPE) is generally used as a converter layer for fast neutron detection. Optimized thickness for HDPE is taken as ∼500 μm [18] for comparison of energy deposition in SiC with and without converter layer. From Fig. 2, it is evident that having a converter over SiC detector would enhance the energy deposition in detector active layer which will result in better efficiency.

Recoil proton would deposit part of its energy in converter before reaching the active layer of the detector. Figure 3 shows the energy which is lost or unexploited in the converter by recoil proton. A substantial amount of energy is being lost in polyethylene converter which would certainly limit the energy resolution of the spectrum and of course, hamper the efficiency.

A material which could assist the charge collection even from the unexploited energy lost in converter would definitely augment the efficiency of the detector and further magnify the energy resolution. A converter layer based on conductive polymers or organic semiconductor could be presumed to unravel this argument. We are proposing perylene as a converter layer after being motivated from [19].

3.3 Perylene as a Converter Layer for SiC Detector

In order to employ perylene as a converter, we have performed Monte Carlo simulations to optimize its thickness for the wide energy range of neutron. Further, a special case of ^{241}Am–Be neutron source has been taken up to analyze the various energy spectrum in SiC detector. Figure 4 represents an efficiency of perylene converter-based SiC detector as a function of converter thickness for different energy neutrons. From this plot, optimum thickness could be determined for the wide energy range of neutron. Optimum thickness could be contemplated as the thickness which can provide adequate recoils in the detector active region. We have estimated ∼500 μm as an optimum thickness for perylene converter layer. The

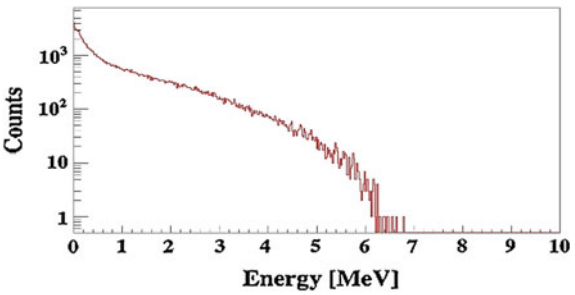

Fig. 3 Unused or lost energy of recoil proton in polyethylene converter

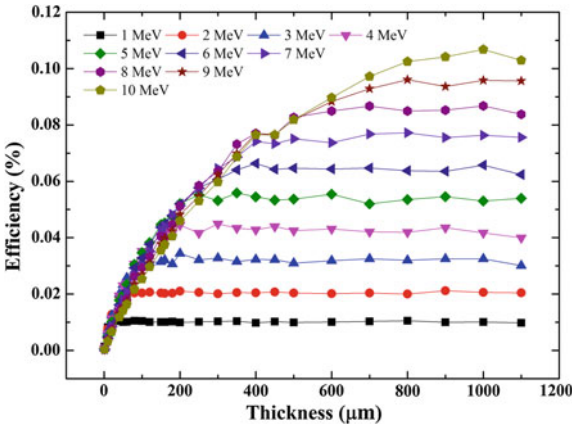

Fig. 4 Efficiency versus perylene thickness for wide energy neutrons

thickness of perylene is also optimized for a particular case of ^{241}Am–Be neutron source which is having a mean energy of ~4.177 meV. It is found that for ^{241}Am–Be neutron source, the optimized thickness is ~500 μm (Fig. 5), which is in good agreement with our wide energy range optimization estimation.

3.4 Calculation of Energy Deposition

Figures 6 and 7 represent the histograms of total energy deposited and energy deposited by recoil proton in the active region of SiC detector, respectively. These energy spectrums show the potential of perylene converter with SiC detector to be employed as a fast neutron spectrometer.

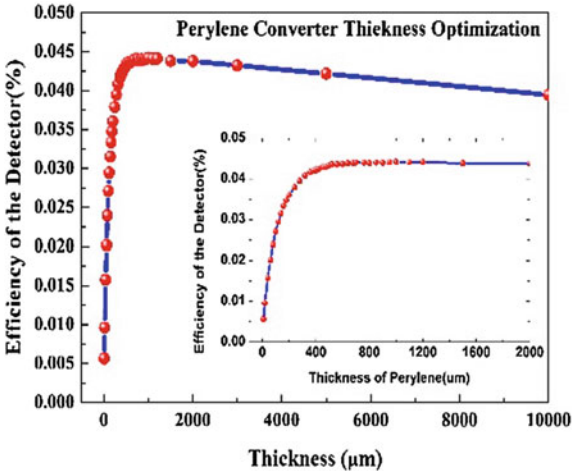

Fig. 5 Perylene thickness optimization for ^{241}Am-Be neutron source

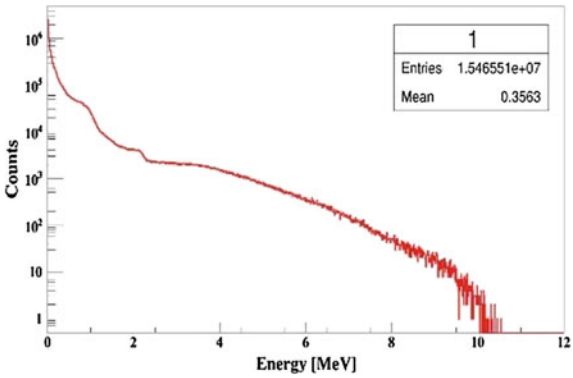

Fig. 6 Total energy deposited in SiC active region

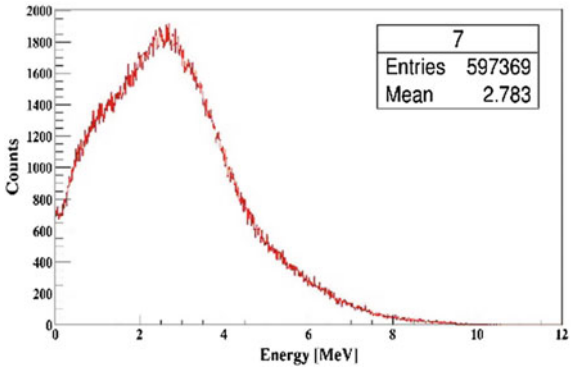

Fig. 7 Energy deposited by recoil protons in SiC active region

4 Conclusion

GEANT4 simulations have been performed to investigate neutron transport and interaction in SiC detector along with perylene converter layer. Reactions due to neutron interactions that are happening in SiC are tabulated along with their mean energy and range. Improvement in SiC detector efficiency has been demonstrated by applying a neutron converter layer, i.e., polyethylene. To minimize the unused deposited energy in polyethylene converter, organic semiconductor material perylene is propounded. The thickness of perylene converter layer has been optimized, and it is found to be $\sim$500 μm. Spectroscopic capabilities of perylene converter with SiC detector has been demonstrated using various histograms. Hitherto, it is unclear, how the difference in charge collection efficiency (CCE) of perylene and SiC will affect the overall CCE of detector, but it could be a worth area to explore further. Our GEANT4 model could further assist in the study of converter layer for fast neutron detection and spectroscopy.

Acknowledgements The first author gratefully acknowledges the grant of research fellowship from Indira Gandhi Centre for Atomic Research, Department of Atomic Energy, India.

References

1. Sivaramakrishna, M., Nagaraj, C.P., Madhusoodanan, K., Chellapandi, P.: Neutron flux monitoring system in prototype fast breeder reactor. Int. J. Eng. Innov. Technol. **3**, 45–53 (2014)
2. Cohen, L., Awschalom, M.: Fast neutron radiation therapy. Annu. Rev. Biophys. Bioeng. **11**, 359–390 (1982)
3. Knoll, G.F.: Radiation Detection and Measurement. Wiley, New York (2010)
4. Bruzzi, M.: Radiation damage in silicon detectors for high-energy physics experiments. IEEE Trans. Nucl. Sci. **48**, 960–971 (2001)
5. Seshadri, S., Dulloo, A.R., Ruddy, F.H., Seidel, J.G., Rowland, L.B.: Demonstration of a SiC neutron detector for high-radiation environments. IEEE Trans. Electron Devices **46**, 567–571 (1999)
6. Dulloo, A.R., Ruddy, F.H., Seidel, J.G., Adams, J.M., Nico, J.S., Gilliam, D.M.: The thermal neutron response of miniature silicon carbide semiconductor detectors. Nucl. Instrum. Methods Phys. Res. Sect. Accel. Spectrometers Detect. Assoc. Equip. **498**, 415–423 (2003)
7. Doty, F.P.: Boron nitride solid state neutron detector. http://www.google.co.in/patents/US6727504 (2004)
8. Moon, B.S., Hahn, C.H., Yoo, D.S., Kim, I.G., Cho, Y.H., Holcomb, D.E.: Measurement of a 2-MeV electron beam flux by using an aluminum-nitride detector. J. Korean Phys. Soc. **51**, 1771 (2007)
9. Mulligan, P., Wang, J., Cao, L.: Evaluation of freestanding GaN as an alpha and neutron detector. Nucl. Instrum. Methods Phys. Res. Sect. Accel. Spectrometers Detect. Assoc. Equip. **719**, 13–16 (2013)
10. McGregor, D.S., Klann, R.T., Gersch, H.K., Yang, Y.H.: Thin-film-coated bulk GaAs detectors for thermal and fast neutron measurements. Nucl. Instrum. Methods Phys. Res. Sect. Accel. Spectrometers Detect. Assoc. Equip. **466**, 126–141 (2001)
11. Ha, J.H., Kim, Y.K.: Fabrication and characteristics of a fully depleted semi-insulating GaAs semiconductor detector for alpha radiation detection at room temperature in air. J. Korean Phys. Soc. **52**, 576 (2008)
12. Ha, J.H., Kang, S.M., Han Soo, K.I.M., Park, S.H., Nam Ho, L.E.E., Song, T.-Y., LEE, J.H.: 4H-SiC PIN-type semiconductor detector for fast neutron detection. Prog. Nucl. Sci. Tech. **1**, 237–239 (2011)
13. Seshadri, S., Dulloo, A.R., Ruddy, F.H.: An advanced SiC nuclear radiation detector. In: Device Research Conference Digest, pp. 114–115 (1997)
14. Franceschini, F., Ruddy, F.H.: Silicon carbide neutron detectors. INTECH Open Access Publisher (2011)
15. Flammang, R.W., Seidel, J.G., Ruddy, F.H.: Fast neutron detection with silicon carbide semiconductor radiation detectors. Nucl. Instrum. Methods Phys. Res. Sect. Accel. Spectrometers Detect. Assoc. Equip. **579**, 177–179 (2007)
16. Ruddy, F.H., Dulloo, A.R., Seidel, J.G., Das, M.K., Ryu, S.-H., Agarwal, A.K.: The fast neutron response of 4H silicon carbide semiconductor radiation detectors. IEEE Trans. Nucl. Sci. **53**, 1666–1670 (2006)
17. Mad Filho, T., Hamada, M.M., Shiraishi, F., de Mesquita, C.H.: Development of neutron detector using the surface barrier sensor with polyethylene (n, p) and 10 B (n, α) converters. Nucl. Instrum. Methods Phys. Res. Sect. Accel. Spectrometers Detect. Assoc. Equip. **458**, 441–447 (2001)

18. Tripathi, S., Upadhyay, C., Nagaraj, C.P., Devan, K., Madhusoodanan, K., Murty, S.A.V.S.: Geant4 simulations of semiconductor detectors (SiC) for fast neutron spectroscopy. In: Annual IEEE India Conference (INDICON), pp. 1–6 (2015)
19. Kargar, A., Loef, E.V.V., Cirignano, L., Shah, K.S.: Organic semiconductors for fast-neutron detection. In: 2011 IEEE Nuclear Science Symposium and Medical Imaging Conference (NSS/MIC), pp. 4545–4549 (2011)
20. Kişnişci, Z., Yüksel, Ö.F., Kuş, M.: Optical properties of perylene-monoimide (PMI) and perylene-diimide (PDI) organic semiconductor thin films. Synth. Met. **194**, 193–197 (2014)
21. Berger, L.I.: Semiconductor Materials. CRC Press, Boca Raton (1996)
22. Agostinelli, S., et al.: Geant4—a simulation toolkit. Nucl. Instrum. Methods Phys. Res. Sect. Accel. Spectrometers Detect. Assoc. Equip. **506**, 250–303 (2003)
23. Allison, J., et al.: Geant4 developments and applications. IEEE Trans. Nucl. Sci. **53**, 270–278 (2006)
24. Geant4 Physics Reference Manual [online]
25. McGregor, D.S., Kenneth Shultis, J.: Reporting detection efficiency for semiconductor neutron detectors: a need for a standard. Nucl. Instrum. Methods Phys. Res. Sect. Accel. Spectrometers Detect. Assoc. Equip. **632**, 167–174 (2011)
26. ROOT a Data analysis Framework|ROOT a Data analysis Framework. https://root.cern.ch/
27. Cheung, R.: Silicon Carbide Microelectromechanical Systems for Harsh Environments. World Scientific (2006)
28. Nava, F., Bertuccio, G., Cavallini, A., Vittone, E.: Silicon carbide and its use as a radiation detector material. Meas. Sci. Technol. **19**, 102001 (2008)
29. Sedlačková, K., Zat'ko, B., Šagátová, A., Pavlovič, M., Nečas, V., Stacho, M.: MCNPX monte carlo simulations of particle transport in SiC semiconductor detectors of fast neutrons. J. Instrum. **9**, C05016–C05016 (2014)

Spectral Analysis and Comparison of Single-Carrier PLC Modules in Narrowband Power Line Communication System

Srihari Mandava, Abhishek Gudipalli and G. Vidhya Sagar

Abstract In recent times, power line communication (PLC) has an ability of communicating the signals and messages making use of the existing power lines without going for new mediums such as optical fibers or radio waves. Considering the voltage, electrical networks are rated as low (1 kV), medium (1–100 kV), and high (>100 kV) networks and the communication problems in these networks increase with increase in voltage. In order to establish high-speed data communications with data rates in the range of megabit/s over power line networks, dedicated communication systems considering the hostile channel properties are required. In addition to signal distortion, losses in cables and multipath propagation, noise from the system also plays a key role to alter the digital communication over power line networks which is dealt in this project. In this work, the signals are obtained with less bit error rate (BER) using Rayleigh fading channel improving the efficiency of the whole system. Different modulation techniques are compared in narrowband power line communication (PLC) systems, and some suggestions are made for the improvement of data transmission in narrowband systems. The best compromise for single-carrier PLC modules between efficiency and architecture complexity is being investigated in this project.

Keywords Binary frequency-shift keying · PSK · ASK · Bit error ratio Rayleigh fading

S. Mandava (✉) · A. Gudipalli · G. Vidhya Sagar
School of Electrical Engineering, VIT University, Vellore, Tamil Nadu, India
e-mail: mandavasrihari@vit.ac.in

A. Gudipalli
e-mail: abhishek.g@vit.ac.in

G. Vidhya Sagar
e-mail: vidhyasagar.g@vit.ac.in

A. Konkani et al. (eds.), *Advances in Systems, Control and Automation*,
Lecture Notes in Electrical Engineering 442, https://doi.org/10.1007/978-981-10-4762-6_19

1 Introduction

PLC is a protocol of communication used to transfer both digital signal and electric signal simultaneously. PLC is also called as power line carrier, power line networking (PLN), and power line digital subscriber line (PDSL). The concept of power line communication was first introduced in the 1950s and was used for controlling the one-way remote relays operating at a frequency of 10 Hz and at a power rating of 10 kW. Later in the 1980s, research was carried out [1]. In the next step, the narrowband power line communication (PLC) was used for telemetry purpose in high-voltage lines with a frequency range of 15–500 kHz of which is still playing its role in power line communication [2]. The very first test for the bidirectional data transfer was done in 1997 by Ascom in Switzerland. Nowadays, the concept of power line communication is used in the smart grids to establish a two-way communication over the existing power distribution network. Modern power networks comprise of a variety of alternate energy sources and much advanced energy consuming devices. These advanced sources include solar power sources, wind mills and smart appliances and electric vehicles on the consuming end.

Load management is the main aim of power line communication. The present methods have the drawbacks of consuming more power for information transmission. The second goal is to make the possibility of electrical meter reading from a distance. A meter reader using PLC is shown in [3] which gets the information at a rate of only 1 bit/s. Tokyo Electric Power Co carried out some successful experiments in the 1970s showing the flow of information in both the directions (bidirectional) with several hundred units [4]. This narrowband PLC technique can also be used for the detection of fraud, power theft, switching on and off loads, load shedding, and demand response. Broadband PLC system was developed by AT&T [3] to provide Internet services over the existing power line network and with the help of the power grid. In this, the frequencies at which the current and data signals vibrate should not match with each other. This method has the disadvantages of noise introduction and electromagnetic compatibility (EMC). Qun et al. designed a power line communication system based upon the FSK-KQ 330 [6] module and analyzed that when there is no data transmission, the signal in the transmit pin is a straight line. It was also seen that the data transmission values at low voltages are nearly same as obtained in the theoretical calculations. Manfred Zimmermann et al. showed the effect of broadband noise on a PLC network in [5]. In this, the PLC system developed at a frequency range of a few kilohertz to a few megahertz does not experience any additive white gaussian noise but is only interfered by narrowband noises and impulsive noises in this particular frequency band. The noise can be a background, narrowbanded, periodic, and asynchronous to the main frequency and periodic impulsive noise.

Dan Raphaeli of Itran Communications et al. [5] showed the differences of OFDM, spread spectrum, and single carrier for high-rate data transmission through PLC. In this work, the FSK was a technique used for transmission in narrowband signal and a major part of the signal was distorted with high spectral density. On the

other hand, the OFDM technique used for the data transmission through broadband could be used on any practical distorting channel. The implementation of OFDM technique is quite tough than the implementation of the FSK techniques used in narrowband PLC system. The spread spectrum was able to transmit at all the band frequencies, and this transmission depends only on the positive signal-to-noise ratio of the spectrum.

This paper will help in study of different modulation techniques in narrowband power line communication (PLC) systems and will help to determine that which of all the techniques used is best on the basis of BER versus SNR ratio and with the help of Simulink model. The signals are obtained with less bit error rate (BER) using Rayleigh fading channel improving the efficiency of the whole system. The best compromise for single-carrier PLC modules between efficiency and architecture complexity is also investigated. In this paper, Sect. 2 gives brief introduction to different modulation techniques, Sect. 3 explains about the classifiers of binary frequency-shift keying (BFSK), amplitude-shift keying (ASK), and phase-shift keying (PSK) used in single-carrier modulation, and Sect. 3 gives the result analysis of the classifiers comparing with each other.

2 Feature Extraction

Modulation is a technique which is used to send signals of low frequency to a large distant place by using another high frequency without much loss of the binary data. The main reason for sending a low-frequency data by combining along with high frequency is that the high frequency has less wavelength and thus because of this reason it suffers less diffraction. The procedure by which original signal is received from a modulated signal is known as demodulation. A modulated wave consists of different carrier or sideband signals. In a PLC system, the process of demodulation is used to extract the binary data which is sent from the sending end. The quality of this data depends upon the modulation and demodulation techniques used for sending the signal from the sending end to the receiving end. There are different types of modulation and demodulation techniques used to transmit the signal from one end to the other end.

2.1 Single-Carrier Modulation

In this, a section of bits are associated with a group of symbols. Fourier coefficients are set for various transmitters, i.e., the users by mapping and demapping of blocks. The reverse section has the modules for IDFT, demapping and to detect user signal. Guards' symbols are implemented between different blocks of symbols to put an end to the interference of intersymbol caused by time widening across the blocks. In single-carrier modulation, mapping is of two types, i.e., localized mapping and

distributing mapping. The mapping which has the subcarriers set for the DFT outputs of input data restricts them to small fraction of the bandwidth in system is called localized mapping and the one in which the DFT outputs of input data are allocated to subcarriers for the whole bandwidth is called distributed mapping.

2.2 Multicarrier Modulation

This is a technique which divides the stream of bits into several bit streams. Each bit stream will have a lower bit rate and are used to modulate several carriers. After receiving the overall transmission, the receiver has then to reassemble the overall data stream received from the individual carriers. The concept of multicarrier modulation is based on several channels which are isolated from other using steep-sided filter. The interference from different available channels is eliminated in this manner. Initially, the multicarrier modulation technique was mainly used in the broadcasting systems such as digital amplitude modulation and video broadcasting. The different multicarrier modulation techniques are orthogonal frequency-division multiplexing (OFDM), generalized frequency-division multiplexing, and filter bank multicarrier.

2.2.1 Orthogonal Frequency-Division Multiplexing

OFDM has number of closely spaced modulated carriers. The receiver receives the complete signal and then demodulates the signal. So when a signal is transmitted, the receiver segregates the received signal from transmitted. The receiver passes the received signal through a filter and the guard is used between the signals to prevent interference with each other. In an OFDM signal, the primary requirement is that the signal must be linear in nature otherwise the overlapping of signals would take place and will cause disturbance the orthogonality of the transmitted signal. The data to be sent by the OFDM signal is passed onto the carriers of the signal so that each carrier takes the payload, thus reducing the data rate on each carrier. When the data rate gets reduced, the main advantage is that interference from the other signals is less and does not affect the data in signal much. This is because of the guard band introduced into the system. Thus, the data is sampled only when signal is stable and no other signals altering the time and phase of the signal.

2.2.2 Generalized Frequency-Division Multiplexing

Generalized frequency-division multiplexing is the latest idea for flexible multiple carrier transmission that provides with extra degrees of freedom as compared to new orthogonal frequency-division multiplexing. In this, the pulse-shaping filter is responsible for out of band radiation of the transmitted signal applied to the

individual subcarriers. In order to reduce the number of carriers, the size of the block is a variable parameter.

2.2.3 Filter Bank Multicarrier

This type of modulation technique depends upon the division of frequency spectrum into many narrowband frequency channels. It completely depends upon the high performance of the DSP processors because channel estimation and equalization becomes a trivial task. With the insertion of some redundancy, the frequency-selective channel becomes a frequency flat subchannel. The required level of selectivity and separation can be achieved by using the filter bank itself.

3 Classifier

The different types of single-carrier modulation techniques used in power line communication system are listed as follows.

3.1 Binary Frequency-Shift Keying (BFSK)

Binary frequency-shift keying [1] is the technique which is used to transmit the binary data through the changes of discrete frequency in a carrier wave. In this type, a discrete pair of frequencies are used which are used to transmit data. In this frequency-shift keying, '1' is called mark frequency and '0' is called space frequency.

$$\mathrm{SBFSK}(t) = A\sin(2\pi[f_c + m(t)f_m]t + \omega_0) \quad 0 \le t \le 100; \tag{3.1}$$

where $m(t)$ = 0 or 1, T is bit duration, A is amplitude, f_c is frequency, and ω_0 is phase.

3.2 Amplitude-Shift Keying (ASK)

Amplitude-shift keying involves the digital modulation in which the carrier wave amplitude gets modified in a completely discrete manner. There can be a number of baseband signals which are given by the formula

$$\begin{aligned} &M = 2m \\ &\mathrm{d}m(t), \quad 0 \le m \le M; \\ &\qquad\quad 0 \le t \le T; \end{aligned} \tag{3.2}$$

On modulation of these signals, the carrier wave is given by

$$S(t) = Am(t)\cos(2\pi f_c t) \quad 0 < t < T \tag{3.3}$$

where A is a constant, $m(t) = 1$ or 0, f_c = carrier frequency and T = the bit duration.

3.3 Phase-Shift Keying (PSK)

Phase-shift keying is the technique which is widely used in the radio communication. It is one of the best suited techniques to use for the purpose of data communications through PLC system. In phase-shift keying, there are defined states or points which are used for sending the bits. When a digital signal is transmitted through a line, it creates amplitude reversals between 1 and −1, thus leading to phase reversals of 1800 phase shifts. The main problem used while using the phase-shift keying is that the user at receiver end is not able to determine that whether it is in space or mark condition.

4 Results

The results before and after modulation with each classifier with and without noise are shown in Figs. 1, 2, 3, 4, 5, and 6.

4.1 Binary Frequency-Shift Keying (BFSK)

See Figs. 1 and 2.

4.2 Amplitude-Shift Keying (ASK)

See Figs. 3 and 4.

4.3 Phase-Shift Keying (PSK)

See Figs. 5 and 6.

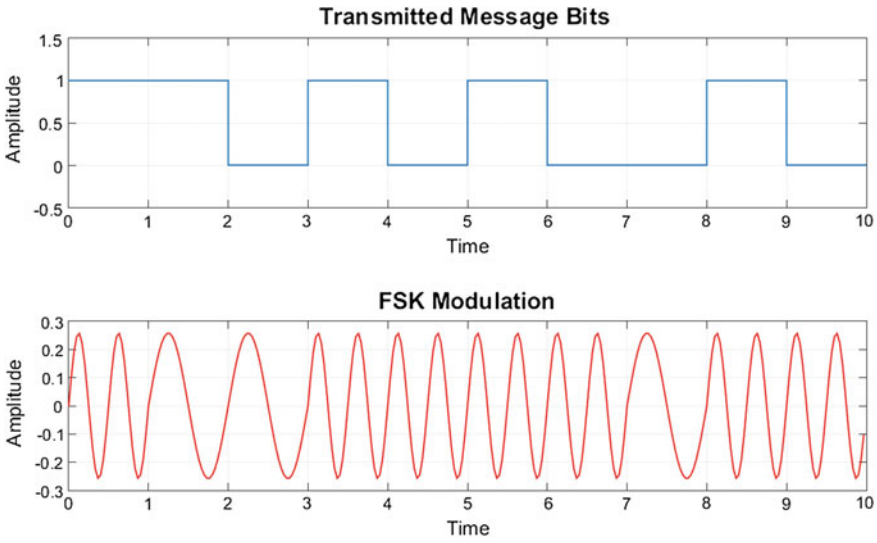

Fig. 1 Transmitted signal after BFSK modulation (without any noise)

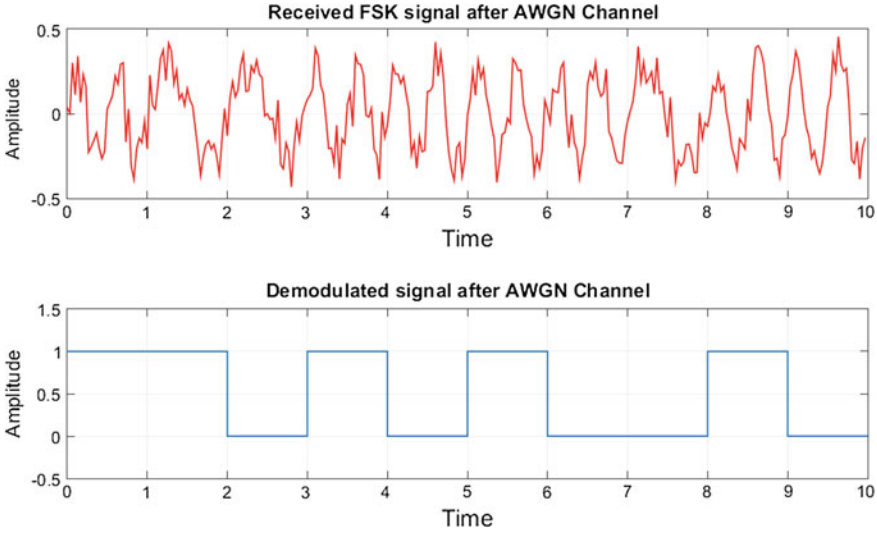

Fig. 2 Transmitted signal after BFSK modulation (after adding white gaussian noise)

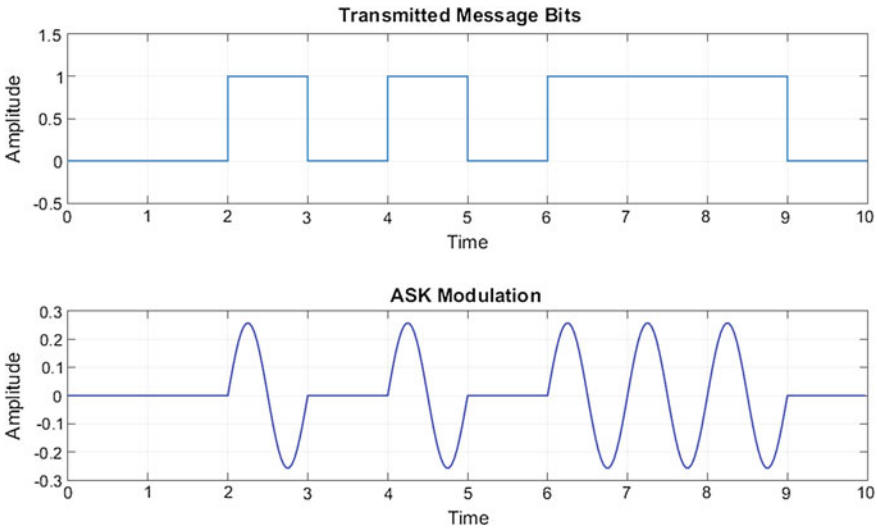

Fig. 3 Transmitted signal after ASK modulation (without adding noise)

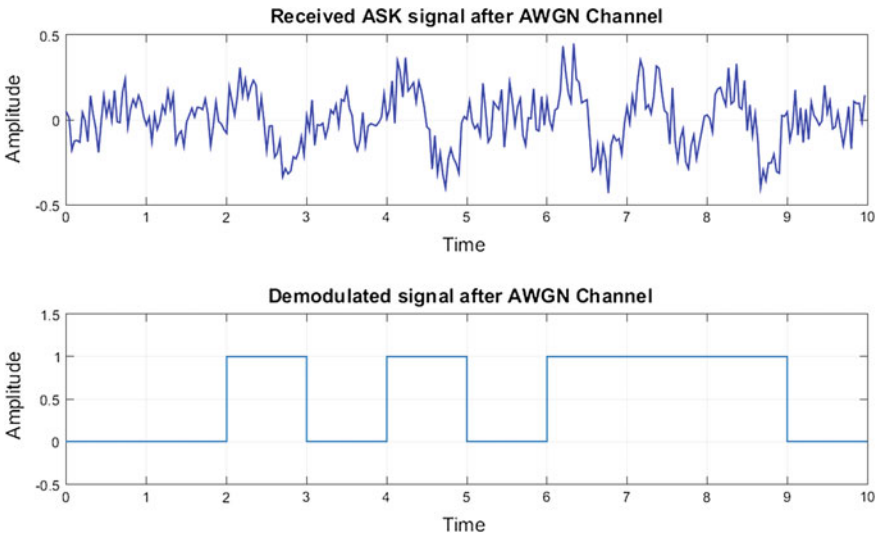

Fig. 4 Transmitted signal after ASK modulation (after adding noise)

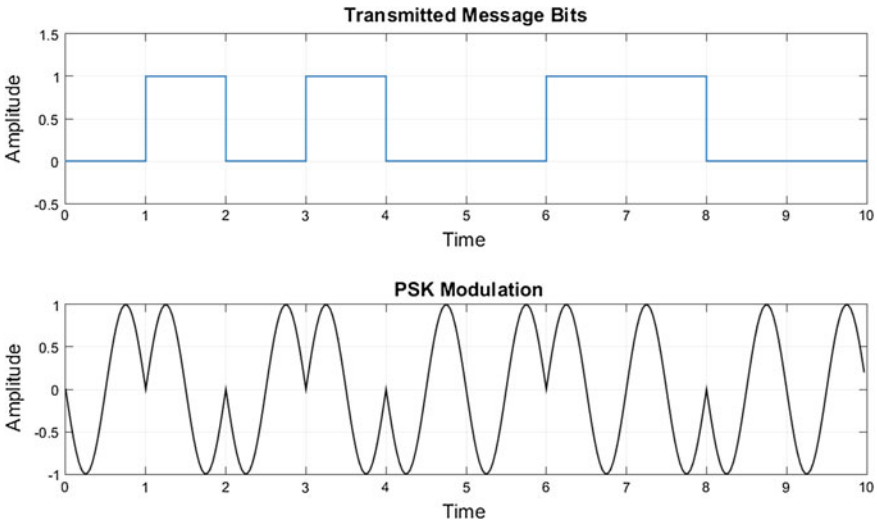

Fig. 5 Transmitted signal after using phase-shift keying (PSK) (without adding noise)

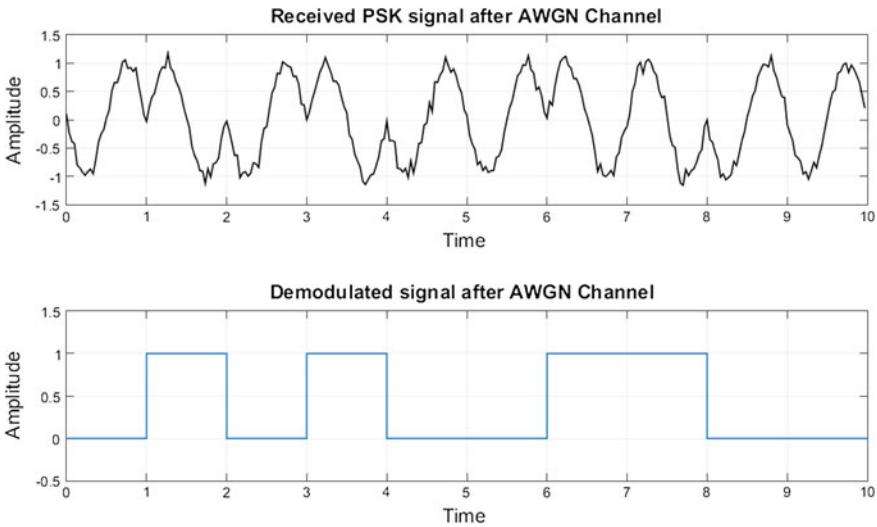

Fig. 6 Transmitted signal after using phase-shift keying (PSK) (after AWGN adding noise)

5 Analysis

Analysis of signals plays a key role in signal communication and signal processing and it is a tough task for all researchers and scientists. It is always important to know the information on the signal's properties and signal analysis is the only tool used for this purpose. As part of signal analysis, spectrum analysis and vector signal analysis are used for analyzing the electrical signals. In this, we tend to solve the problem of excess BER with introducing a Rayleigh fading channel to the system and operate it with the gain. Rayleigh fading is the name which is given to the fading experienced by large number of reflections. This fading uses a statistical approach to analyze the propagation and is used in a number of domains. The Rayleigh fading model is particularly useful when the signal gets scattered between the transmitter and receiver. The attenuation that happens due to multipath fading in wireless channels can be solved by Rayleigh fading (for the case where no line of sight component present). A Rayleigh random variable R has the probability distribution

$$PR(r) = \frac{2r}{\Omega} e^{\frac{-r^2}{\Omega}} \tag{5.1}$$

where $\Omega = E(R^2)$.

For a wireless channel, the envelope of the channel response is modeled to have a Rayleigh distribution. The output graph for each classifier with and without Rayleigh channel is shown in Figs. 7, 8, and 9. The outputs give us a general idea that even on using the Rayleigh fading channel the BER value of the plot remains same as without the Rayleigh gain. On considering the time value of the sequences, the differences can be shown in Figs. 10 and 11.

5.1 BER Analysis

BER analysis is the method to determine the BER versus SNR ratio and get a plot accordingly for a system. In this project the BER analysis is done by getting the BER values of the system at different SNR value having a specific range and sample time. The tool plots graph at all SNR values starting from the lower limit to the upper limits with the ranging sample time. The values of BER also can be displayed if needed. In this simulation work, a general QAM modulator/demodulator baseband is used for the execution of the Amplitude-Shift Keying (ASK) technique. For the exact execution of the work, the noise has also been added which is an AWGN channel. There are two operations: one with complex path gain of the Rayleigh fading channel and one without the gain involved. The results involved in both the scenarios are different as shown in Figs. 7, 8, 9, 10, and 11.

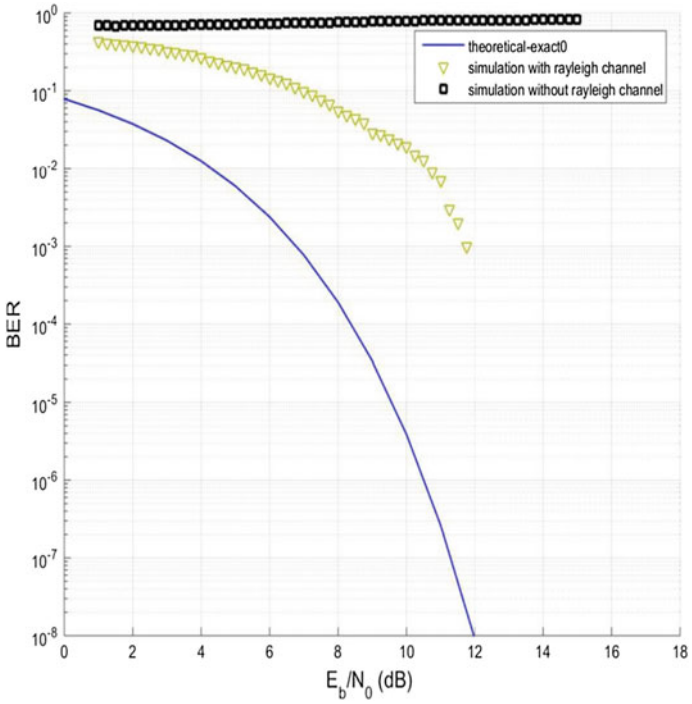

Fig. 7 Graph for ASK technique with and without Rayleigh fading channel

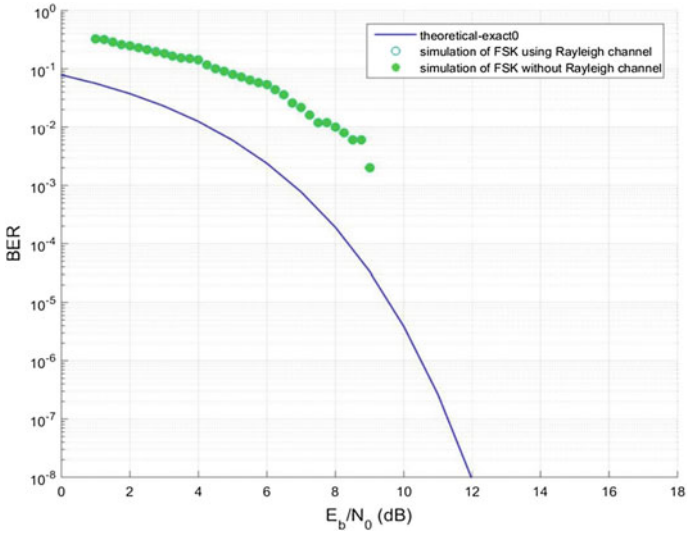

Fig. 8 Graph for FSK technique with and without Rayleigh fading channel

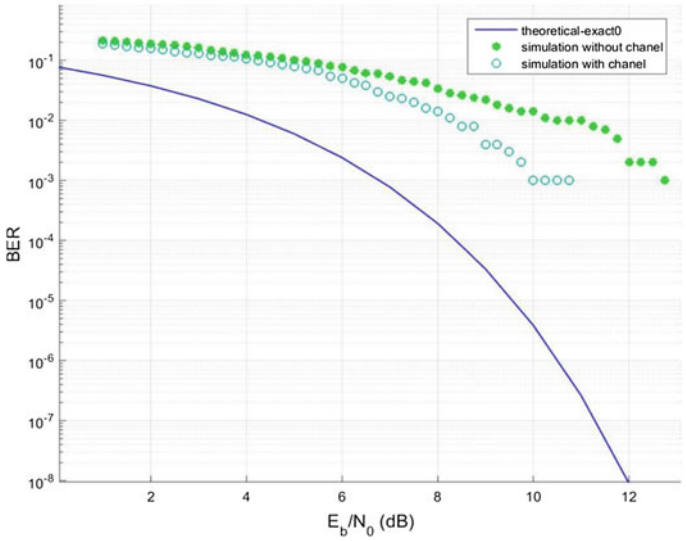

Fig. 9 Graph for PSK technique with and without Rayleigh fading channel

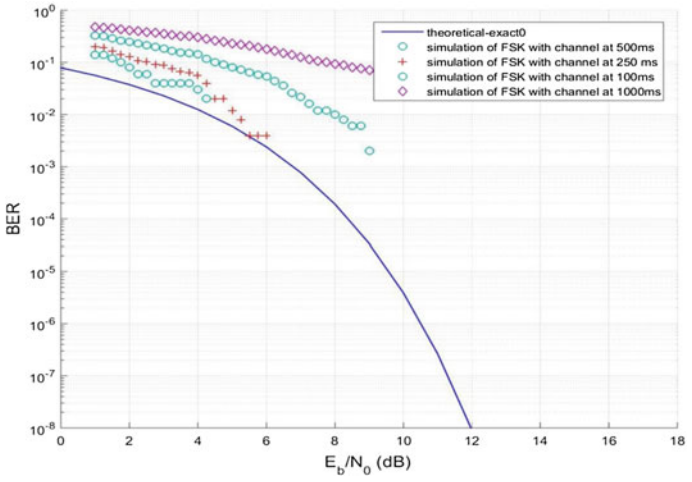

Fig. 10 Graph for FSK technique with and without Rayleigh fading channel at different time sequences

The result suggests that lately increasing the simulation time would result in increase in BER ratio, i.e., the errors for a larger sample time would be high as compared to lower simulation time, with an increase in SNR ratio. The simulation result for the same with different simulation times and with Rayleigh fading channel reduces the errors.

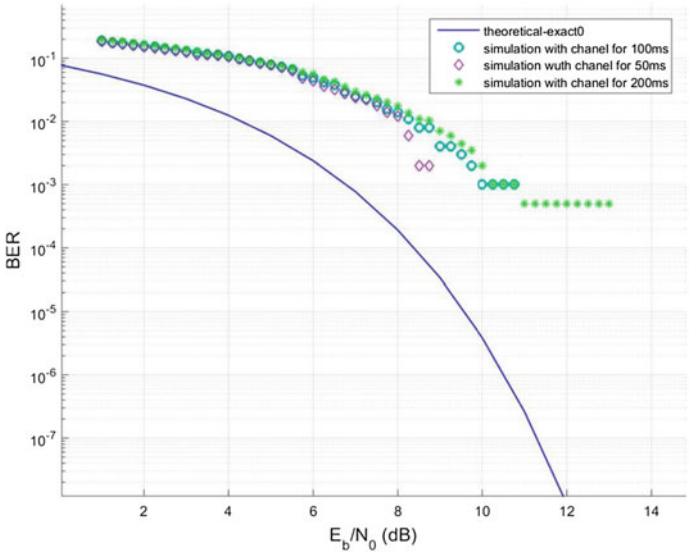

Fig. 11 Comparison of PSK technique at different time periods without Rayleigh fading

6 Conclusion

This paper is aimed to get the comparison of different modulation techniques used in narrowband PLC system. The differences in the modulation techniques were figured out using various MATLAB and Simulink tools. This paper gave us an insight on how the different modulation techniques (ASK, FSK, and PSK) would respond to different parameters such as simulation time which can be seen as the measure of time for which the data is being transferred or the SNR ratio. The simulation results for the techniques brief us about the possible usage of techniques in various scenarios. The PSK modulation technique will be a better option to use than the other two variants but only if the SNR ratio of the system lies below 4 dB for higher SNR values. The technique would fall behind FSK which has a lesser error probability, i.e., lesser BER ratio. This justifies the theoretical results of FSK being better option than PSK for lower bandwidth, i.e., the narrowband systems.

References

1. Yousuf, M.S., El-Shafei, M.: Power line communications: an overview—Part 1. In: 4th International IEE Conference on Innovations in Information Technology, pp. 218–222 (2007)
2. Dostert, K.: Telecommunications over the power distribution grid–possibilities and limitations. IIR-Powerline **6**, 1–9 (1997)

3. Eyre, B.E.: Results of a comprehensive field trial of a United Kingdom customer telemetry system using mains borne signaling. In: Proceedings of the Sixth International Conference on Metering Apparatus and Tariffs for Electricity Supply, IEE Conference Publication, no. 317, pp. 252–256 (1990)
4. Hosono, M.: Improved automatic meter reading and load control system and its operational achievement. In: 4th International Conference on Metering, Apparatus and Tariffs for Electricity Supply, IEEE, pp. 90–94 (1982)
5. Zimmermann, M., Klaus, D.: An analysis of the broadband noise scenario in powerline networks. In: International Symposium on Powerline Communications and its Applications (ISPLC 2000), pp. 5–7 (2000)
6. Qun, Y., Jianbo, Z.: Design of power line carrier communication system based on FSK-KQ330 module. Electrotehnica, Electronica, Automatica **62**(3), 135 (2014)

Three-Level Flying Capacitor Multilevel Inverter Is Used to Suppress Harmonics at the Output of 3-Phase Inverter Drive and Study of Heat at Various Parts of 3-Phase Induction Motor

B. Rajesh and Manjesh

Abstract Harmonics are the major cause for degradation of an induction motor; these unwanted harmonics deteriorate the motor performance. In literature, many researchers have studied that application of multilevel inverter suppresses the harmonics. The multilevel inverter has three major types cascaded, diode clamped, and flying capacitor. The output of multilevel inverter is more sinusoidal than of normal inverter. This work shows normal 2-level inverter constructed with six switches and 3-level flying capacitor multilevel inverter constructed with twelve switches experimentally to study the harmonics and total harmonic distortion (THD). Temperature at various parts of the 3-phase induction motor is obtained by placing J-type thermocouples. The motor is run with 9-Hz input frequency for a period of 4-h duration. *V*/*f* control method is employed to control speed of the motor. Temperatures obtained for 4-h duration with normal inverter and multilevel inverter are compared. The harmonics and THD is obtained by using a power analyzer for both the inverters, and the results are compared. The load for the motor is kept at 500 g for both inverter topologies, the analysis and reduction of harmonic content are employed to study the 3-phase induction motor temperature, and results are presented experimentally.

Keywords Temperature study · 3-level inverter · Harmonics
Total harmonic distortion · Multilevel inverter
Flying capacitor multilevel inverter · Low speed · *V*/*f* control

B. Rajesh (✉) · Manjesh
Department of Electronic Science, Bangalore University, Bangalore, India
e-mail: rajeshb0201@gmail.com

Manjesh
e-mail: manjesh1972@gmail.com

A. Konkani et al. (eds.), *Advances in Systems, Control and Automation*,
Lecture Notes in Electrical Engineering 442, https://doi.org/10.1007/978-981-10-4762-6_20

1 Introduction

The core of most modern dc/ac inverter circuits has the concept of multilevel inverter, which enhances the quality of power by introducing various steps of voltage in line to neutral voltages. The losses are less, and improved electromagnetic compatibility is add-on benefits using multilevel inverters. The multilevel inverters are an enhanced structure of the traditional power inverters which are universally accepted and have found different applications, for example, motor drives. The working of multilevel inverter depends on the construction and number of switches in each leg of the inverter [1, 2]. The multilevel starts form 3-level, and it can be raised to any number of voltage levels. The inverter performance could be improved by increasing the switches per leg in circuit. The number of levels at the output in a multilevel inverter is determined by the number of switches. The voltage levels in the output at the load are increased as the number of switches in the multilevel inverter is increased and inverter output voltage becomes more and more sinusoidal structure. The most important feature of multilevel inverter is its ability to reduce the stress of voltage on each switch; the more number of levels in the DC bus of circuit allows for development in steps. This has the highest priority, especially when DC voltage applied is very high which is required to drive the load. The multilevel inverter's output power fed to an electrical motor which improves the performance of the motor by a extreme level [3, 4]. The content of harmonic voltage applied to terminals of the motor is reduced by large amount. The major source of the motor failures is identified to be high dv/dt effects produced by the traditional or normal inverter drives. The multilevel inverter produces a multi-stepped output voltage; this will prevent failures of motor by the reduction of rate of change of (dv/dt) voltage. The major concern of using a multilevel inverter is that, it requires additional number of switches. The multilevel inverters are classified into three major topologies: cascaded multilevel inverter (CMI), diode clamped multilevel inverter (DCMI), and flying capacitor multilevel inverter (FCMI). FCMI uses a capacitor for clamping the switches in each phase leg to provide the desired extra voltage DC level. This type of circuit construction provides redundancy in switching states which increases the multilevel inverter to provide high capability during power usages. A k-level inverter will require a $(k - 1)$ main DC bus capacitor and a $(k - 1) \times (k - 2)/2$ auxiliary capacitor for each phase leg [5]. In this work, a three-level flying capacitor multilevel inverter is constructed with a normal 2-level inverter, and a three-phase induction motor is driven with both inverters. The motor is fixed with J-type thermocouple at various parts of the 3-phase induction motor, and the temperature is recorded for a period of 4 h with a 500-g motor load. The power analyzer WT-500 is used to measure the harmonics and total harmonic distortion. The motor is run with an input frequency of 9 Hz.

2 Normal or 2-Level Inverter (NID)

The normal or 2-level inverter circuit has six switches. Figure 1 shows the circuit diagram of a three-phase 2-level inverter drive. Switches used in the circuit are MOSFET's (IRF 840); the control signals are provided to the IRF 840 by the microcontroller 89S52 through an opto-isolator MCT2E. The keil micro Vision-3 is used generate control signals, and it is programmed on to the microcontroller by SPI programmer. The three phases in the inverter are 120° out of phase with each other. The switch *Sv* is turned on with a phase delay of 120° form switch *Su* and switch *Sw* is turned on with a lag 120° with respect to *Sv*. The switches can be divided into upper and lower switches. The switches *Su*, *Sv,* and *Sw* are upper switches, and *Su′*, *Sv′*, and *Sw′* are lower switches. The lower switches—*Su′*, *Sv′*, and *Sw′* are complimentary with respect to their upper switches—*Su*, *Sv,* and *Sw*. In same leg, both upper and lower switches should never turn on together; therefore, a dead time of 10^0 is incorporated at the end of each control signal. The pattern in which the switches are turned on is two switches from upper group are ON and one switch from lower group is ON or two switches from lower group are ON and one switch from upper group is ON. The result of this combination of control signal produces a 3-phase output voltage which is used to drive the 3-phase induction motor.

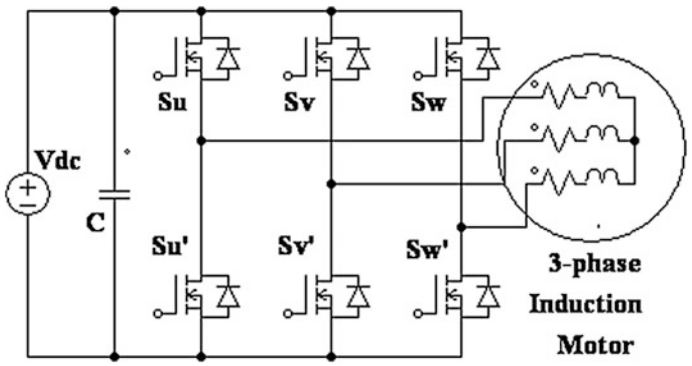

Fig. 1 2-level inverter drive with 3-phase induction motor as a load

3 Flying Capacitor Multilevel Inverter (FCMI)

The 3-level flying capacitor multilevel inverter has twelve switches. The circuit diagram is as shown in Fig. 2 of a three-phase 3-level flying capacitor inverter drive. Switches used in the circuit are MOSFET's (IRF-840); the control signals are provided to the IRF-840 by the microcontroller 89S52 through an opto-isolator MCT2E. The three phases in the inverter are 120° out of phase with each other. The switch *Sv*2 is turned on with a phase delay of 120° form switch *Su*2 and switch *Sw*2 is turned on with a lag 120° with respect to *Sv*2. The switches *Su*1, *Sv*1, and *Sw*1 are turned on with a delay of 20° in each phase with *Su*2, *Sv*2, and *Sw*2, respectively, and the switches are ON for 140° duration. The switches *Su*2, *Sv*2, and *Sw*2 conduct for duration of 170° instead of 180°; this delay is provided for the switches to turn on or off without shorting the circuit in the same leg. The switches can be divided into upper and lower switches. The switches *Su*1, *Su*2, *Sv*1, *Sv*2, *Sw*1, and *Sw*2 are upper switches, and *Su*3, *Su*4, *Sv*3, *Sv*4, *Sw*3, and *Sw*4 are lower switches. The lower switches—*Su*3, *Su*4, *Sv*3, *Sv*4, *Sw*3, and *Sw*4 are complimentary with respect to their upper switches—*Su*2, *Su*1, *Sv*2, *Sv*1, *Sw*2, and *Sw*1. The pattern in which the switches are turned on is two sets of switches from upper group are ON and one set of switches from lower group is ON or two sets of switches from lower group are ON and one set of switches from upper group is ON. The result of this combination of control signal produces a 3-phase output voltage used to drive the 3-phase induction motor.

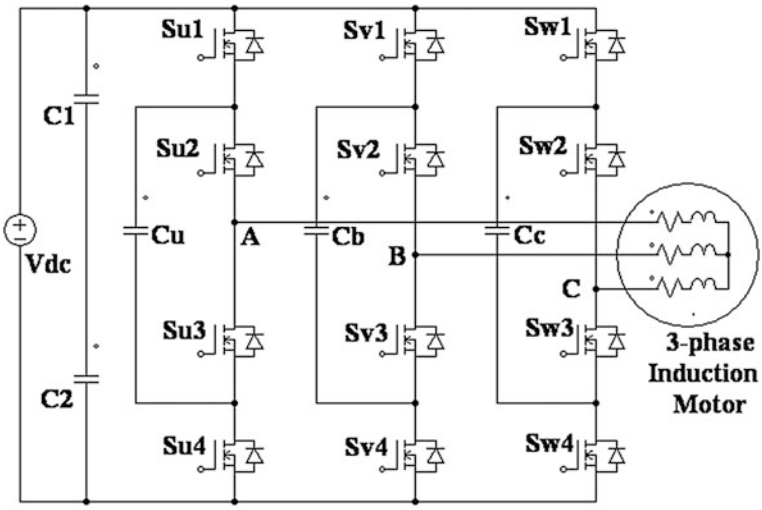

Fig. 2 Flying capacitor inverter drive with three-phase induction motor as a load

4 Results

The three-phase induction motor is inserted with J-type thermocouple at various parts of the induction motor to monitor the temperature. The temperature is logged on to computer using a temperature module kit. The total harmonic distortion (THD) and harmonics are measured at the output of the both 2-level normal inverter and 3-level FCMI drive using a power analyzer WT-500, and for a duration of 4 h, the motor is run to record the temperature and harmonics at the output of the inverter. Figures 3 and 4 show the temperature plot for duration of 4 h for which the motor is run with normal inverter drive and FCMI drive, respectively. The comparison of stator winding temperature for both the inverters is as shown in Fig. 5. The comparison of the percentage of individual voltage harmonics of normal inverter and FCMI is shown in Fig. 6, and in Fig. 7 also the individual current harmonics are compared. The motor has been run for the speed 265 and 267 rpm, respectively, for normal inverter and FCMI with 9-Hz input frequency for both cases. The total harmonic distortion is shown in the Table 1. Fig. 8 shows the output wave form of voltage and current for the normal inverter drive, and Fig. 9 shows vector graph of output voltage and current for normal inverter drive. Figures 10 and 11 show the output voltage and current waveform and vector graph for all three phases current and voltage with FCMI drive.

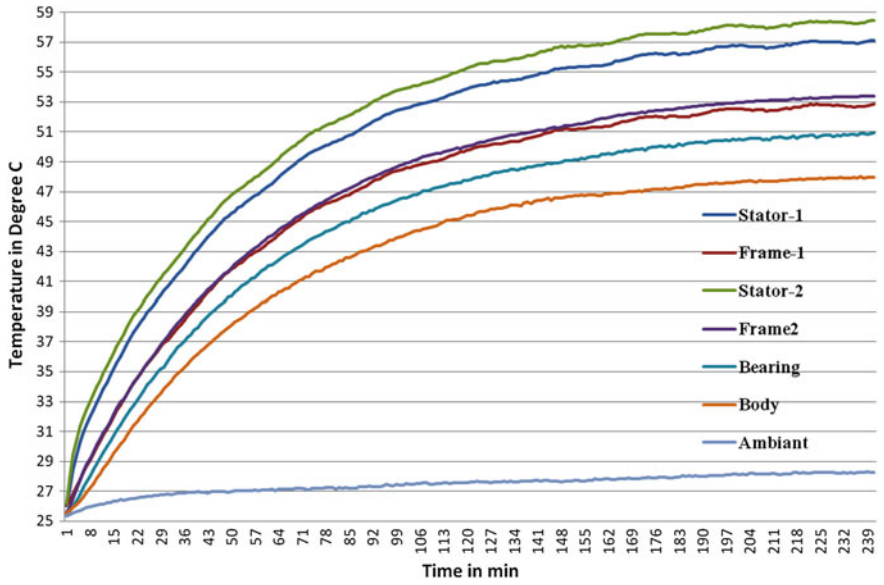

Fig. 3 Practically obtained temperature at various parts of induction motor with 500 g of load for normal inverter drive

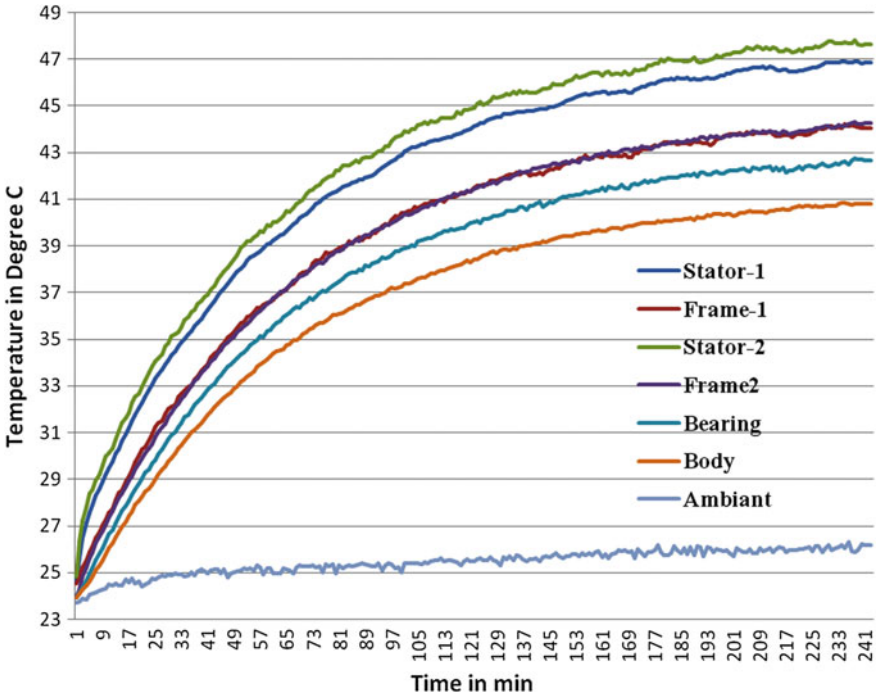

Fig. 4 Practically obtained temperature at various parts of induction motor with 500 g of load for FCMI drive

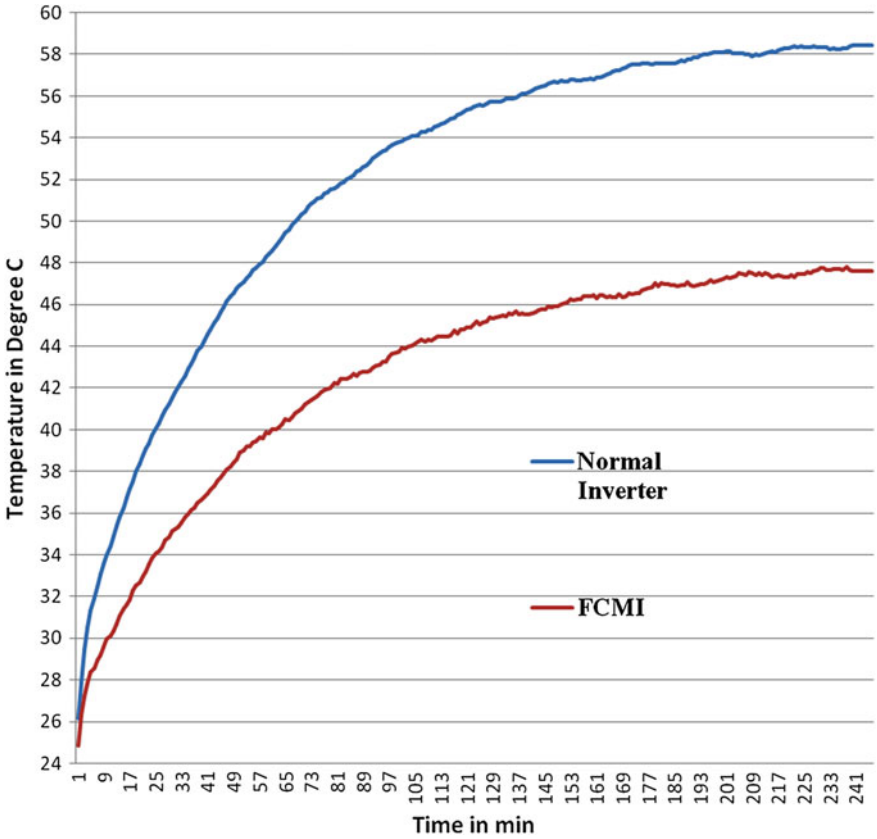

Fig. 5 Practically obtained temperature at stator of an induction motor with 500 g of load for normal inverter drive and FCMI drive

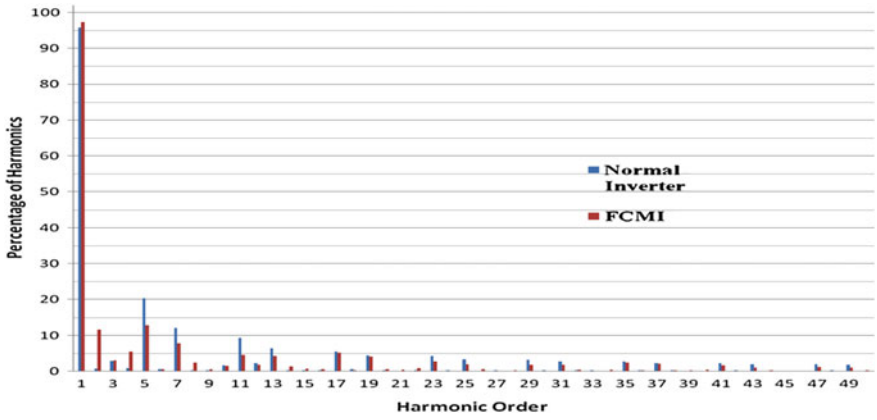

Fig. 6 Harmonic profile of voltage for normal inverter and FCMI

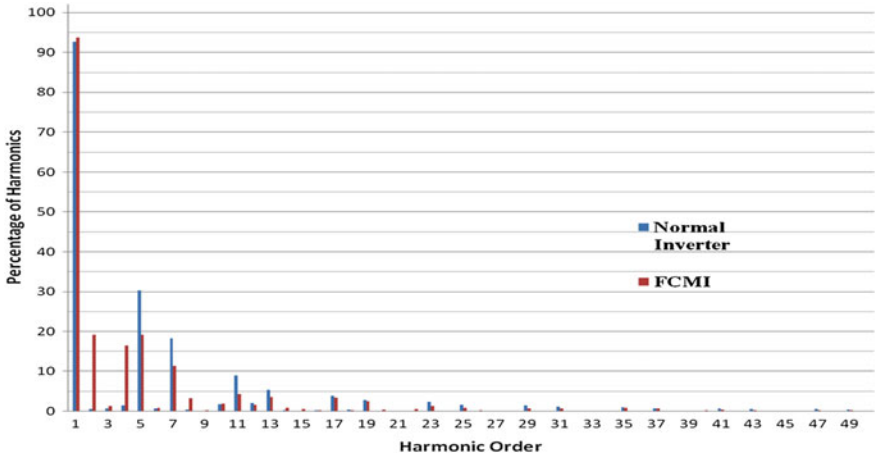

Fig. 7 Harmonic Profile of current for normal inverter and FCMI

Table 1 Total harmonic distortion in percentage for both inverters

THD of	Normal inverter drive	FCMI
Voltage	28.90%	23.27%
Current	37.62%	34.89%

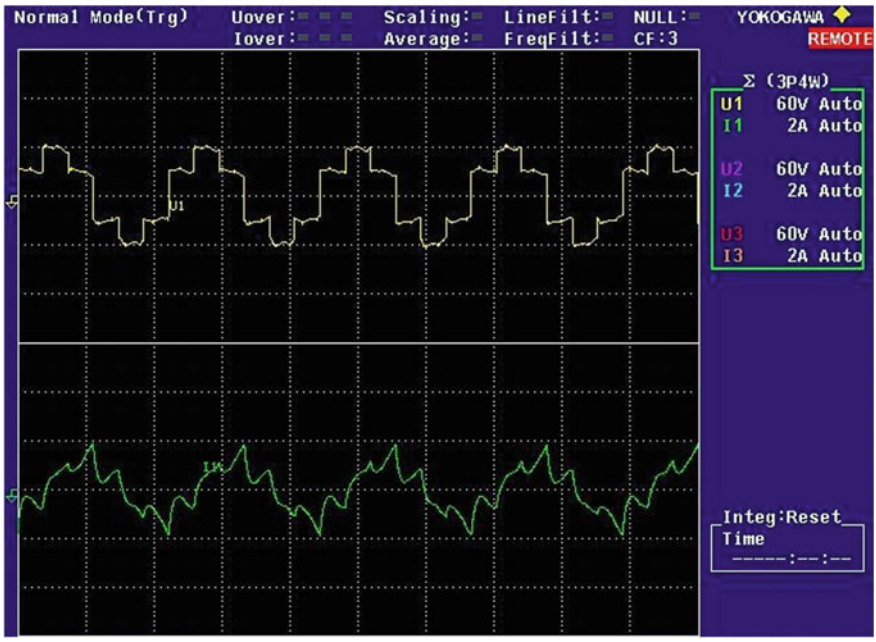

Fig. 8 Practically measured voltage and current waveform for normal inverter drive

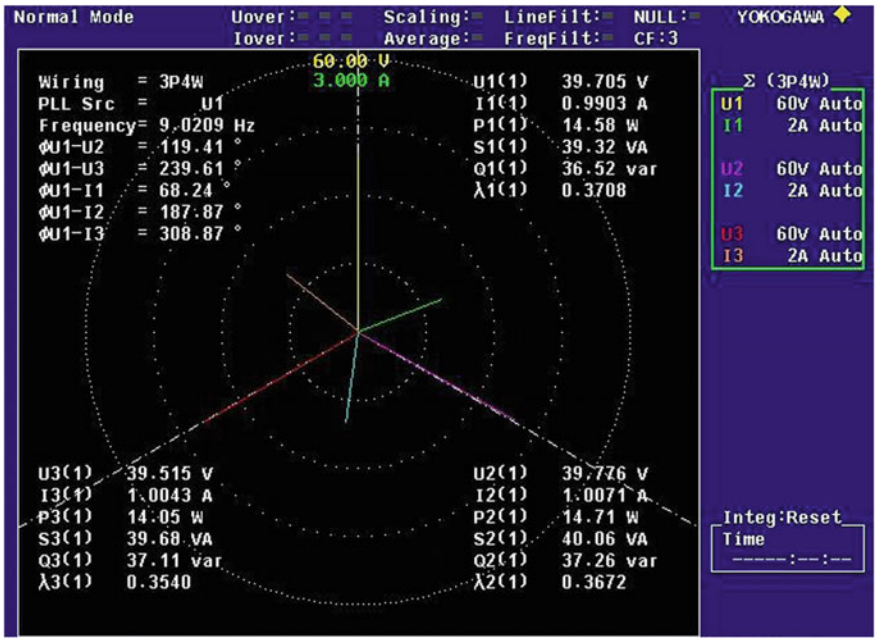

Fig. 9 Practically measured voltage and current vector graph for normal inverter drive

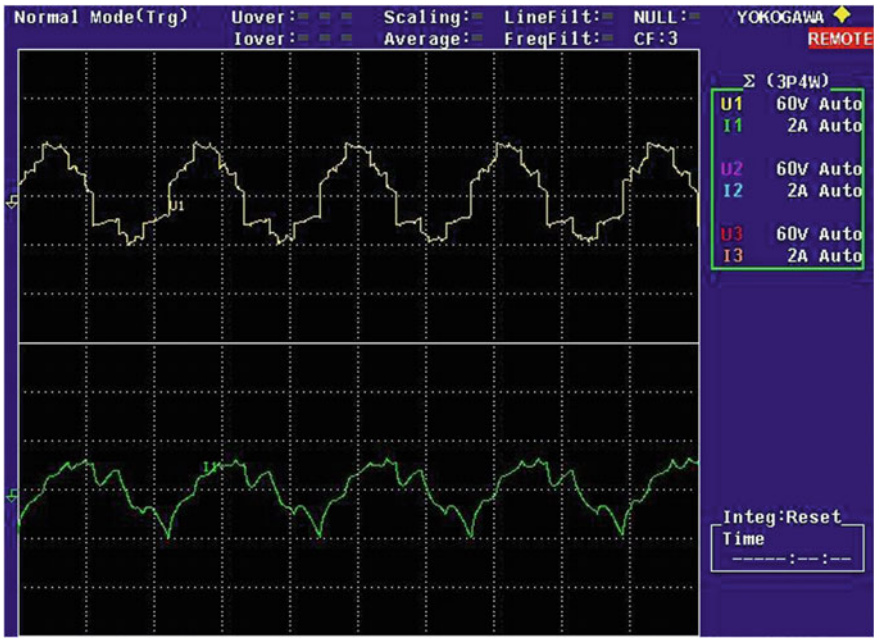

Fig. 10 Practically measured voltage and current waveform for FCMI drive

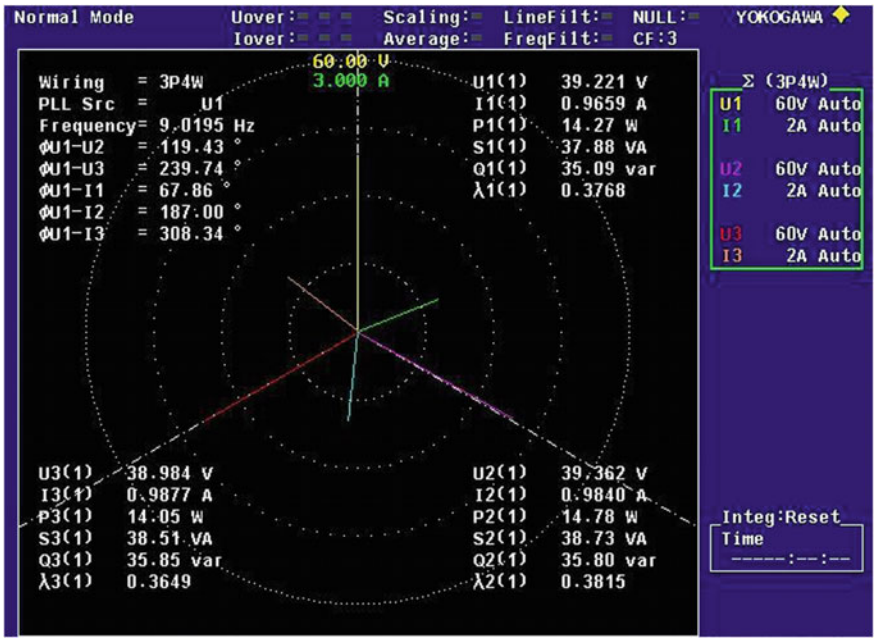

Fig. 11 Practically measured voltage and current vector graph for FCMI drive

5 Conclusion

The three-phase normal inverter drive (NID) and flying capacitor multilevel inverter drive are constructed experimentally to study the temperature at the different parts of three-phase induction motor. The harmonics and THD are also obtained at the output of the inverter using power analyzer with input frequency of 9 Hz. The harmonics and THD obtained for NID and FCMI is analyzed and compared; it is found that the harmonics and harmonic distortion is less using FCMI drive, and also the temperature analysis of the 3-phase induction motor is also studied and compared with NID method; a less rate of rise of temperature rise in the induction motor is found by using FCMI drive method. The most dominant harmonic in 3-phase is fifth harmonic; this harmonic is suppressed for both voltage and current harmonics as shown in Figs. 6 and 7. Table 1 shows the total harmonics distortion of both NID and FCMI. This study enumerates the effect of harmonics on the motor temperature, and reduction of temperature is obtained by using a FCMI in place of NID.

References

1. Mailah, N.F., Saidin, M.S., Othman, S.S.T.: Simulation and construction of single phase flying capacitor multilevel inverter. In: Proceedings of 2010 IEEE Student Conference on Research and Development (SCOReD 2010), 13–14 Dec 2010, Putrajaya, Malaysia, pp. 401–404 (2014)
2. Escalante, M.F., Vannier, J.C., Arzandé, A..: Flying capacitor multilevel inverters and DTC motor drive applications. IEEE Trans. Ind. Electron. **49**(4), 809–815 (2002)
3. Devaraj, S., Anitha, G.S.: Closed loop system of a flying capacitor multilevel inverter using POD-PWM. In: 2016 Biennial International Conference on Power and Energy Systems: Towards Sustainable Energy (2016)
4. Shanmuga Priyan, S., Ramani, K.: Implementation of closed loop system for flying capacitor multilevel inverter with stand-alone photovoltaic input. In: 2013 International Conference on Power, Energy and Control, pp. 281–286 (2013)
5. Kou, X., Corzine, K.A., Familiant, Y.: A unique fault-tolerant design for flying capacitor multilevel inverters, pp. 531–538. IEEE (2003). 0-7803-7817-2/03

Development of Measurement and Data Acquisition Setup Using LabVIEW for Sample Characterization up to Cryogenics Temperature

Anish Bhargav, Javed Ashraf and V.N. Ojha

Abstract In this paper, we present an indigenously developed automated measurement setup comprising of three modules, using LabVIEW software in CSIR-NPL. The first module deals with differential measurements of any thin films, devices, elements, etc., under different magnetic field environment. Differential measurements provide analysis of individual slope of an *I-V* curve. The second is to measure the *I-V* (current-voltage) characteristics of any element or devices. The third module consists of a setup that can be used to measure the *I-V* characteristics of thin films, semiconductor devices, etc., from room to cryogenics temperature. Some of the results obtained using these softwares had been reported in this paper. Also the setup had been validated. The paper encourages the use of virtual instrumentation for accurate and fast measurements.

Keywords NMI · Thin films · LabVIEW · Differential measurements · *I-V*

1 Introduction

The automation has strengthen its root in the manufacturing industries, research and defense laboratories, etc., due to its beauty of making the process faster, more accurate, more productive, and so on. The advent of microcontrollers in 1971 by Gary Boone and Michael Cochran provided a breakthrough in electronics automation [1]. The research laboratories, industries, etc., all over the world are using automation for providing solutions that are reliable, fast, etc. The present work had been carried out in CSIR-NPL. CSIR-NPL is the National Measurement Institute (NMI) of India, which maintains primary and secondary standards for most

A. Bhargav (✉) · V.N. Ojha
CSIR-NPL, Dr. K.S. Krishnan Marg, New Delhi, India
e-mail: bhargavam@nplindia.org

A. Bhargav · J. Ashraf
Department of ECE Engineering, Al-Falah School of Engineering and Technology, Faridabad, Haryana, India

A. Konkani et al. (eds.), *Advances in Systems, Control and Automation*,
Lecture Notes in Electrical Engineering 442, https://doi.org/10.1007/978-981-10-4762-6_21

of the physical quantities, such as voltage, resistance, time, force, temperature, etc., and also maintains SI units [2].

The current-voltage characteristics of a device or element represents the relationship between the current applied and voltage developed across the device or vice versa. It gives an idea about the behavior of an element or device in electrical circuit and also helps in determining basic parameters. In reference to superconductivity, it helps in determining the critical current of the superconductor. It is generally specified in terms of a graph or curve in the datasheet of an electrical/electronic component. On the other hand, differential measurements provide analysis of individual slope of an *I-V* curve. The *I-V* curve shifts or exhibits changes with applied magnetic field [3].

The thin films, elements, and electronic components made from different materials exhibit dissimilar properties at different temperatures [4]. Therefore, it becomes essential to monitor the behaviors of such elements at different controlled temperatures. For example, Niobium, YBCO, etc., become superconductors at cryogenic temperatures. Thus, we have developed a complete automation setup that caters to these needs. The National Instruments LabVIEW (Laboratory Virtual Instrument Engineering Workbench) software had been used to develop this automation setup. It is generally based on graphical programming, where a VI (Virtual Instrument) is created as per user requirement. A VI generally has three components:

1. Front Panel: It acts as an interface to the user.
2. Block Diagram: The inputs and indicators that are placed in the front panel appear in the form of terminals in the block diagram. The block diagram contains structure and functions that perform operations as per the input applied and passes the results to the indicator.
3. Connector Panel: It is used to represent the VI in the block diagrams of other calling VI's [5].

The automation or software control reduces error as it minimizes human involvement, thereby resulting in high precise measurements. Using this software, we had obtained differential characteristics, *I-V* characteristics, and temperature controlled characteristics of thin films, resistor, diodes, etc.

2 Measurement Techniques

2.1 Differential Measurements with Magnetic Field

Differential measurements provide an in-depth analysis of individual slopes of an *I-V* curve. The software that had been developed here is based on Keithley's four wires, source current—measure voltage concept/technique [6]. Here, an alternating current is added to a linear staircase current sweep. The values for this sweep can be

defined by the user. The differential current (d*I*) represents amplitude of the alternating portion of current and is constant throughout the experiment. The voltage is measured at each step of current. Then, the delta voltage between consecutive steps is calculated. The differential voltage (d*V*) is calculated by averaging each delta voltage with the previous delta voltage. The differential conductance (d*G*) is obtained using d*I*/d*V,* whereas differential resistance is obtained using d*V*/d*I*. The magnetic field is applied to the sample under test by energizing the electromagnet with the help of an electric current. The electromagnet used here had been developed at CSIR-NPL and calibrated at "Multiferroics and Magnetic standard" activity of CSIR-NPL. It is traceable to primary magnetic standard "NMR Gaussmeter" whereby one can apply desired amount of electric current to get a particular magnetic field. The software has the provision of applying desired electric current.

2.2 I-V *Measurement*

I-V measurement is based on the concept of sourcing the current and measuring corresponding voltage across the sample under test. We had used current source and voltmeter for this purpose. The current range can be defined with the step value. At each step of current, voltage is measured and the corresponding graph is plotted. This technique is well suited for the elements or devices that follow Ohm's law. However, at nano level and cryogenics temperature, we perform differential measurement.

2.3 Temperature Controlled I-V *Measurement*

Some samples/electronic components exhibit different properties at different temperatures [4]. Hence, temperature controlled *I-V* software had been developed. The measurement setup comprises of temperature controller, current source, voltmeter, and a cartridge heater. The temperature controller uses PID control to reach the desired temperature.

3 Automation Setup

3.1 Differential Measurements with Magnetic Field

The front panel for differential measurement with magnetic field software is shown in Fig. 1.

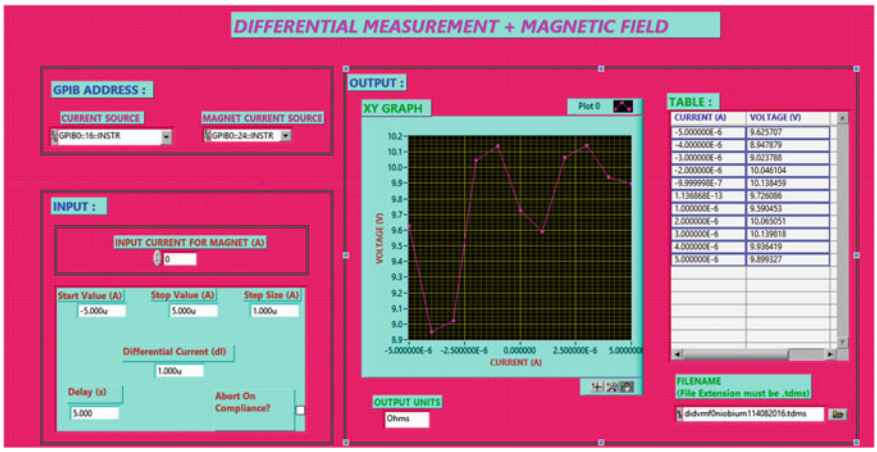

Fig. 1 Front panel of differential measurement with magnetic field software

The sequences of events are as follows:

1. First, we enter the GPIB address of current source and SMU unit (source for magnetic field).
2. Then, we provide the start and stop current along with step size and delay between each successive step of current. The differential current to be applied is also defined here.
3. Then, we provide the value of current for electromagnet (This current is defined using the calibrated curve whereby one can perform the measurements at the magnetic field he desires).
4. Finally, we specify the path and filename, to store the data in the form of excel sheet.
5. The program is then executed and after reaching stop current, it terminates.

3.2 I-V *Measurement*

The front panel of *I-V* measurement software is shown in Fig. 2. In the developed software, we need to enter the GPIB address of each instrument. Then, the inputs are defined, where we provide the starting current value and stop current value i.e., the range is defined. Also step size is defined. In the output section, we have the current and the voltage indicators that show the actual current flowing and voltage being measured by the instruments. The current value and the corresponding voltage value get stored in the table, and the *I* (Current) versus *V* (Voltage) graph is displayed on the front panel. All these front panel sections are wired or programmed in the block diagram.

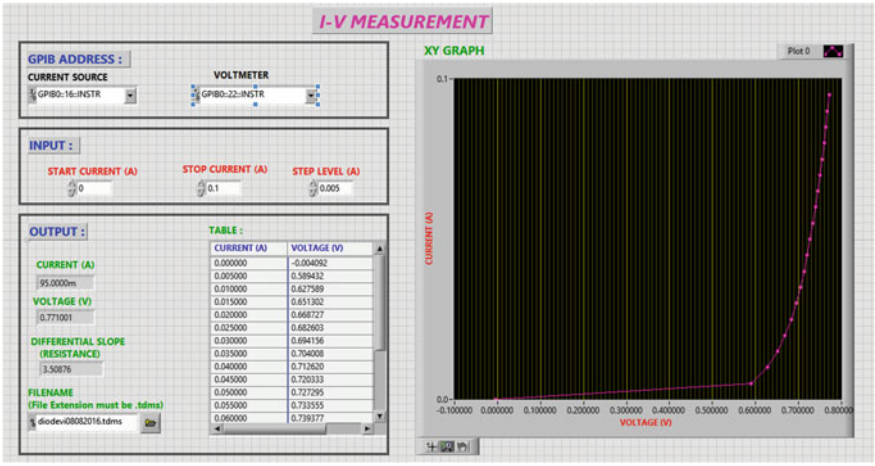

Fig. 2 Front panel of *I-V* measurement software

In the bock diagram, the connections to the various terminals are made. Also, we define the logic for the flow of program. Figure 3 show the measurement in progress.

3.3 *Temperature Controlled* I-V *Measurement*

For temperature controlled *I-V* measurement software, the sequences of events are as follows (front panel is shown in Fig. 4):

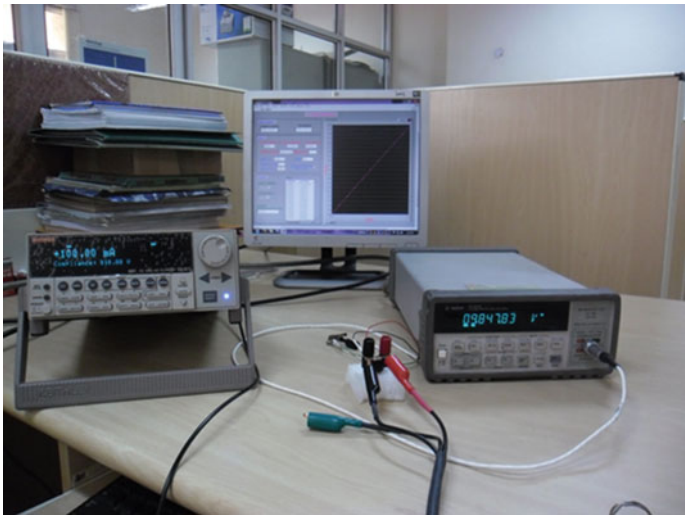

Fig. 3 Real-time *I-V* measurement setup

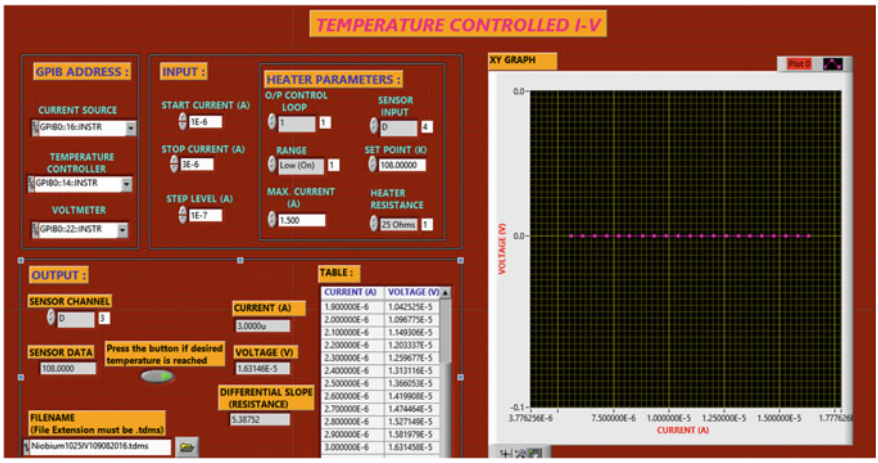

Fig. 4 Front panel of temperature controlled *I-V* measurement software

1. Here, we enter the GPIB address of temperature controller, current source and voltmeter.
2. Then, we specify the desired temperature, along with the start and stop current with step size.
3. Finally, we specify the path and filename where the tabulated data is stored in the form of excel sheet.
4. The program is then executed; it terminates on reaching the stop current.

4 Results

This setup was tested and validated on different elements such as resistors, diode, and thin films. The results obtained are as follows.

4.1 Differential Measurements with Magnetic Field

Differential measurements were carried out on a Niobium thin film and 500 Ω carbon composition resistor at zero magnetic field and at magnetic field of 104 Gauss with differential current of 1 μA. Graphs 1 and 2 show the differential resistance values of 500 Ω resistor at 0 Gauss and 104 Gauss magnetic field. There are no variations in the resistance values as desired.

Similarly, Graphs 3 and 4 show the differential resistance values of Niobium thin film at 0 Gauss and 104 Gauss magnetic field. Graph 5 shows the d*I*/d*V* curve

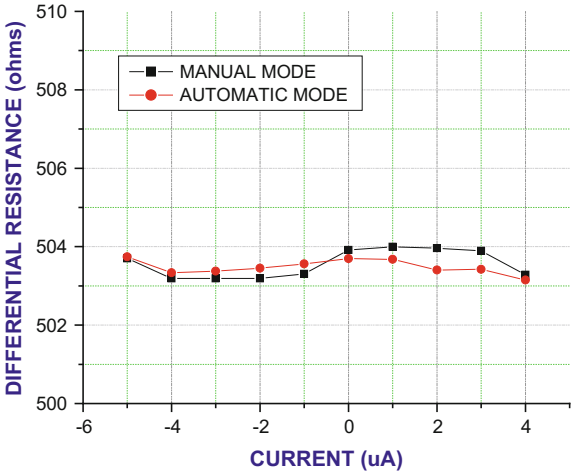

Graph 1 d*V*/d*I* curve of a 500 Ω resistor with magnetic field = 0 G

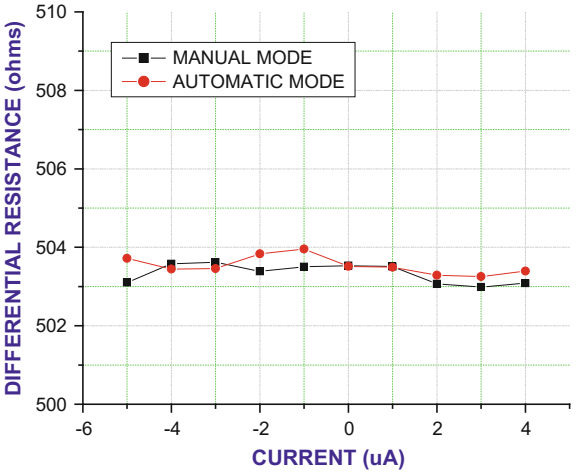

Graph 2 d*V*/d*I* curve of a 500 Ω resistor with magnetic field = 104 G

of a 46 Ω resistor with magnetic field = 0 Gauss. Taking the reciprocal of the conductance values obtained using software, we get desired resistance values, thereby confirming the reliability of this setup.

All the above measurements were carried out at room temperature. The readings obtained in automatic as well as manual mode are almost identical.

Graph 3 d*V*/d*I* curve of Nb thin film at 0 Gauss

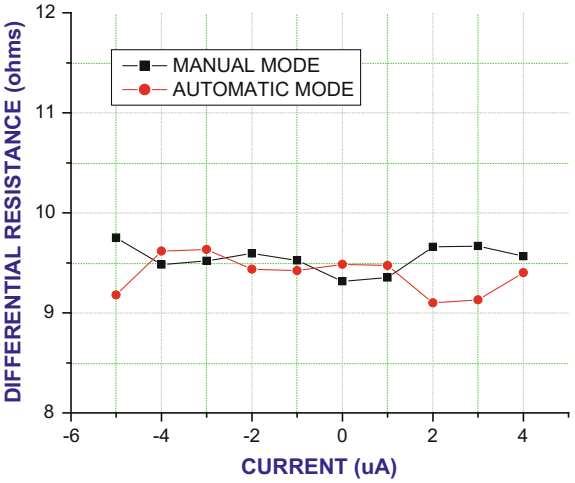

Graph 4 d*V*/d*I* curve of a Nb thin film at 104 Gauss

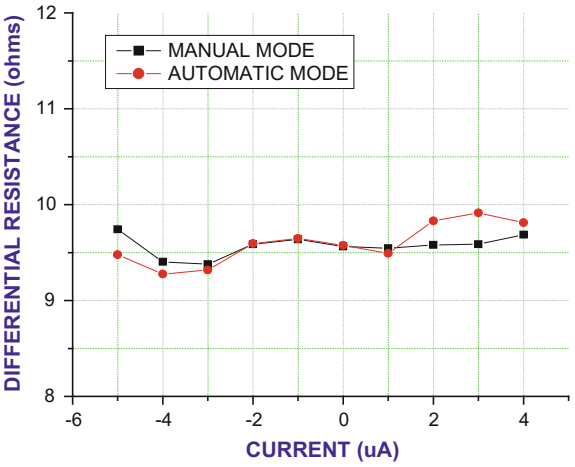

Graph 5 d*I*/d*V* curve of 46 Ω resistor at 0 Gauss

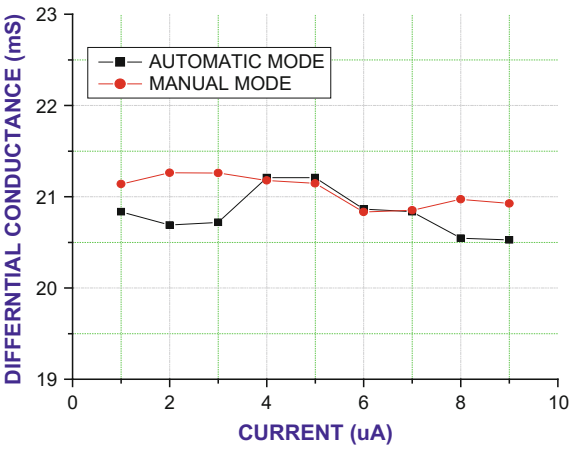

4.2 I-V *Measurement*

The developed automation software was tested on carbon composition resistors, diode, and potentiometer. Graphs 6 and 7 show the *V-I* curve of a silicon diode and *I-V* curve of 5k pot set at 1.46 kΩ. The obtained *I-V* characteristic of the potentiometer is linear as desired.

The *V-I* curve of the diode obtained using the software developed is similar to the curve provided in the datasheet supplied by the manufacturer. The above graph also shows the curves for the readings taken in manual mode using same set of input values and elements. The readings taken in manual mode are almost similar to the readings taken in automatic mode, resulting in validation of the developed software.

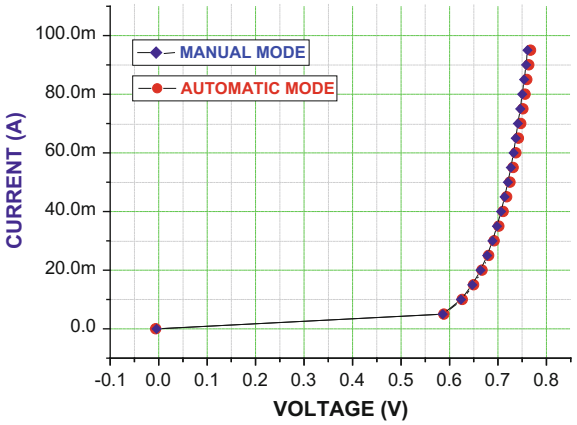

Graph 6 *V-I* curve of a silicon diode

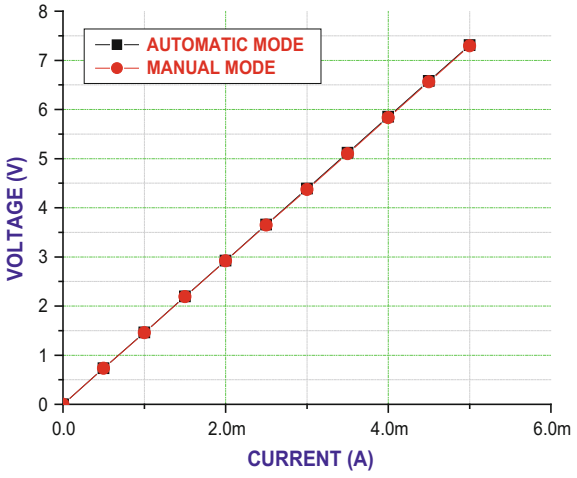

Graph 7 *I-V* curve of a 5k pot set at 1.46 kΩ

4.3 *Temperature Controlled* I-V *Measurement*

The software is tested on Niobium thin film at different temperatures. Graphs 8 and 9 show the *I-V* curve obtained at 175 K and 225 K, respectively, with and without using software. From the curves, we conclude that the readings obtained in manual and automatic modes are almost identical, thereby confirming the reliability of this software. The resistance of this thin film at 175 K is 7 Ω approx. and at 225 K is 8.8 Ω approx. and is constant. We had obtained similar values using the developed software. Table 1 shows the values obtained in manual and automatic mode.

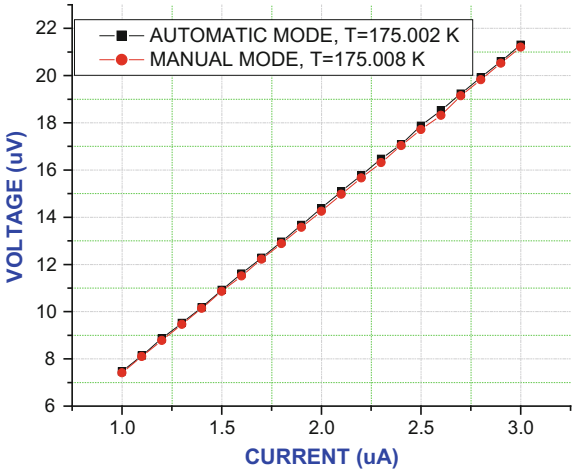

Graph 8 *I-V* curve of Nb film at 175 K

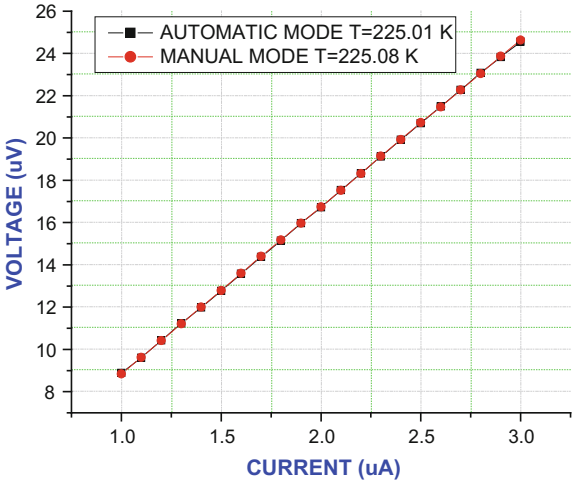

Graph 9 *I-V* curve of Nb film at 225 K

Table 1 Set of readings in manual and automatic mode of Nb film at $T = 225$ K

S. No.	Temperature set = 225 K	Automatic mode	Manual mode
		Actual temperature = 225.01 K	Actual temperature = 225.08 K
	Current (μA)	Voltage (μV)	Voltage (μV)
1	1	8.88	8.85
2	1.1	9.60	9.62
3	1.2	10.43	10.41
4	1.3	11.23	11.21
5	1.4	11.99	12.00
6	1.5	12.77	12.79
7	1.6	13.58	13.60
8	1.7	14.37	14.40
9	1.8	15.14	15.18
10	1.9	15.97	15.97
11	2	16.72	16.74
12	2.1	17.54	17.53
13	2.2	18.33	18.32
14	2.3	19.13	19.15
15	2.4	19.92	19.93
16	2.5	20.70	20.73
17	2.6	21.50	21.47
18	2.7	22.27	22.27
19	2.8	23.08	23.05
20	2.9	23.82	23.87
21	3	24.56	24.63

5 Conclusion

The user-friendly automation setup for differential measurements, *I-V* characteristics, and temperature controlled *I-V* measurements had been developed, tested, and successfully applied for sample characterization. The software had been rigorously tested on different resistors, diodes, pot, thin films, etc. Differential measurements provided an in-depth analysis of the *I-V* curves at different current range. For linear devices, we got linear *I-V* curves, i.e., with increase in current there is a linear increase in the voltage. For non-linear devices, we got the curve as desired. For temperature-controlled *I-V* measurements, we obtained desired temperature with high accuracy and stability, thereby conducting *I-V* measurements at different temperatures successfully. The software control increases the precision and reduces the human error besides resulting in the reduction of measurement time. Also, the setup had been validated as the reading taken in manual mode matches with the readings obtained using the software.

Acknowledgements The authors wish to thank Dr. D.K. Aswal, Director CSIR-NPL; Dr. Ranjana Mehrotra, Head, Quantum Phenomena and Applications Division, Col. Dr. O. P. Malik, Head, ECE Department of Al-Falah University for their constant encouragement and support.

References

1. Augarten, S.: The most widely used computer on a chip: The TMS 1000. State of the art: a photographic history of the integrated circuit. ISBN 0-89919-195-9. Retrieved, 2009-12-23 (1983)
2. Sharma, R., Saxena, A.K., Ojha, V.N., Kothari, P.C.: SI Units (Monograph), p. 17. NPL, New Delhi (2000)
3. Bernstein, P., Picard, C., Hamet, J.F., Prouteau, C., Contour, J.P., Drouet, M.: Effect of a uniform magnetic field on the I-V curves of SFFTs. IEEE Trans. Appl. Supercond. **7**(2) (1997)
4. Dimos, D., Chaudhari, P., Watson, T.J., Mannhart, J., Ru'schlikon.: Superconducting transport properties of grain boundaries in $YBa_2Cu_30_7$ bicrystals. Phys. Rev. **41**(7) (1990)
5. LabVIEW Manual 2013
6. Keithley source meter 6220 manual

Design and Analysis of a Permanent Magnet DC Motor

A. Senthil Kumar, T. Prasath Vijay Raj, A. Tharagesh and V. Prasanna

Abstract Permanent magnet machines are widely used in many applications. The structure of these machines is simple, and it is of low cost. Due to the advance in the power electronic drives and circuits, the control of a PMDC motor is very easier. Because of their excellent torque characteristics and good power factor maintainability, PMDC machines are used extensively in artificial intelligence, aerospace and military applications. Design methodologies are mainly due to armature winding, stator magnets, poles, commutator, brushes which were carried out in an efficient manner in the mathematical form. This chapter presents the mathematical model and analysis of PMDC motor, and it is validated using the simulation software.

Keywords Permanent magnet DC motor · Speed · Exciter
Mathematical model · Transfer characteristics

1 Introduction

The energy conversion device using permanent magnet as exciter can be termed as a permanent magnet machine (PMDC machine). In industrial and automobile applications, the PMDC machines play a major role in starters, wipers, blowers, power window motors and toys. In space applications, these motors are used along with encoders, decoders, and throttle actuators in a wide-bodied aeroplane which

A. Senthil Kumar (✉) · T. Prasath Vijay Raj · A. Tharagesh · V. Prasanna
Department of EEE, Velammal Engineering College, Chennai, India
e-mail: vastham@gmail.com

T. Prasath Vijay Raj
e-mail: prasathvijayraj@gmail.com

A. Tharagesh
e-mail: thararockz79@gmail.com

V. Prasanna
e-mail: prasanna.francis4@gmail.com

A. Konkani et al. (eds.), *Advances in Systems, Control and Automation*,
Lecture Notes in Electrical Engineering 442, https://doi.org/10.1007/978-981-10-4762-6_22

could be operated without the pilots. The whole system is referred to be the 'Smart Actuators'. The PMDC motors for its least maintenance appear to be good for such applications [1–4]. For designing the components in automobiles, high safety measures should be taken, and so the design process needs to be more accurate [5].

These motor drives work efficiently, where the speed varies constantly and also where the variable speed operations need to be achieved [6]. With the advent of alnico (aluminium, nickel and cobalt alloys), the PMDC motor with high efficiency could be designed. Samarium–cobalt made it possible to construct a small-sized, lightweighted and high-efficiency PMDC motor [7].

The working of the PMDC machines is similar to the DC shunt motors except the fact that the stator fields are replaced by the permanent magnets to provide a necessary flux by which the motor operate. Because of the less interaction of the armature field with the main field, the motors experience a linear speed—torque characteristics. If the torque increases, the speed will be decreasing proportionally for a given armature voltage. Because of the permanent magnets, these motors do not need separate excitation for the stator, and hence the size and cost of the motor will also decrease effectively lesser than the conventional DC motors. By controlling the armature, the speed of the motor could be controlled [8, 9].

PM motors are better in the field of control, volume, cost, weight, size and shape in comparison to its counterpart. They exhibit excellent acceleration and deceleration. However, the major drawback is that the field in the motor is permanent and the air gap is limited and fixed, and so the speed could not be controlled externally. Therefore, the efficient speed control is difficult in this motor. The production cost of these motors depends on (i) material cost, (ii) machine assembly cost, (iii) machine controller cost, (iv) operating cost and (v) emergency maintenance cost.

This paper presents the design and analysis of a PMDC motor. The modelling of the motor was also performed, and the results were verified with the help of the MAGNET software. Generally, the modelling is done to represent the mathematical form of the mechanical and electrical system parameters [10]. PMDC machine specifications: (1) output voltage = u (V), (2) output power = w (W), (3) rotational speed = N (rpm), (4) type of duty = continuous, (5) type of construction = totally enclosed.

This chapter describes the following sequence: Sect. 2—Literature, Sect. 3—Detailed design flow, Sect. 4—Performance characteristics analysis, Sect. 5—Simulation results, Sect. 6—Conclusion.

2 Mathematical Model of a PMDC Motor

The mathematical model could be achieved by relating the armature voltage and the motor velocity. By this, the two balanced equations could be derived.

2.1 Electrical Characteristics

The equivalent circuit of a PMDC motor is shown in Fig. 1. The supply voltage and the current are given.

The circuit consists of an induced voltage (V_i) in series with an armature resistor (R_{arm}) and inductance (L_{arm}). The rotation of the flux generates the induced voltage. It is also referred to as the Back emf.

According to the Kirchhoff's voltage law,

$$V_{\text{arm}} - V_{R\text{arm}} - V_{L\text{arm}} - V_i = 0 \tag{1}$$

By Ohm's law, the voltage across the resistor could be written as,

$$V_{R\text{arm}} = i_{\text{arm}} R_{\text{arm}} \tag{2}$$

Similarly, the voltage across the inductor could be written as,

$$V_{L\text{arm}} = L_{\text{arm}} \frac{\mathrm{d}}{\mathrm{d}t} i_{\text{arm}} \tag{3}$$

The Back emf could be represented as,

$$V_i = k_v \omega_{\text{arm}} \tag{4}$$

where k_v is a velocity constant derived by the permanent magnets, reluctance and number of turns; ω_{arm} is an angular velocity of the armature.

Substituting the Eqs. (2)–(4) into Eq. (1) we get,

$$V_{\text{arm}} - i_{\text{arm}} R_{\text{arm}} - L_{\text{arm}} \frac{\mathrm{d}}{\mathrm{d}t} i_{\text{arm}} - k_v \omega_{\text{arm}} = 0 \tag{5}$$

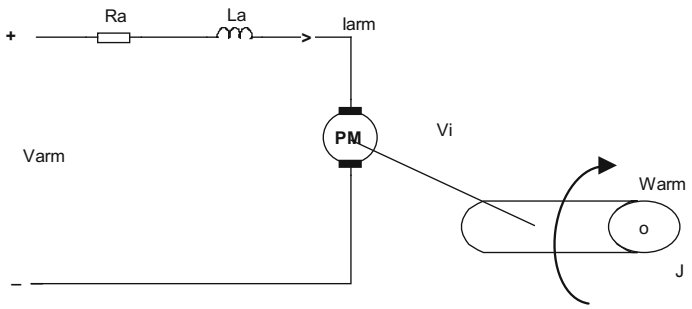

Fig. 1 Electrical representation of a DC motor

2.2 Mechanical Characteristics

The condition for the energy to be balanced is that the sum of the torques should be equal to zero. Hence,

$$T_{\mathrm{e}} - T_{\omega'} - T_{\omega} - T_{\mathrm{L}} = 0 \tag{6}$$

where T_{e} is the electromagnetic torque, $T_{\omega'}$ is the rotational acceleration torque, T_{ω} is the torque due to the velocity of the rotor and T_{L} is the mechanical load torque.

The electromagnetic torque T_{e} with respect to the armature current is written as,

$$T_{\mathrm{e}} = k_t i_{\mathrm{arm}} \tag{7}$$

Similarly, the rotational acceleration torque $T_{\omega'}$ can be represented as,

$$T_{\omega'} = J \frac{\mathrm{d}}{\mathrm{d}t} \omega_{\mathrm{arm}} \tag{8}$$

where J is the inertia of rotor.

The torque associated with a rotor velocity is written as,

$$T_{\omega} = B\omega_{\mathrm{arm}} \tag{9}$$

where B represents the damping coefficient of the mechanical rotational system.

Substituting Eqs. (7)–(9) into Eq. (6) we get the following equation,

$$k_t i_{\mathrm{arm}} - J \frac{\mathrm{d}}{\mathrm{d}t} \omega_{\mathrm{arm}} - B\omega_{\mathrm{arm}} - T_{\mathrm{L}} = 0 \tag{10}$$

2.3 State Space Representation

The Eqs. (5) and (10) could be written as,

$$\frac{\mathrm{d}}{\mathrm{d}t} i_{\mathrm{arm}} = -\frac{R_{\mathrm{arm}}}{L_{\mathrm{arm}}} i_{\mathrm{arm}} - \frac{k_v}{L_{\mathrm{arm}}} \omega_{\mathrm{arm}} + \frac{V_{\mathrm{arm}}}{L_{\mathrm{arm}}} \tag{11}$$

$$\frac{\mathrm{d}}{\mathrm{d}t} \omega_{\mathrm{arm}} = \frac{k_t}{J} i_{\mathrm{arm}} - \frac{B}{J} \omega_{\mathrm{arm}} - \frac{T_{\mathrm{L}}}{J} \tag{12}$$

These equations could be written in the state space form as follows,

$$\frac{\mathrm{d}}{\mathrm{d}t}\begin{bmatrix} i_{\text{arm}} \\ \omega_{\text{arm}} \end{bmatrix} = \begin{bmatrix} -\frac{R_{\text{arm}}}{L_{\text{arm}}} & -\frac{k_v}{L_{\text{arm}}} \\ \frac{k_t}{J} & -\frac{B}{J} \end{bmatrix}\begin{bmatrix} i_{\text{arm}} \\ \omega_{\text{arm}} \end{bmatrix} + \begin{bmatrix} \frac{1}{L_{\text{arm}}} & 0 \\ 0 & -\frac{1}{J} \end{bmatrix}\begin{bmatrix} V_{\text{arm}} \\ T_{\text{L}} \end{bmatrix} \tag{13}$$

$$\begin{bmatrix} y_1 \\ y_2 \end{bmatrix} = \begin{bmatrix} 1 & 0 \\ 0 & 1 \end{bmatrix}\begin{bmatrix} i_{\text{arm}} \\ \omega_{\text{arm}} \end{bmatrix} + \begin{bmatrix} 0 & 0 \\ 0 & 0 \end{bmatrix}\begin{bmatrix} V_{\text{arm}} \\ T_{\text{L}} \end{bmatrix} \tag{14}$$

which could be symbolically expressed as follows,

$$\frac{\mathrm{d}}{\mathrm{d}t}x = A_x + B_u \tag{15}$$

$$y = C_x + D_u \tag{16}$$

where 'x' is a state vector, 'u' is an input vector and 'y' is an output vector.

2.4 Block Diagram with Transfer Function

The block diagram could be developed from the Eqs. (11) and (12). Taking Laplace transform we get,

$$sI_{\text{arm}}(s) - i_{\text{arm}}(0) = -\frac{R_{\text{arm}}}{L_{\text{arm}}}I_{\text{arm}}(s) - \frac{k_v}{L_{\text{arm}}}\Omega_{\text{arm}}(s) + \frac{1}{L_{\text{arm}}}V_{\text{arm}}(s) \tag{17}$$

$$s\Omega_{\text{arm}}(s) - \omega_{\text{arm}}(0) = \frac{k_t}{J}I_{\text{arm}}(s) - \frac{B}{J}\Omega_{\text{arm}}(s) - \frac{1}{J}T_{\text{L}}(s) \tag{18}$$

If the variation in steady-state values are considered, the initial conditions go to zero, all values change with the reference state, and the equations could be represented as follows,

$$I_{\text{arm}}(s) = \frac{-k_v\Omega_{\text{arm}}(s) + V_{\text{arm}}(s)}{L_{\text{arm}}s + R_{\text{arm}}} \tag{19}$$

$$\Omega_{\text{arm}} = \frac{-k_t I_{\text{arm}}(s) - T_{\text{L}}(s)}{J_s + B} \tag{20}$$

Hence, the block diagram could be represented for PMDC motor as shown in Fig. 2.

This block diagram could be simplified by assuming the load torque is constant.

Further, the block diagram could be reduced and the overall transfer function could be found, and it becomes as in Figs. 3 and 4.

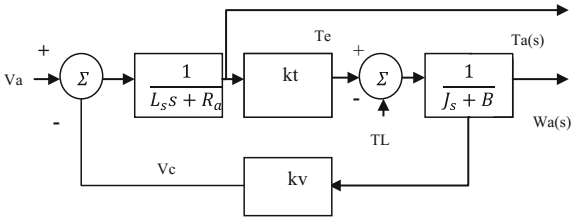

Fig. 2 Block diagram representations of Eqs. (19) and (20)

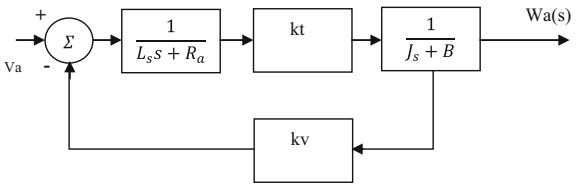

Fig. 3 Block diagram of the PMDC motor

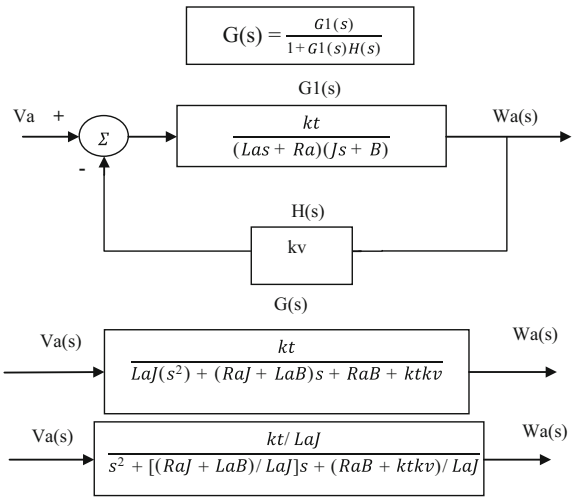

Fig. 4 Reduced block diagram and overall transfer function of the PMDC motor

3 Flow Chart

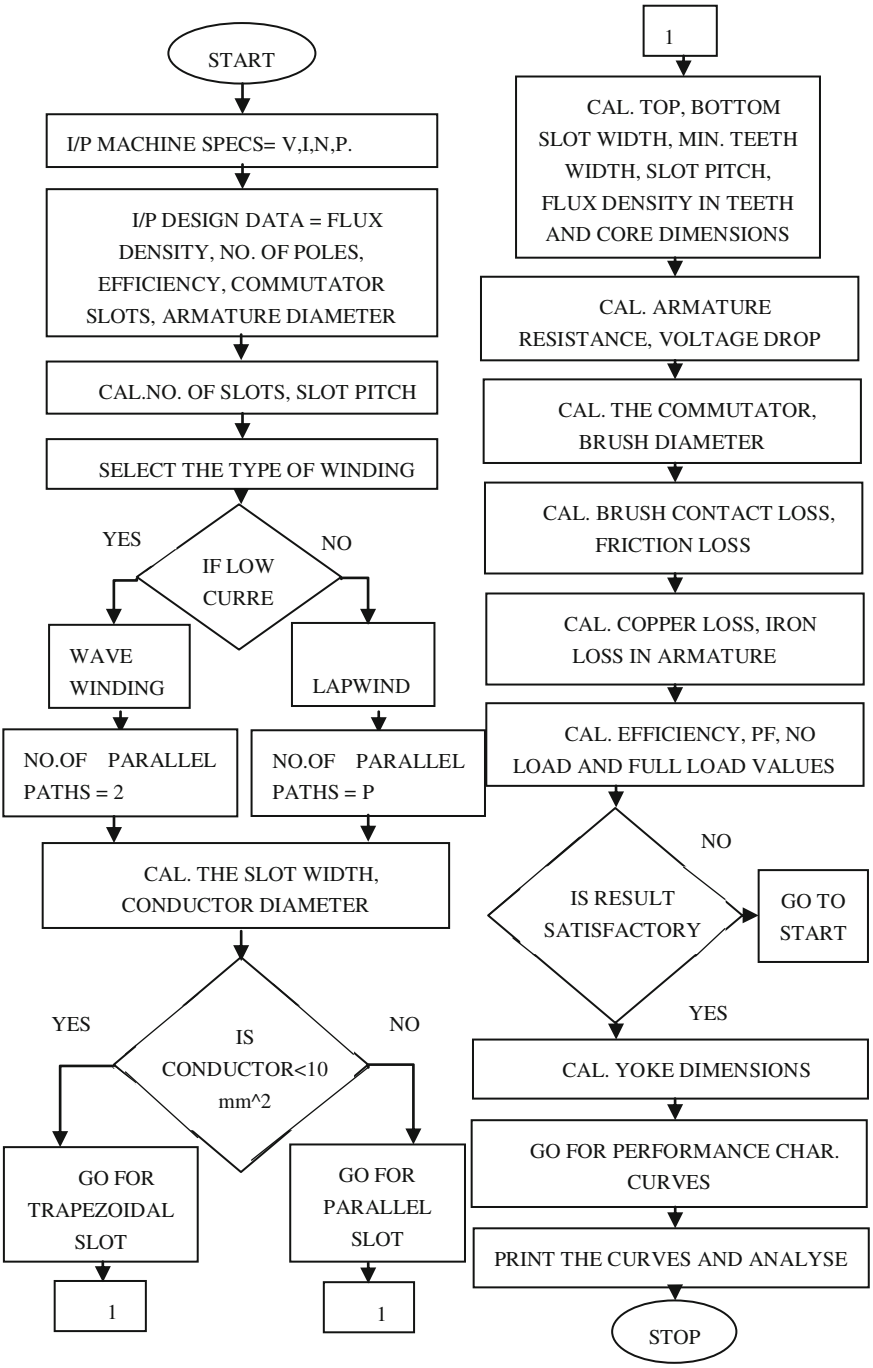
START
I/P MACHINE SPECS= V,I,N,P.
I/P DESIGN DATA = FLUX DENSITY, NO. OF POLES, EFFICIENCY, COMMUTATOR SLOTS, ARMATURE DIAMETER
CAL.NO. OF SLOTS, SLOT PITCH
SELECT THE TYPE OF WINDING
IF LOW CURRE
YES
NO
WAVE WINDING
LAPWIND
NO.OF PARALLEL PATHS = 2
NO.OF PARALLEL PATHS = P
CAL. THE SLOT WIDTH, CONDUCTOR DIAMETER
IS CONDUCTOR<10 mm^2
YES
NO
GO FOR TRAPEZOIDAL SLOT
GO FOR PARALLEL SLOT
1
1
1
CAL. TOP, BOTTOM SLOT WIDTH, MIN. TEETH WIDTH, SLOT PITCH, FLUX DENSITY IN TEETH AND CORE DIMENSIONS
CAL. ARMATURE RESISTANCE, VOLTAGE DROP
CAL. THE COMMUTATOR, BRUSH DIAMETER
CAL. BRUSH CONTACT LOSS, FRICTION LOSS
CAL. COPPER LOSS, IRON LOSS IN ARMATURE
CAL. EFFICIENCY, PF, NO LOAD AND FULL LOAD VALUES
IS RESULT SATISFACTORY
NO
GO TO START
YES
CAL. YOKE DIMENSIONS
GO FOR PERFORMANCE CHAR. CURVES
PRINT THE CURVES AND ANALYSE
STOP

4 Design Calculation

4.1 Given Dimensions

Armature diameter (D)	53.8 mm (Fig. 5)
Slot tip diameter	52.6 mm
Pole arc/pole pitch (Ψ)	0.8875
No. of poles (p)	6
Slot root diameter (d)	39.8

4.2 Number of Slots Calculation

Usually, in 12 V machines, slot pitch (S_s) value lies between 5.5 and 6.5 mm.

No. of slots $S = \pi \times (D/S_s)$

Taking S_s = 5.5 mm,

$S = \pi \times (53.8/5.5), \quad S = 31$

Therefore, no. of slots should lie between 25 and 31.

No. of slots is taken as odd number to avoid the effect of harmonics.

So, the no. of slots can be 25, 27 and 29.

To reduce flux pulsation,

Ratio of $\Psi \times S/p$ = integer $\pm$ 0.5

For S = 25, $\Psi \times S/p$ = 0.8875 $\times$ 25/6 = 3.69 (approx. = 4)

For S = 27, $\Psi \times S/p$ = 0.8875 $\times$ 27/6 = 3.99 (approx. = 4)

For S = 29, $\Psi \times S/p$ = 0.8875 $\times$ 29/6 = 4.28 (approx. = 4)

NO. OF SLOTS = 25

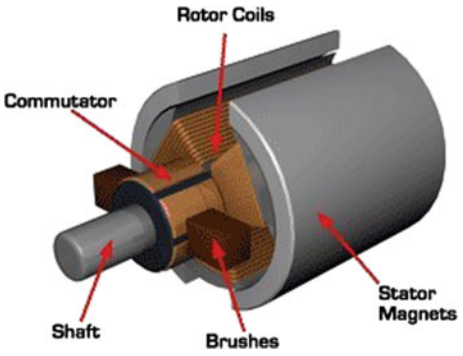

Fig. 5 Armature of a PMDC motor

4.3 Type of Winding

Usually in case of low-current applications, the winding is assumed as wave winding (Fig. 6).
So, for this application, wave winding is used.
Armature winding = wave, double-layer winding.
Double-layer winding is used for achieving higher torque.

4.4 Slot Width Calculation

(Tooth width + slot width) at slot root diameter = $\pi \times d/S$ = 3.14 * 39.8/25 = 4.99 mm (Fig. 7).

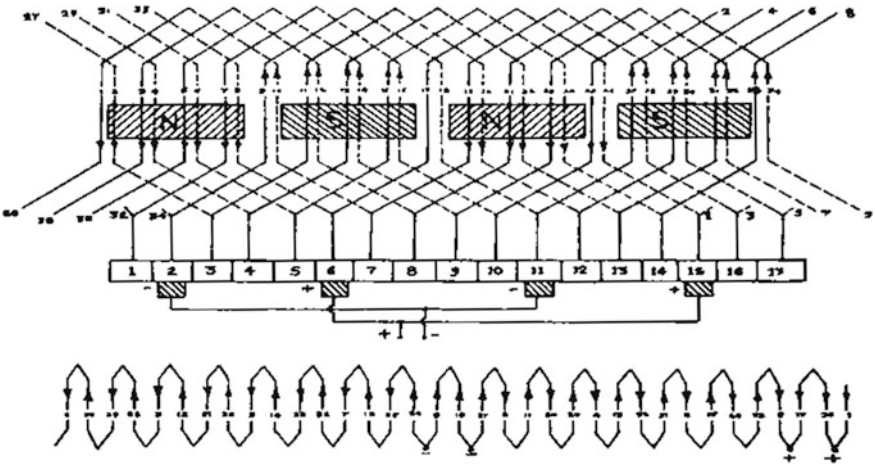

Fig. 6 Wave winding

Fig. 7 Slot diagram

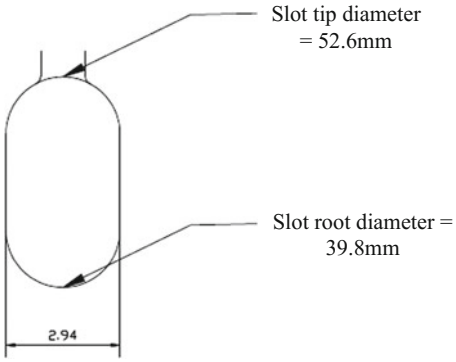

Tooth width at slot root diameter should be at least 1.48 mm to avoid losses due to saturation effect.

Slot width $= 4.99 - 1.2 = 3.79$ mm.

4.5 Calculation of Conductor Dimensions

Lamination is used to avoid shorting between conductors and the core (Fig. 8).

Thickness of lamination used is 0.3 mm.

$$\text{Space for conductor width} = \text{Slot Width} - (2 \times \text{Insulation Thickness})$$
$$= 3.79 - (2 \times 0.3) = 3.19 \text{ mm}$$

Leaving a clearance space of 0.54 mm for varnish, we arrive at the conductor dimension as

Conductor width $= 2.65$ mm

$$\text{Space for conductor thickness} = \text{Slot height} - 3 \times \text{Insulation thickness} = 6.2 \text{ mm}$$

Leaving a clearance space of 0.785 mm for varnish, we arrive at

Space for conductor thickness $= 5.4$ mm

This space is for two conductors (since, it is a double-layer winding)

Conductor thickness $= 5.4/2 = 2.7$ mm

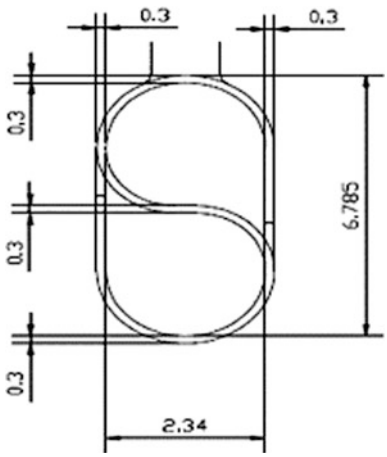

Fig. 8 Slot profile with insulation diagram

4.6 Commutator Design

$$\text{Commutator riser diameter} = 0.836\,D$$
$$= 0.836 \times 53.8 = 44 \text{ mm}$$

Armature barrel diameter = 31 mm

$$\text{Segment width} + \text{Mica separator width} = \pi \times \text{Armature barrel diameter}/\text{No. of slots}$$
$$= 31 \times 3.14/25 = 3.893 \text{ mm}$$

Mica width is taken as 0.56 mm
Segment width = 3.893 − 0.56 = 3.33 mm
Commutator riser diameter = 44 mm
Armature barrel diameter = 31 mm
Mica width = 0.56 mm
Segment width = 3.33 mm

4.6.1 Brush Design

Maximum current density at lock condition in a brush should not be greater than 5 A/mm^2

Lock current = 900 A
Since wave winding is used, no. of parallel path = 2
Current/brush = 900/2 = 450 A
Taking brush width as approx. 2 times segment width + mica width
Brush width = 3.45 × 2 = 6.9–7 mm
Area = 7X mm^2
Current density = current/area = 450/7X
X = 450/35 = 13 mm
Height of brush = 13 mm
Brush width = 7 mm

5 Simulation Results

The simulation results of permanent magnet DC motor are shown in Fig. 9. Here flux lines and flux density distribution of the chosen excitation are studied. The above-mentioned all design analyses are simulated and verified using MAGNET software.

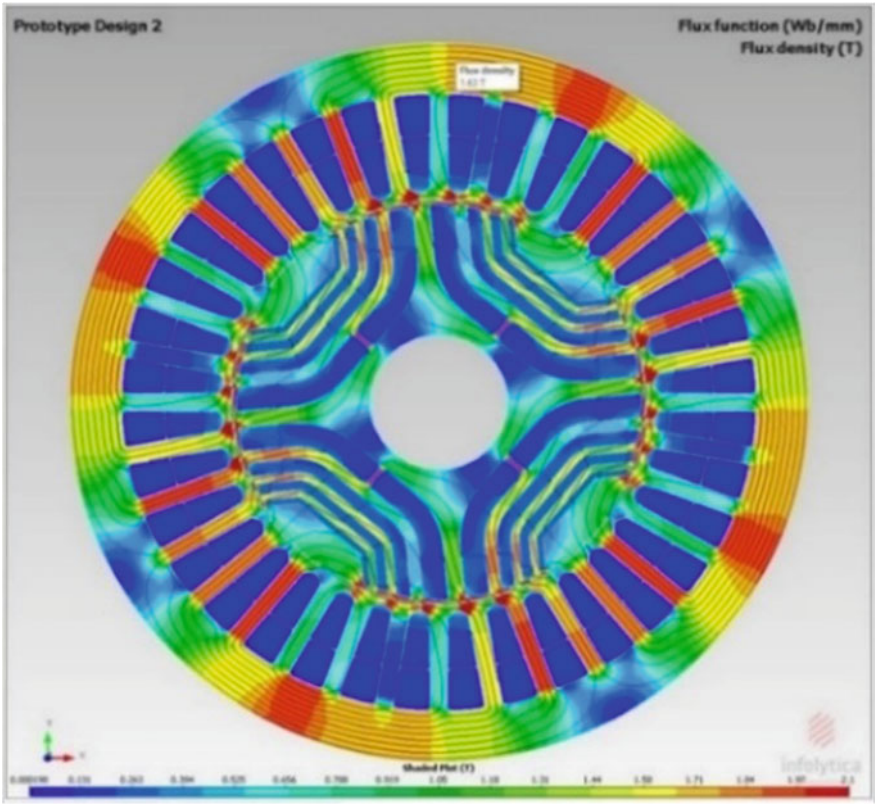

Fig. 9 Simulation results

6 Conclusion

This chapter presents an innovative design and analysis of PMDC motor. The analytical model of a PMDC motor had been verified and validated using MOTOR SOLVE MAGNET software. With the advent of rare-earth PM material like samarium–cobalt, neodymium iron boron, the brushless PM motor, becomes more efficient than induction motor. The output power/volume ratio is high, and better dynamic performance is available with this motor. Construction and maintenance of PMDC motor are also simple. Since the performance and control of this PMDC motor are excellent, it makes the best choice in low-cost and highly efficient applications.

References

1. Kiyoumarsi, A.: Analysis and comparison of a permanent magnet DC motor with a field winding DC motor. J. Electr. Eng. Technol. **4**(3), 370–376 (2009)
2. Kumar, S.B., Ali, M.H., Sinha, A.: Design and simulation of speed control of a DC motor by fuzzy logic technique with Matlab/Simulink. Int. J. Sci. Res. Publ. **4**(7), 1–4 (2014)
3. Singh, A.R., Giri, V.K.: Design and analysis of DC motor speed control by GA based tuning of fuzzy logic controller. Int. J. Eng. Res. Technol. **1**(5) (2012)
4. Kiyoumarsi, A., Moallem, P., Hassanzadeh, M., Moallem, M.: Application of a FEA method in design and analysis of permanent magnet motors. International Journals published by WSEAS Press
5. Wolm, P., Chen, X.Q., Chase, J.G., Pettigrew, W., Hann, C.E.: Analysis of PMDC motor model for application in feedback design for electric powered mobility vehicles in mechatronics and machine vision in practice, 2008, M2VIP 2008. In: 15th International Conference on Auckland, pp 640–645 (2008)
6. Shahgholian, G., Shafaghi, P.: Analysis of a permanent magnet DC motor drive systems
7. Ritunjoy Bhuyan U: Design and performance analysis of permanent magnet DC motor. Int. J. Sci. Eng. Appl. Sci. (IJSEAS) **2**(3) (2016)
8. Javadi, S.H., Moussavi, S.Z., Alasvandi, M.: Speed control of permanent magnet DC motor by using combination of adaptive controller and fuzzy controller. Int. J. Comput. Appl. (0975–8887) **52**(20) (2012)
9. Junak, J., Ombach, G., Staton, D.: Permanent magnet DC motor brush transient thermal analysis. In: International Conference on Electrical Machines in 2008, Paper ID 1109 978-1-4244-1736-0/08 (2008)
10. Venu, K., Rushikesh, C., Rajasekhar, V.: Design and analysis of DC motor with PID controller—a state space approach. Department of Electrical and Electronics Engineering, VNR Vignana Jyothi Institute of Engineering and Technology, Hyderabad, India

Design and Analysis of Performance Characteristics of Electronic Ballast Used for Fluorescent Lamp

J. Lokesh, Akshat Khemka and Poorvi Sharma

Abstract Simulation and measurement are essential to the process of designing electronics. But they have differences in capabilities and limitation of making it happen. This paper presents the detailed implementation of an electronic ballast, for a fluorescent lamp. The circuit is commutated smoothing circuit, power switch, and driving circuit. It is a low-voltage starter, non-stroboscopic, has no noise, energy efficient, and has high power factor with very high switching speed. Characteristic results and measurements are provided with comparison to market available ballast. The circuit has been successfully applied to a 36 W lamp.

Keyword Fast switching · Low ripple · High frequency · Ballast factor

1 Introduction

The fluorescent tube is essentially a low-pressure mercury discharge lamp. The convenience and popularity of fluorescent lamp is underscored by the fact that it accounts for a great amount of light produced on our planet than any other light source. It achieved its portion of dominance starting from the 1980s, and it is estimated that today it accounts for about 80% of the artificial light used in the world. It can be manufactured in almost any shape of white and colored versions.

The main disadvantage of fluorescent lamp is their negative impedance characteristics. So to connect the lamp directly to utility line, we need to prevent the lamp from the excessive flowing current and make sure they work in desired operation region. For this purpose **ballast** are used. In fluorescent light fixtures, two

J. Lokesh (✉) · A. Khemka (✉) · P. Sharma (✉)
Electrical and Electronics Department, Manipal Institute of Technology, Manipal, India
e-mail: lokesh.j@manipal.edu

A. Khemka
e-mail: akshat.khemka@manipal.edu

P. Sharma
e-mail: poorvi.sharma@manipal.edu

A. Konkani et al. (eds.), *Advances in Systems, Control and Automation*,
Lecture Notes in Electrical Engineering 442, https://doi.org/10.1007/978-981-10-4762-6_23

common types of ballast are electronic ballasts and magnetic ballasts. While magnetic ballasts are simple and easy in their design and operating principle, the more sophisticated electronic ballast just has too many advantages. In addition to not causing fluorescent flicker and noise like magnetic ballasts, electronic ballasts are preferred because they are smaller in size and weightless. They are also great for the environment, and they are energy efficient and help us reduce our monthly energy bill. When we use ballast in fluorescent lamps, there is an introduction of harmonics in the line and that causes very poor power factor at input. So these line current harmonics are required to be within standards. The international standards IEC61000-3-2 and its European version EN61000-3-2 are followed for detailed harmonic limits [1].

Important considerations for ballast include high power factor, low-total harmonic distortions, low electromagnetic interference, and no flickering. The electronic ballast has been designed to work for a 36 W fluorescent lamp operating from 220 V ± 10%, 50 Hz utility line. Switching frequency of the lamp is 25 kHz.

2 Circuit Description and Function of Components

The circuit diagram for the electronic ballast is shown in Fig. 1. The fluorescent lamps can be modeled as a resistive load because the converter operates at very high frequency [2, 3]. The circuit is basically divided into four parts:

(a) **Smoothing circuit**: The VD1, VD2, VD3, and VD4 make up the smoothing circuit of the bridge rectifier that converts AC supply of input 230 V to pulsating DC. The output voltage from rectifier will be ranging between zero and $\sqrt{2}$ times rms voltage. It will not work for analog circuit as it will have high level of ripple superimposed on the output.

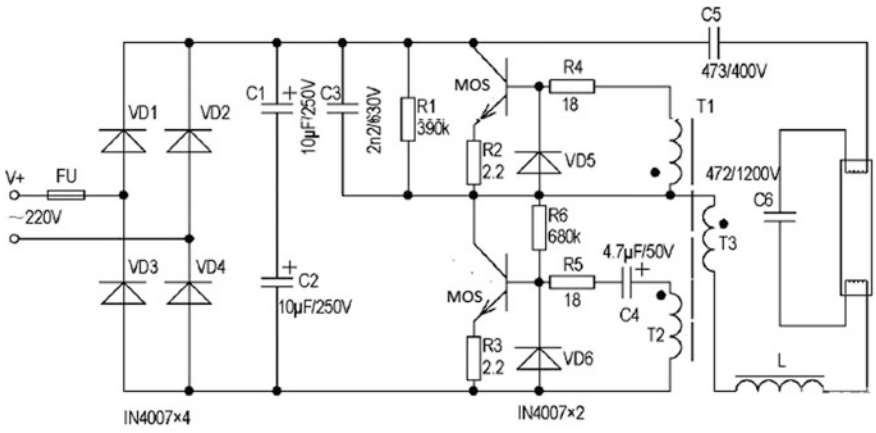

Fig. 1 Proposed electronic ballast circuit diagram

To smooth the output from the rectifier, reservoir capacitors $C1$ and $C2$ are used. When the rectifier voltage goes above the reservoir capacitor voltage, it charges up and it provides the required current from stored charge when the rectifier voltage drops. Capacitors are placed in parallel with the bridge rectifier. It also helps in improving the power factor as the voltage level rises across the capacitor and hence the power factor. The D1N4007 diodes are used in rectifier circuit and the capacitance in circuit can be found using the following equation

$$R_{\text{load}} \times C \gg 1/f \tag{1}$$

where, R_{load} = the total resistance, C = capacitor value and f = ripple frequency; will be double as full wave rectifier is used. So we can find C from Eq. (1). Ripple is generally considered to be 1–20% of the input voltage. The following waveform shows the ripple for a full wave rectifier with capacitor smoothing (Fig. 2).

(b) **Snubber circuit**: They are energy absorbing circuits that are used to protect the circuit from overvoltage or rather absorb the voltage spikes caused by inductance present in the circuit during switching. It is also used to limit the current for the fluorescent lamp to operate without any problems. In this circuit, R1 and C3 are R-C components used.
The design procedure is [3]:
Assuming that the source has very less impedance, then the worst possible peak current in circuit is given by:

$$I_{PK} = V_0/R_S \tag{2}$$

where R_S = snubber resistance, V_0 = open circuit loop voltage.
The circuit dv/dt is determined from the following equation:

$$I_P = C\frac{dV}{dT} \tag{3}$$

Substituting Eq. (2) in (3), we get

$$\frac{dV}{dT} = V \times C/R_S \tag{4}$$

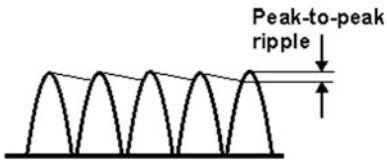

Fig. 2 General full wave rectifier waveform with ripple

By Ohms law, snubber resistance will be

$$R = V_0/I \tag{5}$$

The amount of energy stored in the snubber capacitor is the amount of energy the snubber resistance is to dissipate. It is recommended that to choose AC value that causes the resistor to dissipate one half the wattage rating of resistance.

$$C = P/(f \times (V^2)) \tag{6}$$

(c) **Power switch and driving circuit**: Two MOSFETs VT1 and VT2 are used in the circuit. They have very high switching speed and work in saturation and cut-off states. Resistances *R*4 and *R*5 are put to protect the gate of MOSFETs VT1 and VT2, respectively. Similarly in the case of source, for both the MOSFETs, resistances are present. Diodes *D*5 and *D*6 are also used for protection of MOSFETs. Moreover, they connected in parallel to weaken the memory effect of electric charge greatly between base electrode and emitter, thus improve the switching speed.
The voltage transformer used is a trifilar toroid transformer. It plays a mutual inductance coupling of signal role. It is wounded by single-stranded intersection of core wire and *T*1, *T*2, *T*3 at magnetic ring formation because the intersection of driving circuit and the part to contact has very close interdependence. So the relation between the intersection and the parameters used in the process of production is relatively very difficult to confirm. *T*1 has 3 circles, *T*2 has 3 circles, and *T*3 has 5 circles in this circuit. Electric capacitor *C*4 is connected to VT2 base electrode and emitter, can prevent the base electrode and the launch of sudden change of interpolar electric potential, and can protect VT2 emitter to a certain extent. Capacitance *C*5 prevents the direct current volts direct access to the fluorescent tube and allows high-frequency alternating current voltage of 25 kHz to pass.

(d) **Series resonance circuit**: Choke coil *L*, electric capacitor *C*6 make up the series resonance circuit. The brightness and working current of the fluorescent tube is thus controlled.

3 Testing

3.1 Evaluation of Total Luminous Flux

There are two ways to find the total luminous flux emitted by the lamp or luminaire. (1) Using integrating sphere: If light is emitted uniformly, then the light output emitted by the lamp or luminaire is given by:

$$I = \frac{\text{ø}}{w} \tag{7}$$

where

I is the luminous intensity in a particular direction (luminous flux per solid angle),

Φ is the luminous flux in Lumens (lm), and
ω is the solid angle in steradians (sr).

(2) Using goniophotometer (BZ method). In the zonal method, the light source is assumed as point source and tested under standard test conditions. The following equations are used to find the total light emitted by the lamp. The following equation is used to find the luminous flux between the angle $\theta 1$ and $\theta 2$

$$\text{ø} = I_{\text{mid}} \times \text{ZF} \tag{8}$$

where
ø is the luminous flux.
I_{mid} is the average intensity within the zone.
ZF is zonal factor, and ZF is calculated using following equation:

$$\text{ZF} = 2 \times \pi \times (\cos(n-1)\alpha - \cos n\alpha) \text{ Steradians.} \tag{9}$$

where n is zone number and α is zone angle (angular width).

The accuracy of the value increases as the number of zones increases with decrease in zone angle. The proposed system is tested using goniophotometer, and results are shown in Tables 1 and 2.

3.2 Reference Ballast

As per Indian standards, reference ballast always operates at 50 Hz line frequency. They have constant impedance for long periods of time over a wide range of operating current and are relatively taken care against temperature or magnetic surroundings since the characteristics of any of the magnetic components will get affected by them.

Table 1 Lumen output of the lamp with different ballast

Ballast	Lumen output (lm)
Reference ballast	1454.673
Electronic ballast	1087.12
Proposed ballast	1254.011

Table 2 Comparison of performance characteristics of a proposed ballast and existing ballast in the market

Ballast	BF	BEF
Electronic ballast	0.80	1.975
Proposed ballast	0.86	2.12

Reference ballasts are designed and manufactured specifically to provide stable reference conditions for testing ballasts and lamps ANSI also recommended a standard (ANSI C82.3-1983) for reference ballasts to check the performance characteristics such as ballast factor (BF) and rated light output of ballast with FTL. They are different from commercially available magnetic and electronic ballasts such as those discussed in this report. The performance characteristics of proposed system are measured in terms of ballast factor and ballast efficacy factor (BEF). BF and BEF is given by:

$$\mathrm{BF} = \frac{\text{Luminous lux of the lamp with test ballast (lumens)}}{\text{Luminous flux of the lamp with reference ballast (lumens)}}$$

$$\mathrm{BEF} = \frac{\mathrm{BF} \times 100\,(\%)}{\text{Power}\ (\mathrm{W})}$$

The proposed system is designed for 36 W FTL and the specifications are 230 V, 0.165 A, and 0.95. Ballast loss = 4.5 W. Using Eqs. (8) and (9), the luminous flux with different ballast is obtained and shown in Table 1. The BF and BEF is calculated using above-mentioned equations and listed in Table 2.

4 Conclusion and Future Scope of the Work

This report proposes an electronic ballast topology with very fast switching for fluorescent lamp. There is no flicker at high frequencies. This circuit presents simplicity of control, allowing use of reduced number of components when compared to other topologies, for a given input voltage. Reduction in memory effect by the use of diodes plays a vital role in increasing switching speed. Photometric test has been performed to compare proposed ballast with market available ballast and find the characteristics. Presented ballast circuit has better ballast factor than the market available ballast. It was applied successfully to a fluorescent tube of 36 W with very little losses.

We can also add dimming feature in ballast as it can save tremendous amount of energy and also is an attractive feature that provides mood and brightness effect.

A 4 wire ballast uses a hot (non-dim) and a neutral (ground) plus two voltage conductors for 0–10 vdc control or DALI control protocols. This can further be

extended by using a wireless network to control fluorescent tubes to entire area from one place. If using a wireless network to control the ballast (DALI), we need to take care of the security measures. As fluorescent lamps are widely used at airports, hospitals, and many public places, and if the system is compromised, it can lead to security threats.

References

1. EC 61000-3-2: Electromagnetic compatibility (EMC) Part 3-2: Limits for harmonic current emissions (equipment) input current (2000–08)
2. Rueda, V., Perez, A., Diez, R., Perilla, G.: Battery powered electronic ballast for fluorescent lamp with frequency control. IEEE Trans. Power Electron. **22**(3), 863–870 (2013)
3. Jen-Cheng, H., Lin, J.: Novel single-stage self-oscillating dimmable electronic ballast with high power factor correction. IEEE Trans. Ind. Electron. **58**, 250–262 (2011)
4. Mader, U., Horn, P.: A dynamic model for the electrical characteristics of fluorescent lamp. In: IEEE—IAS/92, Proceedings, pp. 1928–1934, Illinoiscapacitor.com, 'RC SNUBBER CIRCUIT' [Online] (1992)

Ballistocardiogram Signal Denoising Using Independent Component Analysis

B.M. Manjula and Chirag sharma

Abstract Ballistocardiogram (BCG) signal provides measurement of body's reaction force for cardiac blood ejection. BCG signal acquisition and processing techniques have attracted researchers due to its huge applications in biomedical field. These techniques comprise of detection of BCG signals which includes weighing scales, chairs, tables, or beds. There are various signal acquisition processes present, i.e., EEG, fMRI, etc. In last decade, simultaneous recording to EEG and fMRI signal has grown as promising technique in this field of biomedical where brain monitoring or other physical activities need to be monitored. During signal acquisition, original signal gets corrupted due to various conditions which affect the signal. This unwanted signal causes artifact in the original signal, which makes difficult for researchers to analyze and monitor the activities. In order to address this, we propose independent component analysis-based approach for artifact removal. Proposed approach is implemented using MATLAB tool, and experimental study is carried out for various user 'data'set. Outcomes of the filtering method show better filtering or denoising performance.

Keywords Ballistocardiogram · Filtering
Preprocessing independent component analysis

1 Introduction

During last decade, biomedical research has grown tremendously for developing various noninvasive techniques which allows us to study about brain functionality and neural activity, in depth. In biomedical electroencephalogram (EEG) and magnetic resonance imaging (MRI) are the promising techniques to provide better

B.M. Manjula (✉)
Nitte Meenakshi Institute of Technology, Bangalore, India
e-mail: manjula.nmit@gmail.com

C. sharma
Nitte Research and Education Academy, Bangalore, India

A. Konkani et al. (eds.), *Advances in Systems, Control and Automation*,
Lecture Notes in Electrical Engineering 442, https://doi.org/10.1007/978-981-10-4762-6_24

understanding of brain structure and study of brain activity. In later years, EEG and fMRI are combined which is used for electrophysiological information extraction and study of hemodynamic changes which occur in brain [1]. EEG signals provide neural activity of brain with a spatiotemporal resolution which is generated in brain structure by considering centimeter and millisecond order [2]. On the other hand, functional magnetic resonance (fMRI) depends on blood oxygen variation and neural activity, and using this also spatiotemporal information can be extracted with the same order as EEG i.e., with the millimeter and seconds order [3].

In today's scenario of biomedical applications, simultaneous recording of EEG and fMRI is used widely for monitoring brain activities such as epileptic spikes [4], evoked potentials [5], and sleep spindles [6]. EEG 'data' acquisition is performed during MR imaging; due to MR imaging some artifacts are induced into the original EEG 'data' which are mainly classified into two categories: (1) ballistocardiogram (BCG) artifact [7] and (2) imaging artifact [8]. BCG artifacts are caused due to subject's head movement, motion of EEG electrodes, whereas imaging artifacts are caused due to rapid variations in magnetic field. Amplitude and timings are the main components to characterize imaging artifacts. Key features of these artifacts are predictability and regularity which are useful for artifact removal from recorded EEG and fMRI signal. By considering this, various approaches have been proposed in [9–11]. In [9], Allen et al. discussed about the artifacts present in EEG signal and proposed a new recording system for artifact removal.

Similarly, during continuous acquisition of EEG with functional MRI, ballistocarigraphic (BCG) artifacts are induced in the original signals. As we have discussed earlier these signals are generated due to head or electrode movements during acquisition and due to electromagnetic states of the user in MRI Scanner In the last decade, various methods have been proposed to address the issues and complexities of ballitsocarigraphic (BCG) artifact. Ferdowsi et al. [12] developed a new approach for BCG artifact removal by applying source extraction method. This method uses semi-blind source extraction process followed by linear prediction method by considering temporal structures of signal and uses previous information of 'data' for predicting long-term data. Most promising approaches in this field are known as independent component analysis (ICA) [13], "optimal basis sets" (OBSs) [14], adaptive filtering [15], etc. These methods are promising techniques to provide better signal quality and reduced power for BCG signals, but these approaches suffer from signal distortion which results in the signal reduction or distortion of the informative signal for single trial of classification scheme. It shows the better performance if limited trials are provided by considering specific situations. In this type of scenarios, single-trial classification methods provide better performance due to its nature as supervised approach and multivariate capacity which can perform artifact removal for low SNR [16].

During past two decades, various studies have been carried out related to cardiovascular diseases by using BCG signal. These studies show the importance of BCG signal processing approach. Various minor changes occur during BCG signal processing which make it complex and cannot be measured by using these algorithms. In order to address this issue, bed-or-table-based measurement systems were

developed for measuring the reaction forces. However, these schemes are able to provide better and accurate performance during measurement but main challenging issue related to this was implementation cost and requirement of mechanical procedures.

1.1 Issues and Challenges

In this section, we describe the various artifacts which are present in the signal. Artifact signals are not achieved from brain activities, whereas due to acquisition conditions, artifacts are induced in the original signal. Various causes are present which are responsible for artifact in brain signals, such as electrode location, hairy leather, and impedance of electrodes. Causes of artifacts are characterized as three main categories: (1) baseline noise, (2) powerline noise, and (3) occurrences of noise.

A. **Baseline Noise**

This noise causes artifact in the original signal due to poor contact of electrodes which results in low-frequency type artifacts. Another reason of this issue is temperature variation of instruments and amplifiers.

B. **Powerline Noise**

Biological signals are corrupted due to interference of line, wire interference, and other equipment which are used in signal acquisition. These kinds of noises are responsible for spike generation in original signal.

C. **Occurrences of noise**

During the signal acquisition, if above-mentioned noises are not detected and removed then it continues until the signal is acquired. This is called noise occurrences which makes biomedical signal processing more complex. Still there are various issues present in this field of biomedical signal processing which need to be addressed.

In order to address these issues, here in this paper we present a new scheme for BCG signal filtering using independent component analysis-based approach. According to proposed approach, all activities are considered as mixture and spatially stable.

Rest of the manuscript is organized as follows: In Sect. 2, proposed model is discussed, Sect. 3 describes outcomes of proposed model, and finally manuscript is concluded in Sect. 4.

2 Proposed Model

In this section, we describe proposed approach for BCG signal filtering using independent component analysis method. Proposed ICA scheme considers three key components for signal filtering or artifact removal: (i) It is assumed that all activities are mixture and stable for spatial distribution, (ii) propagation delay for source and electrode is considered negligible, and (iii) electrodes are not lesser than sources.

Figure 1 shows the overall working flow of the proposed model for BCG signal filtering using independent component analysis method. Initially, raw 'data' is given input and Preprocessing steps are performed, such as designing the filter, data filtering, and high-pass filtering implementation. By applying preprocessing steps, noise is estimated. On this data, high-pass filtering and ICA are applied which provide filtered output.

2.1 Independent Component Analysis

Independent component analysis approach was first introduced by Jutten and Herault in 1991. In this approach, m mixture in a linear form with m independent components is considered which is given as

$$x_i = d_1 s_1 + d_2 s_2 \ldots + d_m s_m \tag{1}$$

According to ICA model, it is assumed that signal mixture and its components are random variables and these components and variables have zero mean. If zero mean is not achieved then sample mean is subtracted for zero mean modelling. This model is used in this work for BCG signal filtering. Here according to ICA, it is assumed that S signals are recorded simultaneously which are given as

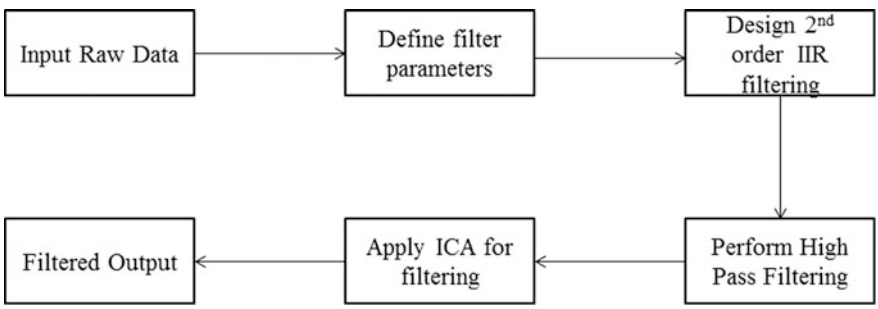

Fig. 1 Overall flow of BCG signal filtering system

$$N(t) = \{n_1(t), n_2(t) \ldots, n_S(t)\} \tag{2}$$

These recorded signals are considered in the form of linear mixture such as $M(M \leq N)$. In this mixture signal of activities, unknown components using ICA are given as

$$I(t) = \{i_1(t), i_2(t) \ldots, i_M(t)\} \tag{3}$$

which includes artifacts and neural activities of the brain

$$S(t) = MI(t) \tag{4}$$

where unknown mixing weight matrix is denoted as M which contains information about signals at each recording.

Once the ICA algorithm process is performed, temporal structure and components are analyzed to extract the artifacts, and responsible components for artifacts are estimated. After estimating the artifact responsible components, its values are fixed to zero which results in a component matrix by considering rejection of artifactual sources. Using this, reconstructed signal can be represented as

$$\widehat{N}(t) = M\widehat{I(t)} \tag{5}$$

$\widehat{N}(t)$ is the artifact removed data.

In this proposed approach, we measure spectral and partial coherence of the input signal's spectrum which provides the measurement of similarity between two signals which are recorded or reconstructed at different stages of signal acquisition.

2.2 Spectral Coherence Computation

In this model, to measure the similarity between input signal and reconstructed signal, spectral coherence is computed for the given signal. This provides normalized cross-spectrum of input signal which can be denoted as

$$C_{a,b}(f) = \frac{F_{a,b}(f)}{\sqrt{F_{a,a}(f)F_{b,b}(f)}} \tag{6}$$

where $F_{a,b}(f) = F_a F_b^*(f)$.

If spectral coherence for the given signal for all frequencies is zero, then it can be concluded that there is no interaction present between two signals; similarly if $\left|C_{a,b}(f)\right| = 1$, then a perfect linear relationship can be estimated between given signals.

2.3 Computation of Partial Spectral Coherence

Another measurement parameter for given signal is computed in terms of partial spectral coherence measurement which is measured by applying inverse computation to cross-spectra for the given signal.

It can be written as

$$PC_{a,b|C}(f) = \frac{\mathcal{G}_{a,b}(f)}{\sqrt{\mathcal{G}_{a,a}(f)\mathcal{G}_{b,b}(f)}} \tag{7}$$

where $\mathcal{G}(f) = F^{-1}(f)$.

3 Results and Discussion

This section provides discussion about simulation study for BCG signal filtering. Proposed approach is implemented using MATLAB 2013b tool.

3.1 Dataset Description

In proposed model, for performance analysis, dataset is obtained from Georgia Institute of Technology Institutional Review Board. This dataset contains 17 users' recordings where ten users are male subjects and seven are female subjects with the age variation of 18–27 years and height variation of 160–180 cm with 60–70 kg variation in weight.

For 'data' acquisition, subjects stand still for 60-s duration on baseline and force plate measurement. After this, each subject was asked to perform stepping for 5 min.

For performance evaluation, we have considered 17 users' recording data. For simulation, sampling frequency, cutoff frequency, and other parameters are considered which are mentioned in Table 1.

According to proposed study, initially data is taken as input in raw signal format which contains artifacts and noises in the signal. Our main aim is to remove artifacts from the signal. In order to do this, raw BCG data is processed through proposed model, where initially, second-order IIR filter is designed and data is filtered for further processing. This data is processed using high-pass filtering method. After achieving high-pass filtered data, mean values of BCG data are removed. On this data, independent component analysis is applied to achieve filtered output using deflation approach which processes signal in one-by-one manner.

Table 2 shows the performance of BCG signal filtering by computing average coherence, minimum coherence, and correlation. These measurements are carried

Table 1 Simulation parameters

Simulation parameter	Considered value
Sampling frequency	256 Hz
Nyquist frequency	Sampling frequency/2
Notch	50 Hz
Cutoff frequency (high-pass filter)	4 Hz
Artifact cleaning tolerance	1.25

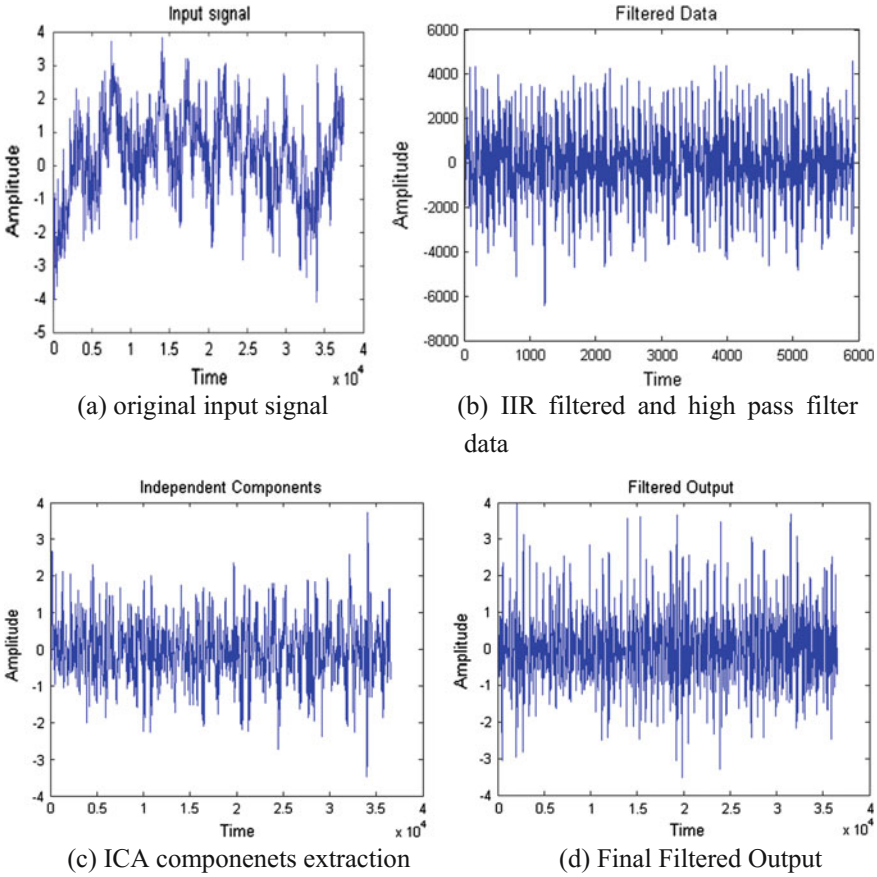

(a) original input signal

(b) IIR filtered and high pass filter data

(c) ICA componenets extraction

(d) Final Filtered Output

Fig. 2 Filtering stages and filtered output

Table 2 Simulation parameters

Input signal	Average of coherence	Minimum of coherence	Correlation
Signal 1 (1008)	0.39	0.15	0.5060
Signal 2 (1004)	0.5389	0.18	0.6668
Signal 3 (1003)	0.41	0.1520	0.4947

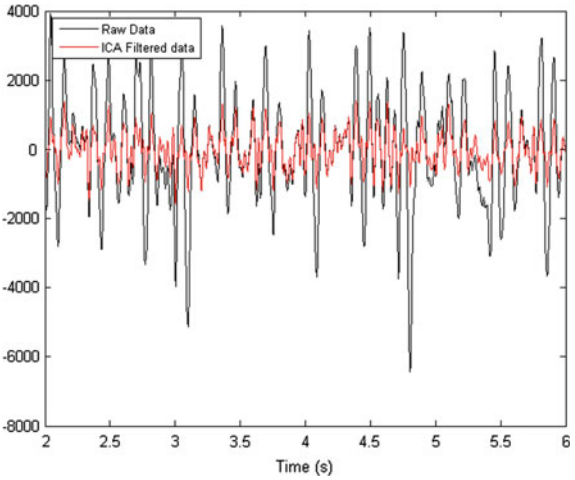

Fig. 3 Raw BCG data and filtered BCG data

out by considering input noisy signal and output artifact removal signal. Coherence shows the similarity between two signals, and here we achieve lesser coherence values between two signals which show that the final output signal is artifact removal signal corresponding to average coherence. Similarly, another parameter computed is correlation which also has same characteristics as coherence.

In Fig. 2, we show filtering steps of BCG signal using proposed approach. Figure 2a is the original signal or raw signal which is takes as input for filtering process. Further, IIR is applied on this data followed by ICA algorithm.

ICA algorithm provides independent components which are used for signal filtering, and Fig. 2d shows final filtered output.

A comparative graphical representation is given in Fig. 3 by considering raw input 'data' and filtered output data.

4 Conclusion

In this work, our main aim is to propose an efficient technique for artifact removal from the biomedical signal. To address this issue, here we propose independent component analysis-based approach for signal filtering. Proposed approach is considered as threefold technique where all the activity signals are considered as the mixture model which has constant or continuous spatial distribution, second, it is assumed that the propagation delay between electrodes and source is negligible, and finally, it is also assumed that electrodes are not lesser than number of sources. Raw 'data is taken as input which is processed through Preprocessing stage of proposed mode. In preprocessing stage, initially second-order IIR filter is designed and later high-pass filtering approach is applied which gives high-pass filtered data. Using this 'data', independent component approach is performed which provides

independent components of each signal, suing these components responsible source is detected and removed which results in signal filtering. Outcome of study shows better filtering performance for various test scenarios.

References

1. Mahadevan, A., Acharya, S., Sheffer, D.B., Mugler, D.H.: Ballistocardiogram artifact removal in EEG-fMRI signals using discrete Hermite transforms. IEEE J. Sel. Top. Signal Process. **2** (6), 839–853 (2008)
2. He, B., Baxter, B., Edelman, B.J., Cline, C.C., Ye, W.W.: Noninvasive brain-computer interfaces based on sensorimotor rhythms. Proc. IEEE **103**(6), 907–925 (2015)
3. Menon, V., Crottaz-Herbette, S.: Combined EEG and fMRI studies of human brain function. Int. Rev. Neurobiol. **66**, 291–320 (2005)
4. Hamaneh, M.B., Chitravas, N., Kaiboriboon, K., Lhatoo, S.D., Loparo, K.A.: Automated removal of EKG artifact from EEG data using independent component analysis and continuous wavelet transformation. IEEE Trans. Biomed. Eng. **61**(6), 1634–1641 (2014)
5. Kidmose, P., Looney, D., Ungstrup, M., Rank, M.L., Mandic, D.P.: A study of evoked potentials from ear-EEG. IEEE Trans. Biomed. Eng. **60**(10), 2824–2830 (2013)
6. Babadi, B., McKinney, S.M., Tarokh, V., Ellenbogen, J.M.: DiBa: a data-driven bayesian algorithm for sleep spindle detection. IEEE Trans. Biomed. Eng. **59**(2), 483–493 (2012)
7. Moco, A., Stuijk, S., de Haan, G.: Ballistocardiographic artifacts in PPG imaging. IEEE Trans. Biomed. Eng. (99), 1–1 (2015)
8. Acharjee, P.P., Phlypo, R., Wu, L., Calhoun, V.D., Adalı, T.: Independent vector analysis for gradient artifact removal in concurrent EEG-fMRI data. IEEE Trans. Biomed. Eng. **62**(7), 1750–1758 (2015)
9. Allen, P.J., Josephs, O., Turner, R.: A method for removing imaging artifact from continuous EEG recorded during functional MRI. NeuroImage **12**, 230–239 (2000)
10. Anami, K., Mori, T., Tanaka, F., Kawagoe, Y., Okamoto, J., Yarita, M., Ohnishi, T., Yumoto, M., Matsuda, H., Saitoh, O.: Stepping stone sampling for retrieving artifact-free electroencephalogram during functional magnetic resonance imaging. NeuroImage **19**, 281–295 (2003)
11. Hoffmann, A., Jäger, L., Werhahn, K.J., Jaschke, M., Noachtar, S., Reiser, M.: Electroencephalography during functional echo-planar imaging: detection of epileptic spikes using post-processing methods. Magn. Reson. Med. **44**, 791–798 (2000)
12. Ferdowsi, S., Sanei, S., Abolghasemi, V., Nottage, J., O'Daly, O.: Removing ballistocardiogram artifact from EEG Using short- and long-term linear predictor. IEEE Trans. Biomed. Eng. **60**(7), 1900–1911 (2013)
13. Srivastava, G., Crottaz-Herbette, S., Lau, K.M., Glover, G.H., Menon, V.: ICA-based procedures for removing ballistocardiogram artifacts from EEG data acquired in the MRI scanner. Neuroimage **24**(1), 50–60 (2005)
14. Niazy, R.K., Beckmann, C.F., Iannetti, G.D., Brady, J., Smith, S.M.: Removal of FMRI environment artifacts from EEG data using optimal basis sets. Neuroimage **28**(3), 720–737 (2005)
15. Bonmassar, G., Purdon, P., Jaaskelainen, I.P., Chiappa, K., Solo, V., Belliveau, J., Brown, E.N.: Motion and ballistocardiogram artifact removal for interleaved recording of EEG and EPs during MRI. Neuroimage **16**(4), 1127–1141 (2002)
16. Tomioka, R., Müller, K.R.: A regularized discriminative framework for EEG analysis with application to brain–computer interface. NeuroImage **49**(1), 415–432 (2010)

Sleep Stage Classification Using S-Transform-Based Spectral Energy Feature

Ankita Mishra and Madhusmita Sahoo

Abstract In this paper, we have presented a novel approach to extract the features of EEG signal from its S-transform, in order to classify human sleep disorder accurately. The estimation of sleep disorder plays an important role in identifying sleep stages. Correct predictions can aid doctors in the diagnosis and further treatment. In this paper, features are extracted in both time and time-frequency domain and classified using a various machine learning algorithm. The recorded EEG datasets are divided into delta, theta, alpha, beta, and gamma sub-bands, and a set of descriptive statistical features are attained from all the sub-bands in the time domain. In the time-frequency domain, spectral energy features are extracted from the S-transform. Finally, classification is done using three different classifiers such as ANN, KNN, and SVM. The extensive numerical simulation results illustrate that the proposed method is providing more classification accuracy.

Keywords Sub-bands of EEG · SVM · KNN · ANN · S-transform
Spectral energy features

1 Introduction

One major activity of the human brain is sleep. Any normal human being spends around one-third of the life in sleeping. According to Rechtschaffen and Kales (R&K), sleep is divided into three different stages: awake, rapid eye movement (REM) sleep and Non-REM (NREM). This NREM sleep is separated into four stages such as stage 1, 2, 3, and 4 [1]. So a total of five stages is encountered by sleep. As the stage 1 and awake has almost same properties, this paper merges these two stages as one. The sleep disorders can be detected by analyzing each stage of

Ankita Mishra (✉) · Madhusmita Sahoo
I.T.E.R., S.O.A. University, Bhubaneswar, India
e-mail: mishra.sonu.ankita@gmail.com

Madhusmita Sahoo
e-mail: madhusmitasahoo@soauniversity.ac.in

A. Konkani et al. (eds.), *Advances in Systems, Control and Automation*,
Lecture Notes in Electrical Engineering 442, https://doi.org/10.1007/978-981-10-4762-6_25

sleep. Thus, the necessity of separating human sleep stages is the crucial part for detection and medication of sleep disorders such as insomnia, sleep apnea, and narcolepsy. As EEG signals are nonstationary in nature, their statistical properties change with time, and hence, it is time averaged. So the estimations based on the time domain features are inadequate to track changes, for examining nonstationary and multicomponent signals. So time-frequency-based techniques are used which surpass traditional techniques based on either time or frequency analysis. The main aim of this paper is to extract essential features, beneficial to improve the classification accuracy. The paper has been assembled as follows: in Sect. 2, a brief discussion on filtering and decomposition of EEG sleep signal into different stages. Section 3 deals with basics of different machine learning algorithms. Section 4 deals with details regarding analysis and classification of the signal in time domain. Section 5 deals with a brief discussion on S-transform. Section 6 deals with the proposed scheme. The simulation results and discussion have been presented in Sect. 6, and this paper concludes in Sect. 7 with a direction toward the future work.

2 Decomposition of EEG Signal

The EEG dataset is downloaded directly through the Internet from the following link http://www.physionet.org/physiobank/database/sleep-edf for our study [1]. Out of 30 recorded signals, 12 are healthy and 18 are non-healthy subjects. Each EEG signal was actual 100,000 samples per second in the raw state. In our work, we have taken 6000 samples. There are two subsets of dataset, namely SC$*$ and ST$*$. SC*s are taken as normal signals, whereas ST*s are taken as abnormal signals. The EEG data were divided into epochs of 30 s and a total of 4700 epochs (350, 310, 2220, 510, 480, and 830 epochs from awake, $S1$, $S2$, $S3$, $S4$, and REM sleep stages, respectively) selection based on Fpz-Cz channel. Typical EEG signals (one from each sleep stage) are shown in Figs. 1 and 2 simulated on MATLAB R2010a.

The five frequency bands of each stage named as δ, θ, α, β, and γ are extracted and filtered using IIR Butterworth band-pass filters. The bands were filtered by taking Butterworth band-pass filters in the order of ten, eleven, eight, and two for alpha, beta, theta, delta, and gamma.

3 Machine Learning Algorithms

Machine learning algorithms normally learn from the training dataset, and once learning is completed it performs co-relational tasks on test data. An artificial neural network (ANN) is a learning algorithm. It is a group of interconnected neurons where a weight is associated with each connection of same or different value. In the process of classification, the weights are modified for prediction of a correctly labeled class of the input layer. In this work, we have taken 300 hidden layers and

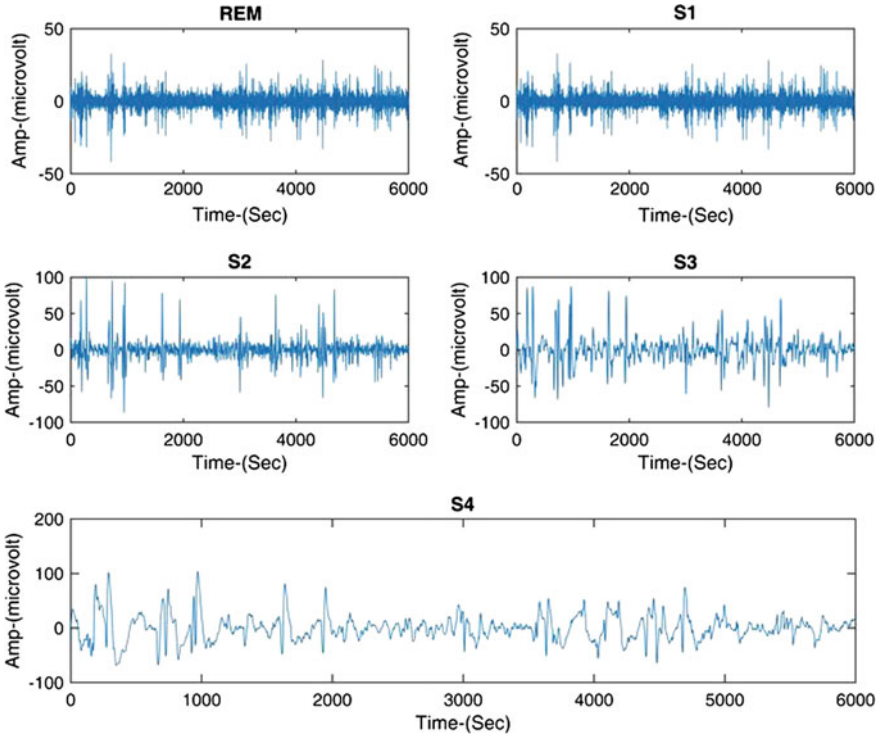

Fig. 1 Sleep stages of normal signal

six output layers. K-nearest-neighbor (KNN) algorithm normally compares a set of training samples with unknown test samples that are stored in an n-dimensional space to measure the closeness of samples. In our work, 150 hidden layers are taken and the Euclidean distance is assigned as 1.

The support vector machine (SVM) [2] is a binary classifier, used to locate a space known as separating hyperplane between the two classes. The nonlinear data can be classified effectively using SVM as compared to any other machine learning algorithm. Accuracy, sensitivity, and specificity are used as evaluation criterions for computing the effectiveness of the algorithm.

$$\text{Sensitivity(Se)} = \left(\frac{\text{TP}}{\text{TP}+\text{FN}}\right) * 100 \tag{1}$$

$$\text{Specificity(Sp)} = \left(\frac{\text{TN}}{\text{TN}+\text{FP}}\right) * 100 \tag{2}$$

$$\text{Average Accuracy} = \left(\frac{\text{TP}+\text{TN}}{\text{FP}+\text{TP}+\text{TN}+\text{FN}}\right) * 100 \tag{3}$$

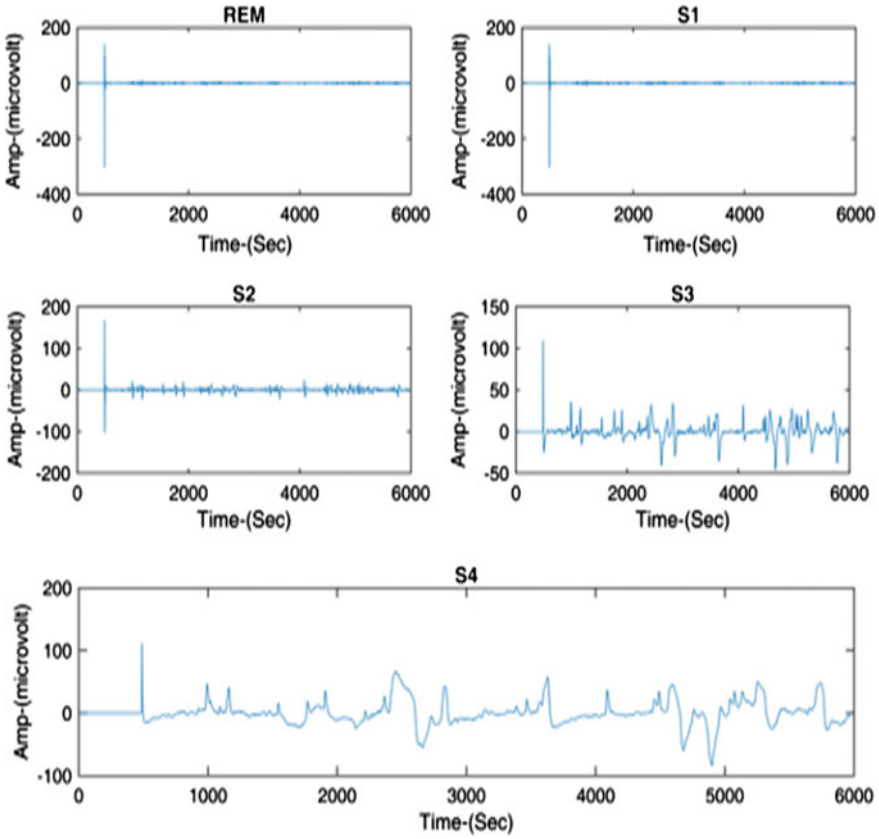

Fig. 2 Sleep stages of Apneic signal

Here, TP, TN, FP, and FN are true positives, true negatives, false positives, and false negatives, respectively.

4 Analysis and Classification in Time Domain

For analyzing the EEG signal in time domain, basic statistical features such as energy, entropy, standard deviation, skewness, and kurtosis are taken into account.

(a) Energy: The signal's power at any period of time is represented by its energy, which is given by:

$$E = \sum_{n=1}^{N} [X_i(n)]^2 \tag{4}$$

Here, N is the total number of samples, n is the number of given sample, and X_i is the value of the sample in each epoch.

(b) Entropy: Uncertain outcomes of signals are given by entropy which is presented as:

$$EN = -\sum_{j=1}^{N} \left[p(X_j) \log_{10}(P(X_j)) \right] \tag{5}$$

(c) Standard deviation: It calculates the distribution of a set of data, which is given by:

$$\text{STD} = \sqrt{\frac{1}{N}\left[\left(\sum_{i=1}^{N} X_i - \frac{1}{N}\sum_{i=1}^{N} X_i\right)\right]^2} \tag{6}$$

(d) Skewness: It is the third moment of distribution of data.

(e) Kurtosis: It is the measure of the 'tailedness' of the probability distribution of a real-valued random variable.

The above analytical parameters are computed for all the stages of EEG signals. Here, three sets of training and testing datasets such as 80–20, 70–30, and 50–50% which include normal and abnormal subject's features are taken for classification.

The simulated results for three different test percentages are presented in Tables 1, 2, and 3. The accuracy is better in SVM, and if more data are used for training, then also accuracy improves further.

Table 1 Classification using ANN

Test %		REM	*S*1	*S*2	*S*3	*S*4	Avg. Acc.
30	S_E	65	66	66	78	70	62
	S_P	72	54	57	70	62	
50	S_E	78	81	80	73	71	58
	S_P	72	65	78	65	70	
20	S_E	75	87	75	75	79	69
	S_P	78	79	72	78	87	

Table 2 Classification using KNN

Test %		REM	*S*1	*S*2	*S*3	*S*4	Avg. Acc.
30	S_E	66	68.5	78	72	55	66
	S_P	69	58	72	60	67	
50	S_E	80	61	55	70	57	65
	S_P	72	71.8	66	65	46	
20	S_E	70	85	57	68	68	68
	S_P	85	100	72	73	67	

Table 3 Classification using SVM

Test %		REM	*S*1	*S*2	*S*3	*S*4	Avg. Acc.
30	S_E	100	100	100	50	100	80
	S_P	82	75	100	25	88	
50	S_E	100	100	75	100	75	78
	S_P	80	80	60	40	86	
20	S_E	100	100	83	66	83	86
	S_P	88	87	87	75	85	

5 Time-Frequency Analysis

The time-frequency depiction of the signal is used to represent the signal in both the time and frequency domains simultaneously, so that we can track variation of frequency components with respect to time [3]. This can be achieved either using STFT or S-transform.

(a) STFT

At each instant of time to represent the spectral or frequency content of the signal, short-time Fourier transform analysis is used. Basically, in STFT, the considered wave form is sliced into a number of short portions/segments and analysis is carried out using Fourier transform on each of the segments. The time-frequency resolution in STFT is poor, because of fixed width of the window [3].

(b) S-transform

Stockwell developed a time-frequency representation which merges the best features of STFT and WT. It can be described as a frequency-dependent STFT or a phase-corrected wavelet transform [4].

Let us say a time series $H(t)$ is given, the local spectrum at time $t = \gamma$ can be evaluated by multiplying $h(t)$ with a Gaussian located at $t = \gamma$. Hence, the 'Stockwell transform' is given by:

$$S(f,\gamma,\delta) = \int h(t)g(t-\gamma)e^{-j2\pi ft}\,dt \tag{7}$$

It can be presented as:

$$P_1(t,f) = h(t)e^{-j2\pi ft} \tag{8}$$

$$S(f,t,\delta) = \int_{-\infty}^{\infty} P_1(t,f)g(t-\delta)dt = P_{1(t,f)} \times g(t-\delta) \tag{9}$$

Steps for determining S-transform:

1. Determine $H(\alpha) = \delta(t)$.
2. Calculate the value of $(H(\alpha) - \delta(\alpha - f))$ where $H(\alpha)$ translated to f.
3. Multiply $G(\alpha, \delta)$ and shift it to $H(\alpha)$.
4. Take the inverse Fourier transform.

Here, the dilation parameter δ is a function of frequency f, $\delta = 1/f$. Thus, the Gaussian window

$$G(t,\delta) = \left(1/\sqrt{2\pi\delta}\right)e^{\frac{t^2}{2\delta^2}} \tag{10}$$

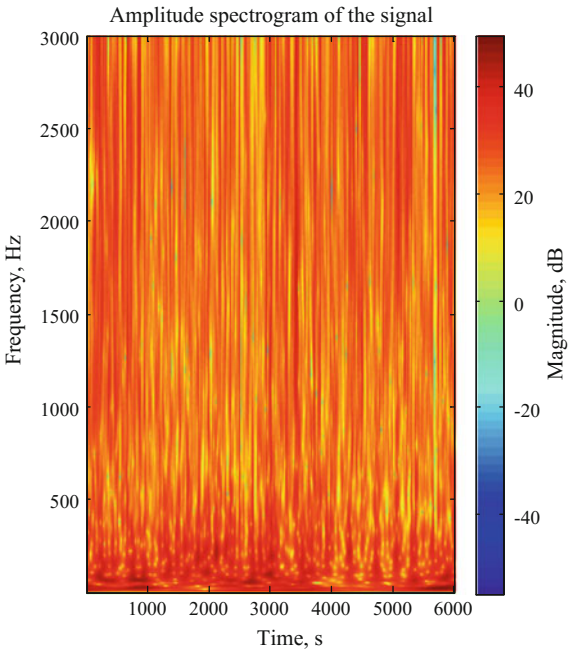

Fig. 3 ST-based normal EEG signal

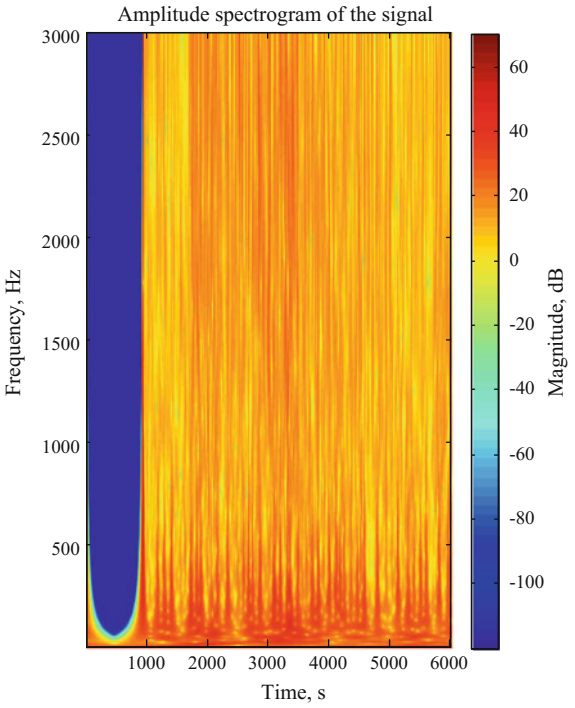

Fig. 4 ST-based sleep apnea EEG signal

With the $\delta = 1/f$ becomes

$$G(t,\delta) = \left(\frac{f}{\sqrt{2\pi\delta}}\right) e^{\frac{-t^2}{2}} \tag{11}$$

Here, the oscillatory exp. Kernel remains stationary in nature, while the time localizing Gaussian is translated. The S-transform independently localizes the real and the imaginary components of the phase and amplitude spectrum [5, 6] (Figs. 3 and 4).

6 Proposed Scheme

In our proposed scheme instead of taking the generalized features, we have taken some special features. These features are computed from its time-frequency matrix. First, the S-transform of each stage is computed, and then energy matrix was extracted. Energy matrix (E) was calculated using the following expression:

$$[E]_{m*n} = \left|[S]_{m*n}\right|^2 \tag{12}$$

$$\left[E_{1*N}^{\max}\right] = \max[S] \tag{13}$$

where M and N are the numbers of frequency and time indices, and S is the S-transform. If X is a given set of the data point or sampled value such as $X = [X_1 \ldots X_N]$, then the statistical parameter was calculated from this energy matrix [4]. Once the features are extracted, some of the data are used for training and others are used for testing purpose using different learning algorithm [7]. Earlier, the same approach has chosen the features were extracted from STFT matrix. From Tables 4, 5, 6, 7, 8, and 9, we can visualize that the S-transform-based approach provides the better result as compared to other approaches using any machine learning algorithm (Figs. 5 and 6).

Table 4 STFT-based classification using ANN

Test %		REM	*S*1	*S*2	*S*3	*S*4	Avg. Acc.
30	S_E	57	69	56	63	64	69
	S_P	60	64	70	62	53	
50	S_E	71	67	62	58	57	68
	S_P	80	72	68	65	47	
20	S_E	82	80	66	68	61	66
	S_P	78	75	52	74	59	

Table 5 STFT-based classification using KNN

Test %		REM	*S*1	*S*2	*S*3	*S*4	Avg. Acc.
30	S_E	60	53	55	45	60	69.6
	S_P	65	67	70	54	66	
50	S_E	66	60	80	54	63	70
	S_P	77	62	62	65	70	
20	S_E	59	66	69	69	45	67.8
	S_P	70	71	80	72	58	

Table 6 STFT-based classification using SVM

Test %		REM	*S*1	*S*2	*S*3	*S*4	Avg. Acc.
30	S_E	65	66	66	78	70	78
	S_P	72	54	57	70	62	
50	S_E	78	81	80	73	71	82
	S_P	72	65	78	65	70	
20	S_E	90	87	75	75	79	81
	S_P	78	79	72	78	87	

Table 7 ST-based classification using ANN

Test %		REM	*S*1	*S*2	*S*3	*S*4	Avg. Acc.
30	S_E	66	68.5	78	72	55	68
	S_P	69	58	72	60	67	
50	S_E	80	61	55	70	57	68
	S_P	72	71.8	66	65	46	
20	S_E	70	85	57	68	68	72
	S_P	85	100	72	73	67	

Table 8 ST-based classification using KNN

Test %		REM	*S*1	*S*2	*S*3	*S*4	Avg. Acc.
30	S_E	75	79	88	85	79	78
	S_P	60	63	88	71.3	82	
50	S_E	92	85	57	35	59	82
	S_P	98	56	48	69	72	
20	S_E	65	64	71	81	77	81.7
	S_P	76	75	62	85	82	

Table 9 ST-based classification using SVM

Test %		REM	*S*1	*S*2	*S*3	*S*4	Avg. Acc.
30	S_E	67	78	81	81	77	93
	S_P	72	82	75	78	83	
50	S_E	83	65	80	84	43	86
	S_P	78	63	82	74	58	
20	S_E	100	78	63	76	75	88
	S_P	92	72	79	84	84	

Here, we have presented each classifier with different test percentages for time and time-frequency analysis in a MATLAB R2010A figure. The bar graphs depict different accuracy for changing test percentages (30, 50, and 20%) for different classifiers. Blue color indicates ANN classifier, green indicates KNN classifier, and the red color is for SVM classifier (Fig. 7).

It can be observed the SVM classifier in each case (time domain, STFT&S-transform analysis) gives better accuracy compared to other classifiers. SVM with the combination of S-transform analysis gives more accurate.

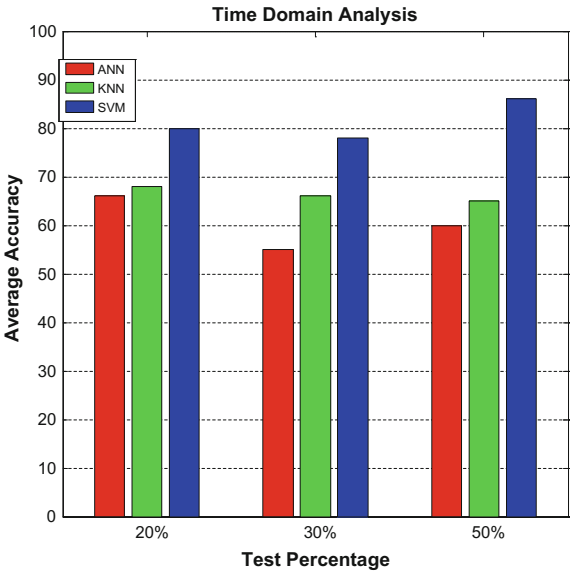

Fig. 5 Time domain analysis for three classifiers

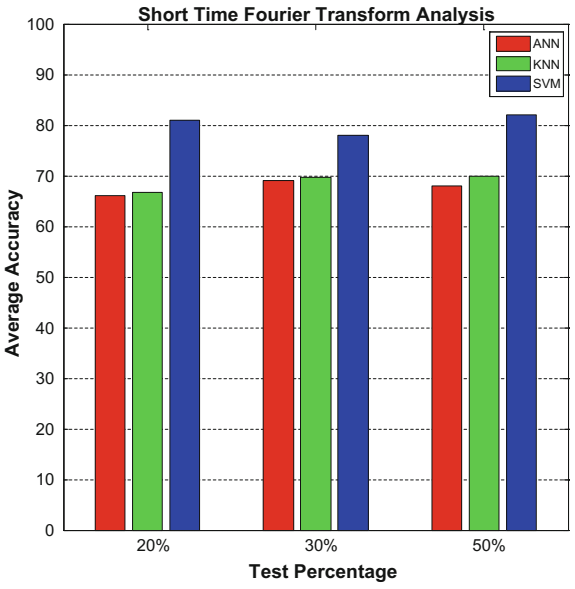

Fig. 6 STFT analysis for three classifiers

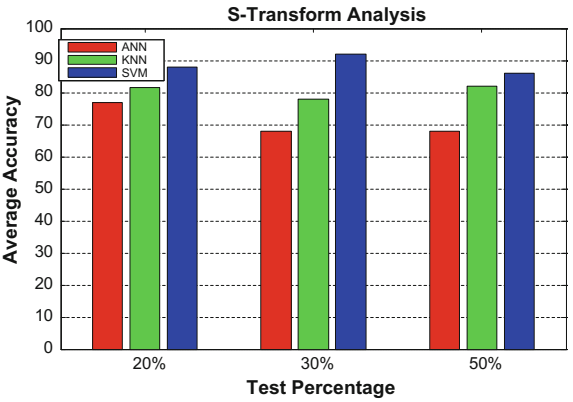

Fig. 7 S-transform analysis for three classifiers

7 Conclusion

In this paper, statistical features and spectral features are calculated from EEG signal to analyze sleep disorder by verifying each sleep stages. In our proposed method, we have taken the spectral energy features for classification. From the extensive simulation, it is clear that our approach with SVM gives the highest accuracy that is 93% as compared to any other method. In future, the result can be improved further if modified S-transform will be considered.

References

1. Physionet, Physiobank, Atm. http://www.physionet.org/physiobank/database/sleep-edfx
2. Patkar, V.P., Joshi, P., Das, L.: Evaluation of PSE, STFT and probability coefficients for classifying two directions from EEG using radial basis function. IEEE J. **6**(15), (2015) (978-1-4799)
3. Jacob, N., Joseph, L.A.: Classification of ECG beats using cross wavelet transform and support vector machines. In: Proceedings of the IEEE Recent Advances in Intelligent Computational Systems (RAICS) (2015)
4. Krishnanand, K.R., Balasubramanyam, P.V., Swain, S.K., Dash, P.K.: Life senior member: S-Transform based spectral energy feature space for fault location approximation. IEEE J. (2010)
5. Ai, L., Nan, L., hua Pu, L.: Application of S-transform in EEG analysis engineering. In: 3rd International Conference on Advanced Computer Theory and Engineering (ICACTE), pp. 669–672 (2010)
6. Mustafal, M., Taib, M.N., Lias, S., Murat, Z.H., Sulatman, N.: EEG spectrogram classification employing ANN for IQ application. IEEE (2013). ISBN 978-1-4678-5618-3
7. Ambulkar, N.K., Sharma, S.N.: Detection of epileptic seizure in eeg signals using window width optimized s-transform and artificial neural networks. In: IEEE Bombay Section Symposium (2015)

MMSE-Based Lattice-Reduction-Aided Equalization for MIMO System in Nakagami-m Channel

Samarendra Nath Sur, Susmita Prasad, Rabindranath Bera and Bansibadan Maji

Abstract Multiple input and multiple output (MIMO) system is proven to be the key technology for future generation communication system. Latest trend in this field is massive (or large scale) MIMO system. But it comes with additional signal processing complexity burden. Also from the point of view of signal restoration at the receiver side, equalizer plays an important role. Therefore, design low-complex receiver is utmost important. This paper deals with the performance analysis of low-complex loop-reduction-based Lenstra-Lenstra-Lovasz (LLL) algorithm. The performance has been analyzed based on the achievable capacity and bit error rate (BER). As also its performance has been evaluated keeping linear receiver such as zero forcing (ZF) and minimum mean-squared error (MMSE) as references.

Keywords MIMO · ZF · MMSE · LLL · BER · Capacity

1 Introduction

In MIMO system, linear receivers such as zero forcing (ZF) or the minimum mean square error (MMSE) criterion, and successive interference cancellation (SIC) are commonly used detection techniques [1]. But, from the point of view of system

S.N. Sur (✉) · S. Prasad · R. Bera
Department of Electronics and Communication Engineering, Sikkim Manipal Institute of Technology, Sikkim Manipal University, Majitar 737136, Sikkim, India
e-mail: samar.sur@gmail.com

S. Prasad
e-mail: susmitaprasad1701@gmail.com

R. Bera
e-mail: rbera50@gmail.com

B. Maji
Department of Electronics and Communication Engineering,
National Institute of Technology, Durgapur, West Bengal, India
e-mail: bmajiecenit@yahoo.com

A. Konkani et al. (eds.), *Advances in Systems, Control and Automation*,
Lecture Notes in Electrical Engineering 442, https://doi.org/10.1007/978-981-10-4762-6_26

performance, all are inferior to the maximum likelihood (ML) detection [2]. But because of the implementation complexity of the ML detector is not used in piratical scenario [3]. In order to reduce the complexity, QR decomposition algorithm is proposed. From the point of view of recent development of MIMO, low-complex receiver system is required [4].

To support the growing demand of high data rate seeking application, large MIMO or massive MIMO is the key technology. Hardware realization of large MIMO is a challenging task due to enormous increase in the complexity of MIMO receiver. Lattice-reduction-aided detection is a favorable approach [5–9], in the context of large MIMO systems. This algorithm utilizes the near orthogonal matrix to improve the BER performance of the system. The widely used lattice-reduction algorithm is called the LLL algorithm [10, 11].

The LLL algorithm-based improved MIMO detectors are utilized and with less complexity in comparison to linear equalizers (LE). However, the LLL algorithm consists of many checking operations, which increase the computations time [12]. Therefore, to encounter this problem a look-ahead check technique has been proposed to avoid the unnecessary complexity [10]. This technique is known as loop-reduction LLL algorithm (LRLLL). This algorithm can be applied to real- and complex-value LLL algorithm [12, 13]. However, in this paper, complex-valued LLL algorithm has been used.

This paper includes the performance study of LRLLL-aided MIMO in presence of Nakagami-m channel. Aim of this paper is to analyze performance improvement of the LRLLL-aided ZF and LRLLL-aided MMSE detectors.

The remaining paper is presented as follows: Section 2 represents mathematical formulation MIMO system. While Sect. 3 represents the loop-reduction-aided LLL algorithm. Section 4 represents the comparative results to evaluate the performance. Sect. 4 provides the conclusion remarks.

2 System Description

We consider MIMO system with N_T transmit and N_R receive antennas. The received signal y can be described by:

$$y = Hx + n \tag{1}$$

where the transmit symbols vector is represented by x, and n is the $N_R \times 1$ additive white Gaussian noise vector. The vector H is a $N_R \times N_T$ complex matrix, representing the channels for the wireless transmission. Here, quadrature phase shift keying (QPSK) modulation is used. As a wireless channel, Nakagami-m channel model is considered.

The pdf of the instantaneous SNR γ for Nakagami-m channel is given by [14]

$$P_{\gamma}(\gamma) = \frac{1}{\Gamma(m)} \left(\frac{m}{\bar{\gamma}}\right)^{m} \gamma^{m-1} \exp\left(\frac{-m\gamma}{\bar{\gamma}}\right), \quad \gamma \geq 0 \tag{2}$$

Typically, H is QR decomposed into two parts as $H = QR$, where Q and R denote unitary and upper triangular matrix of dimension $N_R \times N_T$, respectively.

At the receiver, equalizers are used to estimate the transmitted symbols $\hat{x}$. In case of a zero forcing (ZF) [15], the estimated symbols may be represented by

$$\hat{x} = (\mathcal{H}^T \mathcal{H})^{-1} \mathcal{H}^T y \tag{7}$$

And on the other hand for MMSE [15] receiver, the estimated symbols may be represented by:

$$\hat{x} = P_{\mathrm{d}} (P_{\mathrm{d}} \mathcal{H}^H \mathcal{H} + \sigma_{\mathrm{n}}^2 I)^{-1} \mathcal{H}^H \overline{\mathcal{Y}}$$

where P_{d} is the transmitted data power, and σ_{n}^2 is the noise power at the receiver.

As stated in introduction section, lattice-reduction-aided receiver is more efficient in comparison to linear receiver. Aim of the lattice-reduction techniques is to make the channel matrix H more orthogonal in nature. And this leads to better BER performance. This technique first operated on H to produce reduced channel matrix $\widetilde{H} = HT$. The matrix, T, is unimodular. The mathematical model then can be rewritten as:

$$y = HT\left(T^{-1}x\right) + n = \widetilde{H}z + n$$

Then, the next process is to estimate z with the help of linear receiver such as ZF and MMSE.

3 Results

Figures 1 and 2 represent the comparison of the performances of LRLLL-concatenated ZF/MMSE receiver with conventional ZF and MMSE receiver with the variation in Nakagami fading parameter m and correlation coefficient. As in Fig. 1, with increase in m value the BER performance of the system gets better. At the same time, as in Fig. 2, increase in correlation coefficient degrades the system performance. As represented in Fig. 1, for $m = 5.0$, the required SNR to achieve a BER of 10^{-2} for all the systems is 25 dB (ZF), 21 dB (MMSE), 15 dB (LRLLL-ZF), and 14 dB (LRLLL-MMSE). Therefore, it is clear that there is significant amount of SNR improvement in case of LRLLL-aided system.

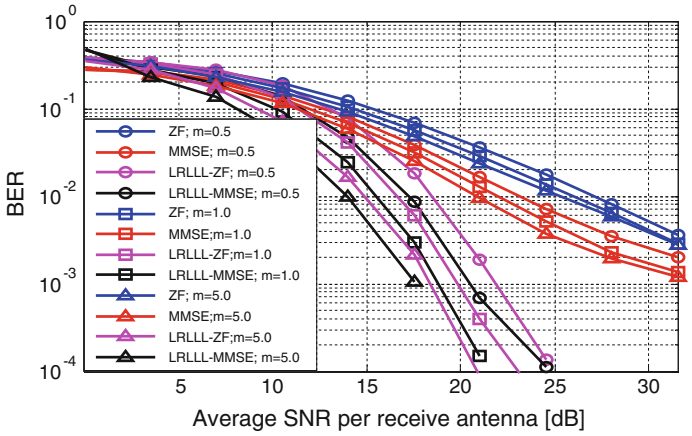

Fig. 1 SNR versus BER curves

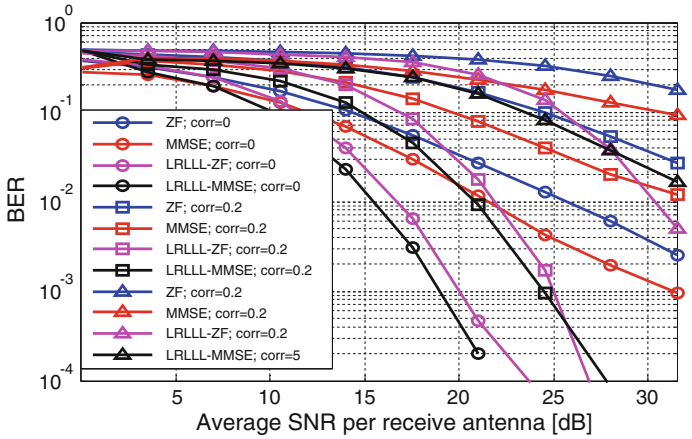

Fig. 2 SNR versus BER curves

Figure 3 shows a comparison between MMSE and LRLLL-MMSE receiver with the change in correlation coefficient. For example, for uncorrelated channel, to have BER of 10^{-3}, the minimum required SNRs are 33 dB (MMSE) and 19 dB (LRLLL-MMSE). Therefore, there is a SNR improvement of 14 dB.

And also out of above said three figures, one can conclude that LRLLL-MMSE is the best receiver and LRLLL-aided receiver significantly improves the system performance.

Figure 4 shows the improvement in channel capacity due to the LRLLL-aided receiver. It also shows that as we increase the *m* value the channel capacity is also

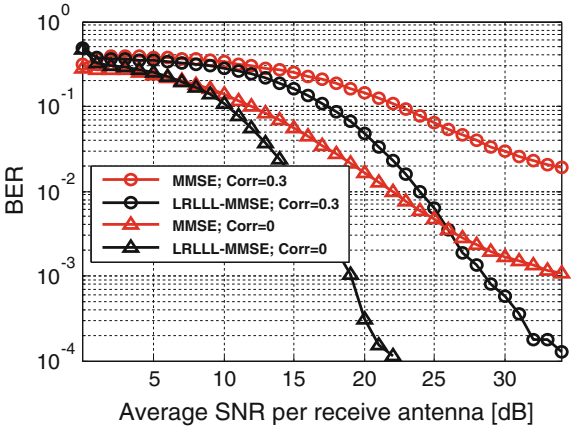

Fig. 3 SNR versus BER curves

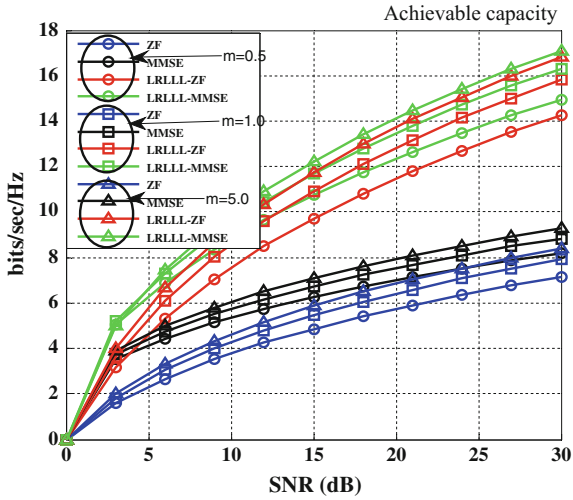

Fig. 4 Achievable capacity variation with SNR

increased. For m = 1 and SNR = 15, the achievable capacities are 5.4 bits/s/Hz (ZF), 6.7 bits/s/Hz (MMSE), 10.9 bits/s/Hz (LRLLL-ZF), and 11.7 bits/s/Hz (LRLLL-MMSE) for all receivers system. Therefore, impact of LRLLL algorithm on the channel capacity is also significant.

4 Conclusion

With the growing demand in high-quality and high secure communication system, the requirement of high end signal processing technique is become more and more inhabitable. But that leads to complex design of system. Therefore, design of

low-complex receiver is become utmost important. This paper represents the performance analysis of lattice-reduction-aided MIMO receivers. From the simulated results, it can be concluded that lattice-aided receiver systems are much more suitable than the conventional linear receiver (ZF and MMSE). Out of all the receiver systems, LRLLL-MMSE receiver performs best under severe channel condition.

References

1. Wolniansky, P.W., Foschini, G.J., Golden, G.D., Valenzuela, R.A.: V-BLAST: an architecture for realizing very high data rates over the rich-scattering wireless channel. In: Proceedings of International Symposium on Signals, Systems, and Electronics (ISSSE), Pisa, Italy (1998)
2. Fincke, U., Pohst, M.: Improved methods for calculating vectors of short length in a lattice, including a complexity analysis. Math. Compt. **44**, 463–471 (1985)
3. Rahman, M., Rohani, E., Xu, J., Choi, G.S.: An improved soft decision based MIMO detection using lattice reduction. Int. J. Comput. Commun. Eng. **3**(4), 264–268 (2014)
4. Ahn, J.-K., Yu, S.-J., Lee, E.-Y., Song, H.-K.: An improved lattice reduction aided detection scheme for MIMO-OFDM system. World Acad. Sci. Eng. Technol. **5**(11), 856–859 (2011)
5. Berenguer, I., Adeane, J., Wassell, I.J., Wang, X.: Lattice-reduction aided receiver for MIMO-OFDM in spatial multiplexing systems. In: Proceedings of IEEE GLOBECOM (2005)
6. Gan, Y.H., Mow, H.W.: Complex lattice reduction algorithm for low complexity MIMO detection. Proc. IEEE PIMRC **2**, 1516–1521 (2004)
7. Wübben, D., Seethaler, D., Jaldén, J., Matz, G.: Lattice reduction. IEEE Signal Process. Mag. **28**(3), 70–91 (2011)
8. Jalden, J., Elia, P.: DMT optimality of LR-aided linear decoders fora general class of channels, lattice designs, and system models. IEEE Trans. Inform. Theory **56**(10), 4765–4780 (2010)
9. Singh, A.K., Elia, P., Jalden, J.: Achieving a vanishing SNR gap to exact lattice decoding at a sub-exponential complexity. IEEE Trans. Inform. Theory **58**(6), 3692–3707 (2012)
10. Lenstra, A.K., Lenstra, H.W., Lovasz, L.: Factoring polynomials with rational coefficients. Math. Ann. **261**(4), 515–534 (1982)
11. Singhal, K.A., Dutta, T., Chockalingam, A.: Lattice reduction aided detection in large-MIMO systems. IEEE 14th Workshop on Signal Processing Advances in Wireless Communications (SPAWC), pp. 589–593 (2013)
12. Liao, C.-F., Chai, L.-W., Huang, Y.-H.: Loop-reduction LLL algorithm and architecture for lattice-reduction-aided MIMO detection. J. Electr. Comput. Eng. **2012**, 1–8 (2012)
13. Gan, Y.H., Ling, C., Mow, W.H.: Complex lattice reduction algorithm for low-complexity full-diversity MIMO detection. IEEE Trans. Signal Process. **57**(7), 2701–2710 (2009)
14. Shin, H., Lee, J.H.: On the error probability of binary and M-ary signals in Nakagami-m fading channels. IEEE Trans. Commun. **52**(4), 536–539 (2004)
15. Jiang, Y., Mahesh, K.V., Li, J.: Performance analysis of ZF and MMSE equalizers for MIMO systems: an in-depth study of the high SNR regime. IEEE Trans. Inf. Theory **57**(4), 2008–2026 (2011)

Fundamental Concepts of Neural Networks and Deep Learning of Different Techniques to Classify the Handwritten Digits

Ambikapathy and Anant Vikram Singh

Abstract This paper discusses the various fundamental techniques and algorithms which are used in neural networks to classify the handwritten digits for the smarter applications in this twenty-first century. This paper gives the deep learning of different tools which is used to classify handwritten digits. The maximum accuracy we achieve from this kind of techniques is approximately 96%. But this accuracy can be improved by advanced techniques to 99%. In recent days, the applications of neural network have been increased tremendously in various fields such as bank and post office to classify handwritten patterns.

Keywords Neural network · Handwriting pattern · Handwritten digit Architecture of neural network

1 Introduction

The neural network technology is the subdivision of artificial intelligence. And this artificial intelligence has more sub divisions. For all those subdivision of AI, the most important requirement is "machine learning"; there are different examples can be made for machine learning concepts such as friend suggestion in the Facebook is the best example; that application gives us suggestion on its own by relating our contacts by analyzing by AI. There is another example is that the suggestion comes in the Google when we type some words, the AI relates the general sentences which can be made and it gives us suggestion, and this kind of actions saves our time and makes our task more smarter way [1]. The current approach in neural network is the object recognition, which makes the machine learning methods as essential [2]. But

Ambikapathy (✉) · A.V. Singh
Department of Electrical & Electronics Engineering,
Galgotias College of Engineering & Technology, Noida, India
e-mail: jesus.ami.phd@gmail.com

A.V. Singh
e-mail: anantv675@gmail.com

A. Konkani et al. (eds.), *Advances in Systems, Control and Automation*,
Lecture Notes in Electrical Engineering 442, https://doi.org/10.1007/978-981-10-4762-6_27

still, there is a problem of over fitting. The recognition of the pattern can be solved with the size of thousand images if those images are augmented with the technology called label-preserving transformations. By this technique, almost the recognition reached to near about human performance. The over fitting can be optimized by data augmentation and dropout techniques [3]. In reality, the objects exhibit several variations in it, so in order to recognize them, we need to use widely recognized training tools as Pinto et al. [4]. The recent study says that it is possible to recognize the datasets even with the millions of images using some standard tools (LabelMe) [5] which has several thousands of segmented images and image net which has more than 15 million high-resolution images under 20,000 categories. The tool which is used in neural network should have the qualities such as scale, accuracy, and diversity. The proper hierarchical structure of any tool can help to get unparalleled ways in computer vision community [6]. To improve the present performance in this field first one should know that the change can improve the present scenario, deciding about the change which can improve the performance called problem in fundamental credit assignment. The two main steps which are involved in primary stage are: (i) the allotment of notation for event orientation to spread the information in NN of networks and (ii) Measure of depth of credit assignment to a path and their problems. The results of both the steps meet at a point to make the output where the image processing can be applied and carried out for the further process to get more advanced and better and smarter solution [7]. After the machine learning, the next technology comes into picture which gives the support to the machine learning and makes the AI smarter is image processing. The human visual system is one of the wonders of the human evolution. It can perform highly complex day-to-day task with utmost ease. Image processing is one of those difficult endeavors. While human brain can easily compute such task, it is highly difficult to accomplish such a problem via computer program. This task will obviously be daunting for a simple computer program, but if we approach this problem by neural networks, this problem can be fairly easy to handle.

2 Neural Networks

What is neural network? And what is the idea behind this? The idea is that the neural network is utilised to develop a system which can mimic the human brain. A neural network, thus, is made up of small functional units called **neurons**. These neurons are nothing but simple mathematical functions, which behave in the same way a biological neuron does. These neurons are interconnected to form **layers**, and these layers are interconnected to form a whole network. Simple neural networks may contain 3–4 layers but today's highly complex neural networks contain up to thousands of layers which are used for all sorts of pattern recognition, image processing, and what not. Let us begin by discussing types of neurons. Basically, there are 2 types of neurons: (a) **Perceptron** and (b) **Sigmoid**.

(a) Perceptron:

A perceptron takes several binary inputs to produce a single binary output.

Figure 1 shows the representation of perceptron which has three inputs, namely x_1, x_2, and x_3, but in actual practice, it can have more than three or less than the three inputs. Then, it comes to the concept of weights. **Weights** represent the importance of input to the output. If an input signal has more weight, then it is more important in determining the output. Generally, the neuron's output is either zero or one, and it is determined by $\sum_j w_j x_j$, and in this case, it may be greater value otherwise lesser value as **threshold** value. It is same like weights, threshold value is generally a real value, and moreover, it is a variable of the neuron. To put it in more precise algebraic terms:

$$\text{Output} = \begin{cases} 0 & \text{if} \quad \sum_j w_j x_j \leq \text{threshold} \\ 1 & \text{if} \quad \sum_j w_j x_j > \text{threshold} \end{cases} \tag{1}$$

We make notational changes to the expression "$\sum_j w_j x_j$" and convert it to "$w \cdot x$".

Where w = weight vector and x = input vector (Fig. 2).

Now, we replace the −ve of threshold value by **bias**, where bias point represents the strength of a neuron how strongly it is being fitted.

A **bias** represents the **firing strength** of a neuron, which means **higher the value of bias, more easy it is for the neuron to respond to a signal and vice versa**. The values of these weights and biases determine the overall response of the

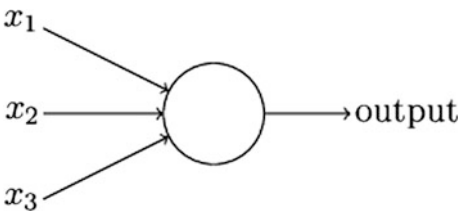

Fig. 1 Representation of function of perceptron

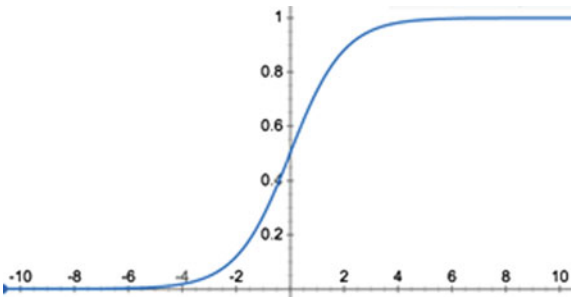

Fig. 2 Plot of pattern of sigmoid neuron

network. To get the best response, a neural network uses certain **learning algorithms** to automatically tune the values of these weights and biases. This tuning is initiated in response to external stimulation. The perceptron algorithm of perceptron was invented by Frank Rosenblatt in the year of 1957 at the place of Cornell Aeronautical Laboratory [8]; this research sponsor is done by the United States Office of Naval Research [9]. The perceptron assumed to be a machine, instead of assuming as a program; it was created and implemented in the hardware, and its name is custom-built hardware, and it is named as "Mark 1 perceptron." This machine was created generally to recognize the images of array of 400 photocells, connected to the "neurons." The different weights are fed or encoded through potentiometers, and weight updates at the time of learning were done by using electric motors [10].

(b) Sigmoid neuron:

The problem with perceptron neuron is that a little change in the input values to the perceptron can have drastic effects in the output of the neural network or artificial neural network. That is why perceptron neurons are not preferred for image recognition. This problem can be solved by replacing the perceptron neuron by sigmoid neuron. A sigmoid neuron also accepts inputs and produces an output but instead of accepting input only in the digit form of 1s and 0s, it can accept inputs in the digit form of both 1s and 0s. It produces output in the form of $\sigma(w \cdot x + b)$, where "σ" is an **activation function**. An activation function is a function of weights and biases which is in turn reason for producing an output. In case of a sigmoid neuron, the activation function's true form is [11]:

$$\sigma(w \cdot x + b) = 1/\left(1 + \exp\left(-\sum_j w_j x_j - b\right)\right) \tag{2}$$

Therefore, small changes in the weights and biases produce easily controllable changes in the output.

The changes in the output are well approximated by the equation:

$$\Delta O/P \approx \sum \frac{\mathrm{d}O/P}{\mathrm{d}W_j}\Delta W_j + \sum \frac{\mathrm{d}O/P}{\mathrm{d}b}\Delta b \tag{3}$$

3 Architecture of Neural Network

A neural network (NN) consists of input and output layers, and it has some hidden layers as well. As the number of these hidden layers increases, the decision-making capability of neural increases (Fig. 3).

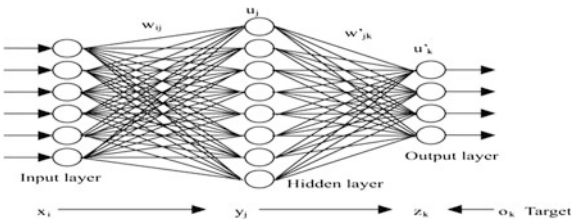

Fig. 3 Plot of pattern of sigmoid neuron

There are two types of neural networks:

(a) **Feed forward networks**: Networks without loops. The information travels in forward direction only. (b) **Recurrent neural networks**: Neural networks with loops. We must define certain algorithms by the help of which our network can **approximate the value of weights and biases**. A **learning algorithm** basically tries to constantly refine the value of weights and biases by trying to minimize a **cost function** [12].

$$C(w, b) \equiv \frac{1}{2n} \sum_{x} ||y(x) - a||^2 \tag{4}$$

w weights associated with the network
b biases associated with the network
x inputs associated with the network

So, our training algorithm does a good job if it can find the values of weights and biases for which the **value of C(w, b)** $\approx$ **0**. To accomplish this task, an algorithm called the **gradient descent algorithm** is used. The idea behind neural network is to develop a system which can learn through some initial data called training data. Gradient descent is one of powerful and most famous algorithms to perform optimization. To understand the gradient descent algorithm, we will replace our variables "w" and "b" with v_1 and v_2. We can understand the working of this gradient descent algorithm by thinking of a ball rolling down the curve C which is a function of v_1 and v_2 with Δv_1 change in the direction v_1 and Δv_2 change in direction v_2. Then, change in $C(v_1, v_2)$ is as follows:

$$\boldsymbol{\Delta C} \approx \frac{\partial \boldsymbol{C}}{\partial \boldsymbol{V_1}} \boldsymbol{\Delta V_1} + \frac{\partial \boldsymbol{C}}{\partial \boldsymbol{V_2}} \boldsymbol{\Delta V_2} \tag{5}$$

We can imagine a ball which is rolling down the valley. So, we will have to choose the value of v_1 and v_2 such that the value of ΔC decreases (so as to minimize the cost function).

ΔC can also be written as the dot product of ∇C and Δv, where

$$\nabla C \equiv \left(\frac{\partial C}{\partial v_1}, \frac{\partial C}{\partial v_2}\right)^T \quad \text{and} \quad \Delta V \equiv (\Delta V_1, \Delta V_2)^T \tag{6}$$

Therefore,

$$\Delta C \approx \Delta V \cdot \nabla C$$

∇C gradient vector relating to the changes in C with changes in V.

ΔV can be written in terms of a variable called **learning rate**.

$$\Delta V = -\eta \nabla C \tag{7}$$

$$\Delta C \approx -\eta \|\nabla C\|^2 \tag{8}$$

This shows that ΔC will always decrease and that is what we want, to minimize the cost function C. So, if the ball is moving downwards, then

$$V' \to V - \Delta V \tag{9}$$

We will update the rules over and over again until we reach global minimum. The learning rate should not be too small or too large. In case of large learning rate, the cost function would not minimize easily by changing values of weights and biases. In case of too small learning rate, the neural network will not learn fast enough [13]. So, as the neural network learns, it constantly updates the rules of weights and biases. Therefore, the new values of weights and biases according to **gradient descent rules are**:

$$w' \to w - \eta \frac{\partial C}{\partial w} \tag{10}$$

$$b' \to b - \eta \frac{\partial C}{\partial b} \tag{11}$$

4 Stochastic Gradient Descent

If the training examples are very large in numbers, the learning rate is very slow.

So, to improve the learning rate, we can divide those training data into number of **batches** of smaller data containing "m" training examples.

$$w' \rightarrow w - \frac{n}{m}\sum \frac{\partial C}{\partial w} \tag{12}$$

$$b' \rightarrow b - \frac{n}{m}\sum \frac{\partial C}{\partial b} \tag{13}$$

We keep picking up different batches of data until we have exhausted all the batches completing **one epoch of training** [14].

5 Back Propagation Algorithm

This is a very popular algorithm used in neural networks to compute the results. It is a common algorithm used for training the neural network. It works by computing the derivatives $\frac{\partial C}{\partial w}$ and $\frac{\partial C}{\partial b}$ so that gradient descent algorithm can be used. This algorithm is based on four equations and those equations are given below in order for the reference,

$$\boldsymbol{\delta}^{\boldsymbol{l}} = \nabla_{\boldsymbol{a}}\boldsymbol{C} \odot \boldsymbol{\sigma}'\left(\boldsymbol{z}_{\boldsymbol{j}}^{\boldsymbol{l}}\right) \tag{14}$$

$$\boldsymbol{\delta}^{\boldsymbol{l}} = \left(\left(\boldsymbol{w}^{\boldsymbol{l}+\mathbf{1}}\right)^{\boldsymbol{T}}\boldsymbol{\delta}^{\boldsymbol{l}+\mathbf{1}}\right) \odot \boldsymbol{\sigma}'\left(\boldsymbol{z}^{\boldsymbol{l}}\right) \tag{15}$$

$$\frac{\partial \boldsymbol{C}}{\partial \boldsymbol{b}_{\boldsymbol{j}}^{\boldsymbol{l}}} = \boldsymbol{\delta}_{\boldsymbol{j}}^{\boldsymbol{l}} \tag{16}$$

$$\frac{\partial \boldsymbol{C}}{\partial \boldsymbol{w}_{\boldsymbol{jk}}^{\boldsymbol{l}}} = \boldsymbol{a}_{\boldsymbol{k}}^{\boldsymbol{l}-\mathbf{1}}\boldsymbol{\delta}_{\boldsymbol{j}}^{\boldsymbol{l}} \tag{17}$$

$\boldsymbol{\delta}^{\boldsymbol{l}}$ Error produced by the jth neuron in the lth layer.

$\nabla_a C$ Measures the rate of change of cost function with respect to the transfer function.

$\boldsymbol{\sigma}'\left(\boldsymbol{z}_{\boldsymbol{j}}^{\boldsymbol{l}}\right)$ = Tells us, how fast the activation function is changing w.r.t the jth neuron [15]. If we know the error and weights of the $(l + 1)$th layer, we can come to know the error of the previous layer. Thus, the error is being back propagated.

$\frac{\partial C}{\partial b_j^l} = \delta_j^l$: The bias gets automatically tuned when we come to know the error of the lth layer (the previous layer). $\frac{\partial C}{\partial w_{jk}^l} = a_k^{l-1}\delta_j^l$:

The weight also gets automatically tuned after the output from the layer prior to the previous layer and the error from the previous layer gets multiplied. Thus, as we have already calculated the derivatives in the 5th step, finally, the weights and biases can be updated for the whole network [16].

6 Problem with the Quadratic Cost Function

If we initialize the weights and biases of a network and we obtain some initial output from that initial value of weights and biases, and if the difference between the initial output and desired output is large, **the network learns very slowly**. So, to avoid the problem of this learning slowdown, we use another cost function called the **cross-entropy cost function**. The cost entropy function looks like this:

$$C = -\frac{1}{n}\sum (y \ln a + (1-y)\ln(1-a)) \tag{18}$$

where

n the no of training inputs.
a corresponding output for input x.

7 Softmax Neurons

Just like perceptron's and sigmoid layer of neurons, there is another type of neurons called softmax neurons which compute the output via softmax functions [17]:

$$a_j^l = \frac{e^{z_j l}}{\sum_k e^{z_k l}} \tag{19}$$

The output from the softmax layer can be thought of as a probability distribution. As we will see later in the results, we achieve a better classification percentage when we use cross-entropy cost function along with softmax layer of neurons than using quadratic cost function along with sigmoid layer of neurons. Now, when we train a neural network for classification, we generally face some problems. One of them is called **over fitting**. Researchers are constantly trying to find new techniques to avoid over fitting. **Over fitting** is a phase when our neural network just memorizes the outputs from training data and fails to generalize new situations and therefore is not able to classify new objects (in this case). (a) **Increasing the number of training examples**: if there will be a huge number of training examples, our network will be able to learn more about the problem and thus will be able to generalize new situations effectively. (b) **Using validation data**: We can divide our

data into training and validation data. It is a set of data through which our network learns about some hyper parameters, e.g., learning rate and number of epochs to train. This data set is used to verify whether any increase in the accuracy of the training data is yielding any increase in the training data set. If it does not happen, it means that our network is over fitting. (c) **Using regularization techniques**: Another technique to reduce over fitting is to use regularization methods. There are many types of regularization methods such as *L*1, *L*2, and dropout [18].

8 Use of Neural Networks in Classifying the Handwritten Digits

This paper will use the concepts defined earlier to classify handwritten digits. Such networks are used by banks to read cheques and by post offices to read handwritten addresses. Now, we will see the effect of different cost functions (those covered in this paper), the various parameters of different values (such as rate of learning, different number of epochs, and number of different hidden neurons) on the classification of accuracy of the neural network. The results have been obtained by programming a neural network through python and the database on which we are testing our network is called MNSIT database, maintained by the US Govt., which contains thousands of scanned handwritten images. Let we use the stochastic learning descent method. Let,

The number of training sample images = 60,000
Quadratic learning rate = 3.0
Number of hidden neurons = 30
Mini-batch size = 10
Classification accuracy = 95.42%

But now, changing the cost function of the cross entropy, the classification accuracy becomes 95.49%. But, these times if we keep the cost function as quadratic and change the number of neurons which are hidden to 100, the classification of accuracy increases up to 96.59%. We have not applied regularization yet. But if we keep the number neurons which are hidden to be 100, keeping all the different parameters same, but change the cost function to cross entropy, the classification accuracy goes up to 96.82%. Now, to test the idea of over fitting (to see whether it really exists or not), we reduce the number of training images to 1000 from 60,000 and keep all the other parameters same. As expected, we encounter the problem of over fitting i.e., our network failed to generalize new situations and our classification accuracy reduced to 82%. To tackle the problem, we increased the number of training images to 50,000 and also applied regularization and found out that our classification accuracy increased to 87%. But, on top of that, if we train our network on validation data, we see that the classification accuracy increases to 97.92%. Now,

if we keep everything same and just change the number of epochs of training to 60, we see that the classification accuracy increases up to 98.02% [19, 20].

9 Conclusion

In this paper, we covered fundamental concepts regarding the neural networks and deep learning and applied those concepts in classifying handwritten digits. The choice of different parameters such as number of hidden layers, number epochs, and rate of learning can be arbitrary according to the need of number of the network. But the right choice can only be arrived at through trial and error and after some experience. Till now, there is no set method to derive the exact learning rate, the exact number of hidden layers etc.

References

1. Deryckere, N., Gevaert, W.: What is the potential of machine learning in a smart city? UG thesis, De Hogeschool west—Vlaanderen (2016)
2. Krizhevsky, A.: Learning multiple layers of features from tiny images. Master's thesis, Department of Computer Science, University of Toronto (2009)
3. Krizhevsky, A., Hinton, G.E.: Using very deep autoencoders for content-based image retrieval. In: ESANN, University of Toronoto, Canada, pp. 1–7 (2011)
4. Pinto, N., Cox, D.D., DiCarlo, J.J.: Why is real-world visual object recognition hard? PLoS Comput. Biol. **4**(1), e27 (2008). pp. 1–9
5. Russell, B.C., Torralba, A., Murphy, K.P., Freeman, W.T.: Labelme: a database and web-based tool for image annotation. Int. J. Comput. Vis. **77**(1), 157–173 (2008)
6. Deng, J., Dong, W., Socher, R., Li, L.-J., Li, K., Fei-Fei, L.: ImageNet: a large-scale hierarchical image database. In: Computer Vision and Pattern Recognition, CVPR09 (2009)
7. Schmidhuber, J.: Deep learning in neural networks: over view. Technical report IDSIA-03-14, The SWISS AI Lab IDSIA, p. 88
8. Simard, P.Y., Steinkraus, D., Platt, J.C.: Best practices for convolutional neural networks applied to visual document analysis. In: Proceedings of the Seventh International Conference on Document Analysis and Recognition, vol. 2, pp. 958–962 (2003)
9. Turaga, S.C., Murray, J.F., Jain, V., Roth, F., Helmstaedter, M., Briggman, K., Denk, W., Seung, H.S.: Convolutional networks can learn to generate affinity graphs for image segmentation. Neural Comput. **22**(2), 511–538 (2010)
10. Sánchez, J., Perronnin, F.: High-dimensional signature compression for large-scale image classification. In: Computer Vision and Pattern Recognition (CVPR), IEEE xplore, pp. 1665–1672 (2011)
11. Le, Q.V., Ranzato, M., Monga, R., Devin, M., Corrado, G., Chen, K., Dean, J., Ng, A.Y.: Building high-level features using large scale unsupervised learning. In: Proceedings of International Conference in Machine Learning, ICML'12 (2012)
12. Lampinen, J., Oja, E.: Clustering properties of hierarchical self-organizing maps. J. Math. Imaging Vis. **2**(2–3), 261–272
13. Lang, K., Waibel, A., Hinton, G.E.: A time-delay neural network architecture for isolated word recognition. Neural Networks **3**, 23–43 (1990)

14. Lange., S., Riedmiller, M.: Deep auto-encoder neural networks in reinforcement learning. In: Neural Networks (IJCNN), The 2010 International Joint Conference on, pp. 1–8 (2010)
15. Madani, O., Hanks, S., Condon, A.: On the undecidability of probabilistic planning and related stochastic optimization problems. Artif. Intell. **147**(1), 5–34 (2003)
16. Maei, H.R., Sutton, R.S.: GQ(λ): a general gradient algorithm for temporal-difference prediction learning with eligibility traces. In: Proceedings of the Third Conference on Artificial General Intelligence, vol. 1, pp. 91–96 (2010)
17. Marquardt, D.W.: An algorithm for least-squares estimation of nonlinear parameters. J. Soc. Ind. Appl. Math. **11**(2), 431–441 (1963)
18. Merolla, P.A., Arthur, J.V., Alvarez-Icaza, R., Cassidy, A.S., Sawada, J., Akopyan, F., Jackson, B.L., Imam, N., Guo, C., Nakamura, Y., Brezzo, B., Vol, I., Esser, S.K., Appuswamy, R., Taba, B., Amir, A., Flickner, M.D., Risk, W.P., Manohar, R., Modha, D.S.: A million spiking-neuron integrated circuit with a scalable communication network and interface. Science **345**(6197), 668–673 (2014)
19. Mesnil, G., Dauphin, Y., Glorot, X., Rifai, S., Bengio, Y., Goodfellow, I., Lavoie, E., Muller, X., Desjardins, G., Warde-Farle, D., Vincent, P., Courville, A., Bergstra, J.: Unsupervised and transfer learning challenge: a deep learning approach. In: JMLR W&CP: Proceedings of Unsupervised and Transfer Learning, vol. 7 (2011)
20. Meuleau, N., Peshkin, L., Kim, K.E., Kaelbling, L.P.: Learning finite state controllers for partially observable environments. In: 15th International Conference of Uncertainty in AI, pp. 427–436 (1999)

Error Rate Analysis of Precoded-OSTBC MIMO System Over Generalized-K Fading Channel

Prabhat Thakur and Keerti Tiwari

Abstract The orthogonal space–time block codes (OSTBCs) increase the diversity order of a multiple-input multiple-output (MIMO) system at a reasonable cost of complexity. However, the precoding technique in which complete channel knowledge is available at the base transceiver station has come into existence with OSTBC for improving the system performance. Moreover, a composite generalized-K channel model has become the key for analyzing both the effects of multipath fading and shadowing. Therefore, this chapter has exploited the precoded OSTBC to improve the bit error rate (BER) performance of MIMO system over a generalized-K fading channel.

Keywords Bit error rate · Generalized-K channel
Multiple-input multiple-output · Orthogonal space–time block codes
Precoding

1 Introduction

The multiple-input multiple-output (MIMO) is a very rapidly growing technology in the wireless communication systems. It has the potential advantages over the single-input single-output (SISO) such as high data rate, low bit error rate (BER), and enhanced signal-to-noise plus interference ratio (SINR) [1]. The MIMO is exploited in the wireless communication by using three frameworks as follows: (1) spatial multiplexing [2], (2) spatial diversity or antenna diversity [3], (3) and beam-forming technique [4]. The use of spatial multiplexing enables us to achieve

P. Thakur · K. Tiwari (✉)
Department of Electronics and Communication Engineering, Jaypee University of Information Technology, Waknaghat, Solan 173234, India
e-mail: keerti.tiwari@mail.juit.ac.in

P. Thakur
e-mail: prabhat.thakur@mail.juit.ac.in

A. Konkani et al. (eds.), *Advances in Systems, Control and Automation*,
Lecture Notes in Electrical Engineering 442, https://doi.org/10.1007/978-981-10-4762-6_28

higher data rates, whereas spatial diversity reduces the BER. Also, the beam-forming increases the SINR significantly with the help of smart antenna [5].

The spatial diversity is responsible for the reliable communication, i.e., low BER and is possible at both transmitting (transmitter diversity [6]) and receiving ends (receiver diversity [7]). Space–time block codes (STBCs) reduce the error rate of MIMO systems by adding spatial diversity in various fading channel conditions. The improved system performance is obtained by transmitting multiple replicas of the same signal from all measured antennas. Thus, the probability of information loss decays at an exponential rate. Then, the OSTBCs have been exploited for the transmitter diversity in the wireless communication with known channel state information (CSI) [8]. However, for real scenarios where CSI is not available at the transmitter, precoded OSTBCs have been presented in the literature [9].

It is cumbersome to design OSTBCs for an arbitrary number of antenna with complex field modulation schemes. Also, multiuser detection at the receiving end in MIMO systems is a prominent challenge. Therefore, to overcome the mentioned limitations, precoding or pre-equalization techniques are used at the transmitting end. The precoding is defined as a process of exploiting the channel-side information at transmitter (CSIT) on the signal before transmission [9].

A number of models have been proposed to consider the effects of fading and shadowing in the wireless channels such as K [10], Weibull–gamma [11], generalized-K [12–16], and extended generalized-K (EGK) [17, 18] fading. However, the generalized-K fading model is receiving the attention due to its flexible modeling that has Rayleigh, Nakagami-*m,* and K fading as its special cases. In [12], Shankar has proposed the concept of the generalized-K fading model. In [19], the authors have designed a memoryless precoder to reduce exact symbol error rate for OSTBCs MIMO communication systems by considering joint transmit–receive correlation. The authors in [20] have presented a linear precoder by using STBCs to minimize the upper bound of the pair-wise error probability. Further, it is illustrated that designed precoder outperforms the preexisting approaches over OSTBCs using Rician channels, especially for high co-related channels. The impact of spatial modulation and precoding design on the SER in OSTBC MIMO systems is illustrated in [21]. Moreover, it is reported that receiver-side correlation degrades the SER, whereas transmit-side correlation improves the same at low-to-medium SNR, and impact is almost negligible at high SNR. In [16], the authors have examined the error exponent of generalized–K fading MIMO channels over OSTBCs and have derived the mathematical expressions for Gallager's random coding and expurgated error. The performance of OSTBC MIMO systems over generalized-K fading channels is presented in [15], and the analytical expressions have also derived for the essential performance metrics such as SER, average outage probability, and channel capacity. In [13], the authors have analyzed the performance of multihop wireless links over generalized-K fading channels. Hendre and Murugan [22] have presented a way to exploit the channel state information (CSI) at the transmitter so that OSTBCs MIMO systems can use the precoding techniques. In addition to this, a mathematical model for designing the codebook of precoded OSTBCs has been provided to minimize the pairwise error probability.

Note that, precoded OSTBC gives improved error rate performance compared to conventional OSTBC. To the best of our knowledge, error rate performance has not been analyzed for precoded-OSTBC MIMO systems over a composite generalized-K fading channel. Therefore, the same is analyzed in this chapter using binary phase shift keying (BPSK) and quadrature phase shift keying (QPSK) modulation.

This chapter is organized as follows: Section 2 presents precoded-OSTBC MIMO system and generalized-K fading distribution. Simulation results and analysis of BER for proposed system are given in Sect. 3. Finally, the Sect. 4 concludes this chapter.

2 System and Channel Model

2.1 Precoded-OSTBC MIMO System

In [23], an approach of a codebook design shared by the transmitter and receiver is recommended for reducing the feedback overhead by constricting the estimated CSI at the receiver. The codebook contains a set of code words which represent channel state conditions. This codebook is used in the precoded-OSTBC system analysis.

Consider a MIMO system which contains the N_T transmit and N_R receive antennas with channel gains $\mathbf{h} \in C^{1\times N_T}$ and space–time code $\mathbf{C} \in C^{L\times T}$ with length L. The code word C is represented as

$$\mathbf{C} = [\mathbf{c}_1\ \mathbf{c}_2\ \mathbf{c}_3\ \mathbf{c}_4 \ldots \mathbf{c}_T] \tag{1}$$

where $\boldsymbol{c}_q = [c_{q,1}\, c_{q,2}\, c_{q,3} \ldots c_{q,L}]^T$, q = 1, 2, 3, … T and value of $L \leq N_T$.

The space–time code word C needs to multiply with precoding matrix $\mathbf{P}$ in the precoded OSTBC. The precoding matrix $\mathbf{P} \in C^{N_T\times L}$ is chosen from the codebook with codebook size n (i.e., CB = $[\mathbf{P}_1, \mathbf{P}_2, \mathbf{P}_3, \ldots \mathbf{P}_n]$) in such a way to improve the overall performance of the communication systems in terms of channel capacity or error rate. If N_T channels are assumed to be static over time period T, then received signal $r \in C^{1\times T}$ can be computed as

$$r = \sqrt{\frac{E_s}{N_T}}\mathbf{hPC} + \mathcal{N} \tag{2}$$

where E_s is the energy of the transmitted signal and $S \in C^{N_T\times T}$.

Now the probability of code-word error in Eq. (2) can be calculated similarly as in Eq. (12.3) of [23]. For a given channel $\mathbf{h}$ and precoding matrix $\mathbf{P}$, the pair-wise code error probability $\Pr(C_i \rightarrow C_j|\mathbf{H})$ is considered and expressed as

$$\begin{aligned}\Pr(C_i \rightarrow C_j|\mathbf{H}) &= Q\left(\sqrt{\frac{\rho\left\|\mathbf{HPE_{i,j}}\right\|^2}{2N_T}}\right) \\ &\leq \exp\left(-\frac{\rho\left\|\mathbf{HPE_{i,j}}\right\|^2}{4N_T}\right)\end{aligned} \tag{3}$$

where $\mathbf{H}$ denotes the channel matrix, ρ is signal-to-noise ratio (SNR) and given as $\rho = \frac{E_s}{N_0}$, here, N_0 is noise power spectral density and $\mathbf{E_{i,j}}$ denotes the error matrix between the code words C_i and C_j for the particular OSTBC scheme. Now to reduce the pair-wise code error probability, the factor $\mathbf{HPE_{i,j}}$ in equation (3) needs to be maximized. The $\mathbf{H}$ and $\mathbf{E_{i,j}}$ are not in our control due to random variations in the channel condition. Therefore, we need to opt $\mathbf{P}$ in order to maximize the $\mathbf{HWE_{i,j}}$, i.e.,

$$\boldsymbol{P_o} = \mathbf{W} \overset{\max}{\rightarrow} \mathrm{CB}\|\mathbf{HP}\|^2 \tag{4}$$

Equation (4) is a constrained optimization problem in which constrained on the value of P should belong to CB. The solution for the unconstrained optimization problem is presented in [9] by exploiting the concept of singular value decomposition (SVD) of channel matrix $\mathbf{H} = \mathbf{U\theta V^H}$. In [9], it is reported that the leftmost L columns of $\mathbf{V}$ provide the optimum solution for Eq. (4), i.e., $\mathbf{P_o} = [v_1, v_2, v_3 \ldots v_L] \cong \widehat{V}_c$.

As $\widehat{\mathbf{V}}$ is the unitary matrix, ith largest eigenvalue of $\mathbf{P_o}$ is $e_i(\mathbf{P_o}) = 1$, for $i = 1, 2, \ldots L$.

For non-deterministic channel, the codebook design is very prominent, and its criterion is given as

$$E\left\{\min_{\mathbf{P} \in \mathrm{CB}} \left(||\mathbf{HP_o}||^2 - ||\mathbf{HP}||^2\right)\right\} \tag{5}$$

where $\mathrm{Ex}(s)$ denotes the expectation of s, and the upper bound for this equation is presented in [23, Eq. 12.7]

$$\begin{aligned}&\mathrm{Ex}\left\{\min_{\mathbf{P} \in \mathrm{CB}} \left(||\mathbf{HP_o}||^2 - ||\mathbf{HP}||^2\right)\right\} \\ &\leq \mathrm{Ex}\left\{e_1^2(\mathbf{H})\right\}\mathrm{Ex}\left\{\min_{\mathbf{P} \in \mathrm{CB}} \left(\frac{1}{2}\left|\left|\widehat{\mathbf{V}}\widehat{\mathbf{V}}^{\boldsymbol{H}}\right|\right|^2 - \left|\left|\mathbf{PP}^{\boldsymbol{H}}\right|\right|^2\right)\right\}\end{aligned} \tag{6}$$

As $e_1^2(\mathbf{H})$ has a particular value, the necessary condition for codebook design is to minimize the value of $E\left\{\min_{\mathbf{P} \in \mathrm{CB}} \left(\frac{1}{2}\left|\left|\widehat{\mathbf{V}}\widehat{\mathbf{V}}^{\boldsymbol{H}}\right|\right|^2 - \left|\left|\mathbf{PP^H}\right|\right|^2\right)\right\}$. The best solution

for this problem is to consider a practical sub-optimal design method using discrete Fourier transform (DFT) presented in as

$$\mathrm{CB} = \left\{\mathbf{P}_{\mathrm{DFT}}, \boldsymbol{\Theta}\mathbf{P}_{\mathrm{DFT}}, \ldots \boldsymbol{\Theta}^{n-1}\mathbf{P}_{\mathrm{DFT}}\right\} \tag{7}$$

$\mathbf{P}_{\mathrm{DFT}}$ is the first code word which is acquired by choosing L number of columns from DFT matrix of size $N_T \times N_T$, and a diagonal matrix $\boldsymbol{\Theta}$ is represented in (8) with free variables $\{u_i\}_{i=1}^{N_T}$ to maximize the minimum chordal distance [23]

$$\boldsymbol{\Theta} = \mathrm{diag}\left[\left\{e^{\frac{j2\pi u_1}{N_T}} e^{\frac{j2\pi u_2}{N_T}} \ldots e^{\frac{j2\pi u_{N_T}}{N_T}}\right\}\right] \tag{8}$$

2.2 Generalized-K Fading

The probability density function (PDF) of generalized-K distributed signal envelop z is given by [18]

$$f_Z(z) = \frac{4z^{k+m-1}}{\Gamma k \Gamma m}\left(\frac{m}{\Omega}\right)^{\frac{m+k}{2}} K_{m-k}\left[2\left(\frac{k}{\Omega}\right)^{\frac{1}{2}} z\right], \quad z > 0 \tag{9}$$

where k, m, $K_v(.)$, $\Gamma(.)$ [24, Eq. (8.310.1)] are the Nakagami-m fading, shadowing parameter, modified Bessel function of order $v(.)$ [24, Eq. (8.432.1)], and the gamma function, respectively. $\Omega = E[Z^2]/m$ identifies mean power, and $E[.]$ is expectation operator. Different combinations of shaping parameters k and m in generalized-K fading distribution indicate variety of fading and shadowing model. Here $k \to \infty$, $m \to \infty$ approximates additive white Gaussian noise (AWGN) channel, $m \to \infty$ approaches Nakagami-m distribution, and $k = 1$ approaches K-distribution. PDF of generalized-K fading distribution in terms of average signal-to-noise ratio (SNR) is represented as [25]

$$f_\gamma(\gamma) = \frac{2\Xi^{\frac{(\alpha+1)}{2}}\gamma^{\frac{\alpha-1}{2}}}{\Gamma k \Gamma m}(\Xi)^{(\alpha+1)/2} K_\beta\left[2\sqrt{\Xi\gamma}\right] \quad \gamma \geq 0 \tag{10}$$

where $\alpha = k + m - 1$, $\beta = m - k$, $\Xi = m\frac{k}{\bar{\gamma}}$, $\gamma = Z^2\frac{E_s}{N_0}$, $\bar{\gamma} = m\,\Omega\,E_s/N_0$, here, γ is instantaneous SNR per received symbol.

3 Simulation Results and Discussion

This chapter evaluates the BER performance of precoded-OSTBC MIMO system for BPSK and QPSK with different fading and shadowing parameters. It is illustrated that for low values of k and m, the BER performance of the MIMO system is worst; however, as the values of both k and m increase to 5, system performance is improved. At low SNR, better performance can be achieved with high values of k and m which is shown in Fig. 1. For k = 5, m = 1, high BER is achieved as compared to k = 1, m = 5 which shows that shadowing gives more impact on BER performance improvement. At k = 1, m = 70, BER of proposed system observes Rayleigh fading scenario [23]. For all simulations, $\Omega = 1$ is taken into consideration. The number of frames and number of packets are 1000 and 100, respectively.

According to [23, Table 12.1], the codebook generator produces the codebook using the design process of (7) with $N_T = 4, L = 2, n = 64$, where $L \leq N_T$. In codebook design, channel gains are expected at the receiver side. Subsequently, the index of the suitable code word is chosen to signify a state of expected channel gain. Each index represents b bits and $n = 2^b$. BER performance of precoded-OSTBC scheme is illustrated in Figs. 1 and 2 for $N_T = 2, N_R = 1$. The precoded-OSTBC scheme gives better performance than the conventional OSTBC scheme without enhancing transmit power or spectral bandwidth.

The generalized-K fading channel is produced by the product of gamma random variables and the channel matrix given for Nakagami-m fading with its independent and identically distributed (iid) entries. Comparing Figs. 1 and 2, it is shown that by

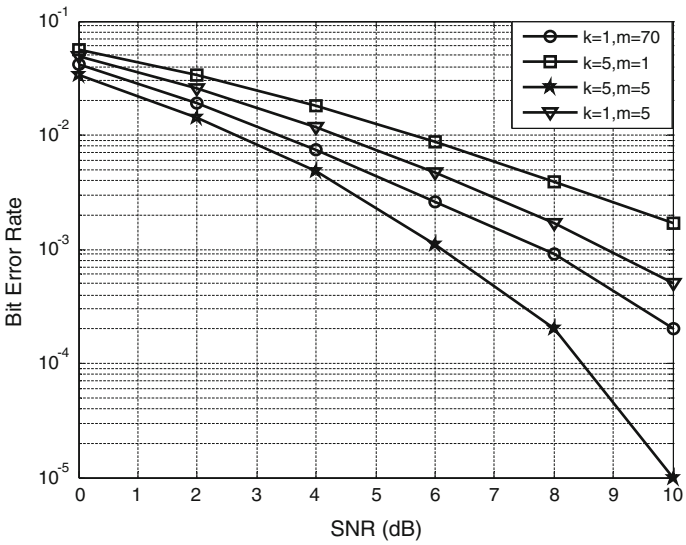

Fig. 1 BER performance of precoded OSTBC for BPSK in generalized-K fading channel ($N_T = 2, N_R = 1$)

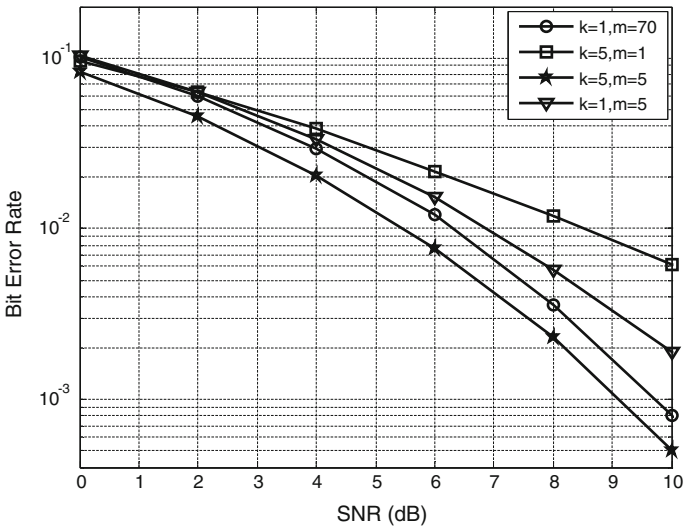

Fig. 2 BER performance of precoded OSTBC for QPSK in generalized-K fading channel ($N_T = 2, N_R = 1$)

increasing modulation order, better BER performance can be achieved. At 10^{-2} BER, BPSK gives approximately 3 dB performance improvement than QPSK. The nature of BER curves for numerically chosen value of k and m for BPSK and QPSK modulation techniques is similar.

Moreover, the error performance is improved at high SNR values with higher modulation order. Simulation results are verified from [23] for a special case (i.e., Rayleigh fading) of composite generalized-K fading which shows that approximately 5 dB less SNR is required at 10^{-2} BER in precoded OSTBC compared to conventional OSTBC MIMO system.

4 Conclusion

In this chapter, we have evaluated the performance of MIMO system with precoded-OSTBC scheme in a composite fading scenario. It is concluded that precoding enhances the system performance approximately 5 dB at 10^{-2} BER compared to conventional OSTBC for a special case of generalized-K fading, i.e., Rayleigh fading. Moreover, it is also illustrated that the shadowing parameter has a significant effect on error rate performance. Further, this work can be extended with spatial multiplexing and spatial modulation using precoding over a composite fading channel.

References

1. Mietzner, J., Schober, R., Lampe, L., Gerstacker, W.H., Hoeher, P.A.: Multiple-antenna techniques for wireless communications—a comprehensive literature survey. IEEE Surv. Tutor. **11**(2), 87–105 (2009)
2. Amin, M.R., Tarapasiya, S.D.: Space-time coding scheme for MIMO systems—literature survey. Procedia Eng. **38**, 3509–3517 (2012)
3. Alamouti, S.M.: A simple transmit diversity technique for wireless communications. IEEE J. Sel. Areas Commun. **16**(8), 1451–1458 (1998)
4. Vouyioukas, D.: A survey on beamforming techniques for wireless MIMO relay networks. Int. J. Antennas Propag. **2013**, 1–22 (2013)
5. Alexiou, A., Hardt, M.: Smart antenna technologies for future wireless systems: trends and challenges. IEEE Commun. Mag. **42**(9), 90–97 (2004)
6. Wornell, G., Trott, M.: Efficient signal processing techniques for exploiting transmit antenna diversity on fading channels. IEEE Trans. Signal Process. **45**, 191–205 (1997)
7. Faissal, E.B., Hussain, B.A.: Efficient performance evaluevation for EGC, MRC, and SC receivers over Weibull multipath fading channel. In: International Conference on Cognitive Radio Oriented Wireless Networks (CROWNCOM), Doha, Qatar, pp. 346–357 (2015)
8. Tarokh, V., Jafarkhani, H., Calderbank, A.R.: Space-time block codes from orthogonal designs. IEEE Trans. Inf. Theory **45**(5), 1456–1467 (1999)
9. Love, D.J., Heath, R.W.: Limited feedback unitary precoding for orthogonal space-time block codes. IEEE Trans. Signal Process. **53**(1), 64–73 (2005)
10. Abdi, A., Kaveh, M.: K distribution: an appropriate substitute for Rayleigh-lognormal distribution in fading-shadowing wireless channels. Electron. Lett. **34**(9), 851–852 (1998)
11. Tiwari, K., Saini, D.S., Bhooshan, S.V.: Antenna selection for MIMO systems over Weibull Gamma fading channel. Perspect. Sci. **8**, 475–478 (2016)
12. Shankar, P.M.: Error rates in generalized shadowed fading channels. Wirel. Pers. Commun. **28**(3), 233–238 (2004)
13. Cao, J., Yang, L.-L., Zhong, Z.: Performance analysis of multihop wireless links over generalized-K fading channels. IEEE Trans. Veh. Technol. **61**(4), 1590–1598 (2012)
14. Miridakis, N.I.: On the ergodic capacity of underlay cognitive dual-hop AF relayed systems under non-identical generalized-k fading channels. IEEE Commun. Lett. **19**(11), 1965–1968 (2015)
15. Xue, J., Zhong, C., Ratnarajah, T.: Performance analysis of orthogonal STBC in generalized-K fading MIMO channels. IEEE Trans. Veh. Technol. **61**(3), 1473–1479 (2012)
16. Xue, J., Sarkar, M.Z.I., Zhong, C., Ratnarajah, T.: Error exponents for orthogonal STBC in generalized-K fading MIMO channels. In: IEEE Wireless Communications and Networking Conference (WCNC), Shanghai, pp. 1925–1929 (2012)
17. Aloqlah, M.S., Nawafleh, F.A.: Performance study of decode and forward based multi-hop relaying in wireless networks over extended generalized-K fading channels. In: International Conference on Computing, Networking and Communications (ICNC), Kauai, HI, pp. 1–5 (2016)
18. Soury, H., Alouini, M.S.: Symbol error rate of MPSK over EGK channels perturbed by a dominant additive laplacian noise. IEEE Trans. Commun. **63**(7), 2511–2523 (2015)
19. Hjorungnes, A., Gesbert, D.: Precoding of orthogonal space-time block codes in arbitrarily correlated MIMO channels: iterative and closed-form solutions. IEEE Trans. Wirel. Commun. **6**(3), 1072–1082 (2007)
20. Bhatnagar, M.R., Hjorungnes, A.: Linear precoding of STBC over correlated Ricean MIMO channels. IEEE Trans. Wirel. Commun. **9**(6), 1832–1836 (2010)
21. Bjornson, E., Jorswieck, E., Ottersten, B.: Impact of spatial correlation and precoding design in OSTBC MIMO systems. IEEE Trans. Wirel. Commun. **9**(11), 3578–3589 (2010)

22. Hendre, V.S., Murugan, M.: Performance of precoded orthogonal space time block code MIMO system for mobile WiMAX system. In: International Conference on Communications and Signal Processing (ICCSP), Melmaruvathur, pp. 5–8 (2013)
23. Cho, Y.S., Kim, J., Yang, W.Y., Kang, C.G.: MIMO-OFDM Wireless Communications with Matlab. Wiley, Singapore (2010)
24. Gradshteyn, I.S., Ryzhik, I.M.: Table of Integrals, Series, and Products, 7th edn. Academic press, New York (2007)
25. Bithas, P.S., Sagias, N.C., Mathiopolous, P.T., Karagiannidis, G.K., Rontogiannis, A.A.: On the performance analysis of digital communications over generalized-K fading channels. IEEE Commun. Lett. **10**(5), 353–355 (2006)

CMOS Based Sinusoidal Oscillator Using Single CCDDCCTA

Ajay Kumar Kushwaha, Ashok Kumar and Sajal K. Paul

Abstract The realization of voltage mode (VM) and current mode (CM) sinusoidal oscillator using current-controlled differential difference current conveyor transconductance amplifier (CCDDCCTA) and all grounded passive elements is proposed. The circuit configuration consists of single CCDDCCTA, two capacitors, and single resistor. The utilization of grounded passive components is good for IC fabrication. The frequency of oscillation can be altered independent of condition of oscillation by external bias currents. The passive sensitivities are low. The PSPICE based OrCAD 16.6 circuit simulator is used to perform simulations. The CCDDCCTA building block has been designed using CMOS 0.25 μm TSMC technology parameters. Simulation results to verify the theory are given.

Keywords Sinusoidal oscillator · CCDDCCTA · Current mode
Voltage mode · Analog building block (ABB)

1 Introduction

Sinusoidal waveform generators are very useful circuits for signal processing, measurement, control systems, and various communication systems [1]. However, various oscillator circuit implementations using a variety of analog building blocks (ABB) are reported [1]. The current mode ABB is designed for high performance,

A.K. Kushwaha (✉) · A. Kumar · S.K. Paul
Department of Electronics Engineering, Indian Institute of Technology
(Indian School of Mines), Dhanbad 826004, India
e-mail: ajay.igecsagar@gmail.com

A. Kumar
e-mail: ashok1987.in@gmail.com

S.K. Paul
e-mail: sajalkpaul@rediffmail.com

A. Konkani et al. (eds.), *Advances in Systems, Control and Automation*,
Lecture Notes in Electrical Engineering 442, https://doi.org/10.1007/978-981-10-4762-6_29

lower power consumption and fast analog signal processing circuits. The CCDDCCTA [2, 3] is a newly developed ABB. Its input block is CCDDCC combined with transconductance amplifier, which has high output impedance ports for current and three high input impedance ports for voltage. The resistance and transconductance are electronically tunable.

The study of various implemented sinusoidal oscillators [1, 4–9] using different current conveyor blocks reveals that these circuits suffer from one or more of the following weaknesses:

(a) No grounded passive components.
(b) Use of excessive passive components.
(c) Use of two or more ABBs.
(d) Non-availability of electronic tunability.
(e) Independent control of condition and frequency of oscillation.

A new CM and VM sinusoidal oscillator with a recently implemented CCDDCCTA block with grounded passive elements has been proposed. The presented oscillator needs single CCDDCCTA, grounded capacitors, and resistor only. The attributes of the presented oscillator can be electronically controlled by external biased current of the CCDDCCTA without alteration of circuit topology. Comparison with available oscillator circuits is also included. Simulation results are included to validate the theory.

2 CCDDCCTA Based Circuit

The electrical symbol of CCDDCCTA block and its internal CMOS structure are given in Figs. 1 and 2, respectively [2].

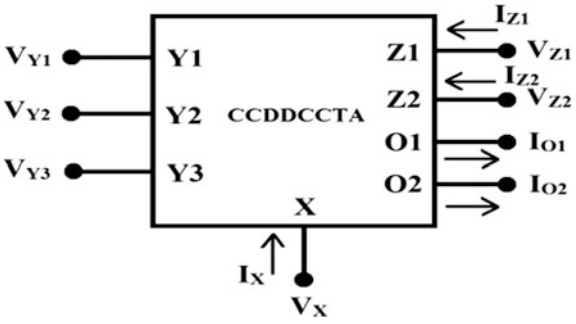

Fig. 1 Electrical symbol of CCDDCCTA

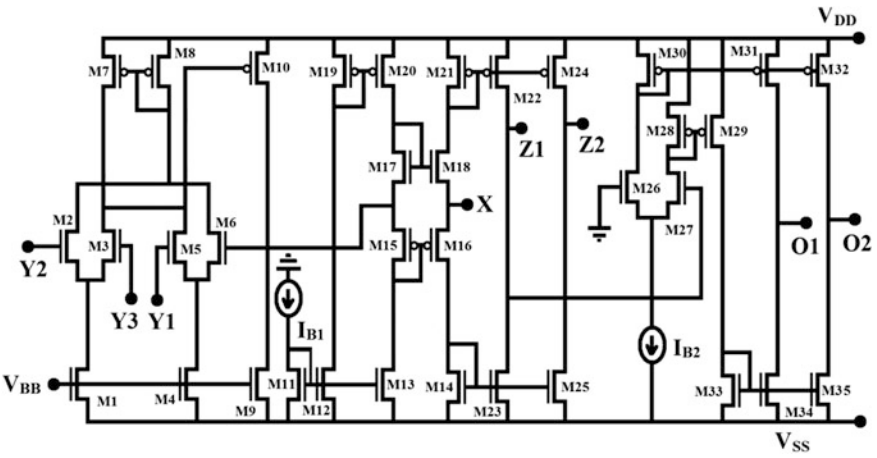

Fig. 2 CMOS implementation of CCDDCCTA

The port connections can be given in matrix as:

$$\begin{bmatrix} I_{Y1} \\ I_{Y2} \\ I_{Y3} \\ V_X \\ I_{Z1} \\ I_{Z2} \\ I_{01} \\ I_{02} \end{bmatrix} = \begin{bmatrix} 0 & 0 & 0 & 0 & 0 \\ 0 & 0 & 0 & 0 & 0 \\ 0 & 0 & 0 & 0 & 0 \\ 1 & -1 & 1 & R_X & 0 \\ 0 & 0 & 0 & 1 & 0 \\ 0 & 0 & 0 & 1 & 0 \\ 0 & 0 & 0 & 0 & -g_{mo} \\ 0 & 0 & 0 & 0 & -g_{mo} \end{bmatrix} \begin{bmatrix} V_{Y1} \\ V_{Y2} \\ V_{Y3} \\ I_X \\ V_{Z1} \end{bmatrix} \tag{1}$$

The internal resistance (R_X) is described as

$$R_x = \frac{1}{g_{m16} + g_{m18}},$$

where

$$g_{mi} = \sqrt{2\mu C_{ox}\left(\frac{W}{L}\right)_i I_{\mathrm{B1}}}, \quad i = 16, 18 \tag{2}$$

Likewise, the transconductance (g_{mo}) is determined as

$$g_{mo} = \sqrt{2\mu C_{ox}\left(\frac{W}{L}\right)_{26,27} I_{\mathrm{B2}}} \tag{3}$$

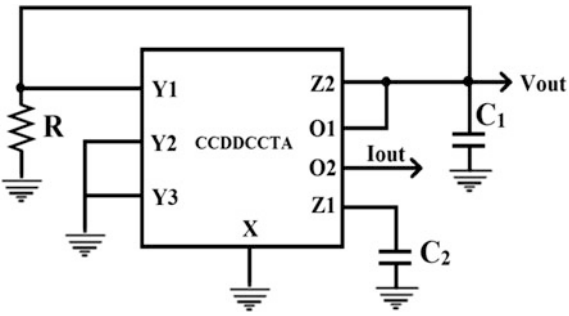

Fig. 3 Proposed current mode (CM) and voltage mode (VM) oscillator

The proposed CM and VM oscillator is presented in Fig. 3 which uses single CCDDCCTA, two capacitors, and one resistor.

The analysis of proposed circuit of Fig. 3 using (1) gives the system characteristic equation as

$$s^2 C_1 C_2 R R_X + sC_2[R_X - R] + g_{mo} R = 0 \tag{4}$$

Evaluation of (4) represents that the circuit of Fig. 3 will work as an oscillator with the condition of oscillation (CO) as

$$\text{CO} : R_X = R \tag{5}$$

If the above CO is satisfied, then circuit gives the frequency of oscillation (FO) as

$$\text{FO} : f_0 = \frac{1}{2\pi}\left(\frac{g_{mo}}{C_1 C_2 R_X}\right)^{1/2} \tag{6}$$

The voltage V_{out} and current I_{out} are the sinusoidal signals; moreover, frequency of oscillation can be tuned by bias currents (I_{B1}) and (I_{B2}). It may also be noted that frequency of oscillation can be varied independent of condition of oscillation by I_{B2}.

3 Sensitivity and Stability of the Oscillator

The sensitivity is a dominant performance parameter of any circuit. The sensitivity of angular frequency with respect to a circuit element, say *Y,* is given as

$$S_Y^{\omega_0} = \frac{Y}{\omega_0}\frac{\partial \omega_0}{\partial Y} \tag{7}$$

The sensitivities as a function of passive and active components are evaluated as

$$S_{C_1}^{\omega_0} = S_{C_2}^{\omega_0} = S_{R_x}^{\omega_0} = -\frac{1}{2}, \quad S_{gmo}^{\omega_0} = \frac{1}{2} \tag{8}$$

It is evident that the all active and passive component's sensitivities are half in magnitude. This is considered low value for sensitivity.

Frequency stability analysis is defined as measure of the ability of an oscillator circuit to produce stable frequency over a long period [6, 9]. The frequency stability (S_F) can be defined as

$$S_F = \left.\frac{d\varphi(k)}{dk}\right|_{K=1} \tag{9}$$

where $\varphi(k)$ and $k = (\omega/\omega_0)$ are the phase function of the open loop transfer function and the normalized frequency, respectively. Considering the current-mode open loop transfer function at $Z2$ port, by choosing $R_X = R$, $g_m = n/R$, and $C_1 = C_2 = C$, We get

$$S_F = \left.\frac{d\varphi(k)}{dk}\right|_{K=1} = 2\sqrt{n} \tag{10}$$

Hence, for high value of n, the value of S_F is high and the high value of frequency stability reveals high stability of oscillator.

4 Simulations and Discussion

The performance of sinusoidal oscillator is examined with PSPICE simulation using 0.25 μm CMOS technology parameter of TSMC. The W/L ratios of CMOS transistors are given in Table 1. The DC voltage supply is taken as ±1.25 V. The bias supplies used in circuit are $V_{BB} = -0.8$ V, $I_{B1} = 25$ μA, and $I_{B2} = 200$ μA.

Table 1 Aspect ratio of transistors

MOS transistors	W/L ratio (μm)
M1, M4, M9, M11–M14, M23, M25, M33–M35	3.0/0.25
M2–M3, M5–M6	1.0/0.25
M10	12.5/0.25
M15	8.0/0.25
M16	9.0/0.25
M18	4.5/0.25
M29	4.35/0.25
M7–M8, M17, M19–M22, M24, M26–M28, M30–M32	5/0.25

To design the frequency of oscillation f_0 = 218 kHz, the component values are taken as C_1 = 0.5 nF, C_2 = 0.5 nF, and R = 1.5 KΩ. The simulated voltage and current output responses including transient state are shown in Figs. 4 and 5, respectively. Figures 6 and 7 show the steady-state voltage and current output responses, respectively. The simulated output frequency spectrums for voltage and current responses are displayed in Figs. 8 and 9, respectively. The total harmonic distortion (%THD) of presented oscillator circuit is found 2.8% at oscillation

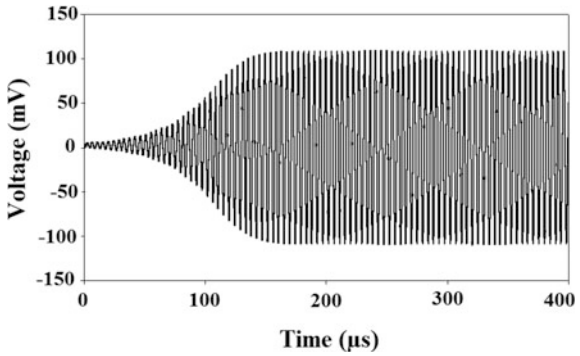

Fig. 4 Voltage output response at initial state

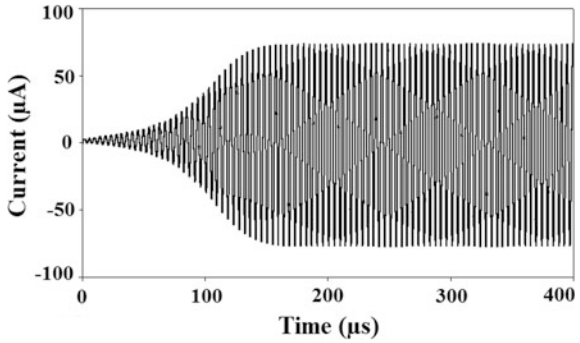

Fig. 5 Current output response at initial state

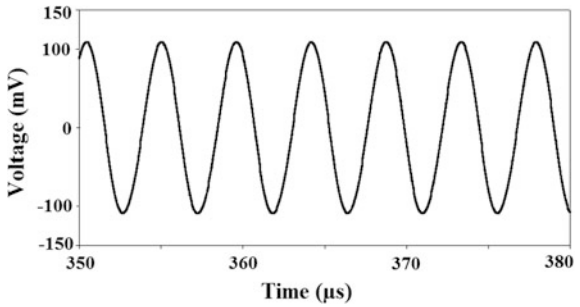

Fig. 6 Steady state voltage output response

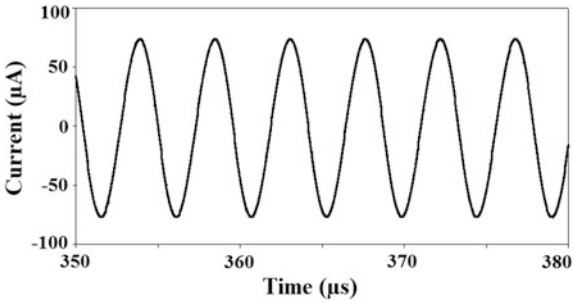

Fig. 7 Steady state current output response

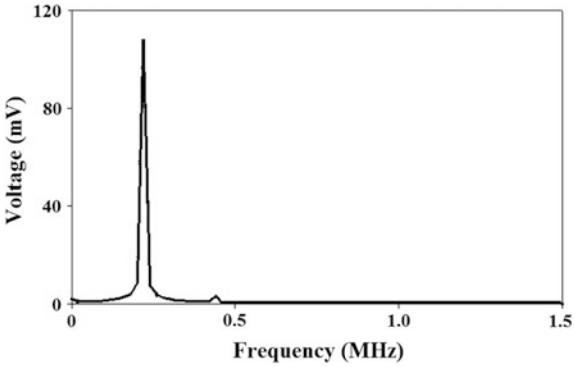

Fig. 8 Frequency spectrum for voltage response

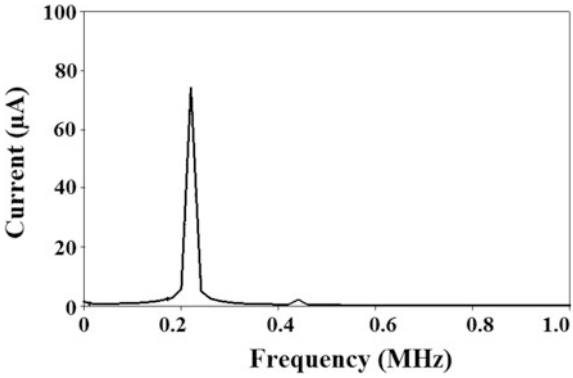

Fig. 9 Frequency spectrum for current response

frequency of 218 kHz, which is well within the tolerance range of 5%. The total power dissipation of the circuit in Fig. 3 is obtained as 1.8 mW. The comparative analysis of different available oscillator circuits is given in Table 2.

Table 2 Comparative analysis of available oscillator circuits

Ref.	ABBs used	Passive components used	Grounded passive components (Yes/No)	Electronic tunability (Yes/No)
[4]	2, CFOA	5	No	No
[5]	1, CFOA	5	No	No
[6]	1, FTFN	7	No	No
[7]	1, MCCCDTA	3	No	Yes
[8]	1, OTRA	5	No	No
[9]	4, CCCII	2	Yes	Yes
Proposed	1, CCDDCCTA	3	Yes	Yes

5 Conclusion

The CM and VM sinusoidal oscillator using CCDDCCTA block is proposed. It uses one CCDDCCTA, two capacitors, and one resistor. The frequency of oscillation is electronically tunable by external bias currents I_{B1} and I_{B2}. It is also found that frequency of oscillator can be varied with I_{B2} without disturbing condition of oscillation. Comparative analysis of available oscillator circuits is also included. Simulated PSPICE results authenticate the proposed theory.

References

1. Senani, R., Bhaskar, D.R., Singh, A.K., Singh, V.K.: Sinusoidal Oscillators and Waveform Generators Using Modern Electronic Circuit Building Blocks. Springer Science + Business media, New York (2016)
2. Pandey, N., Kumar, P., Choudhary, J.: Current controlled differential difference current conveyor transconductance amplifier and its application as wave active filter. ISRN Electron. 1–11 (2013)
3. Kushwaha, A.K., Paul, S.K.: Current mode universal filter using single current controlled differential difference current conveyor transconductance amplifier. Circuit Syst. **6**, 224–236 (2015)
4. Tangsrirat, W., Surakampontorn, W.: Single resistance controlled quadrature oscillator and universal biquad filter using CFOAs. Int. J. Electron. Commun. **63**, 1080–1086 (2009)
5. Abuelma'atti, M.T., Farooqi, A.A., Alshahrani, S.M.: Novel RC oscillators using the current feedback operational amplifier. IEEE Trans. Circuit Syst. **43**, 155–157 (1996)
6. Cam, U., Toker, A., Cicekoglu, O., Kuntman, H.: Current-mode high output impedance sinusoidal oscillator configuration employing single FTFN. Analog Integr. Circuit Signal Process. **24**, 231–238 (2000)
7. Wang, W.: Three current-mode Wien bridge oscillators using single modified current controlled current differencing transconductance amplifier. Mechatron. Autom. Control Syst. (Lecture Notes in Electrical Engineering.) 693–700 (2014). doi:10.1007/978-3-319-01273-5_77

8. Cam, U.: A novel single resistance controlled sinusoidal oscillator employing single operational transresistance amplifier. Analog Integr. Circuit Signal Process. **32**, 183–186 (2002)
9. Bhaskar, D.R., Prasad, D., Senani, R., Jain, M.K., Singh, V.K., Srivastava, D.K.: New fully-uncoupled current-controlled sinusoidal oscillator employing grounded capacitors. Am. J. Electr. Electron. Eng. **4**, 81–84 (2016)

Investigation of Direct Torque Control-Based Synchronous Reluctance Motor Drive for Pumping

V.K. Arun Shankar, S. Umashankar, S. Paramasivam, P. Sanjeevikumar and K. Venkatesh

Abstract This paper discusses direct torque control (DTC) strategy for a synchronous reluctance motor (SynRM). In this article, the SynRM is used to drive the centrifugal pump that requires high power density. A mathematical model of SynRM is formed using dynamic equations. This motor model is then simulated using MATLAB Simulink. The suggested DTC control is analysed for different speeds, and the results are illustrated. The control strategy is simulated, and its performance parameters (flux and current along direct and quadrature axes) are analysed. Simulation results of the synchronous reluctance motor (SynRM) and pump are presented in this paper to determine the performance of the drive.

Keywords Direct torque control (DTC) · Centrifugal pumps
Dynamic modelling · MATLAB · Simulink
Synchronous reluctance motor (SynRM)

V.K. Arun Shankar · S. Umashankar (✉) · K. Venkatesh
Department of Energy and Power Electronics, Vellore Institute of Technology (VIT) University, Vellore, Tamil Nadu, India
e-mail: umashankar.s@vit.ac.in

V.K. Arun Shankar
e-mail: arunshankar.vk@vit.ac.in

K. Venkatesh
e-mail: venkateshkommanaboina@gmail.com

S. Paramasivam
Danfoss Industries Private Limited, Chennai, Tamil Nadu, India
e-mail: paramsathya@yahoo.com

P. Sanjeevikumar
Department of Electrical and Electronics Engineering, University of Johannesburg, Auckland Park, Johannesburg, South Africa
e-mail: sanjeevi_12@yahoo.co.in

A. Konkani et al. (eds.), *Advances in Systems, Control and Automation*,
Lecture Notes in Electrical Engineering 442, https://doi.org/10.1007/978-981-10-4762-6_30

1 Introduction

The rotor structure of a synchronous reluctance motor (SynRM) is robust and simple [1]. They are capable of rotating at very higher speeds in hot climatic conditions also, since there are no windings in the rotor [2, 3].

The modelling and simulation of SynRM are carried out using MATLAB/Simulink software. MATLAB consists of a variety of block sets and toolboxes depending on requirements. For modelling the drive, Simulink provides the necessary components. SynRM was created from the dynamic equations that describe the motor [4]. The electrical parameters must be known for simulation of any machine. These parameters can be either calculated or measured [5, 6].

In asynchronous motors, air-gap flux induces the rotor currents. Whereas for permanent magnet synchronous motor and synchronous reluctance motor, the rotor currents are generated using permanent magnet or field winding [7, 8].

Figure 1 shows the stator and rotor laminations of the synchronous reluctance motor. Mutual flux linkage along d-axis can be calculated using the following equations:

$$\widehat{\psi}_{md} = k_{ws1} N_s \frac{2}{\pi} \tau_p l' \hat{B}_{\delta d} \tag{1}$$

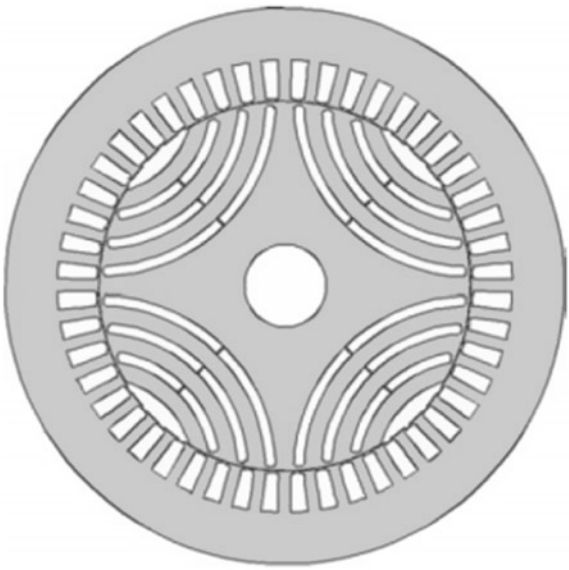

Fig. 1 SynRM—stator and rotor laminations

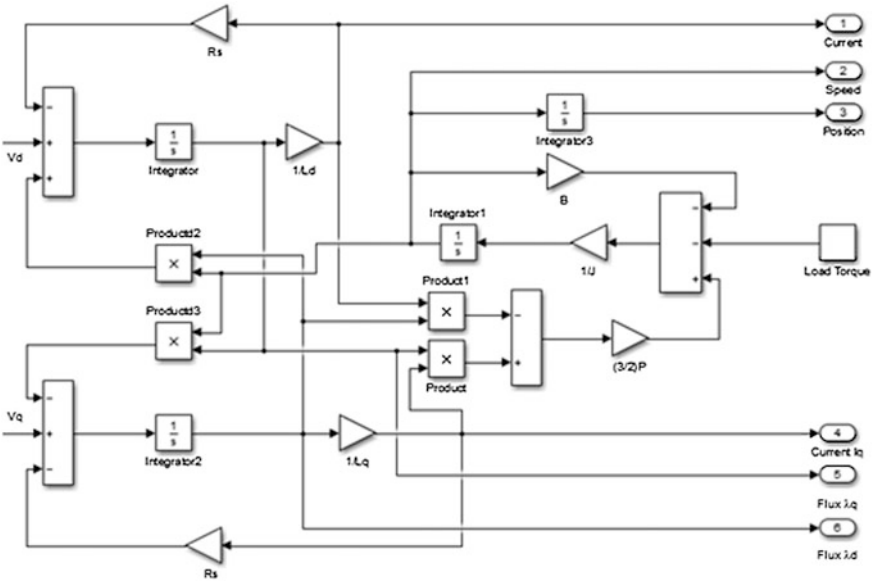

Fig. 2 Simulated SynRM drive in Simulink

Calculating L_d and L_q for any rotor structure, the model of synchronous machine can be treated as synchronous reluctance machine. Figure 2 shows the MATLAB Simulink model of SynRM.

2 Modelling of Controller

In synchronous reluctance motors, rotor position has to be estimated because the stator current vector and rotor position should be synchronized. Whereas, due to the requirement of speed sensor that increases hardware cost, and reduces system reliability, sensorless control of SynRM is gaining more focus by the researchers nowadays.

In a SynRM, because the rotor follows the flux, the position of rotor and fluxes is changed together. Therefore, in this method, the rotor position is estimated using flux linkage. Flux calculation using fundamental models to estimate angles is the most straightforward approach and has several advantages.

In this approach, torque (T_e), speed (ω_r) and flux linkage phase angle (ρ_s), in both transient and steady states, are calculated by using the estimated flux linkages in stator (Ψ_s). The equations of these calculations are shown as follows:

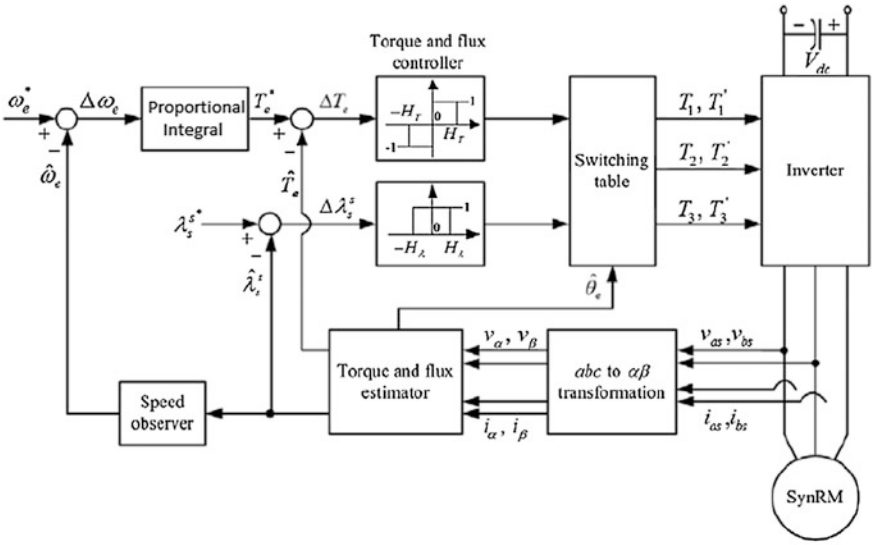

Fig. 3 Block diagram of DTC for synchronous reluctance motor

Table 1 Parameters of SynRM model

Parameters	Values
L_d (H)	1.2
L_q (H)	0.1
Voltage (V)	415
R (Ω)	4
Inertia (kg m^2)	0.125
Damping	0.009
Pole pair	2
f (Hz)	50

$$\psi_\alpha = \int (v_\alpha - R_a I_\alpha)\mathrm{dt} \tag{2}$$

$$\psi_\beta = \int (v_\beta - R_a I_\beta)\mathrm{dt} \tag{3}$$

$$T_e = \frac{3}{2} p(\psi_\alpha I_\beta - \psi_\beta I_\alpha) \tag{4}$$

The DTC control algorithm for speed control of synchronous reluctance motor is shown in Fig. 3. The DTC has flux and torque control loops that are controlled independently. The DTC control also exhibits better performance for flux and torque regulation [9].

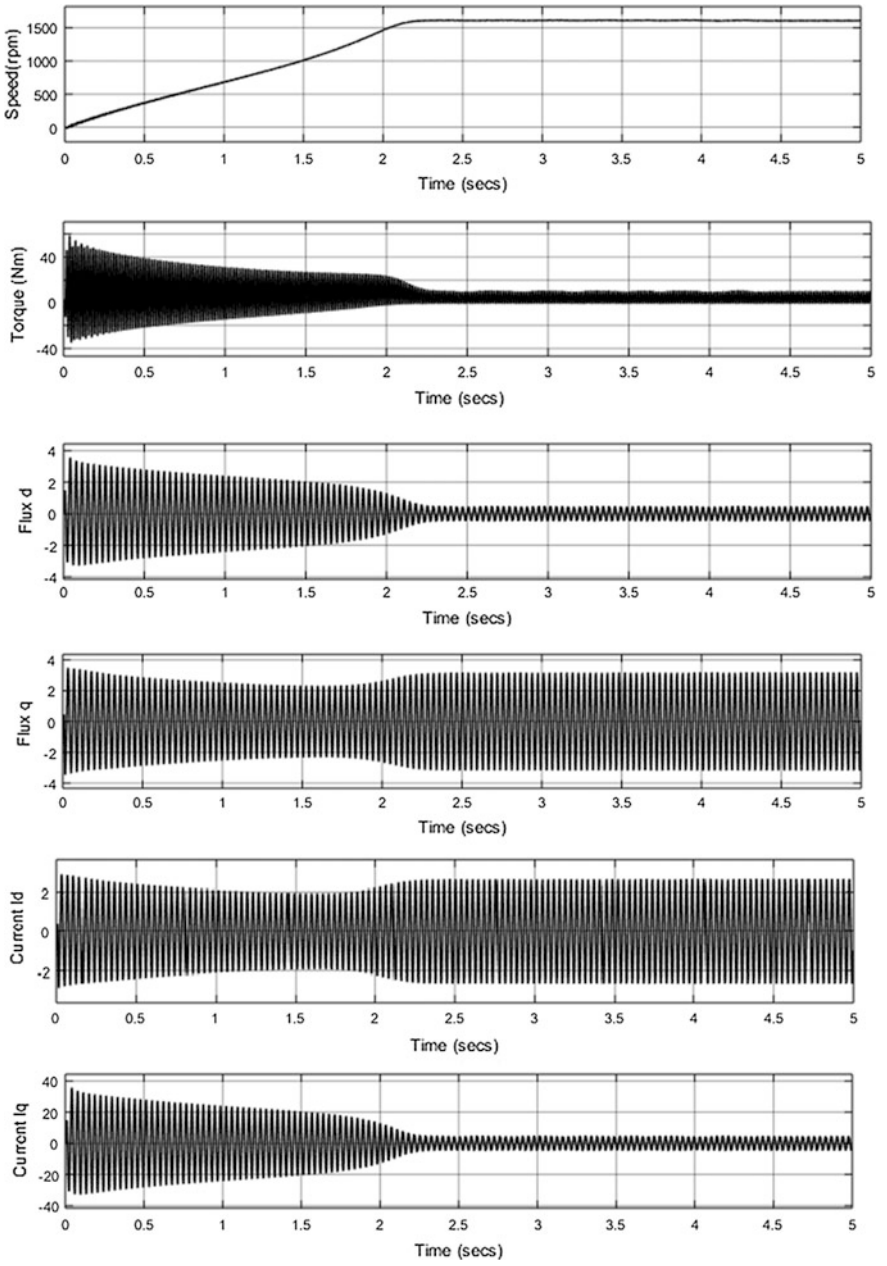

Fig. 4 Output graphs for DTC

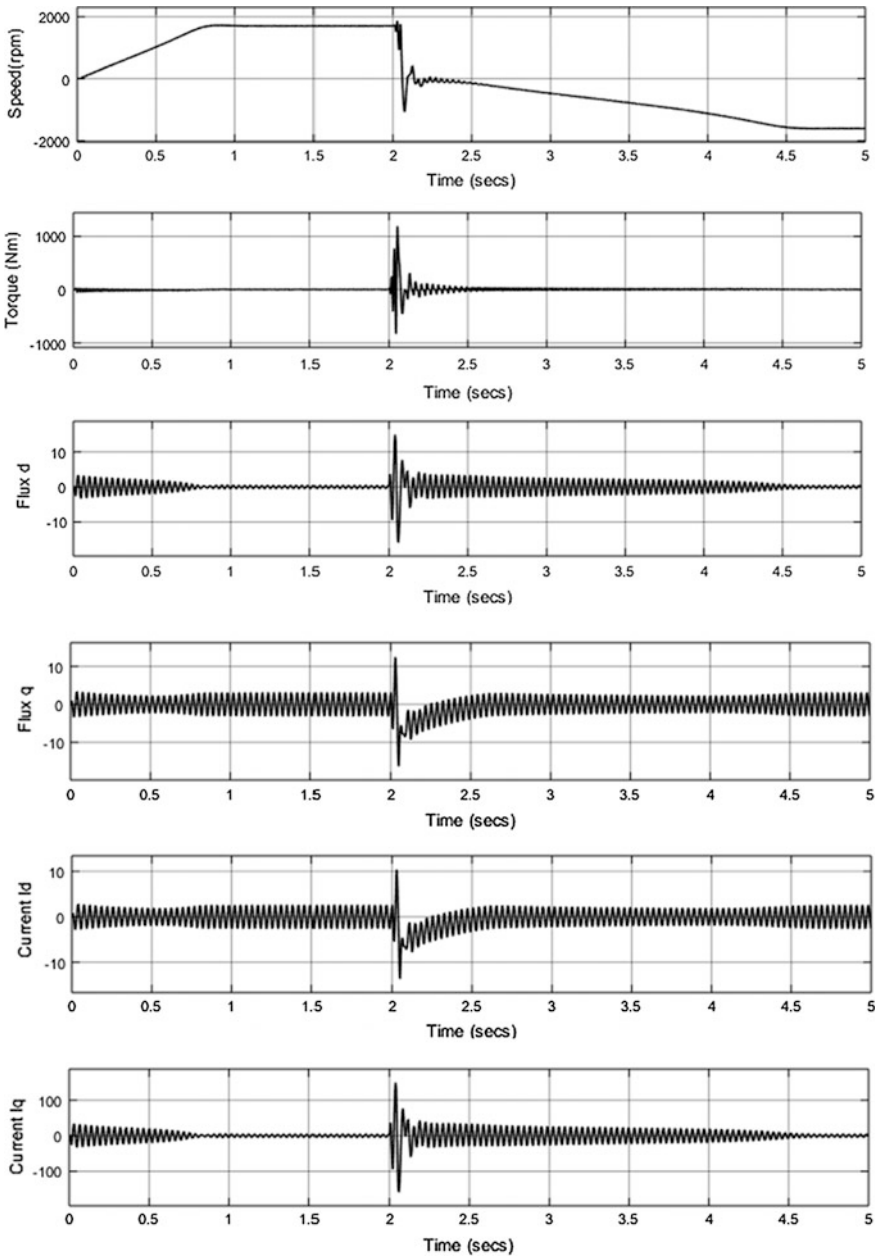

Fig. 5 DTC response for acceleration and deceleration

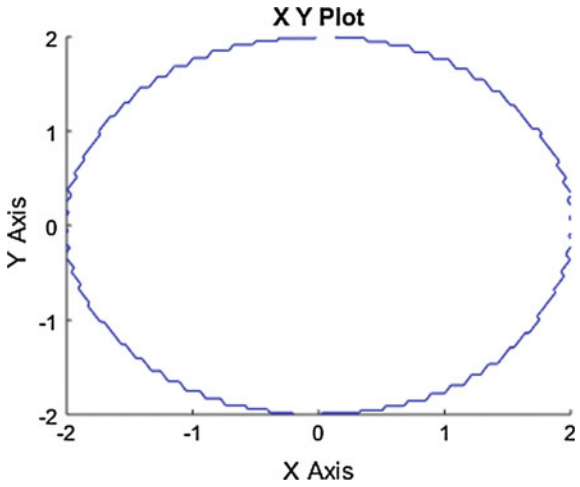

Fig. 6 Stator flux for DTC

3 Simulation Results

Direct torque control was employed with the SynRM model using the parameters given in Table 1, and the results were obtained as shown in Fig. 4.

The speed gets constant at 1750 rpm which is given as the reference value. The final torque is settling to 10 N m. At the beginning of the simulation, the motor is unable to drive the pump load, and the torque fluctuates between negative and positive values. As we can see from Fig. 4, the torque settles when the speed gets settled at 2.3 s. All the other output waveforms are pulsating in nature.

The acceleration and deceleration of a DTC control when load is kept constant are shown in Fig. 5. As we can see from Fig. 5, firstly the speed is accelerated and gets settled at the reference value of 1750 rpm. The motor torque is constant throughout this time. The reference value is changed to −1750 rpm at 2 s. Because of this, the speed is decelerated and finally gets settled at 4.5 s. During this period, the torque fluctuates as the rotor rotating direction is changed.

The stator flux for DTC is given in Fig. 6. X-axis and y-axis represent the stator flux along direct and quadrature axis, respectively.

A centrifugal pump has been used to replace the load, and the output of the pump is observed. The output waveforms of the pump are shown in Fig. 7. Before

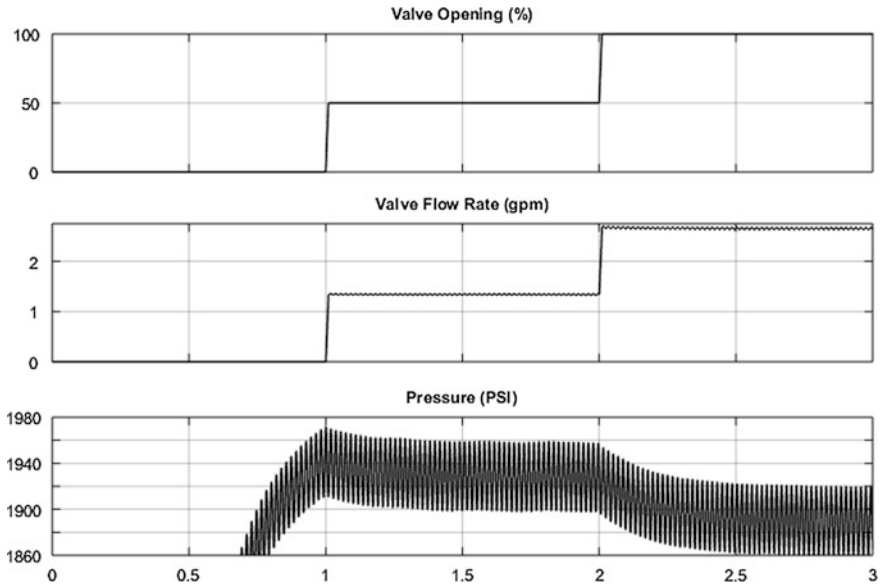

Fig. 7 Pump output for DTC

opening of the valve, the speed should become constant. When the valve is partially opened at 1 s, the valve flow rate increases and the pressure is decreased. This pattern is also observed when the valve is opened again at 2 s.

4 Conclusion

DTC is suitable for high-power applications due to its lesser switching frequency simple control structure. It is concluded that the DTC exhibits a dynamic response to the change in speed command of the synchronous reluctance motor. Also the required control period is short in DTC. The response time in flux and current is very less, and the torque experiences very low ripple even during the acceleration and deceleration of the motor. A major disadvantage of the conventional PI controller is that it requires high response time that has been overcome by the suggested DTC technique. Moreover, the switching frequency of DTC is variable.

References

1. Danfoss Industries.: Facts worth knowing about frequency converters (2014)
2. Pyrhonen, J., Jokinen, T., Hrabovcova, V.: Design of rotating electrical machines, Wiley (2008)

3. Liu, T.H.: Controller design for synchronous reluctance motor drive systems with direct torque control. National Taiwan University of Science and Technology (2011)
4. Mostafa, A.F., Daw., Abaid, E.: Modelling and simulation of reluctance motor using digital computer. Int. J. Comp. Sci. Electron. Eng. (IJCSEE) **1**(2) (2013)
5. Abhishek, S., Arun Shankar, V.K. Umashankar, S.: Investigations on performance evaluation of VFD fed PMSM using DTC control strategies for pumping applications. Int. Conf. Eng., Technol. Sci. (ICETS) (2016)
6. Ahmad, G.: Wide range speed sensorless vector control of synchronous reluctance motor with start up ability. Graduate School of Life Science and Systems Engineering Kyushu Institute of Technology (2007)
7. Arun Shankar, V.K., Umashankar, S., Paramasivam, S., Abhishek, S.: Performance evaluation of fuzzy DTC based PMSM for pumping applications. Ind. J. Sci. Technol. (2016) (in press)
8. Essalmi, A., Mahmoudi, H., Abbou, A., Bennassar, A., Zahraoui, Y.: DTC of PMSM based on artificial neural networks with regulation speed using the fuzzy logic controller. Renew. Sustain. Energ Conf. (IRSEC) 879–883 (2014)
9. Niu, F., Wang, B., Babel, A.S., Li, K., Strangas, E.G.: Comparative evaluation of direct torque control strategies for permanent magnet synchronous machines. IEEE Trans. Power Electron. **31**(2), 1408–1424 (2016)

Modeling and Simulation of Synchronous Reluctance Motor for Pumping Application Using Field-Oriented Control

V.K. Arun Shankar, S. Umashankar, S. Paramasivam, P. Sanjeevikumar and Y. Venkatesh

Abstract This paper presents field-oriented control (FOC) strategy to improve the performance of a synchronous reluctance motor (SynRM) drive system. In this article, the synchronous reluctance motor is used to drive the centrifugal pump that requires high power density. A mathematical model of SynRM is formed using dynamic equations of the motor. This motor model is then simulated using MATLAB Simulink. The suggested control strategy is reviewed, and its control performances (flux and current along direct and quadrature axes) are analyzed. Simulation results are presented to show the efficacy of the approach.

Keywords Field-oriented control (FOC) · Centrifugal pumps
Direct torque control (DTC) · MATLAB · Proportional integral (PI)
Synchronous reluctance motor (SynRM)

V.K. Arun Shankar · S. Umashankar (✉) · Y. Venkatesh
Department of Energy and Power Electronics, Vellore Institute of Technology (VIT) University, Vellore, Tamil Nadu, India
e-mail: umashankar.s@vit.ac.in

V.K. Arun Shankar
e-mail: arunshankar.vk@vit.ac.in

Y. Venkatesh
e-mail: venkateshyaramacha@gmail.com

S. Paramasivam
Danfoss Industries Private Limited, Chennai, Tamil Nadu, India
e-mail: paramsathya@yahoo.com

P. Sanjeevikumar
Department of Electrical and Electronics Engineering, University of Johannesburg, Auckland Park, Johannesburg, South Africa
e-mail: sanjeevi_12@yahoo.co.in

A. Konkani et al. (eds.), *Advances in Systems, Control and Automation*,
Lecture Notes in Electrical Engineering 442, https://doi.org/10.1007/978-981-10-4762-6_31

1 Introduction

The rotor structure of a synchronous reluctance motor (SynRM) is robust and simple [1]. They are capable of rotating at very higher speeds in hot climatic conditions also, since there are no windings in the rotor [2, 3].

The modeling and simulation of SynRM is carried out using MATLAB/Simulink software. MATLAB consists of a variety of block sets and toolboxes depending on requirements. For modeling the drive, Simulink provides the necessary components. SynRM was created from the dynamic equations that describe the motor [4]. The electrical parameters must be known for simulation of any machine. These parameters can be either calculated or measured [5, 6].

In asynchronous motors, air-gap flux induces the rotor currents. Whereas in permanent magnet synchronous motor and a synchronous reluctance motor, the rotor currents are generated using permanent magnet or field winding [7].

Figure 1 shows the stator and rotor laminations of the synchronous reluctance motor. I_d can be calculated using the following equation which is further used to calculate $L_{md.}$

$$I_d = \frac{U_{s,ph}}{j\omega_s L_d} \tag{1}$$

The general equation to calculate L_d is as follows:

$$L_d = L_{md} + L_{s\sigma} \tag{2}$$

Mutual flux linkage along d-axis can be calculated using the following equations:

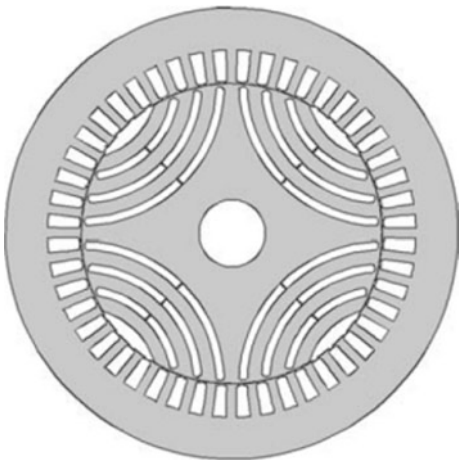

Fig. 1 SynRM—stator and rotor laminations

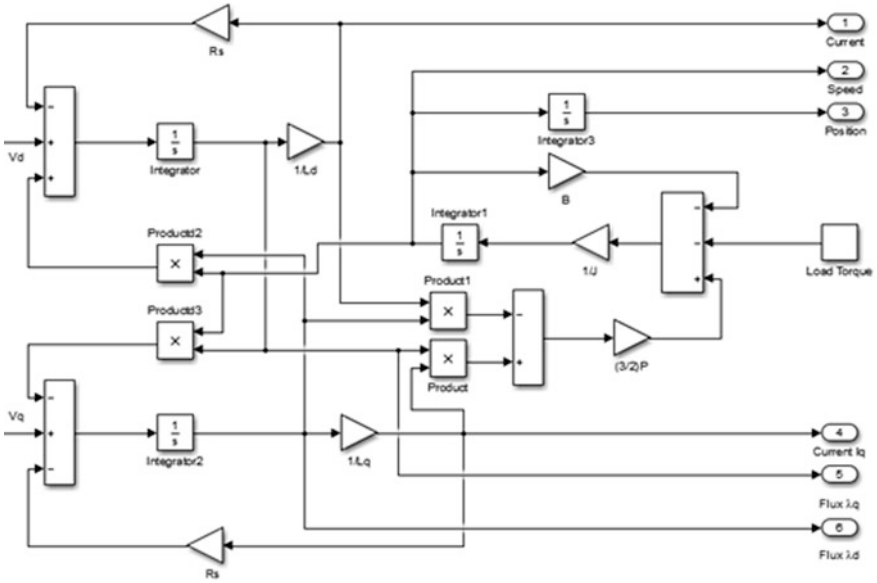

Fig. 2 Simulated SynRM drive in Simulink

$$\hat{\psi}_{md} = k_{ws1} N_s \frac{2}{\pi} \tau_p l' \hat{B}_{\delta d} \tag{3}$$

$$\hat{\psi}_{md} = k_{ws1} N_s \frac{2}{\pi} \frac{\mu_0 \hat{\Theta}_{sd}}{\delta_{\text{def}}} \tau_p l' \tag{4}$$

L_{pd} can be calculated by dividing the Eq. (3) by Eq. (1).

$$L_{pd} = \frac{2}{\pi} \mu_0 \frac{1}{2p} \frac{4}{\pi} \frac{\tau_p}{\delta_{\text{def}}} l' (k_{ws1} N_s)^2 \tag{5}$$

Calculating L_d and L_q for any rotor structure, the model of synchronous machine can be treated as synchronous reluctance machine. Figure 2 shows the MATLAB Simulink model of SynRM.

2 Modeling of Controller

The vector control strategy based on one fact that on the basis of rotor position, we are going to apply voltage vector. This principle is useful for all the drives that exist today. Obtaining the rotor position is not an easy task as it requires sensor to detect rotor position. Sensors have two main shortcomings. It is disturbed by noise, and it is costly.

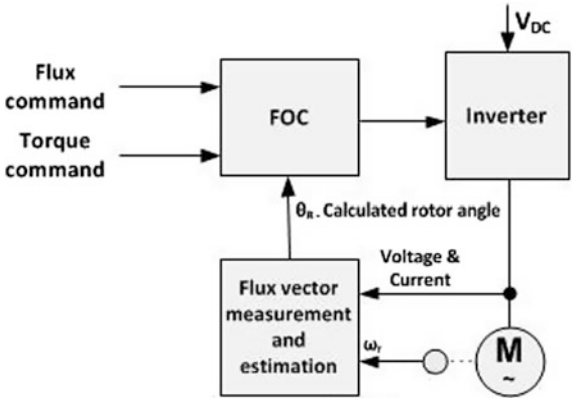

Fig. 3 General vector control block of FOC

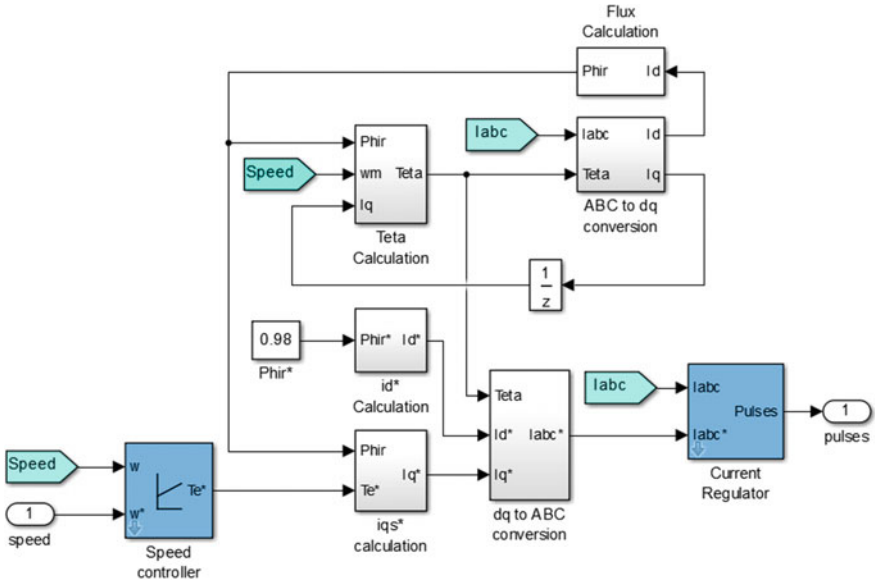

Fig. 4 Vector control block of FOC

The drive system must be efficient in terms of cost and performance. To solve these two problems, the two main transformation of power system is used: Park and Clarke transforms. These transforms are very useful in implementing sensorless drive system. The equation for torque can be written in the form:

$$T_e = \frac{3}{2}\left(\frac{p}{2}\right)\left(1-\frac{L_q}{L_q}\right)\psi_d I_q \tag{6}$$

Figure 3 represents constant I_d FOC control of SynRM. On the basis of magnetizing inductance, the position of rotor is calculated. Using this position, current is controlled and the vector control of FOC is illustrated in Fig. 4.

3 Simulation Results

Field-oriented control was employed with the SynRM model using the parameters given in Table 1, and the following results were obtained as shown in Fig. 5.

A centrifugal pump has been used to replace the load, and the output of the pump is observed. The output waveforms are shown in the Fig. 6. Before opening

Table 1 Parameters of SynRM model

Parameters	Values
L_d (H)	1.2
L_q (H)	0.1
Voltage (V)	415
R (Ω)	4
Inertia (kg m^2)	0.125
Damping	0.009
Pole pair	2
f (Hz)	50

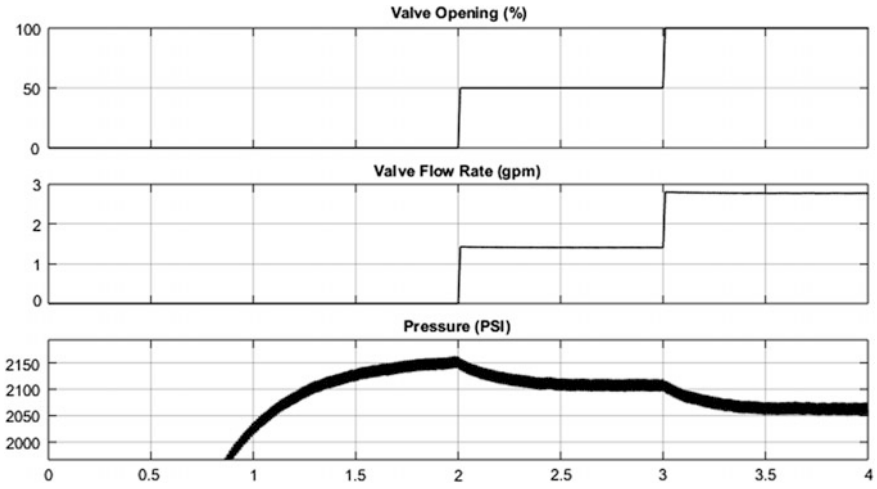

Fig. 5 Pump output for FOC

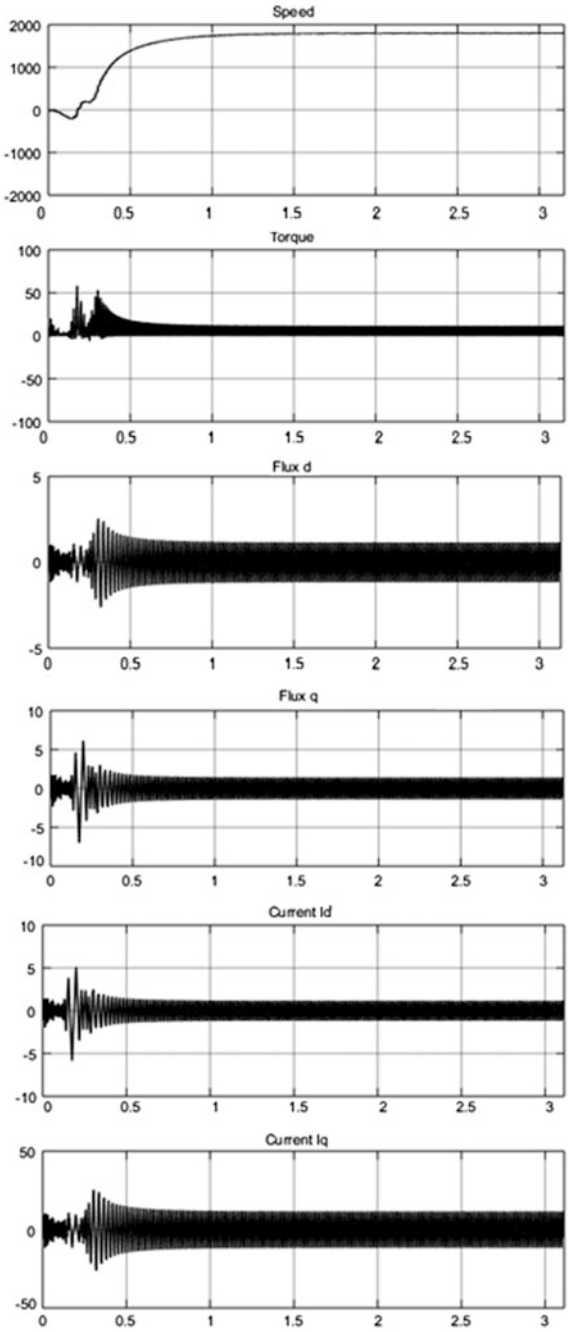

Fig. 6 Output graphs for FOC

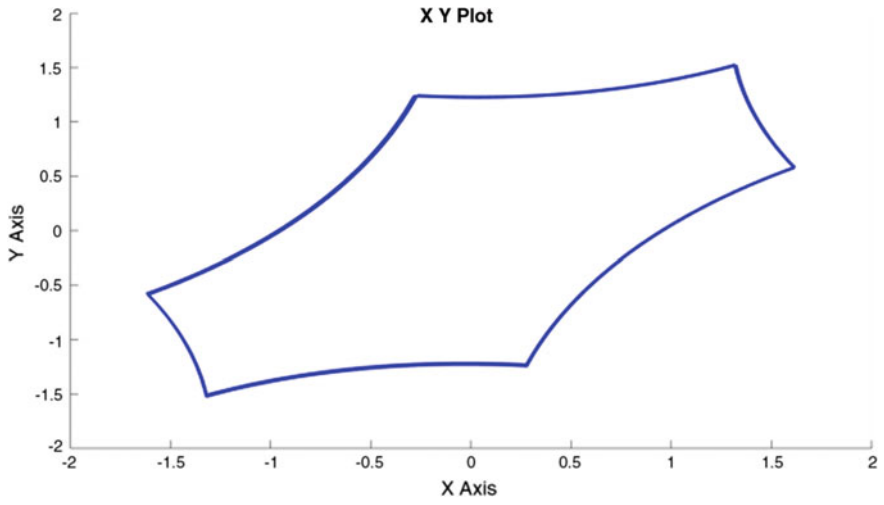

Fig. 7 Stator flux loci for FOC

of the valve, the speed should become constant. When the valve is partially opened at 1 s, the valve flow rate increases and the pressure is decreased. This pattern is also observed when the valve is opened again at 2 s.

From the Fig. 6, the speed gets constant at 1750 rpm which is set as the reference value. The motor torque is not always positive in this case. The torque is settling at a constant value of 10 Nm which is desired for any pumping applications. The torque fluctuates till the speed gets constant. This is because the motor is unable to drive the pump when the speed is low. As the losses, damping and saturation are not considered in designing this model, so the fluxes and the currents are oscillating in nature. These results were also verified.

Figure 7 shows the stator flux loci for FOC. The flux is generated according to voltage vector to run the rotor smoothly.

4 Conclusion

FOC is better in comparison to other control technique as it gives lower torque and flux ripple. It gives similar result to PMSM except lower power and torque density. Its dynamic response is slow as voltage vectors are not easy to calculate when SynRM is disturbed. FOC has higher complexity due to the fact that it uses Clarke and Park transforms; also, it consists of ramp function with PI controller which increases the speed of motor during starting to calculate torque. Position of rotor is also important to calculate and apply required current. The SynRM shows similar dynamic and transient as its predecessor. The major advantage that it offers is fewer ripples as it has no armature circuit and permanent magnet which distort the stator

magnetic field. On controlling with FOC, it reduces ripple. The losses are not considered due to limitation of mathematical modeling. This model is simple but useful in understanding SynRM performance while changing saliency ratio.

References

1. Danfoss Industries.: Facts worth knowing about frequency converters (2014)
2. Pyrhonen, J., Jokinen, T., Hrabovcova, V.: Design of rotating electrical machines. Wiley (2008)
3. Liu, T.H.: Controller design for synchronous reluctance motor drive systems with direct torque control. National Taiwan University of Science and Technology (2011)
4. Mostafa, A.F., Daw., Abaid, E.: Modelling and simulation of reluctance motor using digital computer. Int. J. Comp. Sci. Electron. Eng. (IJCSEE) **1**(2) (2013)
5. Ahmad, G.: Wide range speed sensorless vector control of synchronous reluctance motor with startup ability. Graduate School of Life Science and Systems Engineering Kyushu Institute of Technology (2007)
6. Niu, F., Wang, B., Babel, A.S., Li, K., Strangas, E.G.: Comparative evaluation of direct torque control strategies for permanent magnet synchronous machines. IEEE Trans. Power Electron. **31**(2), 1408–1424 (2016)
7. Hidouri, S.H.N., Sbita, L.: FOC drive scheme for a photovoltaic water PMSM-pumping system. Proc. Eng. Technol. **2**, 27–32 (2013)

Advanced Variable Structure Control for Distributed Power Generation

S.B. Mahajan, Arjun H. Kardile, Shital M. Mule, Ravindra M. Nagarale and P. Sanjeevikumar

Abstract Load frequency control is the core problem in distributed power generation. A novel technique is employed to control frequency with the help of variable structure controller. Here the small-scale hydroelectric power plant (SS-HEPP) is a best alternative source of energy in remote area. SS-HEPP is used for modeling and simulation in MATLAB. Also, the conventional sliding mode controller and PI controller with proposed control strategy are compared.

Keywords Small-scale hydroelectric power plant
Variable structure control · Fuzzy logic · SMC method

S.B. Mahajan (✉) · S.M. Mule
Department of Electrical and Electronics Engineering,
Marathwada Institute of Technology, Satara Parisor, Aurangabad, India
e-mail: sagar25.mahajan@gmail.com

S.M. Mule
e-mail: shitalmule123@gmail.com

A.H. Kardile
Deogiri Institute of Engineering and Management Studies, Aurangabad, India
e-mail: arjunkardile123@gmail.com

R.M. Nagarale
College of Engineering, Ambajogai, India
e-mail: rmnagarale@yahoo.com

P. Sanjeevikumar
Department of Electrical and Electronics Engineering,
University of Johannesburg, Auckland Park, Johannesburg, South Africa
e-mail: sanjeevi_12@yahoo.co.in

P. Sanjeevikumar
R&D Technologies, Chennai, Tamil Nadu, India

A. Konkani et al. (eds.), *Advances in Systems, Control and Automation*,
Lecture Notes in Electrical Engineering 442, https://doi.org/10.1007/978-981-10-4762-6_32

1 Introduction

Electricity has become significant part of industry and modernized civilization. This electricity must be provided to consumer at a specified voltage and frequency to operate gadgets. Due to economic and easy transmission, distribution electricity demand is increasing progressively. But due to restrictions on exhausting energy sources, the efficient use of nonexhausting sources is compulsory to achieve the rising energy burden [1–4]. Sometimes to provide uninterrupted power supply in inaccessible areas of country is problematic. Distributed power generation using available nonconventional sources is best alternative for electrification of remote areas [5–9]. The kinetic energy of flowing water can be utilized for electricity production in small tributary using small-scale hydroelectric power plants (SS-HEPPs). A valuable task is worked out by the SS-HEPP in generation of electricity and the growth of pastoral and remote areas in budding nation [10]. However, cavity among demand of electrical energy and generation is aggregating daily due to increasing electrification and limitations of conventional energy sources. This is increasing the burden on available generating stations. Furthermore, load sharing is compulsory to do by disconnecting small village electricity from grid for few minutes. Relying on small electric loads from distant vicinity on grid supply can be reduced by making use of separate generation units using local renewable resources [11]. Thus, extents having plenty of water storage can also be engaged for SS-HEPP. The hydroelectric power has profuse but unused potential in many region of the globe and can compose a major contribution to energy needs in future [10, 11]. Such electrical power generation is already a flourishing and proficient verified technology, but need to improve controllability of this system [10]. Power plants parameters need to maintain in specific value to obtain the precise and valuable routine[12]. Frequency can be upheld via rejecting the divergence between load and generation demand while voltage magnitude is sustained by means of control circuitry.

1.1 Traditional Frequency Control Methodology of SS-HEPP

In SS-HEPP, the output frequency control mechanism is not in practice due to huge expenditure [11]. In stand-alone SS-HEPP due to lack of storage provision, total power is converted into electrical energy irrespective of overall requirement. Load fluctuations are suppressed with dump load which are usually resistive. Frequency

control of SS-HEPP system with dump load is depicted in Fig. 1; therefore, the actual and dump load can be always continued to have same electric power [10]. The prime necessity of SS-HEPP is water for use of irrigation.

1.2 Construction of Proposed System

In this technique, the valve control mechanism is used to guard the quantity of inlet supply to the SS-HEPP at penstock driven as shown in Fig. 2.

In this case, servo electrical machine is employed whose angular momentum is maintained by controlling command. The advantages of servo electrical machine is that it is well-suited with processor, linear characteristics, quick response, etc. [11]. In this anticipated method, servo electrical DC machine is operated for governing the input supply flow through penstock.

In many methods, for certain operating conditions only linear system is considered while designing the frequency controller. The electrical components have nonlinear characteristics which result in the occurrence of uncertainties in few parameters, and due to this, traditional controller's routine gets changed and affected. Hence, it is very important to plan a good controller which has strength against the parameter variations, uncertainties, and outside turbulence. In this article, a fuzzy-based PI controller is recommended for frequency control of SS-HEPP.

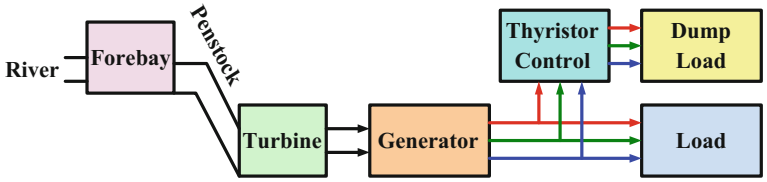

Fig. 1 Frequency control of SS-HEPP system with dump load

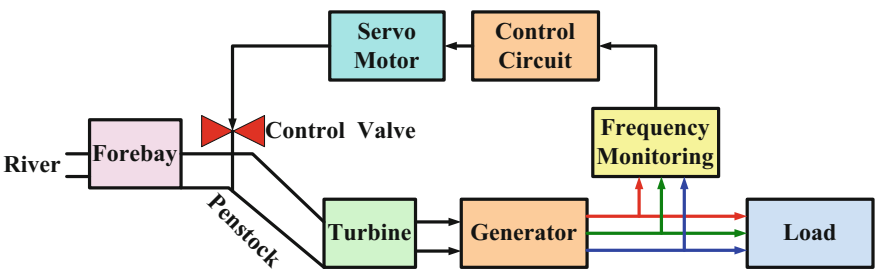

Fig. 2 Small-scale hydroelectric power plant (SS-HEPP) proposed system

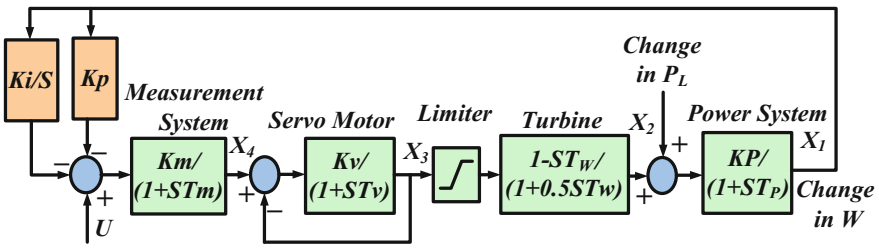

Fig. 3 Non-linear design of SS-HEPP PI controller

2 PI Controller and Fuzzy Logic-Based Controller

Proportional integral controller is used for nonlinear design of SS-HEPP as elaborated in Fig. 3 [12]. The model consists of following parts such as the proportional integral (PI) controller, the dimension system, model of servo electric machine, and rotary mechanical device. At various operating conditions, the performance of PI controller is affected by system nonlinearity and parameter uncertainties [12], so it is appropriate to utilize well-built control method in opposition to these nonlinearity characteristics of the system.

2.1 Conventional Sliding Mode Controller

Sliding mode controller (SMC) is used in control strategy of variable structure control. The key benefits of the SMC are toughness against nonlinearity, external turbulence, and fast active response. Also, this method is simple in design and implementation [13]. In SMC, system state oscillates around sliding surface and does not stay on it due to uncertainties in parameters and restriction of high switching frequency. The oscillations caused in system are called as chattering [12–15]. This occurrence of chattering is unwanted as it may raise the control behavior and stimulate the high frequency [13–15]. SMC is providing a viable solution to control nonlinear system range.

Consider a nonlinear system.

$$x(t) = f(x) + b(x)u(t) + D(t) \tag{1}$$

where nonlinear functions are $f(x)$ and $b(x)$,

$D(t)$ is trouble occurs in the system and system state vector is $x(t)$.

$$\tilde{x}(t) = [x(t) - x_d(t)] \tag{2}$$

where required and error state vector of system is $x_d(t)$ and $\tilde{x}(t)$, respectively.

$$\left.\begin{array}{l} s(t) = \left(\frac{\mathrm{d}}{\mathrm{dt}} + \lambda\right)^{(n-1)} \tilde{x}(t) \\ \lambda > 0 \end{array}\right\} \tag{3}$$

where *s(t)* is switching function.

The control law is specified as,

$$u(t) = u_{\mathrm{eq}}(t) + u_n(t) \tag{4}$$

where $u_{\mathrm{eq}}(t)$ and $u_n(t)$ are elements of the input [12]. Traditionally, $u_n(t)$ is defined by switch sign function as,

$$u_n(t) = k(s)\mathrm{sgn}(s) \tag{5}$$

where $k(x)$ is switching factor, and it is particular more than utmost compared to uncertainty as $s\dot{s} < 0$. The main complexity in this traditional SMC is unwanted chattering in response to system due to the irregular extent in size of $k(x)$ [13]. In fuzzy-SMC, chattering is eliminated and also enhanced the system response.

2.2 *Fuzzy-SMC Design*

When the system state is away from the sliding level, the switching factor $k(x)$ must be augmented in same amount to gain the appropriate response from SMC [13]. To get rid of the chattering, it is proposed to substitute the sign function $k(x)\mathrm{sgn}(s)$ in control law with fuzzy function $u_f = k_{\mathrm{fs}}(t)u_{\mathrm{fs}}(t)$ and the controller utilized is identified as fuzzy-SMC, and Fig. 4 depicts the block diagram of the fuzzy-SMC.

Control law equations are

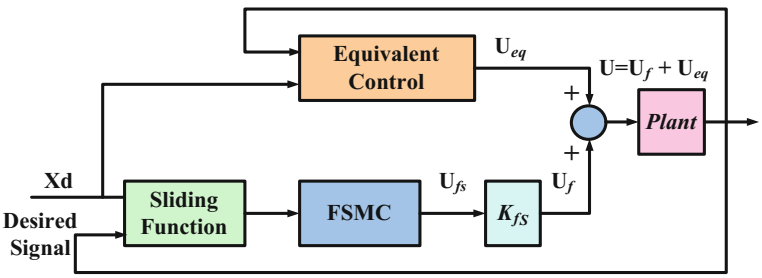

Fig. 4 Block diagram of proposed fuzzy-SMC

$$u(t) = u_{\text{eq}}(t) + k_{\text{fs}} u_{\text{fs}}(t) \tag{6}$$

$$\left.\begin{aligned}
\dot{x_1} &= \tfrac{-1}{T_p} x_1 + \tfrac{K_p}{T_p} x_1 - \tfrac{2K_p}{T_p} x_3 - \tfrac{K_p}{T_p} \Delta P_1 \\
\dot{x_2} &= \tfrac{2}{T_p} x_1 + \tfrac{2}{T_w} x_3 \\
\dot{x_3} &= \tfrac{-(1+K_v)}{T_p} x_1 + \tfrac{K_v}{T_v} x_4 \\
\dot{x_4} &= \tfrac{-1}{T_m} \dot{x_4} - \tfrac{K_m}{T_m} x_5 + \tfrac{K_m}{T_m R} x_1 + \tfrac{K_v}{T_v} u \\
\dot{x_5} &= K_1 x_1
\end{aligned}\right\} \tag{7}$$

$$s(t) = \begin{pmatrix} 1.5(x_1 - x_{1\text{ref}}) + (x_2 - x_{2\text{ref}}) \\ +2(x_3 - x_{3\text{ref}}) + 3.2(x_4 - x_{4\text{ref}}) \end{pmatrix} \tag{8}$$

$$u(t) = u_{\text{eq}}(t) - k_{\text{fs}} u_{\text{fs}} \tag{9}$$

$$u_{\text{eq}}(t) = \frac{T_m}{K_m} \begin{pmatrix} \tfrac{-10}{T_p} x_1 + \tfrac{10K_p}{T_p} x_2 - \tfrac{20K_p}{T_p} x_3 \\ -10\dot{x_{\text{ref}}} + \tfrac{2}{T_w} x_2 + \tfrac{6}{T_w} x_3 - x_{2\text{ref}} \\ + \tfrac{-(1+K_V)}{T_v} x_3 + \tfrac{k_v}{T_v} x_4 - \dot{x}_{3\text{ref}} - \tfrac{-1}{T_m} x_4 \\ - \tfrac{k_m}{T_m} x_5 - \tfrac{k_m}{T_m \cdot R} x_1 - \dot{x}_{4\text{ref}} \end{pmatrix} \tag{10}$$

To realize the fuzzy-SMC on SS-HEPP, the equation of the system state is given in Eqs. (7)–(10). From Eqs. (3) and (6), the equivalent control law and the sliding surface can be obtained to propose fuzzy-SMC shown in Eq. (8).

3 Variables, Membership Functions, and Fuzzy Rule

$$\begin{aligned}
s &= \{N,\ Z,\ P\} \\
\dot{s} &= \{\text{N},\ \text{Z},\ \text{P}\} \\
u_{\text{fs}}(t) &= \{NB,\ NM,\ NS,\ Z,\ PS,\ PM,\ PB\}
\end{aligned}$$

where s *and* $\dot{s}$ are input control variables, and $u_{\text{fs}}(t)$ is output variable

The output and input variables pattern of membership is illustrated in Fig. 5a. Fuzzy logic is an automatic control methodology where on the basis of expert's experience control laws are constructed [12]. Figure 5b depicts the switching function from which fuzzy rule is derived. Derived fuzzy rules are given in Table 1.

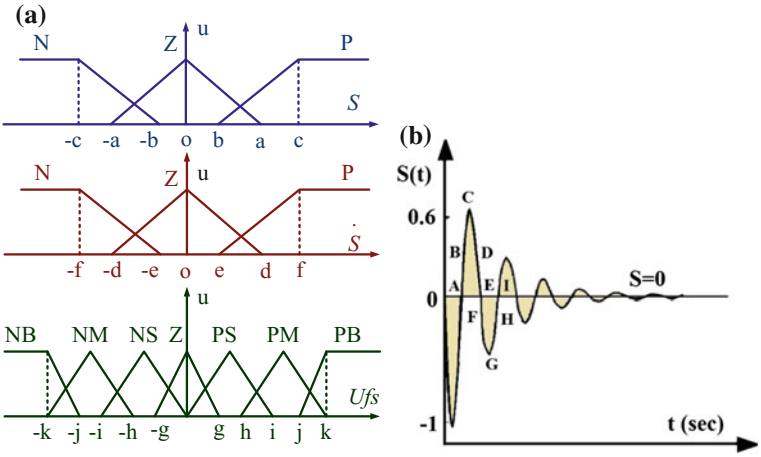

Fig. 5 **a** Output and input pattern of fuzzy-SMC, **b** switching function

Table 1 Rules for proposed fuzzy controller

u_{fs}		S		
		N	Z	P
$\dot{S}$	Z	NS	Z	PS
	N	NB	NB	NM
	p	PM	PB	PB

4 Proposed Control Strategy Simulation Result

To examine the performance of proposed control and traditional control methods simulations are carried at various operating parameters for frequency controlling SS-HEPP.

The simulation model of SS-HEPP in which PI controller is used for the frequency control is shown in Fig. 3. The response of the system for 0.1 pu change in load using PI controller is shown in Fig. 6a. From the simulation model, the settling time of the PI controller system response is observed to be 80 s with the peak overshoot of 3.3. In Fig. 6b response of proposed system is shown. In proposed control strategy, very smooth control signal is achieved as unwanted chattering is removed. In response to proposed control system, the settling time and peak overshoot are reduced to 6 s and 0.58, respectively.

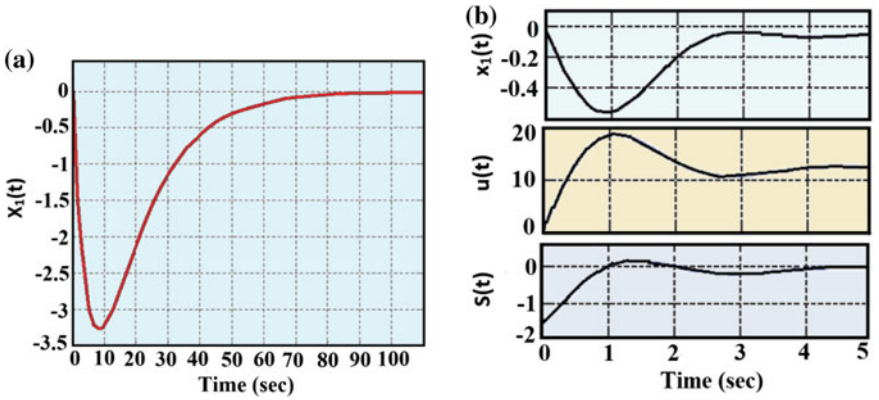

Fig. 6 **a** Frequency response of power plant with PI controller, **b** proposed system response

5 Conclusions

In this article, fuzzy-based sliding mode control strategy is proposed for small-scale hydroelectric power plant (SS-HEPP). The simulation result validated the concept and effectiveness proposed control strategy. Moreover, the proposed control provides a viable solution in load change, parameters variations, outside turbulence, and uncertainties.

References

1. Mahajan, S.B., Sanjeevikumar, P., Blaabjerg, F., Ojo, O., Seshagiri, S., Kulkarni, R.: Inverting Nx and 2Nx non isolated multilevel boost converter for renewable energy application. In: IET International Conference on Clean Energy and Technology, Malaysia (2016)
2. Mahajan, S.B., Draxe, K.P., Pandav, K.M.: A novel asymmetric multilevel inverter with minimum number of switches for renewable power grid applications. In: IEEE International Conference on Green Computing, Communication and Conservation of Energy, India (2013)
3. Mahajan, S.B., Sanjeevikumar, P., Ojo, O., Rivera, M., Kulkarani, R.: Non-isolated and inverting Nx multilevel boost converter for photovoltaic dc link applications. In: IEEE International Conference on Automatica, Chilean Association of Automatic Control, Chile (2016)
4. Mahajan, S.B., Sanjeevikumar, P., Blaabjerg, F., Norum, L.E., Ertas, A.: 4Nx non-isolated and non-inverting hybrid interleaved boost converter based on VLSI cell and cockroft walton voltage multiplier for renewable energy applications. In: IEEE International Conference on Power Electronics, Drives and Energy Systems, India (2016)
5. Mahajan, S.B., Kulkarni, R., Sanjeevikumar, P., Blaabjerg, F., Fedák, V., Cernet, M.: Non isolated and non-inverting cockcroft walton multiplier based hybrid 2Nx interleaved boost converter for renewable energy applications. In: IEEE Conference Power Electronics and Motion Control, Europe (2016)

6. Mahajan, S.B., Kulkarni, R., Sanjeevikumar, P, Siano, P., Blaabjerg, F.: Hybrid non-isolated and non inverting nx interleaved dc-dc multilevel boost converter for renewable energy applications. In: IEEE International Conference on Environment and Electrical Engineering, Florence (2016)
7. Sanjeevikumar, P., Blaabjerg, F., Wheeler, P., Lee, K., Mahajan, S.B., Dwivedi, S.: Five-phase five-level open-winding/star winding inverter drive for low-voltage/high-current applications. In: IEEE Transportation Electrification Conference and Expo Asia-Pacific, Busan (2016)
8. Sanjeevikumar, P., Blaabjerg, F., Wheeler, P., Khanna, R., Mahajan, S.B., Dwivedi, S.: Optimized carrier based five-level generated modified dual three-phase open-winding inverter for medium power application. In: IEEE Transportation Electrification Conference and Expo Asia-Pacific, Busan (2016)
9. Sanjeevikumar, P., Mahajan, S.B., Pandav, K., Siano, P., Oleschuk, V.: Hexuple-inverter configuration for multilevel nine-phase symmetrical open-winding converter. In: IEEE International Conference on Power Electronics, Intelligent Control and Energy System, Delhi (2016)
10. Doolla, S., Bhatti, T.S.: Load frequency control of an isolated small-hydro power plant with reduced dump load. IEEE Trans. Power Syst. **21**(4), 1912–1919 (2006)
11. Doolla, S., Bhatti, T.S.: Automatic generation control of an isolated small-hydro power plant. Electr. Power Syst. Res. **76**, 889–896 (2006)
12. Zargari, A., Hooshmand, R., Ataei, M.: A new control system design for a small hydro-power plant based on particle swarm optimization-fuzzy sliding mode controller with Kalman estimator. Trans. Inst. Measur Control **34**(4), 388–400 (2011)
13. Boiko, I., Fridman, L.: Analysis of chattering in continuous sliding-mode controller. IEEE Trans. Autom. Control **50**(9), 1442–1446 (2005)
14. Hanmandlu, M., Goyal, H.: Proposing a new advanced control technique for micro hydro power plants. Electr. Power Energy Syst. **30**, 272–282 (2008)
15. Tarique, A., Gabbar, H.A.: Particle swarm optimization based turbine control. Intell. Control Autom. **4**, 126–137 (2013)

Investigation of Doubly Fed Induction Generator Behavior Under Symmetrical and Asymmetrical Fault Conditions

Karthik Tamvada, S. Umashankar and P. Sanjeevikumar

Abstract Electrical energy is required to run everyday appliances. It is generated by from conventional energy sources, which are exhaustible; therefore, the importance of non-conventional energy sources is increasing by the hour. Wind energy as an energy source is non-polluting and does not pose any threat to nature. For utilizing this source of energy, it is imperative to find suitable ways to harness it. This paper involves simulation of a DFIG for wind energy applications its investigation under different network fault conditions, both symmetrical and asymmetrical. The simulation is carried out with the aid of Simulink toolbox in MATLAB.

Keywords DFIG · Fault analysis · Modeling · Simulation · Electric grid

Nomenclature

v_{ds}, v_{qs}	Stator voltages in synchronous frame
v_{dr}, v_{qr}	Rotor voltages in synchronous frame
v_s, v_r	Stator and rotor voltage vectors
i_{ds}, i_{qs}	Stator currents in synchronous frame
i_{dr}, i_{qr}	Rotor currents in synchronous frame
i_s, i_r	Stator and rotor current vectors
Ψ_{ds}, Ψ_{qs}	Stator flux linkages in synchronous frame
Ψ_{dr}, Ψ_{qr}	Rotor flux linkages in synchronous frame
Ψ_s, Ψ_r	Stator and rotor flux vectors
R_s, R_r	Stator and rotor resistances
L_s, L_r	Stator and rotor self-inductances per phase

K. Tamvada · S. Umashankar
School of Electrical Engineering, VIT University, Vellore, Tamil Nadu, India
e-mail: umashankar.s@vit.ac.in

P. Sanjeevikumar (✉)
Department of Electrical and Electronics Engineering, University of Johannesburg, Auckland Park, Johannesburg, South Africa
e-mail: sanjeevi_12@yahoo.co.in

A. Konkani et al. (eds.), *Advances in Systems, Control and Automation*,
Lecture Notes in Electrical Engineering 442, https://doi.org/10.1007/978-981-10-4762-6_33

L_m	Magnetizing inductance per phase
L_{ss}, L_{rr}	Stator and rotor self-inductances
ω	Synchronous frequency
ω_r	Rotor electrical frequency
ω_b	Base frequency
T_e	Electromagnetic torque
p	Number of pole pairs

1 Introduction

Wind energy due to its economics and policies, environmental benefits, modularity, scalability, relative ease of installation, mature technology, and penetration in modern power systems [1–3] is the most preferred form of renewable energy. DFIG is a preferred choice in high-power grid-connected wind energy conversion systems, due to the huge economic gains resulting from reduced sizes of power converters and filters [4]. A DFIG is also capable of extracting best wind power for extended wind speeds, reduced mechanical stresses, and four-quadrant operation [5, 6]. It reduces the load stresses on different wind turbine parts, counting the base, tower, and blades. When efficiency of the turbine is higher, longer life time, and energy quality is improved to make these wind turbines inexpensively aggressive, although the initial cost is high [7–9]. Wind power plants are relatively nonlinear containing many uncertainties. The utility grid operators need to anticipate the vulnerability of the grids [10], for regulating wind energy integration into the electric grids. This article attempts to provide an overview on different fault issues related to DFIG connected to the electric grid. In this article, Sect. 2 gives brief overview of network faults effect on DFIG. Section 3 gives the dynamic equations for the modeling of DFIG, and Sect. 4 discusses the DFIG convertors; Sect. 5 provides the numerical simulation results and discussion for response of DFIG to different faults. Section 6 provides the conclusion of the paper. Figure 1 depicts the grid-connected doubly fed induction generator (DFIG).

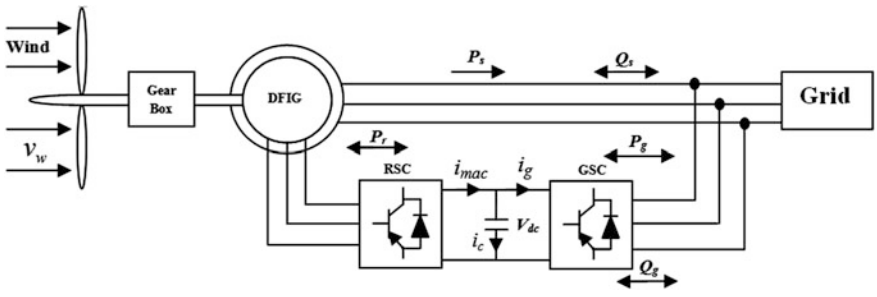

Fig. 1 DFIG configuration while connected to the grid

2 DFIG and Network Faults Types

All the network faults can be classified as symmetrical and asymmetrical faults. Various studies show that the highest chances of occurrence, compared to other types of faults, are for single-phase faults. DFIG enables power production at an effective cost resulting in decreased cost and increased power production capability. But, the DFIG systems are prone to unstable operating conditions during grid fault. This is due to direct interconnection between the electric grid and its stator terminals.

3 Dynamic Modeling of DFIG

Modeling of DFIG in synchronous d-q reference frame involves the use following equations:

$$v_{qs} = R_s i_{qs} + \omega/\omega_b \Psi_{ds} + 1/\omega_b \mathrm{d}/\mathrm{d}t \Psi_{qs} \tag{1}$$

$$v_{ds} = R_s i_{ds} - \omega/\omega_b \Psi_{qs} + 1/\omega_b \mathrm{d}/\mathrm{d}t \Psi_{ds} \tag{2}$$

$$v_{qr} = R_r i_{rs} + (\omega - \omega_r)/\omega_b \Psi_{dr} + 1/\omega_b \mathrm{d}/\mathrm{d}t \Psi_{qr} \tag{3}$$

$$v_{dr} = R_r i_{rs} - (\omega - \omega_r)/\omega_b \Psi_{qr} + 1/\omega_b \mathrm{d}/\mathrm{d}t \Psi_{dr} \tag{4}$$

$$\Psi_{qs} = -L_{ss} i_{qs} + L_m i_{qr} \tag{5}$$

$$\Psi_{ds} = -L_{ss} i_{ds} + L_m i_{dr} \tag{6}$$

$$\Psi_{qr} = L_{rr} i_{qr} - L_m i_{qs} \tag{7}$$

$$\Psi_{dr} = L_{rr} i_{dr} - L_m i_{ds} \tag{8}$$

The electric torque is given by,

$$T_e = 3/2p1/\omega_b (L_m/L_s)(\Psi_{qs} i_{dr} - \Psi_{ds} i_{qr}) \tag{9}$$

4 B2B Configuration of DFIG

The B2B (back-to-back) converter consists of rotor-side converter (RSC) and grid-side converter (GSC). These are voltage source converters that have a capacitor connected at the DC-link acting as the DC-link voltage source. RSC controls the generator speed, and GSC injects reactive power to the electric grid. Decoupled

power control is easily achieved by implementing vector control on the DFIG power converters.

(A) **Rotor-side converter (RSC)**

Overall power conversion for the DFIG takes place here for regulation of active and reactive power. Control of terminal voltages and power factor is also achieved by exchange of reactive power with the electric grid. It is rated less due to which in presence of a disturbance, large amount of currents cannot be safely handled. Considering RSC acting as a current source, the DFIG response is determined by network voltage and frequency; the speed of the rotor; and rotor currents. Under fault conditions, large rotor over-currents persist due to large changes in source voltage. This happens because of the delay associated with rotor voltage control and RSC limitations, necessitating RSC protection.

(B) **Grid-side converter (GSC)**

It is mainly responsible for DC bus regulation. It is also capable of processing active and reactive power. Depending on the operating conditions under faults, source of concern could be torque and active power oscillations. It is also influenced by the requirements of network management.

5 Numerical Simulation Results

The fault analysis is carried for constant wind speed of 15 m/s for L-G fault and L-L-G fault which are asymmetrical network faults along with three-phase fault which comes under the category of symmetrical faults. The converters' control can be carried out by vector control, which would generate the required pulses for the operation of the converters. The fault analysis is carried out with the aid of the Fault block embedded in Simulink. The various faults, both symmetrical and asymmetrical, are implemented on the grid side, and the behavior of the various parameters of the wind energy conversion system (WECS) is analyzed for different faults. Figure 2 shows DC link voltage (V_{Dc}) response to the faults. Figure 3 represents rotor speed (ω_r) response to the faults. Figure 4 depicts real power (P) response to the faults. Figure 5 illustrates reactive power (Q) response to the faults.

Large disturbances lead to high fault currents in RSC, and DC bus voltage rises rapidly. During the aforementioned faults, the converter becomes saturated leading to increase in DC-link bus voltage. This is because the saturated converter absorbs large amount of power. During the faults, the voltage dips resulting in decreased grid voltage. This causes drop in power transfer capability of the GSC, and the additional power cannot be evacuated to electric grid. This bonus power finds its way into the DC-link capacitor leading to incessant growth in its voltage. As observed from Figs. 2, 3, 4, and 5, highest fluctuations occur at the beginning of the fault. For three-phase fault, the magnitude of current can reach up to 3 p.u. nearly

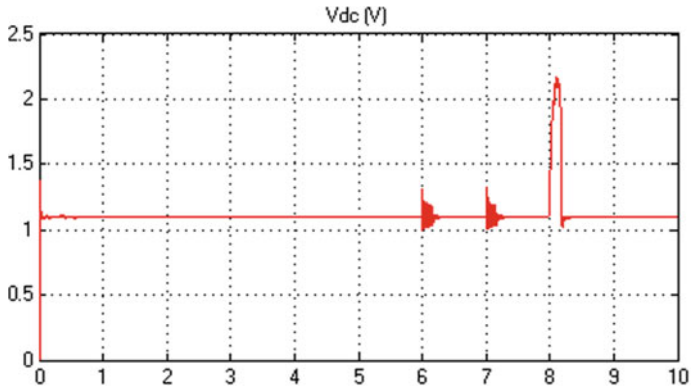

Fig. 2 DC link voltage (V_{Dc}) response to the faults

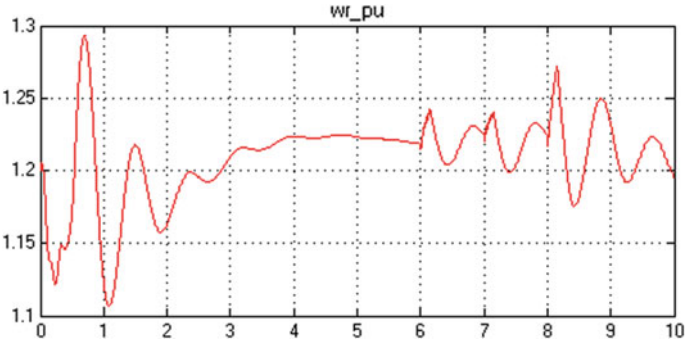

Fig. 3 Rotor speed (ω_r) response to the faults

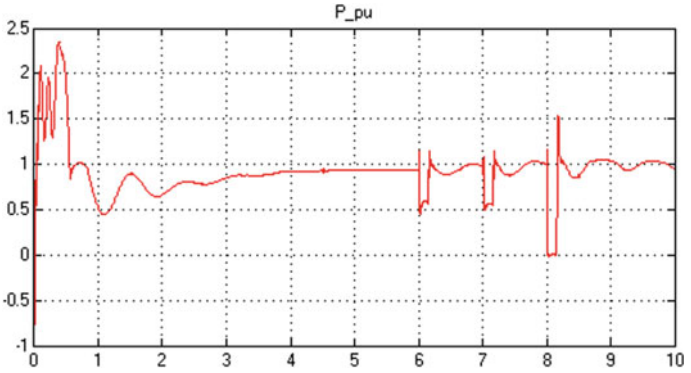

Fig. 4 Real power (P) response to the faults

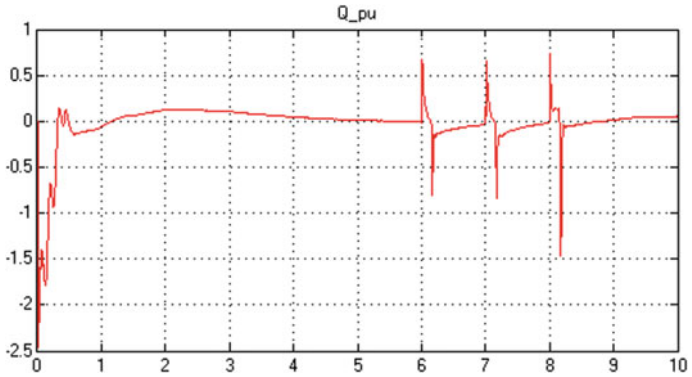

Fig. 5 Reactive power (Q) response to the faults

every time. This may lead to damage of the converters' semiconductor devices unless a overrated converter is used. Under three-phase fault, leakage inductances will be saturated due to an emf that causes rotor converter saturation. Under such conditions, analyzing the DFIG behavior becomes complicated due to deviation from the Superposition principle.

6 Conclusion

DFIG has an edge over other wind power generation technologies making them the favorite choice. In this article, different fault issues related to grid-connected DFIG have been simulated and an attempt is made to assess their severity for DFIG as in order to attain increased wind power penetration in the electric grid. Under severe faults, analyzing the DFIG behavior becomes complicated due to deviation from the Superposition principle. Analysis of fault conditions is necessary as the future of DFIG wind energy systems is to benefit both utility systems and individual consumers of energy in a safe and reliable manner to achieve optimum performance and provide grid resiliency to power quality issues.

References

1. Cheng, M., Zhu, Y.: The state of the art of wind energy conversion systems and technologies: a review. Energy Convers. Manag. **88**, 332–347 (2014)
2. Leung, DYC., Yang, Y.: Wind energy development and its environmental impact: a review. Renew. Sustain. Energy Rev. **16**(1), 1031–1039 (2012)
3. Saqib, M.A., Saleem, A.Z.: Power-quality issues and the need for reactive-power compensation in the grid integration of wind power. Renew. Sustain. Energy Rev. **43**, 51–64 (2015)

4. Carrasco, J.M., et al.: Power-electronic systems for the grid integration of renewable energy sources: a survey. IEEE Trans. Indus. Electron. **53**(4), 1002–1016 (2006)
5. Luna, A., Lima, F.K.A., Santos, D., Rodríguez, P., Watanabe, E.H., Arnaltes, S.: Simplified modeling of a DFIG for transient studies in wind power applications. IEEE Trans. Indus. Electron. **58**, 9–20 (2011)
6. Tohidi, S., Behnam, M.: A comprehensive review of low voltage ride through of doubly fed induction wind generators. Renew. Sustain. Energy Rev. **57**, 412–419 (2016)
7. Zhan, T.-S., Chen, J.L., Chen, S.-J., Huang, C.-H., Lin, C.-H.: Design of a chaos synchronisation-based maximum power tracking controller for a wind-energy-conversion system. Renew. Power Gener. IET **8**, 590–597 (2014)
8. Baloch, M.H., Wang, J., Kaloi, G.S.: Stability and nonlinear controller analysis of wind energy conversion system with random wind speed. Int. J. Electr. Power Energy Syst. **79**, 75–83 (2016)
9. Yang, L., Xu, Z., Østergaard, J., Dong, Z.Y., Wong, K.P.: Advanced control strategy of DFIG wind turbines for power system fault ride through power systems. IEEE Trans. Power Syst. **27**, 713–722 (2012)
10. Colak, I., et al.: Critical aspects of wind energy systems in smart grid applications. Renew. Sustain. Energy Rev. **52**, 155–171 (2015)

PLC-Based Modeling and Control of Heat Exchanger

Abinash Kumar Panda, Fijo M. Francis, Sudha Ramasamy and P. Sanjeevikumar

Abstract In this paper transfer function of a heat exchanger is implemented in MATLAB and is controlled by a PID controller. The controller is implemented in PLC (S7-1200). They both are interfaced using Arduino. The advantage of this method is that without having the actual plant, its response can be studied if the transfer function of a system is available. We have used Arduino Uno for interfacing PLC with MATLAB. The response of the system for three set points was noted. This project also shows that even though Arduino can be used for interfacing, the maximum output voltage of 5 V becomes the limitations. Transfer function of Heat exchanger is used in the recovery of soda in a paper pulp industry.

Keywords Heat exchanger · Programmable logic controller (PLC S7-1200) Proportional-integral derivative (PID) controller · Transfer function

1 Introduction

Usually, we do different type of response analysis in MATLAB using Simulink and command window but real-time control is not possible in these type of implementation. We just get a glimpse of what the system is like, whether the system or

A.K. Panda · F.M. Francis · S. Ramasamy (✉)
School of Electrical Engineering, Vellore Institute of Technology (VIT) University, Vellore, Tamil Nadu, India
e-mail: sudha.r@vit.ac.in

A.K. Panda
e-mail: abinashkp057@gmail.com

F.M. Francis
e-mail: fijomf92@gmail.com

P. Sanjeevikumar
Department of Electrical and Electronics Engineering, University of Johannesburg, Auckland Park, Johannesburg, South Africa
e-mail: sanjeevi_12@yahoo.co.in

A. Konkani et al. (eds.), *Advances in Systems, Control and Automation*,
Lecture Notes in Electrical Engineering 442, https://doi.org/10.1007/978-981-10-4762-6_34

plant is stable or unstable, but the real response of the system cannot be known. We can change the set point and see what happens in real time which is not usually possible in MATLAB and Simulink packages. That will only be known when the system is actually being controlled by a PID controller. Here, the MATLAB will behave like an actual plant, and the controller will control the developed plant in MATLAB in real time. So that we can analyze what actually is happening in between the plant and the controller. In this way, we are developing a new method to check the response of a real-time plant control without having the actual plant with us. To make the plant to interact with the controller, we have to take an interfacing device which will create the behavior of the plant inside it. The interfacing device can be controlled with PLC. To maintain a particular temperature in a heat exchanger will be very difficult, so we have implemented here a PID controller. The controller will try to maintain the current temperature given by the user. This PID logic can be implemented using the HMI which will use the human–machine interface device and maintain the temperature according to the user. But as a whole, the main thing will be done by PID controller implemented inside the PLC. The controller will maintain the temperature without affecting the plant stability. The performance of the system is determined in terms of settling time, peak time, and the percentage overshoot [1]. Generally, we use Ziegler–Nichols method to study different response of the plant, but real-time auto-tuning method is more effective compared to offline tuning like Ziegler–Nichols method This process of fine tuning provides some algebraic rules to tune the PID parameter. This tuning method is defined inside the PID controller which is designed by the S7-1200 manufacturer. The process is verified here as a real-time implementation. In this process, we can implement the stabilization for an nth order system also. Usually, PID control done by using a dedicated test signal, but a real-time plant response is taken as input to the PID controller in this paper [2].

Here the PID controller is discretization PID controller it will be more interactive with the process that we are implementing in. Here, also the sampling time taken as 0.5 and 0.3 s for observations. The PID controller [3] will add one pole or zero according to the plant model and make the system stable. It is more important that the plant properties should not be affected with the help of the implementation of PID controller, so real-time implementation plays an important role in this case [4–6]. There are variety of control schemes such as internal model predictive control, smith predictor control, dynamic matrix control, and cascade control; all these schemes of control system use PID controller as their main control part so if the PID control action will be online, then the desired control scheme can be implemented in an effective way. This enables us to come out from simulation area to a real-time implementation in laboratory [7].

Arduino Uno [8] is a microcontroller which is based on AT-mega 328P. It has 6 analog input pins, 14 digital input and output pins. Out of these, 14 pins and 6 pins can be used as PWM (Pulse-Width Modulated) output pins. It uses 16 MHz quartz crystal. It also has an ICSP (In-circuit Serial Programming) header and a button for reset.

PLC contains three important parts; they are power supply, CPU, I/O modules [8]. The I/O modules can be divided into analog and digital I/O's. The PLC used in our laboratory for the experiment is S7-1200 [9], and its processor is CPU 1214C. It has 4 MB internal load memory (each data log file can contain maximum of 500 KB) and has 14 digital input ports and 10 digital output ports. It also has 2 analog input and 4 pulse output ports and uses Ethernet for communication purpose. It has a math execution speed of 2.3 µs per instructions. Total integrated automation (TIA V13) writes the program into the CPU [8]. Here, set point is taken as digital signal and PWM techniques used for giving the output signal. The range of input signal is usually 0–24 V, and the range of output signal is 0–12 V, which is also matching the range of Arduino input voltage range, so interfacing both the devices becomes easier. The selected heat exchanger is used in the recovery of soda in a paper pulp industry. In paper industry, chemicals are used to separate cellulose from wood and other substances used for the production of paper. After doing this process, these chemicals have to be recovered for the economical operation of the plant. So the resultant product is burned to produce heat, which is used to produce steam and run the turbine to produce electricity.

2 Methodology

Here, the interfacing of MATLAB with PLC using Arduino Mega 2560 is shown in Fig. 1. The plant model in MATLAB is burnt into Arduino [10]. The response of the plant is taken and given to the PLC via its analog input port. The necessary control action is taken by the PID implemented in the PLC is given back to Arduino through its analog input ports. Figure 2 shows the transfer function implementation in MATLAB through Arduino. Here, analog input block is used to read analog input signals. The port numbers are specified as 0–5, and any one port can be chosen to receive the signal from the PLC. Arduino can read 0–10 V in its input port. Arduino converts the voltage into bit value; for example, it assigns 1024

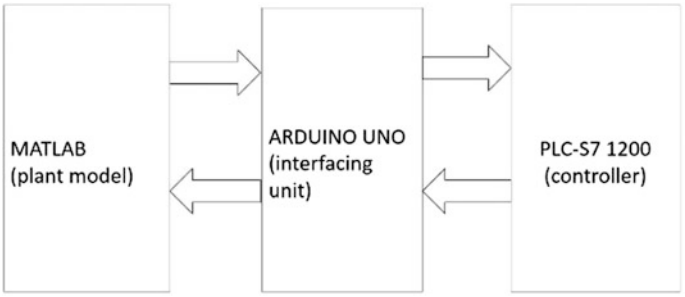

Fig. 1 Generalized block diagram of the control flow from MATLAB to Arduino and from Arduino to PLC

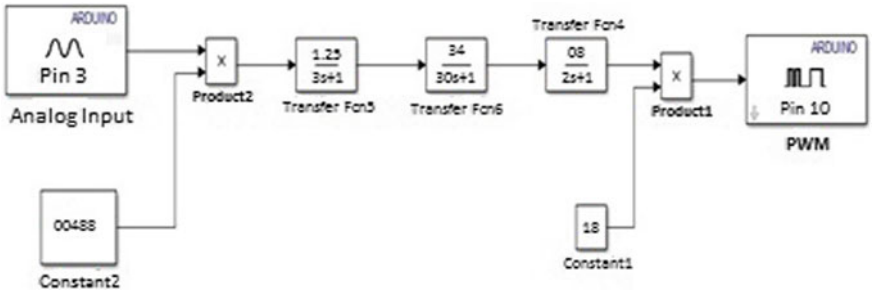

Fig. 2 Plant model implemented in MATLAB

(0011 1111 1111) for 10 V and 512 (0001 1111 1111) for 5 V. The calculation is made (5/1024 is multiplied) to normalize this assigned value in the range of 0–5 V. This voltage is given as input to the valve transfer function; its output is given to the heat exchanger transfer function. The output from the heat exchanger transfer function is taken by the sensor transfer function and given to the Arduino PWM block. The sensor output is converted as duty cycle value by normalizing it and that input is fed to the PWM block which is now determining the duty cycle of PWM. For ex: if duty cycle of 127 PWM block gives 2.5 V, 255 PWM gives 5 V etc. Heat Exchanger model [4] is implemented in MATLAB. The transfer function of heat exchanger gives the relationship between flow of steam entering into the heat exchanger and the temperature of the fluid coming out of the heat exchanger of the other side which is given in Eq. (1). This process of steam inflow into the heat exchanger is usually controlled by the valves. The transfer function of the valve is given in Eq. (2). Now, PLC will control that valve through the appropriate PID parameters which is converted as voltage. This voltage controls the valve which regulates the steam flow. The output side of heat exchanger temperature is fed to the PID controller through the sensor whose transfer function is given in Eq (3).

Transfer function of heat exchanger [4] is given below:

$$G_p(S) = 34/(30s + 1) \tag{1}$$

Transfer function of the control valve:

$$G_c(S) = 1.25/(3s + 1) \tag{2}$$

Transfer function of the temperature sensor is:

$$G_t(S) = 0.08/(2s + 1) \tag{3}$$

The whole process is described in the steps given below:

- The plant, feedback sensor, and actuator transfer function is made available in Simulink through the transfer function block. Arduino and MATLAB are connected through the Arduino Simulink support package in MATLAB [9].
- The PLC is programmed by using TIA V13 software which drives the PLC S7-1200.
- The PID controller is created in the PLC cyclic block.
- All the I/O ports which are needed for the PLC to communicate with Arduino are defined.
- MATLAB and Arduino are interfaced through the ports. The output signal is pulse-width modulated (PWM), and it is given to the Arduino via its analog input port.

3 Interfacing

The PID controller is designed in PLC software as given in Fig. 3. The PID controller can only be implemented in the cyclic block present in PLC. As this is a real-time implementation, the time constraints here are very important. PID is a closed loop controller that is used in many processes to minimize the error value and to achieve the desired set points. It has 3 control actions: proportional (P), integral (I), and derivative (D).

Proportional produces a control action proportional to the present error value. It is adjusted by varying the proportional gain constant. Integral produces a control action that is proportional to the magnitude and duration of the error. It can be varied by varying integral gain constant. It helps the system to reach the set point faster. Derivative control improves the transient performance of the system. It anticipates the error and produces the automatic control action accordingly. It can be adjusted by varying the derivative gain constant. In heat exchanger to maintain its temperature to the desired set point, PID controller is implemented through PLC. The controller should react to the process within a stipulated time; otherwise, the process cannot be controlled in the desired manner. In this way, our method is different from other models. The online fine tuning system given inside the PLC was used for tuning the PID. There are two types of tuning system inside PLC out of which fine tuning mode was implemented. The sampling time was taken to be 0.001 s. By implementing the above mentioned methods, the PID control was implemented in PLC. After tuning process is completed, the PID parameters are set automatically which is shown in Fig. 4. The response is shown in Fig. 5 which also gives the enlarge view of the reading.

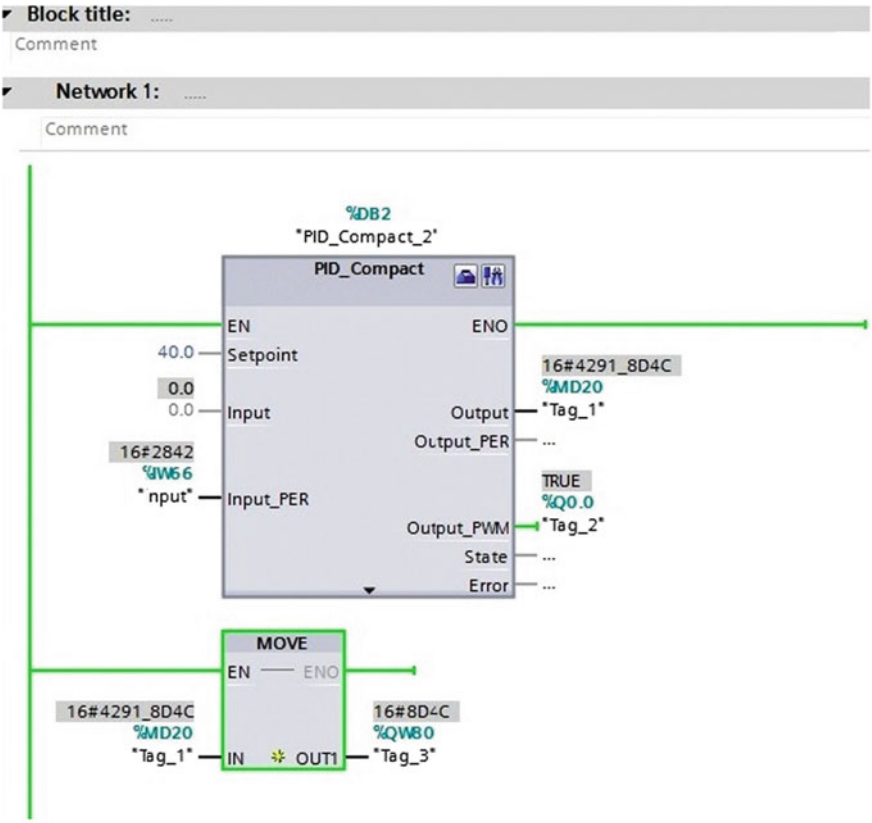

Fig. 3 Block diagram representing the PID control block in PLC S7-1200

4 Results and Conclusion

Figure 6 shows settling time of 2750 s with 45 °C set point. From the above responses when the present temperature of the heat exchanger increases above the set point, the control input is decreasing which implies that the actuator which is controlling the valve will reduce the flow of steam to the heat exchanger. As a result the temperature starts decreasing. The reverse will happen when the present temperature of the heat exchanger decreases below the set point. From Fig. 6, we infer that the plant takes some time to settle to the set point. In Figs. 5 and 6, it is seen that the control action and the temperature are varying rapidly, which is taken after certain interval; it is seen that the temperature has settled to the set point. It is observed that as input increases from the set point, the controller output decreases proportionally and vice versa. It takes some time for the system to auto-tune itself. Since Arduino is having the maximum possible output voltage of 5 V, the rating of the output temperature of the flow from the heat exchanger is restricted within the

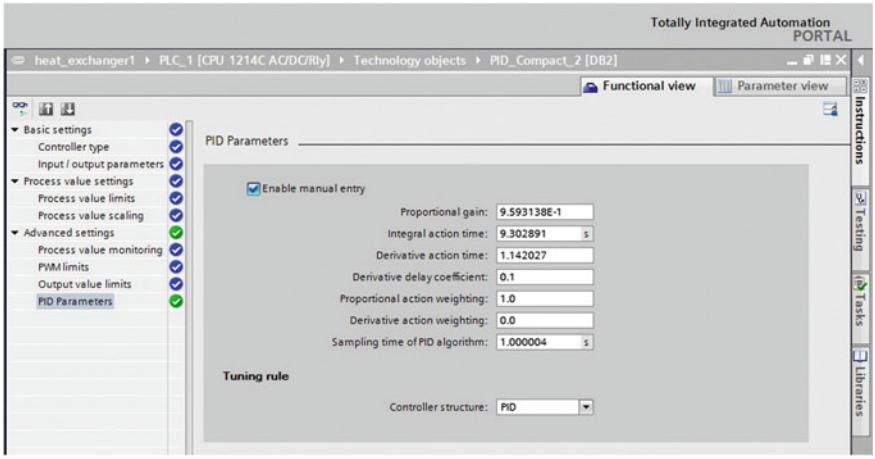

Fig. 4 PID parameters with their sampling time

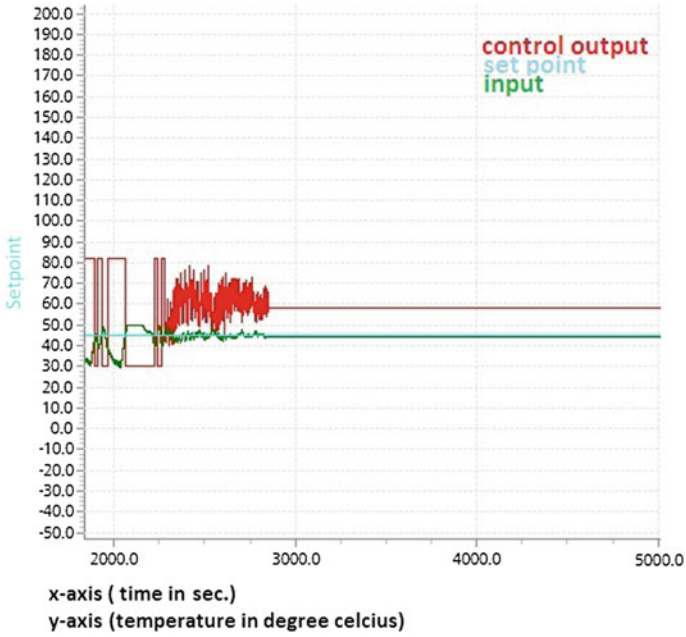

Fig. 5 Time response of the system (*red color* representing control action, *green color* represents the input, and *blue color* represents the set point which is a digital input)

limit. Figure 8 shows the experimental set up developed in this paper which is made in VIT University, Automation laboratory. Table 1 shows the PID parameters of online fine tuning. It is observed here that till the system is being tuned, there will

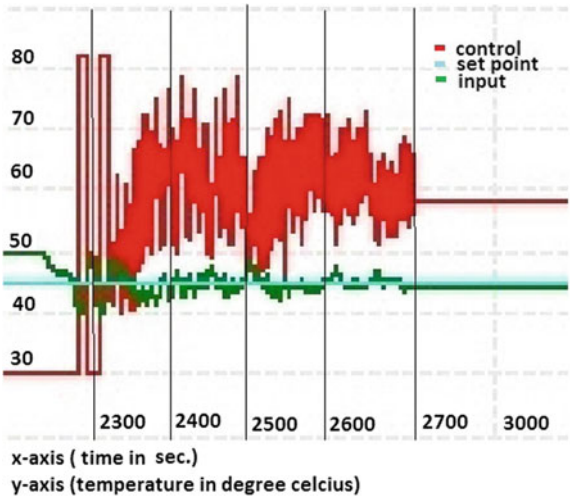

Fig. 6 Time response of the system expanded view of Fig. 5 (*red color* representing control action, *green color* represents the input, and *blue color* represents the set point which is a digital input)

be an implementation of on–off controller which is shown in the Fig. 1 representing the square wave in red color. The settling time here for the 45 °C temperature is 2700 s. The peak overshoot we observed here is 11.11%. The peak time we observed is 2025 s. When the system is first started, it is taking some time to tune; after the system is being tuned, the control action is being implemented, and the system is finally being settled. After the settling time is reached, the temperature of the heat exchange is reached to the desired set point means here the working fluid is

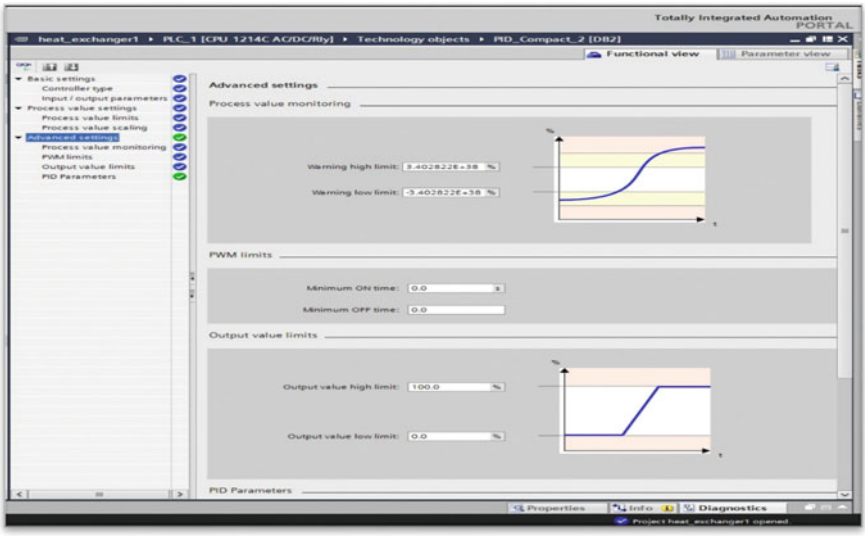

Fig. 7 Figure showing different limits

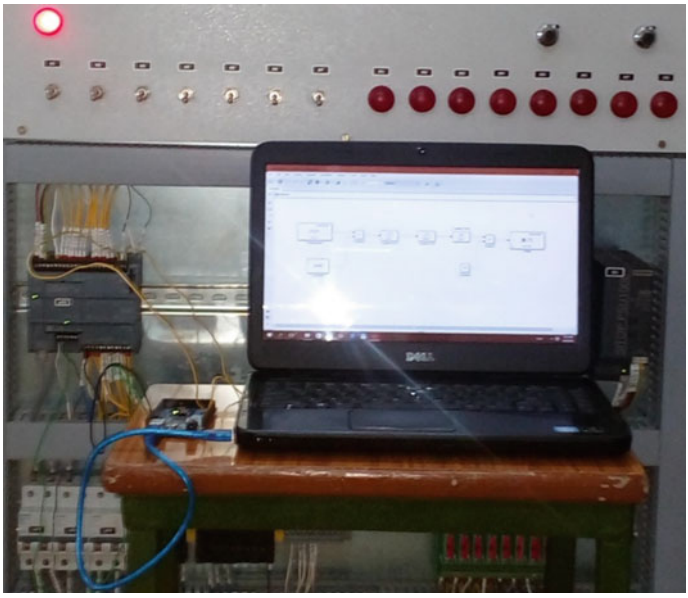

Fig. 8 Representing the set up arrangement in VIT automation laboratory, where the Arduino and the PLC are interfaced and the experiment was conducted

Table 1 Time response of the system

S. No.	Set point (°C)	Peak over shoot	Settling time (s)	Peak time (s)
1	45	11.11%	2700	2025

flowing at the desired temperature, and the corresponding valve opening is maintained at that particular percentage of opening constantly. This project can be applied mainly in the industry HVAC (Heating Ventilation Air Conditioning) systems (Fig. 7).

References

1. Samin, R.E., Jie, L.M., Zawawi, M.A.: PID implementation of heating tank in mini automation plant using programmable logic controller (PLC). In: 2011 International Conference on Electrical, Control and Computer Engineering (INECCE), Pahang, pp. 515–519 (2011)
2. Polak, S., Pavković, D., Zorc, D.: PID controller auto-tuning based on process step response and damping optimum criterion. ISA Trans **53**(1), 85–96 (2014)
3. Ramanathan, P., Sukanya, K.C., Mishra, S., Ramasamy, S.: Study on Fuzzy Logic and PID Controller for temperature regulation of a system with time delay. In: 2013 International Conference on Energy Efficient Technologies for Sustainability (ICEETS), Nagercoil, pp. 274–277 (2013)

4. Dittmar, R., Gill, S., Singh, H., Darby, M.: Robust optimization-based multi-loop PID controller tuning: a new tool and its industrial application. Control Eng Pract **20**(4), 355–370 (2012)
5. Huang, H.-P., Jeng, J.-C., Chiang, C.-H., Pan, Wen: A direct method for multi-loop PI/PID controller design. J Process Contr **13**(8), 769–786 (2003)
6. Zhao, Y.M., Xie, W.F., Tu, X.W.: Performance-based parameter tuning method of model-driven PID control systems. ISA Trans **51**(3), 393–399 (2012)
7. Sharma, C., Gupta, S., Kumar, V.: Modelling and simulation of heat exchanger used in soda recovery—WCE, London, U.K, 6–8 July, 2011
8. http://w3.siemens.com/mcms/programmable-logic-controller/en/basic-controller/s71200/cpu/pages/default.aspx. Accessed on 5 May 2016
9. http://in.mathworks.com/hardware-support/arduino-matlab.html. Accessed on 5 May 2016
10. https://www.arduino.cc/en/Guide/HomePage. Accessed on 5 May 2016

Digitally Controlled Hybrid Liquid Level Detection System Using Programmable Logic Controller and Microcontroller

U.B. Kayande, P. Jaspreetkaur, R.M. Kulkarni, S.B. Mahajan and P. Sanjeevikumar

Abstract In this paper, digitally controlled hybrid liquid level detection (HLLD) system using programmable logic controller (PLC) and microcontroller is articulated. In most of the industries, liquid (chemicals, paint, water, etc.,) is stored at ground levels or in underground tanks and then pumped into overhead tanks as per requirement. This method is advantageous because it is very easy to unload tanks of liquid into underground tanks, and liquid can be pumped as per its necessity. PLC is excellent industrial controller which is used for pump control along with its analog module interfaced to sensor for level detection. This system is efficient but very costly because of analog module. Proposed system eliminates the analog module and replaces it with an embedded microcontroller. In proposed system, PLC analog module is replaced by Arduino microcontroller. This reduces cost of system very much, even the sensors used with microcontroller are comparatively very cheap than those used with PLC directly. In the proposed mechanism, supervisory control and data acquisition (SCADA) system is also interfaced with PLC which monitors the level of liquid and logs the data of liquid usage for analysis. This paper gives detailed information of proposed system along with flowcharts, algorithms, and hardware implementation with actual result of SCADA system.

U.B. Kayande (✉) · P. Jaspreetkaur · R.M. Kulkarni · S.B. Mahajan
Department of Electrical & Electronics Engineering,
Marathwada Institute of Technology, Aurangabad, India
e-mail: udaykayande@gmail.com

P. Jaspreetkaur
e-mail: jaspreetkaurpannu24@gmail.com

R.M. Kulkarni
e-mail: kulkarni.rishi123@gmail.com

S.B. Mahajan
e-mail: sagar25.mahajan@gmail.com

P. Sanjeevikumar
Department of Electrical & Electronics Engineering,
University of Johannesburg, Auckland Park, Johannesburg, South Africa
e-mail: sanjeevi_12@yahoo.co.in

A. Konkani et al. (eds.), *Advances in Systems, Control and Automation*,
Lecture Notes in Electrical Engineering 442, https://doi.org/10.1007/978-981-10-4762-6_35

Keywords Digital control · Liquid level detection
Programmable logic controller · Arduino microcontroller · SCADA

1 Introduction

Resource or raw material supervision is most crucial point in industrial management. Liquid-state raw materials like water, oils, chemicals, paints are more difficult for managing than solids; hence it needs a well-supervised system of control for preserving raw material before it gets processed. Not only controlling expenditure of such materials is important but also measurement of units consumed is equally essential. Wastage of such resources may affect industry in terms of economic loss as well as energy loss [1–4]. In recent years, industries are replacing all the material and resource handling techniques with fully self-governing systems which save time, labor cost, and energy with minimum amount of error [1–3]. Extensive research in area of automation already made industrial processes very fast, effective, and accurate. Industrial automation systems mostly prefer programmable logic controller (PLC) for controlling purpose which is very easy to operate and cost effective over a period of time.

In most cases, liquid-type raw material is stored in large underground tanks as it is easy to unload liquid in such type of storage. Then, this liquid is pumped as per the requirement of process. The existing process is having disadvantage of liquid unexploited due to overflow of the upper tanks, due to delay in turning off pump, to avoid this disadvantage, PLC-based automation is implemented using analog module by interfacing it to ultrasonic sensor [5–10]. Figure 1 depicts the block diagram of conventional PLC control system for pumped liquid storage system.

The cost of such design is very high because analog modules and ultrasonic level sensors are operating on the range of 0–24 V. By considering this drawback, new mechanism is implemented in proposed system which overcomes the existing disadvantage. In the suggested system, analog module of PLC is converted into

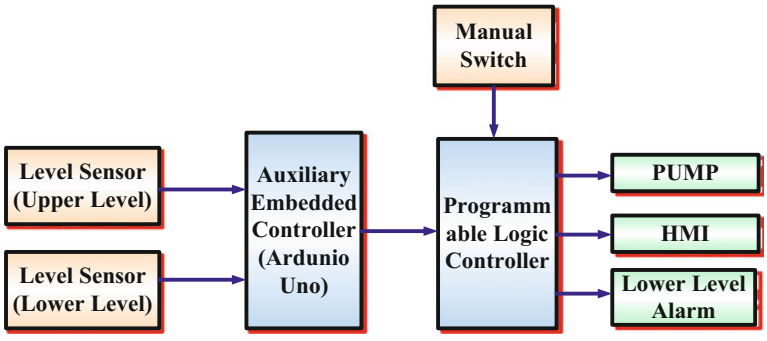

Fig. 1 Block diagram of conventional PLC control system for pumped liquid storage

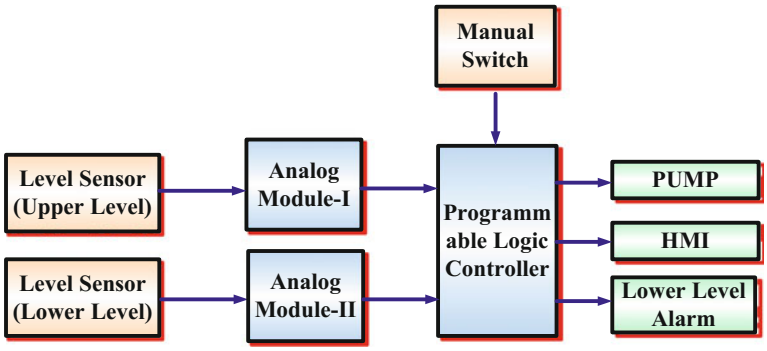

Fig. 2 Block diagram of proposed PLC control system for pumped liquid storage

digital by using Arduino ATmega328 microcontroller which is having in build A to D converter. The designed mechanism is also having additional feature to log liquid dispatch which can explain expenditure of liquid by hours, day, week, month, or a year [7–10].

Effective administrative level control of multiple tanks can be accomplished by proposed system model. Two level sensors are used to deliver the level statistics to the PLC through an auxiliary controller (embedded controller Arduino). PLC works on these records to proceed the required decisions and thereby energizing and de-energizing a drive. This system was implemented in SCADA to create the required human–machine interface (HMI). Figure 2 depicts the block diagram of proposed PLC control system for pumped liquid storage.

2 Connection Diagram of Proposed System

Connection diagram of proposed system is depicted in Fig. 3. Arduino is employed, and it works as an interface between sensor and PLC instead of analog module. The ultrasonic sensors are used with operating voltage of 5 V DC same as that of Arduino. The sensors are interfaced with controller, and then output pins of controller are connected to analog terminals of PLC. Ladder logic loaded in PLC will operate relay (digital output) from the values of these two analog ports. The motor driver circuit operates on the command of the relay. SCADA/HMI is also connected with the PLC by the GUI. SCADA/HMI is used for continuous monitoring and analysis of the water flow in the tanks. Ethernet communication provides data transfer from PLC to SCADA or vice versa; communication cable type may vary with distance. Product required for design of proposed system is given in Table 1 with specification.

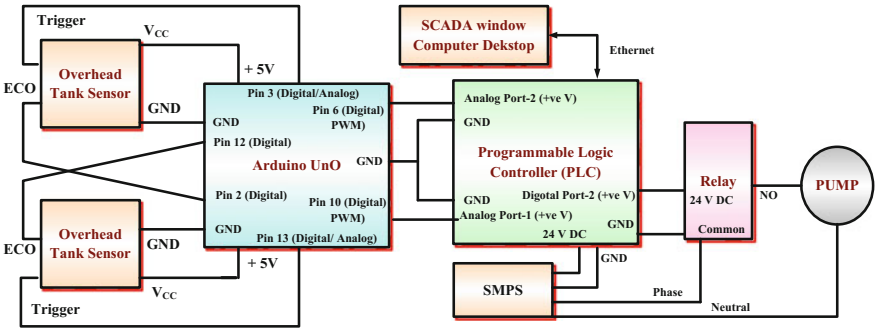

Fig. 3 Complete hardware connection diagram

Table 1 Components with specification required for proposed system

Component	Name of component	Specification
Ultrasonic sensor	HC–SR04	• Working voltage: DC 5 V • Working current: 15 mA • Working frequency: 40 Hz • Max range: 4 m • Min range: 2 cm • Measuring angle: 15° • Trigger input signal: 10 uS TTL pulse • Echo output signal: input TTL lever signal and the range in proportion
Microcontroller	Arduino ATmega328	• Operating voltage: 5 V • Input voltage (recommended): 7–12 V • Digital I/O pins: 14 (of which 6 provide PWM output) • Analog input pins: 6 • DC current per I/O Pin: 40 mA • DC current for 3.3 V pin: 50 mA • Clock speed: 16 MHz
Programmable logic controller (PLC)	Micrologic 1200	Operating voltage: 24 V Digital I/O pins: 40 Analog ports: 2
Relay	Single pole single throw	DC voltage: 24 V
Ethernet cable	–	–

2.1 Sensor to Arduino Interfacing

Numerous services are provided in Arduino Uno which facilitates its communication with other controllers or computers. Digital pins 0 (RX) and 1 (TX), which are existing on ATmega328, provide UART TTL (5 V) serial communication. Arduino is used for converting eco sound of ultrasonic sensor into varying voltage

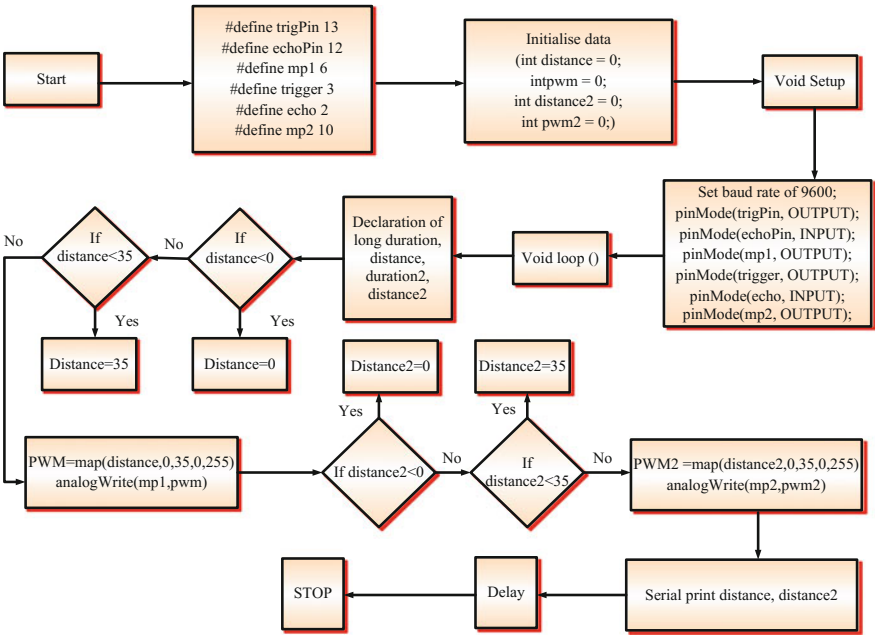

Fig. 4 Flowchart of sensor to Arduino interfacing program

from 0 to 5 V. On the board of Arduino, an ATmega16U2 channel is existing and can offer serial communication over USB and seems to be a simulated com port to software on the computer. This 16U2 firmware customs the standard USB COM drivers without commissioning the external driver. Figure 4 shows the flowchart of the sensor and Arduino interfacing program which can establish communication between two sensors and Arduino. The maximum range of the sensor is used at the respective analog value of 255 and minimum on 0, but practically it cannot be kept at zero; hence it is kept at 35 which corresponds to minimum range of the sensor. Quantities such as long duration, distance, and PWM correspond to sensor 1 reading, whereas duration 2, distance 2, and PWM 2 corresponds to sensor 2. Sensor 1 and sensor 2 readings are then written on analog pins of Arduino which are then given to PLC.

2.2 Arduino and PLC Interfacing

The main controller in proposed system is Allen Bradley Micrologic PLC 12,000. The ladder logic is also developed with use of Allen Bradley software for performance purpose, and it is suitable and specially developed for Allen Bradley PLCs. The total 7 rungs we have used for development purpose. Each rung has separate

logic according to our demand. Mostly, we used normally closed switches (NC) and comparators. Pump can be controlled both manually as well as automatically according to our demand. Separate relay is used for pumping motor. Figure depicts the ladder logic designed for proposed system. The above ladder logic shows our different values of both sensors which are calculated from Arduino output voltage values and bits of arithmetic and logical unit (ALU) of PLC and controller. For tank 1, the values of sensor are max 14,300 and min 2600. For tank 2, the values of sensor are max 13,400 and min 2300. The program is executive with the sequence. (i) Firstly it will check whether the underground tank has sufficient water present or not after coming empty signal from overhead tank. The value for it is 9300, i.e., 25%. (ii) If tank_2 < 100%, then pump will be on and tank_2 will fill-up, same time tank_1 decreases. (iii) If tank_2 full, then pump will be off. (iv) If press manually pump start button, then tank_2 fill-up manually but release button that time pump will be off, otherwise tank fill-up full then automatic stop pump. (v) If press pump stop button, then pump stop manually (only SCADA).

3 Hardware Implementations and Result

Figure 5 shows the actual hardware setup of interfacing of Arduino, PLC, and SCADA of proposed system of liquid level detection, and Fig. 6 shows the mounting of sensor on tank and its control.

SCADA is interfaced with Ethernet-based communications which establish data transfer serially. The InTouch 9.5 HMI is employed to quickly and easily develop custom graphical views of their processes. The results were occupied in four circumstances and were characterized in Variable Table (VAT). The variable depiction along with its status is presented. The manual overrule is turned off to enable automatic procedure. Figures 7, 8, 9, 10, and 11 show different conditions of the proposed system, i.e., (1) overhead tank is empty and underground tank full, (2) water is pumping in overhead tank, (3) underground tank is empty and overhead tank full, (4) alarm indicating level of water lowers in underground tank, (5) water pump manually operated, respectively.

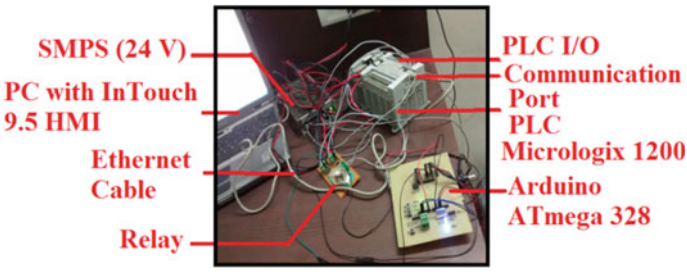

Fig. 5 Setup of Arduino, PLC, and SCADA interfacing of proposed system

Fig. 6 Control and sensing unit of proposed system

Fig. 7 Overhead tank empty and underground tank full

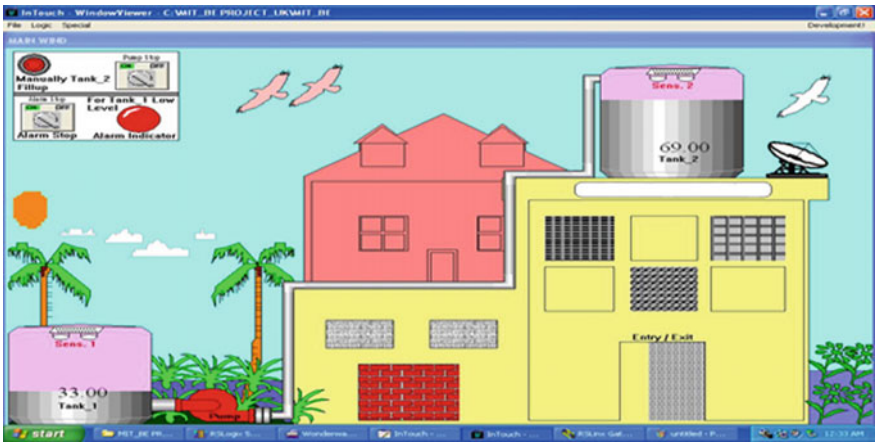

Fig. 8 Water is pumping in overhead tank

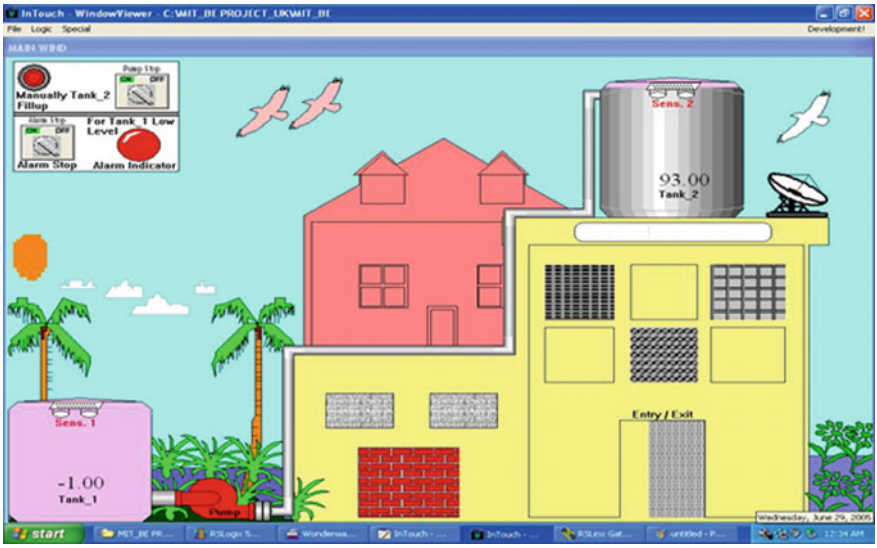

Fig. 9 Underground tank empty and overhead tank full

Fig. 10 Alarm indicated as level of water lowers in underground tank

Fig. 11 Water pump manually operated

4 Conclusion

Digitally controlled hybrid liquid level detection (HLLD) system using programmable logic controller (PLC) and microcontroller is articulated in this paper. Some other automated level detecting schemes are also accessible so far, but most of the methods have some practical limitations and proposed system can resolve these problems with an competent automated liquid level monitoring and controlling system. Without making use of float sensors, accurate results can be acknowledged. Hence, unwanted vibrations and high costs of the float sensors are overwhelmed. A supple, inexpensive, and easy configurable system is established which can solve concern of liquid wastage without any human supervision.

References

1. Jaspreetkaur, P., Kulkarni, R., Mahajan, S.B.: On the automated multiple liquid bottle filling system. In: IEEE International Conference on Circuit, Power and Computing Technologies, India (2016)
2. Mohammed, B.Y., Georg, F.: A formal method based re-implementation concept for PLC programs and its application. In: IEEE conference on Emerging Technology and Factory Automation (2006)
3. Khatri, V.K., Ghangro, A.J., Kumar, J., Haque, S.J.U.: Industrial data acquisition and control system using two PLCs' networked over MPI network. In: IEEE symposium on Industrial Electronics and Application (2009)

4. Da'na, S., Sagahyroon, A., Elrayes, A., Al-Ali, A.R., Al-Aydi, R.: Development of a monitoring and control platform for PLC-based applications. Comput. Stand. Interfaces **30**, 157–166 (2008)
5. Huiqun, Y.U.: The design and realization of PID liquid level control system, based on S7-200 and EM 235. In: IEEE International Conference on Intelligent Computation Technology and Automation (2010)
6. Burali, Y.N.: PLC based industrial crane automation and monitoring. Int. J. Eng. Sci. **1**(3) (2012)
7. Mohamed, E., Elhalwagy, Y.Z., Hashad, A.: Three layer PLC/ SCADA system architecture in process automation and data monitoring. IEEE (2010)
8. Reza, S.M.K., Tariq, S.A.M.: Microcontroller based automated water level sensing and controlling: design and implementation issue. In: Proceedings of the World Congress on Engineering and Computer Science (2010)
9. Javanmard, M., Abbas, K.A., Arvin, F.: A microcontroller-based monitoring system for batch tea dryer. CCSE J. Agric. Sci. **1**(2) (2009)
10. Poh-Kiong, T.: Automated water level management system. Int. J. Comput. Electron. Res. **4**(1) (2015)

Realization of OTRA-Based Quadrature Oscillator Using Third-Order Topology

Bal Chand Nagar and Sajal K. Paul

Abstract A new configuration for realizing third-order quadrature oscillator (TOQO) circuit using operational transresistance amplifier (OTRA) with voltage output is presented. It may also be reported as MOS-C realization, which eases the integrated circuit implementation. It uses two OTRAs, four resistors, and three capacitors. The frequency of oscillation and condition of oscillation are orthogonally controllable. The effect of non-ideality analysis of the circuit is also given and found that at high frequency the effect of parasitic capacitance is negligible. PSPICE simulations and experimental test are provided to verify all the theoretical analysis.

Keywords Operational transresistance amplifier
Third-order quadrature oscillator · Integrated circuits

1 Introduction

Different variants of sinusoidal oscillators, such as single-phase, quadrature, and multi-phase oscillators, generally form important block of a processing system. In communication, such as ASK, PSK, QPSK, quadrature mixers, and SSB modulators applications, there is a requirement of two/multiple sinusoids which are 90° phase shifted. A quadrature oscillator may be used to generate such sinusoids, which can be implemented using second-order and third-order networks. The third-order topology provides good frequency response with high quality factor and low distortion.

There are many methods to design third-order quadrature oscillators (TOQOs) using different active building blocks (ABBs) in the literature. These include realizations using OTA [1], CCII [2], current controlled conveyor (CCCII) [3],

B.C. Nagar · S.K. Paul (✉)
Department of Electronics Engineering, Indian Institute of Technology (ISM), Dhanbad 826004, India
e-mail: sajalkpaul@rediffmail.com

A. Konkani et al. (eds.), *Advances in Systems, Control and Automation*,
Lecture Notes in Electrical Engineering 442, https://doi.org/10.1007/978-981-10-4762-6_36

current differencing transconductance amplifier (CDTA) [4], differential voltage current conveyor (DVCC) [5], combination of two different ABBs (DDCC + OTA and CCCCTA + OTA) [6], operational amplifier [7], operational transresistance amplifier (OTRA) [8, 9], and DVCCTA [10]. The TOQOs [1–5], [7, 8] use three or more ABBs. Moreover, the topology [6] uses two different types of ABBs, which is normally not encouraged. The topologies [7, 8] use more than four resistors. On the other hand, the topology [5] provides neither independent CO nor FO, whereas the oscillators [1, 2, 7] do not provide only independent control of frequency of oscillation (FO). There are only few third-order quadrature oscillator topologies [9, 10], which use only two ABBs. Moreover, the topology [6] uses two different types of ABBs, which is normally discouraged in integrated circuit implementation. The topology [10] uses two DDCCTAs but the hardware implementation of each DDCCTA using commercially available IC needs five numbers of IC AD844 and four numbers of resistor and the topology [9] can not eliminate parasites easily.

A novel third-order QO using OTRAs is proposed. The circuit provides the following useful features: (i) uses only two OTRAs, (ii) provides control of FO independent of CO, (iii) MOS-C realization of the topology eases IC implementation, (iv) moreover, hardware implementation of each OTRA using commercially available IC requires only two numbers of AD844 and one resistor, and (v) low power consumption. The simulation and experimental results are provided.

2 Proposed Circuit

The symbolic representation of OTRA is given in Fig. 1. The port relationships are given in (1).

$$V_0 = R_m\left(I_p - I_n\right), V_p = V_n = 0, \tag{1}$$

where R_m is the transresistance of OTRA and ideally it is infinite [11, 12].

The circuit of the proposed TOQO is represented in Fig. 2. It consists of two OTRAs, four resistors, and three capacitors. V_{01} and V_{02} are two outputs of the TOQO.

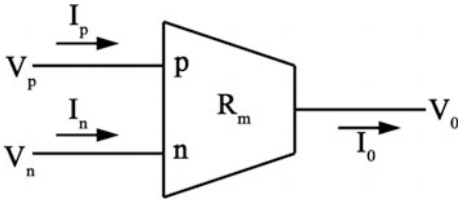

Fig. 1 Symbolic representation of OTRA

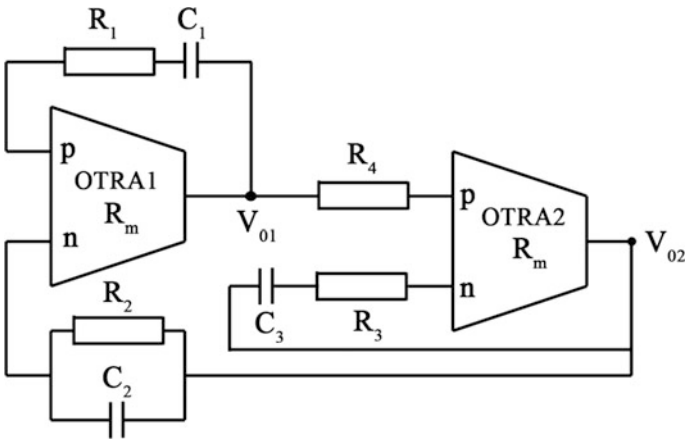

Fig. 2 Proposed TOQO

The characteristic equation is obtained as

$$s^3 C_1C_2C_3R_1R_2R_3 + s^2(C_1C_2R_1R_2 + C_2C_3R_2R_3 + C_1C_3R_1R_3 - C_1C_3R_2R_4) + s(C_1R_1 + C_2R_2 + C_3R_3) + 1 = 0 \quad (2)$$

From Eq. (2), OF and OC can be obtained as
OF:

$$\omega_0 = \sqrt{\frac{C_1R_1 + C_2R_2 + C_3R_3}{C_1C_2C_3R_1R_2R_3}}, \quad (3)$$

OC:

$$C_1C_2C_3R_1R_2R_3 = (C_1C_2R_1R_2 + C_2C_3R_2R_3 + C_1C_3R_1R_3 - C_1C_3R_2R_4)(C_1R_1 + C_2R_2 + C_3R_3), \quad (4)$$

If $R_1 = R_2 = R_3 = R$ and $C_1 = C_2 = C_3 = C$, then FO and CO are modified, respectively, as

$$\omega_0 = \frac{\sqrt{3}}{CR}, \text{ and } 8R = 3R_4. \quad (5)$$

It reveals from Eq. (5) that the FO can be controlled by capacitor(C) without disturbing OC.

The ratio of output signals V_{02} and V_{01} is obtained as

$$\frac{V_{02}(s)}{V_{01}(s)} = \frac{1}{sC_3R_4} = \frac{1}{\omega C_3 R_4} e^{-j90^\circ}, \tag{6}$$

The phase difference between V_{02} and V_{01} is 90°. It ensures that the proposed circuit shown in Fig. 2 is a quadrature oscillator.

The differential input of OTRA allows the implementation of electronically tunable resistor with nonlinearity cancellation in MOS transistors [11]. Figure 3 shows a MOS implementation of resistance whose value may be adjusted by V_A and V_B.

The resistance is expressed as

$$R = \frac{1}{\mu_n C_{ox}\left(\frac{W}{L}\right)(V_A - V_B)} \tag{7}$$

where μ_n, C_{ox}, and W/L represent standard MOS parameters and V_A and V_B are the gate voltages. Thus, MOS implementation of resistance (R_1, R_2, R_3, and R_4) eases the integrated circuit implementation of QO. Figure 4 shows the MOS-C implementation of the proposed TOQO.

The output impedance of the OTRA is very small, ideally zero; hence, the two output voltages, V_{01} and V_{02}, can be connected to the next stage without any extra circuitry, resulting in easy cascading with high output current drive capability.

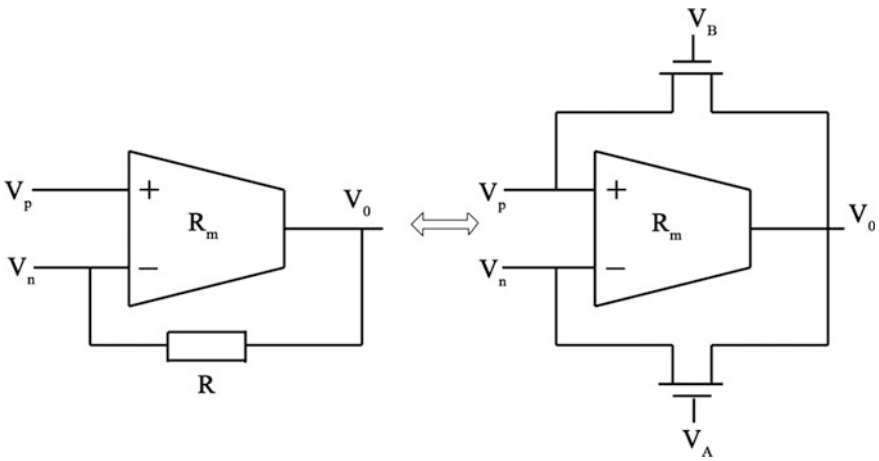

Fig. 3 CMOS realization of linear resistor

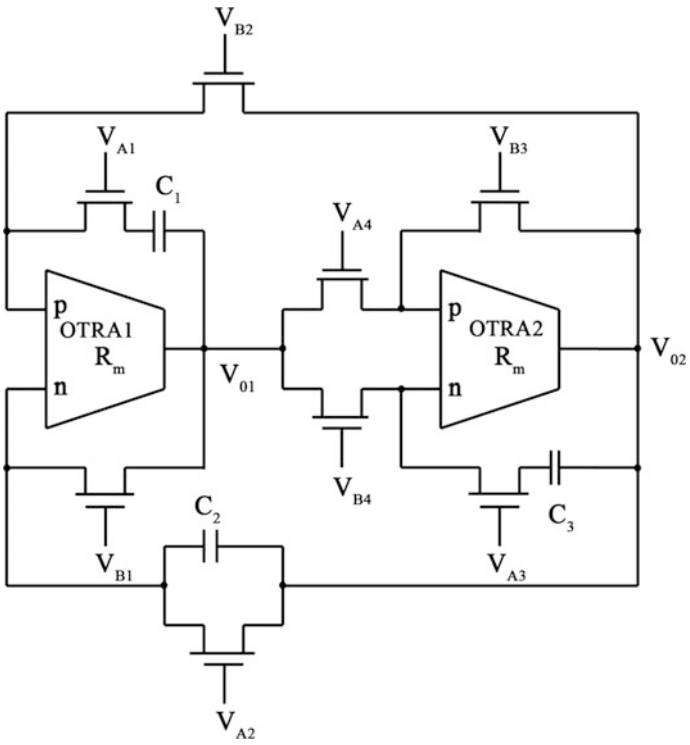

Fig. 4 MOS-C implementation of QO circuit

The sensitivity study shows the variation of output response when we change passive components by a small amount. The sensitivity of oscillation frequency (ω_0) with respect to resistances (R_1, R_2, R_3, and R_4) and capacitances (C_1, C_2, and C_3) can be obtained as

$$S_{R_1}^{\omega_0} = S_{C_1}^{\omega_0} = -\frac{1}{2}\left[\frac{C_2R_2 + C_3R_3}{C_1R_1 + C_2R_2 + C_3R_3}\right], \tag{8}$$

$$S_{R_2}^{\omega_0} = S_{C_2}^{\omega_0} = -\frac{1}{2}\left[\frac{C_1R_1 + C_3R_3}{C_1R_1 + C_2R_2 + C_3R_3}\right], \tag{9}$$

$$S_{R_3}^{\omega_0} = S_{C_3}^{\omega_0} = -\frac{1}{2}\left[\frac{C_1R_1 + C_2R_2}{C_1R_1 + C_2R_2 + C_3R_3}\right], \tag{10}$$

$$S_{R_4}^{\omega_0} = 0. \tag{11}$$

It can be easily observed from Eqs. (8)–(11) that all passive sensitivities are low in magnitude (no more than 0.5), for the proposed TOQO.

3 Non-Ideality Analysis

The R_m using the single pole model may be expressed as

$$R_m(s) = \frac{R_m(0)}{1 + \frac{s}{\omega_0}} \tag{12}$$

where $R_m(0)$ is DC value of R_m, ω_0 is the pole frequency. For high-frequency applications, the $R_m(s)$ may be simplified as

$$R_m(s) = \frac{1}{sC_p}, \quad \text{where} \quad C_p = \frac{1}{R_m(0)\omega_0} \tag{13}$$

It is observed from Eq. (13) that $R_m(s)$ will behave like a reactance for a capacitor having value C_p. Taking the non-ideality effect of $R_m(s)$, the characteristic Eq. (2) modifies to

$$\begin{aligned} &s^4\left(C_1C_3C_p^2R_1R_2R_3R_4\right) \\ &+s^3\left(C_3C_p^2R_2R_3R_4 - C_1C_3C_pR_2R_3R_4 + C_1C_p^2R_1R_2R_4 + C_1C_3C_pR_1R_2R_4 + C_1C_2C_3R_1R_2R_3\right) \\ &+s^2\left(C_p^2R_2R_4 - C_1C_pR_2R_4 + C_3C_pR_2R_4 - C_1C_3R_2R_4 + C_1C_3R_1R_3 + C_2C_3R_2R_3 + C_1C_2R_1R_2\right) \\ &+s(C_1R_1 + C_2R_2 + C_3R_3) + 1 = 0 \end{aligned} \tag{14}$$

It can be readily seen that with $C_p \to 0$, Eq. (14) reduces to their ideal form as in (2). Here, C_p is the parasitic capacitance and it is inversely proportional to dc transresistance gain ($R_m(0)$) and pole frequency (ω_0). For high frequency of operation, C_p^2 is very small and it can be neglected, then the Eq. (14) reduces to

$$\begin{aligned} &s^3\left(C_1C_2C_3R_1R_2R_3 + C_1C_3C_pR_1R_2R_4 - C_1C_3C_pR_2R_3R_4\right) \\ &+s^2\left(C_3C_pR_2R_4 - C_1C_pR_2R_4 - C_1C_3R_2R_4 + C_1C_3R_1R_3 + C_2C_3R_2R_3 + C_1C_2R_1R_2\right) \\ &+s(C_1R_1 + C_2R_2 + C_3R_3) + 1 = 0 \end{aligned} \tag{15}$$

Hence, the modified FO and CO can be obtained as:
FO:

$$\omega_0 = \sqrt{\frac{C_1R_1 + C_2R_2 + C_3R_3}{C_1C_2C_3R_1R_2R_3 + C_1C_3C_pR_1R_2R_4 - C_1C_3C_pR_2R_3R_4}}, \tag{16}$$

CO:

$$\begin{aligned}&\left(C_1C_2C_3R_1R_2R_3 + C_1C_3C_pR_1R_2R_4 - C_1C_3C_pR_2R_3R_4\right) = \\ &\left(C_1C_2R_1R_2 + C_2C_3R_2R_3 + C_1C_3R_1R_3 - C_1C_3R_2R_4 + C_3C_pR_2R_4 - C_1C_pR_2R_4\right) \\ &(C_1R_1 + C_2R_2 + C_3R_3),\end{aligned} \tag{17}$$

Equations (16) and (17) reveal that the FO and CO are affected by C_p. However, when $R_1 = R_2 = R_3 = R$ and $C_1 = C_2 = C_3 = C$, then FO and CO [(16) and (17)] revert back to the form of Eq. (5). Thus, the effect of C_p may be almost eliminated without changing circuit topologies or without adding any additional elements except selecting resistances (R_1, R_2, and R_3) and capacitances (C_1, C_2, and C_3) of equal values.

4 Simulation and Experimental Results

The circuit is simulated using 0.5 µm MOSIS (AGILENT) process parameters. The aspect ratios for PMOS and NMOS transistors are same as in [12], and supply voltages used are $V_{DD} = -V_{SS} = 1.5\ V$ and $V_B = -0.5\ V$ (Fig. 5).

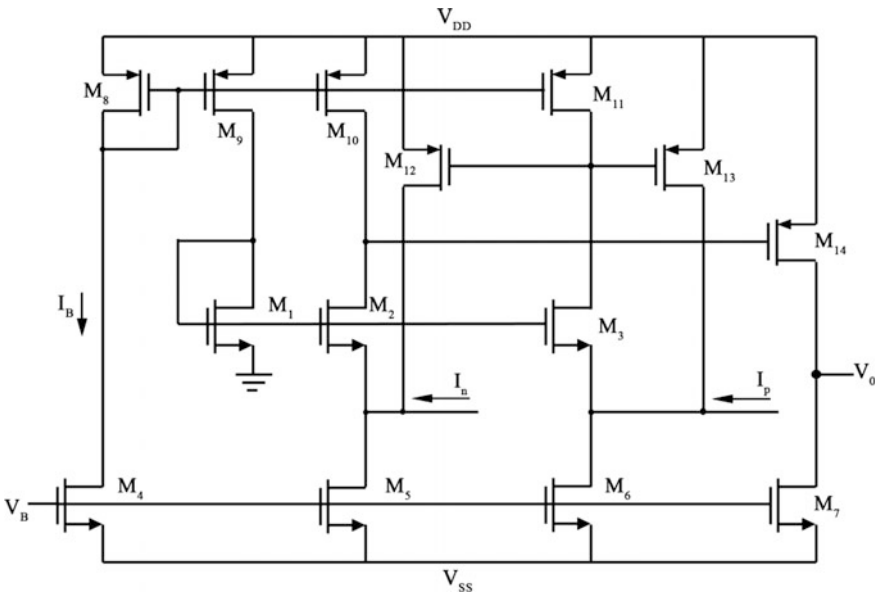

Fig. 5 CMOS implementation of OTRA

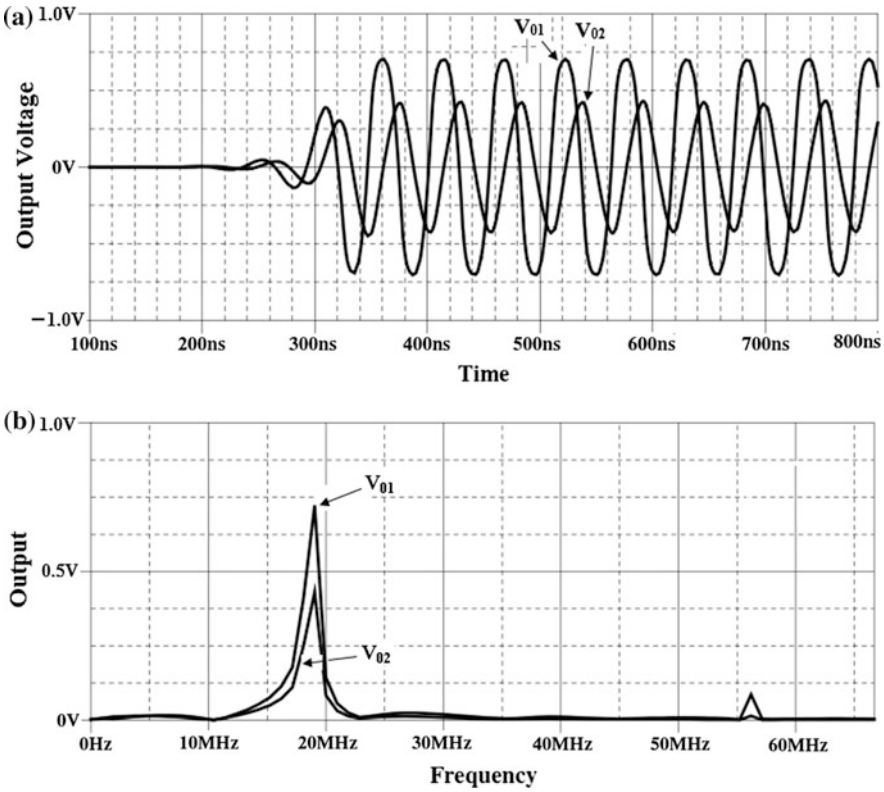

Fig. 6 Simulated results of the proposed TOQO, **a** output response **b** FFT response

The TOQO as shown in Fig. 2 is designed for a frequency of 18.38 MHz with element values as $R_1 = R_2 = R_3 = 1$ kΩ, $R_4 = 2.7$ kΩ, $C_1 = C_2 = C_3 = 15$ pF. The steady-state waveforms of the TOQO are shown in Fig. 6. Figure 6a shows the growth and sustained oscillations. The frequency spectrum (FFT) of the proposed QO as shown in Fig. 6b has FO around 18.58 MHz. A slight deviation in the frequency of the oscillator from theoretical values may be caused by the non-idealities of the OTRA. Total harmonic distortion (%THD) as obtained for proposed oscillator is 1.83%. It proves that the quality of output is good. The power consumption of the oscillator is found to be 1.622 mW. Figure 7 shows the Monte Carlo simulations which provide the strength of the proposed oscillator circuit by taking result of 10 samples for ± 10% variations in R_4. Monte Carlo simulation results thus confirm that the proposed oscillator works well even though the condition of oscillation is disturbed little bit by varying R_4. It also shows the range of the % of samples in different output signal amplitude. Figure 8 shows the variation of FO with R for the oscillator.

A hardware prototype of the proposed circuit as shown in Fig. 2 is also assembled in breadboard to check its functionality experimentally. The OTRA is

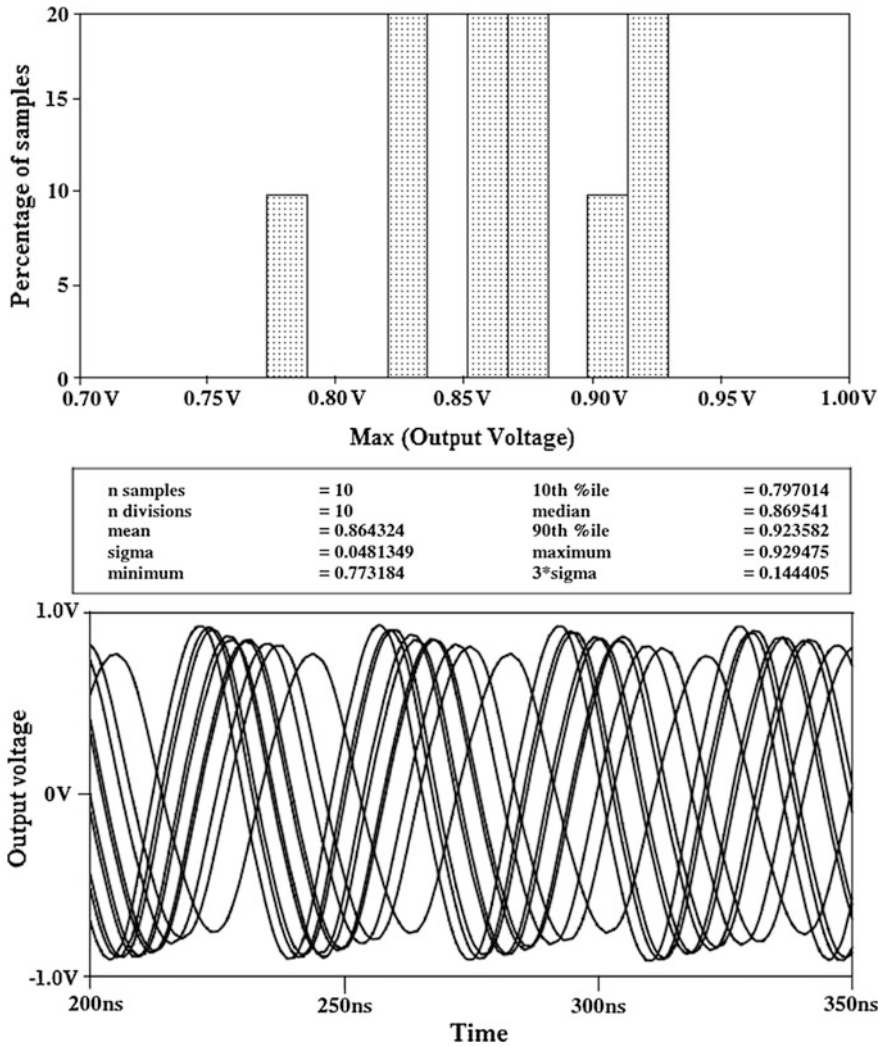

Fig. 7 Result of Monte Carlo simulation of oscillator

constructed using the commercially available CFOA IC AD844AN as shown in Fig. 9 with supply voltages ±6.5 V. The experiment is performed using the element values of resistances and capacitances ($R_1 = R_2 = R_3 = 1$ kΩ, $R_4 = 2.7$ kΩ, and $C_1 = C_2 = C_3 = 15$ pF). The measured values of the resistances and capacitances are obtained as $R_1 = 943$ Ω, $R_2 = 951$ Ω, $R_3 = 940$ Ω, $R_4 = 2.56$ kΩ, $C_1 = 13.64$ pF, $C_2 = 13.58$ pF, and $C_3 = 13.41$ pF for which calculated frequency is found to be 21.55 MHz. The experimental response of the QO is shown in Fig. 10. The measured FO is 21.6 MHz. It shows that the experimental result agrees well with the theoretical value.

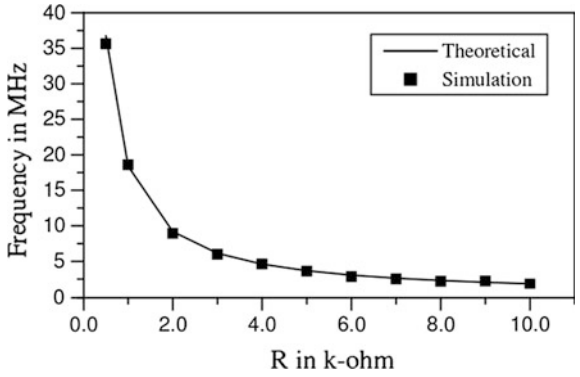

Fig. 8 Plot of *R* versus FO for the oscillator

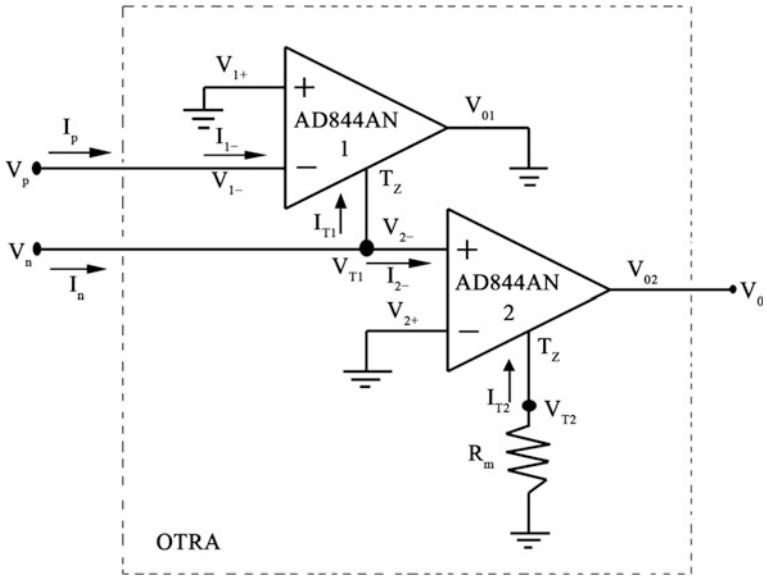

Fig. 9 AD844-based implementation of OTRA

The comparison of the proposed work is discussed here. It reveals that the previously reported third-order current-mode building blocks-based quadrature oscillators have one or more deficiencies such as (a) excessive number of ABBs, (b) excessive number of resistors, (c) non-independent control of CO, (d) non-independent control of FO, and (e) use of mixed ABBs. The proposed quadrature oscillator uses two ABBs, which is minimum in available literature [9, 10]. Moreover, topology [10] has independent control of FO as that of the proposed one, the practical implementation of DVCCTA requires eight IC AD844 and eight extra resistors in comparison with four IC AD844 and two extra resistors in proposed

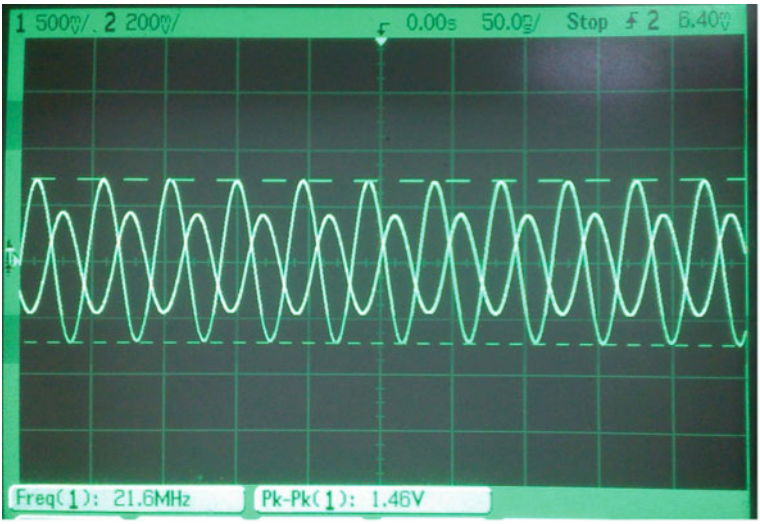

Fig. 10 Experimental output waveform of the third-order QO

one. It is found that the effect of parasitics can easily be eliminated in the proposed circuit, which is not possible in [9].

5 Conclusion

New topologies for realizing voltage-mode third-order QO using OTRA have been presented. The PSPICE simulations are performed using realization of the OTRA based on MOS implementation and also tested experimentally using IC AD844. The proposed design offers the feature of non-ideal parasitic capacitance (C_p) effect elimination without any extra circuit element. Moreover, parasitic resistances R_n and R_p at the input of OTRAs may be absorbed in external resistors (R_1, R_3, and R_4). The proposed circuit gives the following advantageous features: (i) use of minimum ABBs, (ii) independent control of FO, (iii) low passive sensitivity, (iv) low %THD, (v) low power consumption, (vi) MOS-C realization, which eases integrated circuit implementation, and (vii) low output impedance. The functionality of the proposed circuit using simulation as well as experimental technique is found to agree well with the theoretical proposition.

References

1. Prommee, P., Dejhan, K.: An integrable electronic-controlled quadrature sinusoidal oscillator using CMOS operational transconductance amplifier. Int. J. Electron. **89**(5), 365–379 (2002)
2. Horng, J.W., Hou, C.L., Chang, C.M., Chung, W.Y., Tang, H.W., Wen, Y.H.: Quadrature oscillators using CCIIs. Int. J. Electron. **92**(1), 21–31 (2005)
3. Maheshwari, S., Verma, R.: Electronically tunable sinusoidal oscillator circuit. Act. Passive Electron. Compon. Article ID 719376, 1–6 (2012)
4. Horng, J.W., Lee, H., Wu, J.Y.: Electronically tunable third-order quadrature oscillator using CDTAs. Radioengineering **19**(2), 326–330 (2010)
5. Chaturvedi, B., Maheshwari, S.: Third order quadrature oscillator circuit with current and voltage outputs. ISRN Electron. Article ID 385062, 1–8 (2013)
6. Kwawsibsam, A., Sreewirote, B., Jakila, W.: Third-order voltage-mode quadrature oscillator using DDCC and OTAs. In: International Conference on Circuits, System and Simulation, Singapore, pp. 317–321 (2011)
7. Horng, J.W.: Quadrature oscillators using operational amplifiers. Act. Passive Electron. Compon. Article ID 320367, 1–4 (2011)
8. Pandey, R., Pandey, N., Komanapalli, G., Anurag, R.: OTRA based voltage mode third order quadrature oscillator. ISRN Electron. Article ID 126471, 1–5 (2014)
9. Nagar, B.C., Paul, S.K.: Voltage mode third order quadrature oscillators using OTRAs. Analog Integr. Circ. Sig. Process **88**(3), 517–530 (2016)
10. Pandey, N., Pandey, R.: Approach for third order quadrature oscillator. IET Circuits Devices Syst. **9**(3), 161–171 (2015)
11. Salma, K.N., Soliman, A.M.: CMOS operational transresistance amplifier for analog signal processing. Microelectron. J. **30**, 235–245 (1999)
12. Mostafa, H., Soliman, A.M.: A modified CMOS realization of the operational transresistance amplifier (OTRA). Frequenz **60**(3–4), 70–76 (2006)

Mathematical Models for Solving Problems of Reliability Maritime System

A. Nyrkov, K. Goloskokov, E. Koroleva, S. Sokolov, A. Zhilenkov and S. Chernyi

Abstract Mathematical models are proposed, and on their basis, software is developed. Methods of the risk theory are used to minimize the risks. Risk is a consequence of the impact of uncertainty on the achievement of goals. A consequence of influence in the paper refers to the deviation from the goal, expressed in the expected results and the deviation of certain criteria indicators. In this case, we mean any measure of quality. In its turn, risk factors reduce criteria indicators. These factors are divided into categories: general transportation risks and risks of transporting ground. In these categories, one may derive the following risks: incidents at transport resulting from the impact of a set of random factors, including the human one. Furthermore, it should be noted that the occurrence of a risk situation could determine and have a direct impact on the other. As a result, you may experience a chain of risks connected to each other.

Keywords Automatic · Control subsystems · Risk · Transport
Ship's diesel · Kolmogorov

A. Nyrkov · K. Goloskokov · E. Koroleva · S. Sokolov · A. Zhilenkov · S. Chernyi (✉)
Admiral Makarov State University of Maritime and Inland Shipping,
St. Petersburg, Russia
e-mail: sergiiblack@gmail.com

A. Nyrkov
e-mail: apnyrkow@mail.ru

K. Goloskokov
e-mail: Goloskokov@gumrf.ru

E. Koroleva
e-mail: Koroleva@gumrf.ru

S. Sokolov
e-mail: sokolovss@gumrf.ru

A. Zhilenkov
e-mail: zhilenkovanton@gmail.com

A. Konkani et al. (eds.), *Advances in Systems, Control and Automation*,
Lecture Notes in Electrical Engineering 442, https://doi.org/10.1007/978-981-10-4762-6_37

1 Research Problem

During the global crisis, the maritime industry continues to evolve. However, some areas do not show strong growth. Commercial and industrial fleet is a strategic component of every country and region. Mathematical research for the solution of problems of the maritime industry in our time is rather urgent task. Many scientists investigate this industry. The study is a problem in this publication is focused on the use of fuzzy logic and programming.

Modern offshore drilling platforms (ODPs) are completely self-contained objects consisting in terms of automation of a variety of complex subsystems, each of which has, in turn, their own local control and central management for the entire complex. In fact, each of these subsystems, starting from elementary sensors and ending with central control units, is a set of critical components as potential sources of unwanted processes scenarios in the system and, consequently, the cause of the failure. Thus, modern offshore drilling platforms are characterized by a high level of automation of core processes with the congregation of the local automatic control subsystems into a common set of controlled automation systems such as «Amphion», «Cybershot». In general, the ODP is a complex system that operates in non-deterministic conditions associated with low predictable drilling conditions, and the occurrence of an emergency with a high degree of probability can lead to catastrophic consequences [1, 2].

Risk management involves the creation of the environment of proactive or reactive (but with higher reaction rate) decision making within the target ODP system prone to the risks able in real time to identify the possibility of a continuous (i.e., to predict) under these conditions scenarios, within which this process can go down the wrong path.

The difference between the proactive risk management from the reactive one is that with the reactive management overcoming the erroneous scenario begins at its climax, while managing proactively the prediction of occurrence of erroneous scenario is made in the judgment of any prerequisites for its development. Thus, with proactive management, the focus is given not only to the prevention of the development of emerging adverse scenario plans, but also to the methods of early identification of the latter and the effective prevention by all available means, before the scenario starts to be implemented, and its effects have begun to acquire the critical scale.

The need to address the improvement of tools and methods to optimize the controlling of costs determines the relevance of the research. Increasing the practical importance of development and improvement of cost controlling causes the growth of scientific interest in their research.

An important task of the functioning of marine systems is the analysis of statistics of accidents. This generalized indicator can be used to assess the status of the safety of ship movements and reliability onshore and floating structures.

2 Materials and Methods of Research

The main trend in the development of control systems in industry is to transit from centralized to distributed intelligent systems based on network technologies. With the development of microprocessor technology and telecommunications, the opportunity has appeared to place the information processing means near the automation objects. It allows you to create effective control systems with locally distributed equipment—so-called distributed control systems. Operation of power plants and many other objects determines the subject area of the control systems for such objects in real time.

Quality control of ship's diesel generators is a difficult task requiring a high performance of the control system (CS). One of the stages of decision making is the formation of criteria for the performance evaluation, i.e., metrics, which compares the "quality" of possible solutions $x \in X$. In terms of multicriteriality, the most promising approach to the assessment of the problem is the formation of a generalized multiscalar evaluation of $P(x)$ on a set of particular criteria $k_j(x),\ j = \overline{1,m}$. To do this, one must solve the problem of structural–parametric identification of models of formation of $P1(x)$. The effectiveness of the CS is an integrated feature for the set of technical, operational, and economic performance of the equipment. It requires continuous improvement of both individual indicators and approaches to the integrated assessment of the CS efficiency [3–5].

To achieve the objectives, the following items should be developed:

1. A method to develop mathematical models of the operational control system for the ship's diesel generators.
2. Systematization of methods of formation of the elements in the operational control system for the ship's diesel generators.
3. The implementation of the decision-making stages by the person engaged in decision-making (DM) in the operation of the ship's diesel generators.
4. Development of the functional structure of the decision-making system (DMS) using the controlling action adoption system.

The target of research in this paper is management information systems for the ship's diesel generator operation.

The scope of research is the method of complex solution for the problem of decision making using the group accounting for the arguments while assessing the efficiency of the operational control system.

When carrying the tasks outlined in the paper, methods of system analysis and mathematical modeling were used. The main research tool was a software package MATLAB.

3 The Results of Research

In this study, a comprehensive approach to evaluating the effectiveness of the control system is considered from a unified point of performance evaluation, since evaluation of CS without its prediction as incomplete as the forecasting efficiency CS without assessing its current state. Due to the limited knowledge about the processes of intellectual activity in the implementation of decision-making procedure by the decision maker, it is advisable to determine the structure of the multicriteria model for evaluation of the CS effectiveness within the class of polynomial models and, in particular, on the basis of the Kolmogorov–Gabor polynomial [2].

$$F[k_i(x),\ \lambda] = \lambda_0 + \sum_{i=1}^{n} \lambda_i k_i(x) + \sum_{i=1}^{n}\sum_{j=1}^{n} \lambda_{ij} k_i(x) k_j(x) + \\ + \sum_{i=1}^{n}\sum_{j=1}^{n}\sum_{l=1}^{n} \lambda_{ijl} k_i(x) k_j(x) k_l(x) + \cdots, \tag{1}$$

where $F[k_i(x),\ \lambda]$ is unknown functional model of productivity of solutions $x \in X$; $k_i(x), k_j(x), k_l(x)$ are particular criteria characterizing the decision; λ_i, λ_{ij}, λ_{ijl} are isomorphism factors reducing all the summands of a polynomial in one dimension and taking into account the importance ("weight") of each of them. However, even within the Kolmogorov–Gabor polynomial a variety of different models can be synthesized. Therefore, it is necessary to formulate a criterion for selecting a single version of the model. The most important indicator of the "quality" of the model is the accuracy of the approximation of the experimental data, by which the model and its predictive capability are identified, i.e., the accuracy of calculation of output variables for input variables, which are not included in the original (training) pilot sequence [1, 3, 5–7]. This means that it is necessary to synthesize such a model that approximates the objectively existing relationship between the input and output variables, i.e., minimizes some functional of the form

$$\Delta = \min_{S,\lambda} \Theta(Y_m - Y_e), \tag{2}$$

where S, λ are the structure and parameters of the model, respectively;

Θ is the operator characterizing the structure of the criterion;
Y_m is a value of the output variable calculated by the model $Y_i = S(X,\ \lambda)$;
Y_e is an experimentally estimated value of the output variable.

As an operator Θ, either quadratic estimate in the form

$$\Delta_{\mathrm{i}} = \min_{S,\lambda} \sum_{\mathrm{i}=1}^{\mathrm{n}} (Y_{im} - Y_{ie})^2,\ i = \overline{1,n}, \tag{3}$$

known as the least squares criterion [3] or absolute estimate, i.e., absolute error criterion is used.

$$\Delta_{\mathrm{i}} = \min_{S,\lambda} \sum_{\mathrm{i}=1}^{\mathrm{n}} |Y_{im} - Y_{ie}|, \quad i = \overline{1,n}, \tag{4}$$

where n is the number of experimental data.

Due to the particular specific features of the object being modeled, other accuracy estimates may be used. As with any complex system, the "quality" of a mathematical model cannot be described adequately by means of the single criterion. The accuracy of the model, though being important, is the local (particular) assessment of its "quality". Therefore, let us introduce an additional particular criterion such as relevance and complexity of the model. The adequacy of the model will be regarded as the validity of the model, i.e., the stability of its accuracy at all feasible set of input variables. The complexity of the model will be treated as a relative measure, characterizing features and dimensions of the model structure. The relative valuation indicates that compared to the complexity of the models of the same class, for example, the model described by the Kolmogorov–Gabor polynomial is compared.

In this case, the evaluation of the model complexity should take into account the dimensions of the input variables $X \in E^n$, the dimensions of the output variables $Y \in E^m$, the total number of the polynomial members being characterized by the dimensions of the nonzero coefficient tuple λ, and the maximal order of the polynomial. Then, the complexity assessment of the polynomial model will be as follows [2]

$$Q = n + m + \alpha + \beta, \tag{5}$$

where α is the number of the polynomial summands; β is the maximum power of the polynomial terms. n is the number of input variables; m is the number of output variables.

The complexity of the model is determined by its accuracy and adequacy. In particular, if the number of Kolmogorov–Gabor polynomial terms is equal to the number of experimental samples by which the model is identified, so the approximation error, i.e., model error, is zero. However, this does not mean that the model has good predictive qualities, i.e., the ability to predict accurately the value of the output variable for any value of the input variables. This is due to the fact that the initial experimental sample, which is used to identify the model, contains information not only on the actual relationship between input and output, but also on measurement errors, random interferences, etc.

Determination of the model with optimal complexity is associated with the implementation of the principle of external addition [3], which means that the predictive accuracy of the model should be determined based on the "independent" experimental data, which are called test statistics and are not used in solving the

Table 1 Specific features of the initial and constructed fetches

Identified risk	*K*	*S*	*N*	*S**	*S**/*S*
Vibration of the drilling tool with the threat of its failure	2	30	160,000	9	0.245
Overflow of the mud tank with leakage into the environment	2	56	728	11	0.21
Inadmissible power fluctuations in the power supply of the ODP	3	2326	38,996	176	0.08

problem of the model identification. Thus, all the raw experimental data are divided into two sets—a training one that the model is identified and testing one, which is determined by its prognostic quality.

4 Practical Implementation and Verification

The proposed method has been taken as the basis for the creation of risk identification program in order to construct the models in the tasks of diagnosing the emergencies on the ODP. Characteristics of models are shown in Table 1.

Experimental data obtained on the designed models have shown the efficiency and effectiveness of the proposed method and its practical implementation with relatively low-resource requirements of computational devices.

From the data in Table 1, it follows that the use of the proposed method significantly reduces the volumes of sample and does not require multiple passes at the same time for the initial sample. The latter significantly reduces resource consumption for the method, while at the same time maintaining the most important topological properties of the original sample in the subsample being formed and for subsequent analysis [1, 7, 8].

5 Further Reduction of the Samples Being Formed and the Analysis of Identified Risks

Analysis in the context of this paper is referred as for converting data obtained in the process of identifying risks into information based on which it is possible to prioritize the implementation of the identified risk, and, ultimately, to produce the input data required for decision support for risk management.

This function suggests analysis for every identified risk, the result of which is the assessment of each of these risks in terms of consequences and the probability of their occurrence. The latter category in general includes also such a parameter as a recurrence rate in a certain time interval.

The assessment of consequences of a certain risk being realized may be made in terms of the following characteristics of the impact on the equipment and processes:

- Cost—financial losses;
- Time—downtime of the equipment and production interruptions;
- The efficiency of the equipment or process performance;
- The quality of the process implementation or equipment operation.

Thus, the dimensions of the reduced sample formed in terms of the set of representative parameters can be further reduced to two factors, namely the likelihood and magnitude of potential impacts.

The process of formalizing the decision of tasks in a particular domain can be represented in a model and expressed in the set of arrays $M = \langle X, A, Y, F \rangle$, where X, A, Y are arrays of respective control, and fixed and controlled parameters of the environment; F is an array of functional dependencies which link the elements of arrays X, A, Y. In order to realize the dialogue in a better way, let us introduce brief verbal characteristics of the relevant parameters in arrays X, A, Y. In this case arrays X and Y will be represented as set of the following regular pairs: $X = \left\{ (h_i, x_i), i \in I = \overline{1,n} \right\}$; $Y = \left\{ (h_i, Y_i), j \in J = \overline{1,m} \right\}$, and arrays A are a set of following regular triplets $C = \left\{ \left(h_\ell, a_\ell, a_\ell^R\right), \ell \in L = \overline{1,L} \right\}$, where h_i, h_j, h_ℓ are titles of the relevant parameters; x_i, y_j, a_ℓ are their type codes; and $a_\ell^R$are known quantitative values for the fixed parameters.

The model of this type displays the basic laws of the particular environment and dependencies $Y_j = f(x_1, x_2, \ldots, x_n, a_1, \ldots, a_n)$, by which they are linked.

6 Conclusion

Based on the proposed method, it is possible to create the system supervisor, integrated with the central ODP control system that allows not only to minimize the influence of the human factor in the control of alarms and process for verification of information about emergencies, but also to manage the processes in terms of maximum efficiency, by taking into account the possible risks.

Further research in this area can be devoted to the search for new ways to form descriptions of instances as summarized indicators. Implementation of the proposed method with the use of software and hardware supporting parallel computations and distributed data processing is also relevant.

References

1. Nyrkov, A., Sokolov, S., Zhilenkov, A., Chernyi, S., Mamunts, D.: Identification and tracking problems in qualimetry inspections in distributed control systems of drilling platforms. In: IEEE NW Russia Young Researchers in Electrical and Electronic Engineering Conference (EIConRusNW), Saint Petersburg, Russia, pp. 641–645 (2016). doi:10.1016/j.proeng.2015.01.490
2. Chernyi, S., Zhilenkov, A.: Modeling of complex structures for the ship's power complex using XILINX system. Transp. Telecommun. **16**(1), 73–82 (2015). doi:10.1515/ttj-2015-0008

3 Manchur, G., Erven, C.: Development of a mode1 for predicting flicker from electric are furnaces. IEEE Tran. Power Deliv. **7**(1), 416–426 (1992)
4 IEEE working group on power system harmonic, bibliography of power system harmonics, part 1 and Ii, papers 84WM 214-3. IEEE PES Winter Meet. January 29–February 3 (1984)
5 IEEE working group on power system harmonic: power system harmonics: an overview. IEEE Trans. Power App. Syst. PAS-102 (8), pp. 2455–2460, (1983)
6 Singh, B., Al-Haddad, K., Chandra, A.: A review of active filters for power quality improvements. IEEE Trans. Ind. Electron. **46**(5), 960–971 (1999)
7 Govindarajan, S.N.: Survey of harmonic levels on the southwestern electric power company system. IEEE Trans. Power Deliv. **6**(4), 1869–1873 (1991)
8 Nyrkov, A., Sokolov, S., Zhilenkov, A., Chernyi, S.: Complex modeling of power fluctuations stabilization digital control system for parallel operation of gas-diesel generators. In: IEEE NW Russia Young Researchers in Electrical and Electronic Engineering Conference (EIConRusNW), St. Petersburg, pp. 636–640, (2016). doi:10.1109/EIConRusNW.2016.7448264
9 Zhilenkov, A., Chernyi, S.: Investigation performance of Marine equipment with specialized Information Technology. Procedia Eng. **100**, 1247–1252 (2015)
10 Chernyi, S.: Techniques for selecting topology and implementing the distributed control system network. IOP Conference Series: Mater. Sci. Eng. **124**, 012048 (2016)

Tuning PID Controller for Inverted Pendulum Using Genetic Algorithm

C. Sravan Bharadwaj, T. Sudhakar Babu and N. Rajasekar

Abstract The Proportional Integral Derivative (PID) controllers are extensively used as the controllers for controlling the system outputs. The performance of the system is mainly depends on the parameters of the PID controller. To tune these parameters, various techniques are available, and in these methods, there exists drawbacks. To overcome these drawbacks in this paper, the tuning of PID parameters are done by using genetic algorithm, and it is effectively tested on linear inverted pendulum system (LIP). In addition, extensive simulations are performed by varying parameters of the pendulum. For brevity, comparison is made with Z–N methods of tuning, and it is observed that GA-tuned PID controller is giving better performance.

Keywords ITAE · ISE · IAE · Ziegler Nichols method · Genetic algorithm

1 Introduction

The controllers are placing major in the automated industry due to its efficient operation of system. In this PID, controller is extensively used in industry due to its simplicity and effectiveness. To realize any controller, the gains of controller must be determined effectively. To determine the gains of PID controller, more efforts has been devoted to reduce the required time and to optimize the PID parameter values. There are numerous tuning techniques are available based on the

C. Sravan Bharadwaj · T. Sudhakar Babu · N. Rajasekar (✉)
SELECT, VIT University, Vellore 632014, Tamil Nadu, India
e-mail: nrajasekar@vit.ac.in

C. Sravan Bharadwaj
e-mail: sravan.bharadwaj1@gmail.com

T. Sudhakar Babu
e-mail: sudhakar.babu@vit.ac.in

A. Konkani et al. (eds.), *Advances in Systems, Control and Automation*,
Lecture Notes in Electrical Engineering 442, https://doi.org/10.1007/978-981-10-4762-6_38

implementation methods [1]. Tuning methods are mainly classified as: (i) empirical methods (Z–N) (ii) analytical method such as root–locus-based design, and (iii) Optimization methods such as iterative feedback tuning. For the extensive range of industrial applications, Z–N fine-tuning technique suits well, but the main shortcoming of this process is that the operator needs to have clear awareness about plant model [2]. Once it is tuned by Z–N technique, it gives good response, but it is not optimum. If there exists any change in the plant dynamics, then the transient response of the system will vary drastically. To guarantee an independent performance, the controller must have the capability of adapting to the changes in the plant dynamics [3]. Current years, artificial intelligent methods such as fuzzy logic, genetic algorithms (GA), and neural networks are rigorously used due to various features.

Advancements in digital technology have made the controllers automatic. The automatic control system facilitates a wide range of options for control schemes, despite the fact that more than 90% of industrial controllers are still employed based on the PID algorithms, mostly at the low levels, since none of the controller will facilitate the advantages like PID controller. The main features of PID controller are applicability, clear functionality, and simplicity in structure. There are numerous optimization and optimal control procedures available for linear and nonlinear dynamic systems [4–6] to meet the performance optimization requirements of dynamic systems.

The authors in [7] tuned controller constants in a trial-and-error technique, which was time consuming and increased the complexity, and the system response is not satisfactory. More efficient ways to optimize PID gains has been proposed by the authors in [8–10]; in these methods, authors implemented the deterministic optimization procedures based on the integrated absolute error (IAE) standards are used, but these techniques use the predefined MATLAB toolbox and their tuned gains are optimum in only certain operative regions and these techniques are not robust. To bring the inverted pendulum to be stable in vertical position and to control the cart at the preferred position, two PID controllers are required. One can be used for the rod angle control known as angle PID controller, and another for the cart position, and it is referred as cart PID controller [1]. This method increases the complexity of the system. To overcome the drawbacks of existing systems, optimization techniques were widely used for effective operation of system.

Genetic algorithms (GA's) are search techniques motivated by the laws of a genetics and natural selection. The GA is first implemented by Holland based on the Darwin's principal. This can be seen as an optimization technique and is applied to search, machine learning, and optimization tasks [11–13]. GA was effectively adapted to the system dynamics [14]. In this article, gains of PID controller are tuned via GA method for a linear inverted pendulum. To illustrate the effectiveness of genetic algorithm-tuned PID controller, the impulse and step* responses are plotted and are compared with that of the conventional (Z–N) method.

2 Mathematical Model

In this analysis, an inverted pendulum on a moving cart is explored. A pendulum rod is moved around a rigid pivot point fixed to the cart, driven by the stepper motor which is forced to move on the horizontal platform. The rod is set in the vertical position, which is known as an equilibrium point. Main intention is to apply a force to move the cart so that the pendulum stays in the vertical position. The system is shown in Fig. 1, where F is the force in Newton, m is the mass of the pendulum rod in kilogram, M is the mass of the moving cart in kilogram, FV is the force applied to the cart in Newton, F_f is the force due to friction in Newton, g is the acceleration due to gravity in m^*s^{-2}, and θ is the angle of the inverted pendulum measured from the vertical y-axis in radians.

Consider the free-body diagrams shown in Fig. 2. In addition, assume that the coordinates of the center of gravity of the pendulum, (x_G, y_G), are given by:

$$x_G = x + 1 \sin\theta, \quad y_G = 1 \cos\theta \tag{1}$$

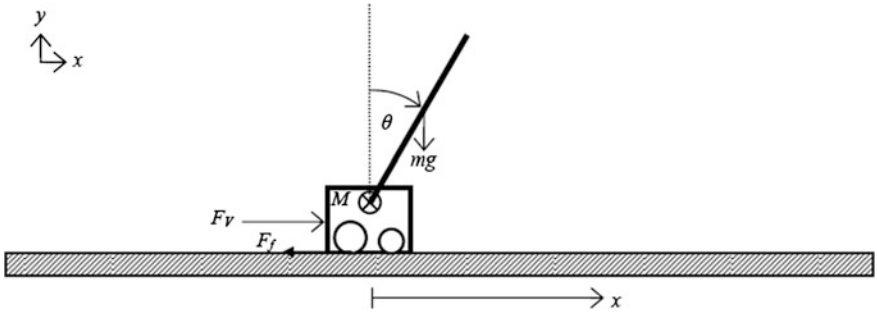

Fig. 1 Representation of the inverted pendulum system

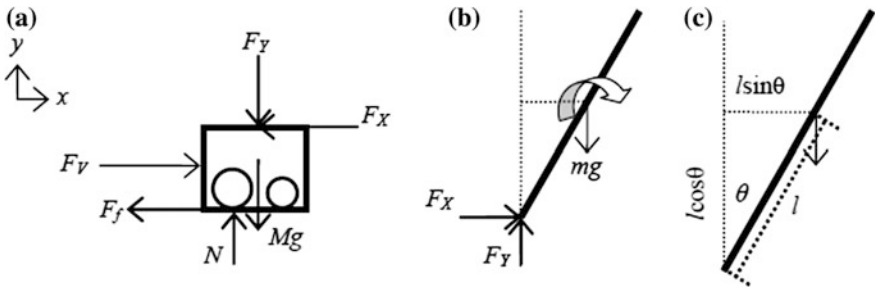

Fig. 2 Free-body schematic of **a** cart **b** pendulum **c** formative the required distances

where l is the distance along the pendulum to the center of gravity and x is the x -coordinate of the cart.

$$M\frac{\mathrm{d}^2x}{\mathrm{d}t^2} = F_v - \left(\frac{\mathrm{d}^2x}{\mathrm{d}t^2} - l\,\sin\theta\left(\frac{\mathrm{d}\theta}{\mathrm{d}t}\right)^2 + l\,\cos\theta\frac{\mathrm{d}^2\theta}{\mathrm{d}t^2}\right) - b\frac{\mathrm{d}x}{\mathrm{d}t} \tag{2}$$

$$F_y = mg - m\left(l\,\sin\theta\frac{\mathrm{d}^2\theta}{\mathrm{d}t^2} + l\,\cos\theta\left(\frac{\mathrm{d}\theta}{\mathrm{d}t}\right)^2\right)$$

From the Newton's laws of motion, the force along horizontal and vertical axis is given as: For any object, the relationship between the moment applied and angular acceleration of the object is given by the following relationship.

$$\sum \bar{M} = I\frac{\mathrm{d}^2\theta}{\mathrm{d}t^2} \tag{3}$$

For the inverted pendulum, moment is summed around its center of gravity, Eq. (3) can be rewritten as

$$F_y\,l\,\sin\theta - F_x\,l\,\cos\theta = I\frac{\mathrm{d}^2\theta}{\mathrm{d}t^2} \tag{4}$$

The equations of motion for the inverted pendulum on a moving cart can be written as

$$\begin{aligned} M\frac{\mathrm{d}^2x}{\mathrm{d}t^2} &= F_v - m\left(\frac{\mathrm{d}^2x}{\mathrm{d}t^2} - l\,\sin\theta\left(\frac{\mathrm{d}\theta}{\mathrm{d}t}\right)^2 + l\,\cos\theta\frac{\mathrm{d}^2\theta}{\mathrm{d}t^2}\right) - b\frac{\mathrm{d}x}{\mathrm{d}t} \\ \left(I + ml^2\right)\frac{\mathrm{d}^2\theta}{\mathrm{d}t^2} &= mgl\,\sin\theta - ml\,\cos\theta\,\frac{\mathrm{d}^2x}{\mathrm{d}t^2} \end{aligned} \tag{5}$$

The model of the pendulum system given in Eq. (5) is nonlinear model and must be linearized in order to get a sensible model for control purposes. The parameter values selected for experimentation were mentioned in Table 1. Linearization will

Table 1 Hardware specifications of LIP [3]

S. No.	Parameter	Value
1	Length (l)	0.25 m
2	Cart mass (M)	1096 g
3	Pendulum mass (m)	09 g
4	Coefficient of friction (b)	0.1 $\mathrm{Nm^{-1}\ s^{-1}}$
5	Inertia (I)	0.0034 kg $\mathrm{m^2}$

be performed about the point $x = 0$ m and $\theta = 0$ radians (appx). Under these assumptions, Eq. (5) can be rewritten as

$$\begin{aligned}(M+m)\frac{\mathrm{d}^2x}{\mathrm{d}t^2} &= F_v - ml\frac{\mathrm{d}^2\theta}{\mathrm{d}t^2} - b\frac{\mathrm{d}x}{\mathrm{d}t} \\ \left(I+ml^2\right)\frac{\mathrm{d}^2\theta}{\mathrm{d}t^2} &= mgl\,\theta - ml\frac{\mathrm{d}^2x}{\mathrm{d}t^2}\end{aligned} \tag{6}$$

By using Laplace transformation to the Eq. (6), it can be written as:

$$\begin{aligned}(M+m)X(s)S^2 &= U(s) - ml\theta(s)S^2 - bX(s)S \\ \left(I+ml^2\right)\theta(s)S^2 &= mgl\,\theta(s) - ml\,X(s)S^2\end{aligned} \tag{7}$$

The output of the system can be written by solving the Eq. (7)

$$\frac{\theta(s)}{X(s)} = \frac{ml\,S^s}{(I+ml^2)S^2 - mgl} \tag{8}$$

3 PID Controller

Tuning of PID controller is a challenging task, even though there are only three parameters in the system, because it must satisfy several criteria within the limitations of PID control. Controller design and tuning seem to be theoretically intuitive; however, it can be tough in real time, if various objectives such as good stability and transient response are to be attained. PID controllers generally provide adequate control by default tunings by using the traditional methods, but performance can be enhanced by fine tuning, and poor tuning may lead to undesirable performance. Typically, initial designs need to be adjusted frequently through simulations until the closed-loop system performs as desired. The most common practice in industries is to utilize PID controller. The schematic of PID is shown in Fig. 3. This set up is acknowledged as parallel form or non-interacting form.

The output of a general PID controller in a parallel form is given as:

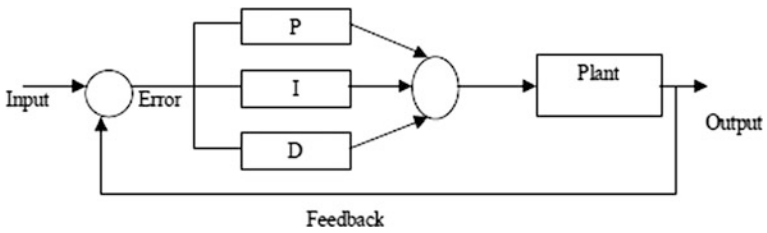

Fig. 3 Schematic of the PID controller in parallel form

Table 2 Z–N method of tuning

Type	P controller	PI controller	PID controller
K_p	$0.5K_c$	$0.45K_c$	$0.6K_c$
T_i	inf	$T_c/2$	$T_c/2$
T_d	0	0	$T_c/8$

$$G_c(s) = K_p\left(1 + \frac{1}{sT_i} + T_d S\right) \tag{9}$$

where K_p,T_i, and T_d are proportional gain, integral, differential time constants. $K_i = K_p/T_i$, $K_d = K_p T_d\, k_p\, k_i$ are derivative and integral gains, respectively.

The tuning of PID means generating the gains of individual controller in a system, for this conventional Z–N method is used. It is based on critical gain K_c and oscillation period T_c. In this technique, the integral time T_i is initially set to infinity, and the derivative time T_d is set to zero. This step is only for the proportional control. K_p will be varied until the system output is oscillatory, and the gain pertaining to this is called as critical gain. In case the output is not oscillatory which indicates Z–N method is not applied. The goal is to minimize the peak overshoot within the limit of 10%. In case the maximum overshoot is greater than 15%, gain adjustment has to be done to decrease it to less than 10%. The parameters tuned using Ziegler–Nichols frequency method [1]; the parameters of PID controller are tuned and shown in Table 2.

4 Genetic Algorithm

Genetic algorithm is a population-based global search algorithm that follows Darwin's principle of survival of the fittest was first proposed by John Holland and his students in the year 1970. The process of GA starts without any knowledge of the output, it will adapt to the environment in which it is working, and the optimization will take place with the help of its operators such as crossover, mutation, and reproduction to attain the global best solution. The method starts with random initial values and explore the search space parallelly. GA's can be applied to complex problems irrespective of its dimensionality, compared to the other gradient techniques which depends on the order of derivative [14].

4.1 Characteristics of Genetic Algorithm

In GA method, solution to the problem is represented as chromosome, and groups of chromosomes form population. Chromosomes are individually awarded with fitness and compared with the other in the population and the success rate is

determined. To attain the better solution, genetic algorithm uses the genetic procedures such as crossover and mutation for generating new set of population. This process is achieved by combining two chromosomes or by changing the bits in chromosomes. Selection of parental chromosomes will be based on the fitness of the parents. By this type of selection, the child chromosomes will have the better characteristics of both parents. Initialization of chromosomes is done with the set of 20–100 chromosomes. In this article, chromosomes are represented in binary. The performance of individual chromosomes is evaluated by a function called objective function. The objective function value for the corresponding chromosome is called as fitness value. The evaluation is based on fitness value and the strongest chromosomes are survived for the next iteration.

Here, each chromosome is having three parts as K_p, K_i, K_d with a length of 30 bit and 10 bit for each parameter.

Steps involved in development and implementation of GA.

1. Initialize the GA parameters.
2. Evaluate the chromosomes for best fitness.
3. Parents should be selected based on the fitness.
4. Reproduction is done by the roulette wheel method.
5. Crossover is introduced to the chromosomes after reproductions.
6. Mutation is done for the resulted chromosomes at lowest probability.
7. Iterate the process from step 2 to 6 until the performance criteria is met. The values of parameters used for the experimentation are given as, Population size = 20, Length of chromosome = 30, Length $K_p = 10$, Length of $K_i = 10$, Length of $K_d = 10$, Max. Generations = 50, $0 \leq K_p \leq 100$, $0 \leq K_i \leq 100$, $0 \leq K_d \leq 100$.

4.2 Objective Function Problem Formulation

Here, the objective function is framed to tune PID gains in such a way that it provides less peak over shoot, small rise time. Each chromosome is evolved, and chromosome having highest fitness considers to be the fittest chromosome. GA uses the fitness values of individuals to produce a new generation set of population comprising of the members with best fitness.

In the evaluation process, the chromosome is divided into 3 parts and it is used for tuning. The newly designed PID gains are placed in the LIP system with unity feedback. For faster evaluation, the Simulink model is designed in other file and is called during the process. The system is given with an impulse input and the error is estimated ITAE.

Integral of time multiplied by absolute error (ITAE)

$$\text{ITAE} = \int_0^t t|e(t)|\mathrm{d}t$$

The ITAE evaluates the error with time and therefore minimizes the error values later on in the response.

5 Results

In this section, the simulations have been performed to evaluate the response of GA-tuned controller. Calculations are performed with 20 chromosomes. The tuned controller is characterized by minimum overshoot, less settling time, and rise time. The best response will then be chosen.

The parameters of GA are chosen as: probability of crossover = 0.8, probability of mutation = 0.3, generations = 50, crossover is single point crossover, and selection is roulette wheel selection. From the Fig. 4, an impulse disturbance of 0.1 PID controller is giving a peak of 0.08, whereas GA-tuned controller is giving around 0.1. Settling time has drastic improvement in GA-tuned PID controller and it is around 0.15 s, whereas in traditional controller it is around 1 s.

Hardware plots are plotted without disturbance in pendulum angle and cart position because of complexity in providing same disturbance with same magnitude since the disturbance is given manually. The cases with disturbance are shown in the simulation results. Different sets of PID gains tuned by GA are verified on hardware, and the plots for both cart position and pendulum angle are plotted for all methods including conventional method. From the hardware response with the 2 types of PID tuning, conventional PID controller will make the pendulum oscillate around the 3.14, but ITAE-based gains provide less oscillations. The experimental setup is shown in Fig. 5.

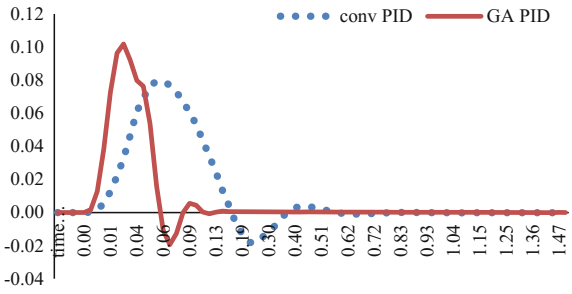

Fig. 4 Comparison between proposed and conventional method for the population size of 20

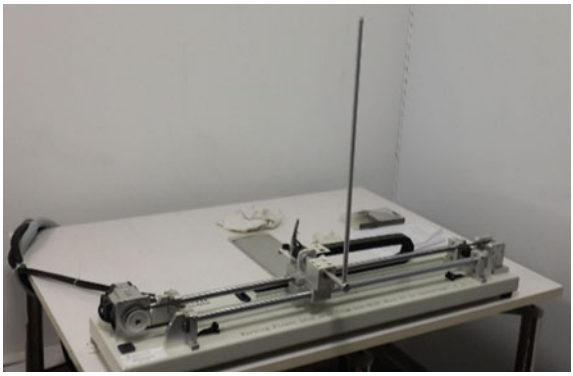

Fig. 5 Hardware implementation of inverter pendulum setup

Table 3 Comparison between PID tuning methods

Method	K_p	K_i	K_d	Error	Max. peak	T_s(s)
Conventional tuning	100	20	15	1.0×10^{-3}	0.08	1.0
ITAE	72	27.1	21.5	0.8×10^{-4}	0.1	0.14

The oscillation in the pendulum angle is because of the output collected from optical encoder. Table 3 gives the details about the tuned parameters based on two methods (conventional and proposed method).

6 Conclusion

From the experimentations, it can be conclude that GA-tuned PID controller will give the faster and good response compared to traditional PID controller tuning methods. These traditional methods will lead us to a starting value of PID controller gains but not the optimal one. Along with this, obtaining gain from classical techniques is more troublesome. It requires more steps, and sometimes trial-and-error procedure is to be followed for reaching the desired performance. With GA tuning, the sound knowledge about the system is not required. The tuning time also will be reduced with the help of GA tuning.

References

1. Prasad, L.B., Tyagi, B., Gupta, H.O.: Optimal control of nonlinear inverted pendulum dynamical system with disturbance input using PID controller and LQR. In: 2011 IEEE International Conference on Control System, Computing and Engineering (ICCSCE), pp. 540–545, IEEE (2011)

2. Ghosh, A., Krishnan, T.R., Subudhi, B.: Brief paper-robust proportional-integral-derivative compensation of an inverted cart-pendulum system: an experimental study. IET Control Theory Appl. **6**(8), 1145–1152 (2012)
3. Lin, G., Liu, G.: Tuning PID controller using adaptive genetic algorithms. In: 2010 IEEE 5th International Conference on Computer Science and Education (ICCSE), pp. 519–523. IEEE (2010)
4. Lewis, L.: Optimal Control. Wiley, New York (1986)
5. Bandyopadhyay, M.N.: Control Engineering: Theory and Practice (Chapter 13). Prentice Hall of India Pvt. Ltd., New Delhi (2004)
6. Burns, R.S.: Advanced Control Engineering (Chapters 9 and 10). Elsevier—Butterworth Heinemann (2001)
7. Yusuf, G.A., Lukman A., Magaji, N.: GA-PID controller for position control of inverted pendulum. In: 2014 IEEE 6th International Conference on Adaptive Science and Technology (ICAST), pp. 1–5. IEEE (2014)
8. Lee, Y., Park, S., Lee, M., Brosilow, C.: PID controller tuning for desired closed-loop responses for SI/SO systems. Aiche J. **44**(1), 106–115 (1998)
9. Lopez, A., Murrill, P., Smith, C.: Tuning PI and PID digital controllers. Instrum. control **42**, 89–95 (2009)
10. Haupt, L.R., Haupt, S.E.: Practical Genetic Algorithms, 2nd edn., p. 685. Wiley, New York (2002)
11. Priya, K., Babu, T.S., Balasubramanian, K., Kumar, K.S., Rajasekar, N.: A novel approach for fuel cell parameter estimation using simple genetic algorithm. Sustain. Energy Technol. Assess. **12**, 46–52 (2015)
12. Rajasekar, N., Jacob, B., Balasubramanian, K., Priya, K., Sangeetha, K., Babu, T.S.: Comparative study of PEM fuel cell parameter extraction using genetic algorithm. Ain Shams Eng. J. **6**(4), 1187–1194 (2015)
13. Balasubramanian, K., Jacob, B., Priya, K., Sangeetha, K., Rajasekar, N., Babu, T.S.: Critical evaluation of genetic algorithm based fuel cell parameter extraction. Energy Procedia **75**, 1975–1982 (2015)
14. Varsek, A., Urbancic, T., Filipic, B.: Genetic algorithms in controller design and tuning. IEEE Trans. Syst. Man. Cybern. **23**(5), 1330–1339 (1993)

LQR PI Controller Design for First-Order Time-Delay Systems

K. Harshavardhana Reddy, Prabhu Ramanathan, Sudha Ramasamy and P. Sanjeevikumar

Abstract In this paper, a linear quadratic regulator-based PI controller is designed to control the first-order time-delay systems. In most of the linear systems, the time delay is commonly found and this delay causes the performance of the system to deteriorate. So to achieve the good performance having delay, need to find the optimal PI controller gains. For this purpose, in this paper PI controller gains are find out by using the LQR, it gives the optimal gain values. In the design of LQR-based PI controller, the selection of Q matrices plays a vital role. So a skew symmetric matrix-based feedback gain matrix is used in selection of Q matrices. The proposed method is validated through various simulation examples. The results are compared to other existing techniques to show the better performance of the proposed method.

Keywords LQR · Skew symmetric matrix · Delay process
Riccati equation · PI controller

K. Harshavardhana Reddy · P. Ramanathan (✉) · S. Ramasamy
School of Electrical Engineering, Vellore Institute of Technology (VIT) University, Vellore, Tamil Nadu, India
e-mail: ishupa@gmail.com

K. Harshavardhana Reddy
e-mail: harshaloka.rs@gmail.com

S. Ramasamy
e-mail: ishuma@gmail.com

P. Sanjeevikumar
Department of Electrical and Electronics Engineering, University of Johannesburg, Auckland Park, Johannesburg, South Africa
e-mail: sanjeevi_12@yahoo.co.in

A. Konkani et al. (eds.), *Advances in Systems, Control and Automation*,
Lecture Notes in Electrical Engineering 442, https://doi.org/10.1007/978-981-10-4762-6_39

1 Introduction

In this paper, a design of optimal PI controller for first-order time-delay systems using LQR theory is proposed. The PI/PID controllers are mostly used in all industrial applications such as chemical process and electrical applications because it has simple design and achieves the good performance [1]. The time-delay problem is found in many industrial control applications, to control the system having time delay is changeling task. A lot of research is going on to find the optimal, robust controller gains for time-delay process [2]. This section provides the exiting methods using the LQR PI controller and methods to find the selection of weight matrices. In the recent past, several works are reported on LQR and implemented on advanced controllers such as self-adjusting LQR, hybrid LQR, fuzzy LQR, and LQR-based PI/PID controllers. In [3], authors explain the design of the PI controller for time-delay process using LQR. Same procedure is also used in this paper. However, the two constraints of LQR problem have been the subject of investigation since 1960s and the problems are selection of weight matrices (Q and R) and solution to algebraic Riccati equation (ARE). These two problems are strongly time dependent on certain operations conditions. Even if all of the control strategies are optimal in nature, different Q and R values will give nonoptimal system performance. In the design of LQR PI controller, the selection of 'R' and weight matrices 'Q' is important to achieve the optimal performance. In [3], the LQR PI controller algorithm was developed for time-delay systems. In this paper proposed the feedback gain matrix-based selection of weight matrices. This methods gives the high integral errors.

In [4], author proposed a genetic algorithm (GA) is to find the weight matrices 'Q' using the feedback regulator, to minimize of integral performance index. In [5], authors used an multiobjective algorithm to selection of weight matrices. This algorithm used an integral time multiplied squared error (ITSE) and integral squared deviation output (ISDCO). In [6], authors proposed an adaptive practical swarm optimization (APSO) to design LQR PI controller for application of laboratory helicopter. This algorithm takes more to time to achieve the global optimization. In [7], the authors designed the LQR PI controller for second-order plus dead-time process using the dominant pole placement technique. This method is an analytical approach to find the weights of q_1 and q_2. From the literature on design of LQR PI controller, weight matrices play vital role and existing methods have certain disadvantages like taking more time because most of the algorithms take more number of interactions to converge. As optimization techniques used are nonlinear, the global solution cannot be guaranteed. To overcome the above problems, a new skew symmetric-based feedback gain matrix is introduced to find the optimal selection of weight matrices Q. The organization of paper as follows: Sect. 1 is literature review of paper, Sect. 2 describes the design of LQR PI controller, Sect. 3 explains the proposed method to selection of weight matrices, Sect. 4 shows the simulation results, and finally, Sect. 5 gives the conclusion of the work.

2 Design of LQR PI Controller

A large number of industrial process are modeled to first-order time-delay system (FOPTD). The transfer model of FOPTD [3] is shown in Eq. (1).

$$T(s) = \frac{c}{s+d} e^{-LS} \tag{1}$$

where d is system matrix, c is control matrix, and L is time delay in seconds.

A linear plant with time delay can be represented as shown in Eq. (2).

$$\dot{z}(t) = Dz(t) + Bu^m(t-L), \quad t \geq 0 \tag{2}$$

The control performance is measured by cost function K represented in Eq. (3).

$$K = \int_0^\infty z^T(t)Qz(t) + u^{mT}(t)Ru^m(t)\mathrm{d}t \tag{3}$$

In Eq. (3), the terms R represented as positive definite matrix and Q is weight matrix in the form of positive definite matrix.

Then, the LQR solution for the cost function is given in Eq. (4).

$$u^m(t) = -R^{-1}C^T Kz(t) \tag{4}$$

where K is positive definite solution of continuous algebraic Riccati equation (CARE) [8] which is shown in Eq. (5).

$$D^T K + KA + Q - KCR^{-1}C^T K = 0 \tag{5}$$

Then the final optimal solution is given as shown in Eq. (6)

$$u^m(t) = -R^{-1}C^T Ke^{D_c L}z(t) \quad \text{for} \quad t \geq L \tag{6}$$

Figure 1 shows the control system block diagram which consists of input, LQR PI controller, process with time delay and output response. Equation (7) gives the formula for PI controller.

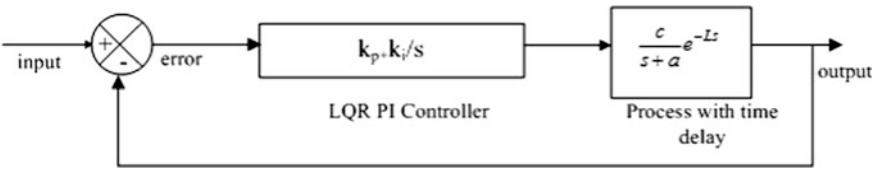

Fig. 1 Block diagram of closed-loop system

$$c(t) = k_p e(t) + k_i \int e(t)\mathrm{d}t \tag{7}$$

In the state space the solution is given as $x(t) = [k_p\, k_i]$.
The state model of the first-order delay system is in Eq. (8)

$$\dot{x}(t) = \begin{bmatrix} 0 & 1 \\ 0 & -d \end{bmatrix} x + \begin{bmatrix} 0 \\ -c \end{bmatrix} u^m(t - L) \tag{8}$$

To derive the PI controller gains, need to find the solution of CARE as shown in Eq. (9) [3].

$$\begin{bmatrix} 0 & 1 \\ 1 & -d \end{bmatrix} \begin{bmatrix} k_{11} & k_{12} \\ k_{12} & k_{22} \end{bmatrix} + \begin{bmatrix} k_{11} & k_{12} \\ k_{12} & k_{22} \end{bmatrix} \begin{bmatrix} 0 & 1 \\ 0 & -d \end{bmatrix} + \begin{bmatrix} q_1 & 0 \\ 0 & q_2 \end{bmatrix} - \begin{bmatrix} k_{11} & k_{12} \\ k_{12} & k_{22} \end{bmatrix} \begin{bmatrix} 0 \\ -c \end{bmatrix} R^{-1} [0 \quad -b] \begin{bmatrix} k_{11} & k_{12} \\ k_{12} & k_{22} \end{bmatrix} = 0 \tag{9}$$

Solving the above Eq. (10) we get the values of k_{11}, k_{12} and k_{22} shown in Eqs. (10)–(12).

$$k_{12} = \frac{\sqrt{q_1 R}}{c} \tag{10}$$

$$k_{22} = \frac{(-Rd + \sqrt{R^2 d^2 + Rc^2(2k_{12} + q_2)})}{c^2} \tag{11}$$

$$k_{11} = ak_{12} + R^{-1} c^2 k_{12} k_{22} \tag{12}$$

The closed-loop feedback gain of the LQR solution is represented in Eq. (13)

$$D_c = D - CF \tag{13}$$

In Eq. (13), F is taken as feedback matrix shown in Eq. (14)

$$F = -R^{-1} [k_{12} \quad k_{22}] \tag{14}$$

After solving the Eq. (13), we get Eq. (15)

$$A_c = \begin{bmatrix} 0 & 1 \\ -R^{-1} c^2 k_{12} & -\sqrt{d^2 + R^{-1} c^2 (2k_{12} + q_2)} \end{bmatrix} \tag{15}$$

From the Eq. (6), we obtained the formulas for the PI controller gain values

The value of $e^{A_c t} = L^{-1}(SI - A)^{-1} = \begin{bmatrix} g_{11}(t) & g_{12}(t) \\ g_{21}(t) & g_{22}(t) \end{bmatrix}$. Then, controller values for interval $t \geq L$ are shown in Eqs. (16) and (17) [3].

$$k_i(t) = R^{-1}c(k_{12}g_{11}(L) + k_{22}g_{21}(L)) \tag{16}$$

$$k_p(t) = R^{-1}c(k_{12}g_{12}(L) + k_{22}g_{22}(L)) \tag{17}$$

Equations (16) and (17) give the gain values for PI controller using LQR solution. The performance of the system depends on 'Q' matrix and 'R' value. In this proposed work, the R value taken as 1, [3, 7].

3 Proposed Method to Selection of Weight Matrices

In this section, the analysis of the output responses for different values of 'Q' has been presented. If the values selected in the weight matrix(Q) are very random then the performance of the system will be poor and therefore the selection of values for 'Q' matrix should be defined as per the considered process.

Figure 2 shows the transient response for various 'Q' matrix values. Here, three cases are taken into consideration to show the performance. Case (i) is selection of 'Q' values randomly as $q_1 = 1$ and $q_2 = 1$, for this the obtained integral absolute error (IAE) is 1.23. For Case (ii), the 'Q' matrix is selected as $q_1 = 2$ and $q_2 = 2$ and the IAE obtained as 1.25. For case (iii), selection of 'Q' values randomly as $q_1 = 2$ and $q_2 = 1$, the obtained IAE is 1.65. From this observation, the selection of 'Q' matrix is random, it will give the high integral error and poor performance as shown in Fig. 2 (Table 1).

As above mentioned, the output performance of the LQR-based controller depends on 'Q' matrices. This paper proposed a skew symmetric matrix [9]-based

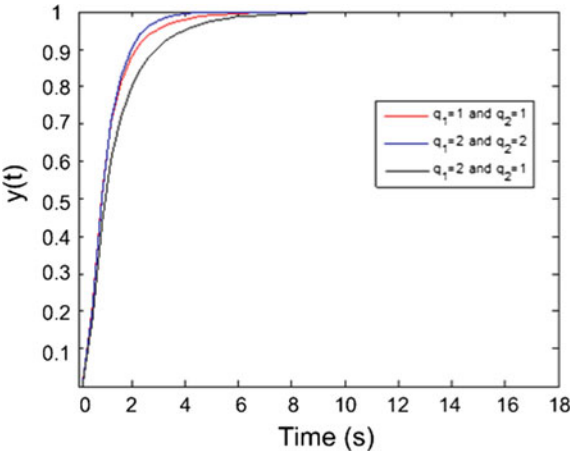

Fig. 2 Transient responses for different values of weight matrixes

Table 1 Comparison of time-domain specifications for different weight matrixes

Weight matrices	System performance	
	Settling time (T_s)	IAE
$q_1 = q_2 = 1$	8	1.23
$q_1 = q_2 = 2$	6	1.25
$q_1 = 1$ and $q_2 = 2$	16	1.65

feedback gain matrix to select the weight matrices 'Q'. The performance of the system gives better optimal response when specific choice of weight matrices is optimum values.

The feedback gain matrix is given Eq. (14), is modified using the skew symmetric matrix, formula is $A^T = -A$; then, it becomes the $A^T + A = 0$. Let us consider the A as the feedback matrix. So Eq. (14) is modified as shown in Eq. (18).

$$A_c = A - ((A - BF) + A - BF)^T) \tag{18}$$

Substituting the values in Eq. (18) and determine the characteristics equation of closed-loop matrix which is equal to the desired closed-loop equation as shown in Eq. (19).

$$\Delta(s) = |sI - A_c| = s^2 + 2 * \xi_m \omega_m + \omega_m^2 = 0 \tag{19}$$

Then we get the optimal values of weight matrices as shown in Eqs. (20) and (21).

$$q_1 = \frac{\omega_m^4}{4b^2} \tag{20}$$

$$q_2 = \frac{(2 * \xi_m * \omega_m - a)^2 - 4 * a^2 - 2 * \omega_m^4}{4b^2} \tag{21}$$

The parameters of proportional and integral gains are obtained by using the values of damping ratio (ξ_m) and natural frequency (ω_m). The selection of these parameters are specified in the range of = [0.7 to 1.0] and L = [1.0 to 1.5] [3, 7].

4 Simulation Results and Discussion

Let us consider the simple first-order delay system model to design the LQR PI controller using the proposed selection of weight matrices method to validate the results through the two examples. Example (1) is shown in Eq. (22).

(A) ***Example 1***

$$G(s) = \frac{0.5}{s+0.5} e^{-0.25s} \tag{22}$$

Calculation made as per procedure; Fig. 3 shows the transient response of the system with proposed method and existing method. For the method proposed by He et al. in [3], the k_p and k_i values are 3.6114 and 6.23, respectively. The output response settles at 7 s with 0.6 peak, and IAE of 1.107.

For proposed method, the controller gain values are given as k_p is 3.1328 and k_i is 3.5797. The output response shows it has lesser settling time 5.2 s with peak time 0.25, and IAE is 0.8688. Table 2 gives a comparison of time-domain specifications and integral error with proposed and existing methods.

(B) ***Example 2***

To validate the proposed method, let us consider the different values of c and d as shown in Eq. (23).

$$G(s) = \frac{0.5}{s+2} e^{-0.3s} \tag{23}$$

For the method proposed by He et al. in [3], the k_p and k_i values are 3.2489 and 4.9215, respectively. The system output performance response settles at 6 s with zero peak, and IAE is 0.8128. For proposed method, the controller gain values are given as k_p is 1.5561 and k_i is 3.5033. The output response shows it has lesser settling time 3.2 s with zero peak time, and IAE is 0.72. Figure 4 shows the output

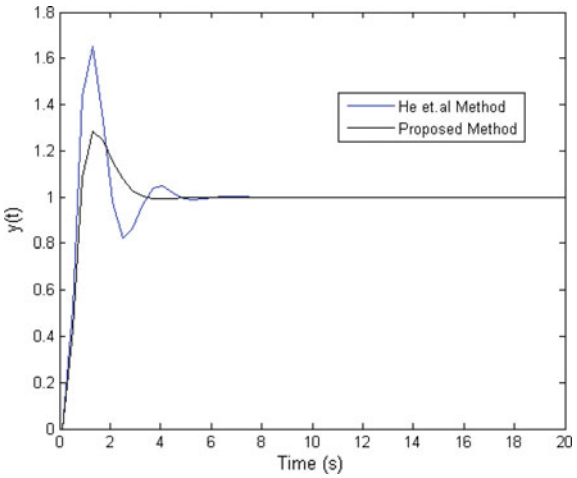

Fig. 3 Transient response for Example 1

Table 2 Comparison of performance indices with proposed and He et al. methods for Example 1

Method	Controller settlings and performance indices						
	K_p	K_i	ξ_m	$\omega_m L$	$T_s(s)$	$T_p(s)$	IAE
He et al. method [3] $q_1 = 45.69$, $q_2 = 1.20$	3.6114	6.23	0.71	1.3	7	0.6	1.107
Proposed method $q_1 = 2900$, $q_2 = 0.77$	3.1328	3.5797	0.71	1.3	5.2	0.25	0.868

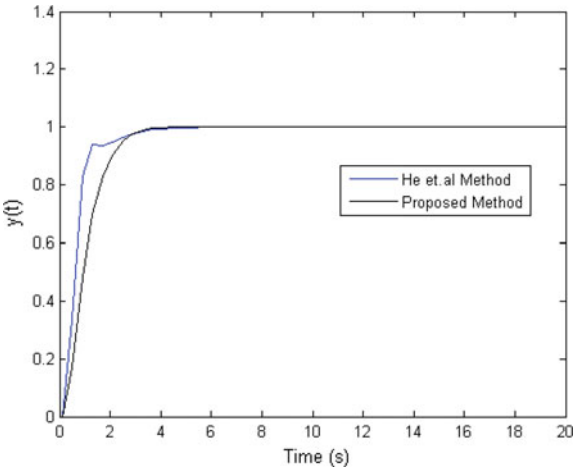

Fig. 4 Transient response for Example 2

Table 3 Comparison of performance indices with proposed and He et al. methods for Example 2

Method	Controller settlings and performance indices						
	K_p	K_i	ξ_m	$\omega_m L$	$T_s(s)$	$T_p(s)$	IAE
He et al. method $q_1 = 1400$, $q_2 = -14.7684$	3.2489	4.9215	0.71	1.3	6	–	0.812
Proposed method $q_1 = 22.037$, $q_2 = -1.0955$	1.5561	3.5033	0.71	1.3	3.2	–	0.72

performance of the proposed controller. Table 3 gives a comparison of time-domain specifications and integral error with proposed and existing methods. As observing this, the proposed method gives the better response when compared to other existing methods.

5 Conclusions

In this paper, the design of LQR-based PI controller is proposed for this type of time-delay systems. The skew symmetric matrix with damping ratio and natural frequency method gives the optimal weight matrices, which leads desired system response to achieve control goals. Simulations results are obtained as shown in Sect. 4, which shows the accuracy of proposed controller and their efficiency in achieving desired time-domain specifications. Further studies are implemented for diverse industrial applications.

References

1. Astrom Karl J.: PID controllers: theory, design and tuning. Instrum. Soc. Am. (1995)
2. Vilanova, R., Visioli, A.: PID Control in the Third Millennium. Springer, London (2012)
3. He, J.-B., Wang, Q.-G., Lee, T.-H.: PI/PID controller tuning via LQR approach. Chem. Eng. Sci. **55**(13), 2429–2439 (2000)
4. Das, S.: LQR based improved discrete PID controller design via optimum selection of weighting matrices using fractional order integral performance index. Appl. Math. Model. **37** (6), 4253–4268 (2013)
5. Das, S., Pan, I., Das, S.: Multi-objective LQR with optimum weight selection to design FOPID controllers for delayed fractional order processes. ISA Trans. **58**, 35–49 (2015)
8. Kumar, E.V., Raaja, G.S., Jerome, J.: Adaptive PSO for optimal LQR tracking control of 2 DoF laboratory helicopter. Appl. Soft Comput. **41**, 77–90 (2016)
7. Srivastava, S.: An optimal PID controller via LQR for standard second order plus time delay systems. ISA Trans. 244–253 (2015)
8. Naidu, D.S.: Optimal Control Systems. CRC Press (2003)
9. Nagrath, I.J.: Control Systems Engineering. New Age International (2006)

Determination of Protein Content of Castor Leaves Using UV-Based Sensor System

Jhimli Kumari Das and Shakuntala Laskar

Abstract Protein is the building block for the growth of all living creatures. The protein content in different food products can be analysed by various invasive and non-invasive methods which can be either direct or indirect way of measurement. This paper proposes non-destructive and indirect in vivo analysis of the protein content by using optical sensor system. The sensor system is based on the study of the optical properties like transmittance and absorbance of the castor leaf. The results are validated with that of the results derived from chemical analysis. The relationship between the protein content and the absorbance of different leaves were found to be highly correlated. The results show that the proposed system can be used to determine the quality of the castor leaf based on its protein content.

Keywords Protein · Castor leaf · Optical sensor system · UV sensors Absorbance

1 Introduction

Protein is an important parameter that determines the quality of the food consumed by various living beings. It also plays a vital role in determining the quality of the silk that is spun by the silkworms. One such silkworm is the Eri silkworm which primarily feeds on castor leaves and is the source of all sort of nutrition for these worms. There are many invasive and non-invasive methods for quantification of protein content in leaves, and the invasive methods are based on chemical analysis which is time-consuming and also destroys the sample. The non-invasive method on

J.K. Das (✉) · S. Laskar
School of Technology, Assam Don Bosco University, Guwahati, India
e-mail: jhimli.das@dbuniversity.ac.in

S. Laskar
e-mail: shakuntala.lashkar@dbuniversity.ac.in

A. Konkani et al. (eds.), *Advances in Systems, Control and Automation*,
Lecture Notes in Electrical Engineering 442, https://doi.org/10.1007/978-981-10-4762-6_40

the other hand is non-destructive and consumes less time, but the most commonly used techniques are very costly and require expertise to operate the device [1–4]. This paper proposes a simple optical sensor system for determination of protein in castor leaves which is non-destructive in nature and is also cost effective. There are many optical systems that are used for determination of protein in variety of food items, and these systems are based on near-infrared spectroscopy. The spectroscopic method is used to measure either transmittance or reflectance of the sample, and the content of protein is related with the values of the optical parameters. The chlorophyll meter is also used for measurement of protein which is related with the nitrogen content in the leaves. The UV absorbance spectroscopy is one of the preferred chemical methods for determination of protein as it gives more accurate protein concentration compared to colorimetric assays.

The proposed sensor system is designed using UV source and detector, and the results obtained from the sensor system were then compared with the readings obtained from the spectrophotometer at 660 nm. The spectrophotometric readings were based on Lowry method which is one of the popular methods for determination of protein content. The sensor system actually records the transmittance values through the sample leaf. The transmittance values were then converted to absorbance by taking log of the transmittance, i.e., log (1/*T*). The absorbance values of spectrophotometer and the sensor system were compared to establish the relation between the protein content of the leaf and the sensor reading.

2 Materials and Methods

The samples of castor leaves were collected from the plants growing in the roadside of the suburban areas of Guwahati, Assam, and not from plants grown under controlled conditions because the device is designed for farmers who do not always grow the plants in prerequisite conditions as sericulture in Assam is carried out along with other farming activities. The leaves were plucked at different climatic conditions like the first sample was collected in the month of January, the second in the month of May and third one in the month of August. The samples collected in the month of January comprised of four leaves from different positions of the plant starting from the leaf at the top that has just opened, and immediately after that the first leaf the second, third and the fourth leaves were taken. The same was repeated for the month of May whereas in the month of August the fifth and the eight leaf from the top was taken. The plants from which the samples were collected were from different locations and also of different variety. The plants for the month of January and May had reddish stems and green leaves, and plant sample for the month of August had green stems and green leaves.

2.1 Chemical Analysis

The chemical analysis to determine the protein content of the leaf samples was done using the Lowry's method which is one of the most commonly used spectrophotometric methods. All the solutions were prepared fresh. The phosphate buffer of pH-7.6 was prepared using 0.2 M monobasic sodium phosphate (NaH_2PO_4) and 0.2 M dibasic sodium phosphate (Na_2HPO_4). This buffer solution was used with the leaf samples for protein extraction. Apart from the buffer solution, alkaline Na_2CO_3 was prepared by dissolving 0.4 g of NaOH in 100 ml of distilled water. Likewise the copper sulphate reagent was prepared by dissolving 0.5 g of $CuSO_4 \cdot 5H_2O$ in distilled water and then adding 1 g of sodium potassium tartarate. The volume of the solution was then adjusted up to 100 ml. This copper sulphate reagent was made alkaline by mixing 1 ml of copper sulphate solution in 50 ml of alkaline solution mentioned above [5].

2.2 Protein Extraction

The protein was extracted by crushing the leaves of four different leaf samples separately in mortar and pestle by adding buffer solution to it. Supposing if 1.5 g of castor leaf is taken, then 1.5 ml of the buffer solution was added to the leaves to prepare the mixture. The mixture was then put in centrifuge tube that is fully covered and kept overnight so that maximum protein can be extracted. The juice from this mixture was extracted by putting the crushed sample in a clean piece of cloth and squeezing it. This juice was then used as the sample whose absorbance reading was observed. 1 ml of each sample of four different leaves was taken in four different test tubes, and 5 ml of alkaline copper sulphate solution was added to it. This solution was then shaked properly and kept for resting for 10 min. After 10 min, 0.5 ml of Folin's reagent was added to it, and the solution was again mixed properly and kept in a dark chamber for another 30 min. The absorbance values at 660 nm of these samples were recorded from a spectrophotometer with respect to a reference of 0.5 M NaOH [5] (Fig. 1).

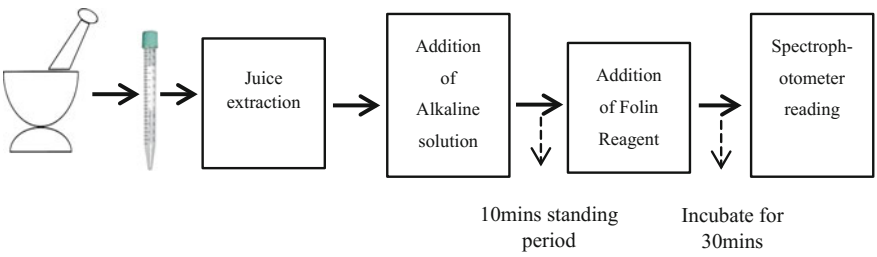

Fig. 1 Steps of protein extraction

2.3 Sensor System

The sensor system comprises of a UV source (390 nm) and a compatible detector (ML8511 sensor). The sensor gives the output in analog voltage that is linearly related with the measured UV intensity (mW/cm^2). After plucking the sample leaf, it is put in a stand between the source and detector, and the transmittance value was recorded in terms of voltage. The reading was also recorded for red LED as it had a wavelength around 660 nm, and it could have been related with that of the spectrophotometer reading. The output transmittance value was then converted to absorbance values by using the basic colorimetric analysis (Fig. 2).

The transmittance can be defined by:

$$T = \frac{I1}{I0} \times 100\%$$

$I1$ is the intensity of light when it passes through the leaf sample, and Io is the reference intensity without the leaf. The absorbance (A) is given by:

$$A = \log(1/T)$$

The distance between the source and the detector was kept as 1.5 cm because if the distance between the two increased then the absorbance value would decrease. Moreover, as the device is supposed to be a small hand-held one, the distance between the source and the detector also has to be less. A figure representing the system is shown in Fig. 3.

2.4 Calibration Experiment

The relationship between the protein content and the absorbance was established by taking a standard protein solution, i.e., a bovine serum albumin (BSA) solution. The Lowry method was used to determine this relationship. In this, 50 mg of BSA

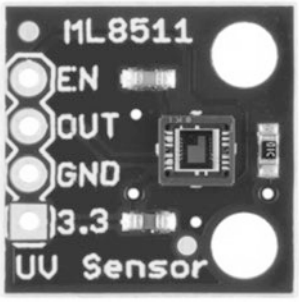

Fig. 2 ML8511 sensor

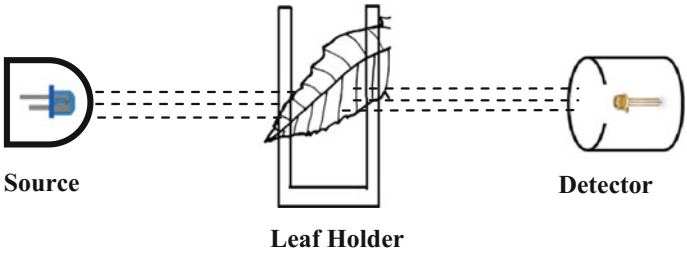

Fig. 3 Schematic diagram of sensor system

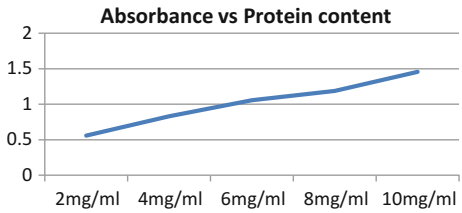

Fig. 4 Relation between absorbance and protein content of standard BSA solution

was dissolved in distilled water, the volume of which later adjusted to 50 ml. Therefore, 1 ml of this solution contained 1 mg of protein. It was observed from the experimentation that with the change in the protein concentration, the absorbance also varied. This variation was linear in nature, i.e., as the protein content increased, the absorbance also increased. A graph plotted from the reading of the spectrophotometer for the same is shown below. This concept was later used to represent the relationship between the absorbance readings from the spectrophotometer with that of the developed sensor system (Fig. 4).

3 Result and Discussion

As discussed above, four leaves from four different plant positions were considered as the samples. The first plant had red stems and a bit dark green leaves. The youngest leaf from the tip of the tree was considered as the first sample, and other three samples were leaves more matured than the previous one. The graph showing the relationship between the absorbance of the spectrophotometer and the sensor system is shown below. From the graph, it is seen that the youngest leaf has minimum absorbance which indicates that the protein content of this leaf is the minimum, whereas the second leaf sample which is from the third plant position has the maximum protein content. The sensor system is less sensitive to the fourth decimal point variation which is evident in the graph. The reading of the same samples was also taken using a red LED, but the relation between the spectrophotometer absorbance and the sensor system absorbance did not match. There

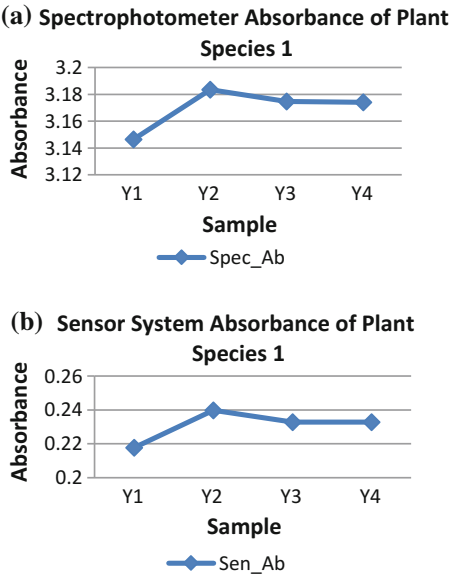

Fig. 5 **a** Absorbance (spectrophotometer) of leaves for the first species of plant, **b** absorbance (sensor system) of leaves for the first species of plant

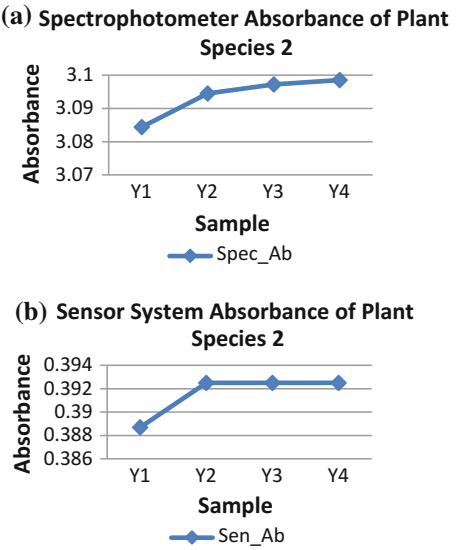

Fig. 6 **a** Absorbance (spectrophotometer) of leaves for the second species of plant, **b** absorbance (sensor system) of leaves for the second species of plant

was a linear increase in absorbance of the sensor system with the increase in maturity of the leaf. Hence, those readings were discarded (Fig. 5).

Likewise the readings for a different species of the castor plant were also considered which had green stems, and the younger leaves were of lighter shade of green compared to the species discussed earlier. Here also it was observed that the sensor system was not sensitive to the variation in the third decimal point as well. But in both the cases, the changes in the spectrophotometer absorbance and the

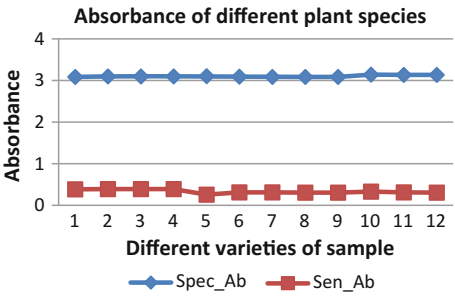

Fig. 7 Absorbance of leaves for different species of plant

sensor system absorbance followed the same trend, i.e., if one increased then the other also increased or remained same due to sensitivity issues (Fig. 6).

Some leaves from different plant like papaya were also studied along with some more matured leaves of the castor plant of the first species. All these readings of the papaya were put together with readings of the second species and shown below. Since the experimentation was carried out for different plant species at different time, there are some variations in the absorbance reading, but the overall trend was similar except for papaya leaves which had different texture and structure of the veins. The absorbance reading of the spectrophotometer was almost ten times more than the sensor system reading (Fig. 7).

4 Conclusion

The observations given above showed that the absorbance values of the spectrophotometer are related with the protein content of the leaf. If the protein content increased, then the absorbance also increased. Later the relation established between the spectrophotometer reading and reading of the sensor system varied in similar manner which indicated that the sensor system can be used to determine the protein content of the leaf. The sensitivity of the system can be increased by using some amplifier circuits. The proposal thus justifies the use of a system that is simple, non-invasive and economical. The system was designed for specific use, i.e., for castor leaves, and this can be modified to be used for other leaves as well.

References

1. Wang, G., Bronson, K.F., Thorp, K.R., Mon, J.: Multiple leaf measurements improve effectiveness of chlorophyll meter for durum wheat nitrogen management. Crop Sci. **54**, 817–826 (2014)
2. Ling, Q., Huang, W., Jarvis, P.: Use of a SPAD-502 meter to measure leaf chlorophyll concentration in Arabidopsis thaliana. Photosynth. Res. **107**, 209–214 (2010)

3. Muñoz-Huerta, R.F., Guevara-Gonzalez, R.G., Contreras-Medina, L.M., Torres-Pacheco, I., Prado-Olivarez, J., Ocampo-Velazquez, R.V.: A review of methods for sensing the nitrogen status in plants: advantages, disadvantages and recent advances. Sensors, 10823–10843 (2013)
4. Tamanna, T.: Biochemical estimation of three primary metabolites from medicinally important plant *Moringa oleifera*. Int. J. Pharm. Sci. Rev. Res. **7**(2), 186–188 (2011)
5. Shah, A.M., Memon, M.S., Memon, A.N., Ansari, A.W., Arain, B.A.: Analysis of protein by spectrophotometric and computer colour based intensity method from stem pea (*Pisum sativum*) at different stages. Pak. J. Anal. Environ. Chem. **11**, 63–71 (2010)
6. Philip, T., Somaprakash, D.S., Qadri, S.M.H.: Effect of fortification of castor (*Ricini Communis* L.) leaves with plant extracts on the biological performance of eri silkworm. Indian J. Seric. **48**(2), 191–193 (2009)
7. Kaffka, K.J., Norris, K.H., Kulcsár, F., Draskovits, I.: Attempts to determine fat, protein andcarbohydrate content in cocoa powder by the nir technique. Acta Aliment. **11**(3), 271–288 (1982)
8. Long, D.S., Engel, R.E., Siemens, M.C.: Measuring grain protein concentration within-line near infrared refl ectance spectroscopy. Agron. J. **100**(2), 247–252 (2008)
9. McDonagh, C., Burke, C.S., MacCraith, B.D.: Optical chemical sensors. Chem. Rev. **108**, 400–422 (2008)
10. Reddy, K.R., Matcha, S.K.: Quantifying nitrogen effects on castor bean (*Ricinus communis* L.), development, growth and photosynthesis. Elsevier B.V., pp. 185–191 (2010)

Hardware in Loop Control of Switched Capacitor Multilevel Inverter for Bus Clamping Modulation

Amarnath Yalavarthi, Akbar Ahmad and Paulson Samuel

Abstract The modified structure of multilevel inverter including a capacitor in series and parallel, providing voltage boost feature, is suitable for both symmetrical and asymmetrical cascaded operations. It produces a more number of voltage levels at the output with reduced number of switching devices when compared to the three basic multilevel inverters, namely diode-clamped, flying capacitor, and cascaded multilevel inverters. The hardware in loop switched capacitor multilevel inverter has been simulated and verified with the most popular and widely used sinusoidal pulse width modulation and space vector-based bus clamping modulation techniques. The vector modulation techniques have advantages of high output voltages and reduced harmonic distortion as they utilize the DC bus effectively. Bus-clamped pulse width modulation has the ability to reduce the switching losses of the converter and has reduced harmonic distortion. This paper provides a comparison between various control algorithms and bus clamping techniques for modified multilevel inverter.

Keywords Switched capacitor multilevel inverter (SCMLI)
Pulse width modulation (PWM) · Total harmonic distortion (THD)
Modulation index (MI) · Sinusoidal pulse width modulation (SPWM)
Bus clamping pulse width modulation (BCPWM)

A. Yalavarthi · A. Ahmad (✉) · P. Samuel
Department of Electrical Engineering, MNNIT Allahabad, Teliyarganj,
Allahabad 211004, India
e-mail: akbar_ree0713@mnnit.ac.in

A. Yalavarthi
e-mail: amaryalavarthi@gmail.com

P. Samuel
e-mail: paul@mnnit.ac.in

A. Konkani et al. (eds.), *Advances in Systems, Control and Automation*,
Lecture Notes in Electrical Engineering 442, https://doi.org/10.1007/978-981-10-4762-6_41

1 Introduction

Research and development are focused on renewable energies, as they are the major future solution to the increasing energy demand. Power electronic converters with improved efficiency play a prominent role in energy harvesting and supply to the grid through dedicated controls [1]. This led to the innovation of a wide range of power converter topologies. The research is still in progress to develop the most efficient and reliable converters. Multilevel inverters have replaced the earlier used three-level inverters because of their high-quality output waveform, low-voltage stress, and reduced switching losses [2–4]. Development of this prototype has given the idea for the latest schemes of the multilevel inverter.

There are three conventional multilevel inverter categories: (1) diode-clamped (neutral point clamped) multilevel inverter (DCMLI) [5], (2) capacitor-clamped (flying capacitor) multilevel inverter (CCMLI) [6], and (3) cascaded multilevel inverter (CMLI) [7]. DCMLI has some drawbacks such as an unequal rating of the devices, the high voltage rating of blocking diode, and the voltage unbalance. CCMLI uses a large number of capacitors and requires a special technique to balance the capacitor voltages. In CMLI, the problem of voltage unbalancing does not arise, but it requires a number of isolated DC supplies for higher levels. Many multilevel inverter topologies with reduced power devices and higher voltage levels have been presented in [8–11].

The two main challenges for the converter are the quality of the output waveform and boosting of the input voltage. At first, transformers are being served for boosting the input voltage. But the use of transformer increases the size and cost of the system and decreases the efficiency. This encouraged the research toward the transformerless topologies. The first transformerless topology with boosting capability was introduced in [12]. This type of converter uses switched capacitor concept to boost the input voltage. But this includes a number of switches and has certain limitations on a number of output levels. Later, many switched capacitor-based topologies have been introduced to overcome those limitations [13–15]. In [14], a topology has been introduced with the advantage of extending a number of levels with reduced number of power switches. This topology has inherent voltage balancing capability and a simplified gating circuit. A new hybrid topology has been introduced in [15] which have an advantage of cascading the units. This topology produces output levels based on the input voltage applied to the cascaded unit.

In this paper, a switched capacitor-based multilevel inverter has been simulated, and the output voltage and current waveform quality have been observed for both SPWM and SVPWM modulation strategies. The simulation and experimental results are presented at different modulation indices for RL load.

2 SCMLI Topology

The proposed converter operation is based on switched capacitor scheme. It has an advantage of boosting the input voltage. Figure 1 shows the configuration of the proposed topology used. The boost in voltage level is obtained by a series–parallel combination of the capacitor with the input voltage. When the capacitor is in parallel to the input voltage, it gets charged, and when in series, it gets discharged supporting the input voltage. Thus, the boost in the voltage level is achieved without the use of a transformer.

Basic unit consists of two power switches, a diode and a capacitor, as shown in Fig. 1. When the switch S_a is turned OFF and S_b is turned ON, capacitor comes in parallel with the supply voltage. During this stage, the capacitor gets charged.

$$V_{\text{out}} = V_C = V_{\text{in}}$$

When the switch S_a is turned ON and S_b is turned OFF, the capacitor network adds to the supply voltage, thereby increasing the available voltage level:

$$V_{\text{out}} = V_C + V_{\text{in}}$$

$$V_{\text{out}} = 2V_{\text{in}} \ (\because V_C = V_{\text{in}})$$

Both the switches S_a and S_b work complimentarily to each other and prevent the supply voltage from being short. The diode in the circuit prevents the capacitor discharging into the source. Thus, the output voltage is greater than input voltage without any transformer, thus reducing the size and cost of the circuit. The level of output voltage depends on the number of SC units used in the circuit. Various levels can be achieved as discussed in Table 1.

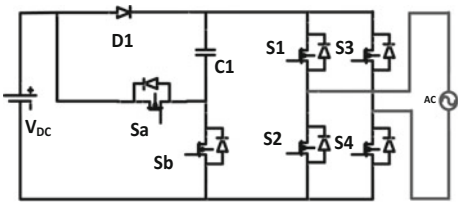

Fig. 1 Switched capacitor multilevel inverter

Table 1 Switching states for five-level output

Level	S_a	S_b	S_1	S_2	S_3	S_4
2 V	1	0	1	0	0	1
1 V	0	1	1	0	0	1
0	1	0	0	1	0	1
1 V	0	1	0	1	1	0
2 V	1	0	0	1	1	0

3 Modulation Methods

The modulation techniques for multilevel inverters can be classified according to the switching frequency. An exceptionally prominent strategy in modern applications is the multiple carrier sinusoidal PWM which uses phase-shifting strategy to lessen the harmonic content in the voltage waveform [16]. Carrier-based PWM is the most famous technique on account of its lucidity and ability to produce suitable output signal. Many multicarrier strategies have been proposed and implemented to reduce the harmonic distortion producing the high-quality output waveform with triangular carrier in comparison with sinusoidal signal. This technique is classified into 2 types: horizontal distribution (phase-shifted) technique and vertical distribution (level-shifted) technique. In phase-shifted pulse width modulation strategy, the equal amplitude and frequency carriers with slight shift in phase are compared with modulating signal to generate driving switching signals [17]. To generate n-level output waveform, $n - 1$ carrier signals are required.

Amplitude modulation index is as follows:

$$m_a = \frac{2 * A_m}{(n-1) * A_c},$$

Frequency modulation index is as follows:

$$m_f = \frac{f_c}{f_m}$$

where A_m and A_c are the amplitudes, and f_m and f_c are the frequencies of the modulating and carrier signals, respectively [16].

The number of cascaded blocks in each phase is represented as N_c with the carriers displaced by an angle using the same control signal to produce output voltage with less distortion. The minimum distortion is achieved when the carriers are shifted with an angle of $\theta_c = 2\pi/N_c$.

In level-shifted pulse width modulation strategy, the carriers with equal amplitude and frequency are shifted vertically [17]. In phase disposition pulse width modulation (PD-PWM), all the carriers are in phase. In phase opposition disposition pulse width modulation (POD-PWM), the carriers above the zero reference are in phase and those below the reference are shifted by 180°. In alternative phase opposition disposition (APOD-PWM), each carrier signal is shifted by 180° from the adjacent carrier.

In bus clamping techniques [18], each phase is clamped to either positive or negative DC bus for a particular duration by adding a common-mode signal:

$$m_R = (M * v_R) + m_{\text{cm}} \tag{1}$$

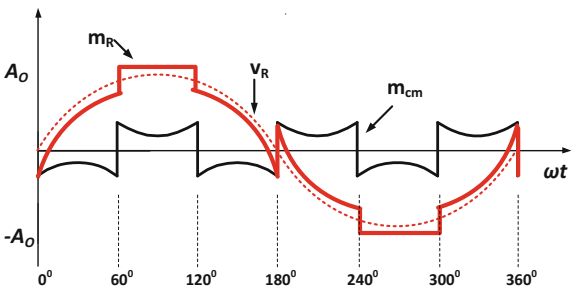

Fig. 2 Common-mode signal and 60° bus clamping modulating signal

$$m_Y = (M * v_Y) + m_{\text{cm}} \tag{2}$$

$$m_B = (M * v_B) + m_{\text{cm}} \tag{3}$$

where v_R, v_Y, and v_B are the three phases, M is the modulation index, m_{cm} is the common-mode signal, and m_R, m_Y, and m_B are the resulting modulating signals. The phase to be clamped and the period of clamping majorly depend on the location of desired reference voltage vector [19]. In 30° clamping, each phase gets clamped for the duration of 30° in every quarter cycle. In 60° clamping, the duration is of 60° for a half cycle of the phase. 60° strategies perform better when compared to 30° clamping at higher modulation indices [20]. In this paper, 60° bus clamping technique has been discussed, and Fig. 2 shows the modulating signal. The common-mode signal is generated based on the following equations:

$$m_{\text{cm}} = \begin{bmatrix} 2A_{\text{C}} - (M * v_{\text{Y}}); & -\pi < \omega_0 t < \frac{-2\pi}{3} \\ -2A_{\text{C}} - (M * v_{\text{R}}); & \frac{-2\pi}{3} < \omega_0 t < \frac{-\pi}{3} \\ 2A_{\text{C}} - (M * v_{\text{B}}); & \frac{-\pi}{3} < \omega_0 t < 0 \\ -2A_{\text{C}} - (M * v_{\text{Y}}); & 0 < \omega_0 t < \frac{\pi}{3} \\ 2A_{\text{C}} - (M * v_{\text{R}}); & \frac{\pi}{3} < \omega_0 t < \frac{2\pi}{3} \\ -2A_{\text{C}} - (M * v_{\text{B}}); & \frac{2\pi}{3} < \omega_0 t < \pi \end{bmatrix} \tag{4}$$

where A_{C} is the peak-to-peak amplitude of the carrier wave and ω_0 is the modulating signal frequency. The common-mode signal using (4) is obtained, and this generated signal is added to each of the phases given in (1)–(3) to get the required modulating signal as in Fig. 2.

4 Result and Discussions

Switched capacitor multilevel inverter has been simulated with the parameters mentioned in Table 2, and the following graphs and observations are noted in the analysis.

The simulations were realized with input DC voltage 100 V with the switching frequency f_C = 5 kHz. It is noted that all the SPWM techniques considered show almost similar performance. It can be observed that 60° clamp PWM with RL load gives best harmonic performance at modulation indices close to unity. The hardware in loop switched capacitor multilevel inverter has been simulated and verified using DSP microcontroller TMS320F240. The MOSFETs utilized in the prototype are IRFP250N with in-built bypass diodes. The experimental prototype is given an input supply of 15 V and the switching frequency of 1 kHz operating at an output phase frequency of 50 Hz with the load parameters R = 10 Ω and L = 12 mH. Figures 3 and 4 show the experimental results of the switched capacitor inverter for both PD and Bus clamping techniques.

Table 2 Circuit parameters considered in simulation study

Input voltage	100 V
Output phase voltage frequency	50 Hz
Carrier frequency	5 kHz
Circuit capacitance	4700 uF
Load (RL)	R = 10 Ω; L = 12 mH

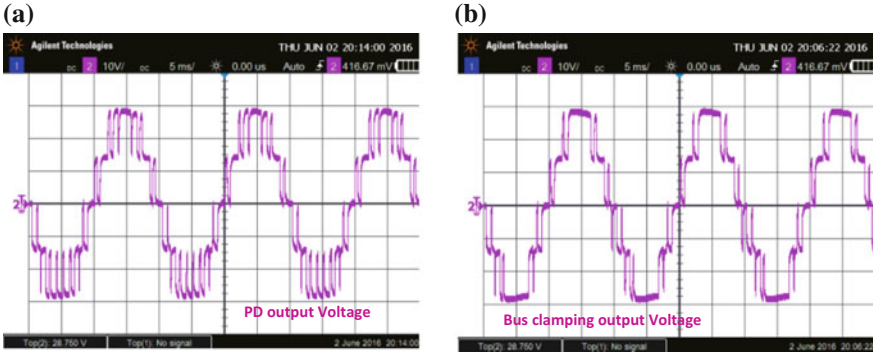

Fig. 3 Five-level voltage waveform **a** PD-PWM and **b** BCPWM

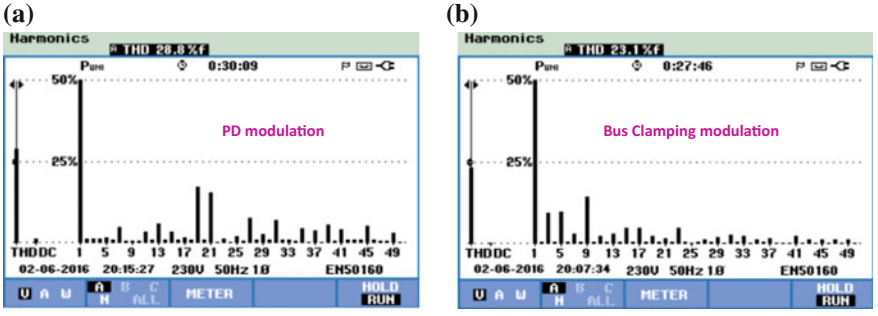

Fig. 4 **a** Output voltage THD for PD technique, **b** output voltage THD for 60° bus clamping technique

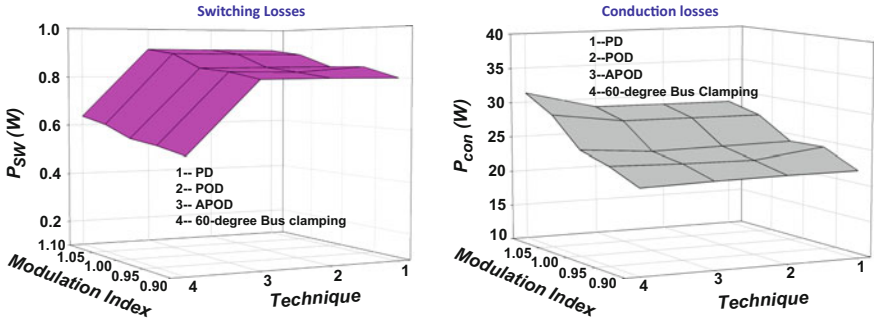

Fig. 5 Comparison of switching and conduction losses at various modulation indices

Switching and conduction losses in SCMLI are compared for SPWM and bus clamping modulation methods at different modulation indexes and are shown in Fig. 5. It is inferred that in comparison with SPWM techniques, bus clamping modulation has reduced switching losses due to clamping of the phase to the peak value as stated in Sect. 3. It is nearly 30% reduction in switching losses noted for bus clamping 60° modulation when compared to SPWM strategies. It is observed that for a given topology, bus clamping strategy has slightly increased conduction losses when compared to other techniques at higher modulation indexes. This is due to high value of fundamental current at the output drawn from the source.

5 Conclusion

Switched capacitor unit has an advantage of boosting the input voltage without the use of transformer and hence finds the motivation for the work to study the performance of the unit with different switching techniques. The most popular and simple SPWM technique has been compared with the bus clamping technique.

From both simulation and experimental results, it is observed that all the SPWM techniques show almost similar performance and the bus clamping technique reduces the harmonic distortion in comparison with SPWM techniques at higher modulation indices. It is further noted that bus clamping technique has reduced the switching losses in the output voltage waveform with the increase in the fundamental value of the voltage. Bus clamping technique results in approximately ten percent reduction in THD, and about one-third of the switching losses reduced than that of the SPWM techniques.

References

1. Rodriguez, J., Lai, J.S., Peng, F.Z.: Multilevel inverters: a survey of topologies, controls, and applications. IEEE Trans. Electron. **49**(4), 724–738 (2002)
2. Panagis, P., Stergiopoulos, F., Marabeas, P., Manias, S.: Comparison of state of the art multilevel inverters. In: Power Electronics Specialists Conference, PESC 2008, IEEE, Rhodes, pp. 4296–4301 (2008)
3. Pharne, I.D., Bhosale, Y.N.: A review on multilevel inverter topology. In: International Conference on Power, Energy and Control, pp. 700–703 (2013)
4. Zinoviev, G.S., Lopatkin, N.N.: Evolution of multilevel voltage source inverters. In: 9th International Conference on Actual Problems of Electronic Instrument Engineering, vol. 01, pp. 125–136 (2008)
5. Nabae, A., Takahashi, I., Akagi, H.: A new neutral-point clamped PWM inverter. IEEE Trans. Ind. App. **IA-17**, 125–136 (1981)
6. Mathew, J., Rajeevan, P.P., Mathew, K., Azeez, N.A., Gopakumar, K.: A multilevel inverter scheme with dodecagonal voltage space vectors based on flying capacitor topology for induction motor drives. IEEE Trans. Power Electron. **28**(1), 516–525 (2013)
7. Malinowski, M., Gopakumar, K., Rodriguez, J., Perez, M.A.: A survey on cascaded multilevel inverters. IEEE Trans. Ind. Electron. **57**(7), 2197–2206 (2010)
8. Mohamad, A.S., Mariun, N., Sulaiman, N., Amran, M., Radzi, M.: A new cascaded multilevel inverter topology with minimum number of conducting switches. In: IEEE Innovative Smart Grid Technologies, pp. 164–169 (2014)
9. Peng, F.Z., Qian, W., Cao D.: Recent advances in multilevel converter/inverter topologies and applications. In: International Conference in Power Electronics, pp. 492–501 (2010)
10. Gupta, K.K., Ranjan, A., Pallavee, B.: Multilevel inverter topologies with reduced device count: a review. IEEE Trans. Power Electron. **31**(1), 135–151 (2016)
11. Lai, J.S., Fang, Z.: Multilevel converters—a new breed of power converters. IEEE Trans. Ind. Appl. **32**(3), 509–517 (1996)
12. Marusarz, R.: A switched capacitor, inductorless DC to AC voltage step-up power converter. In: 20th Annual IEEE Power Electronics Specialists Conference PESC'89 Record, vol. 1, pp. 99–103 (1989)
13. Kanimozhi, M., Geetha, P.: A new boost switched capacitor multilevel inverter using different multi carrier PWM techniques. In: International Conference on Circuit, Power and Computing Technologies, pp. 432–437 (2014)
14. Ye, Y., Cheng, K.W.E., Liu, J., Ding K.: A step-up switched-capacitor multilevel inverter with self-voltage balancing. IEEE Trans. Ind. Electron. **61**(12), 6672–6680 (2014)
15. Babaei, E., Gowgani, S.S.: Hybrid multilevel inverter using switched capacitor units. IEEE Trans. Ind. Electron. **61**(9), 4614–4621 (2014)
16. Kant, P., Ahmad, A., Samuel, P.: Analysis and implementation of multicarrier modulation techniques for Marx multilevel inverter. In: 15th International Conference on Environment and Electrical Engineering Proceedings, pp. 1149–1154 (2015)
17. Sarkar, I., Fernandes, B.G.: Modified hybrid multi-carrier PWM technique for cascaded H-bridge multilevel inverter. In: 40th Annual Conference of the IEEE Industrial Electronics Society, pp. 4318–4324 (2014)
18. Narayanan, G., Krishnamurthy, H.K., Zhao, D., Ayyanar, R.: Advanced bus-clamping PWM techniques based on space vector approach. IEEE Trans. Power Electron. **21**(4), 974–984 (2006)
19. Narayanan, G., Ranganathan, V.T.: Two novel synchronized bus-clamping PWM strategies based on space vector approach for high power drives. IEEE Trans. Power Electron. **17**(1), 84–93 (2002)
20. Bhavsar, T., Narayanan, G.: Harmonic analysis of advanced bus-clamping PWM techniques. IEEE Trans. Power Electron. Lett. **24**(10), 2347–2352 (2009)

Estimation and Modeling of Underwater Acoustic Sensor Network

Jyotsna W. Chavhan and G.G. Sarate

Abstract Underwater wireless communication is a rapidly growing area of research and engineering. The acoustic channel used for propagating the underwater data from transmitter to receiver was having formidable challenges like slow transmission of data, prescribed bandwidth, varying transmission delay, and many more, which gives multipath fading and Doppler effect. Here, we present the underwater acoustic sensor network designed for two underwater wireless sensor nodes which transmit their data using acoustic link from one node to another. The acoustic link between transmitter and receiver is established for underwater data transmission. Acoustic link is having its own limitations like noise interference which is common in acoustic signal, transmission losses increases, time-varying multi-path transmission, Doppler spread is limited, bandwidth is limited up to certain distance, and also it provides high transmission delay. But waves under the water are scattered and propagate very slow which produces the propagation delay in it. Therefore, to overcome these issues, the acoustic channel is particularly modeled based on Gaussian distribution, where the delay varies with time rapidly. As acoustic signal get scattered in almost all directions under the water and it increases fading problem, Doppler spread, Doppler shift and Doppler delay, etc. The orthogonal frequency division multiplexing technique is used to overcome the problem of scattering by using the method called maximum entropy modeling. In this method, the delay between transmitting signal and received signal has been calculated referred as Doppler spread. It also calculates the bit transmitted rate and bit error rate by diving the channel into sub-channels using OFDM. The proposed system is designed and tested for shallow water using two tested nodes. The low-cost sensor nodes are designed which can continuously read the data like temperature, pressure, and salinity below the water, and it can then be transmitted to the receiver which is also kept under the water. The receiver receives the data and

J.W. Chavhan (✉)
Bapurao Deshmukh College of Engineering, Sewagram, Wardha, India
e-mail: jyotsna12.gawai@gmail.com

G.G. Sarate
Government Polytechnic Amravati, Amravati, India
e-mail: ggsanshu@gmail.com

A. Konkani et al. (eds.), *Advances in Systems, Control and Automation*,
Lecture Notes in Electrical Engineering 442, https://doi.org/10.1007/978-981-10-4762-6_42

displays it on laptop. This process demonstrates the vertical and horizontal communication. The system is tested for all atmospheric conditions under different environment. In this work, the system design and its simulation results are shown.

Keywords Underwater acoustic sensor network · Underwater acoustic channel (UW-A) · Orthogonal frequency division multiplexing · Doppler effect Multipath fading effect · Smart antenna approach

1 Introduction

Nowadays, researchers and scientists are doing their research work for underwater areas, which is the growing and emerging field for them. Underwater data are required for many applications like weather forecasting, hazard monitoring, and seaquake monitoring; oceanic data are required for seismic monitoring and many more. This can be possible by developing an underwater communication network by designing certain sensor nodes which can continuously read the underwater data and transfer it to the base station. In this research paper, underwater acoustic sensor network (UWASN) is designed to monitor the underwater data continuously with the help of sensors. The proposed system is designed and tested for shallow water condition using two tested nodes. The low-cost sensor nodes are designed which can continuously read the data like temperature, pressure, and salinity below the water, and it can then be transmitted to the receiver which is also kept under the water; then the received data are transmitted to the base station (laptop), which is kept above the water or nearby sea coastal region which actually continuously monitor the received data. This process demonstrates the vertical and horizontal communication link. Here, the underwater acoustic channel is modeled using maximum entropy modeling technique which calculates the Doppler spread that is 0.5–2 Hz only. Here, the acoustic channel satisfies the smart antenna approach by using IEEE standard 802.15.4, which gives the data transmission rate up to 250 kbps at 2.4 GHz carrier frequency for at least 2 m vertical link and approximately 10 m horizontal link, by keeping the depth of water up to 1.5 m.

The system is tested in a 25 m × 13 m (i.e. 325 m^2) swimming pool with 1–1.5 m depth. Therefore, the acoustic channel is also estimated based on shallow water conditions, since shallow water acoustic communication is consider. For this, the bandwidth was kept up to 2.4 GHz. Here, 16–64 sub-carriers are created with $312.5 \times 10 + 3$ sub-carrier spacing at the frequency of 3.6 MHz, and each sub-carriers are made to process 256 bits per sub-channel. Thus, the smart underwater acoustic communication system can be designed with fast communication and less power consumption.

2 Design of UWASN

2.1 Transmitter Section

Here in this work, we have designed a sensor node based on Fig. 1 as a transmitting node and Fig. 2 as the receiving node. The transmitting node reads the data like temperature, pressure, and salinity of water and transmits it to the receiving node using acoustic link. The design node is having some common specific parameters like (1) input power unit; (2) processing unit; (3) various sensors; (4) smart antennas;

2.2 Receiver Section

Here, the receiver receives the transmitted signal using smart antenna using MAX 232 port which actually converts the received data serially and displays it on the

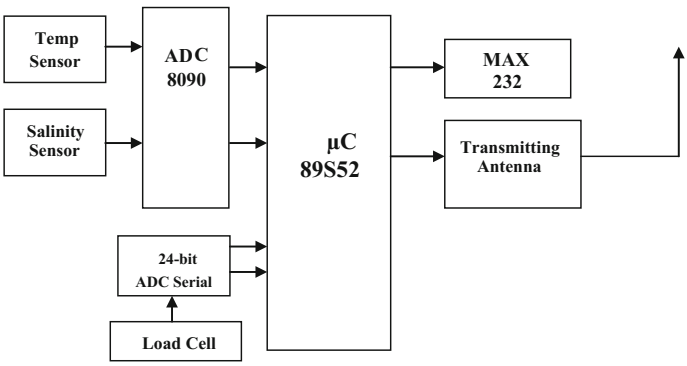

Fig. 1 Transmitter section

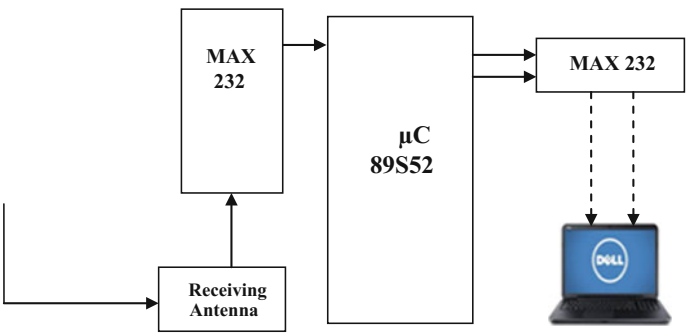

Fig. 2 Receiver section

laptop. The received antenna is a smart antenna which receives the data with the frequency of 2.4 GHz at the speed of 250 kbps. Initially, we made wired connection between underwater receiver node and to the base station; later on, we convert that into complete wireless solution.

3 Underwater Acoustic Channel Modeling

The acoustic channel creates various issues like transmission loss, includes noise, multipath fading, Doppler effects, and propagation delay. These issues determine the temporarily and spatially varying signal of the acoustic channel based on both the factors like bandwidth and frequency. Thus, this factor creates the refracting effect while reading the underwater data of temperature, pressure, and salinity based on the sound speed rather than the light speed. The sound speed is less than the light speed which is within the range of 1450–1540 m/s [1]. Thus, these factors are solved in this research paper, which gives significant values of bit error rate, data transmission rate, transmission delay, noise factor, etc.

3.1 Propagation Delay

The reading parameters like temperature, pressure, and salinity vary with the variation of speed of sound in water. As per the research, the temperature and pressure are almost constant near the surface of water, and the temperature decreases while pressure increases with depth of water. After certain level of depth, the temperature reaches a constant level of 4 °C, and from there, the speed of sound increases with depth [2]. Here Eq. (1) shows the calculation of speed of sound in water.

$$c1 = 1449 + 4.6t + 0.055t^2 + 0.003t^3 + (1.39 - 0.012t)(s - 35) + 0.017d \quad (1)$$

where t is temperature in degree Celsius, s is the salinity; whereas d is the depth of water in meters.

The propagation delay can then be calculated as

$$\tau = \frac{l}{c1} \quad (2)$$

where τ is time in seconds and l is distance in meters.

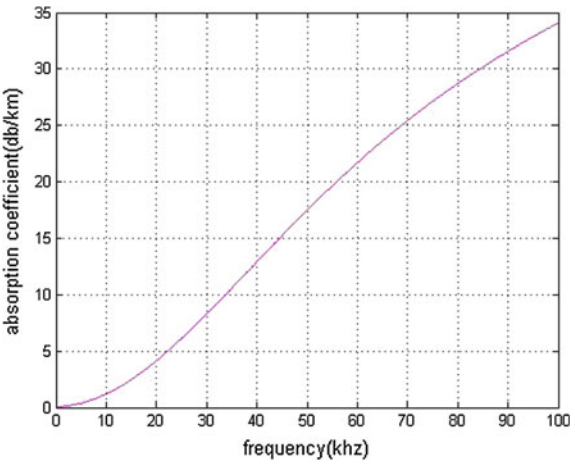

Fig. 3 Absorption coefficient

3.2 *Absorption Coefficient*

Absorption coefficient is an another important factor for acoustic channel. It increases rapidly with increases in frequency as shown in Fig. 3. For this case, the transmitting frequency is 2.4 GHz; therefore, the maximum signal gets attenuated due to high range of frequency, which reduces using the Eq. (3) denoted by α, which is plotted in the form of graph in Fig. 3. In this plot, the absorption coefficient factor reduces due to maximum entropy method for the frequency range about 2.4 GHz. This is already been explained properly in [3]. Here in this case, the acoustic channel was designed and tested for swimming pool where the depth of water was 1 m, and the transmitter and receiver were kept apart from each other around 10 m; therefore, the absorption coefficient was calculated as shown in the equation below, and its result is shown in Fig. 3.

$$\alpha = \frac{0.011f^2}{10+f^2} + \frac{44f^2}{410000+f^2} + 2.75 \times 10^{-4} f^2 + 0.003 \times 10^{-3} \tag{3}$$

4 Underwater Acoustic Channel Estimation

Once the acoustic channel was modeled, it needs to estimate properly based on the designed condition. Here, the channel estimation was done, where various factors were considered along with signal-to-noise ratio, bit error rate, and optimal frequency utilization. The channel to be modeled in such a way that it should be considered for maximum energy allocation within the specified frequency band, so that the channel capacity is maximized [3]. The results that are assessed suggest that despite the fact that frequency spectrum [4, 5] for underwater acoustic

communications, the possibilities in terms of usable frequency bands are not numerous, due to acoustic path propagation and noise characteristics [6].

4.1 SNR and SER

The signal-to-noise ratio identifies the significance of maximum signal received at the receiving end over the distance of 10 m at a frequency of 2.4 GHz, which can be calculated as shown in Eq. (3). In this equation, the transmitted power will be provided as the input power and the amplitude-to-noise ratio can be calculated; its resultant value is provided in the given Eq. (4):

$$\mathrm{SNR}(l,f) = \frac{P(f)}{\frac{A(l,f)}{N_f \Delta_f}} \tag{4}$$

where $P(f)$ is the transmitted power at the given frequency f, A the amplitude of the transmitted signal at the given frequency f travels at 1 m distance, N is the noise added into the received signal at the frequency f, and finally Δ_f is a narrow frequency band. Figures 4 and 5 show the resultant graph of SNR and BER.

4.2 Optimal Frequency

Figure 5 shows the BER of the data transmission reduces as the frequency of the transmitted signal varies from MHz to GHz. Here, we used the ZigBee module

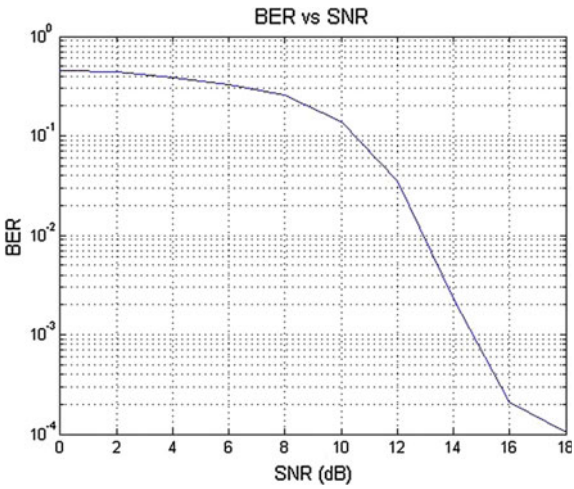

Fig. 4 SNR with BER

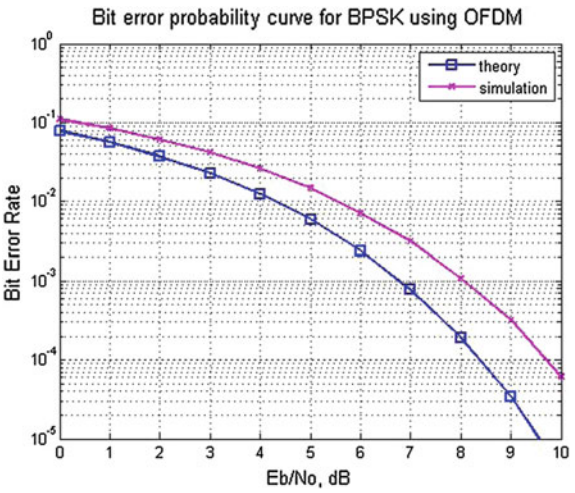

Fig. 5 BER with AN product

using XBee protocol for wireless transmission between transmitter and receiver. This module can work for wide range of frequency from MHz to GHz. Based on its system design and particular nodes, the frequency band is selected for maximum data transmission [7]. Thus, as per Fig. 5, the AN product is used for calculating the product for each distance of 1 m which can provide the maximum narrow band SNR at the receiver end for the optimized frequency *f*. Therefore, while implementing a wireless sensor communication system, a proper transmission bandwidth needs to be chosen so that the transmission power is adjusted for achieving the desired SNR throughout the selected frequency band. Practically, the response of the Doppler effect and noise generated using filtering processes of swimming pool was considered, and optimal transmission frequency was considered.

4.3 Channel Estimation

The designed system is based on 802.15.4 used for ZigBee technique which uses XBee protocol for data transmission using OFDM approach. The data get scattered under the water; therefore, OFDM technique is used; in this method, data are transmitted using the number of sub-carriers with uniform data transmission rate, and the frequency band is sub-divided into these channels. In Xbee-based systems, the IEEE 802.15.4 standard is used for data transmission between the nodes, where the transmission channel is based on OFDMA, which is a multiuser multicarrier modulation technique, in which the channel is divided into number of sub-channels which is used to share the data between several users. The bandwidth of 2.4 GHz scaled is sub-divided into 64 sub-channels each with a frequency of approximately 37.5 MHz [1]. All these sub-channels are correspondingly used to transmit the data

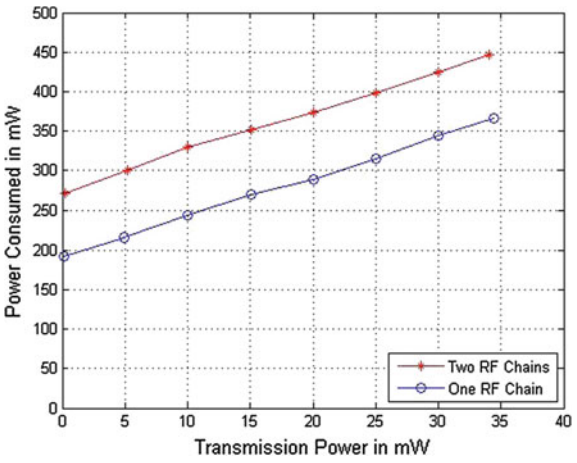

Fig. 6 Transmission power with power consumption

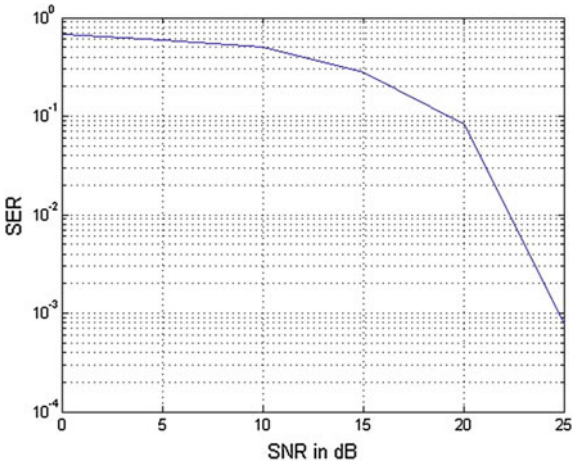

Fig. 7 Simulated BER with 1/2-rate convolution coding

from underwater transmitter to receiver by keeping the OFDM symbol duration at 3.2 μs. In this coding technique, Doppler spread was calculated as 0.5–2 Hz using IEEE standard 802.15.4, and delay spread was around 1 ms (Figs. 6 and 7).

4.4 A Smart Antenna Approach

In this proposed system, we used micro-strip antenna for fast and efficient transmission at the data transmission rate 250 kbps using 2.4 GHz frequency band. To support this antenna, IEEE standard 802.15.4 XBee is also used which actually providing the transmission rate up to 250 kbps. The use of smart antenna helps us to reduce the power consumption at every stage of transmission. The maximum power

Table 1 Simulating result of underwater acoustic sensor network

Parameters	Number of nodes			
	25	50	75	100
Average distance (m)	90.0642	89.235	68.9515	57.6881
Average depth (m)	25	25	25	25
Average energy (J)	0.4050	0.2007	0.2232	0.2052
Average time (ms)	0.22	0.31	0.28	0.38

require to transmit any data from transmitter to receiver is not more than 0.3459 J. The same power consumption can also be simulated for 25 numbers of nodes using 64 sub-carriers, each used 256 bits at 25.6 MHz frequency to transmit using MC-ESE algorithm. Therefore, the simulated results for the system are shown in Table 1.

5 Conclusion

Therefore, here we are concluding that the underwater acoustic sensor network is designed using two underwater low-cost homemade sensors. The nodes can transmit the data from the transmitter to the receiver using acoustic channel at the frequency of 2.4 GHz. The system is simulated, and corresponding results are shown in Table 1. Here the designed system was tested in swimming pool of 325 m^2 dimension, where the depth was kept as 1 m and the distance between the nodes was around 10 m maximum. The system was transmitting the data at the range of 250 kbps using XBee protocol of ZigBee module, which actually using for underwater data transmission. The underwater acoustic communication channel is designed using maximum entropy modeling technique by selecting acoustic channel simulation and performing root mean square. Doppler spread is 0.5–2 Hz. The acoustic communication channel satisfies smart antenna approach by using IEEE standard 802.15.4 which gives the data transmission rate up to 250 kbps at 2.4 GHZ carrier frequency for at least 2 m vertical communication link and approximately 2 m horizontal link by keeping the depth of water up to 1 m, since shallow water acoustic communication is consider. For this, the bandwidth was kept up to 2.4 GHz. The system can generate the maximum signal-to-noise ratio (SNR) that is up to 1.477 dB, and its signal-error-rate (SER) is calculated as −14.9513 dB.

References

1. Grythe, K., Hakegard, J.E.: Non-perfect channel estimation in OFDM-MIMO based underwater communication. IEEE J. (2009)
2. Linton, L., Conder, P., Faulkner, M.: Multiuser communications for underwater acoustic networks using MIMO-OFDM-IDMA. Center for Telecommunications and Micro-Electronics (CTME), Victoria University, Melbourne, Australia

3. Boayue, A.: Characterization of underwater acoustic communication statistical characteristics of the underwater multipath channels statistical characteristics of the underwater. Master of Science in Communication Technology, Norwegian University of Science and Technology, Department of Electronics and Telecommunications (26 Aug 2013)
4. Socheleau, F.-X., Laot, C., Passerieux, J.M.: Concise derivation of scattering function from channel entropy maximization, Draft (30 Apr 2010)
5. O Rourke, M.J.: Simulating underwater sensor networks and routing algorithms in MATLAB. Master of Science School of Engineering and Computer Science Engineering Science University of the Pacific Stockton, California (2013)
6. Thottappilly, A.: OFDM for underwater acoustic communication. Master of Science in Electrical Engineering, Blacksburg, Virginia (17 Aug 2011)
7. Ali, T., Jung, L.T., Faye, I.: Diagonal and vertical routing protocol for underwater wireless sensor network. Procedia Soc. Behav. Sci. (2014)

A New Development Methodology for High Precision ISP

Dommeti Rajesh, A.V. Praveen, G. Anusha and Mallikarjuna Rao Pasumarthi

Abstract For general image sensing applications in avionics, it is necessary to keep the line of sight (LOS) of the sensor insensitive to the carrier's body rates. Such application requirement necessitates the usage of an inertial stabilized platform (ISP). Any ISP generally consists of a two- or three-axis gimbal system with the payload, i.e., sensors or cameras on the inner gimbal. The dynamics of such a system are complicated, and it is a difficult task to attain the objective of stabilization. Parameter estimation techniques are used to derive a state space model of the gimbal system dynamics from the experimented data or design data of the gimbal system. In this paper, a state space model is estimated using a prediction error method for a cross-coupled two-axis inertial stabilization platform and the results of both cross-coupled and state space estimation method are compared. The model satisfies the characteristics of the original system for a required frequency range.

Keywords Inertial stabilized platform · Gimbal systems
Parameter optimization · Line of sight retention

D. Rajesh (✉) · A.V. Praveen · M.R. Pasumarthi
Department of Electrical Engineering, Andhra University College of Engineering(A), Andhra University, Visakhapatnam 530003, Andhra Pradesh, India
e-mail: rajesh.dommeti@gmail.com

A.V. Praveen
e-mail: venkatapraveenrs@gmail.com

M.R. Pasumarthi
e-mail: electricalprofessor@gmail.com

G. Anusha
Department of Electrical Engineering, Andhra University College of Engineering for Women, Andhra University, Visakhapatnam 530003, Andhra Pradesh, India
e-mail: g.anusha.1996@gmail.com

A. Konkani et al. (eds.), *Advances in Systems, Control and Automation*,
Lecture Notes in Electrical Engineering 442, https://doi.org/10.1007/978-981-10-4762-6_43

1 Introduction

Every image sensing and target tracking application requires an image processing device which is supposed to follow and track the target with high precision. Such devices are generally placed on moving vehicles which cause disturbances in the line of sight (LOS) of sensor and also degrade the quality of the image. Inertial stabilized platforms (ISP) are employed for the purpose of decoupling the movement of the body from the sensor's LOS [1]. The sensor will be placed in the inner elevation gimbal, and they are carried by the outer azimuth gimbal. The dynamics of such a structure are derived using Newton's second law or Lagrange equations [2, 3]. These equations are hard to derive if one assumes a dynamic mass imbalance in the system. Several papers have been published on gimbal dynamics assuming a linear and balanced system, but did not account for the dynamic mass unbalance which would occur once the body starts rotating [4]. A single axis gimbal which explained the single axis ISP well, but could not extend it to a multiaxis gimbal system is presented in [5]. If one assumes all the nonlinearities present in the system like friction torque or cable restraint torque to be linear or nonexistent, then the derived equations of motion will be an approximation of the actual systems dynamics and not exact [6]. Hence, for such complicated systems one may revert to system identification and parameter estimation techniques. This requires one to perform an experiment or a series of experiments on the actual system and then estimate a model of the system which, due to the advances in computational techniques and computing devices, will give a more accurate model than that obtained mathematical derivation. The motive behind implementing the parameter estimation techniques is to make the ISP system simple by the virtue of mathematical complexity so as to achieve better tuning of the controllers. In addition to that adopting the prediction error method attain that purpose better than subspace algorithms and facilitates improved understanding of the gimbal dynamics [7]. System identification was used to find the state space model of the gimbal dynamics, but a balanced gimbal system assumed thereby reducing the complexity of it [8]. Here, an unbalanced gimbal system is modeled and simulated. Then, its parameters are estimated using the prediction error estimation method.

This paper is organized as follows: Section 2 gives a derivation of the gimbal dynamics based on Newton's laws of motion and Lagrange's equations, and then dynamic unbalance and kinematic coupling are explained. Section 3 gives a brief introduction about system identification and parameter estimation using which a state space model has been derived. The obtained state space representation is then simulated giving the same signal as the original model and the two responses are compared.

2 Gimbal Dynamics

The two-axis gimbal is considered as shown in Fig. 1. It is placed on the main body via shock absorbers, and the outer gimbal is the azimuth gimbal and the inner gimbal is the elevation gimbal [1]. The sensor is placed on the inner gimbal, and its

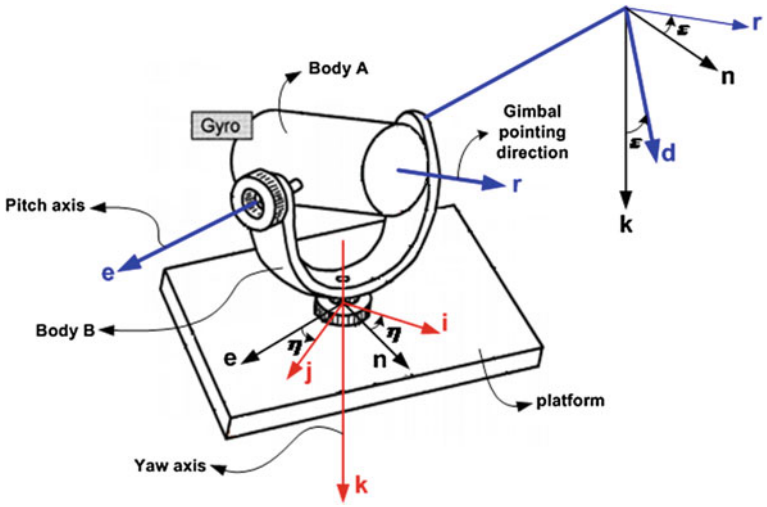

Fig. 1 Two-axis inertial stabilization system—axis representation

velocities in y and z direction are measured with the help of a rate gyro placed on the elevation gimbal. Three sets of coordinate frames are attached to each of the body, azimuth and elevation gimbals, (i, j, k) to the body, (n, e, k) to the outer gimbal, and (r, e, d) to the inner gimbal with A representing the inner gimbal, by representing the outer gimbal and P represents the main vehicle. The coordinate transformation matrices from P to B and B to A are as shown.

$$ {}^{B}_{P}C = \begin{bmatrix} \cos\eta & \sin\eta & 0 \\ -\sin\eta & \cos\eta & 0 \\ 0 & 0 & 1 \end{bmatrix} \quad {}^{A}_{B}C = \begin{bmatrix} \cos\varepsilon & 0 & -\sin\varepsilon \\ 0 & 1 & 0 \\ \sin\varepsilon & 0 & \cos\varepsilon \end{bmatrix} \tag{1} $$

Angular velocities are assigned to each frame with respect to coordinate their respective planes. The equations relating the angular velocities of different frames are as follows:

$$ \begin{cases} \omega_{Bn} = \omega_{Pi}\cos\eta + \omega_{pj}\sin\eta \\ \omega_{Be} = -\omega_{Pi}\sin\eta + \omega_{pj}\cos\eta \\ \omega_{Bk} = \omega_{Pk} + \dot{\eta} \end{cases} \tag{2} $$

$$ \begin{cases} \omega_{Ae} = \omega_{Be} + \dot{\varepsilon} \\ \omega_{Ad} = \omega_{Bn}\sin\varepsilon + \omega_{Bk}\cos\varepsilon \\ \omega_{Ar} = \omega_{Bn}\cos\varepsilon - \omega_{Bk}\sin\varepsilon \end{cases} \tag{3} $$

With Eq. (2) representing the transformation between main body and outer gimbal, and Eq. (3) is the relation between outer and inner gimbals angular velocities. The angles η and ε are the angles between the outer gimbal and the main

body and the inner and outer gimbals, respectively, with $\dot{\varepsilon}$ and $\dot{\eta}$ representing the rate of change of the angles.

The azimuth and elevation channel relationships are derived using the torque equation from Newton's law

$$T = J \cdot \alpha \tag{4}$$

This is the case when the plane in which the object is rotated on a stationary frame. When both are rotating, the equation becomes

$$\bar{T} = \frac{\mathrm{d}}{\mathrm{d}t}\bar{H} + \bar{\omega} \times \bar{H}; \quad \bar{H} = J \cdot \bar{\omega} \tag{5}$$

The angular velocities of the main body, inner, and outer gimbal are given in the following notations based on Fig. 1.

$$^{P}\bar{\omega}_{P/I} = \begin{bmatrix} \omega_{Pi} \\ \omega_{Pj} \\ \omega_{Pk} \end{bmatrix}, \quad ^{B}\bar{\omega}_{B/I} = \begin{bmatrix} \omega_{Bn} \\ \omega_{Be} \\ \omega_{Bk} \end{bmatrix}, \quad ^{A}\bar{\omega}_{A/I} = \begin{bmatrix} \omega_{Ar} \\ \omega_{Ae} \\ \omega_{Ad} \end{bmatrix} \tag{6}$$

The inertia matrices of the inner and outer gimbal are given under the following notation:

$$^{A}J_{\text{inner}} = \begin{bmatrix} A_r & A_{re} & A_{rd} \\ A_{re} & A_e & A_{de} \\ A_{rd} & A_{de} & A_d \end{bmatrix} \quad ^{A}J_{\text{outer}} = \begin{bmatrix} B_n & B_{ne} & B_{nk} \\ B_{ne} & B_e & B_{ke} \\ B_{nk} & B_{ke} & B_k \end{bmatrix} \tag{7}$$

The inertia matrix is not diagonal since mass unbalance is taken into consideration. The equation for the angular momentum of the elevation gimbal is as given below represents the moment of inertia of the elevation gimbal:

$$^{A}\bar{H}_{\text{inner}} = {}^{A}J_{\text{inner}}\bar{\omega}_{A/I} = \begin{bmatrix} A_r\omega_{Ar} + A_{re}\omega_{Ae} + A_{rd}\omega_{Ad} \\ A_{re}\omega_{Ar} + A_e\omega_{Ae} + A_{de}\omega_{Ad} \\ A_{rd}\omega_{Ar} + A_{de}\omega_{Ae} + A_{Ad}\omega_{Ad} \end{bmatrix} = \begin{bmatrix} H_r \\ H_e \\ H_d \end{bmatrix} \tag{8}$$

From which the torque acting on the elevation channel of the gimbal is found to be by Eq. (8) in (5).

$$A_e\dot{\omega}_{Ae} = T_{EL} + T_{D-EL} \tag{9}$$

$$\begin{aligned} T_{D-EL} = {} & (A_d - A_r)\omega_{Ar}\omega_{Ad} - A_{re}(\dot{\omega}_{Ar} + \omega_{Ae}\omega_{Ad}) + A_{rd}\left(\omega_{Ar}^2 - \omega_{Ad}^2\right) \\ & - A_{de}(\dot{\omega}_{Ad} - \omega_{Ae}\omega_{Ar}) \end{aligned} \tag{10}$$

$T_{D\text{-}EL}$ is the disturbance torque due to the gimbals inertia.

The load acting on the azimuth gimbal is a combination of both the payload and the elevation gimbal. The torque acting on it is as follows:

$$\bar{T} = \frac{\mathrm{d}}{\mathrm{d}t}\bar{H}|_B + \bar{\omega}_{B/I} \times \bar{H} \tag{11}$$

$$\bar{H} = \begin{bmatrix} H_i \\ H_j \\ H_k \end{bmatrix} = {}^{B}J_{\text{outer}}\bar{\omega}_{B/I} + {}^{A}_{B}C^{TA}J_{\text{inner}}\bar{\omega}_{A/I} \tag{12}$$

$$\begin{aligned} H_k = {} & B_{nk}\omega_{Bn} + B_{ke}\omega_{Be} + B_k\omega_{Bk} - (A_r\omega_{Ar} + A_{re}\omega_{Ae} + A_{rd}\omega_{Ad})\sin\varepsilon \\ & + (A_{rd}\omega_{Ar} + A_{de}\omega_{Ae} + A_d\omega_{Ad})\cos\varepsilon \end{aligned} \tag{13}$$

$$\begin{aligned} \left(\bar{\omega}_{B/I} \times \bar{H}\right)_k = {} & \omega_{Bn}(B_{ne}\omega_{Bn} + B_e\omega_{Be} + B_{ke}\omega_{Bk} + A_{re}\omega_{Ar} + A_e\omega_{Ae} + A_{de}\omega_{Ad}) \\ & - \omega_{Be}(B_n\omega_{Bn} + B_{ne}\omega_{Be} + B_{nk}\omega_{Bk}) - \omega_{Be}(A_r\omega_{Ar} + A_{re}\omega_{Ae} + A_{rd}\omega_{Ad})\cos\varepsilon \\ & - \omega_{Be}(A_d\omega_{Ar} + A_{de}\omega_{Ae} + A_d\omega_{Ad})\sin\varepsilon \end{aligned} \tag{14}$$

$$J_{eq}\dot{\omega}_{Bk} = T_{Az} + T_{d1} + T_{d2} + T_{d3} \tag{15}$$

where J_{eq}, T_{d1}, T_{d2}, T_{d3}, and T_{d4} are simplified as

$$J_{eq} = B_k + A_r\sin^2\varepsilon + A_d\cos^2\varepsilon - A_{rd}\sin(2\varepsilon) \tag{16}$$

$$T_{d1} = \left[B_n + A_r\cos^2\varepsilon + A_d\sin^2\varepsilon + A_{rd}\sin(2\varepsilon) - (B_e + A_e)\right]\omega_{Bn}\omega_{Be} \tag{17}$$

$$\begin{aligned} T_{d2} = {} & -[B_{nk} + (A_d - A_r)\sin\varepsilon\cos\varepsilon + A_{rd}\cos(2\varepsilon)] \times (\dot{\omega}_{Bn} - \omega_{Be}\omega_{Bk}) \\ & - (B_{ke} + A_{de}\cos\varepsilon - A_{re}\sin\varepsilon) \times (\dot{\omega}_{Be} + \omega_{Bn}\omega_{Bk}) \\ & - (B_{ne} + A_{re}\cos\varepsilon + A_{de}\sin\varepsilon) \times \left(\omega_{Bn}^2 - \omega_{Be}^2\right) \end{aligned} \tag{18}$$

$$\begin{aligned} T_{d3} = {} & \ddot{\varepsilon}(A_{re}\sin\varepsilon - A_{de}\cos\varepsilon) + \dot{\varepsilon}[(A_r - A_d)(\omega_{Bn}\cos(2\varepsilon) - \omega_{Bk}\sin(2\varepsilon))] \\ & + \dot{\varepsilon}[2A_{re}(\omega_{Bn}\sin(2\varepsilon) + \omega_{Bk}\cos(2\varepsilon))] + \dot{\varepsilon}[(A_{de}\sin\varepsilon + A_{re}\cos\varepsilon)(\omega_{Ae} + \omega_{Be}) - A_e\omega_{Bn}]. \end{aligned} \tag{19}$$

3 Kinetic Coupling

In the above equations, the terms of the type A_{re}, A_{rd}, A_{de} denote the inertia terms of the respective gimbals with respect to two axes and are called as products of inertia. Such terms are zero for symmetrical bodies. In addition to the asymmetrical nature of the ISP, angular coupling between the two channels is also present, meaning that the angular motion with respect to one axis disrupts the position of the LOS with

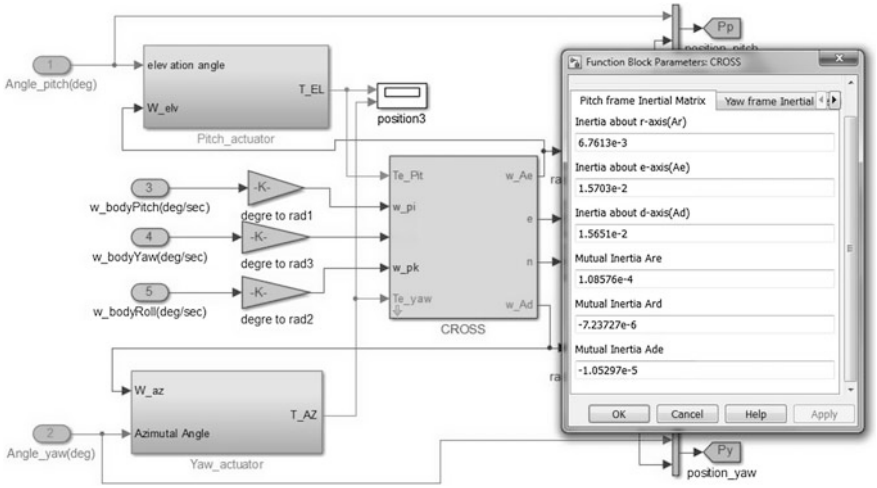

Fig. 2 Simulation diagram of the system with body rates

respect to another axis. These two situations were considered while deriving the torque equations. The simulation diagram is shown in Fig. 2.

Two different case studies are taken with inertial matrices in order to generalize the theory of parameter estimation that applied to two-axis gimbal systems.

Case (i): The simulation is assigned with existing system values with 650 g seeker plate and with true dimensions. The inertia matrices are taken from physical CAD model and are assigned to unbalanced cross-coupled block.

$$
{}^{A}J_{inner} = \begin{bmatrix} 6.7613e^{-3} & 1.08576e^{-4} & -7.23727e^{-6} \\ 1.0857e^{-4} & 1.5703e^{-2} & -1.05297e^{-5} \\ -7.2372e^{-6} & -1.05297e^{-5} & 1.5651e^{-2} \end{bmatrix}
$$

$$
{}^{B}J_{outer} = \begin{bmatrix} 3.50961e^{-2} & 6.21373e^{-6} & 6.21373e^{-6} \\ 6.21373e^{-6} & 1.58219e^{-2} & -1.24045e^{-4} \\ 6.21373e^{-6} & -1.24045e^{-3} & 3.14724e^{-2} \end{bmatrix}
$$

Case (ii): In this example, a dual axis camera gimbal structure was considered and represented with unbalanced inertial matrix as well as actuation system data [3].

$$
{}^{A}J_{\text{inner}} = \begin{bmatrix} 1e^{-3} & -2e^{-3} & -4e^{-3} \\ -2e^{-3} & 8e^{-4} & -1e^{-3} \\ -4e^{-3} & -1e^{-3} & 6e^{-3} \end{bmatrix}
$$

$$
{}^{B}J_{\text{outer}} = \begin{bmatrix} 3e^{-3} & -2e^{-3} & -4e^{-3} \\ -2e^{-3} & 4e^{-4} & -1e^{-3} \\ -4e^{-3} & -1e^{-3} & 3e^{-4} \end{bmatrix}.
$$

4 Parameter Estimation Using Prediction Error Method

Parameter estimation and system identification are two concepts with the same procedure of calculation with disguised goals or applications. The latter gives a model that explains the system's responses, while the former also gives a vector containing the parameters of the system. Since the advent of computers, this has become quite achievable. So to obtain the mathematical model of the gimbal system without manually deriving the entire equations, one can adopt one of the above processes depending on their application. The MATLAB System Identification tool is used here, which can give a linear (transfer function or state space) or a nonlinear model of a system. The block named cross in Fig. 2 contains the equations derived in Sect. 2. The cross-coupled block is connected to actuate motors, one each for elevation and azimuth channels. By applying system identification toolbox, the cross-coupled block is to be replaced by an estimated model in order retain system characteristics.

To find the state space model for the gimbal system using prediction error method, in which the past inputs, outputs, and tries to predict the future output. A parameter vector has kept updating based on the error in the predicted value for every iteration. It is an iterative procedure using a gradient search algorithm. This method computes the parameters of the model from complex transfer function into the state space model to pertain its original characteristics. The system identification toolbox in MATLAB is used to obtain the state space model of the gimbal system

The original model was simulated initially under excitation with random signal as inputs and the system's response to it are sampled into the toolbox. Using indent commands, the data appear in the working data box and the required operation performed. This model is validated in the toolbox by choosing the model order of estimation. The procedure is repeated more types of inputs to incorporate the characteristics of the original system. More the number of experiments tends to guaranteed for the valid mode. So higher sample number, then the goodwill be the estimated model.

5 Simulation and Results

The two case studies are estimated with different inputs using system identification toolbox and obtained estimated model and are shown below. Both the original and estimated models are tested with the same input, i.e., unit step and corresponding output signals are observed in each case for elevation, yaw channels and their position, stabilization loops.

Case (i): The estimated state space model with A, B, C, and D is given by

$$A = \begin{bmatrix} 5.219 & -34.41 & -256.1 & 26.08 \\ -8.504 & -217.9 & -1694 & 341.2 \\ -4.944 & 26.15 & 193.4 & -21.17 \\ 24.84 & 5.452 & 81.73 & -74.12 \end{bmatrix}$$

$$B = \begin{bmatrix} 128.8 & 16.66 & 16.66 & 16.66 & 16.66 \\ 3368 & 127.1 & 127.1 & 127.1 & 127.1 \\ -108.5 & -12.76 & -12.76 & -12.76 & 131.1 \\ -1095 & -11.72 & -11.72 & -11.72 & 435 \end{bmatrix}$$

$$C = \begin{bmatrix} 3.935 & 0.6258 & 10.14 & 1.341 \\ -0.8946 & 0.262 & 0.9114 & 0.5898 \\ -0.8962 & 0.2517 & 0.8217 & 0.5872 \\ 3.763 & 0.6706 & 10.18 & 1.515 \end{bmatrix}$$ with D matrix being zero

The results corresponding to case (i) are given in Figs. 3, 4, 5, and 6. In which, (a) subplot shows the original system response and (b) subplot shows estimated model response characteristics. From the time and frequency domain characteristics, it shows that the estimate system replicates the original system to provide a simplified model to tune the PID controllers.

Case (ii): The estimated state space model with A, B, C, and D is given by

$$A = \begin{bmatrix} 19.76 & -82.06 & 16.65 & 54.14 \\ 10.1 & -38.53 & 6622 & 21.46 \\ 7.003 & -24.35 & -5.105 & 2.567 \\ 3.674 & -7.61 & 3.94 & 1.003 \end{bmatrix}$$

$$B = \begin{bmatrix} 120 & -1.148e^{-2} & 6.154e^{-2} & -5.006e^{-2} & 162.4 \\ -131.1 & -2.094e^{-2} & 2.102e^{-2} & -7.85e^{-2} & 76.12 \\ -854.5 & -8.991e^{-2} & 1.918e^{-2} & 7.073e^{-2} & -68.82 \\ 7.579 & -1.176e^{-2} & -2.56e^{-2} & -1.383e^{-2} & -6.311 \end{bmatrix}$$

$$C = \begin{bmatrix} -0.3017 & 1.806 & -1.621 & -2.886 \\ 0.008499 & -0.02739 & 0.01647 & -0.1408 \\ -0.008938 & -0.005439 & 0.006731 & -0.1413 \\ -1.203 & 30773 & -1.314 & -2.069 \end{bmatrix}$$ with its D matrix also being zero.

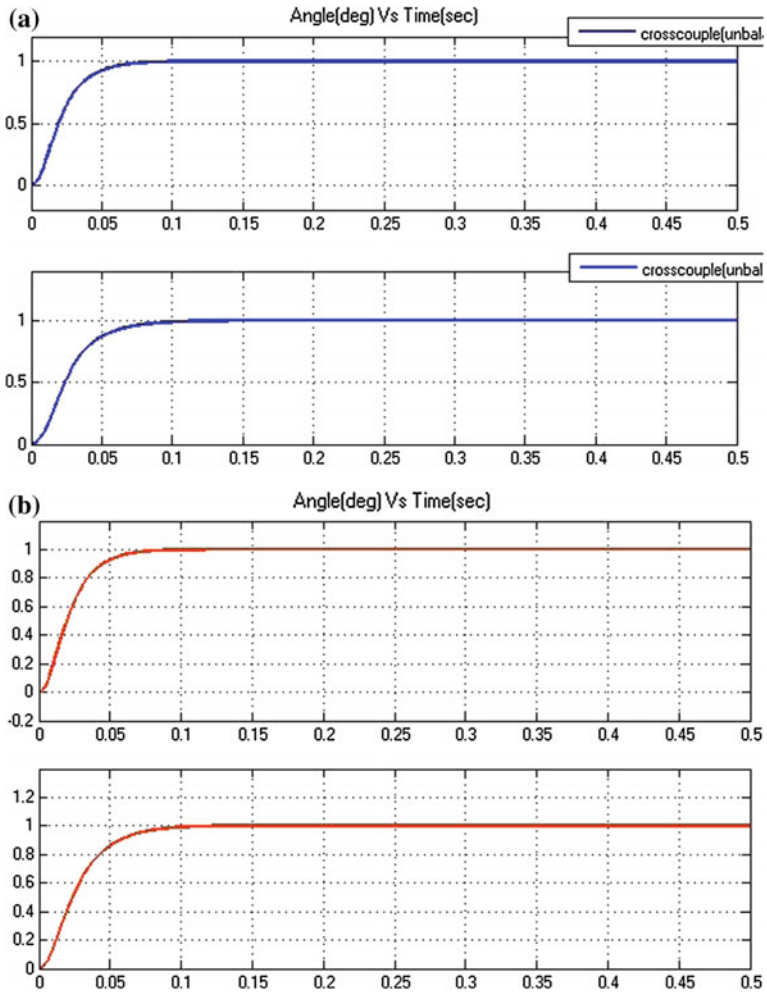

Fig. 3 Step position responses of elevation and yaw channel **a** cross-coupled, **b** estimated

The results pertaining to the case (ii) are given below in Figs. 7, 8, 9, and 10. Where subplots (a), (b) show original and estimated system characteristics, respectively. From the time and frequency domain characteristics, estimated state space model replicates the original system. Hence two case studies, the procedure can be generalized to two-axis gimbal ISP systems to represent whole complex system into a simple state model. The ultimate goal of this kind of complex problem is that to simplify the system to enhance the tuning procedure of the controller without any approximations.

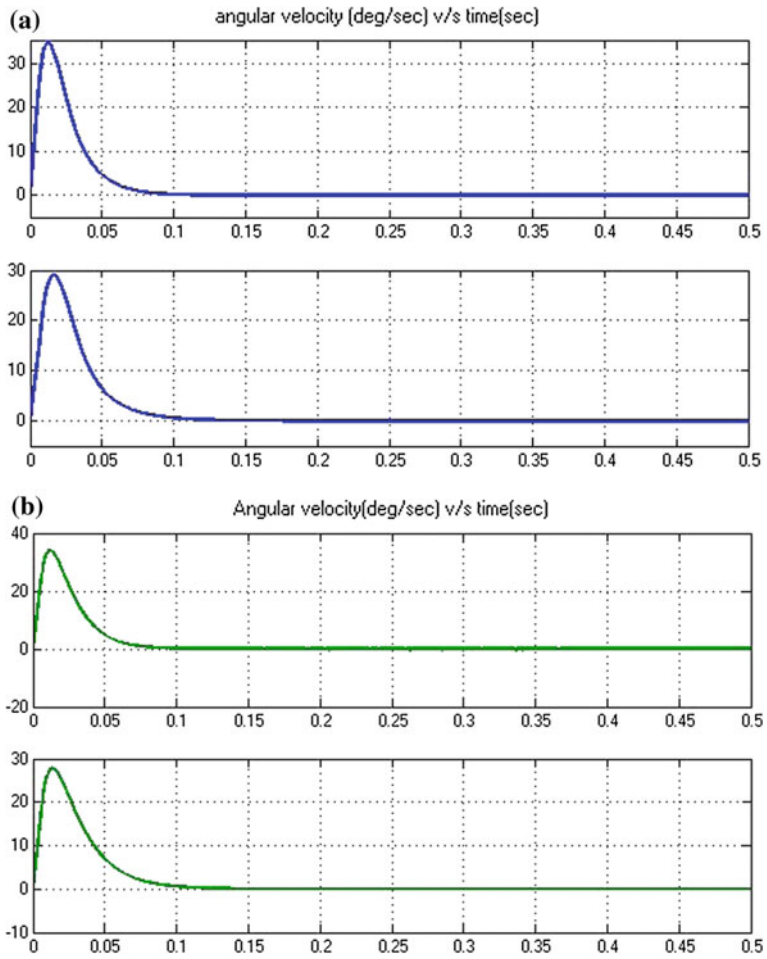

Fig. 4 Stabilization loop responses of elevation and yaw channel **a** cross-coupled, **b** estimated

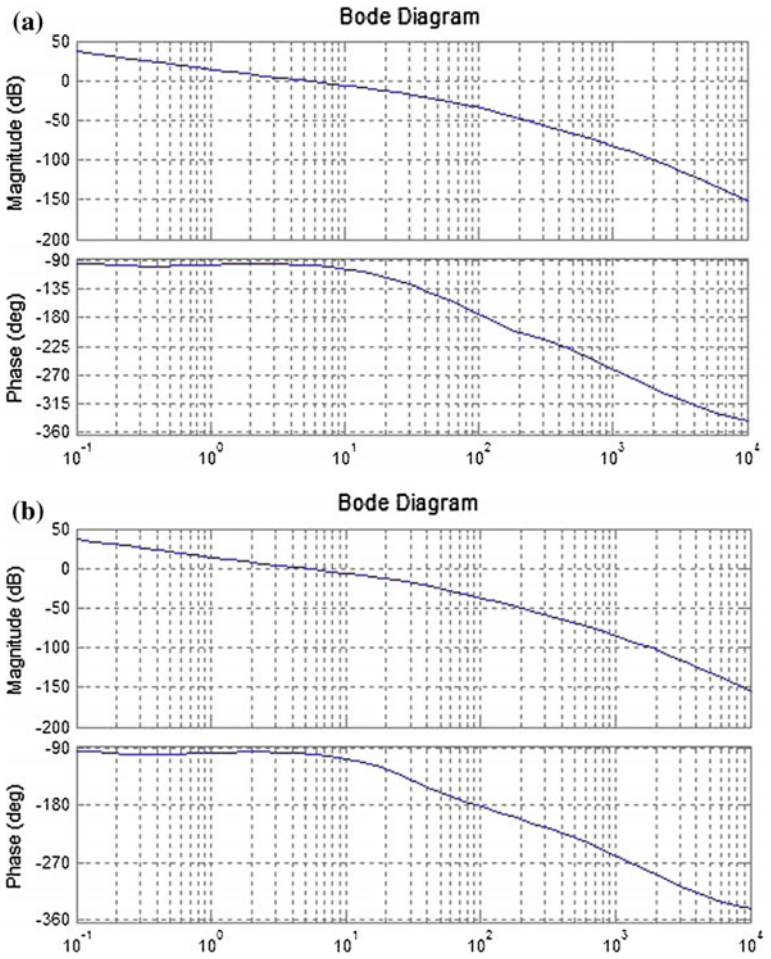

Fig. 5 Frequency responses of elevation position loop **a** cross-coupled, **b** estimated

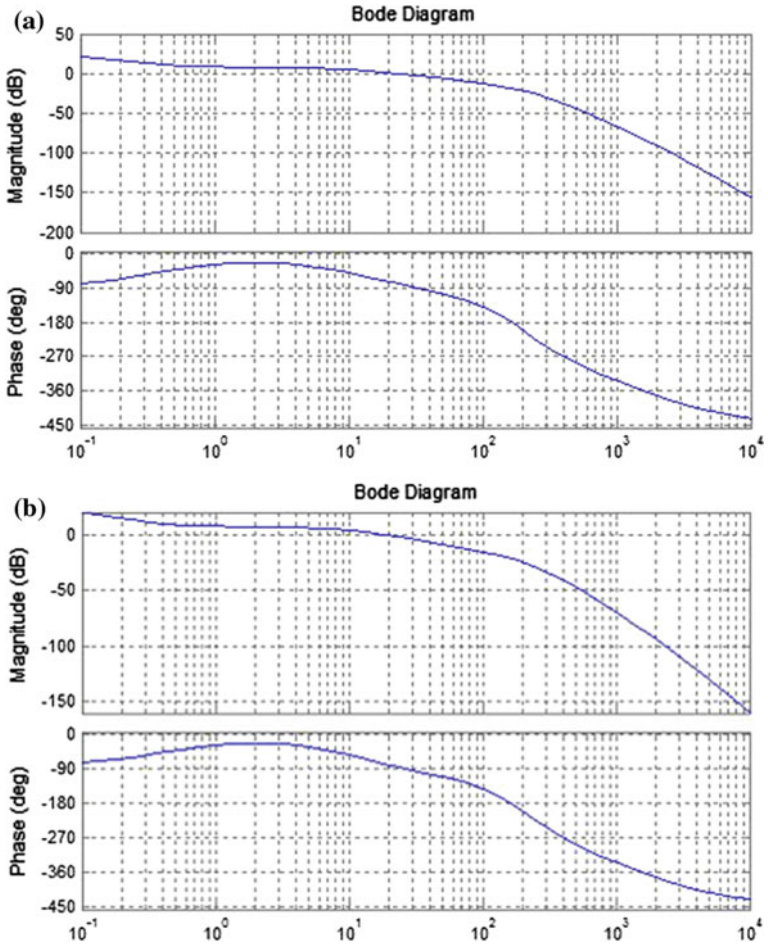

Fig. 6 Frequency responses of elevation stabilization loop **a** cross-coupled, **b** estimated

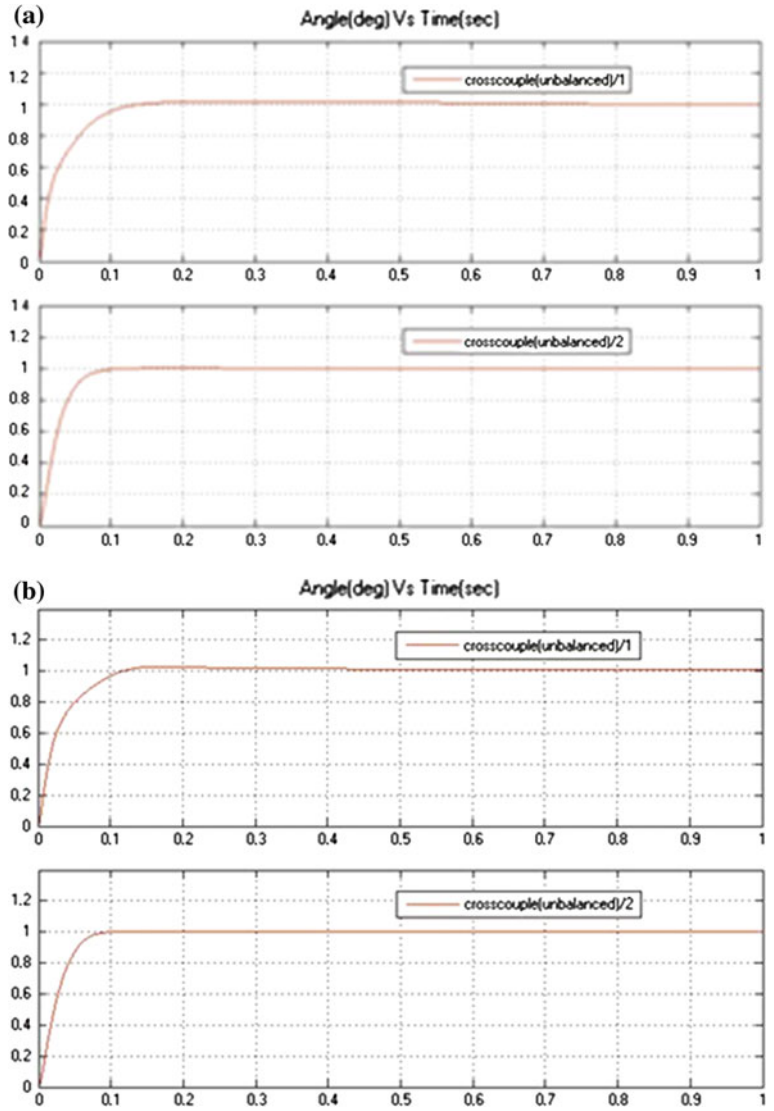

Fig. 7 Step position responses of elevation and yaw channel **a** cross-coupled, **b** estimated

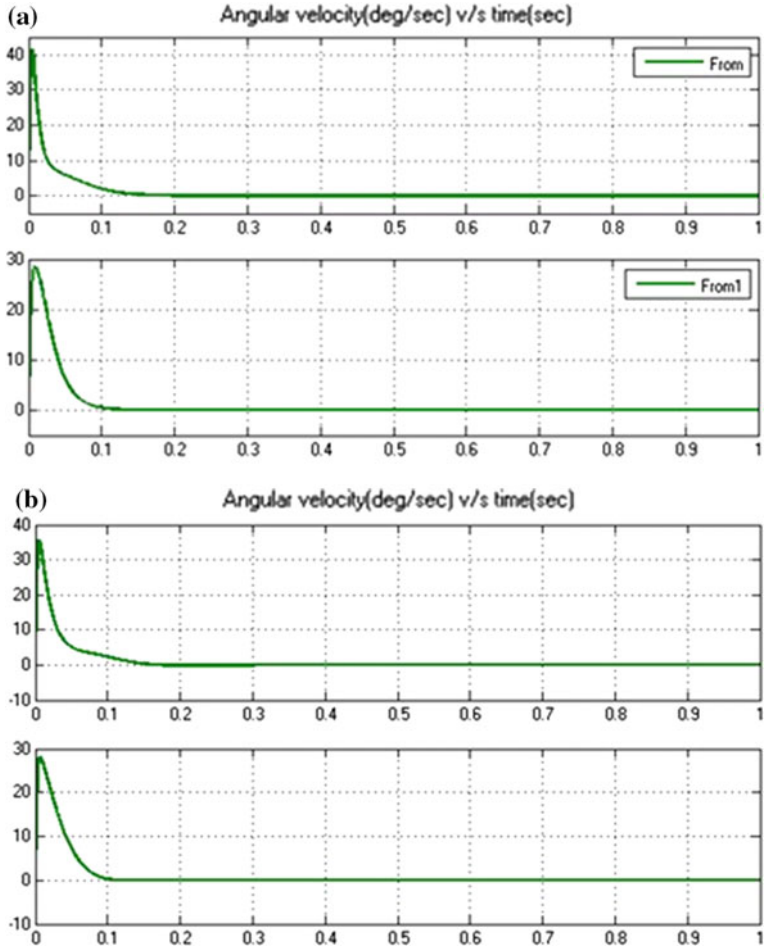

Fig. 8 Stabilization loop responses of elevation and yaw channel **a** cross-coupled, **b** estimated

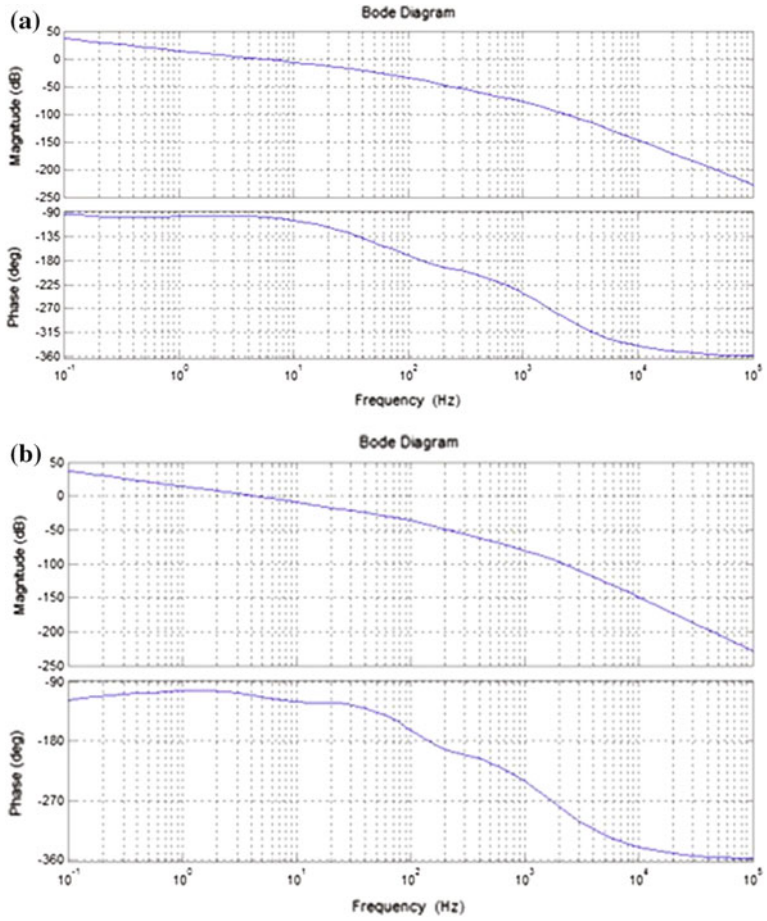

Fig. 9 Frequency responses of elevation position loop **a** cross-coupled, **b** estimated

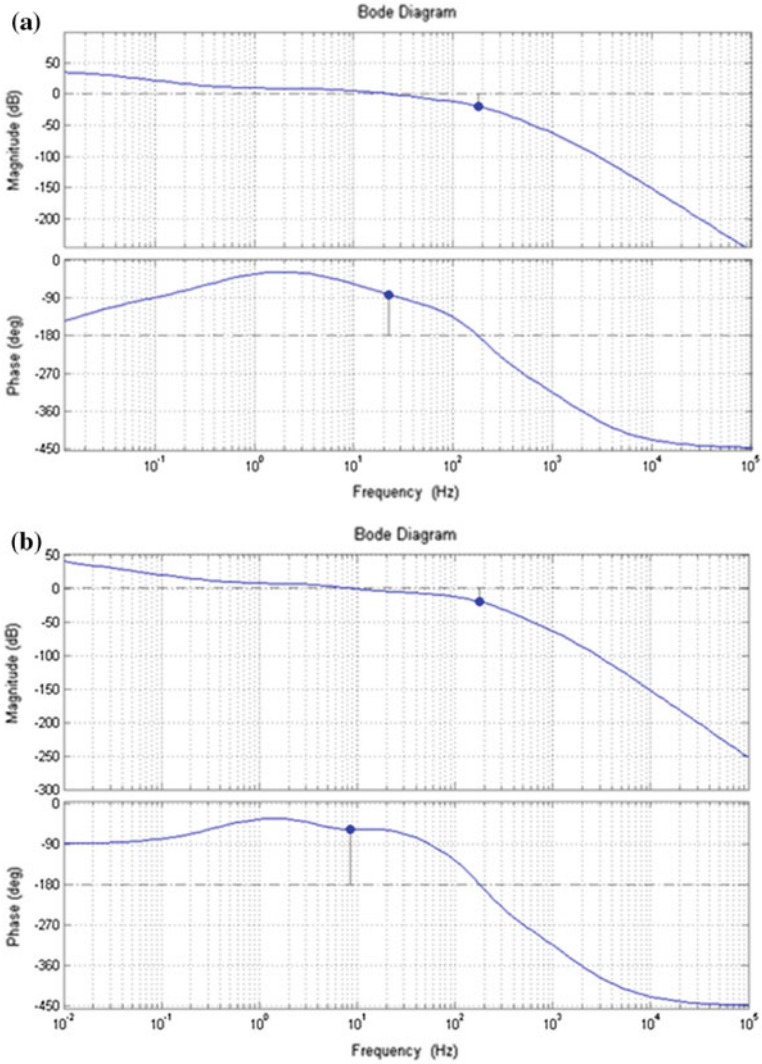

Fig. 10 Frequency responses of elevation stabilization loop **a** cross-coupled, **b** estimated

6 Conclusion

The cross-coupled model obtained by considering all nonlinearities of the inertial stabilization platform is more complex in nature, and it is very difficult to determine the parameters of PID controllers for two channels. Parameter optimization block facilitates the same characteristics of cross-coupled model with less complexity in tuning the position loop and stabilization loop controllers. This approach is identical for any two-axis gimbal systems with various sets of parameters. The parameter estimated model retains all characteristics of the original physical system.

References

1. Masten, M.: Inertial stabilized platforms for optical imaging systems. IEEE Control Syst. Mag. **28**(1), 47–64 (2008)
2. Ekstrand, B.: Equations of motion for a two-axes gimbal system. IEEE Trans. Aerosp. Electron. Syst. **37**(3), 1083–1091 (2001)
3. Abdo, M., Reza, A., Toloei, A., Reza, M.: Research on the cross-coupling of a two axes gimbal system with dynamic unbalance. Int. J. Adv. Rob. Syst. **1** (2013)
4. Khodadadi, H.: Robust control and modeling a 2-DOF inertial stabilized platform. In: International Conference on Electrical, Control and Computer Engineering 2011 (InECCE) (2011)
5. Otlowski, D.R.: Mass properties factors in achieving stable imagery from a gimbal mounted camera. In: Airborne Intelligence, Surveillance, Reconnaissance (ISR) Systems and Applications V (2008)
6. Hilkert, J.M., Hullender, D.A.: Adaptive control system techniques applied to inertial stabilization systems. In: Acquisition, Tracking, and Pointing IV (1990)
7. Ljung, L.: System Identification: Theory for the User. Prentice-Hall, Englewood Cliffs, NJ (1987)
8. Ha, J.: A study on the control method of a ship borne launcher using a system identification method. In: 2015 19th International Conference on System Theory, Control and Computing (ICSTCC) (2015)

Simple FOPI Tuning Method for Real-Order Time Delay Systems

Utkal Mehta, Vincent Lechappe and Om Prakash Singh

Abstract Fractional-order controllers (FOC) can be more adequate to control systems with complex dynamics than integer-order controllers; however, how to obtain FOC is still being explored vigorously. This paper deals with a tuning approach for FOC with primary requirements of simplicity in technique and robustness. A simple analytical method to tune fractional-order proportional-integral (FOPI) controller for known system transfer functions is proposed. Study shows the simplicity and efficiency of the presented design method over some previously published approaches.

Keywords Fractional-order PI controller · Robustness · Time delay systems Optimal tuning

1 Introduction

There are many techniques for PID tuning, classical rules, optimization programs, model-based tuning, and many other tested in industry so far [1]. Even though the PID is simple, many challenge to tune the controller parameters practically. Recently, real-order PID controller design shows considerable interest in academic research and industry [2–8]. This is mainly due to the fact that real-order transfer for controller can better represent the various systems of engineering and sciences [1]. In general, real-order transfer function considered for PID is called the

U. Mehta (✉) · V. Lechappe
School of Engineering and Physics, The University of the South Pacific, Suva, Fiji
e-mail: utkal.mehta@usp.ac.fj

V. Lechappe
e-mail: vincent.lechappe@usp.ac.fj

O.P. Singh
Department of Electronics and Communication Engineering,
Sikkim Manipal Institute of Technology, Majitar, Sikkim, India
e-mail: opsing@gmail.com

A. Konkani et al. (eds.), *Advances in Systems, Control and Automation*,
Lecture Notes in Electrical Engineering 442, https://doi.org/10.1007/978-981-10-4762-6_44

fractional-order PID (FOPID) controller. Moreover, it is evident from significant research that FOC have additional merits of handling complex system dynamics compared to conventional PID. After inducing the concept of FOPID controller in [1], a stabilization problem of fractional systems using FOPID controllers was also studied by Hamamci [9]. Especially, due to the computational tool such as FOMCON toolbox [10] available, design verification of real-order transfer function is possible in Simulink study. Literature study shows that number of design approaches have been reported to suggest good FOPID parameter values. Some methods were applied successfully in many practical non-integer examples such as control of hard disk drive servo systems, control of power electronic converters, velocity control of a servo system, control of composite hydraulic cylinders, and control of head flow. All previous techniques experience certain limitations, such as to solve simultaneously two or more nonlinear algebraic relations to calculate the unknown parameters of FOPID. However, in this way, there is a possibility to place the non-optimum solution if pitiable guess of initial values is used.

In this work, an effort is made to develop explicit tuning method for FOPI controller considering the real-order dead time systems. In this way, the proposed method can be applied to integer and fractional systems also. The objective is to derive simple and fast tuning formula that industry can adopt easily for various PID tune-controlled systems. The main objective is to design parameters of FOPI such that it optimizes load disturbance rejection. The exact formula is derived with required constraint imposed on the Nyquist curve. The loop transfer function of closed-loop must, therefore, satisfy robustness index.

2 A Real-Order (Fractional) Transfer Function

A general transfer function of any real order can be written in the s-domain as follows,

$$G(s) = \frac{b_m s^{\beta_m} + b_{m-1} s^{\beta_{m-1}} + \cdots + b_0 s^{\beta_0}}{a_n s^{\alpha_n} + a_{n-1} s^{\alpha_{n-1}} + \cdots + a_0 s^{\alpha_0}} \mathrm{e}^{-\theta s} \tag{1}$$

where $a_i \in N$ for $i = 0, \ldots, n$, $b_j \in N$ for $j = 0, \ldots, m$, $\alpha_k \in R_+$ for $k = 0, \ldots, n$, $\beta_l \in R_+$ for $l = 0, \ldots, m$ and θ represents the constant time delay. Due to the real number order, the transfer function is also called "fractional-order." It includes, in particular, traditional integer-order time delay systems.

3 FOPI Controller

It is well-known that PI controller is most simple and widely tested relatively in industry [1, 11]. There are many refined control techniques such as model predictive control and Smith predictor and are developed on PI. In this paper, the FOPI is considered as fractional-order controller and can be represented as $C(s)$ to show the proposed controller synthesis effectively.

$$C = \left(K_p + \frac{K_i}{s^{\lambda}}\right) \tag{2}$$

where K_p, K_i and λ are the positive real tuning parameters. The real number λ represents the fractional-order.

3.1 Design and Tuning

Any control design wants to realize decent load disturbance rejection and also to robust from parameter variations. We desire to have tuning rules of controller be simple and still result in good closed-loop behavior. Based on robustness specifications, such as gain margin, phase margin, and maximum sensitivity, many classical PI/PID tuning methods were developed and also quite well adopted in the practice [1]. Generally it is possible to change the system characteristics of $G(j\omega)_{s=j\omega}$ in (1) such that the overall closed-loop system performs fine. How can we say the system's performance is up to the satisfaction? When the effect of load disturbances will be less and it must be stable always whenever moderate changes in system parameters. In general, it is desired to choose $C(s)$ tuning parameters so the system under controlled is not disturbed with variations in system dynamics. A study tells that this requirement can be obtained via sensitivity specification. A sensitivity problem for same purpose was discussed in [11]. According to defined specification for sensitivity, the system remains stable to variations in system dynamics if the robustness is specified by:

$$\frac{1}{M_r} = \max_{0 \le \omega < \infty} |\mathrm{Re}(G_L)| \tag{3}$$

where, $G_L(s) = G(s)C(s)$. Figure 1 shows the geometrical illustration of the above specification. A range of M_r gives the constraint of the distance between the imaginary axis and the Nyquist curve of $G_L(j\omega)$, and it is measured from the left-half of the complex plane. Moreover, a specification in (3) turns out to be sufficient condition for designing a controller.

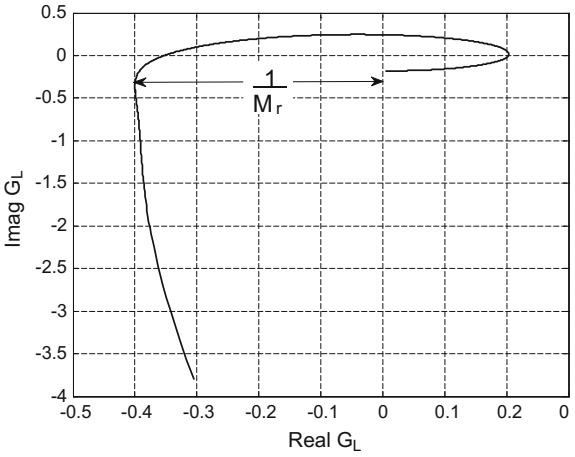

Fig. 1 Geometrical illustration of Eq. (3)

By analyzing the loop transfer function in complex frequency domain and substituting $s = j\omega$ and $j^{\lambda} = e^{\frac{j\lambda\pi}{2}} = \left(\cos\frac{\lambda\pi}{2} + j\sin\frac{\lambda\pi}{2}\right)$, $G_L(j\omega) = G(j\omega)C(j\omega)$, equation becomes

$$G_L(j\omega) = \left(K_p + K_i\omega^{-\lambda}\cos\frac{\lambda\pi}{2} - jK_i\omega^{-\lambda}\sin\frac{\lambda\pi}{2}\right)(A(\omega) + jB(\omega)) \tag{4}$$

where, $A(\omega) = \mathrm{Re}[G(j\omega)]$ and $B(\omega) = \mathrm{Im}[G(j\omega)]$.

Let's define,

$$f(K_p, K_i, \lambda, \omega) = \mathrm{Re}[G_L(j\omega)] = A(\omega)\left(K_p + K_i\omega^{-\lambda}\cos\frac{\lambda\pi}{2}\right) + B(\omega)K_i\omega^{-\lambda}\sin\frac{\lambda\pi}{2} \tag{5}$$

In this design, the criteria is imposed to have a line parallel to the imaginary axis along with the Nyquist curve of $G_L(j\omega)$ (see Fig. 1) and a distance between them must be constant say, $1/M_r$ and also halts on the left-half of the s-plane. To accomplish this constraint, following two expressions are obtained,

$$f(K_p, K_i, \lambda, \omega) = -\frac{1}{M_r} \tag{6}$$

$$\frac{\partial f}{\partial \omega}(K_p, K_i, \lambda, \omega) = 0 \tag{7}$$

By substituting (5) into above equations, respectively, we get

$$A(\omega)\left(K_p + K_i\omega^{-\lambda}\cos\tfrac{\lambda\pi}{2}\right) + B(\omega)K_i\omega^{-\lambda}\sin\tfrac{\lambda\pi}{2} = -\tfrac{1}{M_r} \tag{8}$$

$$\begin{aligned} &A'(\omega)K_p + A'(\omega)K_i\omega^{-\lambda}\cos\tfrac{\lambda\pi}{2} + \cdots \\ &\cdots A(\omega)K_i(-\lambda\omega^{-\lambda-1})\cos\tfrac{\lambda\pi}{2} + B(\omega)K_i(-\lambda\omega^{-\lambda-1})\sin\tfrac{\lambda\pi}{2} + \cdots \\ &\cdots B'(\omega)K_i\omega^{-\lambda}\sin\tfrac{\lambda\pi}{2} = 0 \end{aligned} \tag{9}$$

Here, $\partial A/\partial\omega$ and $\partial B/\partial\omega$ are denoted by $A'(\omega)$ and $B'(\omega)$ in the rest of the paper. Now, for given ω and λ, both K_p and K_i can be estimated from two expressions (8) and (9). Hence, the complete region of the parameters can also be generated for $0<\omega<\infty$ and $0<\lambda<2$. Obviously, any arbitrary set (K_p, K_i, λ) will satisfy the condition in (6) and also follows the relation

$$\frac{\partial f}{\partial\lambda}(K_p, K_i, \lambda, \omega) = 0. \tag{10}$$

By stating that each set is not unique to a given value of M_r. The task is remained to find the optimal set (K_p, K_i, λ) while it satisfies the M_r constraint. In addition, the value of M_r can be set up as suitable trade-offs between performance and robustness in any given dynamic models.

In order to estimate the optimal set of (K_p, K_i, λ) and given M_r, we need to know the optimal point of frequency ω. For this, the well-known integrated error criterion can be used, defined by

$$\mathrm{IE} = \int_0^\infty e(t)\mathrm{d}t \tag{11}$$

Here, the unit step input gives the error $e(t)$. In [1], it shows that the value of IE is directly related to the controller parameters, i.e., IE = $1/K_i$. Thus, the controller parameters can be calculated by maximizing K_i (to reduce the error quickly) subject to requirements (6) and (7). So, the expressions (8) and (9) define subtly K_i as a function of K_p and λ. One can write the derivative function to find maximum of this function as

$$\mathrm{d}f = \frac{\partial f}{\partial K_p}\mathrm{d}K_p + \frac{\partial f}{\partial K_i}\mathrm{d}K_i + \frac{\partial f}{\partial\lambda}\mathrm{d}\lambda + \frac{\partial f}{\partial\omega}\mathrm{d}\omega \tag{12}$$

It is obvious that K_i is maximum to have the condition satisfies $\mathrm{d}K_i = 0$. Same way for K_p, one can formulate the relationship as

$$\frac{\partial f}{\partial K_p}(K_p, K_i, \lambda, \omega) = 0. \tag{13}$$

Use of (7) in (13), results

$$A(\omega) = 0. \tag{14}$$

It means that f is a maximum at particular frequency when the real part of system transfer function is zero. We define this frequency point as the local extremum point, $\omega = \omega_{90}$. Substituting (14) into (8)–(10), we obtain the following three expressions,

$$K_p = \frac{1}{M_r A'(\omega_{90})}\left[\frac{B'(\omega_{90})}{B(\omega_{90})} - \frac{\lambda}{\omega_{90}} + \frac{A'(\omega_{90})}{B(\omega_{90})}\frac{\cos\frac{\lambda\pi}{2}}{\sin\frac{\lambda\pi}{2}}\right] \tag{15}$$

$$K_i = -\frac{\omega_{90}^{\lambda}}{M_r B(\omega_{90})\sin\frac{\lambda\pi}{2}} \tag{16}$$

$$\omega_{90} = \frac{2\lambda}{\pi}\tan\frac{\lambda\pi}{2} \tag{17}$$

Two expressions (15) and (16) are explicit formulas. Additionally, it is desirable to relate third controller parameter λ in terms of measured system frequency ω_{90}. The aim is to derive an explicit formula to tuning rule. By analyzing the Eq. (17) for various values of λ, $\lambda \in (0, 2)$, following interpolating equation fits the data well

$$\begin{aligned} \lambda = xe^{-\omega_{90}} + y; \quad \text{where } (x, y) &= (-0.18, 1.10) \text{ if } \omega_{90} < 1 \\ &= (-0.28, 0.98) \quad \text{if } \omega_{90} \geq 1 \end{aligned} \tag{18}$$

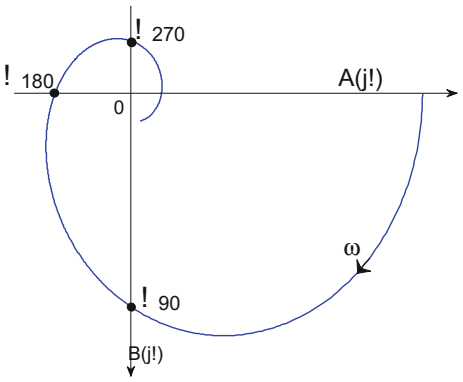

Fig. 2 Measured ω_{90} of $G(j\omega)$ from Nyquist plot

The above expression calculates tuning parameter λ. Practically, ω_{90} is obtained from the Nyquist plot of the frequency response of $G(j\omega)$, i.e., $G(j\omega)|_{\omega=\omega_{90}} = -jB(\omega_{90})$, as shown in Fig. 2.

3.2 *Choice of* M_r

The choice of M_r provides us desirable property of closed-loop system to be insensitive with parameter variations. The controller parameters will vary depending on the changes of M_r, but the system will always remain stable. To understand this point further, let us take the fractional-order system with transfer function,

$$G_1(s) = \frac{e^{-s}}{s^{0.5}+1}. \tag{19}$$

For this transfer function, ω_{90} is calculated as 1.1624 from the frequency response of $G_1(j\omega)$. Tuning rule is evaluated for robustness range, $1.4 < M_r < 3.2$ for G_1, and responses are shown in Figs. 3 and 4. It was observed that responses obtained with $M_r \geq 2.0$ proved little or no overshoot, whereas output with

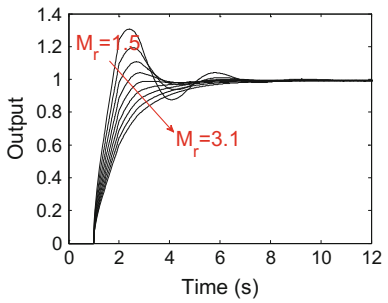

Fig. 3 Outputs for G_1 with various M_r

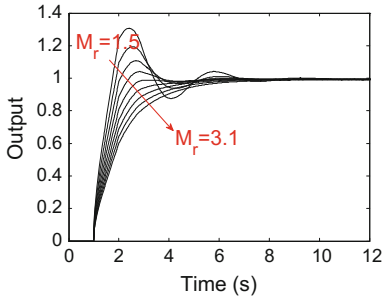

Fig. 4 Control inputs for G_1

$M_r = 1.5$ observed oscillatory with a larger overshoot but faster. This indicates that M_r value can be useful to tune parameter values. Note that M_r value is also to be decided based on the stability margin. A large value of M_r indicates that the stability margin of the control system is high. Obviously, it is desirable in system control at the time to design any controller values.

4 Example

A higher order FO system proposed by Bettayeba and Mansouric [7] and Das et al.'s [8] has the transfer function

$$G_2(s) = \frac{4.47}{s^{2.47} + 5.23s^{1.02} + 4.47} e^{-0.12s} \tag{20}$$

The fractional-order controller obtained by Bettayeba and Mansouric [7] was

$$C(s) = \frac{s^{0.02}}{1 + 8.22s^{0.11}} 9.62\left(1 + \frac{1}{1.17s^{1.02}} + 0.19s^{1.45}\right) \tag{21}$$

For the same transfer function model, Das et al.'s [8] method gave the FOPID controller as

$$C(s) = \left(0.84 + \frac{1.23}{s^{1.002}} + 0.27s^{0.93}\right) \tag{22}$$

Letting tuning parameter $M_r = 2.5$, the FOPI controller designed by the proposed method is

$$C(s) = \left(0.4311 + \frac{0.9923}{s^{0.9298}}\right) \tag{23}$$

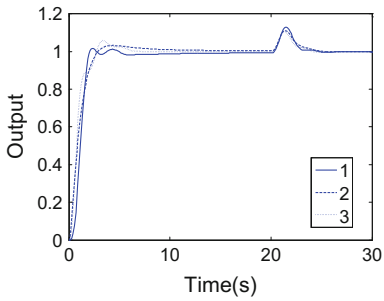

Fig. 5 Outputs for G_2 by *1* proposed method, *2* by Battayeba's method [7], and *3* by Das's method [8]

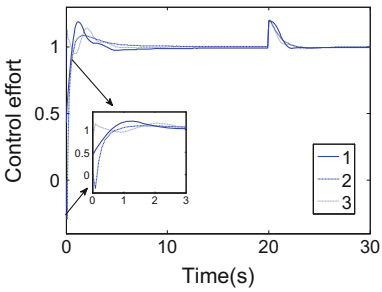

Fig. 6 Control efforts for G_2 by *1* proposed method, *2* by Battayeba's method [7], and *3* by Das's method [8]

for the system frequency $\omega_{90} = 1.7191$. For comparison with other methods, responses to a unity setpoint change and disturbance of +0.2 at $t = 20$ s are given in Figs. 5 and 6, respectively. It is observed that G_2 controlled by the proposed controller could obtain smaller control effort with small overshoot and settling time. The total variation in control input was measured as 2.12 for [8] and 2.21 for [7]; while that for the proposed method was measured only 1.87. The merit of the proposed method is visible since it gives the desired properties with less control input effort. Moreover, the percentage overshoot was measured 2.82 and 5.89 for [7] and [8], respectively.

5 Conclusion

This paper presents a general FOPI design method for any order transfer function with various dynamics, including with and without time delays, low and high real orders. The method uses the integrated error criterion with a desired robustness specification and solves for the FOPI controller parameters in the frequency domain. Explicit tuning rules succeed for various real-order systems with a single robustness parameter to be selected by the user. This investigation helps to explore online automatic tuning procedure for fractional controller which is very attractive in a practical point of view.

References

1. Åström, K.J., Hägglund, T.: Advanced PID control. ISA-Research Triangle Park, NC 27709 (2006)
2. Podlubny, I.: Fractional-order systems and $PI^{\lambda}D^{\mu}$ controllers. IEEE Trans. Auto Control **44** (1), 208–214 (1999)
3. Monje, C.A., Vinagre, B.M., Feliu, V., Chen, Y.: Tuning and auto-tuning of fractional order controllers for industry applications. Control Eng. Pract. **16**(7), 798–812 (2008)
4. Chen, Y.Q., Petras, I., Xue, D.: Fractional order control—a tutorial. In: American Control Conference (ACC'09), June 2009, pp. 1397–1411

5. Das, S., Saha, S., Das, S., Gupta, A.: On the selection of tuning methodology of FOPID controllers for the control of higher processes. ISA Trans. **50**(3), 376–388 (2011)
6. Merrikh-Bayat, F.: General rules for optimal tuning the $PI^{\lambda}D^{\mu}$ controllers with application to first-order plus time delay processes. Can. J. Chem. Eng. **90**(6), 1400–1410 (2012)
7. Bettayeba, B., Mansouric, R.: Fractional IMC-PID-filter controllers design for non-integer order systems. J. Proc. Control **24**, 261–271 (2014)
8. Das, S., Pan, I., Das, S.: Multi-objective LQR with optimum weight selection to design FOPID controllers for delayed fractional order processes. ISA Trans. **58**, 35–49 (2015)
9. Hamamci, S.: An algorithm for stabilization of fractional-order time delay systems using fractional-order PID controllers. IEEE Trans. Auto. Control **52**(10), 1964–1969 (2007)
10. Tepljakov, A., Petlenkov, E., Belikov, J.: FOMCON a MATLAB toolbox for fractional-order system identification and control. Int. J. Microelectron. Comput. Sci. **2**(2), 51–62 (2011)
11. Wang, Y.G., Shao, H.H.: Optimal tuning for PI controller. Automatica **36**(1), 147–152 (2000)

Particle Swarm Optimization-Based Closed-Loop Optimal State Feedback Control for CSTR

Geetha Mani, Natarajan Sivaraman and P. Sanjeevikumar

Abstract Complete state vector information is necessary for implementing the state feedback control via algebraic Riccati equation (ARE). However, all the states are usually not available for feedback because it is often expensive and impractical to include a sensor for each variable. Hence, to estimate the unmeasured variables, a state estimation technique is formulated to estimate all the states of the process. One of the major problems of closed-loop optimal control design is the choice of weighted matrices, which will result in optimal response. The conventional approach involves trial-and-error method to choose the weighted matrices in the cost function to determine the state feedback gain. Some of the drawbacks of this method are as follows: it is tedious, time-consuming, optimal response is not obtained, and manual selection of weighting matrices is also not straightforward. To overcome the above shortcomings, swarm intelligence is used to obtain the optimal weights, which provide superior performance than the conventional trial-and-error approach. The proposed approach performance is assessed by weight selection using PSO, which is compared with manual tuning that satisfies the closed-loop stability criteria. Further, the proposed controller performance is evaluated not only for stabilizing the disturbance rejection, but also for tracking the given reference temperature in a continuous stirred tank reactor (CSTR).

Keywords CSTR · LQR · Kalman filter · LQG · PSO

Geetha Mani (✉)
School of Electrical Engineering, Vellore Institute of Technology (VIT) University, Vellore, Tamil Nadu, India
e-mail: geethamr@gmail.com

N. Sivaraman
Mercedes-Benz Research & Development India, Bangalore, India
e-mail: s.natarajan90@gmail.com

P. Sanjeevikumar
Department of Electrical and Electronics Engineering, University of Johannesburg, Auckland Park, Johannesburg, South Africa
e-mail: sanjeevi_12@yahoo.co.in

A. Konkani et al. (eds.), *Advances in Systems, Control and Automation*,
Lecture Notes in Electrical Engineering 442, https://doi.org/10.1007/978-981-10-4762-6_45

1 Introduction

The challenge involved to design an optimal state feedback controller by means of LQR is selecting matrices Q and R that should satisfy both the design criteria and the reduction in control effort. Conventionally, trial-and-error method is being followed to find the weighting matrices, but optimal response is not obtained with this type of search. Therefore, to overcome the difficulty in selecting weighting matrices of LQR, in the last decade, few approaches using evolutionary algorithms for optimization were reported [1]. In the existing literature, the control design is considered by using evolutionary algorithms and these methods do not require explicit gradient information for optimization. Outlines the evolutionary algorithm in control engineering aspect [2].

In particular, by using genetic algorithms (GAs), the problem with pole placement was solved carefully, formulating it as multi-objective optimization problem [3]. Recently, it was found that tuning the PI and PID controllers using particle swarm optimization (PSO) method improves the response time. Further, PSO also outperforms other evolutionary algorithms like GAs. It also became a reliable tool for control optimization problem [4].

In [5], for model-based predictive control (MBPC) application to determine the optimal control sequence, EAs were used. In particular, the focus is on nonlinear systems that have constrained input. To avoid the infeasibility, specialized genetic coding and operators were developed. Favorable results were obtained for long control horizons by applying the resulting scheme in a simulated batch-fed fermenter.

Tsai et al. [6] proposed the controller design for automatic fighter tracking problems using the variable feedback gain based on PSO, in which the performance of the PSO-based LQR was proved to be better than the LMI-based LQR for the automatic fighter tracking applications. Solihin and Akmeliawati [7] proposed employing PSO for optimizing the stabilizing controller design via LQR applied for an inverted pendulum and designed stabilizing controller for a single inverted pendulum using LQR. Then, the gains of the LQR are chosen by minimizing the objective function via PSO. Proposed methodology is given in the next section. Section 3 is about the discussion on simulation results followed by the conclusion given in Sect. 4.

2 Proposed Methodology

The closed-loop optimal control of CSTR with quadratic performance measure is presented. This leads to state regulation and set point tracking. The proposed method is shown in Fig. 1.

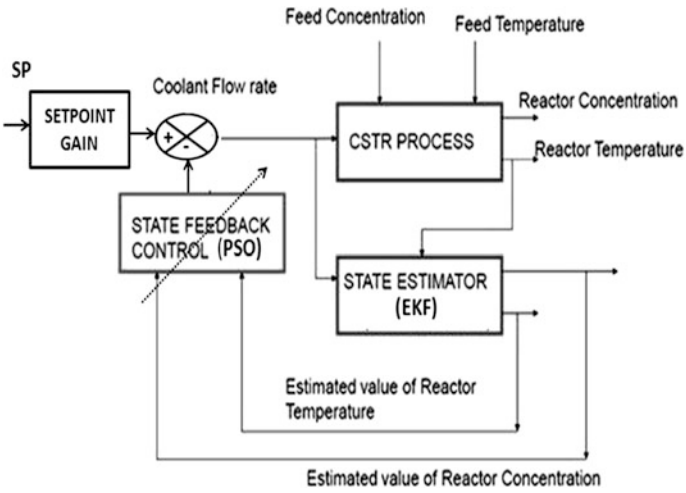

Fig. 1 Proposed PSO-based closed-loop optimal state feedback control

The linearized state space model of CSTR is obtained to implement the state feedback controller, and EKF has given in [8]. The generalized algorithm for both regulatory and tracking control is given by [9].

Consider an LTI plant as

$$\dot{x}(t) = Ax(t) + Bu(t) \tag{1}$$

$$y(t) = Cx(t) \tag{2}$$

where $x(t)$ and $u(t)$ represents the state and an input vector. The constant system model parameters are indicated by A and B, respectively. It is assumed that the pair (A, B) could be stabilizable. The performance index is given in (3)

$$J = \frac{1}{2}\int_0^\infty [x'(t)Q_0x(t) + u'R_0u(t)]\mathrm{d}t \tag{3}$$

where Q_0 is a nonnegative definite matrix and R_0 is a positive definite matrix. The solution is as follows:

Step 1 By using Riccati equation

$$-\overline{P}A - A'\overline{P} - Q_0 + \overline{P}BR_0^{-1}B'\overline{P} = 0 \tag{4}$$

where $P \in R^{n\times m}$ is a nonnegative definite matrix that satisfies the matrix Riccati equation,

Step 2 Estimated state using an extended Kalman filter (EKF)

$$\widehat{X}(t) = A\widehat{x}(t) + Bu(t) + K(t)(y(t) - C\widehat{x}(t)) \tag{5}$$

$$K(t) = P(t)C'(t)V^{-1}(t) \tag{6}$$

Then, the Kalman gain is:

$$V(t) = C(t)P(t)C(t)' + R_0 \tag{7}$$

Step 3 To find optimal control

$$u^*(t) = -\left(R_0^{-1}B'P(t)\right) * \widehat{x}(t) \tag{8}$$

Step 4 To find set point gain $\overline{g}$ for tracking system

The error is

$$e(t) = z(t) - y(t) \tag{9}$$

where $z(t)$ is the desired signal (set point).

The performance index is taken as

$$\lim_{t_f \to \infty} J = \lim_{t_f \to \infty} \frac{1}{2} \int_0^\infty (e'(t)Q_0e(t) + u'(t)R_0u(t))\mathrm{d}t \tag{10}$$

To find $\overline{P}$:

$$-\overline{P}A - A'\overline{P} + \overline{P}BR_0^{-1}B'\overline{P} - C'QC = 0 \tag{11}$$

To find $\overline{g}$

$$\dot{\bar{g}}(t) = \left[\overline{P}E - A'\right]\bar{g}(t) - Wz(t) \tag{12}$$

where $E = BR_0^{-1}B'$ and $W = C'Q_0$

$$\text{Optimal control } u(t) = -R_0^{-1}B'\left[\overline{P}x(t) - \overline{g}(t)\right] \tag{13}$$

Weighting matrices Q_o and R_o play a vital role in optimization. Its compositions have a larger impact on the system performance [3]. The number of matrix elements in Q_o and R_o depends on state variable and the input variable. Let the numbers in diagonal-off is considered to be zero. Then, the quadratic performance index is weighted ISE of the states and inputs if the diagonal matrices are chosen. The trial-and-error approach is simpler which makes the designers to select the Q_o and R_o matrices without restriction. On the other hand, selection process is very tedious

because it involves iteration and time-consuming process and requires suitable experience and also awareness about the physical problem. Further, it iterates for a very long time to find the best value for the elements in Q_o and R_o matrices.

Thus, by employing the PSO technique, the above problem could be averted. It finds the optimum solution for the LQG. The obtained solution is used to minimize difference between the reference input and actual process variable. Flowchart for weight selection of LQG based on PSO algorithm is shown in Fig. 2. Particles in PSO represent the diagonal elements of Q_o and R_o matrices, and the elements are chosen to be positive real. Firstly, the position and velocity of the particles are initialized, and for each particle, the solution of Riccati equation is found. It is followed by calculating the corresponding feedback gain matrix. The fitness of each particle is calculated using the current position value. By using the integral square error (ISE), the fitness value is calculated. The position is updated by comparing the present ISE value with the previous best ISE value. If it is found to be less, then the current values are set as best $p_{i,}$ otherwise the current ISE value is retained. Among all the particles, whichever is having minimum ISE value is selected as a global best p_g.

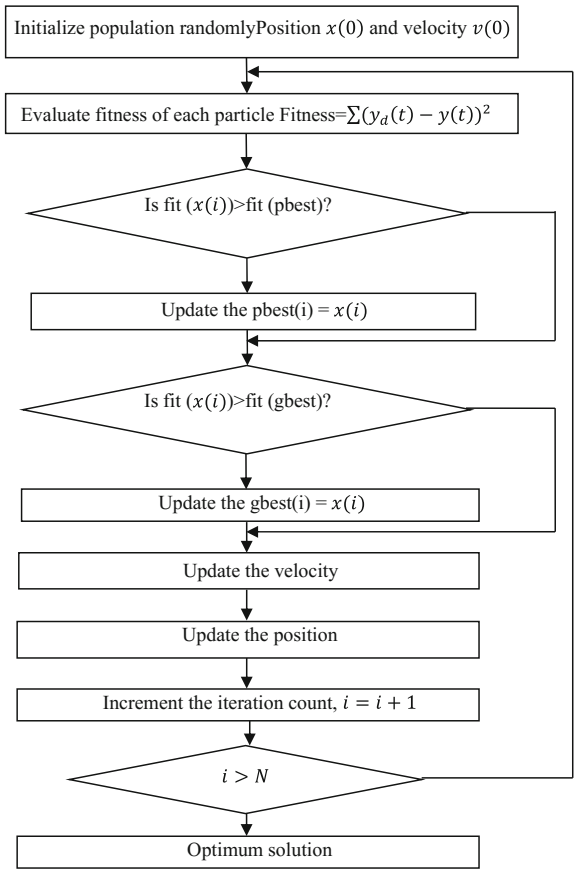

Fig. 2 PSO flowchart for weight selection

2.1 Formulation of Fitness Function

In order to arrive at the proper global optimal solution, formulation of the fitness function is essential. It decides on convergence rate. Integral of the square error (ISE), integral of the time-weighted absolute error (ITAE), and integral of the absolute error (IAE) are some of the commonly used fitness functions to design controllers. The fitness function used in this paper is ISE, and it is given in (14)

$$f = \text{ISE} = \int_0^{T_i} [y_d(t) - y(t)]^2 \mathrm{d}t = \int_0^{T_i} e^2(t) \mathrm{d}t \tag{14}$$

The optimization problem finds the state feedback controller gain matrix $K = [\, k_1 \quad k_2 \,]$ by which the fitness function ISE is minimized.

3 Comparative Analysis on Simulation Performed

Linearized state space model of CSTR is used for simulation purpose in all process. Feed temperature, feed flow, and concentration are assumed to be constants. Manipulated input variable is given as a coolant flow rate. Reactor concentration and temperature are taken as state variables. The open-loop poles of CSTR system are $-2.39 + 3.03i$ and $-2.39 - 3.03i$. The system is stable and satisfies both controllable and stabilizable conditions. The pair [state matrix (A), output matrix (C)] is measurable. The stability of closed-loop system is guaranteed by the C matrix where C is $C^{\mathrm{T}}C = Q$. So, the tuning parameter values of LQG controller are found out using manual tuning (trial-and-error method) selected as Q_o = Diag{1 1} and $R_o = 1$ to satisfy the closed-loop stability.

The tuning parameters of Kalman filter preferred are the following:

Process noise covariance matrix Q = Diag{0.0025, 0.0025}
Measurement noise covariance matrix $R = 0.0025$
Initial state error covariance matrix $P = 1000I_{(2\times2)}$.

PSO Parameters:

Swarm size: 100; number of generations: 400; cognitive acceleration constant: $c_1 = 1.3$
Social acceleration constant: $c_2 = 1.3$; inertia weight $w_{\min} = 0.4$, $w_{\max} = 1.1$
Distribution range [0 1] and [1 10]
The simulation under both set point tracking and regulatory control was performed based upon the situation that would be on reality.

Case 1: Set point Tracking

The objective of the controller is to track the temperature, which is given as set point irrespective of disturbances prevailing in the process by properly adjusting

coolant flow rate. The corresponding state feedback gain is determined using LQG whose weighting matrices are tuned in offline by PSO and manual tuning.

Table 1 shows the tuning parameters used for manual method and PSO (two different distributions) optimization methods along with the state feedback gain matrix, set point gain function for tracking application, and closed-loop eigenvalues of the system. From Fig. 3, it could be observed that the closed-loop eigenvalues of the system tuned via PSO in the search interval [1 10] are located comparatively far from the imaginary axis, which suggest that the stability of the system is improved.

Simulation result in Fig. 4 shows that the proposed PSO-based optimal control approach tracks the set point better when compared to trial-and-error approach. The output variation of the controller (coolant flow rate) for servoresponse is shown in Fig. 5.

In order to assess the performance of the controller, the integral square error is calculated between desired set point temperature and actual output temperature for all the three methods and the observation is given in Table 2. The value of ISE in

Table 1 State feedback controller gains obtained using PSO

S. No.	Tuning method	Tuning parameters	State feedback gain matrix	Closed-loop eigenvalues	Set point gain
1	Trial-and-error	Q_o = Diag {1 0} R_o = 1	K = [−140.01 − 0.875]	−2.788 + 3.29i	−1.66
2	PSO range [0 1]	Q_o = Diag {3.69 1.92} R_o = 2.09	K = [−130.66 −0.8144]	−2.76 + 3.27i −2.76 + 3.27i	−1.6367
3	PSO range [1 10]	Q_o = Diag {344.67 789.25} R_o = 16.43	K = [−1068 −9.852]	**−6.93 + 5.57i −6.93 − 5.57i**	−7.05

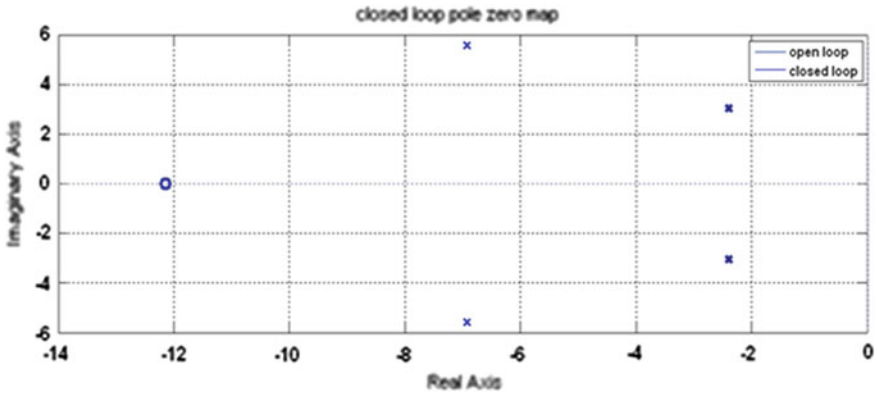

Fig. 3 Eigenvalue distribution

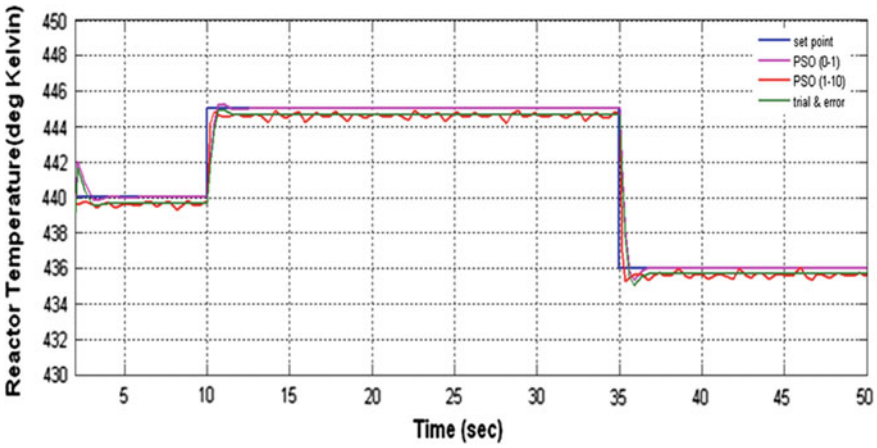

Fig. 4 Comparison of set point tracking response

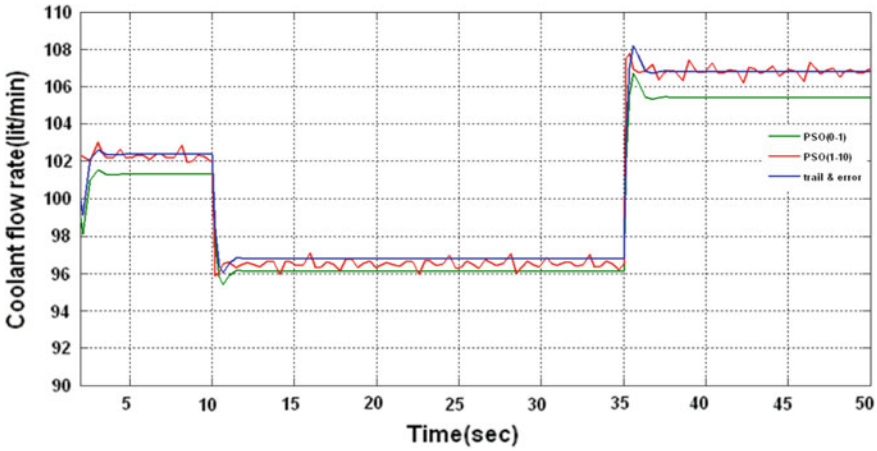

Fig. 5 Comparison of controller output (coolant flowrate) response in set point tracking

case of PSO when distributed range is [0 1] gives the least among the three methods. It has no offset, exactly tracking the set point variation. The EKF estimates the concentration of the reactor based on measured temperature value. Figure 6 shows the comparison of servoresponse of estimated concentration of the reactor.

Case 2: Regulatory Response

In regulatory control, the temperature and concentration of reactor state variable track zero even disturbances occur in the feed flow rate and feed temperature. Figure 7 shows the comparatively closed-loop regulatory response of PSO and

Table 2 Comparison of performance index for set point tracking

S. No.	Tuning method	ISE
1	Trial-and-error	0.102
2	PSO range [0 1]	**5.702e−8**
3	PSO range [1 10]	0.1766

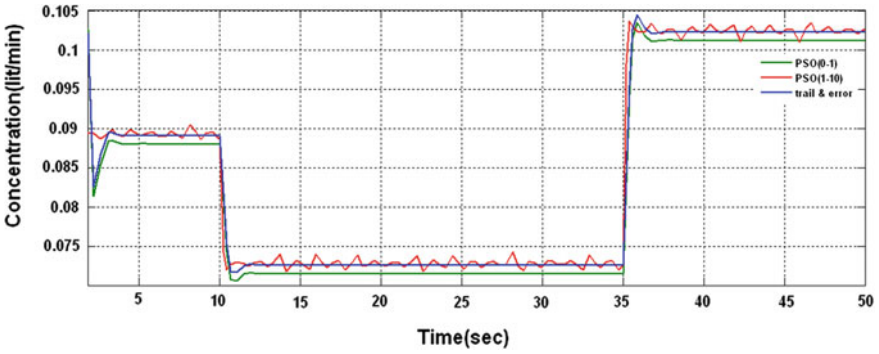

Fig. 6 Comparison of the servo response of estimated concentration

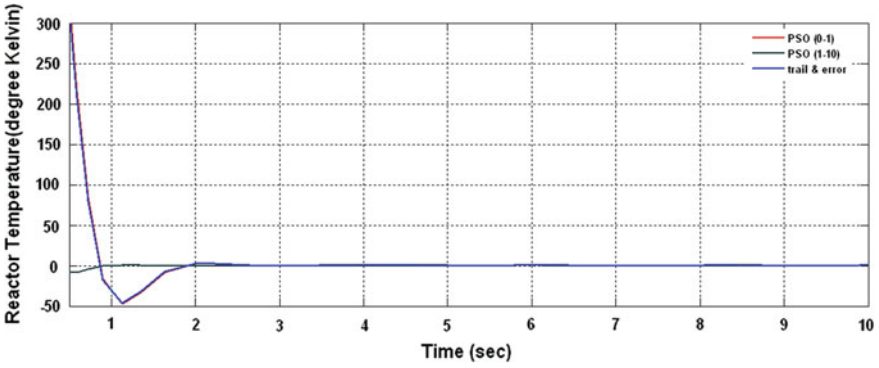

Fig. 7 Comparison of regulatory response of optimal control

manual tuning method. The temperature of the reactor tracks the zero after some initial transients. Integral square error between the actual and estimated variables is chosen as a performance index to evaluate the performance of the controller.

Table 3 shows the PSO in search interval [0 1] gives least ISE value in both the state variables (temperature and concentration). Figure 8 shows the coolant flow variation in closed loop. The estimated value of concentration is shown in Fig. 9.

So, PSO in the search interval [0 1] gives optimal tuning parameters of the system in both servo and regulatory mode.

Table 3 Comparison of performance index of tuning methods for regulatory control

S. No.	Tuning method	ISE concentration	ISE temperature
1	Trial-and-error	0.0006	0.005
2	PSO range [0 1]	**0.00014**	**0.0018**
3	PSO range [1 10]	0.0013	0.061

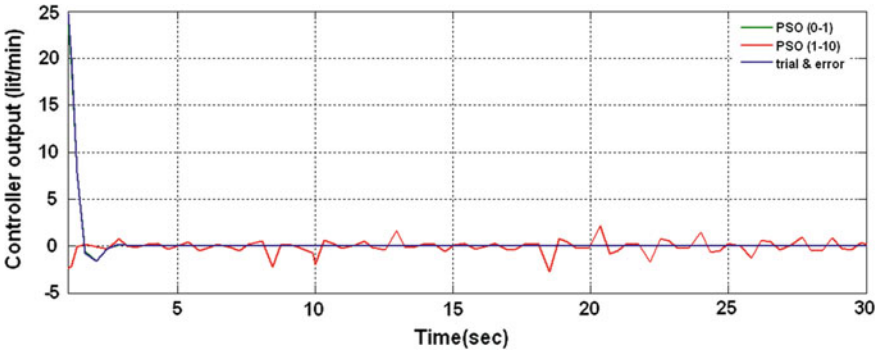

Fig. 8 Comparison of controller output response in regulatory mode

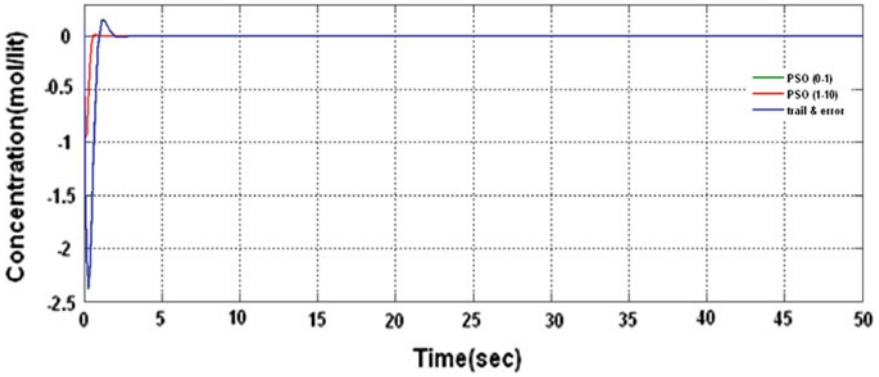

Fig. 9 Comparison of regulatory response of estimated concentration

4 Conclusion

This paper presents the novel PSO-based optimal weight selection of state estimation-based optimal controller. It is proposed to stabilize the CSTR process control and to achieve the trajectory tracking of given temperature set point. The proposed method is effective when compared to trial-and-error approach for determining the optimal weighting matrices for designing the optimal controller.

This approach makes the controller designer to ease the process of choosing the optimal weighting matrices. Comparative analysis is made between the proposed method and the trial-and-error-based method. The proposed method outperforms in terms of the ISE performance index. It could be observed from the simulation results. Further, the stability is improved in terms of both set point tracking and disturbance rejection.

References

1. Omer, O., Levent, C., Erol, U.: A novel method of selection of Q and R matrices in the theory of optimal control. Int. J. Syst. Control **1**(2), 84–92 (2010)
2. Fleming, P., Purshouse, R.: Evolutionary algorithms in control systems engineering: a survey. Control Eng. Pract. **10**(11), 1223–1241 (2002)
3. Sanchez, G., Villasana, M., Strefezza, M.: Multi-objective Pole Placement with Evolutionary Algorithms. Lecture Notes in Computer Science, vol. 44, pp. 417–425 (2007)
4. Gaing, Z.L.: A particle swarm optimization approach for optimum design of PID controller in AVR system. IEEE Trans. Energy Convers. **19**(2), 384–391 (2004)
5. Onnen, C., Babuska, R., Kaymak, U., Sousa, J.M., Verbruggen, H.B., Isermann, R.: Genetic algorithms for optimization in predictive control. Control Eng. Pract. **5**(10), 1363–1372 (1997)
6. Tsai, S.J., Huo, C.L., Yang, Y.K., Sun, T.Y.: Variable feedback gain control design based on particle swarm optimizer for automatic fighter tracking problems. Appl. Soft Comput. **13**(1), 58–75 (2013)
7. Solihin, M.I., Akmeliawati, R.: Particle swam optimization for stabilizing controller of a self-erecting linear inverted pendulum. Int. J. Electr. Electron. Syst. Res. **3**, 410–415 (2010)
8. Geetha, M., Jerome, J., Arun Kumar, P.: Critical evaluation of non-linear filter configurations for the state estimation of continuous stirred tank reactor. Appl. Soft Comput. **25**, 452–460 (2014)
9. Naidu, D.S.: Optimal Control Systems. CRC Press, Florida (2003)

Design of a Piezoresistive Microaccelerometer with High Sensitivity for Medical Diagnostic

Sonali Biswas and Anup Kumar Gogoi

Abstract The design of a piezoresistive microaccelerometer and its performance analysis have been presented in this paper. The objective is to design a tremor diagnostic system operating at frequency range from 0.1 to 25 Hz and ±2 g. In this paper, mainly the analysis has been done based on the temperature effect, drift, and doping. The microaccelerometer designed has been simulated using the finite element method-based software COMSOL 4.3 with the following dimensions; proof mass: 3200 × 3200 × 250, flexure: 1000 × 250 × 20, frame: 5200 × 230 × 250, piezoresistor: 100 × 25 × 2 (all dimensions are in μm). Here basically, the impact of strain on the temperature and doping has been studied. Sensitivity is dependent upon the piezoresistive coefficient; therefore, the temperature and the doping concentration have a direct impact upon the sensitivity of the device. The designed microaccelerometer has a sensitivity of 10.5 mV/V/g, and Wheatstone bridge is employed as the signal pickup circuit to reduce the cross-axis sensitivity.

Keywords Microaccelerometer · Proof-mass · Piezoresistive Wheatstone bridge

1 Introduction

Piezoresistive microaccelerometers find wide application in several areas, and many exciting developments have taken place making it suitable for various micro-electro-mechanical system (MEMS) applications. There has been an improvement in the performance level in terms of sensitivity, resolution, bandwidth, linearity, and miniaturization [1–4]. However, specific application demands

S. Biswas (✉) · A.K. Gogoi
Department of Electronics and Electrical Engineering, Indian Institute of Technology Guwahati, Guwahati 781039, India
e-mail: b.sonali@iitg.ernet.in

A.K. Gogoi
e-mail: akg@iitg.ernet.in

A. Konkani et al. (eds.), *Advances in Systems, Control and Automation*,
Lecture Notes in Electrical Engineering 442, https://doi.org/10.1007/978-981-10-4762-6_46

necessary design specifications in terms of performance and sensitivity. High-performance MEMS accelerometer in terms of sensitivity, resolution, and low noise floor is still an active area of research. In this paper, the design of a piezoresistive microaccelerometer operating from 0.1 to 25 Hz and the performance analysis of the same have been done for obtaining high sensitivity. Several neurodegenerative diseases cause tremor in patients and are characterized by a rhythmic roughly sinusoidal oscillatory movement ranging from 0.1 to 25 Hz. Therefore, MEMS accelerometer is used to measure the tremor, namely rest, kinetic, and postural operating with maximum acceleration amplitude of ±2 g. Piezoresistive accelerometer has high sensitivity, DC response, and easy readout. The disadvantage is that piezoresistors are highly temperature sensitive and suffer from thermal drift [5]. The piezoresistance coefficients depend on the doping concentration and temperature [1, 2]. In this paper, mainly the effect of temperature, offset, and doping has been studied and simulated. Sections 2–4 describe the effect of strain and the piezoresistive coefficient and components. In Sect. 5 and its subsections, the simulated results have been given mainly taking into account the temperature effects and the doping on the response characteristic and sensitivity characteristic of the sensor output.

2 Effect of Strain on Piezoresistor

The basic principle of a piezoresistor is given by Eq. (1), where the bulk resistivity is ρ, the length (L), and the area (A).

$$R = \rho L / A \tag{1}$$

From the above equation, we see the resistance value changes with applied strain in two ways:

1. Dimension
2. Resistivity

The piezoresistors undergo change in resistance when strain is applied and its behavior is linear as shown in Eq. (2). Here, the dimensional change is negligible compared to the change in resistivity.

$$\Delta R/R = G\Delta L/L \tag{2}$$

Therefore, gauge factor is

$$G = (\Delta R/R)/(\Delta L/L) = \Delta R/\varepsilon R \tag{3}$$

where ε is the strain. In the above equation, when we introduce Poisson's ratio (λ) which is the negative ratio of transverse to axial strain, we get the gauge factor as in Eq. (4).

Table 1 The piezoresistor material properties

Property	Units	Value
Density	ρ	2330 kg/m^3
Young's modulus	Y	1.69e^{11}
Poisson's ratio	λ	0.28 kg/m^3

$$G = (\Delta R/R)/\varepsilon = 1 + 2\lambda + \delta\rho/\rho \tag{4}$$

As compared to the dimensional change, the resistivity change is larger by a factor of 50 for a semiconductor, when strain is applied hence we take into account the change in resistivity. In the above Eq. (4), the first two terms occur due to change in dimension, and the third term occurs due to change in resistivity, dominant for semiconductor gauges.

Hence we get

$$G_\mathrm{l} = \pi_\mathrm{l} Y + 1 + 2\lambda \tag{5}$$

where G_l denotes the longitudinal gauge factor, π_l is the piezoresistive coefficient along longitudinal direction, and Y is the Young's modulus and is anisotropic with respect to crystal direction [1].

For semiconductors, we have $\pi_\mathrm{l} \gg 1 + 2\lambda$ therefore using ($Y = \sigma_\mathrm{l}/\varepsilon$) where σ_l denotes longitudinal stress, we get

$$\Delta R/R = \pi_\mathrm{l}\sigma_\mathrm{l} \tag{6}$$

In the present work, the microaccelerometer has total eight p-doped single crystal silicon piezoresistors with the following material properties as in Table 1.

3 Piezoresistive Coefficient

The piezoresistors when doped, the piezoresistive coefficients are influenced by its relative orientation to crystallographic direction. Equation (7) gives a symmetric relativity matrix relating electric field component E_i and current density component i_i which is the Ohm's law [2, 3].

$$\begin{pmatrix} E_x \\ E_Y \\ E_Z \end{pmatrix} = \begin{pmatrix} \rho_1 & \rho_6 & \rho_5 \\ \rho_6 & \rho_2 & \rho_4 \\ \rho_5 & \rho_4 & \rho_3 \end{pmatrix} \begin{pmatrix} i_x \\ i_y \\ i_z \end{pmatrix} \tag{7}$$

Here, the normal stresses are (σ_{xx}, σ_{yy}, σ_{zz}) and shear stresses are (τ_{xy}, τ_{yz}, τ_{zx}). Thus, the various components of the stress sensor can be denoted as $\sigma_{xx} \rightarrow T_1$, $\sigma_{yy} \rightarrow T_2$, $\sigma_{zz} \rightarrow T_3$, $\sigma_{yz} \rightarrow T_4$, $\sigma_{xz} \rightarrow T_5$, $\sigma_{xy} \rightarrow T_6$. The relation between changes of resistivity and the applied stress and strain can be given by (8) and (9), where the

isotropic resistivity of unstressed crystal is ρ_0 and the six independent components of the resistivity matrix are ρ_1 to ρ_6. Π is the component of piezoresistance sensor, and T is the component of stress sensor [3].

$$\begin{bmatrix} \Delta\rho_1/\rho_0 \\ \Delta\rho_2/\rho_0 \\ \Delta\rho_3/\rho_0 \\ \Delta\rho_4/\rho_0 \\ \Delta\rho_5/\rho_0 \\ \Delta\rho_6/\rho_0 \end{bmatrix} = (\pi)(t) \tag{8}$$

$$= \begin{pmatrix} \pi_{11} & \pi_{12} & \pi_{12} & 0 & 0 & 0 \\ \pi_{12} & \pi_{11} & \pi_{12} & 0 & 0 & 0 \\ \pi_{12} & \pi_{11} & \pi_{12} & 0 & 0 & 0 \\ 0 & 0 & 0 & \pi_{44} & 0 & 0 \\ 0 & 0 & 0 & 0 & \pi_{44} & 0 \\ 0 & 0 & 0 & 0 & 0 & \pi_{44} \end{pmatrix} \begin{pmatrix} T_1 \\ T_2 \\ T_3 \\ T_4 \\ T_5 \\ T_6 \end{pmatrix} \tag{9}$$

The fundamental piezoresistance coefficients are π_{ll} (longitudinal), π_{12} (transverse), and π_{44} (shear) [1].

4 Piezoresistive Component

Different orientation relative to the crystallographic axis there exist a nonzero coefficient matrix [Π]. Table 2 shows the longitudinal and transverse piezoresistive coefficient for some typical cases [3, 6].

The piezoresistivity component is shown in Table 3 [3, 6]. The gauge factors for longitudinal and transverse are given, and we need to calculate according to our orientation. In our case for the piezoresistive accelerometer designed, first the longitudinal coefficient is calculated for $\langle 110 \rangle$ orientation given by $(\Pi_{11} + \Pi_{12} + \Pi_{44})/2$. Then, the longitudinal gauge factor is obtained by using Eq. (5), and the change in resistance to original resistance, i.e., $\Delta R/R$ can be obtained using (6).

Table 2 Piezoresistive coefficient in some commonly used configuration

Direction of strain	Direction of current	Configuration	Piezoresistive coefficient
$\langle 100 \rangle$	$\langle 100 \rangle$	Longitudinal	Π_{11}
$\langle 100 \rangle$	$\langle 010 \rangle$	Transverse	Π_{12}
$\langle 110 \rangle$	$\langle 110 \rangle$	Longitudinal	$(\Pi_{11} + \Pi_{12} + \Pi_{44})/2$
$\langle 110 \rangle$	$\langle 110 \rangle$	Transverse	$(\Pi_{11} + \Pi_{12} - \Pi_{44})$
$\langle 111 \rangle$	$\langle 111 \rangle$	Longitudinal	$(\Pi_{11} + 2\Pi_{12} + 2\Pi_{44})/2$

Table 3 Piezoresistivity components for single crystal silicon

Piezoresistivity coefficient 10^{-11} Pa^{-1}	n-type resistivity 11.7 Ω cm	p-type resistivity 7.8 Ω cm
Π_{11}	−102.2	6.6
Π_{12}	53.4	−1.1
Π_{44}	−13.6	138.1

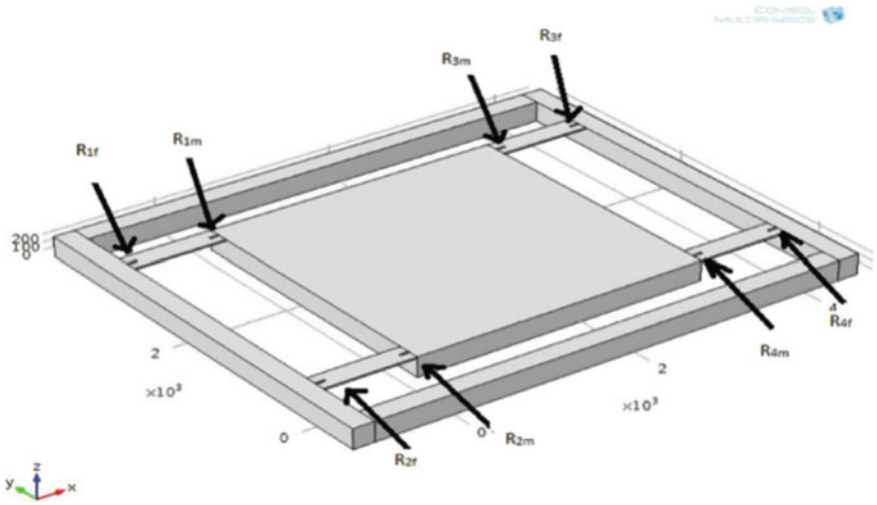

Fig. 1 Simulated MEMS accelerometer structure (3-D view)

5 Results and Discussion

The device has a quad proof-mass with four flexures, two on either side. Eight *p*-doped silicon types of piezoresistors are implanted on the flexures, and the entire structure is surrounded by a fixed frame. The device with the geometric configuration proof-mass: 3200 × 3200 × 250, flexure: 1000 × 250 × 20, frame: 5200 × 230 × 250, piezoresistor: 100 × 25 × 2 (all dimensions are in μm) has been simulated using finite element method software COMSOL 4.3 as in Fig. 1.

5.1 Thermal Drift of the Offset Voltage

Piezoresistors are positioned in such a way that maximum stresses can be obtained for any minimum deflection. In our case, four *p*-doped piezoresistors are placed. The nature of the accelerometer as an effect of acceleration has been shown in Table 4 [4]. Initially under perfect equilibrium, the output voltage must be equal to zero. Due to the effect of temperature, the values of its four resistances will change

Table 4 Nature of the piezoresistor along different axes when acceleration is applied

Piezoresistor	*X*-direction	*Y*-direction	*Z*-direction
R_{1m}	Tensile	Tensile	Tensile
R_{1f}	Compressive	Compressive	Compressive
R_{2m}	Compressive	Tensile	Tensile
R_{2f}	Tensile	Compressive	Compressive
R_{3m}	Compressive	Compressive	Tensile
R_{3f}	Tensile	Tensile	Compressive
R_{4m}	Tensile	Compressive	Tensile
R_{4f}	Compressive	Tensile	Compressive

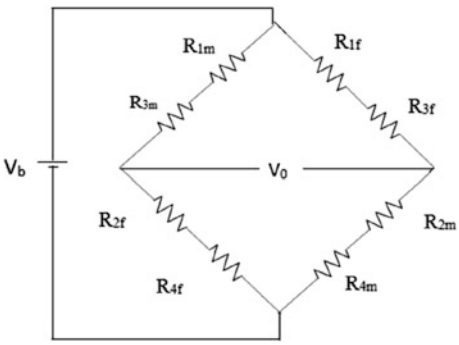

Fig. 2 Wheatstone bridge configuration with piezoresistors as sensing elements

and an offset voltage is obtained [4–8]. As the temperature changes are identical in all the elements, the ratio of their resistance does not change, and hence the output voltage of the sensing elements does not change. The temperature drift can be corrected using the full-bridge configuration.

As piezoresistances are temperature sensitive, Wheatstone bridge helps in eliminating the temperature effect on the output, thereby reducing the cross-axis sensitivity. The eight piezoresistors connected in a Wheatstone bridge manner is shown in Fig. 2 [6]. Here, the resistors R_{im} and R_{if} in Fig. 1 denote the sensing element near to the mass and near to the frame, respectively.

5.2 *Effect of Temperature on the Sensitivity*

Piezoresistive accelerometers are temperature dependent [4]. Even if the acceleration remains constant, the accelerometer output varies with temperature as reported in [4]. Temperature coefficient of piezoresistive sensor is of two types; first the temperature coefficients of offset (TCO) and second the temperature coefficient of sensitivity (TCS). The signal pickup circuit we have used here is the Wheatstone bridge which reduces the offset or the TCO. In our case, the material is silicon, and based on the amount of doping concentration, the resistivity ranges from 0.1 to

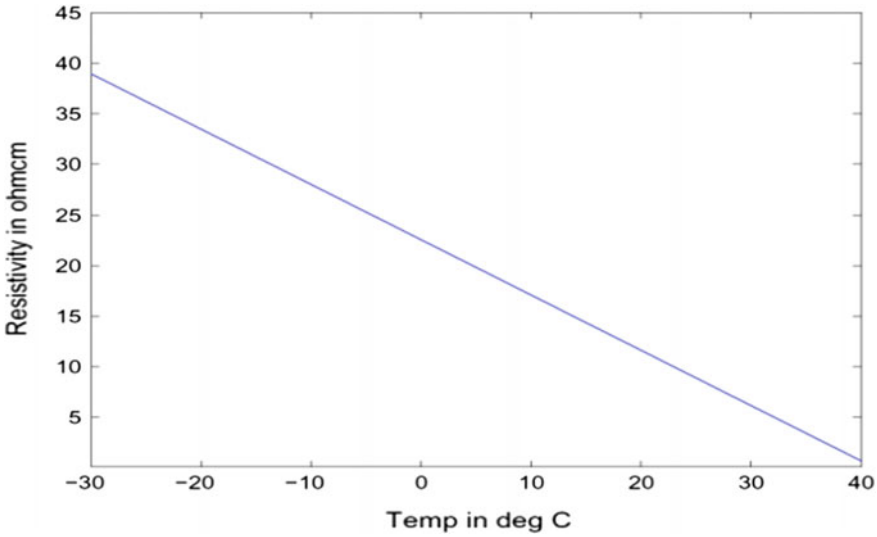

Fig. 3 Variation of resistivity at different temperature

60 Ωm. The temperature coefficient of silicon is 0.07/°C. Silicon is a semiconductor that has the conduction band and the valence band moderately separated. Hence as the temperature increases, the conductance increases or the resistance decreases. As resistance is directly proportional to resistivity, resistivity also decreases. Considering a variation in temperature, the resistivity is seen to decrease with increase in temperature as obtained in Fig. 3.

As the piezoresistive coefficients are temperature sensitive, the piezoresistor sensitivity depends upon the TCS [4]. It is seen that with the increase in temperature, the piezoresistive coefficients decrease and hence the output voltage also decreases as reported in [4] as given in Fig. 4 [4]. At lower temperature range, we have higher temperature drift.

5.3 Effect of Doping Concentration on the Sensitivity

Different levels of doping concentration and different types of doping have an impact upon the piezoresistive coefficients. With an increase in temperature and doping concentration, the value of the piezoresistive coefficient for p-type and n-type silicon decreases. As reported in [2], the doping concentration and the operating temperature have a direct influence on the longitudinal piezoresistive coefficient. At constant operating temperature that ranges between −75 and 75 °C, the piezoresistive coefficient decreases both with the increase in the doping concentration and the temperature. When the level of doping is increased, it decreases

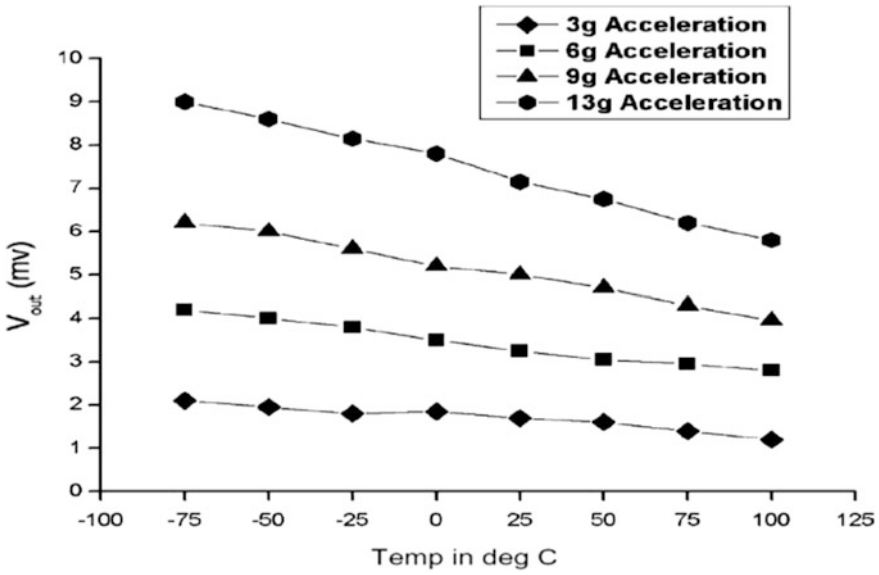

Fig. 4 Variation of Wheatstone bridge output at different temperature with acceleration [4]

the signal output and hence reduces the sensitivity. For our case, we have chosen p-doped silicon. In intrinsic crystalline silicon, there is approximately 5×10^{22} atoms/cm. The doping chosen here is p-doped silicon with 5×10^{17} atoms/cm^3. This specification lies in between the typical range for lightly doped that ranges from 10^{13}/cm^3 to 10^{18}/cm^3. Continuous increase of doping level leads to the substantial decrease of the sensitivity. Moreover, it gives the acceptable signal stability and caters to the desired properties in the device that the semiconductor silicon is intended for. High doping level at high operating temperature may degrade the performance of the accelerometer in terms of sensitivity.

5.4 Sensitivity

Considering the p-type single crystal silicon as the piezoresistive sensing element with orientation $\langle 110 \rangle$, we choose the piezoresistive coefficient, namely Π_{11}, Π_{12}, and Π_{44} and obtain the longitudinal coefficient. Considering the bridge input voltage of 5 V and Young's modulus of 1.69e^{11}, we obtain the bridge output. The sensitivity for the ± 2 g specification has been obtained as 10.5 mv/V/g. The sensitivity has been obtained for various input acceleration due to gravity and has been plotted in Fig. 5. The plot shows that the dependence of sensitivity on g value is nonlinear. There is low cross-axis sensitivity due to the Wheatstone bridge pickup circuit thus enhancing the performance.

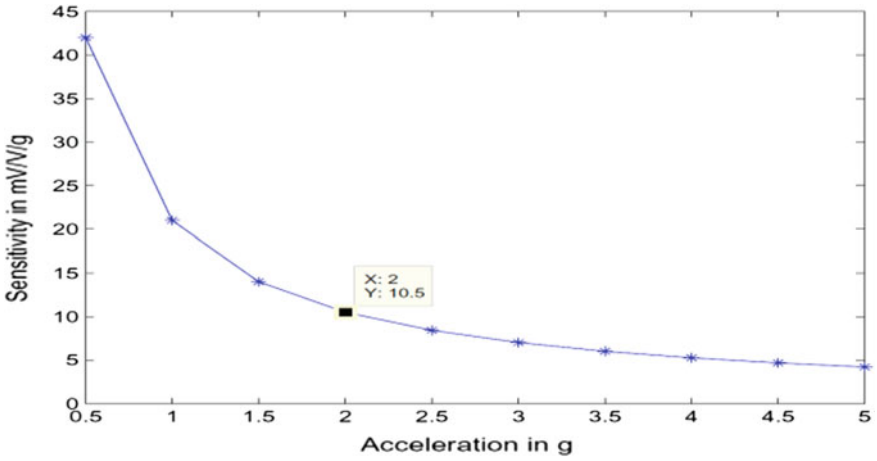

Fig. 5 Sensitivity with variation in input acceleration due to gravity

6 Conclusion

A complete study of the temperature effect, offset, doping concentration on the piezoresistive MEMS accelerometer of ±2 g has been done and simulated for low cross-axis sensitivity and high-performance medical diagnostic application. The tremor diagnostic system essentially requires bandwidth ranging from 0.1 to 25 Hz with dynamic range of ±2 g. The piezoresistive coefficient decreases both with the increase in the doping concentration and with the increase in temperature. As sensitivity is dependent upon the piezoresistive coefficient, therefore temperature and the doping concentration have a direct impact upon the sensitivity of the device. The sensitivity for the ±2 g specification has been obtained as 10.5 mV/V/g.

References

1. Kanda, Y.: Piezoresistance effect of silicon. Sens. Actuators **A28**, 83–91 (1991)
2. Keyes, R.W.: The effect of elastic deformation on the electrical conductivity of semiconductors. In: Seitz, F., Turnbull, D. (eds.) Solid State Physics, vol. 11, pp. 149–221. Academic Press, New York (1960)
3. Liu, C.: Foundation of MEMS, pp. 207–244. Pearson (2011)
4. Kal, S., Das, S., Maurya, D.K., Biswas, K., Ravi Sankar, A., Lahiri, S.K.: CMOS compatible bulk micromachined silicon piezoresistive accelerometer with low off-axis sensitivity. J. Microelectron. **37**, 22–30 (2006)
5. Otmani, R., Benmoussa, N., Benyoucef, B.: The thermal drift characteristics of piezoresistive pressure sensor. Phys. Procedia **21**, 47–52 (2011)

6. Biswas, S., Gogoi, A.K.: Design and simulation of piezoresistive MEMS accelerometer for the detection of pathological tremor. In: Proceeding of IEEE SoutheastCON, pp. 1–5. Lexington, KY, Mar 2014
7. Biswas, S., Gogoi, A.K.: Design and analysis of FEM based MEMS accelerometer for detection of postural tremor in thyrotoxicosis. In: Proceeding of International Conference on Advanced Electronics System (ICAES), IEEE Computer Society, pp. 113–116 Sept (2013)
8. Biswas, S., Gogoi, A.K.: Design issues of piezoresistive MEMS accelerometer for an application specific medical diagnostic system. J. IETE Tech. Rev. **33**(1), 11–16 (2016)

Recognition of Human Speech Emotion Using Variants of Mel-Frequency Cepstral Coefficients

Hemanta Kumar Palo, Mahesh Chandra and Mihir Narayan Mohanty

Abstract In this chapter, different variants of Mel-frequency cepstral coefficients (MFCCs) describing human speech emotions are investigated. These features are tested and compared for their robustness in terms of classification accuracy and mean square error. Although MFCC is a reliable feature for speech emotion recognition, it does not consider the temporal dynamics between features which is crucial for such analysis. To address this issue, delta MFCC as its first derivative is extracted for comparison. Due to poor performance of MFCC under noisy condition, both MFCC and delta MFCC features are extracted in wavelet domain in the second phase. Time–frequency characterization of emotions using wavelet analysis and energy or amplitude information using MFCC-based features has enhanced the available information. Wavelet-based MFCCs (WMFCCs) and wavelet-based delta MFCCs (WDMFCCs) outperformed standard MFCCs, delta MFCCs, and wavelets in recognition of Berlin speech emotional utterances. Probabilistic neural network (PNN) has been chosen to model the emotions as the classifier is simple to train, much faster, and allows flexible selection of smoothing parameter than other neural network (NN) models. Highest accuracy of 80.79% has been observed with WDMFCCs as compared to 60.97 and 62.76% with MFCCs and wavelets, respectively.

Keywords Human speech emotion · Mel-frequency cepstral coefficient Probabilistic neural network · Feature extraction · Wavelet analysis

H.K. Palo · M.N. Mohanty (✉)
Department of Electronics and Communication Engineering,
Siksha 'O' Anusandhan University, Bhubaneswar, Odisha, India
e-mail: mihir.n.mohanty@gmail.com

H.K. Palo
e-mail: hemantapalo@soauniversity.ac.in

M. Chandra
Department of Electronics and Communication Engineering,
Birla Institute Technology, Ranchi, India
e-mail: shrotriya69@rediffmail.com

A. Konkani et al. (eds.), *Advances in Systems, Control and Automation*,
Lecture Notes in Electrical Engineering 442, https://doi.org/10.1007/978-981-10-4762-6_47

1 Introduction

Currently due to involvement of ambiguous and multi-modal expressive behavior, emotion inference in daily human interaction remains a challenge. Mostly the emotional expressions are in the form of facial or bodily movements, although speech is sole medium of emotional expression during telephone conversation. For such task, detection of emotion arguably remains a challenge. The recognition system demands extraction of suitable features that can best represent speech emotions.

Among different feature extraction techniques such as prosodic, spectral, voice quality, nonlinear, MFCC uses frame-based approach and is widely accepted for speech and emotion analysis [1–3]. Although popular, MFCC feature extraction process does not involve the temporal dynamics among features that is essential for emotional analysis. The drawback can be minimized using derivative and acceleration coefficients of MFCC and has been approached by different researchers [4, 5]. However, MFCC-based features including deltas give information on amplitude and energy, hence unable to provide adequate information on speech emotion. To improve the recognition further, multi-resolution capability of wavelet analysis in extracting MFCC features has been proposed for speaker verification [6]. These literatures suggest for a possibility in enhancement of accuracy if the advantages of both wavelet analysis and differential MFCC are combined. Hence, a novel effort has been made to extract the wavelet-based delta MFCC (WDMFCC) features for comparison purpose.

Most classifiers used in speech analysis are statistical, NN-based, fuzzy logic, and combination of these [1–7]. GMM and HMM have the ability to model the pattern involving large feature sets. Smaller dataset and difficulty in modeling the emotions using conventional statistical classifiers such as GMM and HMM have opened up new avenues for NN-based classifiers [7]. As compared to multilayer perceptron (MLP), PNN is much faster, simpler, easy to implement, and more accurate [8]. Requirement of only one parameter adjustment and absence of any constraint in choosing the parameter with precision makes it superior to RBFN. This has motivated the authors to opt for probabilistic neural network (PNN) classifier in this work.

The organization of the paper is as follows: The feature extraction techniques and the classification model used are explained in Sects. 2 and 3, respectively. A detailed description on the simulation result with a comparison among the state of the art and the proposed features is described in Sect. 4. The conclusion and future research direction are provided in Sect. 5.

2 Feature Extraction Techniques

Initially, standard features based on wavelet analysis and MFCC are extracted and compared for their effectiveness in terms of recognition accuracy and mean square error (MSE). Next to it, delta MFCC features are extracted and compared with the

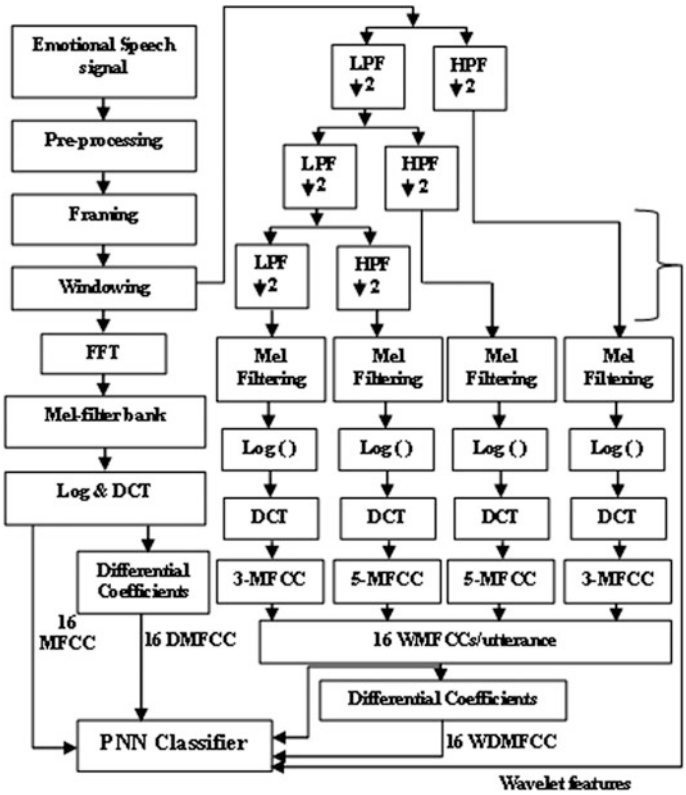

Fig. 1 Proposed feature extraction technique

wavelet-based MFCC and proposed wavelet-based delta MFCC features. The proposed feature extraction technique is shown in Fig. 1.

2.1 MFCC

One of the most dominant and effective cepstrum-based features is MFCC that uses a Mel-scale to wrap the original signal frequency into Mel-frequency. This way both human auditory and hearing mechanism are taken into account since human ear is logarithmic in nature. The relationship used to convert the windowed signal frequency f into Mel-frequency f_m is given by

$$f_m = 2595 \log_{10}\left(\frac{f}{700} + 1\right). \tag{1}$$

2.2 Wavelet Analysis

In wavelet analysis, the emotional speech signal $s(n)$ is decomposed into approximated and detailed coefficients using a series of low-pass and high-pass filters, respectively [9]. For the low-pass filter having an impulse response $h(n)$, the output can be represented as a convolution and is given by

$$X_L(n) = s(n) * h(n) = \sum_{k=-\infty}^{\infty} s(k)h(n-k) \tag{2}$$

Similarly, the output of the high-pass filter is the convolution of the filter impulse response and the signal under consideration. The sub-sampled output of the filters by a factor of two can be represented as

$$X_L(n) = \sum_{k=-\infty}^{\infty} s(k)h(2n-k) \tag{3}$$

$$X_H(n) = \sum_{k=-\infty}^{\infty} s(k)h(2n+1-k). \tag{4}$$

2.3 MFCC in Wavelet Domain (WMFCC)

The steps of extraction of WMFCC feature are explained below.

(1) Signal decomposition: Initially, decompose the signal into detailed d_i and approximation a_i coefficients at ith level, respectively. A three-level decomposition with Daubechies-4 (dB-4) has been performed here. Emotional utterances of Berlin database has been used for this work having a sampling frequency of 16 kHz. Thus, for 8 kHz bandwidth, the sub-bands are distributed in the range of 0–1, 1–2, 2–4, and 4–8 kHz due to filtering.
(2) The MFCC feature extraction technique as shown in Fig. 1 is applied individually for these sub-bands. Five WMFCCs from each sub-bands of 1–2 and 2–4 kHz and three WMFCCs from each band of 0–1 and 4–8 kHz have been extracted. More WMFCCs are extracted from the middle bands (1–4 kHz) to obtain more perceptual information as the speech signal often lies in this band. The number of WMFCC coefficients obtained this way is reduced to 16 coefficients per utterance.

2.4 Delta MFCC (DMFCC)

The delta MFCC (M_Δ) features of emotional utterances are extracted using the relation:

$$M_\Delta = \beta \times \sum_{q=1}^{2} n \times [\mathrm{MFCC}(r+q) - \mathrm{MFCC}(r-q)], \quad r = 1, 2, \ldots N \tag{5}$$

where MFCC_Δ is the delta features, and to scale the frequency, a value of $\beta = 2$ has been used. N is the number of delta features per utterance, whereas q is the indexing parameter associated with analyzing window.

2.5 Proposed Wavelet Delta MFCC (WDMFCC)

In the proposed technique, the use of wavelet analysis has provided both time and frequency information of the signal, while traditional MFCCs provided the energy or amplitude information. Application of derivatives of MFCC has inducted the dynamic characteristics with the WMFCC features. The steps of extracting WDMFCC features are explained below.

a. Extract the wavelet features as explained earlier using Eqs. (3) and (4) as shown in Fig. 1.
b. Apply the MFCC feature extraction technique to the wavelet features as explained in WMFCC feature extraction technique.
c. Apply the derivative algorithm as given in Eq. (5) to the WMFCC features to extract 16 WDMFCC features per utterance of an emotion.

3 Classification Method

PNN is a nonparametric network having input, pattern, summation, and decision layers as the main constituent sections as shown in Fig. 2.

For any input emotion pattern E with dimension of the vector x and smoothing parameter δ, the output of the pattern layer can be represented as

$$\delta_{u,v}(E) = \frac{1}{(2\pi)^{\frac{x}{2}}\delta^x} \exp\left[-\frac{(E - E_{u,v})^T (E - E_{u,v})}{2\delta^2}\right] \tag{6}$$

where $E_{u,v}$ denotes the neuron vector and is considered to be the center of the kernel function. Here $u = 1, 2, \ldots, U$ is the number of emotional states; $v = 1, 2, \ldots V_u$ and

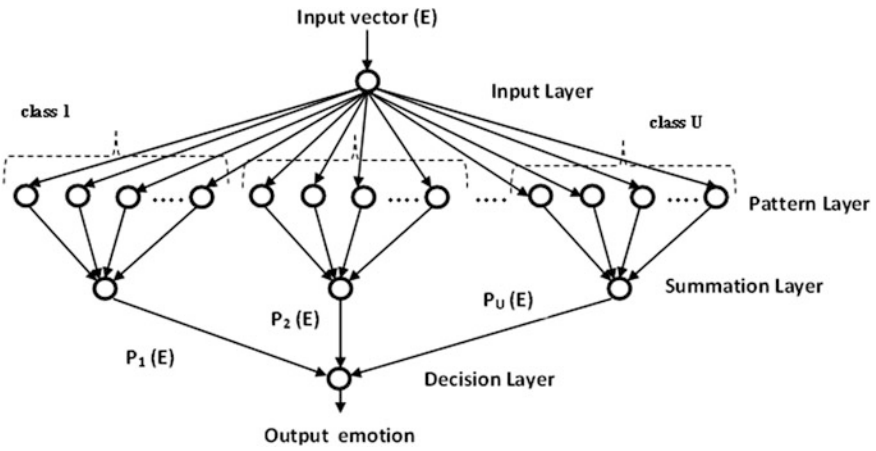

Fig. 2 The structure of PNN

V_u is the total number of feature values in class S_u as given in Eq. (2). Based on the probability distribution function (PDF) of all the neuron, the summation layer summarizes and averages all the neuron outputs of the designated class so as to classify the pattern E to that class S_u.

$$p_u(E) = \frac{1}{(2\pi)^{\frac{x}{2}}\delta^x}\frac{1}{V_u}\sum_{v=1}^{V_u}\exp\left[-\frac{(E-E_{u,v})^T(E-E_{u,v})}{2\delta^2}\right] \tag{7}$$

The decision layer takes a decision on the predicted class using Bayes' approximation of the summation layer neuron output:

$$\widehat{S}(E) = \arg\max\{p_u(E)\} \tag{8}$$

where the computed class of the pattern E is represented by $\widehat{S}(E)$.

4 Results and Discussion

Berlin emotional speech database (EMO-DB) [10] has been chosen to distinguish five emotional states such as angry, anxiety, happy, sad, and neutral. The utterances used for training of the classifier are not involved in testing or validation purpose. Approximately 70% of the data are used for training, and 20% each are used for testing and validation of every emotional state.

The recognition accuracy using the extracted features with PNN classifier is given in Table 1. Comparison of the results has gone in favor of WDMFCC as compared to others. Use of both temporal information due to involvement of

differential values of MFCC and exploration of multi-resolution capability of wavelet analysis is the prime reason of the accuracy improvement.

Wavelet-based features like WMFCC and WDMFCC are better than delta MFCC and MFCC features as observed in Table 1. It is found that involvement of either differential information or wavelet approach in modifying the MFCC extraction technique has enhanced the robustness of the resultant features as compared to the standard MFCC or wavelet features.

A comparison of MSE has provided similar results as shown in Fig. 3. It is found that standard wavelet-based features are more reliable as compared to MFCCs both in terms of classification accuracy and MSE.

To find the response time of the classifier with different MFCC features extracted, the time elapsed both during feature extraction and classification has been compared in Table 2.

Table 1 The recognition accuracy using the extracted features with PNN classifier

Features	Angry (%)	Anxiety (%)	Happy (%)	Neutral (%)	Sad (%)	Average accuracy (%)
MFCC	64.55	62.78	61.44	57.12	58.96	60.97
Wavelets	66.71	64.35	63.42	59.30	60.01	62.76
DMFCC	65.80	64.81	65.54	62.06	61.37	63.92
WMFCC	86.60	84.58	76.21	68.63	66.49	76.50
WDMFCC	89.27	86.64	80.39	75.48	72.15	80.79

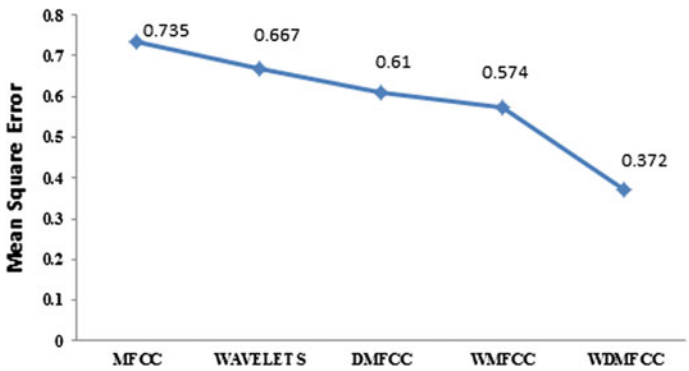

Fig. 3 Comparison of MSE using variants of MFCC with PNN classifier

Table 2 Real-time comparison of different features using PNN classifier for 45 utterances per emotion

Features	MFCC	Wavelets	DMFCC	WMFCC	WDMFCC
Feature extraction time/utterance (s)	0.1159	1.244	0.18809	0.32604	2.19
Classification time/emotion (s)	15.50	13.13	10.56	11.54	13.12
Recognition accuracy (%)	60.97	62.76	63.92	76.50	80.79

5 Conclusion

There is an improvement in feature reliability involving the differential values of MFCC coefficients due to inclusion of temporal emotional information. Application of multi-resolution capability in extraction of MFCC features has resulted more reliable information than standard MFCC as the classification results suggest. Involvement of both wavelet analysis and differential algorithm used for modification of standard MFCC found to be a novel effort in this direction. Other modification techniques that can add valuable emotional information to MFCC features can open up new avenues in the field of emotion recognition.

References

1. Kari, B., Muthulakshmi, S.: Real time implementation of speaker recognition system with MFCC and neural networks on FPGA. Indian J. Sci. Technol. **8**(19), 1–11 (2015)
2. Mohanaprasad, K., Pawani, J.K., Killa, V., Sankarganesh, S.: Real time implementation of speaker verification system. Indian J. Sci. Technol. **8**(24), 1–9 (2015)
3. Subhashree, R., Rathna, G.N.: Speech emotion recognition: performance analysis based on fused algorithms and GMM Modelling. Indian J. Sci. Technol. **9**(11), 1–8 (2016)
4. Mishra, A.N., Chandra, M., Biswas, A., Sharan, S.N.: Robust features for connected Hindi digits recognition. Int. J. Signal Process. Image Process. Pattern Recogn. **4**(2), 79–90 (2011)
5. Kwon, O.W., Chan, K., Hao, J., Lee, T-W.: Emotion recognition by speech signals. In: Interspeech (2003)
6. Kumar, P., Chandra, M.: Hybrid of wavelet and MFCC features for speaker verification. In: 2011 World Congress on Information and Communication Technologies, IEEE, pp. 1150–1154 (2011)
7. Ayadi, E., Kamal, M.S., Karray, F.: Survey on speech emotion recognition: features, classification schemes, and databases. Pattern Recogn. **44**(3), 572–587 (2011). Elsevier
8. Specht, D.: Probabilistic neural networks. Neural Netw. **3**, 109–118 (1990)
9. Palo, H.K., Mohanty, M.N., Chandra, M.: Efficient feature combination techniques for emotional speech classification. Int. J. Speech Technol. **19**, 135–150 (2016)
10. Burkhardt, F., Paeschke, A., Rolfes, M., Sendlmeier, W., Weiss, B.: A database of German emotional speech. In: Proceedings of the Interspeech, Lissabon, Portugal, pp. 1517–1520 (2005)

Optimal and Novel Hybrid Feature Selection Framework for Effective Data Classification

Sivakumar Venkataraman and Rajalakshmi Selvaraj

Abstract Data mining methods are frequently applied in the framework of data classification. Under data mining methods, feature selection (FS) algorithms are essential for dealing with various dimensional data sets that may contain features in the range of small, medium, and large dimensions. Handling large number of features always raises the issues regarding the classifier accuracy and running time. A novel hybrid feature selection technique build on symmetrical uncertainty and genetic algorithm is proposed. The experiments' results on UCI datasets using this hybrid framework proved that proposed feature selector is efficient through minimizing the volume of initial features and accurate by providing better detection performance in the classification algorithms comparing with other feature selectors in the literature. It is evident from the earlier research work the prosed method promotes in optimizing and improves the performance. In summary, the proposed feature selection method has outperformed other methods in minimizing the selected features, classification performance and reduces the executing time.

Keywords Data mining · Feature selection · Classification
Symmetrical uncertainty and genetic algorithm

1 Introduction

Data analytics researchers need relevant and high-quality data from huge amount of stored data. Feature selection method helps in reducing the dimensionality of features by removing redundant, irrelevant, or noisy data through which improvisation in classification accuracy with minimum processing of data can be achieved.

S. Venkataraman (✉)
Faculty of Computing, Botho University, Gaborone, Botswana
e-mail: sivakumar.venkataraman@bothouniversity.ac.bw

S. Venkataraman · Rajalakshmi Selvaraj (✉)
Department of Information Systems, BIUST, Gaborone, Botswana
e-mail: selvarajr@biust.ac.bw

A. Konkani et al. (eds.), *Advances in Systems, Control and Automation*,
Lecture Notes in Electrical Engineering 442, https://doi.org/10.1007/978-981-10-4762-6_48

Due to increase of dimensionality of records and features in data repositories, there is shift in maintaining the records related to each and every individual. Formally, in recent times, data mining techniques are used to discover a novel and useful pattern from the historical data. Many research ideas are openly still needed to solve this. Mostly classification framework gives an effective result for classifying the datasets. Usually, large and high dimensional datasets contain complex information with errors, and in such a situation, classification algorithm plays a vital role.

By using the feature subset selection process, the relevant subset features can be determined from the original features. The process of ranking features according to their significance in improving the performance of classifiers is called as ranking-based feature selector. Under KDD process, feature selection is only one essential step that improves the detection performance of the classifiers, minimizes the time taken to build the data mining model, and reduces the number of initial features because there are no quality features and no quality results in the classifiers.

FS methods are classified as filter and wrapper method. Based on this key idea, several FS methods are introduced in machine learning paradigm. Wrapper method is used to select the features based on the accuracy estimate, and filter method is used to select the features not based on the accuracy estimate; rather, it uses the data characteristics with the relevancy or correlation measures. Filter-based approaches are not dependent on classifiers and usually faster and more scalable than wrapper-based methods. Moreover, they have low computational complexity too. Recently, numbers of hybrid approaches are also being proposed to achieve a good balance in the feature selection criteria by combing both filter and wrapper method.

2 Related Works

In [1], the author discussed the impact of the noise in the class labels by analyzing the traditional mutual information-based filter feature selection algorithm. This proposed idea brings the solution for the nearest neighbors-based entropy estimator to minimize the class label errors. In [2] the author presents an empirical study on many feature selection and classification algorithms to analyze their performance on diverse biological datasets. This study reveals combination of RFE with SVM and LR as best generalization model to perform feature selection and classification. In [3], the author has proposed a rule-based feature selection algorithm to improve the detection performance of multiclass support vector machine. In [4], the author has applied a hybrid algorithm combines the genetic algorithm with K-nearest neighbor for predicting the binding of protein–water from its X-ray crystallographic protein structure data. In [5], the author has proposed a redundancy demoting (RD) approach for making improvement in ranking by demoting the redundant features. For instance, for diagnosing the erythemato-squamous disease with the help of feature selection based on *F*-score measure has been applied [6]. In [7], the author proposed genetic algorithm (GA) as commonly used global searches for optimization. This method is used in feature selection process among various

applications and has exposed to be a good tool [8–12]. A recommended way of solving this issue is to group genetic algorithm and some memetic (search) operations [13, 14]. This helps in fine-tuning the search process and improves the quality of the results generated from genetic algorithm with relation to accuracy and efficiency. Recently, these types of evolutionary algorithms are called hybrid evolutionary algorithms (EAs), memetic algorithms (MAs), Lamarckian evolutionary algorithms, Baldwinian EAs, and local search or cultural genetic algorithms. These algorithms are not used for convergence to high-quality results only, also for further efficient search mechanism [13, 14]. Selecting only the minimum relevant features from the original subset is the main challenge in feature selection. This work aims to develop 'symmetrical uncertainty and genetic algorithm (SU-GA)'-based feature selector named universal and novel feature selector. The goal of this study is to make accurate prediction with the help of least number of significant features. In this research work, the features undergo memetic (genetic) evolution such as 'include' and 'remove' to select the features. The examined results prove the proposed SU-GA-based classifier attains significant dimensionality reduction in various dimensional datasets from the UCI machine learning repository [15].

3 Proposed Method

3.1 Symmetrical Uncertainty

The symmetrical uncertainty (SU) between features and the target concept are used to obtain the best features for classification. Features with a larger SU value obtain greater weight. SU measures the relationship among X, Y variables based on the information theory. It can be calculated as follows.

$$\mathrm{SU}(X, Y) = 2\frac{I(X, Y)}{H(X) + H(Y)}$$

Considering $I(X, Y)$ as the MI among X, Y. $H(..)$ as an entropy function for X, Y features. The SU admits the normalized range value [0,1] as correction factor value is 2. If SU value is 1, then the information of one feature is absolutely predictable. If SU value is 0, then X, Y are not associated.

3.2 Genetic Algorithm

The amount for genetic algorithm (GA) [16] is stated randomly for all individual chromosome that encrypt the feature subsets. Each chromosome are assembled with binary string, and the binary string encrypting describes that the value '1' ('0')

shows the particular feature is selected (omitted). The Obj_Fun (Objective Function) for subset are obtained from the aptness of individual chromosome as,

$$\text{Fitness}(c) = \text{Max}(\text{Obj\_Fun } (\text{SFc}))$$
$$\text{Obj\_Fun}(\text{SFc}) = \alpha * (1/\tau) + (\text{RCF} * \text{Recall}) + (\text{PCF} * \text{Precision})$$

where

τ No. of ones in the SFc
α No. of minimum features selected
RCF Recall credibility factor
PCF Precision credibility factor

Considering SFc as the SF subset arranged with Chromosome c. Obj_Fun (SFc) estimates the feature subset contribution. If Chromosomes with similar aptness value obtained, then the first priority of surviving will be provided to the less number of SF.

3.3 Proposed SU-GA Feature Selector

The proposed hybrid feature selection algorithm including feature ranking and optimal feature selection (FR-OFS) method adopts the filter method with wrapper method to attain the optimal subset features. First phase, the proposed algorithm selects very few relevant features, by computing the SU values between features and the target concept. Second phase, GA is used to search the optimal subset of features with higher accuracy obtained in the first phase with symmetrical uncertainty. The number of GA is set based on features rank rendering from the examined results from SU. Features having higher SU value will have the higher possibility, where the feature can be selected, that states the resembling bits will have more possibility to be select in the chromosome. Each individual's fitness is evaluated using GA such as the value of the result by using the fitness function. The chromosomes might subjectively have transformed by the crossover and mutation functions. This impacts the aptness value is carried out by both crossover and mutation operation. The procedure is repeated until acceptable results are obtained. The features are chosen at the end of this space called as reliable features. The proposed SU-GA feature selector is shown in Figs. 1 and 2.

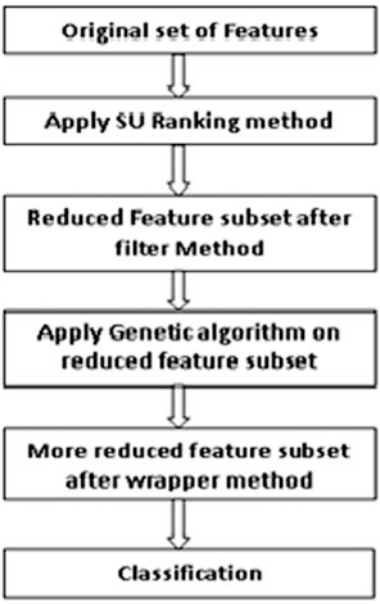

Fig. 1 Proposed SUGAFS method

Input: Full data set.

Step 0. Start
Step 1. Load Dataset
Step 2. Compute SU value of each feature
Step 3. Select the features with larger SU value.
Step 4. Initialize the population P with selected features.
Step 5. Evaluate the fitness value of the individuals.
Step 6. While Termination criteria not Satisfied
{
Select parents for reproduction
Perform recombination and mutation
Evaluate population
}
Step 7. Output the Selected feature subset.
Step 8. Stop.

Output: Selected Feature subset.

Fig. 2 Hybrid feature selection algorithm

4 System Implementation and Experimental Results

The implementation of proposed SU-GA Feature selector is on twofold. Firstly, the SU value of each feature is examined, and the features are prioritized based on the highest SU value, and those features having lesser SU are eliminated by considering

as an irrelevant and redundant feature. Both WEKA and MATLAB tool box are used to successfully implement the proposed hybrid feature selector SU-GA. In the second phase, genetic algorithm is applied on the selected feature subset by SU to find out the optimal feature with out compromising the classification accuracy. The final set of optimal features selected by the proposed hybrid feature selector SU-GA is tested with the help of various benchmark classification algorithms in the literature by using the classification accuracy, number of reduced features, and time taken to build a model by using 10-fold crossvalidation as a test method.

4.1 Experimental Setup

Totally, 10 benchmark dataset from UCI machine learning repository is chosen for carrying out the experiments on the existing and proposed feature selector in terms of number of feature selected by each method, the improvement in detection performance of classifiers by each method and time taken to build a model by each method are empirically evaluated and tested on various datasets including Soybean, Lung Cancer, Ionosphere, and Dermatology. The summary of this datasets such as the number of attributes and instances in each dataset is shown in Table 1.

Different classification algorithm, namely NB, J48, SMO, and JRIP, are applied on both original as well as number of features selected by SU, GA, and proposed SU-GA feature selector. The proposed method is implemented using WEKA and MATLAB tool box. The features having higher SU values are identified through ranker search algorithm available in WEKA. The number best-ranked features by SU was given as an input to the GA toolbox available in the MATLAB to select only the optimal feature set through eliminating both irrelevant and redundant features effectively. Finally, it varies supervised classifiers applied on both original and optimal subset of features selected by the proposed method. The classification accuracy, number of selected feature by each method, and time taken for classifiers are clearly proved that the proposed method is superior than other existing feature selector in the literature. The results are presented in Tables 3 and 4.

Table 1 Datasets for research

Dataset name	Attributes name	No. of instances
Ionosphere	35	351
Soybean	36	683
Diabetes	9	768
Segment challenge	20	1500
Vote	17	435
Dermatology	35	366
Lung cancer	57	32
Wine	14	178
Hepatitis	20	155
Vehicle	19	846

4.2 Results and Discussions

In this experiment, three widely used evaluation measures features selected; classification accuracy and processing time are adopted to evaluate the proposed method. This proposed SUGAFS algorithm and other two feature selection algorithms SU and GA are implemented in WEKA and MATLAB. These three algorithms are tested and compared on ten discrete UCI datasets. The results abstained from SU, genetic feature selection methods, and the proposed method have been tabulated. Tables 2, 3, 4, 5, 6, 7, and 8 exemplify the number of features selected, classification performance, and the time taken by the proposed method with SU and GA methods. This experiment shows the proposed method is more effective when compared with available feature selection methods.

4.3 Feature Selection

FS is a process of driving the subset features from the original feature space. The proposed method has been applied in all datasets to select the relevant features by removing the irrelevant one. Table 2 shows the features selected by using SU, GA, and SU-GA. The results indicate that the proposed method selects the least number of features than other two methods for all the ten datasets. Notably, this method selects around ten percentage of attributes for segment challenge and vote datasets. For lung cancer and vehicle data, it selects only around twenty percentage of features. If the selected features are decreased, the performance of classification algorithm does improve this advocates the necessity of feature selection. Therefore, effective feature selection may improve the accuracy and performance of learning algorithms (Fig. 3).

Table 2 Features selected by different FS methods

Datasets	All	SU	GA	SU-GA
Ionosphere	34	17	14	13
Soybean	35	18	22	16
Diabetes	8	4	4	3
Segment	19	10	8	4
Vote	16	8	4	2
Dermatology	35	18	22	11
Lung cancer	57	28	21	13
Wine	14	7	12	6
Hepatitis	20	10	11	8
Vehicle	19	10	11	4
Total	257	130	129	80

Table 3 Classification accuracy by different methods on various datasets

Dataset	NB				J48				SMO			
	All	SU	GA	SU-GA	All	SU	GA	SU-GA	All	SU	GA	SU-GA
Ionosphere	82.6	87.2	90.3	90.6	91.5	91.7	92.6	92.0	88.6	88.0	88.0	88.3
Soybean	93.0	90.6	92.1	89.3	91.5	90.6	90.8	90.5	93.7	93.4	93.5	93.4
Diabetes	76.3	75.4	77.5	76.4	73.8	74.3	74.9	74.6	77.3	76.0	76.8	75.9
Segment	81.1	76.9	82.9	82.8	95.7	94.9	95.4	94.9	91.9	90.2	89.4	82.1
Vote	90.1	91.3	96.1	95.6	96.3	95.2	96.1	95.6	96.1	95.6	95.6	95.6
Dermatology	97.3	91.8	98.1	92.9	94.0	88.0	94.3	90.4	95.4	84.1	97.3	98.2
Lung cancer	50.0	68.8	75.0	78.1	50.0	62.5	62.5	62.5	40.6	62.5	65.6	68.8
Wine	97.2	96.1	97.2	97.8	93.8	94.4	93.8	94.4	98.3	96.6	98.3	96.6
Hepatitis	84.5	84.5	84.5	85.8	83.9	82.6	83.2	83.9	85.2	83.2	83.2	83.2
Vehicle	44.8	43.4	48.5	44.1	72.5	69.5	68.3	66.1	74.3	66.7	58.0	46.7
	79.7	80.6	84.2	83.3	84.3	84.4	85.2	84.5	84.1	83.6	84.6	82.9

Table 4 Classification accuracy by different methods on various datasets

Dataset	NB				J48				SMO			
	All	SU	GA	SU-GA	All	SU	GA	SU-GA	All	SU	GA	SU-GA
Ionosphere	89.5	88.9	89.5	88.9	92.9	91.7	92.3	91.7	91.2	92.0	92.6	92.9
Soybean	84.3	82.3	80.8	81.0	92.1	90.3	91.7	88.6	93.4	93.0	94.0	93.3
Diabetes	71.2	72.1	73.6	73.4	73.8	72.0	74.0	72.0	75.4	77.2	75.5	76.4
Segment	87.4	87.1	88.2	87.1	96.9	96.4	97.9	96.9	96.7	96.3	94.5	91.5
Vote	94.9	95.6	95.6	95.6	95.6	94.3	95.2	95.6	94.7	95.2	95.9	95.4
Dermatology	86.7	86.4	87.4	89.3	94.8	91.5	94.2	90.4	96.2	92.1	96.4	93.7
Lung cancer	62.5	65.6	62.5	62.5	56.2	62.5	65.6	65.6	37.5	53.1	65.6	71.9
Wine	88.8	88.8	88.8	88.8	97.2	96.6	96.6	97.2	97.2	98.3	99.4	98.3
Hepatitis	76.1	76.8	77.4	79.4	80.0	81.9	83.9	80.0	80.0	83.9	83.9	82.6
Vehicle	65.7	64.9	66.0	65.7	77.0	73.8	72.8	64.7	81.7	70.1	71.1	64.2
	80.7	80.8	81.0	81.2	85.7	85.1	86.4	84.3	84.4	85.1	86.9	86.0

Table 5 Average performance of different classification algorithms

Classification algorithms	All	SU	GA	SU-GA
NB	79.7	80.6	84.2	83.3
J48	84.3	84.4	85.2	84.5
SMO	84.1	83.6	84.6	82.9
JRIP	81.6	82.5	81.6	83.0
DT	80.7	80.8	81.0	81.2
Rand Frst	85.7	85.1	86.4	84.3
Multi Perptn	84.4	85.1	86.9	86.0
Kstar	81.9	83.5	84.3	83.7
Average	82.8	83.2	84.3	83.7

4.4 Classification Performance

In order to evaluate how well original features and each selected feature by different feature selector including SU, GA and SU-GA will able to improve the detection performance of various classifiers is empirical evaluated. The various classification algorithms are used in numerous sets in predicting the results, and the value are observed. It is observed that the selected features by SU-GA feature selector will able to improve the detection performance of all the classifiers. However, this method selects more number of features as compared with the proposed method which selects only 30% of features. It is worth to note that the difference of classification performance between GA and the proposed method is very small with better running time and number of features selected. And also, the proposed method is effective and efficient when compared with other available feature selection methods.

Table 5 shows the average learning accuracy and observed the proposed SU-GA feature selector improves the detection performance of JRIP and decision table algorithms and is comparatively improved than the other methods. This experimentation concludes that the attributes reduced through SUGAFS, and classification accuracy may increase or remain comparatively identical. The exploratory results illustrate the classification accuracy from the chose feature subset indicates prevalent results than all other existing strategies (Fig. 4).

4.5 Processing Time

In the third phase, several tests are carried out to assess the running time of the proposed method across all the datasets. It is also conducted that the same experiments for SU and GA feature selection methods. After obtaining the results, the performance of the three feature selection methods are compared with the original dataset in terms of running time. The detailed results are provided in Tables 6, 7 and 8. From the experimental results, it can be noted that the proposed feature selection method drastically reduces the running time of a learning algorithms.

Table 6 Computational time of different methods on various datasets

Dataset	NB				J48				SMO			
	All	SU	GA	SU-GA	All	SU	GA	SU-GA	All	SU	GA	SU-GA
Ionosphere	0.01	0.00	0.00	0.00	0.08	0.01	0.01	0.01	0.00	0.08	0.08	0.01
Soybean	0.00	0.00	0.00	0.00	0.03	0.01	0.01	0.01	1.49	1.24	1.12	1.08
Diabetes	0.01	0.00	0.00	0.00	0.01	0.00	0.01	0.00	0.09	0.07	0.06	0.01
Segment	0.02	0.01	0.00	0.00	0.04	0.03	0.02	0.02	0.4	0.13	0.28	0.11
Vote	0.00	0.00	0.00	0.00	0.00	0.00	0.00	0.00	0.09	0.01	0.01	0.01
Dermatology	0.01	0.00	0.01	0.00	0.03	0.02	0.03	0.00	0.28	0.26	0.21	0.08
Lung cancer	0.00	0.00	0.00	0.00	0.00	0.00	0.00	0.00	0.02	0.01	0.02	0.01
Wine	0.00	0.00	0.01	0.00	0.01	0.01	0.01	0.01	0.02	0.02	0.02	0.02
Hepatitis	0.00	0.00	0.00	0.00	0.05	0.00	0.00	0.01	0.05	0.01	0.01	0.01
Vehicle	0.01	0.00	0.00	0.00	0.04	0.02	0.02	0.00	0.07	0.05	0.05	0.05

Table 7 Computational time of different methods on various datasets

Dataset	NB				J48				SMO			
	All	SU	GA	SU-GA	All	SU	GA	SU-GA	All	SU	GA	SU-GA
Ionosphere	0.05	0.14	0.13	0.02	0.04	0.11	0.1	0.02	2.27	0.65	0.54	0.43
Soybean	0.24	0.19	0.23	0.08	0.19	0.22	0.29	0.07	31.78	15.67	15.94	13.47
Diabetes	0.17	0.05	0.04	0.01	0.16	0.12	0.13	0.03	0.66	0.45	0.46	0.32
Segment	0.16	0.08	0.07	0.02	0.13	0.08	0.07	0.05	5.31	3.00	2.53	1.88
Vote	0.15	0.01	0.00	0.00	0.15	0.02	0.01	0.00	0.84	0.42	0.2	0.14
Dermatology	0.07	0.12	0.17	0.02	0.14	0.11	0.1	0.01	23.66	7.39	10.68	4.77
Lung cancer	0.00	0.01	0.00	0.00	0.01	0.01	0.01	0.00	5.75	1.43	0.78	0.36
Wine	0.1	0.01	0.01	0.01	0.01	0.01	0.01	0.01	0.29	0.15	0.23	0.13
Hepatitis	0.01	0.01	0.01	0.01	0.09	0.01	0.01	0.02	0.36	0.15	0.15	0.13
Vehicle	0.06	0.03	0.03	0.01	0.07	0.06	0.06	0.05	2.09	0.95	1.13	0.63

Table 8 Processing time average by different FS methods

Classification algorithms	All	SU	GA	SU-GA
NB	0.006	0.002	0.003	0.00
J48	0.029	0.01	0.011	0.006
SMO	0.251	0.188	0.186	0.139
JRIP	0.065	0.055	0.058	0.022
DT	0.101	0.065	0.069	0.018
Rand Frst	0.099	0.075	0.079	0.026
Multi Perptn	7.301	3.026	3.264	2.226
Kstar	0.00	0.00	0.00	0.00
Average	0.98	0.43	0.46	0.30

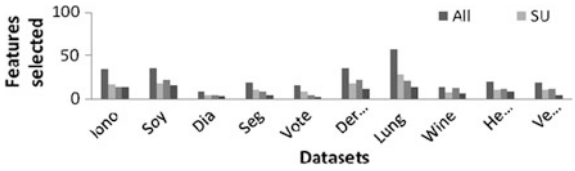

Fig. 3 Number features selected on UCI datasets

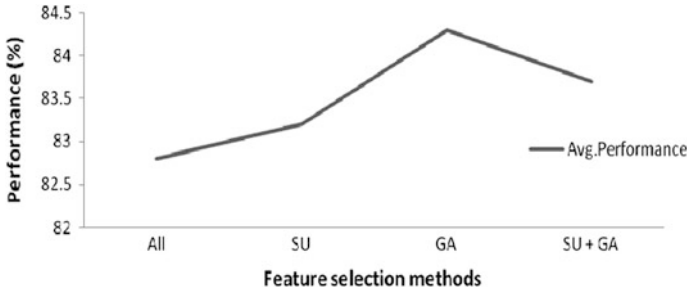

Fig. 4 Performance of FS methods

It is found that the average running time of the proposed model significantly improves the processing time than any other FS methods.

From the experiment, it has observed the following points are in favor of the proposed method:

1. Running time for all classification algorithms is lesser than other methods.
2. GA feature selection method takes much time than other two feature selection methods because of its global search nature.
3. The average processing time of the proposed method is considerably lesser than other two feature selection methods (Figs. 5 and 6).

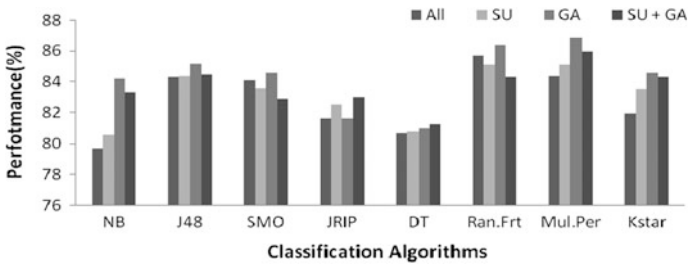

Fig. 5 Processing time average by different FS methods

Fig. 6 Processing time average by different FS methods

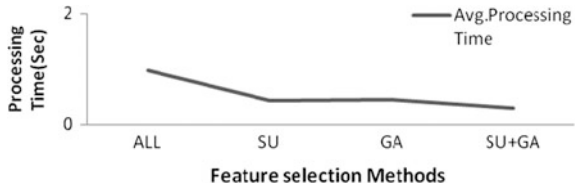

5 Conclusion

In this work, both SU and GA are combined named as hybrid feature selector for the purpose of eliminating both irrelevant and redundant features and to select only the most relevant features for improving data classification. The performance of the proposed feature selector was evaluated in terms of three quality measures such as number of selected features, detection performance of classifiers, and time taken to build the model with the dataset from University of California Irvine dataset. The proposed SU and GA should probably become part of the standard tool box of feature selection method for effective data classification. The proposed method can more clearly be stated as follows:

1. SU and GA are combined named as SU-GA hybrid feature selector for selecting only most relevant features for supervised. The system is aimed at making improvements over the existing work in three perspectives such as reduction in feature set, improvement in classification accuracy, and finally, minimizing the running time of achieving the goal.
2. The proposed method significantly reduces processing time than any other feature selection methods with minimal number of features. The result of SU-GA imparts higher classification accuracy rate for some dataset with minimum selected features and minimum running time.
3. The proposed features and learning paradigm SU-GA are promising strategies to be applied on any data classification problems.

References

1. Frenay, B., Doquire, G., Verleysen, M.: Estimating mutual information for feature selection in the presence of label noise. Comput. Stat. Data Anal. **71**(1), 832–848 (2014)
2. Hemphill, E., Lindsay, J., Lee, C., Mandoiu, I., Nelson, C.E.: Feature selection and classifier performance on diverse bio-logical datasets. BMC Bioinf. **15**(13) (2014)
3. Ganapathy, S., Kulothungan, K., Muthurajkumar, S., Vijayalakshmi, M., Yogesh, P., Kannan, A.: Intelligent feature selection and classification techniques for intrusion detection in networks: a survey. EURASIP J. Wirel. Commun. Netw. (2013)
4. Raymer, M.L., Doom, T.E., Kuhn, L.A., Punch, W.F.: Knowledge discovery in medical and biological datasets using a hybrid bayes classifier/evolutionary algorithm. IEEE Trans. Syst. Man Cybern. **33**(5), 802–810 (2003)
5. Osl, M., Dreiseit, S., Cerqueira, F., Netzer, M., Pfeifer, B., Baumgartner, C.: Demoting redundant features to improve the discriminatory ability in cancer data. J. Biomed. Inform. **42**(4), 721–725 (2009)
6. Xie, J., Wang, C.: Using support vector machines with a novel hybrid feature selection method for diagnosis of erythemato-squamous diseases. Expert Syst. Appl. **38**, 5809–5815 (2010)
7. Holland, J.H.: Adaptation in Natural Artificial Systems, 2nd edn. MIT Press (1992)
8. Deutsch, J.M.: Evolutionary algorithms for finding optimal gene sets in microarray prediction. Bioinformatics **19**(1), 45–52 (2003)
9. Jirapech-Umpai, T., Aitken, S.: Feature selection and classification for microarray data analysis: evolutionary methods for identifying predictive genes. BMC Bioinf. **6**, 148 (2005)
10. Li, L., Weinberg, C.R., Darden, T.A., Pedersen, L.G.: Gene selection for sample classification based on gene expression data: study of sensitivity to choice of parameters of the GA/KNN method. Bioinformatics **17**(12), 1131–1142 (2001)
11. Li, L., Pedersen, L.G., Darden, T.A., Weinberg, C.R.: Computational analysis of leukemia microarray expression data using GA/KNN method. In: Proceeding of the 1st Conference on Critical Assessment of Microarray Data Analysis, CAMDA (2000)
12. Ooi, C.H., Tan, P.: Genetic algorithm applied to multi-class prediction for the analysis of gene expression data. Bioinformatics **19**(1), 37–44 (2003)
13. Moscato, P.: On evolution, search, optimization, genetic algorithms and martial arts: toward memetic algorithms. Technical Report Caltech Concurrent Computation Program, Rep. 826, California Institute of Technology, Pasadena, CA (1989)
14. Zhu, Z., Ong, Y.S., Dash, M.: Wrapper-Filter feature selection algorithm using a memetic framework. IEEE Trans. Syst. Man Cybern. Part B **10**(4), 392–404 (2006)
15. Hettich, S., Blake, C., Merz, C.: UCI repository of machine learning databases. http://www.ics.uci.edu/mlearn/MLRepository.html (1998)
16. Moretti, S., van Leeuwen, D., Gmuender, H., Bonassi, S., Van Delft, J., Kleinjans, J., Patrone, F., Merlo, D.F.: Combining Shapley value and statistics to the analysis of gene expression data in children exposed to air pollution. BMC Bioinf. **9**(361), 1–21 (2008)
17. Aitkenhead, M.J.A.: Co-evolving decision tree classification method. Expert Syst. Appl. **34**(1), 18–25 (2006)
18. Baker, J.E.: Adaptive selection methods for genetic algorithms. In: Proceedings of International Conference in Genetic Algorithm and Their Applications, pp. 101–111 (1985)
19. Hualonga, B., Jingb, X.: Hybrid feature selection mechanism based high dimensional date sets reduction. Energy Procedia **11**, 4973–4978 (2011)
20. Tan, F., Fu, X., Zhang, Y., Bourgeois, A.G.: A genetic algorithm—based method for feature subset selection. Soft Comput. **11**, 111–120 (2008)
21. Jinyan, L., Huiqing, L.: Kentridge bio-medical data set repository. http://datam.i2r.a-star.edu.sg/datasets/krbd (2001)
22. Keinan, A., Sandbank, B., Hilgetag, C.C., Ellison, I., Ruppin, E.: Fair attribution of functional contribution in artificial and biological networks. Neural Comput. **16**(9), 1887–1915 (2004)

23. Qi, Z., Tian, Y., Shi, Y.: Robust twin support vector machine for pattern classification. J. Pattern Recognit. **46**(1), 305–316 (2013)
24. Senthamarai Kannan, S., Ramaraj, N.: A novel hybrid feature selection via Symmetrical Uncertainty ranking based local memetic search algorithm. Knowl. Based Syst. **23**, 580–585 (2010)
25. Shao, Y.H., Chen, W.J., Zhang, J.J. et al.: An efficient weighted Lagrangian twin support vector machine for imbalanced data classification. J. Pattern Recognit. **47**(9), 3158–3167 (2014)
26. Weka.: Machine Learning Software in Java. The University of Waikato software documentation. http://www.cs.waikato.ac.nz/_ml/wek
27. Eswa, J., Yang, J.H., Honavar, V.: Feature selection using a genetic algorithm. IEEE Intell. Syst. **13**(2), 44–49 (1998)
28. Yildirim, P.: Filter based feature selection methods for prediction of risks in hepatitis disease. Int. J. Mach. Learn. Comput. **5**(4), 258–263 (2015)

Sensorless Direct Torque Control of Induction Motor Using Neural Network-Based Duty Ratio Controller

H. Sudheer, S.F. Kodad and B. Sarvesh

Abstract Improvements in the sensorless direct torque control of an induction motor by employing fuzzy logic switching controller (FLSC) plus neural network-based duty ratio controller (NNDRC) are explained in this paper. The conventional direct torque control (CDTC) of an induction motor suffers from major drawbacks such as high ripples in motor torque and flux response, poor performance during low speed and starting, and switching frequency variations due to hysteresis bands. Duty ratio controller evaluates the time for which active switching state is applied (δ), and for the remaining time period, zero switching vector is applied. The simulation results show that by using FLSC with NNDRC, considerable reduction in torque and flux ripples and improvement in dynamic response of drive compared to CDTC are achieved.

Keywords Induction motor (IM) · Direct torque control (DTC)
Neural network (NN) · Fuzzy logic switching controller (FLSC)
Duty ratio controller (DRC)

1 Introduction

Direct torque control was first introduced by Takahashi and Naguchi for the fast response and high-performance applications [1, 2]. Over the years, DTC gained popularity over field-oriented control due to advantages such as an absence of

H. Sudheer (✉)
Faculty of Science and Technology, IFHE Hyderabad, Hyderabad, India
e-mail: hsudheer@ifheindia.org

S.F. Kodad
PES Institute of Technology and Management, Shimoga, India
e-mail: kodadsf@rediffmail.com

B. Sarvesh
JNTUA, Anantapur, India
e-mail: bsarvesh56@gmail.com

A. Konkani et al. (eds.), *Advances in Systems, Control and Automation*,
Lecture Notes in Electrical Engineering 442, https://doi.org/10.1007/978-981-10-4762-6_49

coordinate transformations, current regulators, and voltage modulation circuit [2, 3]. However, conventional direct torque control (CDTC) suffers from major disadvantages such as (a) high flux and torque ripples predominantly during starting and at low-speed operation [4–6], (b) variable switching frequency due to hysteresis bands and variable motor speed [4–6], and (c) current and torque distortion when sector changes [6]. In order to overcome the disadvantages, several techniques are developed by researchers such as direct self-control, DTC with SVM, and DTC-SVM with neuro-fuzzy logic controllers as given in [7]. In recent years, researchers employed the use of artificial intelligent (AI) techniques such as fuzzy logic, neural networks, and neuro-fuzzy for direct torque control. The execution of the CDTC switching table with fuzzy logic is given in [8, 9] which results in the reduction of torque and flux ripples to some extent. The torque ripple reduction using a simple duty ratio controller is first proposed in [10]. The duty ratio algorithm proposed by [11] demonstrates that active voltage vector is applied for only the part of a sampling period, while the zero voltage vector is applied for the remaining time period results in the torque ripple reduction. In this paper, CDTC first improved using fuzzy logic-based switching controller called fuzzy DTC (FDTC). As explained in the [12], speed sensor elimination was important in the industry. The sensorless control results in lower cost and reduced hardware complexity. The CDTC is first improved by a fuzzy logic switching controller (FLSC) which used 180 fuzzy rule base. In this paper, optimal duty ratio using ANN is implemented. The performance of FDTC with neural network-based duty ratio (NNDRC) controller is assessed using MATLAB/Simulink simulation results. Simulation results indicate that there are considerable improvements in both dynamic and steady-state responses of an induction motor using FDTC with NNDRC when compared to CDTC.

2 Conventional Direct Torque Control (CDTC)

In CDTC, the torque and flux are controlled by the selection of the optimal switching vector of inverter based on torque, flux errors, and stator flux angle [1, 3]. The selection of inverter switching vector is done using a classical switching table, such that flux and torque are bound within the hysteresis limits, thereby enabling the fast transient response of the drive. The challenges in DTC are the estimation of the torque and flux parameters and development of an optimal switching table. The induction motor is fed by voltage source inverter (VSI). Motor stator currents (i_a, i_b) and rotor flux angle are feedback to current-based model reference adaptive system estimator [12], which estimates torque and speed of the induction motor. The speed error is given to the discrete PI controller of $K_P = 2$, $K_I = 300$. The PI controller output is limited using saturator $T_e^* = \pm 8$ Nm. The estimated torque (T_e) compared with its reference value (T_e^*) generates a torque error (e_T) which is processed through three-level hysteresis comparator so as to limit the torque error. The reference flux of the motor is estimated based on motor parameters given by:

$$\varphi_s^* = \sqrt{\frac{4L_s^2 L_r}{3pL_m^2}} \tag{1}$$

The estimated flux compared with reference flux generates flux error (e_φ) which is processed through two-level hysteresis comparator. Depending on the stator flux angle, the stator flux plane is divided into six sectors. If the stator flux angle lies between −30° and +30° is sector 1, +30° to +90° is sector 2 and so on. The hysteresis comparator outputs 'e_T', 'e_φ' and sector ($S(n)$) are given to a switching table, which selects the optimal switching state S_a, S_b, S_c of voltage source inverter. The optimal switching vector is selected based on present sector, flux error, and torque error [13].

3 DTC Using Fuzzy Logic Switching Controller (FDTC)

The major reasons for high torque and flux ripples are fixed magnitude hysteresis bands and application of switching vector for the complete sample time period. Fuzzy logic supports the variable membership function which aids in selecting optimal switching vector. Using fuzzy logic torque error (e_T), flux error (e_φ) and stator flux space (θ) are divided into multiple subsections which enable the precise and optimal selection of the switching vector The torque hysteresis band, flux hysteresis band, and switching table are replaced by FLSC as depicted in Fig. 1.

Fuzzy logic is an excellent tool to implement switching table. The optimal voltage vector is selected using the rule base developed by an expert having knowledge about process or plant. The expert's intelligence is included using a set

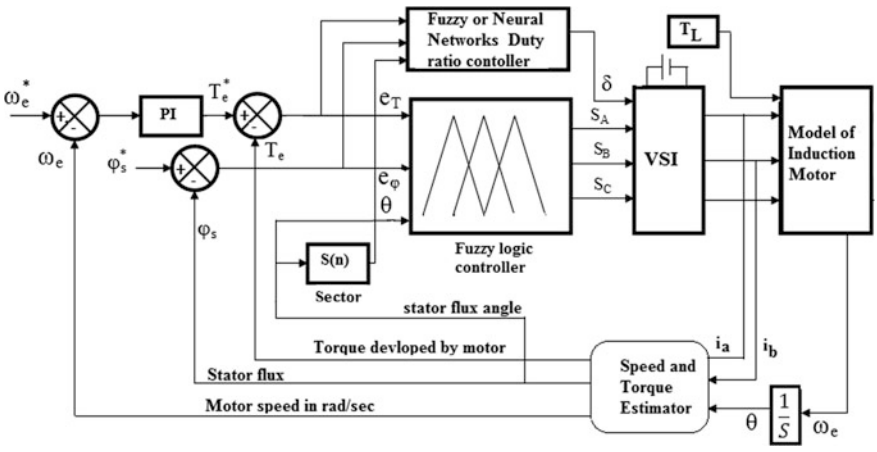

Fig. 1 Block diagram of DTFC with NFDRC

of fuzzy rules. Fuzzy logic variable are assigned to membership values which lies in between 0 and 1. FLSC has 3 input's flux error ($\varphi_s^* - \varphi_s$), torque error ($T_e^* - T_e$), stator flux angle (θ_s), and one output switching state (n) [4, 14]. 3 inputs cannot be applied to FLSC directly; they are fuzzified before applying to the fuzzy rule base. In fuzzification process, the inputs are fuzzified using fuzzy membership functions.

The mapping of inputs and output depends on a rule base. The fuzzy rule is developed based on expert knowledge and intuition in order to meet the objective of controlling. Since there are three MFs for e_φ, five MFs for e_T, and twelve MF s for θ signals, $3 \times 5 \times 12 = 180$ fuzzy rules are developed to select one of seven MFs for the output [9, 15]. The rule base proposed in [4] is employed. For example, *Rule: If e_T is PL, e_φ is P, and θ is θ_1, then the output is V_1.* The fuzzified output is developed using 'Min-Max' fuzzy inference method [4]. The aggregation gives a range of output in fuzzified form, which is converted into crisp value using defuzzification. Out of available methods of defuzzification, the mean of maximum (MoM) method is employed. The output of FLSC determines the switching vector V_n (n = 0–6) that needs to be applied to VSI so the output is converted in S_A, S_B, and S_C switching signals using the Boolean expression.

4 Duty Ratio Controller Using Neural Network (NNDRC)

In most of the literature, duty ratio controller is applied to CDTC for torque ripple reduction. The basic idea of duty ratio control is the selected active switching state of VSI that is applied for just enough time that the motor torque and flux reach their reference values. Once T_e reaches T_{ref}, a zero switching state is applied for the remaining switching time period ($1 - \delta$). The NNDRC determines a time duration for which active voltage is applied. The selection of an optimal duty ratio is a nonlinear function of torque error, reference flux, and flux angle in the particular sector [13]. A nonlinear function which gives optimal duty ratio for every switching cycle is difficult to implement using conventional methods.

The NNRDC is implemented using feed-forward neural network with one hidden layer that is trained for the evaluation of an optimal duty ratio. The neural network is developed using neural network toolbox in 'MATLAB.' The NNDRC has three inputs: torque error, reference flux, and stator flux angle and one output duty ratio. 80,000 samples of inputs and output are collected to develop the neural net. Using '*nftool*' command, the neural network fitting tool is generated. Inputs and targets are imported from a file stored in Mat file.

The feed-forward, backpropagation neural network with a hidden layer of 20 neurons with '*Tansig*' (sigmoid transfer function) is selected, and an output layer of one neuron with '*Purelin*' (linear transfer function) is selected as shown in Fig. 2. The neural networks are trained using Levenburg–Marquardt algorithm by setting validation and testing as 15%. ANN learns by adaptation of weights in order to reach the target of mean square error equal to zero. The best validation at 1000

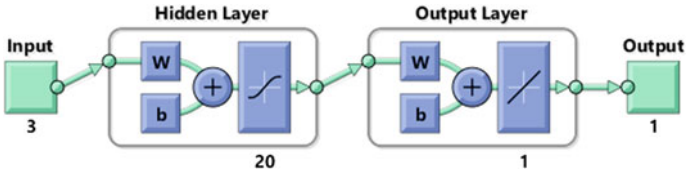

Fig. 2 Neural network-based duty ratio controller architecture

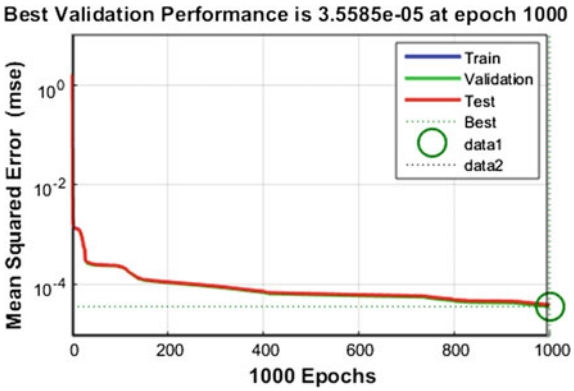

Fig. 3 Training performance of NN DRC

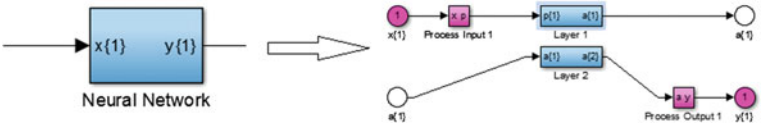

Fig. 4 Simulink model of neural network-based DRC

epoch is shown in Fig. 3. Once the training is finished, the neural network Simulink block is generated using '*gensim*' as shown in Fig. 4 which is placed in the Simulink model of FDTC with NNDRC. The trained neural network will select the optimal duty, and the selected optimal duty ratio (δ) is applied to switching vector of VSI.

5 Simulation Results and Discussions

To evaluate the performance of FDTC with NNDRC in the improvement of the dynamic and steady-state responses of drive, respective 'Simulink' models are simulated using MATLAB software. To measure dynamic and the steady-state

performances of the drive, induction motor is initially subjected to a reference speed of 50 rad/s and subjected to a sudden change from 50 to 100 rad/s at $t = 0.4$ s. In order to test the effectiveness of a feedback loop and robustness of the drive initially, the motor load torque is 0 Nm and subjected to a sudden load of 4 Nm at $t = 0.2$ s. All simulations are performed for a sampling time of 1/10,000 s, i.e., equivalent to the sampling frequency of 10 kHz.

Figure 5 shows the speed response, torque response, flux response, and stator current's response of CDTC of the induction motor. During starting, the motor is able to reach a reference speed of 50 rad/s in $t = 0.05$ s, but the speed response contains peak overshoot of 9% and few oscillations. At $t = 0.5$ s, it is subject to step change with $\omega_{ref} = 100$ rad/s. The drive is able to track the speed of 100 rad/s with load torque of 4 Nm, but the speed response contains an overshoot of 2.5% and oscillations as shown in Fig. 5.

The motor torque contains ripples and peak overshoot of 6 Nm when subjected to a step change of 4 Nm. During steady state, torque response contains ripples of 4 ± 1.2 Nm. The flux response contains the ripples 0.924 ± 0.076 Wb. As shown

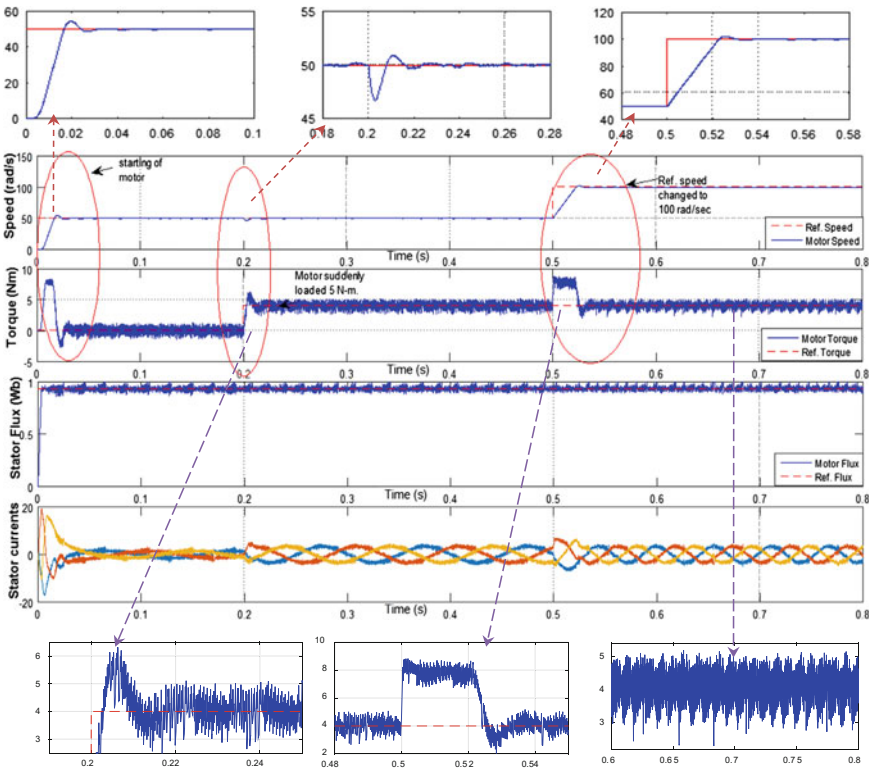

Fig. 5 Speed, torque, stator flux, and stator current's response of CDTC

in the figure, the stator currents are not purely sinusoidal and contain ripples during transient and steady state.

Figure 6 shows the speed response, torque response, flux response, and stator current's response of FDTC with NNDRC (neural network-based duty ratio controller) of an induction motor. During starting, motor is able to reach a reference speed of 50 rad/s in $t = 0.07$ s, but the speed response had a zero peak overshoot and reaches a steady state of 50 rad/s without any oscillations. At $t = 0.5$ s, it is subject to step change with $\omega_{ref} = 100$ rad/s. The drive is able to track the speed of 100 rad/s with a load torque of 4 Nm. The speed response does not contain peak overshoot and oscillations as shown in Fig. 6. The motor torque overshoot is reduced to 4.4 Nm when subjected to a step change of 4 Nm. During steady state,

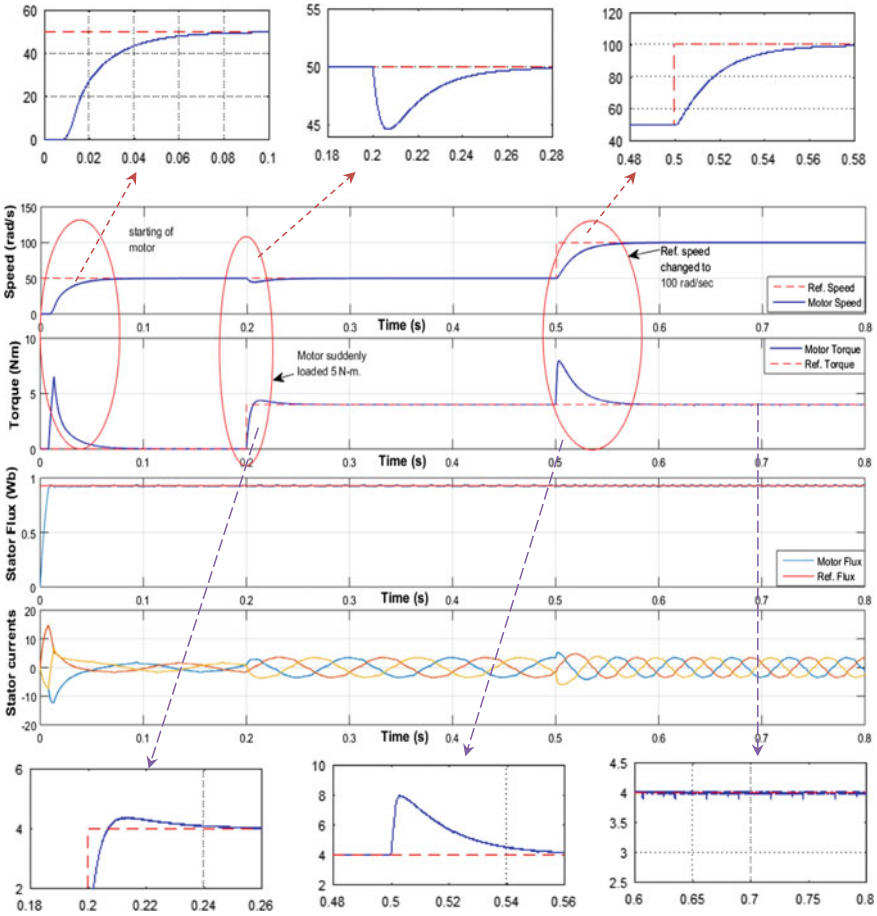

Fig. 6 Speed, torque, stator flux, and stator current's response of FDTC with NNDRC

torque ripples are reduced from 4 ± 1.2 Nm in CDTC to 4 ± 0.01 Nm. The flux response shows that smooth flux response, and ripples are reduced to 0.924 ± 0.016 Wb, as shown in Fig. 6. The stator currents are pure sinusoidal, contain very fewer ripples during transient and steady state compared to CDTC.

6 Summary/Conclusion

This paper proposes the use of fuzzy logic switching controller along with neural network-based duty ratio controllers for improvements in sensorless direct torque control of induction motor. The fuzzy logic switching controller selects an optimal switching state to meet the torque demand and reference speed of induction motor. In FDTC with NNDRC, active switching state is applied for a time determined by optimal duty ratio (δ) developed by duty ratio controller for each sampling period, and for the remaining time ($1 - \delta$), a zero switching state is applied. Simulation results show that using FDTC with NNDRC, the torque and flux ripples are reduced to 99 and 86.84%. Dynamic and steady-state response of the induction motor is improved using proposed schemes.

References

1. Takahashi, T.N.: A new quick-response and high-efficiency control strategy of an induction motor. IEEE Trans. Ind. Appl. **22**(5), 820–827 (1986)
2. Takahashi, I., Ohmori, Y.: High-performance direct torque control of an induction motor. IEEE Trans. Ind. Appl. **25**(2), 257–264 (1989)
3. Kazmierkowski, M.P., Kasprowicz, A.B.: Improved direct torque and flux vector control of PWM inverter-fed induction motor drives. IEEE Trans. Ind. Electron. **42**(4), 344–350 (1995)
4. Sudheer, H., Sarvesh, B., Kodad, S.F.: Improved fuzzy logic based DTC of induction machine for a wide range of speed control using AI based controllers. J. Electr. Syst. **12**(2), 301–314 (2016)
5. Kang, J.-K., Sul, S.-K.: New direct torque control of induction motor for minimum torque ripple and constant switching frequency. IEEE Trans. Ind. Appl. **35**(5), 1076–1082 (1999)
6. Grabowski, P.Z., Kazmierkowski, M.P., Bose, B.K., Blaabjerg, F.: A simple direct-torque neuro-fuzzy control of PWM-inverter-fed induction motor drive. IEEE Trans. Ind. Electron. **47**(4), 863–870 (2000)
7. Buja, G.S., Kazmierkowski, M.P.: Direct torque control of PWM inverter-fed AC motors—a survey. IEEE Trans. Ind. Electron. **51**(4), 744–757 (2004)
8. Zhang, Y., Zhu, J., Zhao, Z., Xu, W., Dorrell, D.G.: An improved direct torque control for three-level inverter-fed induction motor sensorless drive. IEEE Trans. Power Electron. **27**(3), 1502–1513 (2012)
9. Gdaim, S., Mtibaa, A., Mimouni, M.F.: Design and experimental implementation of DTC of an induction machine based on fuzzy logic control on FPGA. IEEE Trans. Fuzzy Syst. **23**(3), 644–655 (2015)
10. Telford, D., Dunnigan, M.W., Williams, B.W.: A novel torque-ripple reduction strategy for direct torque control [of induction motor]. IEEE Trans. Ind. Electron. **48**(4), 867–870 (2001)

11. Zhu, P., Kan, Y., Chen, J.: Improve direct torque control performance of induction motor with duty ratio modulation. In: Proceedings of IEMDC'03, vol. 2, pp. 994–998 (2003)
12. Vonkomer, J., Zalman, M.: Induction motor sensorless vector control for very wide speed range of operation. In: 12th International Carpathian Control Conference (ICCC), Velke Karlovice, pp. 437–442 (2011)
13. Sudheer, H., Kodad, S.F., Sarvesh, B.: Optimal duty ratio controller for improved DTFC of induction motor using fuzzy logic. In: SCEECS, Bhopal, India, pp. 1–6 (2016)
14. Toufouti, R., Meziane, S., Benalla, H.: Direct torque control strategy of induction motors. Acta Electrotechnica et Informatica. **1**(7), 1–7 (2007)
15. Kuric, I., Zalman, M.: Direct Torque and flux control of Induction machine and fuzzy controller. J. Electr. Eng. **56**(9–10), 278–280 (2005)

Design and Simulation of a Single-Output Multichannel Charger for Lithium-Ion Batteries

Vipin Valsan and Agidi Oghenemaro Emmanuel

Abstract Recently, the usage of portable electronic gadgets such as laptops and mobile devices has grown massively. These developments have led to an alarming increase in demand for rechargeable batteries. Benefits of lithium-ion batteries include but are not limited to high operating voltage, high energy density and low maintenance because it has no memory making it the most widely used rechargeable battery in today's electronic industry [1]. With Li-ion batteries being in such high demand, numerous researches have been conducted to develop a suitable charging system for them. In recent times, majority of these researches have been focused on charging the lithium-ion battery for automobile application. In this paper, a single-output charger for charging lithium-ion batteries of different specification is presented and simulated. A TTC dynamic model of Li-ion battery is modeled in MATLAB/Simulink. A DC–DC buck converter is designed and a PI controller is integrated into the system for stabilizing the output. The novelty of the proposed system is that it can be used to charge multiple devices sequentially. From the experimental results obtained, the proposed charging system has the ability of charging Li-ion batteries of laptops and mobile phones with a current ripple of less than 1%.

Keywords Lithium-ion · Buck converter · Charger · Simulink · Battery

V. Valsan (✉)
Department of Electrical and Electronics, Manipal Institute of Technology, Manipal University, Manipal, India
e-mail: vipin.valsan@manipal.edu

A.O. Emmanuel
Department of Electrical and Electronics Engineering, University of Benin, Benin City, Edo State, Nigeria
e-mail: agidioghenemarho@yahoo.com

A. Konkani et al. (eds.), *Advances in Systems, Control and Automation*,
Lecture Notes in Electrical Engineering 442, https://doi.org/10.1007/978-981-10-4762-6_50

1 Introduction

In recent years, the number of portable electronic gadgets such as tablets, mobile phones, and laptops has increased tremendously. This development has resulted in an increase in demand for portable batteries. Rechargeable batteries are often preferred in these devices because in the long run they represent a more cost-effective solution. Today, secondary batteries such as NiCd and NiMH are inadequate in satisfying consumer's requirements as a result of their generally bulky size and low energy capacity [2]. In contrast, advantages such as low maintenance, no memory effect, portability, and high energy density have made lithium-ion battery the prominent battery for portable electronic systems.

With the demand of rechargeable batteries constantly on the rise in the consumer market comes the complimentary increase in the demand for chargers to keep these batteries in constant operation. The performance and life span of Li-ion batteries largely depends on the quality of their chargers. Conventionally, the charging of lithium-ion batteries occurs in two stages: Firstly, constant current (CC) is applied to charge the battery until the battery voltage reaches the predetermined upper voltage limit. This constant current stage is followed by a constant voltage charging stage until the battery current attains a predefined value. This approach is referred to as the constant current–constant voltage (CC-CV) charging method, and it is often employed in commercial battery charging ICs [1], but this method is mostly applied to charge batteries of specific ratings. Similarly, various lithium-ion battery chargers have been developed for charging multiple cell [2], but again the drawback of this design as with majority of available multi output designs is that it can only be used for a specific voltage rating.

In this paper, a single-output charger for charging lithium-ion batteries of different specification is presented and simulated. The proposed charger system comprised of a bridge rectifier, capacitor filter, a DC–DC buck converter, a PI controller, and a switching circuit at the output.

Also, in this paper a dynamic model of lithium-ion battery is established using TTC equivalent circuit model in MATLAB/Simulink. The parameters of the dynamic model are obtained from experimental results. These parameters are varied with current and state of charge (SOC), thus allowing various circuit designs to be made using the parameters of the battery. These battery models are capable of predicting current–voltage (I–V) performance and predicting the runtime of the battery [3].

This paper is arranged as follows: Sect. 2 explains the charger system; Sect. 3 describes the Li-ion battery; Sect. 4 provides some experimental test results of the charger and the Li-ion battery; Sect. 5 presents results of the charger combined with the battery; Sect. 6 describes Discussion and Conclusion.

2 Charger System

2.1 Architecture/Hardware Configuration/Charger Overview

The general overview of the charger is shown in Fig. 1. The rectifier (bridge) is used to convert alternating voltage signal from the supply source to pulsating DC voltage, and the filter circuit (capacitor) is used to smoothen the DC output. The output of the filter is fed to the input of the buck converter which depends on the switching circuit provides output voltage and current for charging the batteries.

A PWM signal is used to switch the buck converter (MOSFET) for a specified duty cycle. The output voltage is controlled by a proportional integral (PI) controller. The entire charger system design can be divided into three major sections: buck converter, controller, and the switching circuit. The rectifier section is a bridge rectifier and capacitor, and its operation is as basic as any rectification process in power electronics.

2.2 Buck Converter

Of all available DC–DC converters available, the buck converter is the simplest form that can reduce DC voltage without the application of a transformer. The conventional buck converter is shown in Fig. 2 [4].

For this paper, the ideal switch shown in the conventional buck converter is replaced by a MOSFET. The buck converter operates by switching the MOSFET between ON and OFF states at high frequency. A pulse width modulation (PWM) signal controls the duty cycle of the MOSFET to regulate buck converter's output. At the beginning of each switching cycle, the gate signals turn the MOSFET

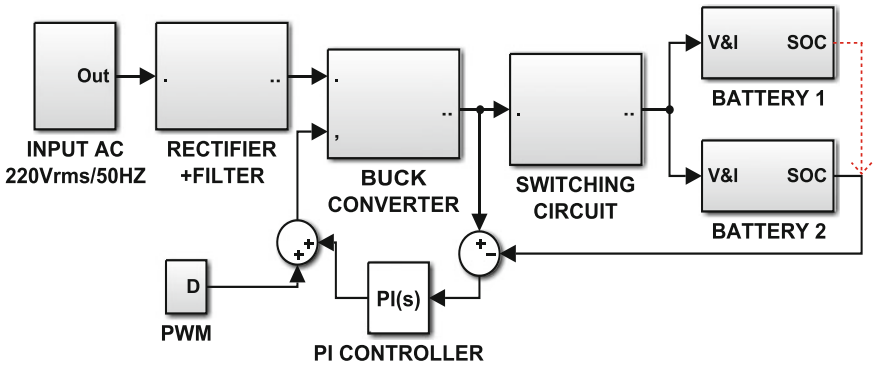

Fig. 1 General overview of the dual charger

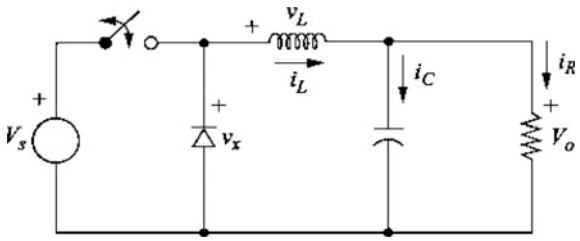

Fig. 2 Conventional buck converter

on and reverse bias the diode; therefore, the potential difference between input and output of the converter is applied across the inductor which results in a linear increase in inductor current. When the MOSFET turns off, the voltage across the inductor becomes negative and the inductor current decreases linearly. The energy stored in the inductor is transferred to the load. The relationship between the output voltage and the input voltage is given as

$$V_{\text{out}} = V_{\text{in}} * D \tag{1}$$

where duty cycle D is $\frac{t_{\text{on}}}{T}$.

t_{on} is the period for which the MOSFET is on, and T is the total period of the MOSFET.

2.2.1 Component Selection

Given the current ripple requirement, the value of the required inductor can be obtained using Eq. (2).

$$L = \frac{V_{\text{o}}(1 - D)}{F_s * \Delta iL} \tag{2}$$

V_{o} is the output voltage; F_s is the frequency of one switching cycle; ΔiL is the peak-to-peak inductor current ripple given by the design specifications; and D is the duty cycle of the switch. Because both duty cycle and the output voltage are changing during charge operation, the output capacitor is used to filter out the inductor ripple current. If the capacitance is large enough, most of the ripple current will flow through the output capacitor. The value of the capacitor is given by (3).

$$C = \frac{I_{\text{ripple}}}{8 * F_s * \Delta V} \tag{3}$$

2.2.2 Transfer Function of Buck Converter

By applying KVL and Laplace transform to the buck converter circuit shown in the diagram, the small signal analysis open-loop transfer function of the ideal buck converter is given as

$$\frac{V_o}{D} = \frac{V_{in}R}{s^2 + s\left(\frac{1}{RC}\right) + \left(\frac{1}{LC}\right)} \tag{4}$$

where R is the load.

In practical applications, the capacitor and inductor both have internal resistance denoted as ESR and DCR, respectively. The presence of these affects the output ripple of the buck converter. The new transfer function taking ESR and DCR into consideration becomes

$$\frac{V_o}{D} = \frac{V_{in}(R_0 r_c Cs + R_0)}{s^2(r_c LC + R_0 LC) + s(L + r_c r_L C + r_L R_0 C + R_0 r_c C) + (r_L + R_0)} \tag{5}$$

R_0 = load resistance, r_c = ESR, r_L = DCR.

2.3 Controller Design

The PI controller is used in this circuit to eliminate forced oscillations and steady-state error. The conventional transfer function of a PI controller is derived in Fig. 3.

$$u(t) = K_p e(t) + \frac{K_p}{T_i}\int_t^0 e(t)\mathrm{d}t \tag{6}$$

$$\frac{U(s)}{E(s)} = K_p\left(1 + \frac{1}{T_i s}\right) \tag{7}$$

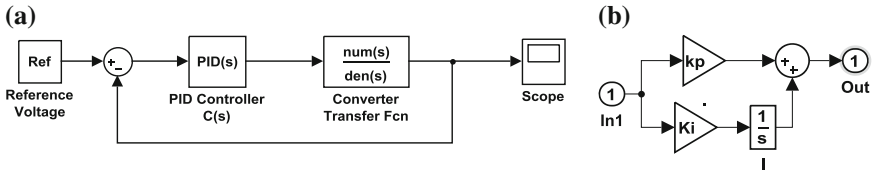

Fig. 3 **a** PI controller tuning, **b** Simulink representation of PI controller

$$\frac{V_{\text{out}}}{V_{\text{in}}} = K_p + \frac{K_i}{s} \tag{8}$$

T_i integral time

The values of K_i and K_p are obtained from MATLAB using the auto-tune PI function. With the transfer function known, the values of $R1$, $R2$, $C1$, $C2$, and R can be calculated for analogue circuit implementation.

Obtaining controller values/controller component selection,

P controller output in percent of full scale
E_p process error in percent of the maximum

$$K_p = \frac{R2}{R1} * \text{Proportional constant}$$
$$Ki = \frac{1}{R1C} * \text{integral constant}$$

Therefore, the analogue controller transfer function is given as

$$\frac{V_{\text{out}}}{V_{\text{in}}} = \frac{R2}{R1} + \frac{1}{R1C_s} \tag{9}$$

2.4 DPDT Switching Circuitry

Figure 4 is the DPDT switching circuit for a dual-lithium-battery charger designed in this paper. When the switch is in position 1, a particular voltage and current are being supplied to the load, and when the switch is in position 2, a different set of

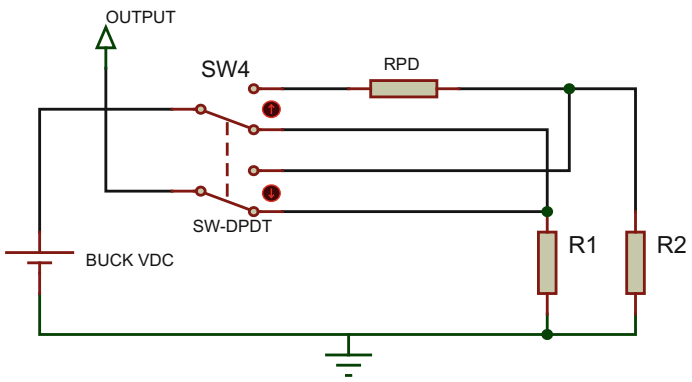

Fig. 4 Model DPDT switching circuit on Labcenter PROTEUS

voltage and current are now available at the output. To calculate the voltage drop resistance Rpd,

let the converter output be V_o,
larger voltage rating battery be $V_1 = V_o$, and
smaller voltage rating battery be V_2.
Then,

$$\text{Rpd} = \frac{V_o - \text{Rated Battery Voltage}}{\text{Rated battery current}} \tag{10}$$

3 Battery Modeling

To show the properties of the battery, an equivalent dynamic circuit model shown in Fig. 5 is proposed [3].

The model above comprises of a DC voltage source, two RC parallel networks, and a resistor in series. the DC source denoted as OCV is the open circuit voltage, the internal resistance of the DC source is represented by series resistance R_s, and the terminal voltage of the cell is represented by V_t while the two RC parallel networks ($R1$, $C1$; $R2$, $C2$) are used to depict the voltage transient response of the battery. The usable capacity of the battery is varied with different value of current in consideration of the rate capacity effect. The battery's state of charge (SOC) is determined from the value of the usable capacity of the battery. All parameters obtained from this model are dependent on the current and SOC of the battery [3].

Figure 6 shows the simulation model of the Li-ion battery in MATLAB/Simulink. The output of the model is the battery's terminal voltage which is a controlled voltage source. The five subsystems seen in the proposed model are employed to regulate the battery's terminal voltage: They include SOC calculation, OCV calc, RC values, voltages of RC parallel networks, and VRS. SOCo is the initial state of charge while SOC is the real-time state of charge.

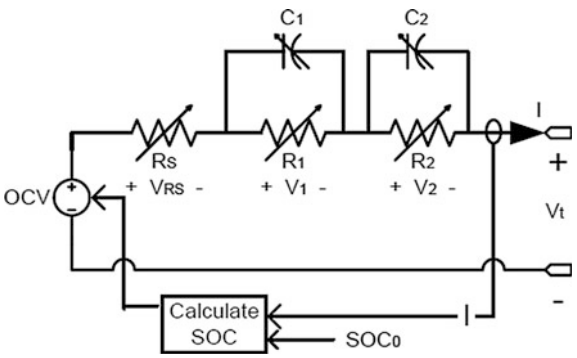

Fig. 5 Equivalent TTC circuit of lithium-ion cell

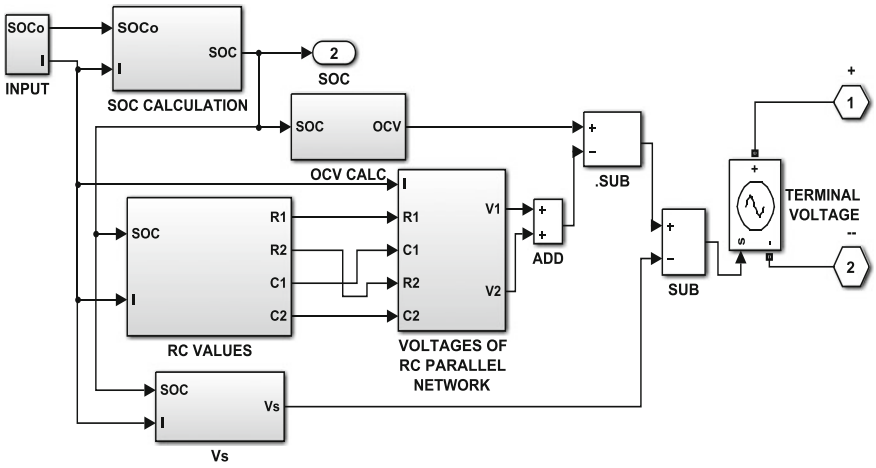

Fig. 6 Lithium-ion cell battery model in MATLAB/Simulink

4 Experimental Tests

As test for the proposed multichannel charger system, experiments were carried out on two lithium-ion batteries used in everyday electronic device.

Target Specification

1. Lenovo laptop battery with charging voltage of 20 V and current specification of 3250 mAh and
2. Nokia E63 battery with charging voltage of 3.7 V and current specification of 1500 mAh.

4.1 Battery Test

In this paper, two lithium-ion batteries of different voltage ratings (20 and 3.7 V) are modeled according to the mathematical expressions obtained. Battery system lookup tables were fed with respective battery parameter relationship that had been obtained. The continuous discharge test (CDT) in conjunction with the pulse discharge test (PDT) was carried out to obtain the parameters of the lookup tables (Fig. 7).

Here, the SOC decreases with time. This implies that the battery is discharging (Fig. 8).

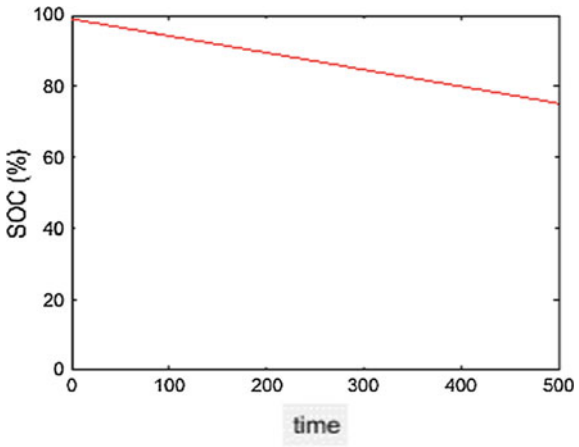

Fig. 7 SOC of laptop battery with respect to time

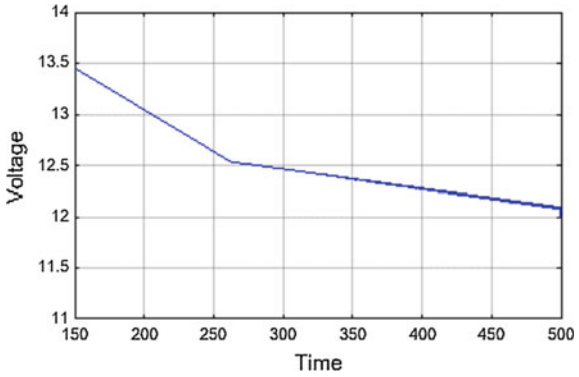

Fig. 8 Terminal voltage of battery with respect to time

Here, the V_t decreases as time increases. This implies that the battery is discharging.

4.2 Charger Tests

V_{out} = 323.6 V. A capacitor of 0.1 μF is chosen to filter out the ripples (Fig. 9).

4.3 Buck Converter

ESR of the capacitor is given as follows: $\frac{\Delta V}{\Delta iL} = 6.15$;

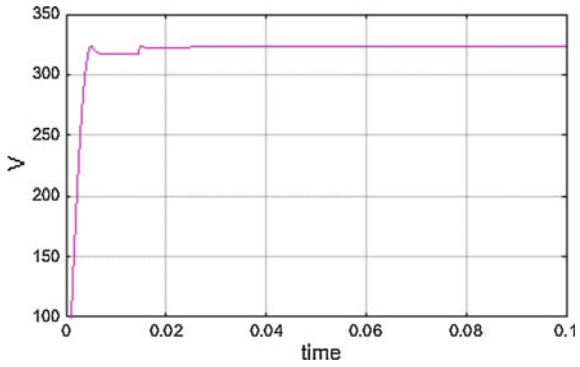

Fig. 9 Output of rectifier and filter section

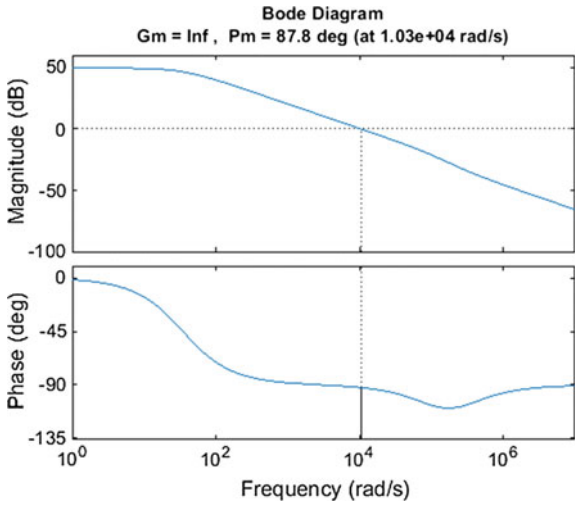

Fig. 10 The bode plot of non-ideal converter

DCR depends on the manufacturer, for this experiment, we assume the value of 0.5. The buck converter transfer function from Eq. (7) becomes

$$\frac{V_o}{D} = \frac{0.008164s + 1990}{1.575e - 6s^2 + 0.192s + 6.65} \tag{11}$$

From the Bode plot, it is shown that the system is stable with phase margin of 87.8° at a frequency of 10,300 rad/s (Fig. 10).

With MATLAB auto-tune features, controller values K_i and K_p are determined $K_p = 0.0015$; $K_i = 0.183$.

The controller transfer function is given as (Fig. 11)

$$C = 0.00155 + \frac{0.183}{s} \tag{12}$$

Integrating the PI controller with the buck converter produces a stable system with crossover frequency of 38.5 rad/s and phase margin of 60°.

5 Results and Discussion

See Figs. 12 and 13.

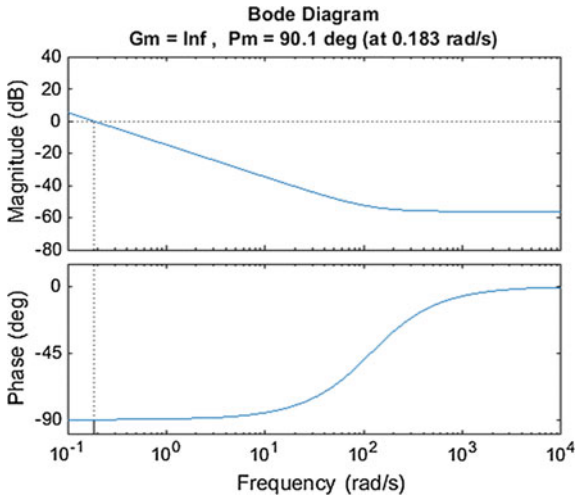

Fig. 11 The bode plot of final controller

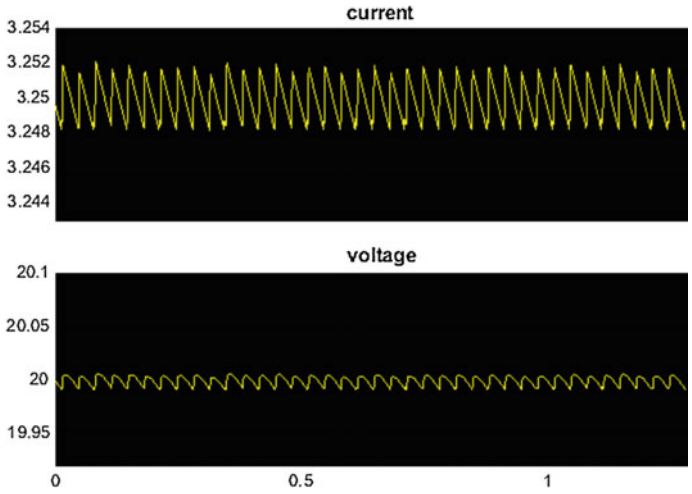

Fig. 12 The output of the entire system when connected to the laptop battery is shown in Fig. 12. It has a voltage range of 19.992 to 20.005 V (0.065%) and output current range of 3.248 to 3.252 A (0.12%)

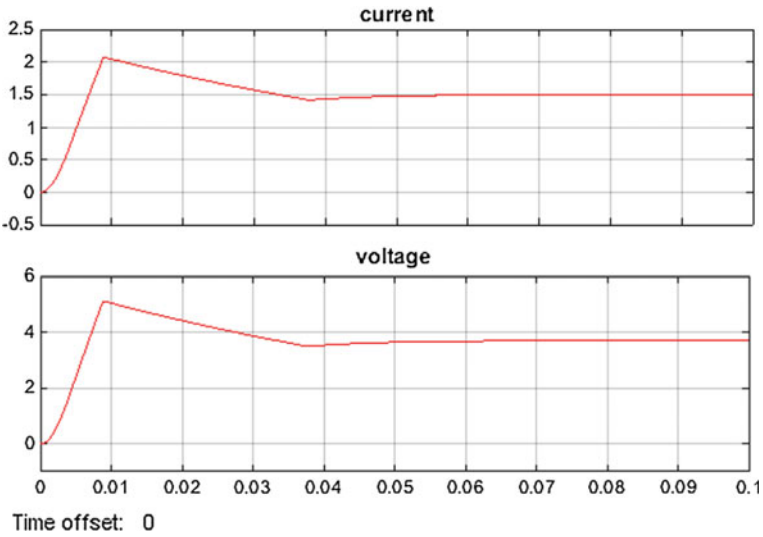

Fig. 13 Output voltage and current of the mobile phone when being charged voltage range of 3.6995–3.7001 V, current range of 1.499–5.001 A at steady state

6 Conclusion

In this paper, a single-output multichannel charger system for charging lithium-ion batteries was presented. To monitor the charging voltage and current, two lithium-ion batteries are modeled in MATLAB/Simulink. The proposed charger system operates in two modes for which it provides a specific constant current and voltage. The charger system presented above has advantages such as high efficiency, low output current and voltage ripple, simplicity, and when implemented portable.

In this paper, temperature effect and other hardware implementation constraints are not considered. These topics and other cost-effective designs will be provided in the future research.

References

1. Kaushal, N., Singh, C.P.: Design of FPGA based lithium-ion battery charger. Phil. Trans. Roy. Soc. London **A247**, 529–551 (1955)
2. Rahimi, A.M.: A Lithium Ion Battery Charger for Charging up to Eight Cells, 3rd edn, vol. 2, pp. 68–73. Oxford, Clarendon (1892)
3. Yao, L.W., Aziz, J.A., Kong, P.Y., Idris, N.R.N.: Modeling of lithium-ion battery using MATLAB/Simulink, In: IECON 2013–39th Annual Conference of the IEEE Industrial Electronics Society (2013)
4. Hart, D.W.: Power Electronics. McGraw-Hill (2011). ISBN: 0071289305

Design of Spectrum Sensing System

Riya Paul, Pamoli Nath and Soumyasree Bera

Abstract Current spectrum management is licensed in a definite frequency band, and since a large part of radio spectrum allocation is already done, vacant bands are not available to either effectively use new services or develop existing ones. As a solution to this, it is required to find means for improved spectrum utilization creating situations for access of dynamic spectrum. In these days, spectrum scarcity is a prime hurdle faced by all users. This problem gives rise to the idea of cognitive radio, where available channels for communication are detected and instantly moved into vacant channels. In this paper, matched filtering and energy detection methods are covered, where our motive is the all-time presence of spectrum to all users.

Keywords Cognitive radio · Energy detection · Spectrum sensing
Matched filtering · SNR

1 Introduction

The available electromagnetic radio spectrum is highly scarce. This issue is solved by the use of cognitive radio (CR) technology [1]. Cognitive radios [2] are designed to ensure a trustworthy communication for all network users. According to interaction with environment, cognitive radio can change its parameters in which it operates. Spectrum sensing, spectrum management, spectrum sharing, and spectrum mobility are its four major functional blocks. In spectrum sensing, the presence of

Riya Paul (✉) · Pamoli Nath · Soumyasree Bera
Sikkim Manipal Institute of Technology, Sikkim Manipal University,
Majitar, Sikkim, India
e-mail: paul.riya12@gmail.com

Pamoli Nath
e-mail: pamolinath@gmail.com

Soumyasree Bera
e-mail: soumyasree.bera@gmail.com

A. Konkani et al. (eds.), *Advances in Systems, Control and Automation*,
Lecture Notes in Electrical Engineering 442, https://doi.org/10.1007/978-981-10-4762-6_51

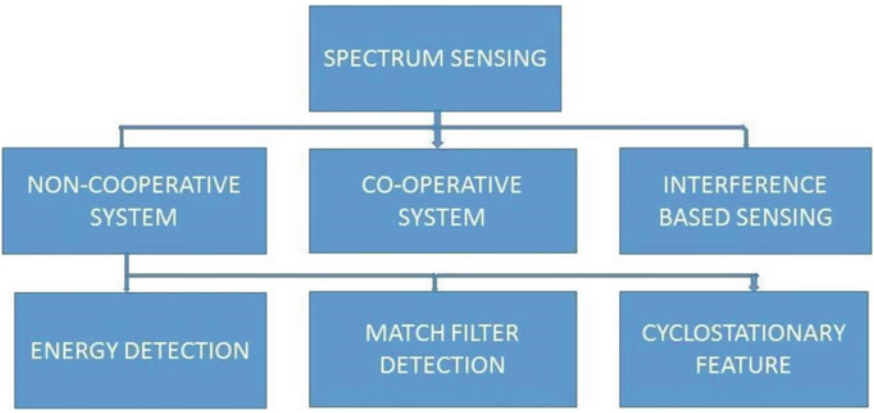

Fig. 1 Classification of spectrum sensing

spectrum and licensed user is determined. Spectrum management predicts the time of availability for use to the unlicensed users. Spectrum sharing distributes the spectrum holes among the secondary users taking care of the spectrum cost. Spectrum mobility maintains uninterrupted communication for a better spectrum [3].

Figure 1 shows the classification of spectrum sensing methods [4]. Among these, the non-cooperative system is studied in this paper. Three signal processing techniques are used for spectrum sensing [4] in the literature: matched filter, energy detection, and cyclostationary feature detection. Matched filtering, though optimal, needs full knowledge of primary signaling. But when nothing is assumed, an energy detector is used. In this paper, we have covered matched filtering technique and energy detection techniques.

2 Methodology

2.1 Energy Detection

Energy detection is the signal detection technique which uses an energy detector to state the absence or presence of signal in the band. It is an efficient approach to spectrum sensing since its computational technique is not that complex and can be implemented in both time domain and frequency domain [5]. Noise power knowledge in the band to be sensed is required by the energy detector to adjust the threshold of detection. Though not the best, energy detection is simple to implement, so it is widely used. The signal is detected as the energy detector output is compared with the threshold. It is suitable for wideband spectrum sensing. It works according to the following block diagram:

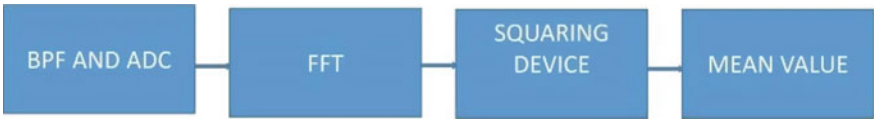

Fig. 2 Frequency-domain representation of energy detection

2.2 Match Filtering Process

A matched filter is a network in which the output peak-signal-to-noise (power) ratio of a radar receiver is maximized which again maximizes a target detectability. Here, the signal detection is first done using various codes, which are described later. Matched filter is a trusty detection technique but requires the primary user signal knowledge beforehand. The block diagram of matched filter is shown in Fig. 3.

3 Simulation Results

At first, the desired transmitted signal is generated and the noise is added to give the real time effect of channel during transmission. The same signal can also be treated as channel ouput which then becomes the received signal. The presence or absence of the transmitted signal is evaluated from this received signal. The received signal is then passed through the different sensing techniques following the methods shown in Figs. 2 and 3, respectively. For each case, a particular threshold level is set, and comparing the signal level with this level, it is concluded whether a spectrum is sensed or not. Further, the experiment is continued to find out the detection probability of each of the sensing techniques for different signal-to-noise ratios (SNR), so as to define up to which SNR, the system is able to detect the presence or absence of any spectrum.

3.1 Energy Detection Method

Energy detection method [6] is the simplest form of detection techniques, and the details of the method are already being discussed in the previous section (shown in Fig. 2).

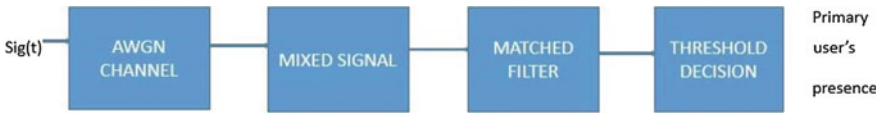

Fig. 3 Match filtering using spectrum sensing

In this method, at first, a simple sinusoidal signal is being generated and the same is being considered as the transmitted signal. The generated signal is shown in Fig. 4. Figure 5 shows the signal that is being fed to the sensing system at a particular SNR.

The performance of the designed energy detection technique is tested and verified in terms of two properties—(i) probability of detection (Pd) versus SNR and (ii) probability of false alarm (Pfa) versus SNR. At first, Pd versus SNR is plotted as shown in Fig. 6, which depicts that the system is able to detect the presence of spectrum when the SNR is positive. Therefore, the system will work in positive SNR, but it fails when the SNR is negative.

The next performance that is being tested is the Pfa versus SNR (in Fig. 7) which is just the reverse implication of probability of detection; i.e., at higher SNR, the chances of false detection is negligible, whereas at lower SNR, Pfa is very high.

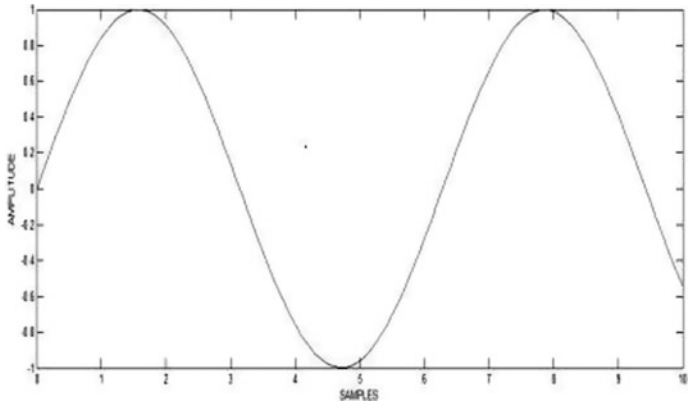

Fig. 4 Original transmitted signal

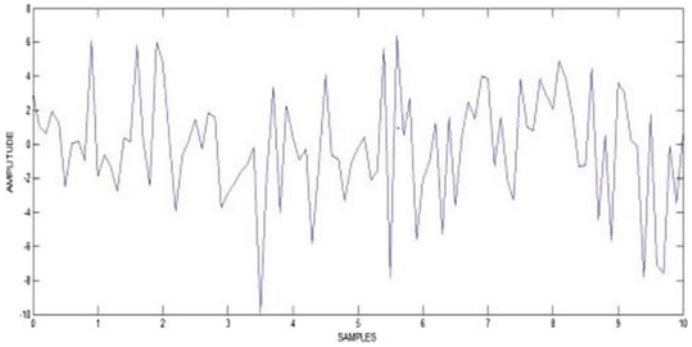

Fig. 5 Signal received by the sensing system

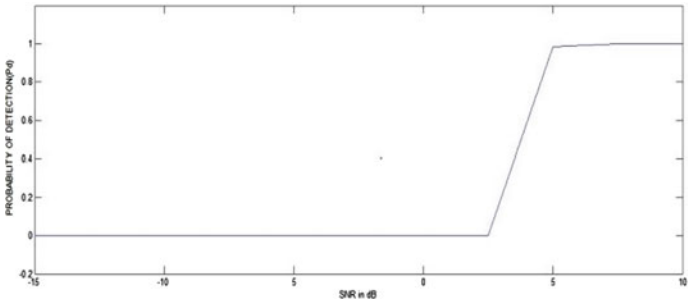

Fig. 6 Probability of detection versus SNR

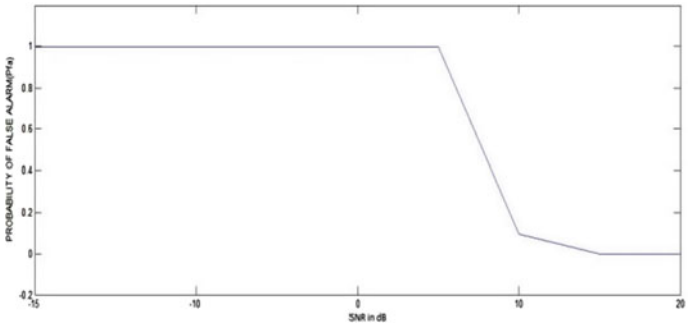

Fig. 7 SNR versus Pfa

3.2 Match Filtering Method

The second sensing technique that has been designed is match filtering [7] where the receiver is able to detect only the known type of spectrum and rejects the rest. Therefore, to create such waveform, coded signal is considered as the transmitted signal. At first, the various coded signals are designed and their correlation property is tested (such as barker code, P1 code, P2 code, P3 code, P4 code), and the code with best correlation property is selected as the transmitted signal, i.e., P4 code.

The autocorrelation of the generated transmitted signal (P4 coded) is shown in Fig. 8. After the generation, it is being polluted by adding noise to it so as to provide the channel effect (refer Fig. 9).

As discussed previously that the performance of the system is tested in terms of its Pd versus SNR and Pfa versus SNR, same is being implemented in this case as well.

Therefore, Figs. 10 and 11 depict the Pd versus SNR and Pfa versus SNR of the match filtering method.

But the constraint of this method is that it is able to detect only known type of signal unlike the energy detection technique [8].

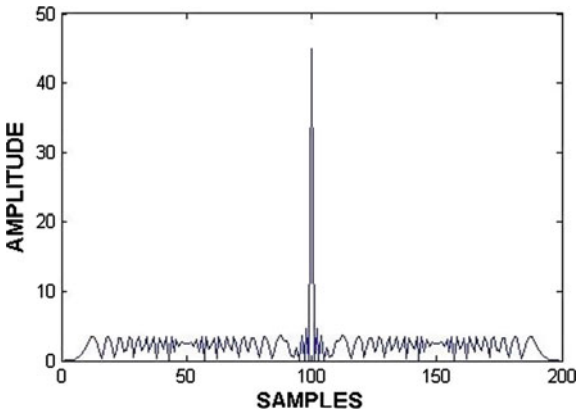

Fig. 8 Autocorrelation of transmitted P4

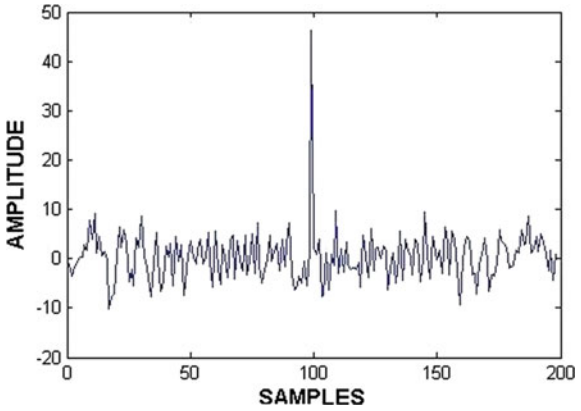

Fig. 9 Autocorrelation of transmitted P4 and noise

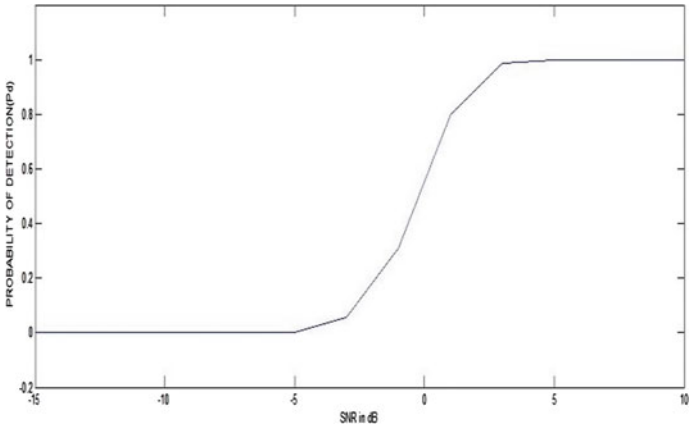

Fig. 10 Pd versus SNR of match filtering technique

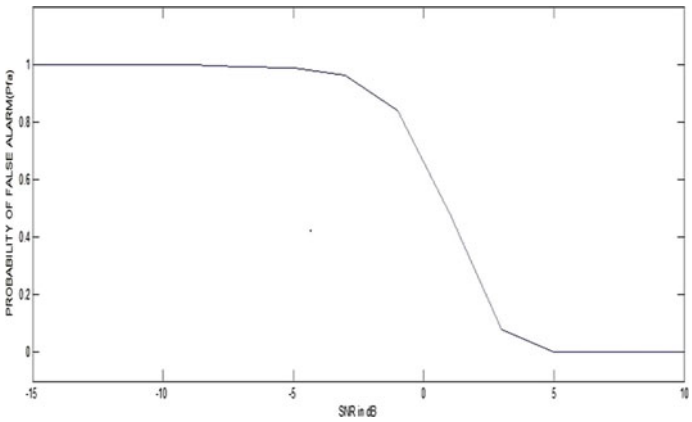

Fig. 11 Pfa versus SNR of match filtering technique

4 Conclusion

This paper presented a comparative study of all detection codes using matched filtering and energy detection techniques. As SNR goes beyond 5 dB, a good probability of detection of signal is found (from Fig. 6). Though we have used matched detection technique here, it is totally code-dependent, which makes cyclostationary process a better one. In the future, spectrum sensing analysis can be done using cyclostationary method also. Its hardware implementation can be done which will make the process more efficient.

References

1. Malik, S.A., Shah, M.A., Dar, A.H., Haq, A., Khan, A.U., Javed, T., Khan, S.A.: Comparative analysis of primary transmitter detection based spectrum sensing techniques in cognitive radio systems. Aust. J. Basic Appl. Sc. **4**(9), 4522–4531 (2010)
2. Cordeiro, C., Challapali, K., Birru, D., Shankar, N.S.: IEEE 802.22: the first worldwide wireless standard based on cognitive radios. In: Proceeding of IEEE DySPAN, pp. 328–37 (2005)
3. Stoianovici, V., Popescu, V., Murroni, M.: A Survey on Spectrum Sensing Techniques in Cognitive Radio-Bulletin of the Transilvania University of Brasov, vol. 50 (2008)
4. Huang, X., Han, N., Zheng, G., Sohn, S., Kim, J.: Weighted-collaborative spectrum sensing in cognitive radio. CHINACOM, pp. 110–114 (2007)
5. Abdulsattar, M.A., Hussein, Z.A.: Energy detection technique for spectrum Sensing In Cognitive Radio: a survey. Int. J. Comput. Netw. Commun. (IJCNC) **4**(5) (2012)

6. Subhedar, M., Birajdar, G.: Spectrum sensing techniques in cognitive radio networks: a survey. Int. J. Next Gener. (IJNGN) **3**(2) (2011)
7. Shobana, S., Saravanan, R., Muthaiah, R.: Matched filter based spectrum sensing on cognitive radio for OFDM WLANs. Int. J. Eng. Technol. (IJET) **5**(1) (2013)
8. Ganesan, G., Li, Y.: Cooperative spectrum sensing in cognitive radio, part I: two user networks, IEEE Trans. Wireless Commun. 2204–2213 (2007)

Modeling and Simulation of Switched Reluctance Motor

Jignesh A. Makwana, Pramod Agarwal and Satya P. Srivastava

Abstract This paper explores mathematical modeling techniques of switched reluctance motor. Several interesting techniques have been compared for different requirement. Embedded function has been developed in MATLAB to map the magnetic nonlinearity of the motor. A magnetic characteristic derived from the developed function is compared with the actual magnetic characteristics of the motor. Furthermore, methods to transpose 'Simulink' SRM model to 'simpowersystem' have been explored and compared.

Keywords Reluctance motor · Modeling · Simulation · Magnetic nonlinearity

1 Mathematical Model of SRM

Main objective of motor modeling is to derive a nonlinear function to relate the mechanical output (torque, speed) of the motor to the electrical input (voltage, current). In conventional motors, torque can be represented as a function of motor current or its component. As against it, motor torque is nonlinear function of phase current and angular position of rotor. The phase current is also a function of both flux-linkage and rotor angle.

Figure 1 represents simplified model of the SRM. It has only single source of magnetic field production, i.e., stator winding, and there is no winding on the rotor. Magnetic material (rotor) placed in between this magnetic field experience a force of attraction. Voltage balance equation for the phase can be written as (1) as applied phase voltage is equal to summation of the voltage drop across phase resistance and rate of change of flux-linkage. Flux-linkage Eq. (2) is derived using integration. Electrical characteristics of the SRM obtained from the Eqs. (1) and (2) are shown

J.A. Makwana (✉)
Electrical Engineering Department, Faculty of Engineering, MEFGI, Rajkot, India
e-mail: Jigneshmakwana326@gmail.com

P. Agarwal · S.P. Srivastava
Electrical Engineering Department, IIT Roorkee, Roorkee, Uttrakhand, India

A. Konkani et al. (eds.), *Advances in Systems, Control and Automation*,
Lecture Notes in Electrical Engineering 442, https://doi.org/10.1007/978-981-10-4762-6_52

in Fig. 2 where black box $i(\psi, \theta)$ represents three-dimensional nonlinear relation among phase current, flux-linkage, and rotor angle. In the simplified model, torque characteristic represents nonlinear relation among motor torque, phase current, and rotor angle. The dynamics of the mechanical system as represented by Eq. (3) is shown in Fig. 3. Therefore, to model the SRM, magnetic nonlinearity is the only challenging task.

$$V_a = i_a R_a + \frac{\mathrm{d}\psi_a}{\mathrm{d}t} \tag{1}$$

$$\psi_a(t) = \int_0^t (V_a - i_a R_a)\mathrm{d}t \tag{2}$$

$$T_e - T_L = J\frac{\mathrm{d}\omega}{\mathrm{d}t} + B\omega_m \tag{3}$$

Linear model of the SRM can be derived by neglecting the magnetic saturation and utilizing idealized inductance profile. Phase voltage equation of the SRM can

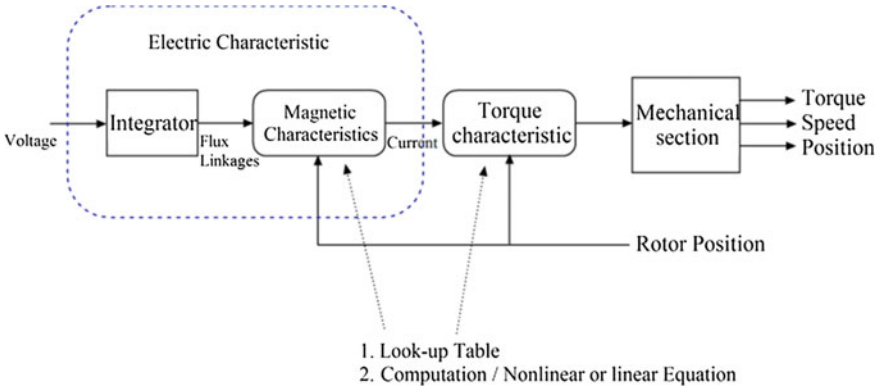

Fig. 1 Block diagram of SRM model

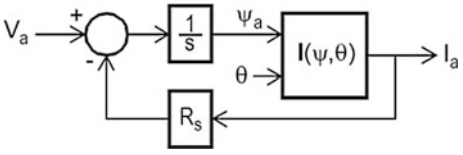

Fig. 2 Simulink model of electric characteristics of the SRM

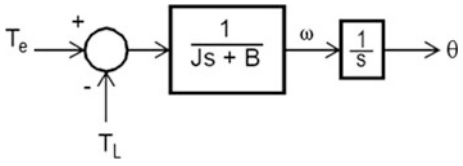

Fig. 3 Simulink model of basic mechanical loading

be represented as shown in Fig. 2 where the current $i(\psi, \theta)$ can be derived from the idealized inductance profile and phase flux $\psi = L(\theta) \cdot i$. The torque developed by the individual phases of the motor can be derived by simplified torque equation $T = \frac{i^2}{2}\frac{dL}{d\theta}$. The total instantaneous torque of the motor is given by the summation of the all phases. Linear model of the SRM is sufficient for the implementation of the controller; however, the nonlinear model is required for the realization of complete SRM drive and to investigate the dynamic behavior of the entire system.

Many practices have been in use to model the magnetic nonlinearity of the SRM; out of which, several methods are covered in the following sections.

1.1 Method-1: Look-Up Table-Based Approach

The look-up table-based approach [1–3] is very accurate method to represent the magnetic nonlinearity of the SRM. The model of SRM discussed here is designed in [1] for the electric vehicle propulsion, where the goal is optimal efficient operation of the drive. Magnetic characteristics of the SRM is shown in Fig. 4, which represents number of magnetic curves at the different rotor angle [1]. Look-up table is used to store the magnetic characteristics as a three-dimensional data. The flux-linkage calculated from the Eq. (2) and the rotor angle are used as an index to select the phase current. One more Look-up table is used to represent torque characteristics of the motor. The torque characteristic of the SRM is shown in the Fig. 5, which represents nonlinear relation among torque, phase current, and rotor

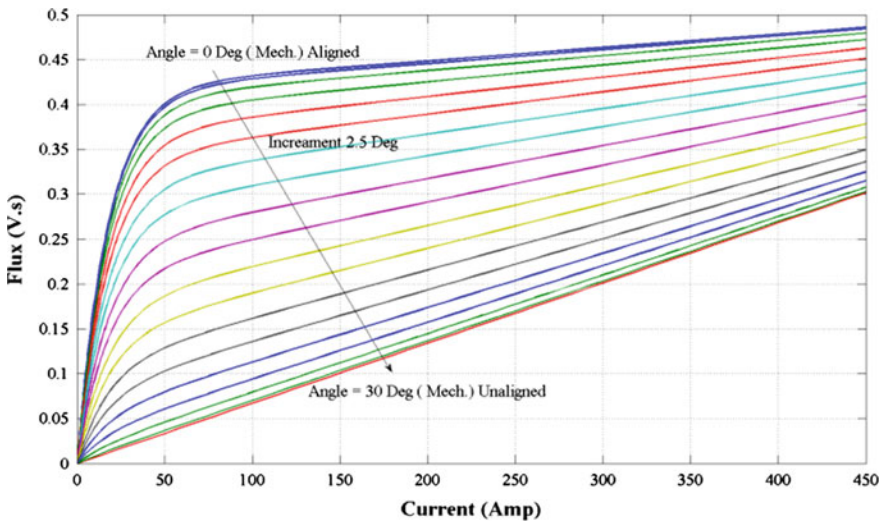

Fig. 4 Magnetic characteristics of SRM

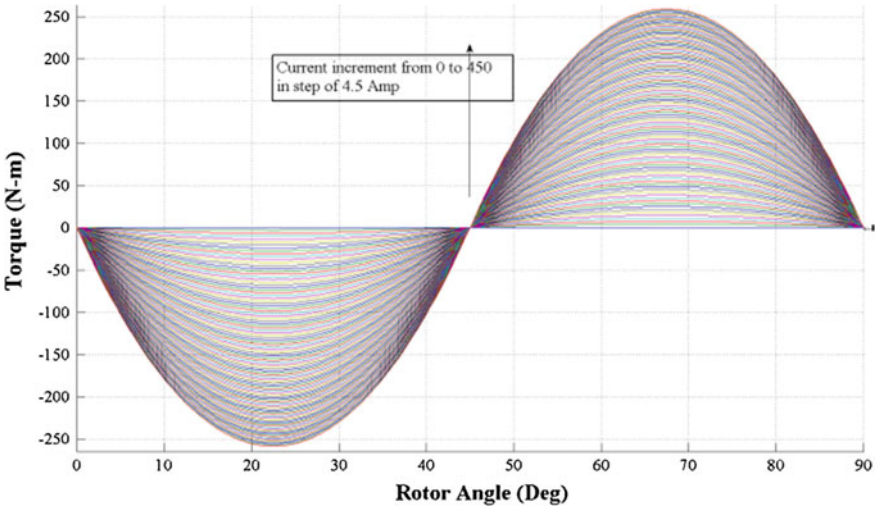

Fig. 5 Torque characteristics of SRM

angle. The look-up table-based approach to map nonlinear characteristics of the SRM reduces involvement of the dynamics equations and thus reduces the process time. This method is the most accurate method to model a physical SRM, if precise data of the magnetic as well as torque characteristics are available.

However, it requires a large amount of experimental workout to obtain the motor characteristics. The accuracy of the model depends on the experimental technique used to obtain the precise motor parameter as well as on the accuracy of the measuring instruments. This method is time consuming and costly but is an accurate modeling technique of the SRM. The experimental procedure required to obtain the motor magnetic characteristics is well explained in [3].

This method is suitable to model an existing SRM, where it is required to study the entire motor performance with high grade of accuracy along with the different types of converter and control techniques. PC-based design and FEA software packages such as PC-SRD and PC-FEA are available, which makes it possible to derive the magnetic parameters of the motor from the dimensional detail and winding parameters of the motor. It saves the time to model a SRM based on look-up table; however, it requires a skill to deal with an available software package.

1.2 Method 2: Analytical Modeling Technique

It is possible to develop a mathematical expression to represent the magnetic nonlinearity of the motor with the help of exponential or trigonometric functions. Many modeling techniques have been published in the literatures to map the magnetic nonlinearity in the form of mathematical equation, where the goal is to

determine number of unknown parameters from the motor parameters with calculations and analytical reasoning [4–7]. The piecewise analysis is covered in [7] to connect the fundamental geometry and turns per phase of the motor with an analytical terminal description.

$$\psi(i,\theta) = a_1(\theta)[1 - e^{[a_2(\theta)i]}] + a_3(\theta)i \tag{4}$$

Equation (4) summarizes the magnetic characteristics of the SRM over all the rotor position and current, where $a_1(\theta)$, $a_2(\theta)$, and $a_3(\theta)$ are the unknown coefficient needs to be determined. The derivative of flux represents an incremental inductance as a function of unknown coefficient as

$$l(i,\theta) = \frac{\partial\psi(i,\theta)}{\partial i} = -a_1(\theta)\cdot a_2(\theta)\cdot e^{[a_2(\theta)i]} + a_3(\theta) \tag{5}$$

Unsaturated phase inductance 'L' can be represented as a function of rotor angle as given below:

$$L(\theta) = -a_1(\theta)\cdot a_2(\theta) + a_3(\theta) \tag{6}$$

Equation (6) is simplified as,

$$a_2(\theta) = \frac{a_3(\theta) - L(\theta)}{a_1(\theta)} \tag{7}$$

It is required to determine three unknown coefficients $a_1(\theta)$, $a_3(\theta)$, and $L(\theta)$, which depend on rotor angle. The piecewise linear models assumed for the coefficients are shown in Fig. 6. The angle θ_a and θ_u refer to aligned and unaligned position of the rotor, respectively. The stator/rotor pole arc is fully covered by the rotor/stator pole arc, from the rotor angle θ_a to the angle θ_1, and just after θ_1 pole arcs start uncovering. The angle θ_2 represents a position, where both the pole arcs just become fully uncovered. The process of the determination involves determining all eleven parameters listed in Table 1. Seven parameters are found based on simple calculation, two are based on values from tables and two are found iteratively. Angular breakpoints are found directly from the motor design parameter. Inductive constant L_{max} is found from the equation, while determination of L_{corner} and L_{min} require dimensional detail of the rotor and stator pole, to find out the constant from the table [7]. The magnetization coefficient $a_1(\theta_a)$ and $a_3(\theta_a)$ are found iteratively. The values for $a_1(\theta_u)$ and $a_3(\theta_u)$ are then taken as constant fraction of $a_1(\theta_a)$ and L_{min}, respectively. Step-by-step procedure of finding each parameter is covered in [7].

If all the eleven parameters are known, then coefficients $a_3(\theta)$, $L(\theta)$, and $a_1(\theta)$ can be found from the simple equations. The MATLAB embedded function is designed to represent a nonlinear relation among flux-linkage, phase current, and rotor angle approaching analytical modeling technique. Flowchart of the embedded

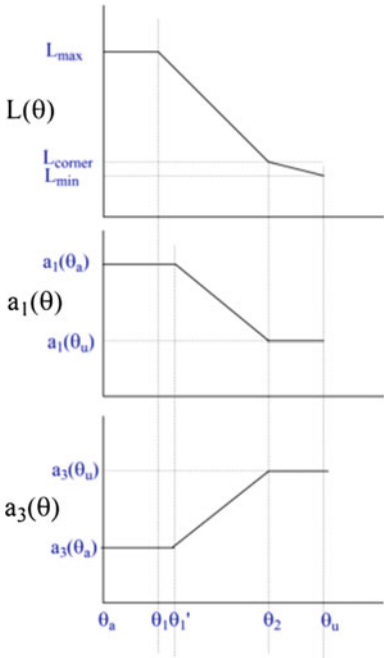

Fig. 6 Piecewise linear model assumed for unsaturated phase inductance, magnetization coefficient a_1 and a_3, as a function of rotor angle

Table 1 Eleven parameters needs to be determine

Magnetization coefficient	Inductive constant	Angular breakpoints
$a_1(\theta_a)$	L_{max}	θ_1
$a_3(\theta_a)$	L_{corner}	θ_1'
$a_1(\theta_u)$	L_{min}	θ_2
$a_3(\theta_u)$		θ_u

function design is shown in Fig. 7 where it is assumed that all the eleven parameters are known. The embedded function provides the value of the flux-linkage for the given phase current and rotor angle. The design parameters of the motor are listed in the Table 2. The magnetization coefficient, inductance constant, and angular breakpoints are derived from the design parameter of the SRM, as summarized in Table 2 design parameter of 60 kW SRM (Table 3).

The magnetic characteristics derived using embedded function is compared with the actual magnetic characteristics of method-1 in Fig. 8. The accuracy of the nonlinear function mapping is quite reasonable for the low phase current value. The phenomena of pole corner saturation and saturation of yoke reduce the accuracy of the mapping, at the higher current level. The details about motor geometry and winding turns are sufficient for the analytical modeling technique; however, several pre-calculations are required. This method reduces the time and cost of the modeling technique compared to method-1, where it was required to collect a large

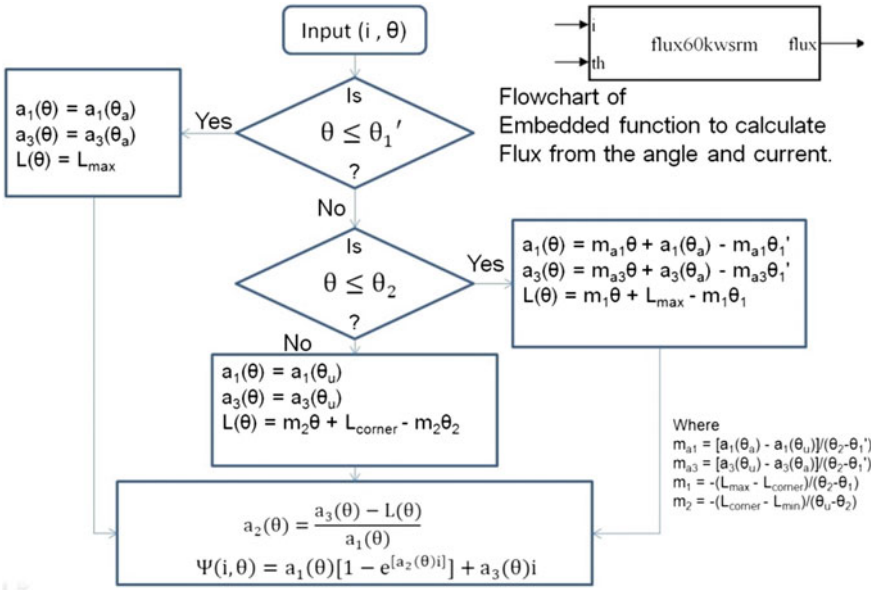

Fig. 7 Flowchart of the embedded function design to represent a magnetic nonlinearity

Table 2 Design parameter of 60 kW SRM

Motor parameters	Value
Shaft radius (R_{sft})	0.0143 m
Rotor back iron radius (R_{rbi})	0.034 m
Radius behind rotor pole (R_{rph})	0.041 m
Width of rotor pole base (W_{rpb})	0.032 m
Rotor radius at airgap (R_r)	0.055 m
Radial airgap (l_g)	0.0002 m
Stator radius at airgap (R_{sa})	0.0552 m
Radius at top of stator pole (R_{sbi})	0.082 m
Outside radius (R_o)	0.1 m
Active length (G)	0.3 m
Rotor pole arc (θ_r)	45°
Stator pole arc (θ_s)	32°
Number of rotor pole (N_r)	4
Turn per phase (N)	13

number of data from experimental setup. The method also eliminates requirement of experimental skill, which was needed in method-1. The analytical modeling method is suitable for the performance evaluation of the power electronics converter and different control techniques as well as to predict the performance of the motor.

Table 3 Eleven parameters of the three phase SRM

Magnetization coefficient	Inductive constant (mH)	Angular breakpoints (°)
$a_1(\theta_a)$ = 439.6 mWb	L_{max} = 23.68	θ_1 = 6.5
$a_3(\theta_a)$ = 177.7 μH	L_{corner} = 1.19	θ_1' = 12.83
$a_1(\theta_u)$ = 43.96 mWb	L_{min} = 0.67	θ_2 = 38.5
$a_3(\theta_u)$ = 636.5 μH		θ_u = 45

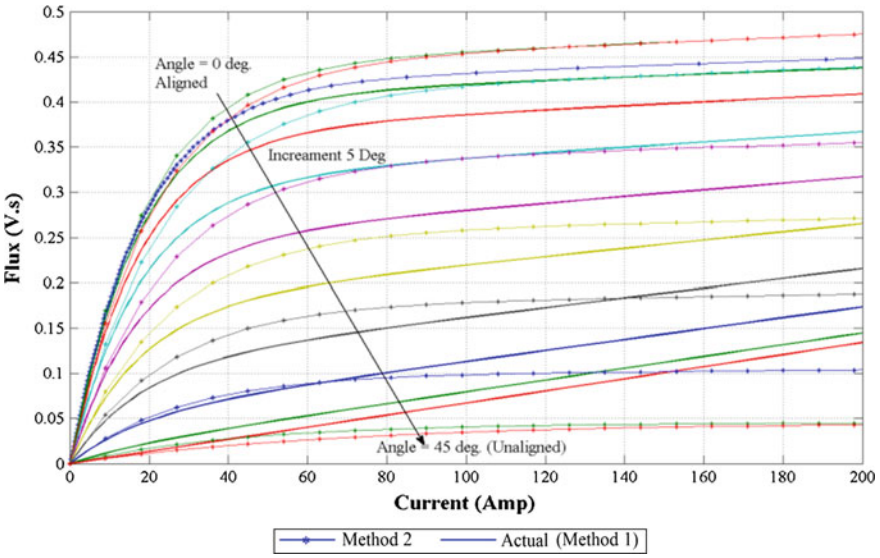

Fig. 8 Magnetic characteristics of the SRM represented by the MATLAB embedded function

The electromagnetic torque is a nonlinear function of the phase current and rotor angle, which is due to nonlinear magnetic characteristics of the motor. The torque produced by the phase of the SRM can be calculated as the derivative of the machine co-energy [1] as

$$Te(i,\theta) = \frac{\partial}{\partial\theta} W_c(i,\theta) \tag{8}$$

where 'W_c' is the co-energy. The co-energy can be obtained from the flux-linkage as

$$W_c = \int \psi(i,\theta) \cdot \mathrm{d}i \tag{9}$$

Figure 9 shows the torque characteristics of the SRM, calculated from the magnetic characteristics. The electromagnetic torque can be obtained using Eqs. (8) and (9).

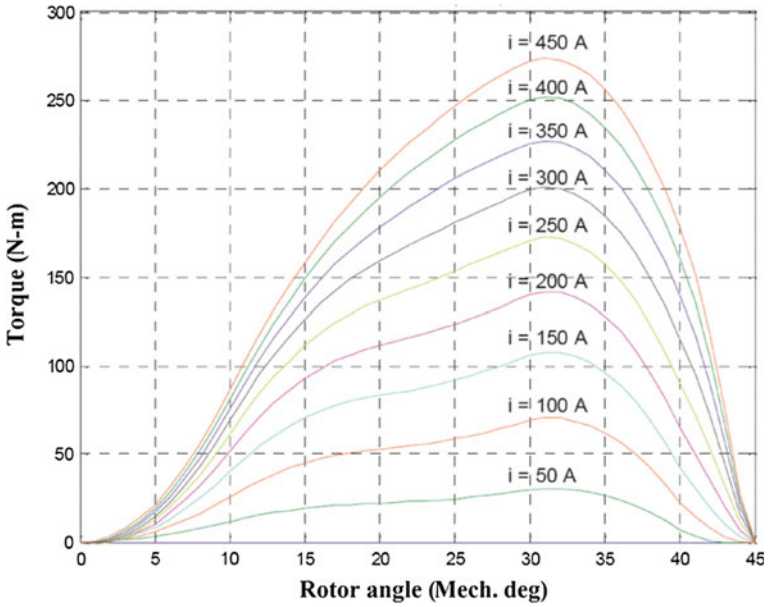

Fig. 9 Torque characteristics of the SRM, calculated from the Eq. (8)

1.3 Method 3: Inductance-Based Modeling

The inductance-based modeling technique considers nonlinear relation of inductance-current-angle relation to represent a magnetic nonlinearity of the SRM, instead of flux-current-angle relation [8, 9]. The phase-winding inductance is a nonlinear function of rotor angle and phase current. The variation of the phase inductance with the rotor position is expressed by a limited number of Fourier series terms. The coefficients of the Fourier series are determined by the values of the inductance at the aligned position, unaligned position, and midway position. The nonlinear relation between the phase inductance and the current is represented by the polynomial functions. The coefficients of the polynomial are derived by static characteristics obtained from experimental results or finite element analysis. The dynamic phase equation can be represented as a function of phase inductance as

$$\begin{aligned} V_{\text{ph}} &= R_{\text{s}} i + \frac{\text{d}[L(\theta, i) i]}{\text{d}t} = R_{\text{s}} i + L(\theta, i) \frac{\text{d}i}{\text{d}t} + i \frac{\text{d}\theta}{\text{d}t} \frac{\text{d}L(\theta, i)}{\text{d}t} \\ &= R_{\text{s}} i + L(\theta, i) \frac{\text{d}i}{\text{d}t} + \frac{\text{d}L(\theta, i)}{\text{d}t} \omega_{\text{m}} i \end{aligned} \tag{10}$$

where 'ω_{m}' is the motor speed in rad/sec, 'i' is the phase current, and '$L(\theta, i)$' is the equivalent inductance of the phase. The leakage inductance and the mutual

inductance of the winding are neglected. The phase equation can be simplified further as

$$V_{\text{ph}} = R_s i + L(\theta, i)\frac{\mathrm{d}i}{\mathrm{d}t} + e(\theta, i) \tag{11}$$

where $e(\theta, i)$ is the back EMF $= \dfrac{\mathrm{d}L(\theta, i)}{\mathrm{d}t}\omega_m i$.

The equivalent inductance of the phase is represented as a three terms of the Fourier series as

$$L(\theta, i) = L_0(i) + L_1(i)\cos(\theta) + L_2(i)\cos(2\theta) \tag{12}$$

and thus, the back EMF can be represented by the derivative as—

$$e(\theta, i) = -\omega_m(L_1(i)\sin(\theta) + 2L_2(i)\sin(2\theta)\cdot i \tag{13}$$

The current dependent coefficients $L_0(i)$, $L_1(i)$, and $L_2(i)$ are expressed by the three-order polynomials as—

$$\begin{aligned} L_0(i) &= \frac{1}{2}\left[\frac{1}{2}(L_{\text{a}} + L_{\text{u}}) + L_{\text{m}}\right] \\ L_1(i) &= \frac{1}{2}(L_{\text{a}} - L_{\text{u}}) \\ L_2(i) &= \frac{1}{2}\left[\frac{1}{2}(L_{\text{a}} + L_{\text{u}}) - L_{\text{m}}\right] \end{aligned} \tag{14}$$

where 'L_{a}' is the aligned position inductance, 'L_{m}' is the midway position inductance and 'L_{u}' is the unaligned position inductance. The aligned position inductance and midway position inductance are function of the phase current, while the inductance at the unaligned position can be assumed as the independent of the phase current. The inductances L_{a}, L_{m}, and L_{u} are represented as—

$$\begin{aligned} L_{\text{a}} &= L(\theta = 0, i) = \sum_{m=0}^{k} a_m i^m \\ L_{\text{m}} &= L\left(\theta = \frac{\pi}{2}, i\right) = \sum_{m=0}^{k} b_m i^m \\ L_{\text{u}} &= L(\theta = \pi, i) \end{aligned} \tag{15}$$

where 'k' is the degree of approximation. The coefficients, a_{m}-and b_{m} are determined by curve fitting methods such that the inductance profile obtained using Eq. (12) would best fit into the profile obtained experimentally.

2 Comparison of the Modeling Techniques

Both the method-2 and method-3 provide analytical solution to account for the magnetic nonlinearity of the SRM. Method-3 requires experimental data of inductance profile $L(\theta, i)$ of the SRM to obtain coefficient of Fourier series. It provides reasonable accuracy compared to the method-2; however, it requires experimental setup which increases the cost and time of implementation. Also the computation time of the simulation model is comparatively high as it involves derivative calculations. This method is suitable to analyze the performance of the converter as well as to obtain the dynamic performance of the SRM drive. The method-2 does not require experimental data; however, it involves extensive calculations to derive polynomial coefficients. Even though the coefficients are computed with good precision, accuracy of method-2 is somewhat less due to error in flux derivative calculation. The details about motor geometry and winding turn parameters are required initially. This method takes minimum time and cost to derive the simulation model as compared to other methods. It gives high accuracy for low current level, while effect of magnetic saturation reduces the accuracy of the model at the higher current level. The method can be used to investigate the performance of various converter topologies and control techniques, which helps in its performance and design optimization. The method-1 accounts for the nonlinearity of the SRM magnetic characteristics while it minimizes the simulation time. This is because it avoids all partial derivatives and utilizes a look-up table which approximates the relation flux-current position and torque-current position. However, it requires large number of experimental data, and thus, it takes maximum time to derive simulation model of the SRM. Nevertheless, the method provides highest efficiency among all other methods, and it also has advantage of minimum computation time which results in faster simulation.

Several techniques have been published in past which use artificial intelligent techniques to model nonlinearity of SRM [10]. All this techniques tries to achieve highest accuracy to replace look-up table-based approach. But it is computational intensive and required prior knowledge of magnetic characteristics.

3 MATLAB Simulink Model of the SRM

The nonlinear model of the SRM is derived using method-1. The look-up tables are used to represent the magnetic characteristics (Fig. 4) as well as the torque characteristics (Fig. 5) of the 60 kW SRM. The Simulink model of the SRM is shown is Fig. 10 where look-up tables ‘ITBL’ and ‘TTBL’ store the flux-angle-current and current-angle-torque relation, respectively. The motor model produces the torque and speed for the voltage applied to the phase. The model of the converter is developed using ‘simpowersystem’ library components. It is also possible to model

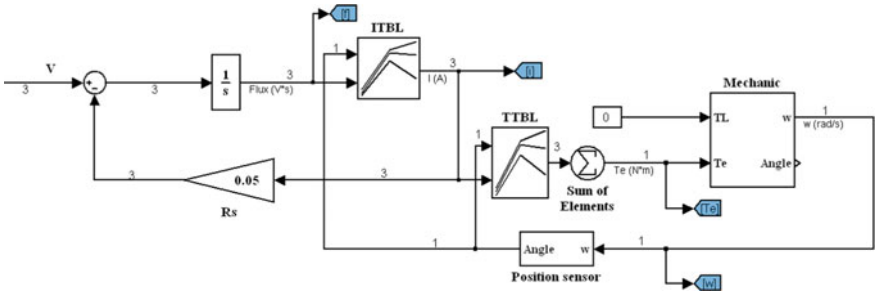

Fig. 10 Simulink model of the SRM

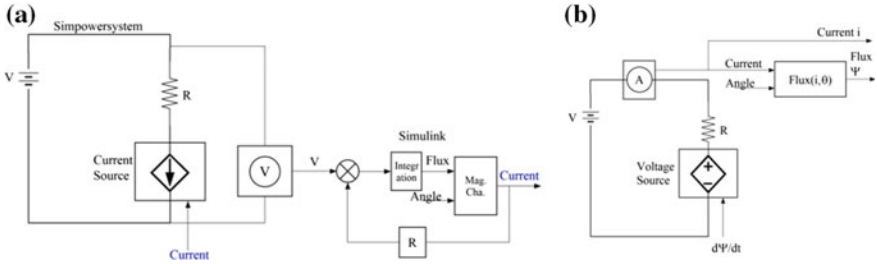

Fig. 11 'Simulink' to 'Simpowersystem' using **a** controlled current source **b** controlled voltage source

various converters and control techniques using the Simulink library. However, 'simpowersystem' library of the MALTAB offers flexibility and easy to model a power electronic and power system components using the node-based circuit simulation approach. The main advantage of using a 'simpowersystem' library to develop the model of converter is that actual devices used in the drive system can be modeled quickly because of readily available modules of the power electronics switches. It offers a great flexibility to study the different converter topologies and certain practical issues can be clearly understood.

Two methods are developed to incorporate the model of converter, designed with 'simpowersystem' library, and the model of the motor, designed with 'Simulink' library. The first method uses the resistive element and the dependent current source from the 'simpowersystem' library to represent a phase of the motor as shown in Fig. 11a [1, 11]. The switching device in series with the motor phase is not shown for the simplicity. The node voltage across the motor phase is converted into the single line signal using the voltage measurement block of the 'simpowersystem' library, and it is applied to the Simulink model of the motor. The motor model produces current, torque, and speed according to the applied phase voltage. The phase current in the 'simpowersystem'-based phase model depends upon the phase current of the 'Simulink' model. Thus, phase voltage applied to the phase of the 'simpowersystem' model results in the production of torque and speed in the

'Simulink' model; while at the same time, the phase current of the 'Simulink' model reflects to the phase of 'simpowersystem' model.

The controlled voltage source-based method is applicable where the flux-linkage is to be estimated from the phase current and rotor angle, as in method-2. The resistive element and dependent voltage source from the 'simpowersystem' library form a motor phase. The phase current is transformed to the single line signal using ampere meter. The voltage source depends on the rate of change of flux-linkage generated from the embedded function, and thus, phase current is governed by the Eq. (11).

4 Conclusion

Present paper provides guidelines in selecting mathematical modeling technique for particular application. Developed embedded model provides great flexibility and fast simulation compared to look-up table-based approach. This method is suitable for performance analysis of SRM-based drive and converter, whereas look-up table-based approach is must when accuracy is the main concern as like in state observer-based sensorless motor control techniques. Furthermore, this paper presents that transpose of SRM model developed in MATLAB 'Simulink' library to 'simpowersystem' library is possible with the use of controlled voltage source and controlled current course. It is important to model complete SRM drive where converter of the motor needs to design in 'simpowersystem' library with available models of semiconductor devices.

References

1. Le-Huy, H., Brunelle, P.: A versatile nonlinear switched reluctance motor model in Simulink using realistic and analytical magnetization characteristics. In: 31st Annual Conference of IEEE Industrial Electronics Society, IECON 2005, pp. 1–6 (2005)
2. Krishnan, R.: Switched Reluctance Motor Drives: Modeling, Simulation, Analysis, Design, and Applications, CRC Press LLC (2001)
3. Miller T.J.E.: Electronic Control of Switched Reluctance Machines: Newnes (2001)
4. Miller, T.J.E., Glinka, M., McGilp, M., Cossar, C., Gallegos-Lopez, G., Ionel, D., Olaru, M.: Ultra-fast model of the switched reluctance motor. In: IEEE Thirty-Third IAS Annual Meeting Industry Applications Conference, pp. 319–326 (1998)
5. Miller, T.J.E., McGilp, M.: Nonlinear theory of the switched reluctance motor for rapid computer-aided design, IEE Proc. B Electr. Power Appl. pp. 337–347 (1990)
6. Torrey, D.A., Lang, J.H.: Modelling a nonlinear variable-reluctance motor drive. IEE Proc. B Electr. Power Appl. **137**(5), 314–326 (1990)
7. Torrey, D.A., Niu, X.M., Unkauf, E. J.: Analytical modelling of variable-reluctance machine magnetisation characteristics. IEE Proc. Electr. Power Appl. pp. 14–22 (1995)
8. Franceschini, G., Pirani, S., Rinaldi, M., Tassoni, C.: SPICE-assisted simulation of controlled electric drives: an application to switched reluctance drives. IEEE Trans. Ind. Appl. **27**(6), 1103–1110 (1991)

9. Mahdavi, J., Suresh, G., Fahimi, B., Ehsani, M.: Dynamic modeling of nonlinear SRM drive with Pspice. In: IEEE Thirty-Second IAS Annual Meeting Industry Applications Conference, IAS'97, pp. 661–667 (1997)
10. Makwana, J.A., Agarwal, P., Srivastava, S.P.: ANN based sensorless rotor position estimation for the Switched Reluctance Motor. In: 2011 Nirma University International Conference on Engineering, Ahmedabad, Gujarat, pp. 1–6 (2011)
11. Murthy, S.S.: Modeling of a switched reluctance motor in sensorless and with sensor modes. J. Power Electron. **6**(4), 315–321 (2006)

Fast Terminal Sliding Mode Control for High Pressure Rated Modified CSTR System

B. Senthil Kumar and K. Suresh Manic

Abstract This paper presents Continuous Sliding Mode controllers applied to nonlinear high pressure rated modified CSTR system which has been linearized to one operating point. Firstly, the first-order sliding mode control or classical sliding mode control has been discussed, and second-order super twisting control is used to attain robustness properties in the presence of uncertain bounded External disturbances when applied to the system. Later, Terminal Sliding Mode Control and Fast Terminal Sliding Mode Control are presented which result in faster convergence of state variables with respect to initial values of the system. The convergence of state variables to the equilibrium point occurs in finite time. The simulation results show the improved control performances and the properties of continuous Sliding Mode Controllers when applied for maintaining pH control for High Pressure Rated Modified CSTR system where it has unmodelled dynamics as the external bounded disturbance.

Keywords Sliding Mode Control · Terminal Sliding Mode Control
Fast Terminal Sliding Mode Control · Chattering · Modified CSTR

1 Introduction

pH is the degree of acidity or alkalinity of a solution. It is measured as $-\log[H^+]$, and the range of pH value is between 0 and 14. The logarithmic relationship between hydrogen ion concentration and pH value, pH process is highly nonlinear [1]. The nonlinearity present in the system has been linearized to one equilibrium point, and transfer function has been attained. Control of pH is a difficult task due to

B. Senthil Kumar (✉)
Faculty of Electrical Engineering, Anna University, Chennai, India
e-mail: vlrsenthil@gmail.com

K. Suresh Manic
Department of EEE, Sriram Engineering College, Chennai 602024, India
e-mail: ksureshmanic@gmail.com

A. Konkani et al. (eds.), *Advances in Systems, Control and Automation*,
Lecture Notes in Electrical Engineering 442, https://doi.org/10.1007/978-981-10-4762-6_53

the nonlinearity and higher sensitivity to disturbances of the process. The deep sea condition is mimicked using high pressure rated environmental CSTR system to study the growth of micro-organisms. For that, pH inside set-up has to be maintained at a predetermined level at elevated pressure. Due to various conditions like elevated pressure, enzymes produced by microbes inside the environmental CSTR, the pH value is going to vary frequently. For the survival of microbes, this variation should be controlled. Around the neutral point (pH value 7), the pH curve has a huge gain, i.e. even a small change in acid/base flow is going to vary the pH value drastically. The control of pH around this region is really challenging.

The system has to be modelled accurately for the design of controller. In this work, it is modelled as a first-order plus dead (FOPDT) system from the real-time open-loop response [2, 3]. The system is having significant delay due to various reasons like the delay for uniform mixing of acid/base in the five litre environmental CSTR [4]. This paper presents the robustness properties for the FOPDT system using Sliding Mode Control, where the system is regulated under plant parametric uncertainties and disturbances act along the input which is bounded.

Sliding Mode Controllers are used for the regulation of chemical process and realizing robustness properties [5, 6]. Sliding Mode Control is a robust control method used whenever there is a mismatch in the system where it comes from unknown bounded external disturbance acting on the system [7, 8]. In this paper, the state space methods are used and Linear State Feedback Control is studied along with different type of Sliding Mode Controllers such as First Order SMC, Super Twisting Control, Terminal Sliding Mode Control and Fast Terminal Sliding Mode Control [9–11].

2 Control Strategy

2.1 First-Order SMC

The first-order SMC is a reduced order controller which has a linear sliding surface and becomes invariant when it reaches the sliding surface, and the control is discontinuous when applied to the system on the other hand super twisting controller is a second-order controller where the control is a continuous type.

The delay time has been converted to a first-order system.

$$e^{-sT} = \frac{1}{1+sT} \tag{1}$$

A nonautonomous system of the form $\dot{X} = Ax(t) + Bu + Bd$ to be considered where $x(t) \in \Re, A \in \Re, B \in \Re, u \in \Re$, and d is a bounded external disturbance acting along with the input. The sliding mode controllers are designed which drive the system asymptotically to the Equilibrium point [4, 5].

Constant rate reaching law

$$\dot{S} = -K\,\mathrm{sign}(s) + d \quad \text{where } K > d_{\max} \tag{2}$$

Constant plus proportional rate reaching law

$$\dot{S} = -Ks - Q\,\mathrm{sign}(s) + d \quad \text{where } K > Q > d_{\max} \tag{3}$$

Super twisting law

$$\begin{aligned} \dot{S} &= -K_1|s|^{1/2}\mathrm{sign}(s) + z \\ \dot{Z} &= -K_2\mathrm{sign}(s) + d \end{aligned} \quad \text{where } K_1 > 0,\ K_2 > 0 \tag{4}$$

Here, K, Q, K_1 and K_2 are the tuning parameters that design the reaching rate, and d is the external bounded disturbance acting along the input.

2.2 Terminal Sliding Mode Control

Terminal Sliding Mode Control has a nonlinear sliding surface where the states reach in finite time and are stable; the Terminal is referred to as Equilibrium point [9].

$$\dot{x_1} = x_2 \tag{5a}$$

$$\dot{x_2} = f(x) + g(x)u \tag{5b}$$

Let the TSM manifold is defined as

$$S = x_2 + \beta x_1^{q/p}, \quad \beta > 0 \tag{6}$$

where the sliding manifold is a non-Lipchitz in nature, and p and q are odd integers, $q < p$

$$\dot{S} = \dot{x_2} + \beta\frac{q}{p}x_1^{\frac{q}{p}-1}\dot{x_1} \tag{7}$$

Substituting (5a) and (5b) and the control is obtained as

$$u = -g^{-1}(x)\left[f(x) + \beta\frac{q}{p}x_1^{\frac{q-p}{p}}x_2 + K\mathrm{sign}(s)\right] \tag{8}$$

where $K > 0$ and $\dot{S} = -K\,\mathrm{sign}(s)$

During sliding mode, $S = 0$

$$\dot{x_1} = x_2 = -\beta x_1^{\frac{q}{p}} \tag{9}$$

where p and q are odd integers, and p-q is an even number. It implies that x_1 goes to zero in time t_1 and remains there all time $t \geq t_1$, since $\dot{x_1} = 0$. If $p = q$, then TSM becomes a linear sliding surface.

2.3 Fast Terminal Sliding Mode Control

To achieve faster convergence, a new manifold is defined as

$$S = x_2 + \alpha x_1 + \beta x_1^{q/p} \tag{10}$$

and during sliding $\dot{S} = 0$ the reduced order system during sliding will be

$$\dot{x_1} = -\alpha x_1 - \beta x_1^{q/p} \tag{11}$$

When the initial value of x_1 is far away from origin αx_1, that is $\dot{x_1} \approx -\alpha x_1$ be the dominating region and the convergence rate be faster. When the initial values of x_1 is near to origin $\beta x_1^{q/p}$ [10].

For SISO system,

$$\dot{x_i} = x_{i+1} \quad i = 1, 2\ldots, n-1 \tag{12a}$$

$$\dot{x_n} = f(x) + g(x)u \tag{12b}$$

For this second-order SISO system,

$$S_2 = \dot{S_1} + \alpha_2 S_1 + \beta_2 S_1^{q_2/p_2} \tag{13a}$$

$$S_3 = \dot{S_2} + \alpha_2 S_1 + \beta_2 S_1^{q_2/p_2} \tag{13b}$$

3 Numerical Example

The high pressure rated modified CSTR [1] is given by

$$G(s) = \frac{0.272e^{-5.005s}}{3.2s + 1}$$

The system is converted into state space form using Eq. (1), and the matrix is given as

$$A = \begin{bmatrix} 0 & 1 \\ -0.5122 & -0.0624 \end{bmatrix} \quad \text{and} \quad B = \begin{bmatrix} 0 \\ 1 \end{bmatrix}$$

The constant rate reaching law is given by Eq. (2) and the response been obtained (Figs. 1 and 2).

The control variable is given for constant rate reaching law which is a discontinuous control (Fig. 3).

The terminal sliding mode control as given by Eq. (5a) and (5b) is shown in Fig. 4.

The sliding surface for terminal sliding mode control for initial values $x_1 = 10$ and $x_2 = 10$ is given in Eq. (7) (Fig. 5).

The control variable is given in Eq. (8) (Fig. 6).

The fast terminal sliding mode control for initial values of $x_1 = 100$ and $x_2 = -100$ is give in Eq. (12a) and 12b (Fig. 7).

The phase plane plot for finite time convergence is shown in Fig. 8.

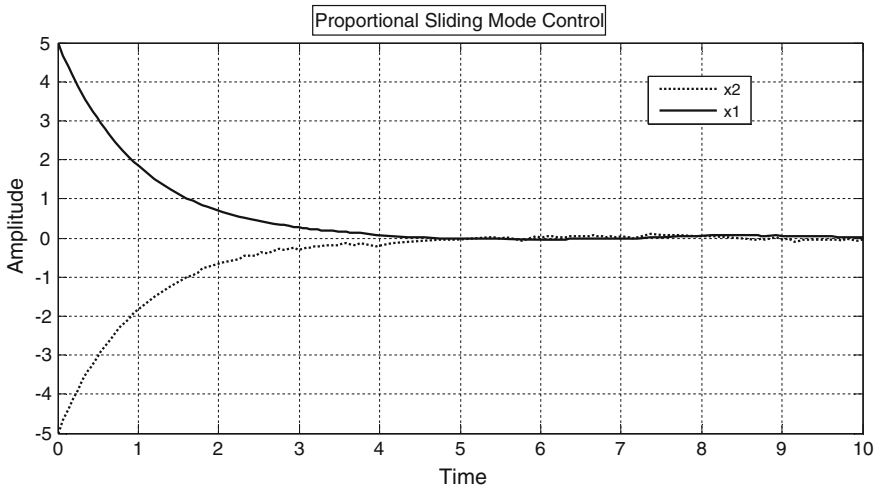

Fig. 1 Response for constant rate reaching law

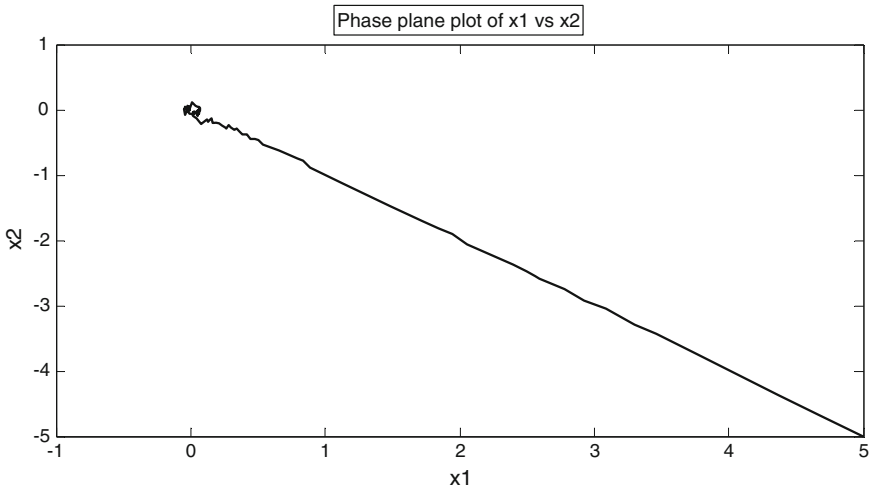

Fig. 2 Phase plane plot for constant rate reaching law

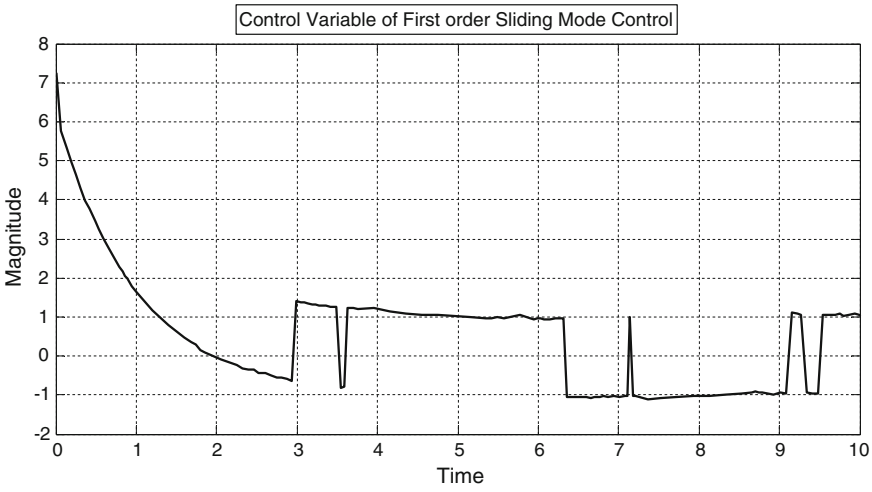

Fig. 3 Discontinuous control for constant rate reaching law

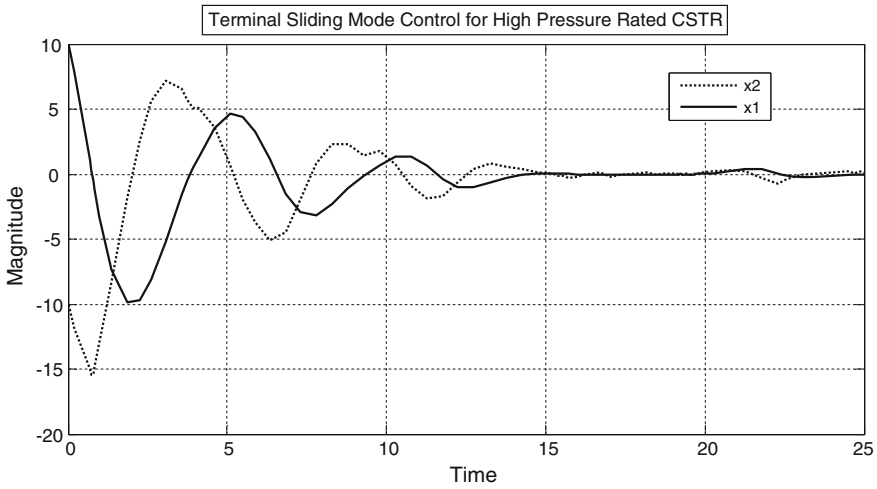

Fig. 4 Terminal sliding mode control for high pressure rated modified CSTR

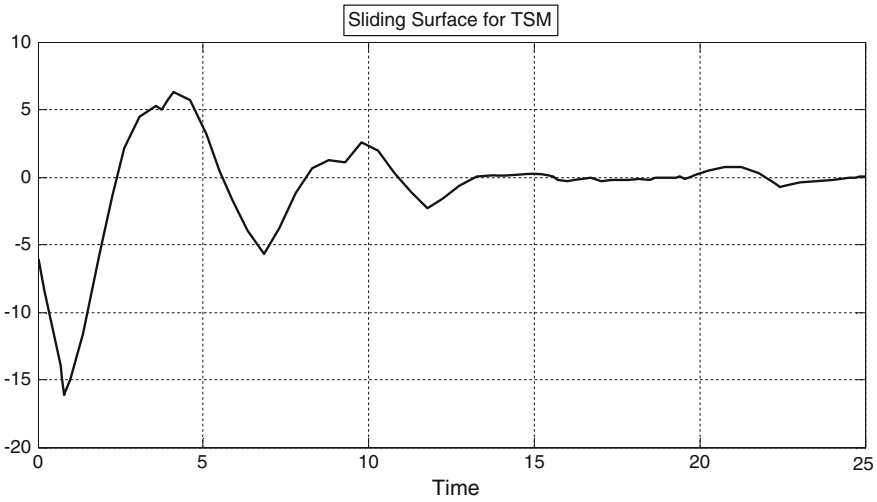

Fig. 5 Sliding surface for terminal sliding mode control

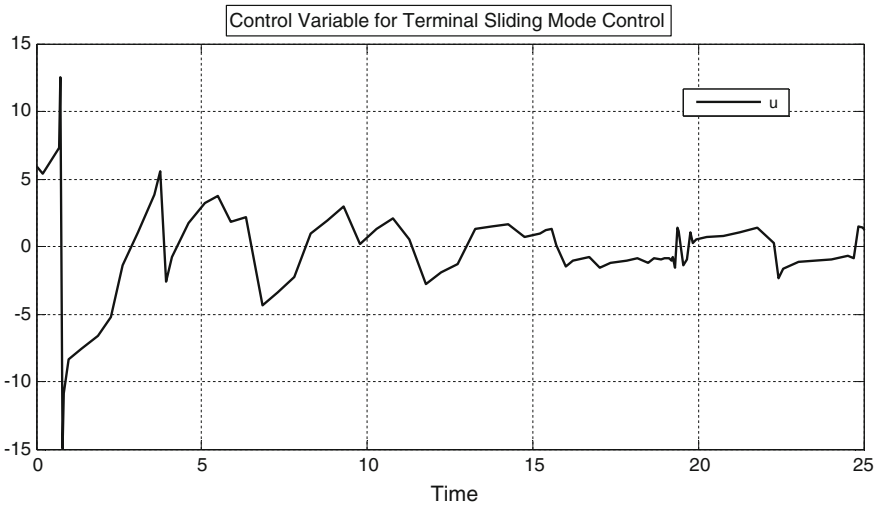

Fig. 6 Control variable for terminal sliding mode control

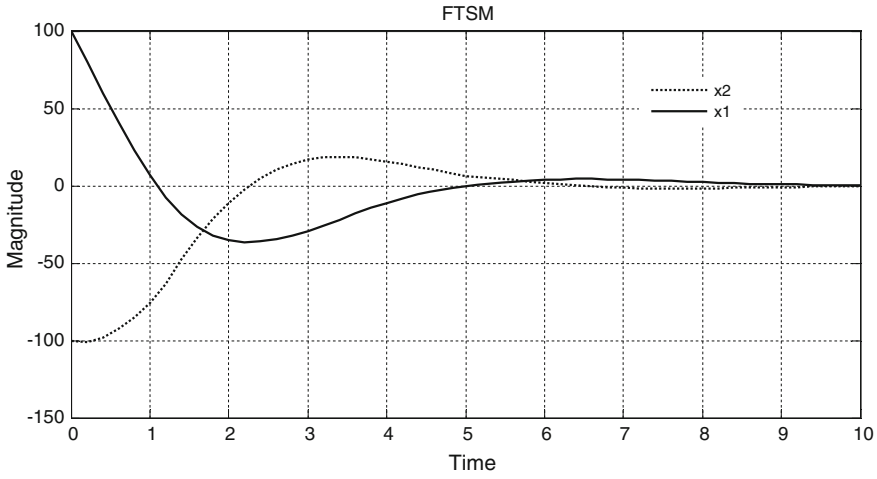

Fig. 7 Response for fast terminal sliding mode control

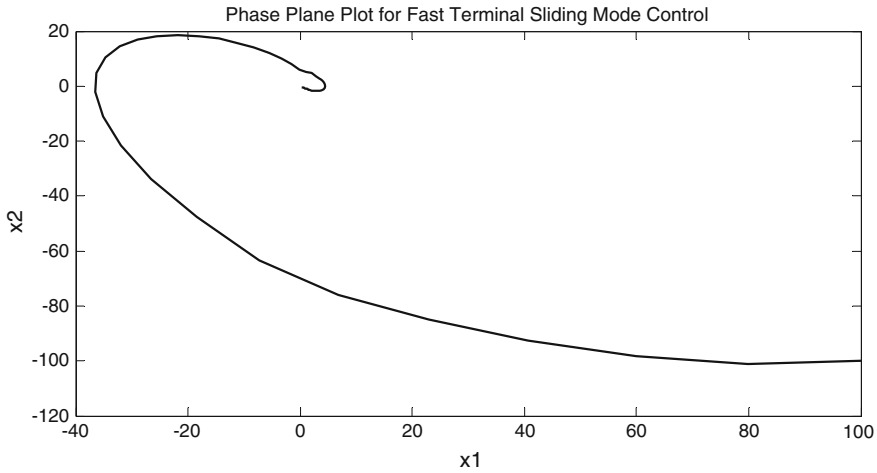

Fig. 8 Phase plane plot for FTSM x_1 versus x_2

Table 1 Result and comparison of control input for various Sliding Mode Controllers

Controllers	$\|u\|_2$	$\|u\|_\infty$	Initial values		Sliding surface
			X_1	X_2	
Proportional rate reaching law	19.43	7.249	5	−5	Linear
Terminal Sliding Mode Control	32.1362	14.9451	10	−10	Nonlinear
Fast Terminal Sliding Mode Control	164.5313	76.79	100	−100	Nonlinear

4 Conclusion

The system which is a first-order plus dead time has uncertainties when modelled which has been controlled using first-order sliding mode control where robust properties has been realized. The realization shows Figs. 2 and 8 the phase plane analysis for the First Order Sliding Mode Control Fig. 2, Terminal Sliding Mode control Fig. 8 the convergence rate is finite near the equilibrium point and Convergence rate is faster for Faster Terminal Sliding Mode Control when the initial values are too far from the origin. The control variable which is discontinuous in the case of First-Order Sliding Mode control has lot of chattering which occurs due to signum function, Whereas in the case of Terminal Sliding Mode control and Fast Terminal Sliding Mode Control, the sliding surface is nonlipschitz, that is nonlinear surface, but convergence rate is finite; with respect to magnitude of the control input, there are some variations.

References

1. Kannangot, J., Lakshmi, P., Thiruppathi, K.: Design of fuzzy logic-based ph controller for high-pressure-rated modified CSTR system. In: Suresh, L.P., Dash, S.S., Panigrahi, B.K. (eds.) Proceedings of Artificial Intelligence Evolution Algorithms Engineering Systems ICAEES 2014, vol. 1, pp. 803–811. Springer India, New Delhi (2015)
2. Vijayan, V., Panda, R.C.: Design of a simple setpoint filter for minimizing overshoot for low order processes. ISA Trans. **51**, 271–276 (2012)
3. Vijayan, V., Panda, R.C.: Design of PID controllers in double feedback loops for SISO systems with set-point filters. ISA Trans. **51**, 514–521 (2012)
4. Bequette, B.W.: Process Control: Modeling, Design, and Simulation. Prentice Hall Professional (2003)
5. Kumar, B.S., Manic, K.S.: Sliding mode control for a minimum phase unstable second order system. Appl. Mech. Mater. **573**, 285–290 (2014)
6. Anusha Rani, V., Kumar, B.S., Manic, K.S.: Sliding mode control for robust regulation of chemical processes. Indian J Sci. Technol. **9**, 1–12 (2016)
7. Shtessel, Y., Edwards, C., Fridman, L., Levant, A.: Sliding mode control and observation (2014). doi:10.1007/978-0-8176-4893-0
8. Edwards, C., Spurgeon, S.K.: Sliding Mode Control: Theory and Applications (1988)
9. Yu, X., Man, Z.: Model reference adaptive control systems with terminal sliding modes. Int. J. Control **64**, 1165–1176 (1996)
10. Xinghuo, Y., Zhihong, M.: Fast terminal sliding-mode control design for nonlinear dynamical systems. IEEE Trans. Circ. Syst. I. Fundam. Theory Appl. **49**, 261–264 (2002)
11. Camacho, O., Rojas, R., García, W.: Variable structure control applied to chemical processes with inverse response. ISA Trans. **38**, 55–72 (1999)

Experimental/Simulation Study to Check the Significance of Proximity Effect

Asha Shendge

Abstract Nowadays, due to smart grid technologies, the working on off seashore wind/solar renewable energy where power carried through medium of submersible cables, transient peaks have significance to investigate proximity effect of a conductor system. To investigate these phenomena, author has experimented energized pipe conductor in close proximity to aluminum plate. The return path is provided by aluminum plate to check the significance of proximity effect. The field measurements are carried out, and also, simulation is done with numerical method FDTD. Then, comparison is done between experimental measurements and simulations. As the height of conductor varies from earth, distribution of current becomes uneven. It could be concluded the proximity effect is represented by height variation from earth return path.

Keywords FDTD (Finite-difference time-domain)
Electromagnetic transient program (EMTP) · Z line impedance
Y line admittance · Proximity effect

1 Introduction

The electromagnetic behavior of parameters of conductor/cable is represented by line impedance Z and line admittance Y. The simulation models need Z and Y for conductor system. While doing simulation using electromagnetic transient program (EMTP) routine [1] it calculates conductor and cable transients using Z, the series impedance using formulae derived by [2–5] that do not reflects the presence of proximity effects. EMTP assumes cylindrically symmetric of currents and electromagnetic quantities and calculates skin effect. In case there is current deviating from cylindrical distribution the assumption that only skin effect present due to Z in case nature cylindrically symmetric of currents and quantities is no longer true. However,

Asha Shendge (✉)
Electrical Engineering Department,
G.H. Raisoni Institute of Engineering and Technology, Pune, India
e-mail: asha.shendge@raisoni.net; ashashendge@gmail.com

A. Konkani et al. (eds.), *Advances in Systems, Control and Automation*,
Lecture Notes in Electrical Engineering 442, https://doi.org/10.1007/978-981-10-4762-6_54

more than one conductor or stranded cable is closer to each other, and also, frequency f is increased proximity effect becomes more pronounced. To approach, the author has already experimented [6] proximity effect for simple conductor system.

To investigate current distribution on conductor due to change in the height of injection point, in order to investigate new formulae when conductor is used in close proximity are the subject of interest. The FDTD helps to analyze the proximity effect significance for conditions where conductors are close to each other in energized conductor.

2 Experimental Setup

Figure 1 shows the laboratory setup. For investigation, aluminum pipe with 2 m length and 5 cm radius was used. 100 V was applied using source as pulse generator (PG). The source resistance was 1 kΩ. 100-Ω resistor through lead wire is connected at receiving end. Then, it is terminated into aluminum plate as return path. At center point of disk, the transient voltage was applied. For height h = 5.5 cm, top, center, and bottom voltage is injected. It helps to observe effect of close proximity for height change. The receiving end resistor positions as bottom, center, and top of pipe are changed for nine conditions. The distribution of current which flows through the conductor to ground was measured.

Figure 2 illustrates detailed view of front and rear side of pipe. Points T, C, and B represent top, center, and bottom positions of injection and receiving end resistor.

Figure 3 represents circuit diagram for injection and resistor connection for cases.

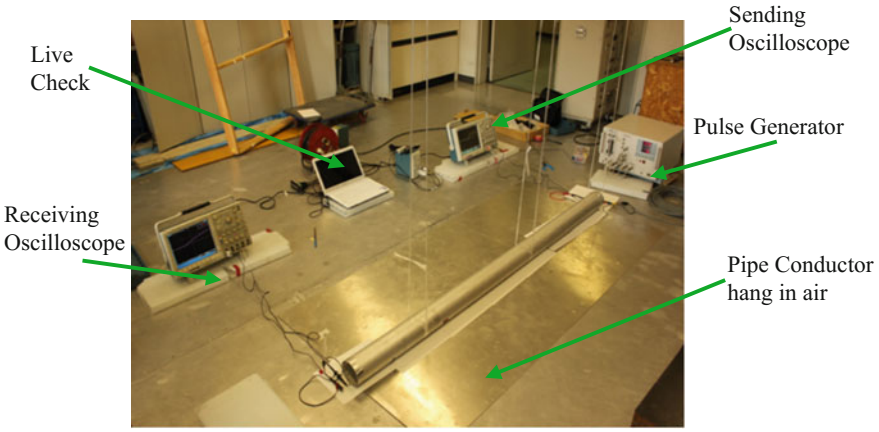

Fig. 1 Laboratory setup

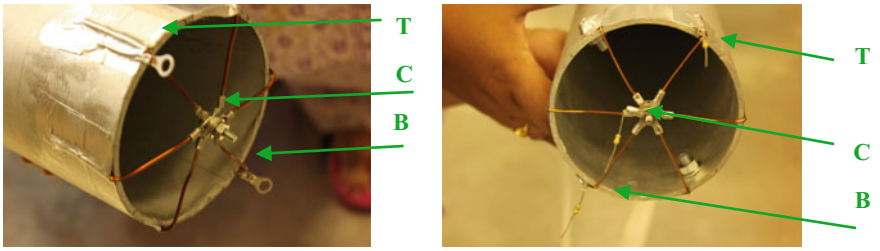

(a) Front side (b) Rear side

Fig. 2 Detailed view of pipe conductor

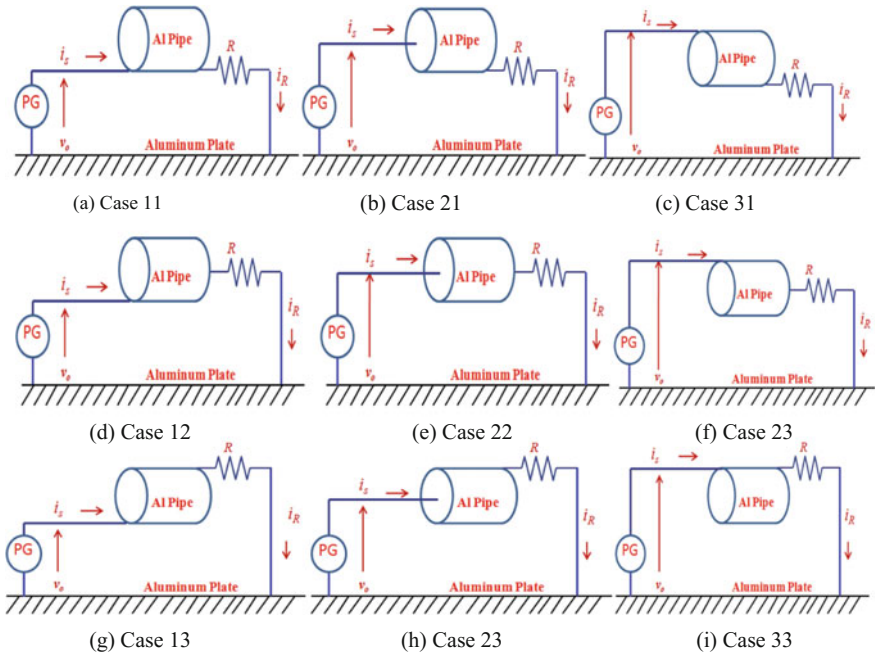

(a) Case 11 (b) Case 21 (c) Case 31

(d) Case 12 (e) Case 22 (f) Case 23

(g) Case 13 (h) Case 23 (i) Case 33

Fig. 3 Circuit representation for each conditions of experiment

3 Numerical Simulation

Whenever circuit theory approach could not solve transient problems, then electromagnetic theory comes into picture. Numerical analysis is carried out by Maxwell's equations. Digital computers can handle Maxwell's equations expressed in differential forms that are valid integral forms is a discrete in nature. These forms of Maxwell's equations are the basic fundamentals of the finite-difference time-domain

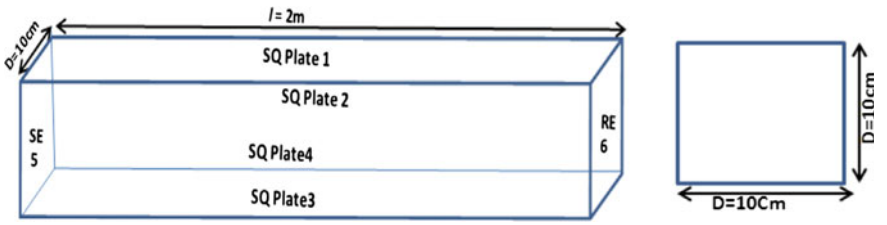

(a) Front view (b) Side view

Fig. 4 FDTD simulation model

(FDTD) method. These equations give the solution of electromagnetic propagation problems [7] which can calculate various incidents and reflected and scattered fields.

3.1 FDTD Model

In this paper, Visual Simulation Test Laboratory developed by Central Research Institute of Electrical Power Industry, Japan [8], is adopted. Pipe conductor cannot be simulated directly by Visual Simulation Test Laboratory. The pipe is represented by 4 conducting square plates. The pipe with width equal to equivalent of diameter of aluminum pipe is constructed while doing simulation. The OC (open-circuit) and SC (short-circuit) test conditions at receiving end as per experimental circuit were simulated. The time period was 20 ns. $\Delta_s = 5$ mm is the cell size of an analytical space for VSTL simulation. An aluminum plate is assumed to be earthed with resistivity $\rho_c = 2.8 \times 10^{-8}$ Ωm. For simulation purpose there was around 40–50 cells boundary was set by apart. Injecting voltage was the measured waveform.

For injection of current and termination of receiving end by resistor, two square plates were enclosed to front end as well as rear end as shown in Fig. 4.

4 Experimental and Simulated Result

4.1 Measured Result

The applied input voltage and injected current for all nine conditions represented in Fig. 3 were step type. The input voltage is 100 V, and injected current is 0.2 A. Figures 5 and 6 show receiving end voltages and currents for different injection positions to conductor for three injection positions.

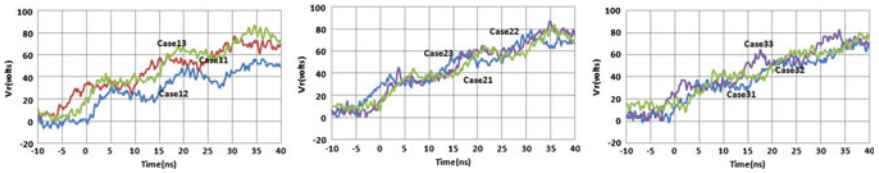

(a) INJ-Bot (b) INJ-Cen (c) INJ-Top

Fig. 5 Receiving end voltage

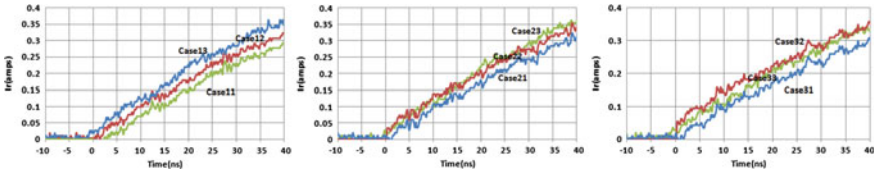

(a) INJ – Bot (b) INJ-Cen (c) INJ-Top

Fig. 6 Receiving end current

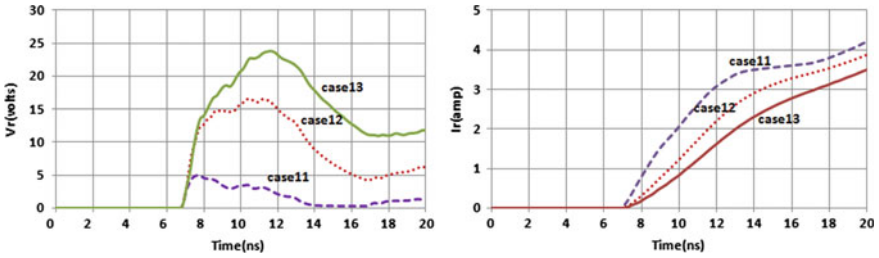

(a) Receiving end voltage (b) Receiving end current

Fig. 7 Simulation for INJ-BOT

4.2 FDTD-Simulated Result

Figure 7 shows receiving end voltages and currents for bottom injection positions to conductor for three injection positions.

5 Discussion and Conclusion

The study on conductor system is carried out to check the influence of proximity on sending end current voltage and receiving end current voltage by two ways by measurements and using FDTD simulation. The bottom injection, center injection,

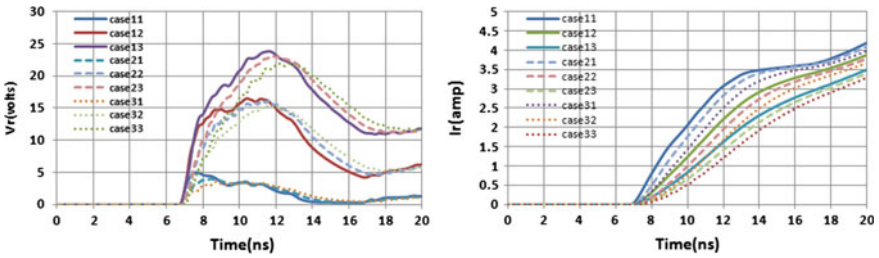

(a) Receiving end voltage (b) Receiving end current

Fig. 8 Comparison of for INJ-POINT

and top injection are considered for study. The numerical method FDTD shows appreciable significance for close conditions as shown in Fig. 8. It is predicted that this methodology will be of benefit to new researchers who are working on off seashore wind, solar renewable energy where power is carried through submersible cables.

References

1. Scott-Mayer, W.: EMTP Rule Book. Bonneville, Portland, OR (1994)
2. Schelkunoff, S.A.: The electromagnetic theory of coaxial transmission lines and cylindrical shields. Bell Syst. Tech. J. **13**, 532–579 (1934)
3. Carson, J.R.: Wave propagation in overhead wires with ground return. Bell Syst. Tech. J **5**, 539–554 (1926)
4. Ametani, A.: A general formulation of impedance and admittance. IEEE PAS **99**(3), 902–908 (1980)
5. Dommel, H.W.: Manual of Line Constants, B.P.A. (1976)
6. Shendge, A.: A study on a conductor system for an investigation of proximity effect. Sci. Res. J. Electromagn. Anal. Appl. **4**(11), 440–446 (2012)
7. Yee, K.S.: Numerical solution of initial boundary value problems involving Maxwell's equations in isotropic material. IEEE Trans. Antennas Propag. **14**(3), 302–307 (1996)
8. CRIEPI: Visual Simulation Test Lab (2000) http://criepei.denken.or.jp/

Denoising of MRI Images Using Curvelet Transform

Ranjit Biswas, Debraj Purkayastha and Sudipta Roy

Abstract Most of the medical images are usually affected by different types of noises during acquisition, storage, and transmission. These images need to be free from noise for better diagnosis, decision, and results. Thus, denoising technique plays an important role in medical image analysis. This paper presents a method of noise removal for brain magnetic resonance imaging (MRI) image using curvelet transform thresholding technique combined with the Wiener filter and compares the result with the curvelet and wavelet-based denoising techniques. To assess the quality of denoised image, the values of peak signal-to-noise ratio (PSNR), mean square error (MSE), and structural similarity index measure (SSIM) are considered. The experimental results show that curvelet denoising method depicts better result than wavelet denoising method, but the combined method of curvelet with Wiener filtering technique is more effective than the wavelet- and curvelet-based denoising method in terms of PSNR, MSE, and SSIM.

Keywords Wiener filter · Wavelet transform · Curvelet transform · Denoising

1 Introduction

Medical images are having an important role for diagnosis of diseases. These images are obtained from various methods such as MRI, CT, and X-ray imaging. Nowadays, these images are captured using digitized systems. During the

R. Biswas (✉)
Department of Information Technology, Ramkrishna Mahavidyalaya, Kailashahar, Tripura 799277, India
e-mail: ranjit_tb@yahoo.co.in

D. Purkayastha · S. Roy
Department of Computer Science & Engineering, Assam University, Silchar 788011, India
e-mail: cyberdebraj@gmail.com

S. Roy
e-mail: sudipta.it@gmail.com

A. Konkani et al. (eds.), *Advances in Systems, Control and Automation*,
Lecture Notes in Electrical Engineering 442, https://doi.org/10.1007/978-981-10-4762-6_55

acquisition process, the images may be corrupted by different types of noise and it is very important to remove the noise to get better interpretation. Removal of noise from digital images is a big challenge for the researchers. Huang et al. [1] proposed a type of median filtering technique which is much faster and was implemented in 2D. Later, Ney [2] implemented a technique of dynamic programming for implementing nonlinear smoothing filters, which gives a good result in removing noise but keeps much more information around the curves by penalizing when there is large difference in two consecutive samples and rewarding when these are close. Saluja et al. [3] proposed an adaptive Wiener filter based on wavelet transform to calculate coefficients of weighted high-pass filtering. Boulfelfel et al. [4] investigated the usage of Wiener filter and PSE filter in CT images and developed a 3D filter that performs better than 2D filters.

The transform domain filtering contains wavelet transform, ridgelet transform, and curvelet transform. Lang et al. [5] used wavelet analysis of undecimated wavelet transform on unidimensional signals to remove noise which was one of the earlier implementations of wavelet in noise removal. To remove noise and to compress image, Chang et al. [6] used adaptive wavelet soft threshold using data-driven method called as Bayes Shrink method for threshold estimation. Mojsilovic et al. [7] classified the stages of liver disease using wavelet transform. One of the important thresholding techniques—Visu Shrink developed by Donoho et al. [8, 9] using wavelet shrinkage. Another technique called SURE (Stein's Unbiased Risk Estimator) shrink also developed by Donoho et al. [10], which is based on SURE estimator developed by Steinin [11]. Stein name it as Unbiased Risk Estimator. SURE estimator estimates mean of random normal variable which is independent. Zhang [12] proposed and implemented diffusion in image domain and also in wavelet domain.

Candes and Donoho [13] showed ridgelet transform of images. Based on ridgelets, curvelet transform came into existence. The disadvantage of wavelet denoising is that it does not perform well while denoising in the curves in an image and results in loss of details. Starck and Candes in [14] proposed a curvelet transform based on Candes's ridgelet technique. This technique can efficiently represent a curve because it has ability to select and identify curves along with time and frequency relations. This technique also uses wavelet shrinkage for thresholding. Ulfarsson et al. [15] removed speckle noise efficiently from SAR images using curvelet domain transform. Liu et al. [16] studied and analysed the curvelet based on ridgelet. Ali et al. [17] developed a method to fuse CT image and MR image, and the fusion is done in curvelet domain.

2 Denoising Techniques

There are two fundamental approaches to image denoising, viz. spatial domain filtering and transform domain filtering methods.

2.1 Wavelet Transform

Wavelet is very useful for nonlinear representation of signals. Wavelet basically decomposes the image into its time and frequency relation components. Thus, the image is transformed into frequencies rather than pixel. In the wavelet domain, the noisy image is decomposed into four subsamples according to their low (L) and high (H) frequency bands called LL, LH, HL, and HH. The LL subsample is again decomposed into four subsamples at level two [3] and so on as per the requirement of the computation.

2.2 Curvelet Transform

Stark and Candes [14] solved the problem of wavelet transform by proposing curvelet transform based on ridgelet transform. Ridgelet implementation was done by converting it into radon transform. In the ridgelet transform, support interval or the scaling is done by anisotropy scaling relationship, denoted by Eq. (1).

$$\text{width} = \text{length}^2 \tag{1}$$

This was done in the first generation of curvelet transform using multiscaling ridgelet where the curve is divided into blocks and the subblocks are approximated into a straight line and ridgelet analysis is done upon it. The basic curvelet decomposition steps are given as follows.

The subband decomposition is done by Eq. (2).

$$f \mapsto (P_0 f, \Delta_1 f, \Delta_2 f, \ldots) \tag{2}$$

where P_0 are subband filters, and $\Delta_s, s \geq 0$, and subbands $\Delta_s f$ contain details about 2^{-2s} wide. The smooth windows are $w_Q(x_1, x_2)$ which are localized in diadic squares and which is defined by Eq. (3).

$$Q = [k_1/2^s, (k_1+1)/2^s] \times [k_2/2^s, (k_2+1)/2^s] \tag{3}$$

Then, the resulting square is renormalized to unit scale, which is represented by Eq. (4).

$$g_Q = T_Q^{-1}(w_Q \Delta_S f), \quad Q \in Q_S \tag{4}$$

where $(T_Q f)(x_1, x_2) = 2^s f(2^s x_1 - k_1, 2^s x_2 - k_2)$ is a renormalization operator.

After the renormalization, the ridgelet transform is done by Eq. (5).

$$\alpha_{\mu} = \langle g_Q, p_{\lambda} \rangle \tag{5}$$

3 Thresholding Technique

Thresholding in transform domain is achieved by hard thresholding and soft thresholding to remove unwanted noise signals. Hard thresholding removes all the value after a certain limit, and soft thresholding lowers the intensity of noise towards zero values, which is defined by Eqs. (6) and (7).

$$y(t)_{\text{Hard}} = \begin{cases} x(t) & |x(t)| \geq T \\ 0 & |x(t)| < T \end{cases} \tag{6}$$

$$y(t)_{\text{Soft}} = \begin{cases} \text{sign}(x(t)) \cdot (|x(t)| - T) & |x(t)| \geq T \\ 0 & |x(t)| < T \end{cases} \tag{7}$$

where T is threshold value, and x and y are input and output coefficients in the respective transform domain.

The threshold value in wavelet domain is calculated by Donoho et al. [10], using Visu Shrink method. Visu Shrink is based on universal thresholding as explained in the following Eq. (8).

$$T_w = \sigma\sqrt{\log(N)} \tag{8}$$

where T is the threshold value, N is the size of image, and ∂ is the noise variance.

The threshold value in curvelet transform is calculated by value of 3*sigma and 4*sigma [18] used for the coarse-scale and fine-scale elements (9).

$$T_c = 3 * \text{sigma} + \text{sigma} * (s == \text{length}(C)) \tag{9}$$

where C is the size of decomposed images, and s = 2 to length of C.

4 Proposed Technique

A new technique is proposed here using curvelet transform thresholding technique combined with the Wiener filter. The curvelet transform helps to overcome the problem of wavelet transform, and noise is removed using it first, and then, the Wiener filter is used to remove the residual noise.

5 Parameter Estimations

To evaluate the performance of the techniques, we have considered the values of peak signal-to-noise ratio (PSNR), mean square error (MSE), and structural similarity index measure (SSIM), which are defined by Eqs. (10), (11), and (12).

$$\text{PSNR} = 10 \cdot \log_{10}\left(\frac{\text{MAX}_I^2}{\text{MSE}}\right) \tag{10}$$

$$\text{MSE} = \frac{1}{mn}\sum_{i=0}^{m-1}\sum_{j=0}^{n-1}[f(i,j) - g(i,j)]^2 \tag{11}$$

where mn is size of image, MAX_I is maximum probable pixel value of the image, $f(i, j)$ is the noisy image, and $g(i, j)$ is denoised image.

$$\text{SSIM}(x, y) = \frac{(2\mu_x\mu_y + C_1)(2\sigma_{xy} + C_2)}{(\mu_x^2 + \mu_y^2 + C_1)(\sigma_x^2 + \sigma_y^2 + C_2)} \tag{12}$$

where μ_x, μ_y are local means, σ_x, σ_y are standard deviations, and σ_{xy} is cross-covariance for images x, y.

6 Experimentation

In this work, the proposed technique along with other existing techniques is experimented on MRI images of brain. The experiments are performed using MATLAB on MRI images of size 256 × 256 following the wrapping technique on curvelet software package. White Gaussian noise is added in MRI images with different sigma, i.e., σ = 10, 20, 30, 40, 50, 60, 70. Then, the various types of denoising techniques were implemented, viz. Wiener filter, wavelet thresholding, curvelet thresholding, and curvelet thresholding, with Wiener filter.

7 Results and Discussion

After applying different denoising methods to noisy MRI brain image, results were compared visually and using quality metrics values of PSNR, MSE, and SSIM. The experimental results show that the proposed combined method of curvelet with Wiener filter-based image denoising is performed more effectively compared to other methods. Tables 1, 2 and 3 show the PSNR, MSE, and SSIM values obtained by each method for MRI brain image with different sigma, i.e., σ = 10, 20, 30, 40,

Table 1 Comparison of PSNR values for brain MRI image

Sigma σ	Wiener	Wavelet hard	Wavelet soft	Curvelet hard	Curvelet soft	Combined
10	31.452	29.198	28.154	30.351	28.153	42.179
20	26.611	23.952	23.529	24.336	23.011	43.364
30	23.708	20.875	20.686	20.932	20.050	44.630
40	23.708	18.743	18.660	18.608	17.978	45.943
50	19.849	17.064	17.037	16.829	16.400	47.543
60	18.456	15.729	15.718	15.462	15.133	48.500
70	17.297	14.590	14.583	14.318	14.057	50.421

Table 2 Comparison of MSE values for brain MRI image

Sigma σ	Wiener	Wavelet hard	Wavelet soft	Curvelet hard	Curvelet soft	Combined
10	46.550	78.219	99.460	59.973	99.496	3.937
20	141.890	261.756	288.531	239.570	325.069	2.997
30	276.860	531.575	555.183	524.607	642.812	2.239
40	276.860	868.621	885.359	895.977	1035.770	1.655
50	673.310	1278.371	1286.375	1349.516	1489.665	1.145
60	927.760	1738.323	1742.991	1848.875	1994.280	0.918
70	1211.600	2260.087	2263.393	2405.855	2554.956	0.590

Table 3 Comparison of SSIM values for brain MRI image

Sigma σ	Wiener	Wavelet hard	Wavelet soft	Curvelet hard	Curvelet soft	Combined
10	0.729	0.672	0.657	0.688	0.634	0.988
20	0.556	0.409	0.400	0.401	0.345	0.989
30	0.503	0.281	0.276	0.253	0.204	0.990
40	0.503	0.216	0.213	0.170	0.131	0.991
50	0.471	0.177	0.176	0.119	0.088	0.994
60	0.471	0.149	0.148	0.087	0.062	0.995
70	0.470	0.131	0.131	0.064	0.045	0.996

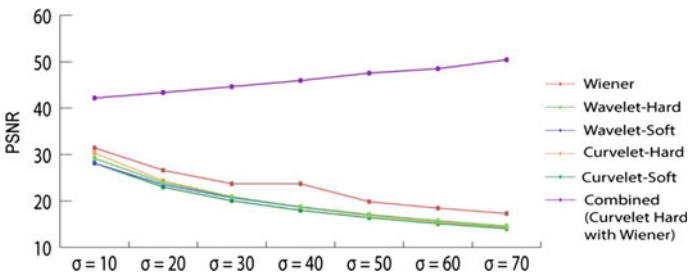

Fig. 1 PSNR values of MRI brain image

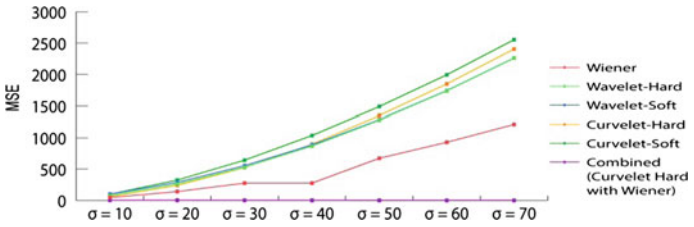

Fig. 2 MSE values of MRI brain image

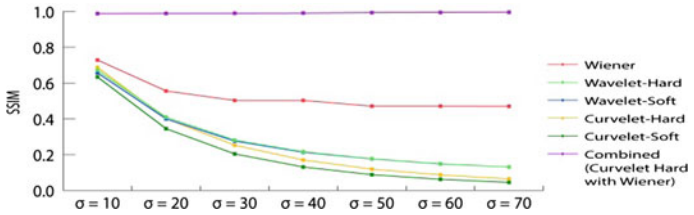

Fig. 3 SSIM values of MRI brain image

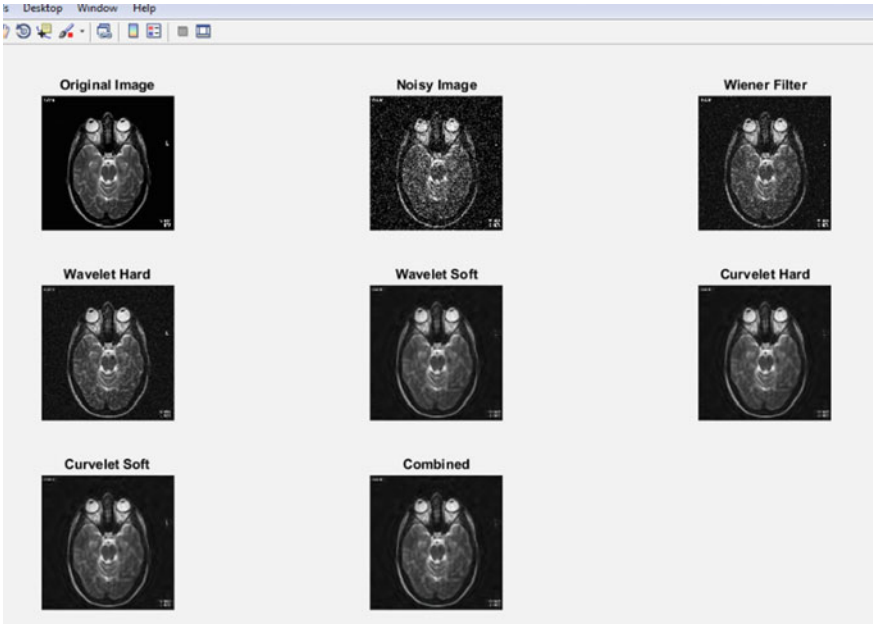

Fig. 4 Experimental results of MRI brain image denoising (where $\sigma = 40$)

50, 60, 70. The noise level of the image gradually comes down for the high PSNR value and the low MSE value. We have analysed that the combined method of curvelet with Weiner filter gives the higher PSNR and SSIM value and lower MSE value compared to other techniques. These are represented graphically in Figs. 1, 2, and 3, whereas in Fig. 4, the noisy image and resulting images of different methods corrupted by Gaussian noise with $\sigma = 40$ are shown. The visual quality of the image also becomes better in this combined curvelet with Wiener filter technique.

8 Conclusion

In this paper, we have studied wavelet, curvelet, and proposed filtering method and their effect in terms of the considered assessment parameters. The experimental results show that curvelet based approach performs better than the wavelet-based method. It also clearly indicates that curvelet with Wiener filter method outperforms compared to the other denoising methods, i.e., Wiener, wavelet, and curvelet. Also, the combined method does a very good job even when the noise is high as revealed from the experimental results. The curvelet denoising method removes the noise mostly lying in low frequency subbands, but some of the white Gaussian noise is spread in high frequency subbands also. So Weiner filter combined with curvelet transform is used here to remove that residual noise to some extent and the results were satisfactory.

References

1. Huang, T., Yang, G., Tang, G.: A fast two-dimensional median filtering algorithm. IEEE Trans. Acoust. Speech Signal Process. **27**(1), 13–18 (1979)
2. Ney, H.: A dynamic programming technique for nonlinear smoothing. In: IEEE International Conference on ICASSP, pp. 62–65 (1981)
3. Saluja, R., Boyat, A.: Wavelet based image denoising using weighted highpass filtering coefficients and adaptive wiener filter. In IEEE International Conference on Computer, Communication and Control (IC4-2015) (2015)
4. Boulfelfel, D., Rangayyan, R.M., Hahn, L.J., Kloiber, R.: Three dimensional restoration of single photon emission computed tomography images. IEEE Trans. Nucl. Sci. **41**(5), 1746–1754 (1994)
5. Lang, M., Guo, H., Odegard, J.E.: Noise reduction using an undecimated discrete wavelet transform. IEEE Signal Process. Lett. **3**, 10–12 (1995)
6. Chang, S.G., Yu, B., Vetterli, M.: Adaptive wavelet thresholding for image denoising and compression. IEEE Trans. Image Process **9**, 1532–1546 (2000)
7. Mojsilovic, A., Popovic, M., Sevic, D.: Classification of the ultrasound liver images with the 2nx1-d wavelet transform. In: Proceedings of IEEE International Conference Image Proceedings, vol. 1, pp. 367–370 (1996)
8. Donoho, D.L., Johnstone, I.M.: Ideal spatial adaptation via wavelet shrinkage. Biomefrika **81**, 425–455 (1994)
9. Donoho, D.L.: De-noising by soft thresholding. IEEE Trans. Inf. Theory **41**(3), 613–627 (1995)

10. Donoho, D.L., Johnstone, I.M.: Adapting to unknown smoothness via wavelet shrinkage. J. Am. Stat. Assoc. **90**, 1200–1224 (1995)
11. Stein, C.M.: Estimation of mean of a multivariate normal distribution. Ann. Stat. **9**, 1135–1151 (1981)
12. Zhang, X.: A denoising approach via wavelet domain diffusion and image domain diffusion. Multimedia Tools Appl. 1–17 (2016)
13. Candes, E.J., Donoho, D.L.: Ridgelets: a key to higher-dimensional intermittency? Phil. Trans. R. Soc. Lond. A **357**, 2495–2509 (1999)
14. Starck, J.L., Candes, E.J., Donoho, D.L.: The curvelet transform for image denoising. IEEE Trans. Image Process. **11**, 670–684 (2002)
15. Ulfarsson, M.O., Sveinsson, J.R., Benediktsson, J.A.: Speckle reduction of SAR images in the curvelet domain. In: Proceeding of the International Geoscience and Remote Sensing (IGARSS), vol. 1, pp. 315–317 (2002)
16. Liu, Y., Liu, Y.: Study on the basic principle and image denoising realization method of curvelet transform. In: International Conference on Multimedia Technology, pp. 1–4 (2010)
17. Ali, F.E., El-Dokany, I.M., Saad, A.A., El-Samie, F.E.A.: Fusion of MR and CT images using the curvelet transform. In: National Radio Science Conference, pp. 1–8 (2008). doi:10.1109/NRSC.2008.4542354
18. Candes, E.J., Demanet L., Donoho D.L., Ying, L. http://www.curvelet.org/

Epileptic Seizure Detection from EEG Signals Using Best Feature Subsets Based on Estimation of Mutual Information for Support Vector Machines and Naïve Bayes Classifiers

A. Sharmila and P. Geethanjali

Abstract The detection of epileptic abnormality from electroencephalogram (EEG) signals is achieved using pattern recognition system. In this work, to distinguish the epileptic seizure from normal EEG signal, pattern recognition is applied. Novel pattern recognition is studied with the conventional features which are extracted from discrete wavelet transform (DWT) sub-bands D3-D5 and A5 to detect epileptic seizure with support vector machine (SVM) and naïve Bayes (NB) classifier for 14 varying combinations of set A to D with set E. The open source EEG data which is provided by University of Bonn, Germany, and Christian Medical College and Hospital (CMCH), India, are used in this work. Further, the DWT coefficients obtained from D3-D5 to A5 sub-bands increases the computational burden of the classifier. So, feature selection based on the estimation of mutual information theory is applied to the DWT coefficients to obtain significant features required for the classifier to get better accuracy with lesser computational burden. The results show that SVM performs well for 9 data sets and NB performs better for 4 varying data sets. However, SVM and NB performed equally well in differentiating normal open EEG and epileptic data and afford an accuracy of 100%. In using CMCH data, SVM provides 100% accuracy with only top 2 ranked features.

Keywords Electroencephalogram (EEG) · Epilepsy
Discrete wavelet transform (DWT) · Mutual information (MI)
Naïve Bayes (NB) · Support vector machine (SVM)

A. Sharmila · P. Geethanjali (✉)
School of Electrical Engineering, Vellore Institute of Technology University, Vellore, India
e-mail: pgeethanjali@vit.ac.in

A. Sharmila
e-mail: asharmila@vit.ac.in

A. Konkani et al. (eds.), *Advances in Systems, Control and Automation*,
Lecture Notes in Electrical Engineering 442, https://doi.org/10.1007/978-981-10-4762-6_56

1 Introduction

A valuable tool which is proven in the study of conditions whose special effects are perceptible in the electrical brain activity is an electroencephalogram (EEG). Epilepsy is a condition which is characterized by spatially well-localized occurrence or prevalent transient recurrent seizures observable in the EEG [1]. Nearly, 1% of world population grieves from epilepsy, and it is one of the most common neurological disorders [2]. Owing to the difficulty in seizures prediction, the epilepsy study implicates that recording of the EEG over extensive periods of a few days continuously. Therefore, an expert must visually analyze huge number of data to detect the activity associated to epilepsy. To assist the experts in this long and tiresome process, over the years several attempts have been made to improve computerized epileptic seizure detection systems. In these systems, different techniques have been taken with varying degrees of success.

The main aim of this study is to recognize a pattern recognition scheme which is based on best feature subset using estimation of mutual information theory for efficient seizure detection with NB and SVM classifier with most relevant features. In this work, for first time, an attempt has been made to use the 6 varying data set combinations such as AC-E, AD-E, BC-E, BD-E, and ABC-E. The study presented here inspects both openly existing five EEG data sets A, B, C, D, and E provided by Department of Epileptology at University of Bonn, Germany [3] and the data sets of normal and epileptic patients which have been provided by Department of neuroscience, CMCH, India. Further, in this study, signals have been decomposed into various sub-bands frequencies using discrete wavelet transform (DWT). The three statistical features such as mean absolute value (MAV), standard deviation (SD), and average power (AVP) were derived from D3-D5 and A5 of DWT coefficients. With the intention of avoiding the redundancy of features, the derived features are ranked and studied using NB and SVM classifier based on top ranked features using feature selection based on mutual information theory to differentiate the epileptic signal from non-epileptic signals.

1.1 EEG Data Segmentation

In this work, open source EEG database [3] which is provided by University of Bonn, Germany, has been used. Also, the EEG data consists of 12 normal and 12 epileptic patients acquired for the duration of 26 s from 29 channels which is provided by Department of Neuroscience, CMCH, India has been used. The digitized data has a sampling rate of 500 Hz, and it is filtered using band-pass filter with the cut-off frequencies of 0.53–100 Hz. In this study, 13,000 samples are segmented into 6 equal data segments of size 2000 samples; in which, the remaining samples are discarded in each channel data. Thus, a total of 72 segments are attained from 29 channels data for each normal subject and epileptic patients.

1.2 Discrete Wavelet Transform (DWT)

Since the EEG signals are non-stationary, it is difficult to capture frequency content with time of actions, so in this work, fast Fourier transform (FFT) and time domain analysis are not preferred. The time-frequency representation using discrete wavelet transform is preferred in this work to capture frequency content with the time of occurrence. Five-level wavelet decomposition is done, and statistical features such as mean absolute value (MAV), standard deviation (SD), and average power (AVP) which are extracted from the DWT coefficients such as D3, D4, D5, and A5 are considered in this work, because utmost the frequency content necessary for analyzing the epileptic seizure signal is available in that sub-bands [4].

2 Feature Selection and Ranking

Certain features which are extracted from the DWT coefficients might be redundant, and hence, they increase the classifier computational burden even if not providing the information useful for classification [5]. So, in this work, to avoid taking redundant features applied to the classifier, a feature selection based on mutual information (MI) which provides the top significance features based on ranking is chosen [6]. The estimation of mutual information between features and associated class labels using quantized feature space has been employed.

2.1 Classification

The necessity of the classifier in this pattern recognition system is to detect the epileptic seizure in EEG data with NB and SVM classifier. These classifiers are used to categorize the epileptic seizure EEG from the other EEG using the derived DWT statistical features obtained based on feature ranking. A comparison has been done between the NB and SVM classifiers with top ranked to last ranked features. The classifiers are assessed using accuracy, sensitivity, and specificity. Lesser training data is required for classification using NB than SVM.

3 Results

This main goal of this pattern recognition study is to detect epileptic seizure from the EEG signals based on feature selection with relevant leading ranked features. In this work, pattern recognition system has been developed based on best MAV, AVP, SD features subsets from D3-D5 to A5. In SVM, 60% of data is used for

training and 40% of data is used for testing data. Whereas, in NB, 20% of data is used for training and 80% of data is used for testing data in all the 14 varying combinations.

Table 1 shows the classification table of NB and SVM for the ranked features in the descending order, and Table 2 shows the comparison of these NB and SVM classifiers with highest ranked features. For all the 14 data sets combinations, the first and second ranking features are applied to the classifier, then the next two ranked i.e. in the order of 4, 6, 8, 10, and 12 features are applied to classifiers. The performance of NB and SVM is studied using statistical parameters such as classification accuracy (CA), sensitivity (SEN), and specificity (SPEC). Upon feature selection, the NB performance could be improved with lesser training data. In the data set combination A-E, the leading 10 ranked features provide 100% classification accuracy with NB and the ranked features such as 11 and 12 are not essential for this data set classification, and so it is not required for the classifier, and therefore, these features are neglected. In case of SVM, with the all 12 ranked features, 100% CA is attained.

In using the B-E data set combination, the highest CA of 99.58% is obtained with NB for the leading 6 ranking features and with SVM, the highest CA of 99.12% is achieved using the leading four ranking features. In using the C-E data set combination, highest CA of 99.12% is achieved with SVM using the leading ten ranked features, and the highest CA of 99.58% is achieved with NB using all 12 ranking features. In using data sets combination D-E, with SVM, the highest CA of 97% is attained for leading four ranked features and the highest CA of 93.5% is attained with NB using the leading two ranked features. So, to classify the data set D-E, NB requires features whereas SVM requires 4 features. In the data set combinations AB-E, CA of 99.67% is attained with leading 6 ranked features with NB, and CA of 99.61% is achieved with SVM for only leading 2 ranked features. In case of using the data set combination AC-E, CA of 99.55% is accomplished with the leading 10 features with NB and with SVM, CA of 99.41% is achieved with leading 10 ranked features. In the data set combination AD-E, the CA of 97.83% is achieved with SVM, and it is 96.67% for only leading 2 ranked features with NB. The other features are not required for the classifiers and therefore it is neglected.

In case of data set combination BC-E, highest CA of 97.94% is attained for leading 4 ranked features with NB and it is 98.33% with SVM for leading 4 ranked features. In case of BD-E data set combination, the highest CA of 95.5% is attained with SVM for leading 10 ranked features and it is 91.44% with NB for leading 8 ranked features. In the data set CD-E combination, using leading 4 ranked features, the highest CA of 96.19% is achieved with NB and it is 97.58% with SVM for only leading 2 ranked features. In the data set combinations ABC-E, the highest CA of 98.58% is attained with NB for leading 6 ranked features, and with SVM, it is 98.81% for all the 12 ranked features. In the data set ACD-E combination, the highest CA of 97.62% is achieved with NB for leading 4 ranked features and CA 98.06% is attained with SVM for the leading 2 ranked features. In the data set BCD-E combination, the highest CA of 94.04% is attained with NB for leading 4 ranked features and it is 96.68% with SVM for leading 8 ranked features. In case of

Table 1 Classification table of NB and SVM for the ranked features in descending order

Datasets	Total No. of ranked feature	NB			SVM		
		CA (%)	SEN (%)	SPEC (%)	CA (%)	SEN (%)	SPEC (%)
A-E	2	99.75	100	99.5	**99**	98.68	100
	4	99.83	100	99.66	99.5	99	100
	6	99.91	100	99.83	99.5	99.17	100
	8	99.91	100	99.83	99.5	99.17	100
	10	**100**	100	100	99.75	100	99.5
	12	100	100	100	**100**	100	100
B-E	2	99.25	99.33	99.16	98.37	100	96.8
	4	99.5	99.66	99.33	**99.12**	100	98.2
	6	**99.58**	99.5	99.66	98.87	100	97.7
	8	99.41	99	99.83	98.87	100	97.7
	10	99.41	98.84	100	98.25	100	96.6
	12	99.33	98.68	100	98.25	100	96.6
C-E	2	98.58	97.86	99.32	98.37	97.77	98.9
	4	99.25	98.84	99.66	98.75	99.24	98.2
	6	99.16	98.67	99.66	98.5	99.23	97.7
	8	99	98.35	99.66	98.25	99.23	97.3
	10	99.16	98.67	99.66	**99.12**	99.24	99
	12	**99.58**	99.66	99.5	99.25	99.25	99.2
D-E	2	**93.5**	89.66	98.15	96.87	96.52	97.2
	4	92.08	87.18	98.46	**97**	96.3	97.7
	6	91.25	85.92	98.43	96.12	95.11	97.1
	8	90.25	84.45	98.39	96.12	95.33	96.9
	10	89.91	83.97	98.37	96.12	95.33	96.9
	12	89.75	83.73	98.37	95.62	93.76	97.6
AB-E	2	99.16	99.91	97.71	**99.16**	99.74	98.8
	4	99.44	100	98.36	99.16	99.74	98.8
	6	**99.67**	99.91	99.17	99.16	99.74	98.8
	8	99.5	99.74	99	99.08	100	98.6
	10	99.11	99.66	98.02	98.91	100	98.4
	12	99.33	99.74	98.51	98.91	100	98.4

(continued)

Table 1 continued

Datasets	Total No. of ranked feature	NB			SVM		
		CA (%)	SEN (%)	SPEC (%)	CA (%)	SEN (%)	SPE C (%)
AC-E	2	99.16	99	99.32	98.75	99.23	98.51
	4	99	98.92	99.15	99.25	99.24	99.25
	6	99.38	99.33	99.49	99.25	99.24	99.25
	8	99.48	99.41	99.49	99.25	99.24	99.25
	10	**99.55**	99.58	99.49	**99.41**	98.75	99.74
	12	99.55	99.91	98.84	99.25	98.27	99.74
AD-E	2	**96.67**	96.04	98.04	**97.83**	95.83	98.86
	4	96.33	95.5	98.04	97.66	94.71	99.23
	6	96.16	95.42	97.83	97.25	93.58	99.22
	8	95.16	93.99	97.94	97	93.33	98.97
	10	94.67	93.53	97.36	97	93.33	98.97
	12	94.38	93.43	96.63	96.91	93.11	98.97
BC-E	2	89.38	88.07	93.05	97.41	97.92	97.17
	4	**97.94**	97.31	99.29	**98.33**	99.22	97.91
	6	99.71	99.91	99.28	98.33	99.22	97.91
	8	97.05	96.13	99.19	98.33	99.47	97.79
	10	97.27	96.52	99.28	98	99.21	97.43
	12	97.55	96.91	98.94	98.33	98.71	98.14
BD-E	2	89.05	86.73	96.32	93.75	89.15	96.17
	4	90.38	88.4	96.11	95.41	91.56	97.45
	6	91	88.4	97.19	95.33	91.54	97.32
	8	**91.44**	89.32	97.44	95.41	91.56	97.45
	10	91.44	89.32	97.44	**95.5**	91.58	97.57
	12	91.22	89.12	97.02	95.33	91.34	97.44
CD-E	2	96.55	95.96	97.82	**97.58**	94.48	99.23
	4	**96.19**	95.34	98.01	97.41	94.03	99.23
	6	95.27	94.07	98.13	97.08	93.14	99.22
	8	94.61	93.25	97.9	96.75	93.28	98.59
	10	94.38	93.09	97.52	97	93.75	98.72
	12	94.22	93.08	96.96	96.58	92.43	98.84
ABC-E	2	98.08	98.72	96.17	97.31	93.85	98.49
	4	98.54	98.78	97.8	98.37	97.22	98.75
	6	**98.58**	98.56	98.62	98.37	97.22	98.75
	8	98.21	98.56	97.13	98.43	97.7	98.67
	10	98.2	98.56	97.12	98.5	97.47	98.83
	12	98.5	98.89	97.31	**98.81**	97.98	99.08

Table 1 continued

Datasets	Total No. of ranked feature	NB			SVM		
		CA (%)	SEN (%)	SPEC (%)	CA (%)	SEN (%)	SPE C (%)
ACD-E	2	96.33	95.77	98.3	**98.06**	94.24	99.4
	4	**97.62**	97.54	97.88	97.93	93.38	99.5
	6	97.33	97.17	97.87	97.93	93.79	99.4
	8	96.91	96.9	96.92	97.75	93.12	99.4
	10	96.91	96.89	96.96	97.56	92.47	99.4
	12	96.37	96.47	96.05	97.43	92.23	99.3
BCD-E	2	93.04	92.72	94.27	95.18	89.1	97.3
	4	**94.04**	93.49	96.16	96.5	91.34	98.3
	6	93.67	93.23	94.77	96.5	91.34	98.3
	8	93.58	93.27	94.77	**96.68**	91.6	98.4
	10	93.7	93.23	95.53	96.62	91.38	98.4
	12	93.58	93.27	94.77	96.43	90.73	98.4
ABCD-E	2	95	95.18	94.17	96	87.2	98.4
	4	95.36	95.38	95.28	97.2	90.95	98.8
	6	**95.53**	95.53	95.5	97.25	90.78	98.9
	8	95.2	95.33	94.53	97.25	91.16	98.8
	10	95.1	95.47	93.3	**97.3**	91.19	98.9
	12	**95.1**	95.51	93.14	97	89.35	99.1

the data set ABCD-E combination, with SVM the highest CA of 97.3% is attained for leading 10 ranked features and it is 95.53% with NB for leading 6 ranked features. Moreover, the SVM affords better CA, SEN, and SPEC for leading 2 ranked features in using the data sets combinations such as AB-E, AD-E, CD-E, and ACD-E as shown in Table 2.

From Fig. 1, it is inferred that the average CA of SVM is 98.13% and it is 97.13% with NB for the leading ranked features. SVM is well performed for 9 varying data sets combinations, and NB is well performed for 4 varying data set combinations. In case of the data set combination A-E, NB and SVM performed equally with difference in the leading ranked features. In general, performance of the SVM is well performed to detect the epileptic seizure from EEG signals using best feature subsets based on mutual information theory. The leading ranked features which afford highest CA are the most relevant features for the classifiers.

In this work, an attempt has been made to use CMCH database, and the results of clinical inference are presented in Table 2. From 29 channels, a total of 348 features are extracted from the coefficients D3-D5 and A5 with 72 segments. Subsequently, because of 29 channel, there are larger number of features, so initially applied the feature selection method and obtained feature ranking for each individual features and the top ranked features in the order of 2, 4, 6, 8, 10, 12, and 14. The leading

Table 2 Classification table of NB and SVM for the leading 14 ranked features

Data sets	Total No. of ranked feature	Naïve Bayes			SVM		
		CA (%)	SEN (%)	SPEC (%)	CA (%)	SEN (%)	SPEC (%)
Normal subjects-Epileptic patients	2	97.61	100	95.45	94.44	100	90
	4	97.61	100	95.45	100	100	100
	6	97.61	100	95.45	100	100	100
	8	**98.86**	**100**	**97.67**	100	100	100
	10	98.86	100	97.67	100	100	100
	12	98.86	100	97.67	100	100	100
	14	98.86	100	97.67	100	100	100

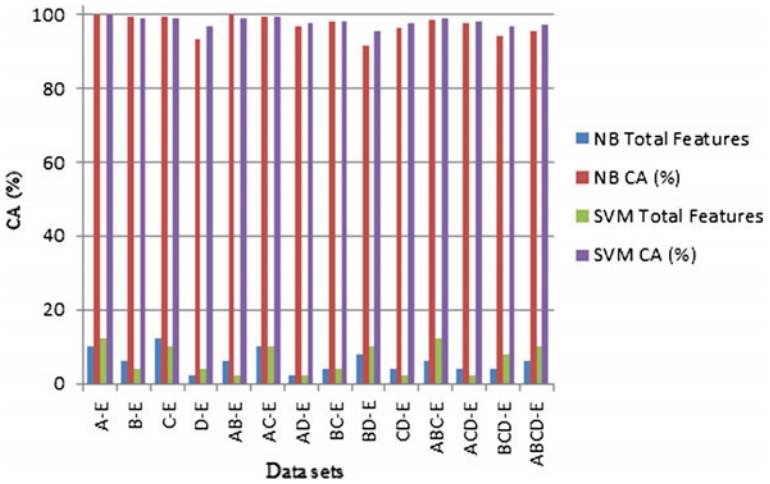

Fig. 1 Classification plot of NB and SVM (CA versus data sets)

ranked features are applied to NB and SVM classifier to achieve the highest CA as shown in Table 2.

It is observed from Table 2 that the highest CA of 100% is attained with SVM for leading 4 ranked features, and it is 98.61% with NB for leading 8 ranked features. Also, increase in the other leading ranked features up to 28 has not shown any improvement in the result of NB.

4 Conclusions

In this pattern recognition system, the EEG data from normal and epileptic subject has been analyzed to attain good accuracy with lesser time. The best subset statistical features of MAV, SD, and AVP derived from DWT coefficients based on mutual information are important in the detection of epileptic seizure. It has been inferred from the results that pattern recognition system attains highest accuracy of 100% in using NB and SVM for leading 10 and 12 ranked features for the data set combination A-E. In CMCH data set, an accuracy of 100% is obtained with SVM for only leading 4 ranked features and the highest accuracy of 98.86% is achieved with NB for leading 8 ranked features. This pattern recognition system based on the leading ranked statistical features from DWT achieves the best accuracy using SVM classifier for 9 data set combinations and attains best accuracy in NB for 4 data sets combination, and both SVM and NB provide better accuracy for 1 data set in using University of Bonn database. It is inferred that SVM is well performed with feature selection technique, and NB shows improved result with smaller training data.

References

1. Lehnertz, K.: Epilepsy and nonlinear dynamics. J. Biol. Phys. **34**, 253–266 (2008)
2. Duncan, J.S., Sander, J.W., Sisodiya, S.M., Walker, M.C.: Adult epilepsy. Lancet **367**, 1087–1100 (2006)
3. EEG Database from University of Bonn. Accessed 16 June 2013. http://epileptologie-bonn.de/cms/front_content.php?idcat=193
4. Subasi, A.: EEG signal classification using wavelet feature extraction and a mixture of expert model. Expert Syst. Appl. **32**(4), 1084–1093 (2007)
5. Acharya, U.R., VinithaSree, S., Suri, J.S.: Use of principal component analysis for automatic detection of epileptic EEG activities. Expert Syst. Appl. **39**(10), 9072–9078 (2012)
6. Pohjalainen, J., Okko, R., Serdar, K.: Feature selection methods and their combinations in high-dimensional classification of speaker likability, intelligibility and personality traits. Comput. Speech Lang. **29**(1), 145–171 (2015)

Intelligent Routing in MANET Using Self-Adaptive Genetic Algorithm

R.M. Nareshkumar, S. Phanikumar and Manoj Kumar Singh

Abstract At present, communication technology provides support for different varieties of mobile networks, and among them, mobile ad hoc network (MANET) is of prime importance and challenging. Topological change with time is the inherent characteristics in MANET. This occurs either to save the energy or mobility observed with nodes. Therefore, routing problem under MANET is also dynamic and can be formulated as a dynamic optimization problem. It is essential that the solution should have a high level of adaptability to define dynamic routing. In this paper, high level of adaptiveness has achieved by designing the different strategies under genetic algorithm like redefinition of solution population, small random perturbation, and sharing the gained knowledge to current solution. The proposed solution has achieved optimal routing in a very efficient way under dynamic topology.

Keywords Wireless sensor network · Routing · Energy efficiency
Evolutionary computation · Genetic algorithm

1 Introduction

In all types of networks, quality of routing solution is the prime deciding factor for overall network performance. Dynamic characteristics of topology in MANET transform the routing as a dynamic optimization problem. To get the best solution, it is necessary that high level of adaptiveness should be there. In an informal way,

R.M. Nareshkumar
GITAM University, Hyderabad, India
e-mail: nareshkumarmustary@gmail.com

S. Phanikumar
Department of Computer Engineering, GITAM University, Hyderabad, India
e-mail: phanikumar.s@gmail.com

M.K. Singh (✉)
Manuro Tech Research Pvt. Ltd., Bangalore, India
e-mail: mksingh@manuroresearch.com

A. Konkani et al. (eds.), *Advances in Systems, Control and Automation*,
Lecture Notes in Electrical Engineering 442, https://doi.org/10.1007/978-981-10-4762-6_57

routing problem under dynamic condition can be defined as: for a pair of nodes as source and destination in wireless network carries an upper bound of delay and requirement is to find a minimum cost path on a topology graph which is without loop. Either energy-saving perspective or nodes mobility, there is a change in topology or objective is to find quickly the new optimal minimum cost path which satisfies the delay constraint.

Mathematical formulation of the objective can be represented as: in MANET, $G(V, E)$. There is a request of unicast routing between a pair of nodes and has been an upper bound of delay Δ. Routing can be consider as finding a number of paths $\{O_i | i \in \{0, 1, \ldots\}\}$ sequentially over a set of graph $\{G_i | i \in \{0, 1, \ldots\}\}$, which must satisfy the delay constraint as given in (1) and carry the minimum cost path as given in (2).

$$\Delta(O_i) = \sum_{l \in O_i(s,r)} d_l \leq \Delta \tag{1}$$

$$\mathrm{CF}(O_i) = \mathrm{Min}_{O \in G_i} \left\{ \sum_{l \in O_i(s,r)} \mathrm{CF}_l \right\} \tag{2}$$

In practical aspect, dynamic condition of many systems is very natural, and achieving the optimal solution under the dynamic environment is a very challenging task. There is need to explore the changing landscape very quickly to have the optimal solution and track the change over the landscape. Natural computing methods are based on natural models, hence there is a high level of adaptiveness inherently exists. Among the various possibilities under natural computing methods like evolutionary computation, swarm intelligence, are well established and have shown their usefulness in various applications.

Due to a huge number of applications in practical life, numbers of researchers have given attention over the dynamic routing problem. Multiple path possibilities can be achieved through the multipath routing, and for MANET, environment-related issues have been discussed in [1]. To reduce the communication overhead and storage demand, [2] has proposed the Fuzzy logic-based routing solution with consideration of input parameters like delay, signal power, and mobility. Comparative performance analysis of routing protocol AODV and DSR has been presented in [3], and their applicability for MANET has also discussed. Routing which is based on trust has discussed in [4]. Forwarding ratio has been considered to estimate the direct trust, and indirect trust has been obtained from neighbor's recommendation. Based on clustering method, routing for mobile nodes has been discussed in [5]. For a multiple node pair as source and destination, end-to-end delay minimization method has been proposed in [6]. Black hole nodes detection or their effects on routing have been achieved through DSR-based routing in [7]. Achievement of optimal routing path through A-star evaluation function has been proposed in [8]. Swarm intelligence like ant colony has been applied in [9] to develop the routing algorithm for emergency-oriented wireless system. Energy-efficient routing algorithms can increase the life span of WSNs; hence it is

very important that routing solution should take care in the estimation of optimal path of routing. In [10], orientations toward homogeneous and heterogeneous WSNs-based classification of existing routing algorithms from energy efficiency perspective have been discussed.

2 Proposed Solution

To obtain minimum distance, we have designed various adaptive forms of genetic algorithms like redefinition of population in genetic algorithm (RGA), random perturbations in genetic algorithms (PGA), and knowledge-based genetic algorithms (KGA). In MANETs, there are a number of applications where dynamic topology exists, for example, in the case of track animals, soldier strategy in war field. In natural systems, evolution can be considered as the best example of adaptability, hence genetic algorithm platform has taken to develop the solutions, but the existing challenge is to find the optimal connectivity quickly for a change in topology. To handle all these issues, in this research, three different approaches have been developed: (a) apply a completely new solution population with event, (b) keep applying a small amount of perturbation in population, and (c) use the knowledge of some previous better solutions to the current population. To simulate the MANET, a defined range of area is decided, and nodes position can be represented through the uniformly distributed random number on X coordinate and Y coordinate direction. Connectivity between nodes is decided through the estimation of Euclidean distance on the communication range.

3 GA with Redefine Population on Time (RGA)

To handle the change, a completely new population, which has a high level of diversity introduced at the time of change, is observed. The pseudo-code for RGA has given below.

Pseudo-code for RGA
1. Initialization of population
2. Apply crossover and mutation operator to produce offspring.
3. Mixer population [MPOP] ← [Parent Pop; Offspring Pop]
4. Fitness estimation $(f_{vi}) \leftarrow f_{\boldsymbol{fun}}(MPOP)$
5. Next Generation population ← Tournament selection (f_{vi})
5. Topology change detection $\leftarrow f\left(f_{vi} - f_{v(i-1)}\right)$;
6. If change detected: Current Generation = Generate New population; Else Current Generation = Next Generation;
7. If termination does not occur, Go to step 1.

4 GA with Continuous Perturbation (PGA)

A new member is always incorporated in the population of each iteration to have better diversity so that under dynamic condition a better solution could explore. With this approach, it is possible to handle dynamic conditions faster and free from event detection procedure. The pseudo-code for PGA has given below.

Pseudo-code for PGA
1. Initialization of population;
2. Apply crossover and mutation operator to produce offsprings;
3. Mixer population [MPOP] ← [Parent Pop; Offspring Pop];
4. Fitness estimation $(f_{vi}) \leftarrow f_{fun}(MPOP)$
5. Next Generation population [NPOP] ← Tournament selection (f_{vi});
6. $pos_{\min} = f_{\min}(NPOP)$
7. $NPOP(POS)$ = A new solution;
8. If termination does not occur, Go to step 1.

5 GA with Sharing Knowledge (KGA)

If there is a possibility to use the knowledge available with some previous generation best solutions to current generation, there is a very good chance to handle dynamic topology in an efficient manner because they may have the knowledge to handle the change in the topology with the time, in result the optimal solutions can be achieved with very less time and chances of failure are minimized. The pseudo-code for KGA has given below.

Pseudo-code for KGA
1. Initialization of population
2. Apply crossover and mutation operator to produce offsprings.
3. Mixer population [MPOP] ← [Parent Pop; Offspring Pop]
4. Fitness estimation $(f_{vi}) \leftarrow f_{\text{fun}}(\text{MPOP})$
5. Next Generation population [NPOP] ← Tournament selection (f_{vi})
6. Store the best members from NPOP in SB_i
7. Replace the weaker solution from NPOP by solution available in $SB_i - 1$
8. If termination does not occur, Go to step 1.

6 Experimental Design

Simulation experiments have done in MATLAB environment. A set of 50 nodes has been applied in experiment in square region, having area of 200 × 200 square unit. The communication range of each node has taken as 50 units and after estimation of Euclidean distance from each node to all other nodes, topology connectivity decides. For all the experimental case, size of population is taken as 50. Crossover has applied with 1 probability if it is feasible else equal to zero. Mutation has applied with 0.1 probabilities.

6.1 Chromosome Representation

We have applied a constraint-based definition in an initial population definition of routing path to a desired source and destination. Following steps have been applied in the representation of chromosomes:

(i) Define the source sensor as starting number.
(ii) Obtain the possible neighbors.
(iii) Apply uniform random process to select a connected sensor among possible neighbors.
(iv) If selected node is not a destination sensor, add the selected sensor as the next node in routing path.
(v) Repeat the process from (ii), until the destination source does not meet.

6.2 Connectivity-Based Crossover Operator and Mutation

In MANETs, it is not possible to define the crossover over the length of solution at any arbitrary position, because if there is no connectivity exists with immediate neighbors, it will become unfeasible solution. It is again not possible to compensate the quality of unfeasibility through any penalty approach, as it applies for most other types of problem. We have designed the crossover operation through an attractor approach, which is not based on similar position in solution, instead it is based on node connectivity, where possible distribution of connectivity is exchanged. These attractors are the common nodes available in both parents' solutions. Among possible locations of attractors, one location is selected randomly to form the offspring.

As shown in Fig. 1, parents P1 and P2 have taken for crossover. There are two attractors available in chromosomes (N3, N2) and (N2, N6), where the first position (like N3) is the position from 1st parent and a second position (N2) is the position from second parent. Other positions are not allowed to crossover, because they will

(a)

	Source	N1	N2	N3	N4	N5	N6	Destination	Chrom.Length
P1	1	6	5	8	7	13	11	15	8
P2	1	9	8	10	2	12	5	15	8

(b)

										Chrom.Length
O1	1	6	5	8	10	2	12	5	15	9
O2	1	9	8	7	13	11	15			7

Fig. 1 Connectivity-based crossover, **a** parents selected for crossover, **b** generated offsprings after crossover operation

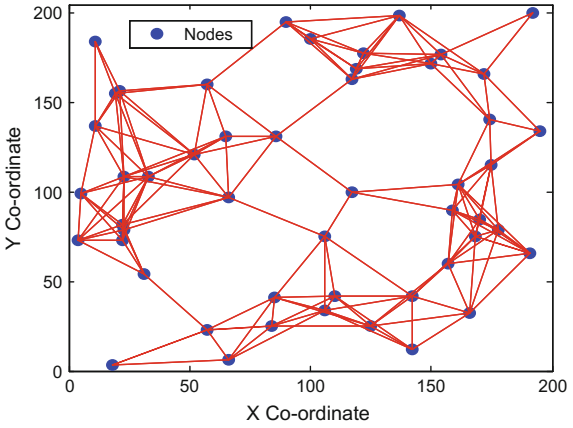

Fig. 2 Simulated network with 50 nodes

make the solution unfeasible. It is also observed that crossover can cause the change in chromosome length. In this paper, possible domain of change under mutation with each node is the possible number of nodes, which are connected with their neighbors only.

In the simulated network as shown in Fig. 2, three different topology changes have been applied by different events. Topology corresponding to third event has shown in Fig. 3. These topology changes have occurred at the 10th, 20th, and 30th unit of time. Different algorithms, RGA, PGA, and KGA, have been applied to find the routing path between node numbers 11 and 49. Topological changes have been applied at the same time independently for all algorithms. Corresponding to topology 3, convergence characteristics have shown in Figs. 4, 5, and 6. Performances of obtaining routing path for all three topologies corresponding to different events have shown in Table 1. It is observed that every time there is the largest cost of the route appeared by RGA and more time required achieving the final value. Performances of KGA are always better in terms of low-cost route and time required to get new route once changes take place in topology.

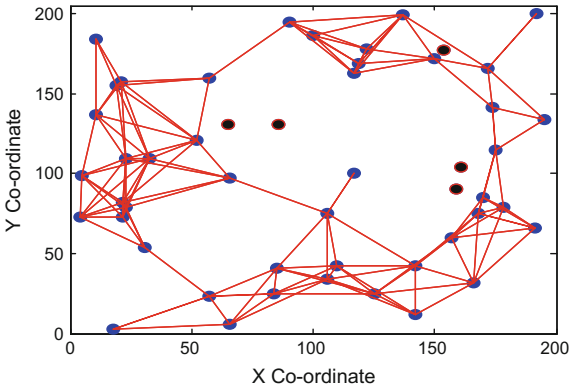

Fig. 3 Network with changed topology as 3rd event

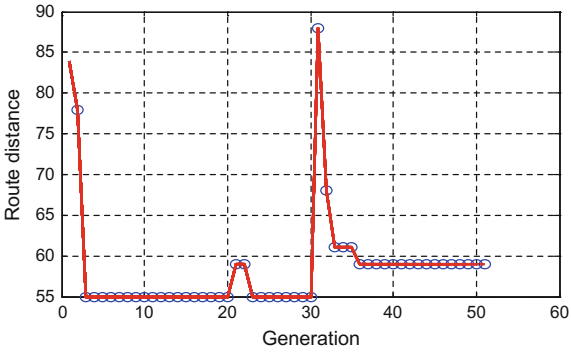

Fig. 4 Convergence characteristics of RGA-based routing

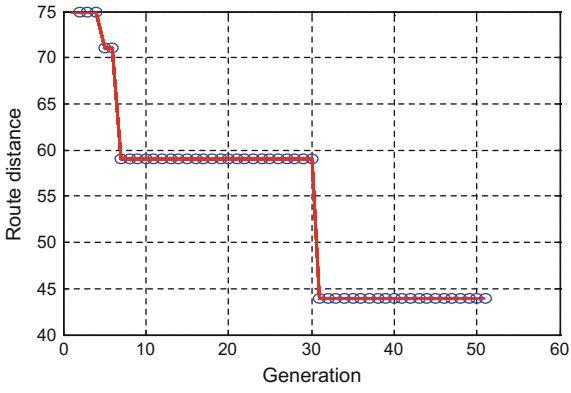

Fig. 5 Convergence characteristics of PGA-based routing

It is observed by experiments that RGA may take a longer period to generate optimal solutions, and there may be a chance in between topology changes further which makes the situation worst; obtained results are no way useful. If there is a

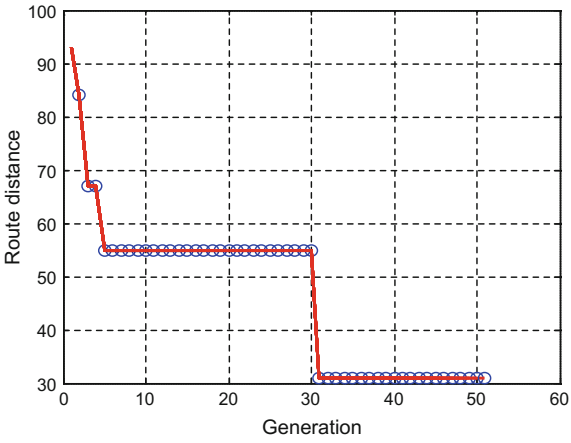

Fig. 6 Convergence characteristics of KGA-based routing

Table 1 Performances over different topologies of the network created by different events

Topology with events	Method	Pre-event cost value	At event cost value	Maximum cost after post-event	Stable cost value after post-event	Stability period
Event1	RGA	59	59	81	61	5
Event1	PGA	59	59	59	59	0
Event1	KGA	55	55	55	55	0
Event2	RGA	61	61	73	55	6
Event2	PGA	59	59	59	59	0
Event2	KGA	55	55	55	55	0
Event3	RGA	55	55	67	61	5
Event3	PGA	59	59	44	44	1
Event3	KGA	55	55	31	31	1

high level of change occurs in topology, it may difficult to find the optimal solutions within a time span by the PGA. KGA has shown the superior results in all cases in terms of the high level of adaptive characteristics and faster exploration of the global solution. This is possible because of experience from the past event helps to handle the new event better manner, if it occurs.

7 Conclusion

The objective of achieving the optimal routing in dynamic environment of MANET has obtained from various different variations of adaptiveness under genetic algorithms. Core requirements of routing under MANET of getting the global solution

of desired route between two nodes and settle down faster if there is any change occurred in topology has achieved. In this research, three different concepts have been proposed to increase the adaptability under dynamic topology environment. Knowledge sharing-based adaptive genetic algorithm has shown outstanding performance.

Acknowledgement This research has done in Manuro Tech Research Pvt. Ltd., Bangalore, India, under Innovative solution for Future Technology program.

References

1. Mueller, S., Tsang, R.P., Ghosal, D.: Multipath routing in mobile ad hoc networks: issues and challenges. In: Performance Tools and Applications to Networked Systems, vol. 2965, pp. 209–234. LNCS (2004)
2. Gupta, S., Bharti, P.K., Choudhary, V.: Fuzzy logic based routing algorithm for mobile ad hoc networks. In: High Performance Architecture and Grid Computing, vol. 169, pp. 574–579. Communications in Computer and Information Science (2011)
3. Singh, S., Kush, A.: Evaluation of routing schemes for MANET. In: High Performance Architecture and Grid Computing, vol. 169, pp. 568–573. Communications in Computer and Information Science (2011)
4. Sardar, M., Majumder, K.: A new trust based secure routing scheme in MANET. In: Proceedings of the International Conference on Frontiers of Intelligent Computing: Theory and Applications (FICTA), vol. 247, pp. 321–328. ASIC (2013)
5. Vinutha, C.B., Nalini, N.: Energy aware optimal clustering and reliable routing based on Markov model. In: Wireless Sensor Networks, WiSPNET (2016)
6. Sen, T.K., Mahobiya, C.: Delay optimal multicast routing for wireless ad-hoc networks. In: IEEE International Conference on Engineering and Technology (ICETECH), pp. 575–580 (2016)
7. Deshmukh, S.R., Chatur, P.N.: Secure routing to avoid black hole affected routes in MANET. In: Symposium on Colossal Data Analysis and Networking (2016)
8. Septiana, R., Soesanti, I., Setiawan, N.A.: Evaluation function effectiveness in wireless sensor network routing using A-star algorithm. In: 4th International Conference on Cyber and IT Service Management (2016)
9. Chenguang, H., Tingting, L., Weixiao, M., Chunpeng, L.: An ant colony-based direct communication model routing algorithm for wireless emergency communications system. In: International Wireless Communications and Mobile Computing Conference (2016)
10. Yan, J., Zhou, M., Ding, Z.: Recent advances in energy-efficient routing protocols for wireless sensor networks: a review. IEEE Access **4**, 5673–5686 (2016)

Comparison of Various Decoding Algorithms for EG-Low Density Parity Check Codes

J. Chinna Babu, C. Chinnapu Reddy and M.N. Giri Prasad

Abstract he latest advancements in low-density parity-check (LDPC) codes have been resulted in reducing the decoding complexity. Hence, these codes have excelled over turbo codes, BCH codes, and linear block codes in terms of evaluating the performance in higher decoding rate; hence, these decodable codes are the trending topic in coding theory of signals. Construction of LDPC codes is being elaborated in this proposed paper which further helps to study decoding and encoding of these binary and non-binary low-density parity-check codes, respectively. In this proposed design architecture, we have considered the SBF and MLDD algorithms employed here utilize reliability estimation to improve error performance and it has advantages over bit flipping (BF) algorithms. This algorithm can be improved with still more security level by having a trade-off between performance and data transmission. It can also be enhanced by implementing it in real-time applications for data decoding and correction, for smaller-size datum.

Keywords LDPC codes · Decoding algorithm · Shannon limit · Delay
SBF · MLDD

1 Introduction

For error-free transmission of data from source to its destination over a noisy channel, error coding is needed. Error coding uses mathematical formulae to encode the data for error-free transmission and the resultant code word is decoded at the

J. Chinna Babu (✉)
JNTUA, Anantapur, Andhra Pradesh, India
e-mail: jchinnababu@gmail.com

C. Chinnapu Reddy
O/o CTE, SPFU AP, TEQIP-II, Vijayawada, Andhra Pradesh, India
e-mail: ccreddyece@gmail.com

M.N. Giri Prasad
Department of ECE, JNTUA, Anantapur, Andhra Pradesh, India
e-mail: mahendragiri1960@gmail.com

A. Konkani et al. (eds.), *Advances in Systems, Control and Automation*,
Lecture Notes in Electrical Engineering 442, https://doi.org/10.1007/978-981-10-4762-6_58

receiver to obtain the relevant information. Various error decoding schemes are selected, depends on the occurance of error types. Based on the rate of occurance of errors, we may consider the communication channel. This Channel deals that, whether the data retransmission is possible or not [1].

LDPC codes are the linear error decoding and correcting codes, where LDPC codes represent low-density parity-check codes. Here, the term 'low density' replies to one of the characteristic parity-check matrix H, which may contain only few numbers of ones in comparison with zeros. These low-density parity-check codes are undoubtedly the best error detection and correction codes in existence at present scenario. The parity data or redundant data is added to the original message so that the original message can be decoded at the receiver end without the need for the data retransmission and also the errors can be detected and corrected if any errors are present. Such codes are called error-correcting codes (ECCs) or forward error-correcting codes (FECs) [2–4].

Error-correcting codes are usually classified as two types:

- Convolution codes: The codes which are using convolution process are being processed based on the bit after bit mechanism.
- Block codes: The codes which are using blocking process are being processed based on the block after block mechanism.

LDPC codes are defined by a sparse parity-check matrix and also by Tanner graph.

2 Matrix Representation

Hence, these LDPC codes which are proposed are functionally represented by a sparse matrix, which is having parity information. This well-defined matrix represented by H is generated by a random process and it was subjected to the sparse constraints. An LDPC code was defined by the parity-check H-matrix which indicates null space and it was defined with the following specified properties.

- Each of the rows may contain p many number of ones.
- Each of the columns may contain r many number of zeros.
- The number of ones in among any two preceded columns which are common, denoted by lambda and it is not greater than one.
- Both of these numbers of ones p and zeros r are less, compared with the variable code length size and number of the available rows in parity matrix H. Since these numbers of ones p and zeros r are very less, sparse parity matrix H has less number of ones, and therefore, it is a sparse parity-check matrix. Hence, the code is specified by a parity-based matrix H and it is often known as a low-density parity-check code, and it can be specified by a matrix.

For example:

$$H = \begin{bmatrix} 0 & 1 & 0 & 1 & 1 & 0 & 0 & 1 \\ 1 & 1 & 1 & 0 & 0 & 1 & 0 & 0 \\ 0 & 0 & 1 & 0 & 0 & 1 & 1 & 1 \\ 1 & 0 & 0 & 1 & 1 & 0 & 1 & 0 \end{bmatrix}$$

The size of the above matrix is $n \times k = 8 \times 4$, which means there are 'n' number of variable nodes and 'k' number of check nodes.

2.1 Tanner Graph Representation

The above mentioned graph contains number of variable nodes are 'n' and number of check nodes are 'k'. The connection between variable node and check node exists, if the element of nth column and kth row of H-matrix has one.

There are two types of LDPC codes:

1. Binary LDPC codes: These are irregular low-density parity-check codes as the row weights and column weights are different.
2. Non-binary LDPC codes: All the rows and columns have equal weights. Hence, these are regular LDPC codes.

The above matrix is considered as (w_r, k) where $w_r = 2$ is row weight and $k = 3$. Figure 1 indicates the parity-check matrix H with dimensions $n \times m$. This matrix is represented for a (8, 4) code. The Tanner graph is a bipartite representation of H-matrix, where c-nodes (f_0, f_1, f_2, f_3) are called check nodes or node constraints and v-nodes (c_0-c_7) are called variable nodes. This check node indicates f_i, and it is mapped to the v-node c_j, if the element h_{ij} of low-density parity-check matrix H is one [5–8].

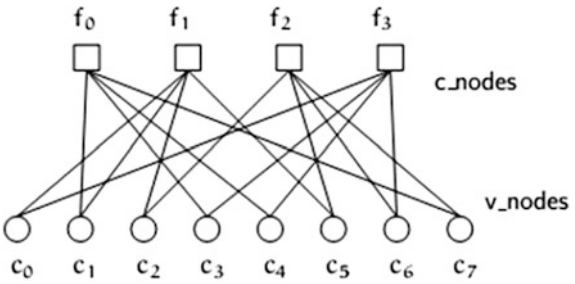

Fig. 1 Graphical representation of H-matrix for the above example

3 Decoding of LDPC Codes

Many algorithms are developed for decoding and encoding of both binary and non-binary LDPC codes based on soft-decision-decoding (SDD) and hard-decision-decoding (HDD) schemes. The generic block diagram of decoding algorithm for LDPC codes is as shown in Fig. 2 [1, 2].

The basic procedure for decoding of low-density codes includes the following steps.

- Check node issues some constraints to the variable *v*-nodes.
- If the variable *v*-nodes satisfy these constraints, the input code to decoder is assumed to be true and transmits that data to the output.
- Else the error is detected and corrected and is then passed to the output.

The scheme used for decoding and encoding of LDPC codes is an iterative process. The algorithms considered in this paper for comparison are soft-bit flipping (SBF) algorithm, majority logic decoder/detector (MLDD) algorithm.

3.1 Soft-Bit Flipping (SBF) Decoder Algorithm

Soft-bit flipping algorithm is the most efficient one among several decoding algorithms. This SBF algorithm has good error performance and it has less hardware complexity.

The following steps give the procedure for decoding of LDPC codes using SBF algorithm

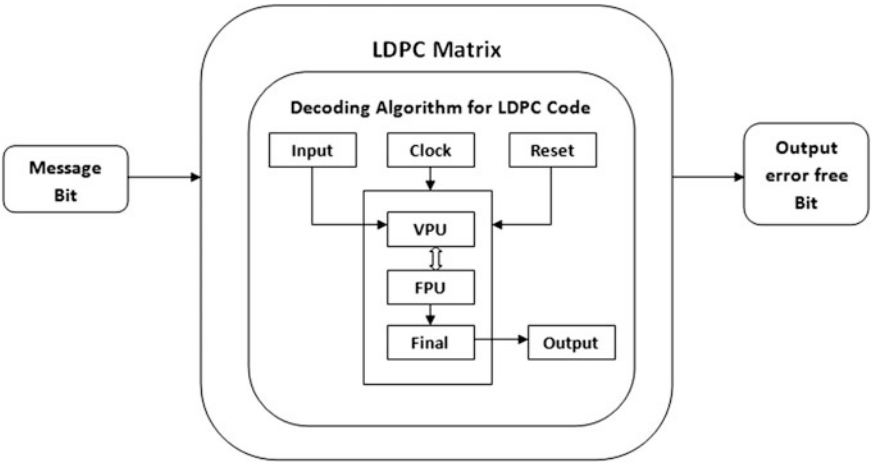

Fig. 2 Generic block diagram of decoder for low-density parity-check codes

1. The parity-check sums are the constraints made by check nodes to be satisfied by variable nodes. The resulting bits are called syndrome bits. If all the computed syndrome bits are zero represents that all parity-check equations are to be satisfied, then the decoding process was halted.
2. The syndrome bits which resulted ones are detected for each of the bit code position, denotes f_i where $i = 0$ to $n - 1$.
3. The proportional set of bits Ω with maximum value of (f_i) should be identified.
4. The proportional bits in set Ω should be complemented.
5. Steps from 1 to 4 should be repeated until entire syndrome bits become zero. At this stage, the iterations are stopped.

In this paper, Fig. 3 shows the serial hybrid SBF decoder. The decoder consists of buffer input (which holds the code bits), a rollback buffer (which holds the result of flipped bits), a buffer output (holds the error-free code bits), check nodes, variable nodes, a flip unit (flips the bits when the constraints are not met), a variable node processing unit (VPU), and a check node processing unit (CPU), where shift registers (shifts the bits as the iteration progresses) are used [9–12].

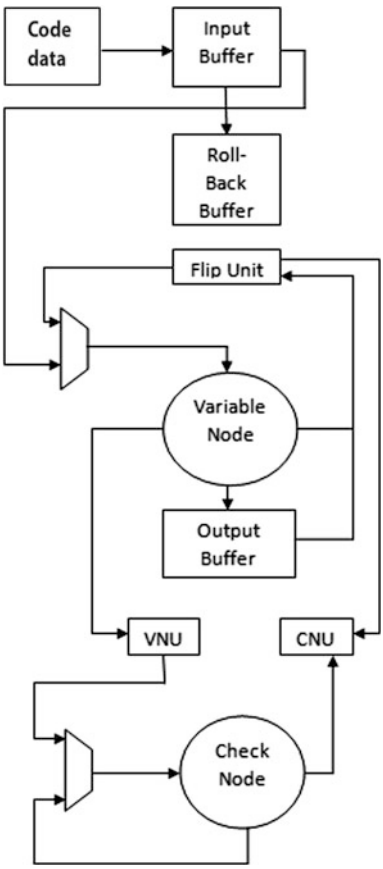

Fig. 3 Block diagram of SBF decoder

3.2 *Majority Logic Decoder/Detector (MLDD) Algorithm*

Majority logic decoder/detector algorithm acts as an error detector and corrector with reduced number of iterations than MLD algorithm. This algorithm is applicable for binary LDPC codes [13–15] (Fig. 4).

The computational procedure for MLDD decoding algorithm is given by the following procedural steps.

1. The code word is stored in the cyclic shift register.
2. At each tap, the check sums are calculated by the XOR matrix, which are the constraints provided by check nodes to the variable nodes.
3. After all the check sums are calculated, the majority gate decides whether the output bits are majority ones or zeros.
4. If more number of zeros is there, then the input bit is considered to be true and the data is rotated and same process continues for 3 cycles. If all are true, the data is assumed to be correct and is forwarded to the output.
5. If more number of ones is there, then the bit under operation is complemented and rotated. Check sums are again calculated, and the process repeats until the entire check-sum equations are zeros.

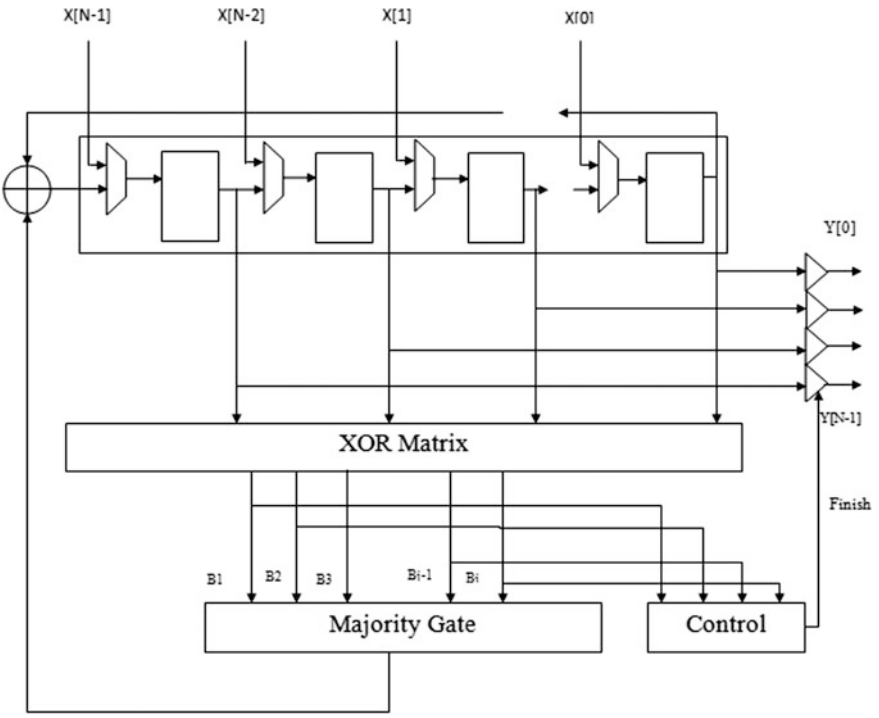

Fig. 4 Block diagram of MLDD algorithm

4 Synthesis Results

By using the Xilinx ISE Design Suite, the Verilog codes for SBF and MLDD algorithms are executed and the synthesis results are obtained [15] (Figs. 5 and 6).

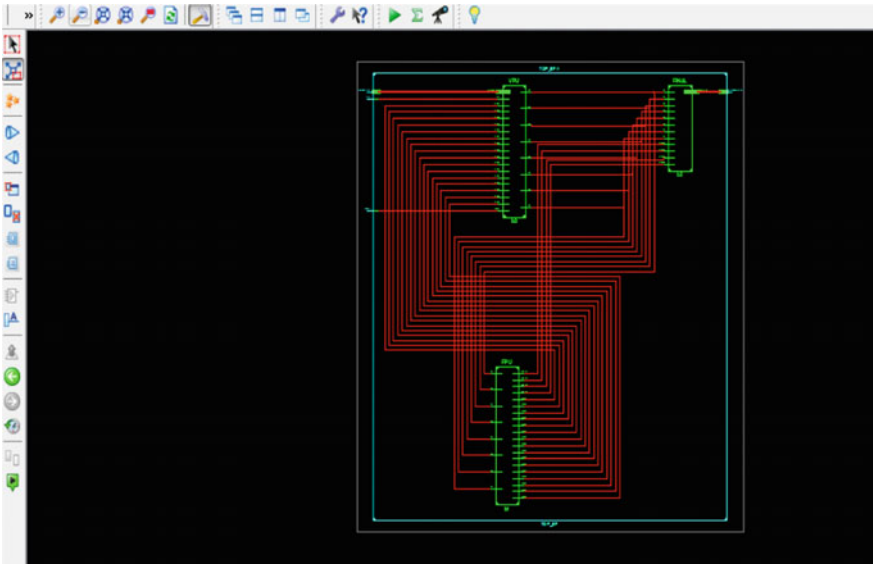

Fig. 5 Overall schematic of soft-bit flipping (SBF) decoding algorithm

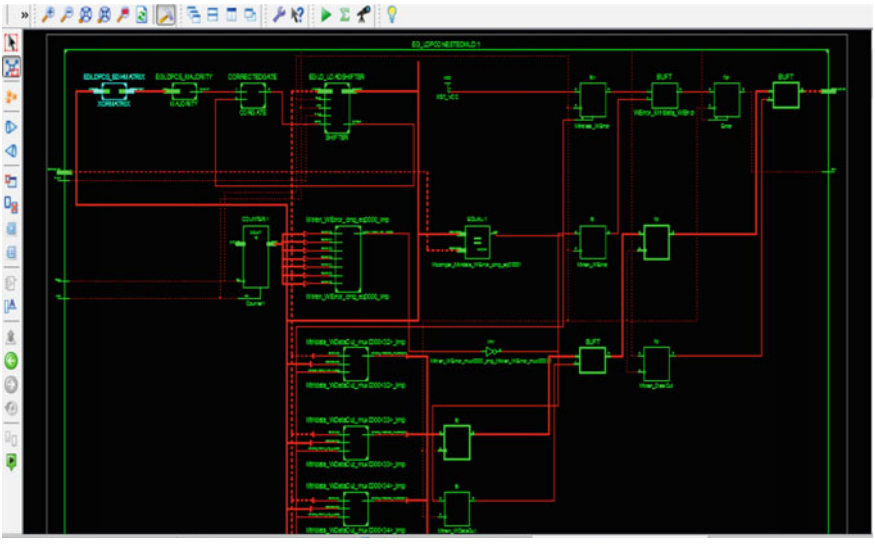

Fig. 6 Overall schematic of majority logic decoder/detector (MLDD) algorithm

Table 1 Comparison of area and delay for SBF decoder for various technologies

Technology	Clock frequency (MHz)	Area report	Delay report (ns) (slack time)
AMI 0.5 μm	25	No. of gates = 194	6.98
	20	No. of gates = 194	3.02
AMI 1.2 μm	25	No. of gates = 261	31.98
	50	No. of gates = 261	11.98
TSMC 0.35 μm	25	No. of gates = 202	31.98
	200	No. of gates = 202	3.62

Table 2 Comparison of SBF and MLDD decoding algorithms in terms of device utilization summary

Logic utilization	SBF decoding algorithm	MLDD decoding algorithm
No. of slices	25	133
No. of flip flops	10	200
No. of 4-input LUTs	46	196
No. of bonded IOBs	18	130
GCLKs	1	1

5 Comparison Results

The results of various structural parameters of above mentioned algorithms have been compared and tabulated is as shown in Tables 1 and 2.

Table 1 shows the area and delay reports obtained for SBF decoder for different technologies at different clock frequencies. These results are obtained from the Spectrum of tool package (Table 2).

Target device: xc3s1200e-5-ft256.

6 Conclusion

The good error-correcting capabilities of geometric LDPC codes are gaining more prominence in many fields. As the technology is advancing, many decoding algorithms for the LDPC codes have been developed. In this chapter, the soft-bit flipping (SBF) algorithm and majority logic decoder/detector (MLDD) algorithm for decoding LDPC codes have been investigated and the results obtained by simulating and synthesizing are compared in terms of hardware consumption and delay. From these results, it is concluded that hardware complexity of min-sum algorithm is higher than that of MLDD algorithm and SBF algorithm. SBF decoder requires less hardware components than other. Whereas the delay is less for MLDD algorithm followed by SBF decoder. Considering hardware complexity, speed, and power consumption, the best decoder can be selected according to the application.

References

1. Gallager, R.G.: Low density parity check codes. IRE Trans. Inf. Theory **IT-8**, 21–28 (1962)
2. MacKay, D.J.C., Neal, R.M.: Near Shannon limits performance of low density parity check codes. Electron. Lett. **32**(18), 1645–1646 (1996)
3. MacKay, D.J.C.: Good error correcting codes based on very sparse matrices. IEEE Trans. Inf. Theory (1997)
4. MacKay, D.J.C.: Gallager codes those are better than turbo codes. In: Proceedings of 36th Allerton Conference on Communication, Control, and Computing (1998)
5. Zhang, J., Fossorier, M.P.C.: A modified weighted bit-flipping decoding of low-density parity-check codes. IEEE Commun. Lett. **8**(3), 165–167 (2004)
6. Chen, J., Dholakia, A., Eleftheriou, E., Fossorier, M.P.C., Hu, X.-Y.: Reduced-complexity decoding of LDPC codes. IEEE Trans. Commun. **53**(8), 1288–1299 (2005)
7. Palanki, R., Fossorier, M.P.C., Yedidia, J.S.: Iterative decoding of multiple-step majority logic decodable codes. IEEE Trans. Commun. **55**(6), 1099–1102 (2007)
8. Savin, V.: Min-max decoding for non-binary LDPC codes. In: Proceedings of IEEE ISIT, pp. 960–964 (2008)
9. Cho, J., Sung, W.: High-performance and low-complexity decoding of high-weight LDPC codes. J. Korea Inf. Commun. Soc. **34**(5), 498–504 (2009). (in Korean)
10. Zhang, C., Wang, Z., Sha, J., Li, L., Lin, J.: Flexible LDPC decoder design for multi-Gb/s applications. IEEE Trans. Circuits Syst. I, Reg. Papers **57**(1), 116–124 (2010)
11. Zhang, X., Siegel, P.H.: Quantized min-sum decoders with low error floor for LDPC codes. In: IEEE International Symposium on Information Theory, pp. 2871–2875, (2012)
12 Kou, Y., Lin, S., Fossorier, M.: Low density parity check code based on finite geometries: a rediscovery and more. IEEE Trans. Inf. Theory (1999)
13 Fossorier, M.P.C., Mihaljevic, M., Imai, H.: Reduced complexity iterative decoding of low-density parity check codes based on belief propagation. IEEE Trans. Commun. **47**(5), 673–680 (1999)
14 Kschischang, F.R., Frey, B.J., Loeliger, H.-A.: Factor graphs and the sum–product algorithm. IEEE Trans. Inf. Theory **47**(2), 498–519 (2001)
15 Chinna Babu, J., Chinnapu Reddy, C., Giri Prasad, M.N.: Comparison of technologies for the implementation of SBF decoder for geometric LDPC codes. Ind. J. Sci. Tech. **9**(30), (2016)

Development of a System for Quantitative Assessment of Vocal Loading

P. Mahalakshmi, Ritwik Dhawan, Kartik Bharadwaj and Milind Kar Ray

Abstract Great vocal well-being is a key worry to proficient voice clients such ad instructors and artists. Consequently, to improve the utilization of voice and appropriate recovery to reestablish vocal well-being is the need of the day. A framework has been created to give a way to quantitative vocal stacking appraisal for the avoidance of voice issues. The advancements in signal processing have helped us to achieve this goal. Time dose, cycle dose, energy dose, and distance dose are the vital voice dosage measures citied in writing. The initial two measurements are ascertained in the study. The parameters which determine these measurements are voicing time, fundamental frequency of speech, and intensity of speech. Silence/unvoiced/voiced classification of speech signal has been done. The fundamental frequency has been extracted by cepstrum analysis. Voice doses are calculated using the above parameters, and tests are done on male and female audio samples. In this study, MATLAB platform is used for speech signal recording as well as analysis.

Keywords Vocal dose · Cepstrum · Quefrency · Pre-emphasis Short-time energy

P. Mahalakshmi (✉) · R. Dhawan · K. Bharadwaj
School of Electrical Engineering, VIT University, Vellore, Tamil Nadu, India
e-mail: pmahalakshmi@vit.ac.in

R. Dhawan
e-mail: ritwik.professionalid@gmail.com

K. Bharadwaj
e-mail: krishi.bharadwaj@vit.ac.in

M.K. Ray
School of Electronics Engineering, VIT University, Vellore, Tamil Nadu, India
e-mail: milind.karray@gmail.com

A. Konkani et al. (eds.), *Advances in Systems, Control and Automation*,
Lecture Notes in Electrical Engineering 442, https://doi.org/10.1007/978-981-10-4762-6_59

1 Introduction

As per World Health Organization measurements, discourse and dialect issue unfavorably influence the relational abilities of no less than 3.5% of the human populace [1]. The level of disarranges fluctuates from mellow weaknesses like elocution mistakes to more serious ones including listening to misfortune, aphasia, and cranial–facial inconsistencies. A discourse issue alludes to the trouble in comprehension or assembling words to impart thoughts.

Around 25% of the US populace is occupied with work that is "vocally requesting," and it is watched that they create visit voice issues [2]. Cases of experts with overwhelming vocal requests incorporate educators, artists, legal counselors, salespeople, heart stimulating exercise teachers, on-screen characters, and assembling administrators. These experts require over the top vocalization or talk louder than a higher clamor level to be heard accurately. Aside from the above issue, the ecological contamination, sudden changes in dampness, or presentation to pharmacological operators can make vocal overlay tissues bothered or powerless against harm. While in some cases, certain disease or damage may obstruct the vocal folds or larynx. Consequently, there is a need to quantify the measure of voice use among these experts and to screen the event of the voice issues keeping in mind the end goal to set up word-related security limits. In this manner, a superior mechanical answer for voice estimation is completely essential in the present situation.

2 Theoretical Background

2.1 Speech Production

From flag-situated perspective, the generation of discourse is generally depicted as a two-level process [3]. At first, the sound is started and it is sifted on the second level [4]. The creation of discourse is viewed as a superposition of start, phonation, verbalization, and prosodic association forms [5].

2.2 Source Filtering

The source filter model explains that the spoken word is comprised of a source component originating from the vocal cords which is then shaped by a filter imitating the work of vocal tract [6]. Figure 1 shows this concept.

Fig. 1 A simple model of speech

The source is a signal $x(t)$ which is fed to the filter. Here, the input is called the excitation signal, and filter refers to the vocal tract which acts as a linear time-invariant system with the impulse response $h(t)$. It is also the speech transfer function since it adds voice to the words. The speech is the output $y(t)$ which is simply a convolution of the source signal $x(t)$ with the filter's input response $h(t)$ as stated below in (1).

$$y(t) = x(t) * h(t) \tag{1}$$

2.3 Vocal Dose Measures

The trauma to vocal fold tissue caused by loud or prolonged vocalization can be thought as an exposure problem over time which is generally quantified by dose [7]. The term "vocal dosimetry" has been adapted to the occupational voice problems caused by long-term exposure of the vocal fold tissues to vibration. The important vocal dose measures are **time dose**, **distance dose**, **cycle dose, and energy dose** [7]. The parameters needed to compute these dose measures are the voicing time and the fundamental frequency of speech.

- **Time Dose**

Time dose (D_t) is the measure of total time in seconds during which the vocal folds are vibrating and is defined as follows:

$$D_t = \int K_v \mathrm{d}t \tag{2}$$

where the limits are from 0 to t and t represents the total time for which the speech is recorded and K_v is voicing step function.

- **Distance Dose**

Distance dose (D_d) is the accumulated distance traversed by the vocal folds in a vibratory trajectory and is defined as follows:

$$D_d = \int K_v(4A)F_0 \mathrm{d}t \tag{3}$$

where A is the vocal fold vibration amplitude, with $4A$ being the distance traveled by the vocal fold tissue in the vibratory cycle, and F_0 is the fundamental frequency of speech.

- **Cycle Dose**

Cycle dose (D_c) is the measure of the accumulated number of oscillations of the vocal folds and is defined as follows:

$$D_c = \int K_v F_0 dt \tag{4}$$

- **Energy Dose**

Energy dose (D_c) is the measure of the amount of energy dissipated as heat in the vocal fold during vibration and is defined as follows

$$D_e = 0.5 \int K_v \eta (A/T)^2 \omega^2 dt \tag{5}$$

where η is the viscosity of the vocal fold tissue, T is the thickness of the vibrating part of the glottis, and $\omega = 2 * \pi * F_0$ is the angular frequency.

3 Methodology and Implementation

The aim is to extract relevant parameters namely speech signal intensity, RMS value of the signal, fundamental frequency, and voicing time and then subsequently calculate the above-mentioned doses. Figure 2 explains the steps involved in signal processing. First, the signal acquisition takes place, and then, this signal is fed for pre-emphasis where the power of high-energy frequencies is boosted for enhancing the signal. After this, the signal is taken in segmented frames and the frames are windowed smoothly. The short-time energy analysis is done, and RMS value of the signal is estimated. Based on the energy received, the signal is classified as S/UV/V (silence/unvoiced/voiced).

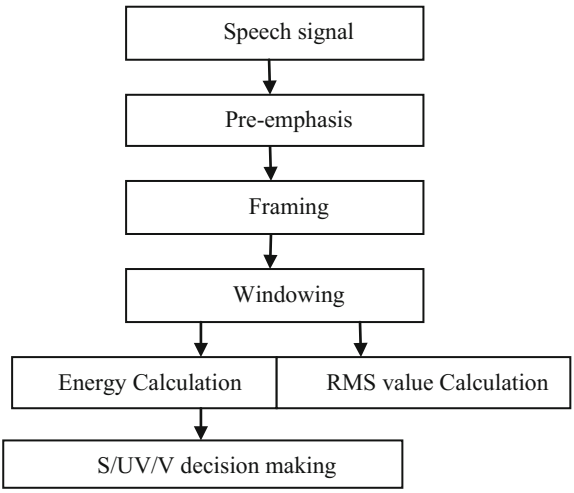

Fig. 2 Steps involved in signal processing

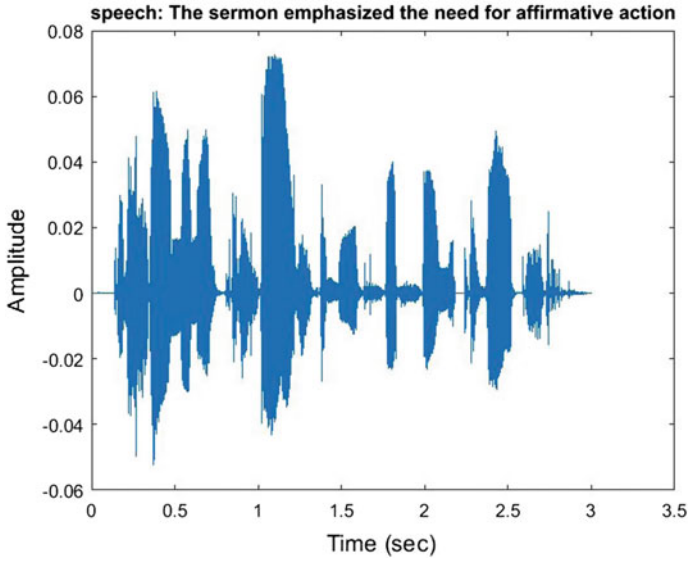

Fig. 3 Speech signal is "The sermon emphasized the need for affirmative action"

Finally, the fundamental frequency of the speech is determined by means of cepstrum analysis. Using this frequency, the cycle dose and time dose are plotted for further analysis and recommendation for the test subject.

3.1 Speech Signal Acquisition

Signal acquisition is achieved through a head-mounted microphone which is fed into the computer and stored as (.wav) file in MATLAB software for analysis. Since human speech signals fall mostly below 4 kHz, a sampling frequency of 8 kHz is used to extract all the necessary data from the speech signal.

3.2 Pre-emphasis

Due to the nature of glottal pulse, a drop in energy is seen across the high frequencies as compared to the low frequencies. Therefore, a boost is needed for these high frequencies in order to improve the speech recognition accuracy which is done by pre-emphasis which is basically a technique to increase the energy of the high frequencies and spectrally flatten signal. It is similar to first-order FIR filtering, and the transfer function is given by (6).

$$H(z) = 1 - \alpha z^{-1} \tag{6}$$

where $H(z)$ is the transfer function, α is the pre-emphasis factor, and its typical value is 0.95.

3.3 Framing and Windowing

The speech being a non-stationary signal, the speech analysis is therefore carried out on short segments having each frame of 32 ms (256 samples) with adjacent frames being separated by 1 sample each. Consecutively, a smoothing window is applied to each segment to reduce the edge effect. The Hamming window is used which tapers the signal to zero at the beginning and end of each frame. Hamming window is described by (7).

$$w(n) = 0.53836 - 0.56164 \cos(2 * \pi * n/(N-1)) \tag{7}$$

where $0 < n < (N - 1)$ and $N = 256$ (frame size).

3.4 Short-Time Energy

An automatic classification for the S/UV/V signal is achieved which is based on the energy content in the signal. The energy content is found using short-time energy (E_n) which is defined as (8).

$$E_n = \sum_{m=-\infty}^{\infty} (x[m], w[n-m])^2 \tag{8}$$

This energy is computed every point in the input data, and a decision is made for each point accordingly. The signal with zero energy is classified as silence (S), the signal with energy less than 0.5 is classified as unvoiced signal, whereas the signal with energy ranging from 0.5 to 1 corresponds to voiced signal. The RMS (root mean square) value is also estimated.

3.5 Fundamental Frequency Estimation

A dependable approach to get a gauge of the prevailing principal recurrence for the long, spotless, stationary discourse signs is to utilize the cepstrum. The cepstrum is a Fourier investigation of the logarithmic plentifulness range of the flag. In the event

that the log sufficiency range contains numerous standard music, then the Fourier examination of the range will demonstrate a pinnacle contrasting with the isolating between the music, i.e., the key recurrence. Viably, the flag range is dealt with as another flag, and after that, the periodicity in the range itself is searched for. The x-hub of the cepstrum has units of quefrency, and crests in the cepstrum are called rahmonics. To get a gauge of the essential recurrence from the cepstrum, we search for a crest in the quefrency locale to average discourse central frequencies [8].

4 Results

The sample speech is taken in MATLAB software as (.wav) file as shown in Figure 3.

Figure 4 shows the short-time energy plot of the above sample speech.

The fundamental frequency extraction has been performed as shown in the Fig. 5. The peak in the cepstrum corresponds to the fundamental frequency (200 Hz) for that segment of speech.

The Goldilocks section has customarily been utilized by specialists for voice assessments when vast varieties in power, principal recurrence, and voice quality are required [9]. We have used a portion of the passage, and the same is given below.

> Once upon a time, there lived three bears. They lived in the woods. One of the bears was papa bear. One was mama bear, and one was baby bear.

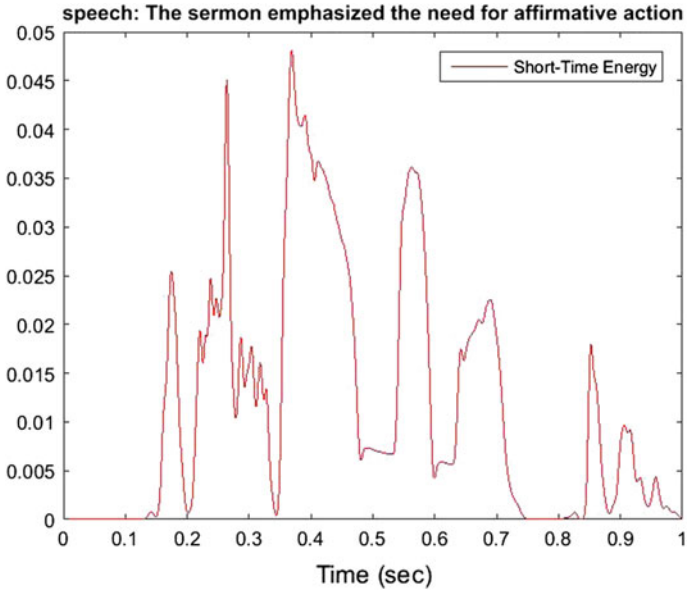

Fig. 4 Short-time energy plot of speech signal

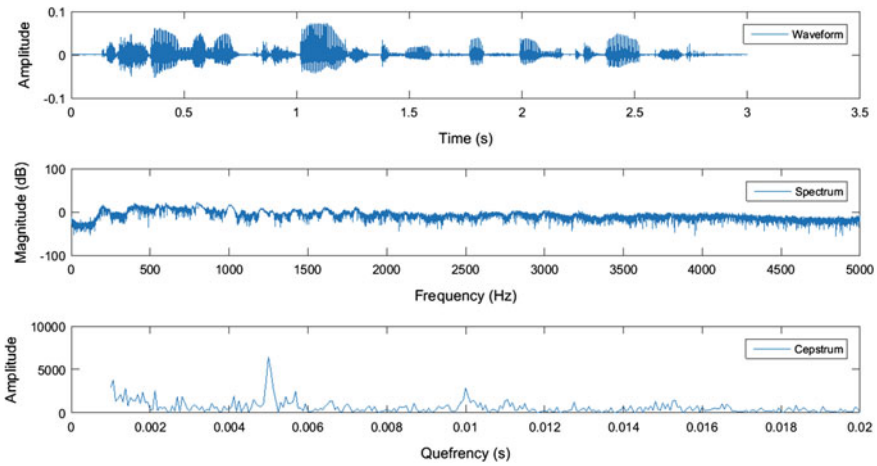

Fig. 5 Fundamental frequency estimation from cepstrum

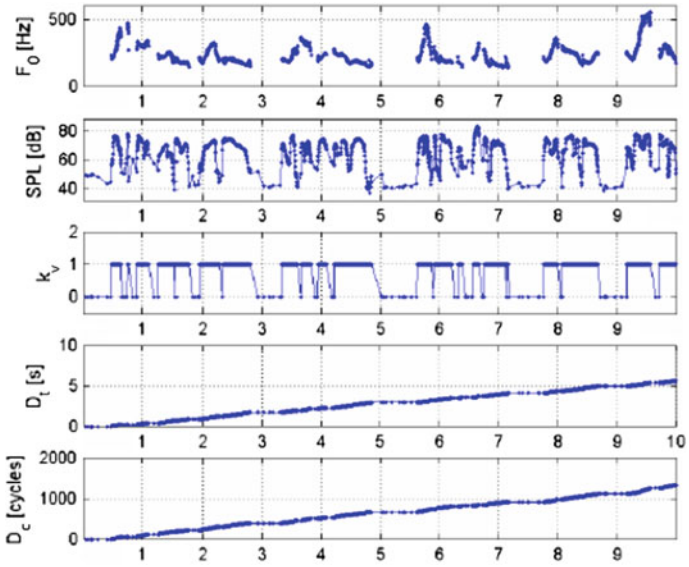

Fig. 6 Goldilocks passage fundamental frequency and vocal doses

The voice sample for duration of 10 s is taken. The cepstrum analysis of the above signal is performed.The fundamental frequency is found out and the corresponding cycle dose is computed as 1324 cycles and the time dose as 5.61 s as shown in Figure 6.

5 Conclusion

The system presented here has been developed for vocal dose measurement which allows measurement of the time dose and the cycle dose. The important parameters used to decide these doses are voicing time and fundamental frequency of speech. The criterion used for distinguishing voice segments from unvoiced and silence is the energy level of the speech. The fundamental frequency is estimated by cepstrum analysis of the signal. We hope that these parameters will help figure out a safe limit for vocal use and to determine the amount of recovery time needed once this safe limit is exceeded. Hopefully, these measures can be related to vocal fatigue among people in vocally demanding professions. In future, study can be extended for calculation of energy dose and distance dose, incorporating a sound pressure level meter in the data acquisition system and with proper calibration procedures.

References

1. Turk, O., Arslan, L.M.: Software Tools for Speech Therapy and Voice Quality Monitoring. http://signal.ee.bilkent.edu.tr/defevent/papers/cr2060.pdf
2. Titze, I.R.: Guide to vocology. In: The National Centre for Voice and Speech, NCVS (2002)
3. Koreman, J.: Decoding Linguistic Information in the Glottal Airflow. Ph.D. Thesis, University of Nijmegen (1996)
4. Fant, G.: Acoustic Theory of Speech Production. Mounton, The Hague, Nertherlands. http://www.ling.cam.ac.uk/li9/m4_0809_acoustictheoryspeechproduction.pdf (1960)
5. Laver, J.: Principles of Phonetics. Oxford University Press, Oxford (1994)
6. Mark, H.: Lecture 8: source-filter model of speech production. In: B214: Phonetic Science: Acoustics of Speech and Hearing. University College London
7. Popolo, P.S., Rogge Miller, K., Svec, J.G., Titze, I.R.: Technical considerations in the design of a wearable dosimeter. In: The National Centre for Voice and Speech Online Technical Memo, no. 5, version 1.1 (2002)
8. O'Shaughnessy, D.: Speech Communication: Human End Machine, Addison-Wesley. ISBN No: 9780201165203
9. Svec, J.G., Popolo, P.S., Titze, I.R.: The Goldilock's passage for frequency extraction, voicing detection, SPL calculation and vocal dose determination in speech. In: The National Centre for Voice and Speech Online Technical Memo, no. 1, version 1.4 (2003)

Solution for Multi-area Unit Commitment Problem Using PSO-Based Modified Firefly Algorithm

Samikkannu Prabakaran, Selvaraj Tamilselvi, Perianayagam Ajay-D-Vimal Raj, Mahalingam Sudhakaran and Selvamuthukumaran Rajasekar

Abstract A new approach applying particle swarm optimization (PSO) and firefly algorithm (FA) has been proposed for solving economic dispatch and multi-area unit commitment problems, in this paper. In FA, the flashing behavior depends on the random movement factor, which gets fixed and causes the solution to vary uncertainly. Hence, PSO algorithm is used to optimize the random movement factor of FA. Using the proposed PSO-based FA, the ON/OFF status of generating units of multi-area system is determined. The effective equality and inequality constraints are considered to solve the multi-area system. The proposed algorithm is implemented in MATLAB working platform and is applied to four areas with 26 generating unit systems for a 24-h schedule. The performance of proposed method has been compared with other recent reported results. The implication of proposed method is clarified and verified by numerical results.

Keywords Multi-area unit commitment · Operating cost · FA
Random movement factor · PSO

S. Prabakaran
Department of Electrical and Electronics Engineering,
SCSVMV University, Kanchipuram, Tamil Nadu, India
e-mail: Prabakaran110768@gmail.com

S. Tamilselvi
Department of Electrical and Electronics Engineering,
SSN College of Engineering, Chennai, India
e-mail: tamilselvi.manjuraj@gmail.com

P. Ajay-D-Vimal Raj (✉) · M. Sudhakaran
Department of Electrical & Electronic Engineering, Pondicherry Engineering College,
Pondicherry University, Pillaichavadi, Puducherry, India
e-mail: ajayvimal@pec.edu

M. Sudhakaran
e-mail: sudhakaran@pec.edu

S. Rajasekar
Researcher of NEC Laboratories, NEC Asia Pacific Pte. Ltd., Singapore, Singapore
e-mail: rajaseka6387@gmail.com

A. Konkani et al. (eds.), *Advances in Systems, Control and Automation*,
Lecture Notes in Electrical Engineering 442, https://doi.org/10.1007/978-981-10-4762-6_60

1 Introduction

The load of a practical power network varies persistently, and thus it is not prudent to use all the units needed to fulfill the peak loads [1]. Power system must be gone about as an essential reliable component to supply the load [2]. From the reliable point of view, unit commitment (UC) plays a real part in the everyday operation, arranging and controlling techniques of powerful networks [3, 4]. It is the determination of the optimum operating on a schedule of various electric power production units, in addition to meet the determined demand over a transient period, with the minimum total operating cost [5–10]. Commonly, it is mentioned as a varied combinatorial and nonlinear improvement issue with substantial measurements and coupling constraints [11–13]. Different strategies, for example, dynamic programming, sequential system, genetic calculations, unit de-commitment strategies, mixed integer program, and expert frameworks have been utilized for UC issues [14–16]. Despite precisely a power pool that included a few generation areas connected using tie-lines, destination is to attain the cost-effective generation policy that would provide the confined demand without damaging tie-line limit requirements [17]. This is called as Multi-Area Unit Commitment (MAUC) optimization issues.

MAUC issues are expanding with the number of constraints, measurements and several areas. In the event that there are no restrictions for exchanging power between interconnected areas, the power pool might be considered as an extensive single area and MAUC would be simple [18]. It enhances the market proficiency and framework reliability by imparting the assets crosswise area limits [19]. The MAUC schedule was optimized, wherein the basic necessity list plan was actualized, employing minimal path, maximal flow technique, which is generally created to tackle transportation issue. Analogous to single area UC (SAUC), numerically, MAUC's goal capacity is to minimize the aggregate expense of working all units over a specified time horizon. The aggregate working expense includes fuel expenses, operation and maintenance charge (OMC), and start-up expenses, with the transmission losses being consolidated in the incremental cost rate evaluation [20].

This paper describes a modified FA for solving multi-area unit commitment problem. Here, particle swarm optimization (PSO) algorithm is used to optimize the random movement factor and the performance of FA is improved. The multi-area unit commitment problem has been formulated in such a way to reduce the total system operating cost. The proposed method is used for computing the allocation of generation of units in hourly basis to get optimal value. This paper is organized as follows: Sect. 1 analyzes recent research work; Sect. 2 discusses problem formation and the proposed method; Sect. 3 depicts the results; and Sect. 4 concludes the paper.

2 Problem Formulation for MAUC

The main objective function of the MAUC problem is to minimize the total operating cost of entire generation, simultaneously satisfying the load demand. The total operating cost involves start-up cost, shutdown cost, and fuel cost. The fuel cost equation is in general a quadratic equation of power output of every generating unit, at each hour. The start-up cost of each generator is an exponential function of the time that the unit remains off. MAUC is used for commitment schedule of the generators in multiple areas which are connected through tie-lines.

$$\text{MinTOC} = \sum_{h=1}^{N_A} \sum_{n=1}^{t} \sum_{m=1}^{N_H} \left[\text{Fc}_{m,n}^{h}(P_{m,n}^{h}) + \text{Sc}\left(X_{m,n}^{\text{off}}\right)\left(1 - U_{m,n-1}^{h}\right)\right] \times U_{m,n}^{h} \quad (1)$$

$$m = 1 \ldots N_H, n = 1 \ldots t, h = 1 \ldots N_A$$

where

$$\text{Fc}(P_m^h) = a_m^h (P_m^h)^2 + b_m^h (P_m^h) + c_m^h \quad (2)$$

$$\text{Sc}\left(X_{m,n}^{\text{off}}\right) = H_m + C_m\left(1 - \text{e}^{\left(X_{m,n}^{ofdf}\right)}\right) \quad (3)$$

$$\eta = 2a_m^h P_m^h + b_m^h \quad (4)$$

where TOC represents the total operating cost of the entire system; $U_{m,n}^{h}$, the commitment state (1 for ON and 0 for OFF); $P_{m,n}^{h}$, the power generation of unit m in area h at n hour; and $\text{Fc}(P_{m,n}^{h})$, the fuel cost of unit m in area h at n hour. $\text{Sc}\left(X_{m,n}^{\text{off}}\right)$ signifies the start-up cost of unit m, $\left(a_m^h, b_m^h, c_m^h\right)$ characterize the cost coefficient parameters of unit m in area h, η is the production cost of supplying the incremental energy; H, the start-up coefficient in hot condition; C, the start-up coefficient in cold condition; N_A, the number of areas; t, the total time span in hours; and N_H, the number of units in area h.

For optimizing the above problems in objective functions, the equality and inequality constraints such as spinning reserve limitations, system power balance constraints, import export constraints, minimum uptime and downtime constraints, and initial ON or OFF state of every unit.

2.1 Equality Constraints

System power balance constraint

$$\sum_{h} P_n^h = \sum_{h} D_n^h + L_n \tag{5}$$

Import Export balance

$$\sum_{m} E_n^h - \sum_{h} I_n^h + L_n = 0 \tag{6}$$

where P_n^h represents power generation in area h at nth hour, D_n^h, the local demand of area h at nth hour; I_n^h, the total import power to area h at nth hour; L_n, the real power loss of the system; and E_n^h, the total export power to area h at nth hour.

2.2 Inequality Constraints

Spinning reserve constraint

$$\sum_{m} P_{m,n\max}^h \geq D_n^h + R_n^h + E_n^h - I_n^h \quad n = 1, 2, \ldots t. \tag{7}$$

Generation limits of each unit

$$P_{n,\min}^h \leq P_n^h \leq P_{n,\max}^h \quad m = 1 \ldots N_H, n = 1 \ldots t, h = 1 \ldots N_A \tag{8}$$

Minimum uptime/downtime constraints

$$\left(X_{m,n-1}^{\text{on}} - T_m^{\text{on}}\right) * \left(U_{m,n-1}^{\text{on}} - U_{m,n}\right) \geq 0 \tag{9}$$

$$\left(X_{m,n-1}^{\text{off}} - T_m^{\text{off}}\right) * \left(U_{m,n} - U_{m,n-1}\right) \geq 0 \tag{10}$$

Import/Export line constraints
Upper limits

$$\sum_{m} P_{m,n}^h \leq D_n^h + E_{n\max}^h \tag{11}$$

Lower limits

$$\sum_{m} P_{m,n}^h \geq D_n^h - I_{n\max}^h \tag{12}$$

Area generation limits

$$\sum_{m} P_{m,n}^{h} \leq \sum_{m} P_{n\max}^{h} - R_{n}^{h} \quad h = 1\ldots N_A, n = 1\ldots t \tag{13}$$

$$\sum_{m} P_{m,n}^{h} \leq \sum_{m} P_{n\min}^{h} \quad h = 1\ldots N_A, n = 1\ldots t \tag{14}$$

where $P_{m,n\max}^{h}$ signifies the maximum generation of power from unit m, in area h at nth hour; R_{n}^{h}, the spinning reserve to area h at nth hour; and $P_{n\min}^{h}$, the minimum power generation in area h at nth hour; $X_{m,n}^{\text{off}}$ represents the time for which unit m remains OFF at nth hour; $X_{m,n}^{\text{on}}$ denotes how long the unit m remains ON at nth hour; T_{m}^{on} and T_{m}^{off} represent minimum up- and downtimes of unit m, respectively; $E_{n\max}^{h}$ represents the maximum total export power to area h at nth hour; $H_{n\max}^{h}$ gives the maximum total import power to area h at nth hour; and $P_{n\min}^{h}$ gives the minimum generation of power in area h by unit m at nth hour.

2.3 Multi-Area Economic Dispatch

The aim of multi-area economic dispatch (MAED) is to find out the allocation of generation of every unit in the system and transfer of power among the areas such that the total production cost is minimum. The objective is to select η_{sys} each hour to reduce the operation cost. The actual output value generated in unit m has determined the system incremental production cost through minimum and maximum generation coordination, and it will not work in shut down mode.

$$P_{n}^{h} + D_{n}^{h} + E_{n}^{h} - I_{n}^{h} \tag{15}$$

where

$$P_{n}^{h} = \sum_{m=1}^{N_H} P_{m,n}^{h} \tag{16}$$

Shutdown mode

$$P_{m} = 0 \tag{17}$$

Coordinate mode

$$\eta_{\min,m} \leq \eta_{\text{sys}} \leq \eta_{\max,m} \tag{18}$$

Minimum mode

$$\eta_{\min,m} > \eta_{\text{sys}} \tag{19}$$

Maximum mode

$$\eta_{\max,m} > \eta_{\text{sys}} \tag{20}$$

In case, multi-area system is bound by several constraints as given in above equations, and then the generation in each area has to be setup in any of the following modes, discussed below.

Area coordination mode

$$\eta^h = \eta_{\text{sys}} \tag{21}$$

$$D_n^h - I_{\max}^h \leq \sum_m P_{m,n}^h \leq D_n^h + E_{\max}^h \tag{22}$$

Limited export mode

The generating units in the limited export mode are lower in one particular area than other areas, so areas may generate limits on upper bound, according to Eq. (10) or (13), and hence

$$\eta^h < \eta_{\text{sys}} \tag{23}$$

For area h, the area η^h satisfies the generation requirement to attain the optimal incremental cost.

Limited import mode

An area may reach its lower power generation bound, based on Eq. (11) or (14) due to higher generation cost.

$$\eta_{\min}^h > \eta_{\text{sys}} \tag{24}$$

where η_{sys} represents the production cost of delivering the last incremental energy to satisfy the complete demand; $\eta_{\min,m}$, the minimum production cost for unit m; $\eta_{\max,m}$, the maximum production cost for unit m; and η^h,the production cost of area h.

2.4 Tie-Line Constraints

As a rule, tie-line parameters are estimated by the transportation model. However, it is inappropriate for multi-area unit commitment and hence we have made use of the quadratic cost function. In fact, tie -line flows are not directly linked to the generation of area to tackle the tie-line constraints; area η iterations are located within

the η_{sys} iteration loop. In each and every η_{sys} iteration, Eqs. (10), (11), (13), and (14) are verified to assess the operation mode of each and every area. In case the generation of area h, P_n^h, does not fall within the gamut of coordination range prescribed by Eq. (21), the area is likely to function either at the upper or the lower limit mode, and in accordance with Eqs. (24) and (25), the η employed in the area would be dissimilar from η_{sys}. The local η iterations are carried out among the dedicated units in area h till the area generation approaches the specific bounds.

In MAUC, the system generating the balance equation simplify the real power loss with the outside system to zero from Eq. (5), therefore

$$\sum_h P_n^h = \sum_h D_n^h \tag{25}$$

The cost-effective area may have more power above the demand, and the unnecessary additional power gets transferred through tie-lines. Further, it may cause certain export losses, and then the excess power is transferred to other areas. Due to the power balance equation, there may be a little power deficit and it requires certain generation imports. The minimum power generation level in these areas is the local demand less the amount of capacities in all the tie-lines. When the tie-lines are attached to an area having higher deficit, the direction of flow gets reversed.

2.5 *Modified Firefly Algorithm to Solve the Formulated MAUC Problem*

PSO-based modified firefly algorithm is proposed in this paper, for solving an optimization task of MAUC problem. PSO algorithm is applied to optimize the randomization parameter of firefly, and the performance of the algorithm is enhanced. Using the PSO algorithm, a set of α_t values generated and the best value is selected by which α_t give minimum unit generator deviation. Therefore, the algorithm could converge to the optimum solution more quick by reducing the randomness. The steps of proposed modified FA are explained as follow,

The PSO algorithm requires the parameters followed below:

(i) Maximum and minimum velocity that limit $v_i(t)$ within the range.
(ii) An inertial weight w.
(iii) Two random numbers r_1 and r_2 which decide the influence of $p_i(t)$ and $g_i(t)$ on the velocity updation.
(iv) Two multipliers $C1$ and $C2$.

$$v_i(t+1) = wv_i(t) + c_1 r_1(p_i(t) - x_i(t)) + c_2 r_2(g_i(t) - x_i(t)) \tag{29}$$

$$x_i(t+1) = x_i(t) + v_i(t+1) \tag{30}$$

Steps of PSO-based firefly algorithm

Step 1: Set the initialize parameters of the algorithm such as the absorption coefficient, γ; β_0, the attractiveness; and α, the randomness parameter with the maximum number of iteration.
Step 2: Generate the initial population of each area from the given generator limits, $P^h_{n,\min} \le P^h_n \le P^h_{n,\max}$

$$\{x_1, x_2, x_3, x_4\} = \left\{[P^1_1, P^1_2, \ldots P^1_n], [P^2_1, \ldots P^2_n], [P^3_1, \ldots P^3_n], [P^4_1, \ldots P^4_n]\right\} \tag{31}$$

where, x_1 is the vector of generator value of area 1 such as $P^1_1, P^1_2, \ldots P^1_n$, x_2 is the vector of generator value of area 2 such as $P^2_1, P^2_2, \ldots P^2_n$, x_3 is the vector of generator value of area 3 such as $P^3_1, P^3_2, \ldots P^3_n$, and x_4 is the vector of generator value of area 4 such as $P^4_1, P^4_2, \ldots P^4_n$.
Step 3: In this step, the operating cost of the system is calculated, i.e., the fitness function of the generator limits. Evaluate the fitness value from Eq. (1)
Step 4: Generate the randomness value of α^{PSO}_t of FA from the give limits $\alpha^{\text{PSO}}_{t,\min} \le \alpha^{\text{PSO}}_t \le \alpha^{\text{PSO}}_{t,\max}$

$$\alpha^{\text{PSO}}_t = \frac{\alpha^{\text{PSO}}_{t,\min} + \left(\alpha^{\text{PSO}}_{t,\max} - \alpha^{\text{PSO}}_{t,\min}\right)/\text{Generation}}{\text{Maximum Generation}} \tag{32}$$

Step 5: Then, calculate the fitness function of generator value which was generated by α^{PSO}_t. The fitness function is to minimize the difference between initial generator value and α^{PSO}_t-based updated generator value.

$$\text{Fitness} = P^h_n(\text{initial}) - P^h_n\left(\alpha^{\text{PSO}}_t\right) \tag{33}$$

Step 6: Initially, the values of $p_i(t)$ and $g_i(t)$ of Eq. (1) are set as $p_i(0) = g_i(0) = x_i(0)$ for all particles. The iterative optimization process begins, once the particles are initialized and select the best α^{PSO}_t.
Step 7: Set the iteration count.
Step 8: Movement of the firefly m which gets attracted to other new attractive firefly n can be calculated with the best α^{PSO}_t by the following expression,

$$x^{t+1}_m = x^t_m + \beta_0 e^{-\gamma r^2_{mn}}\left(x^t_n - x^t_m\right) + \alpha^{\text{PSO}}_t \in^t_m \tag{34}$$

where α_t^{PSO} is the randomization parameter which is updated by PSO algorithm. The calculation procedure is explained as,

Step 9: Check for the maximum iteration, and select the best solutions.

Step 10: If the iteration does not satisfy the maximum value, increase the iteration count, and follow Step 2.

Step 11: Once the global fitness value is obtained and process gets terminated.

The flowchart of the PSO-based FA is given in Appendix I.

3 Results and Discussion

The proposed multi-area unit problem was formulated which was solved by the PSO-based firefly algorithm. The proposed method was implemented in MATLAB working platform, and the performance was evaluated with four area thermal generating system. In the test system, every area comprises of 26 generators, which have the start-up cost functions and generating cost functions. The dataset of the units is listed in [17]. The cost functions of the generators are categorized by sliding order since the generating units of the four areas are some extent different. The implementation parameters of proposed PSO-based firefly algorithm are given in Table 1. Bar chart of load demand of four area system is illustrated in Fig. 1.

Using the above demand profile, the total operating cost of multi-area system is calculated for each hour of a day using the firefly and PSO-based firefly algorithm.

The convergences performance of FA is the proposed method illustrated in Fig. 2. The proposed method takes very less iteration to reach the minimum fitness value when compared with FA. Therefore, convergence performance is also confirmed the effectiveness of proposed method. Moreover, the computational times of FA and PSO-based FA are observed for calculating a solution of the problem which is given in Table 2. The FA has less elapsed time to check the constraints. But, the proposed method takes more computational time to FA but the solution is accurate when compared with FA.

Table 1 Implementation parameter of PSO and FA

Parameter	PSO	FA
No. of generation	100	100
No. of iteration	500	500
A	–	1
B	–	0.3
Γ	–	0.5
C_1	0.12	–
C_2	1.2	–
W	0.9	–

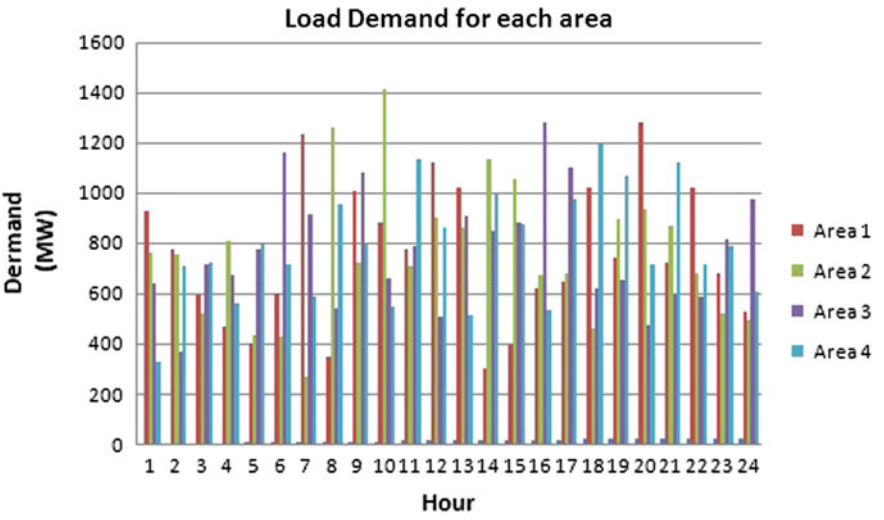

Fig. 1 Load demand profile in each area

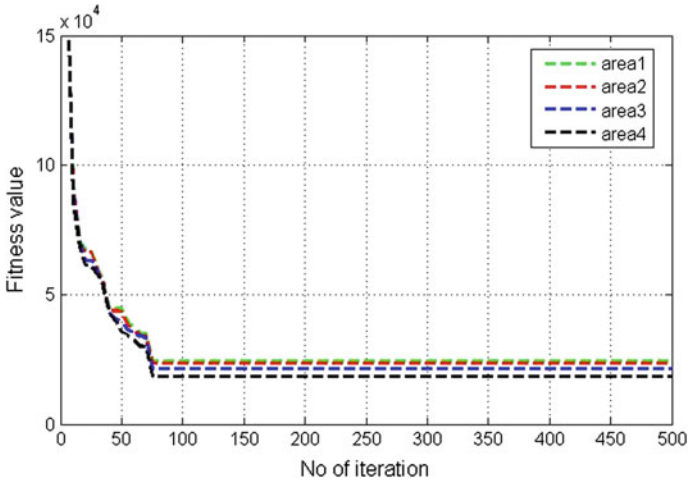

Fig. 2 Convergence performance of PSO-based FA

Table 2 Computational time of FA and PSO-based FA

MAUC method	Elapsed time (s)
FA	45
PSO-based FA	58

4 Conclusion

A PSO-based FA was proposed for selecting minimum operating cost of multi-area unit commitment problem. The proposed method was implemented, and the performance was tested four areas with 26 generating unit systems for a 24-h schedule. Then, the total operating cost is calculated and compared for proposed method, FA, PSO, EP, and DP. From that, the proposed method obtained minimum operating cost as 2540439.466 $ without violating the system demand with the computational time as 58 s. Moreover, the numerical results are confirmed and the proposed method effectively solves the multi-area unit commitment problem. The future research will focus on introducing new optimization algorithm and incorporating more operational consideration of transmission constraints.

References

1. Chowdary, N., Billinton, R.: Unit commitment in interconnected generating systems using a probabilistic technique. IEEE Trans. Power Syst. **5**, 1231–1238 (1990)
2. Wang, Q., Watson, J-P., Guan, Y.: Two-stage robust optimization for contingency-constrained unit commitment. IEEE Trans. Power Syst. **28**, 2366–2375 (2013)
3. Wu, Z., Chow, T.W.S.: Binary neighbourhood field optimization for unit commitment problems. IET Gener. Transm. Distrib. **7**, 298–308 (2013)
4. Damousis, I.G., Bakirtzis, A.G., Dokopoulos, P.S.: A solution to the unit-commitment problem using integer-coded genetic algorithm. IEEE Trans. Power Syst. **19**, 1165–1172 (2004)
5. Petridis, V., Kazarlis, S., Bakirtzis, A.: Varying fitness functions in genetic algorithm constrained optimization: the cutting stock and unit commitment problems. IEEE Trans. Syst. Man Cybern. B Cybern. **28**(5), 629–640 (1998)
6. Victoire, T.A.A. Jeyakumar, A.E.: Unit commitment by a tabu-search-based hybrid-optimization technique. IEE Proc. Gener. Transm. Distrib. **152**, 563–574 (2005)
7. Xiong, P., Jirutitijaroen, P.: Two-stage adjustable robust optimization for unit commitment under uncertainty. IET Gener. Transm. Distrib. **8**, 573–582 (2014)
8. Xiong, P., Jirutitijaroen, P.: A stochastic optimization formulation of unit commitment with reliability constraints. IEEE Trans. Smart Grid **4**, 2200–2208 (2013)
9. Maifeld, T.T., Sheble, G.B.: Genetic-based unit commitment algorithm. IEEE Trans. Power Syst. **11**, 1359–1370 (1996)
10. Wang, B., Li, Y., Watada J.: Supply reliability and generation cost analysis due to load forecast uncertainty in unit commitment problems. IEEE Trans. Power Syst. **28**, 2242–2252 (2013)
11. Saber, A.Y., Senjyu, T., Yona, A., Funabashi, T.: Unit commitment computation by fuzzy adaptive particle swarm optimization. IET Gener. Transm. Distrib. **1**, 456–465 (2007)
12. Chung, C.Y., Yu, H., Wong, K.P.: An advanced quantum-inspired evolutionary algorithm for unit commitment. IEEE Trans. Power Syst. **26**, 847–854 (2011)
13. Li, Y-F., Pedroni, N., Zio, E.: A memetic evolutionary multi-objective optimization method for environmental power unit commitment. IEEE Trans. Power Syst. **28**, 2660–2669 (2013)
14. Chen, C-L.: Key issues of wind capacity integration in congested areas of the Taiwan power system. IET Renew Power Gener. **8**(1), 10–21 (2014)
15. Ting, T.O., Rao, M.V.C., Loo, C.K.: A novel approach for unit commitment problem via an effective hybrid particle swarm optimization. IEEE Trans. Power Syst. **21**(1), 411–418 (2006)

16. Pappala V.S., Erlich,I : IEEE Trans. Power Syst. **25**(3), 1696–1704
17. Ouyang Z, Shahidehpour, S.M.: Heuristic multi-area unit commitment with economic dispatch. IEE Proc C-Gener. Transm and Distrib. **138**(3), 242 (1991)
18. Wang C., Shahidehpour S.M.: A decomposition approach to nonlinear multi-area generation scheduling with tie-line constraints using expert systems. IEEE Trans. Power Syst. **7**(4), 1409–1418
19. Ahmadi-Khatir, A., Bozorg, M., Cherkaoui, R.: IEEE Trans. Power Syst. **28**(3), 2819–2829
20. Yingvivatanapong C., Lee W-J., Liu E.: IEEE Trans. Power Syst. **23**(1), 196–203

Wi-Fi-Based Low-Cost Monitoring of ECG and Temperature Parameters Using Arduino and ThingSpeak

Kartik Bharadwaj, Ritwik Dhawan, Milind Kar Ray and P. Mahalakshmi

Abstract Health monitoring is one of the most important parameters to diagnose a patient, and it can be done in many ways. Temperature monitoring and pulse rate of a patient is one of the ways. Temperature sensor and pulse rate sensor have been used to get the physiological data from a patient's body. These data can be used to monitor the health of the patient. The acquired data is then sent to a website server from which the doctors can check the patient's vital signs anytime. Therefore, low-cost monitoring can be used in remote areas where people are not able to afford the healthcare. Future improvement can be done by sending an email containing the status of the health parameters to the doctor in case of emergency.

Keywords Wi-Fi module · Arduino · ECG · Processing · ThingSpeak · Eagle

1 Introduction

Technology defines the twenty-first century in an apt way. Mobile and Internet have become the heart and soul of today's global scenario. From social networking to media outreach, from military to medical fields, all have become an integral part of the Internet. Many hospitals and modern healthcare clinics in urban cities have state-of-the-art medical instruments. Though the cost of these instruments is high, it does provide accurate medical information about a patient's body. This, therefore, saves time and patient's life too. But, due to alarming rate in the health effects of

K. Bharadwaj · R. Dhawan · M.K. Ray · P. Mahalakshmi (✉)
School of Electrical Engineering, VIT University, Vellore, Tamil Nadu, India
e-mail: pmahalakshmi@vit.ac.in

K. Bharadwaj
e-mail: krishi.bharadwaj@vit.ac.in

R. Dhawan
e-mail: ritwik.professionalid@gmail.com

M.K. Ray
e-mail: milind.karray@gmail.com

A. Konkani et al. (eds.), *Advances in Systems, Control and Automation*,
Lecture Notes in Electrical Engineering 442, https://doi.org/10.1007/978-981-10-4762-6_61

patients, doctors are now busier than ever. This reduces the attention span given to each patient and sometimes may also lead to unavailability of doctors in critical times. Also, the ever increasing cost of medical devices restricts access to people in remote areas.

In medicine, checking is the perception of an infection, condition, or one or a few medicinal parameters after some time. It can be performed by consistently measuring certain parameters by utilizing a medicinal screen nearby screen and additionally by more than once performing restorative tests. The process of wirelessly transmitting the patient's data from one station to a remote station is termed as biotelemetry. Remote healthcare system (RHS) is a healthcare system that makes the patient to use a portable medical setup to perform a standard check-up and report the patient's data to a healthcare expert instantly. The data is sent to the doctor by using a software application installed on the patient's electronic device such as computer, smart phone, or tablet [1]. Remote human services framework has begun to end up a captivating point among specialists, medicinal professionals, designs, and also IT organizations. In any case, the use of remote medicinal services framework where doctors can screen patient's well-being parameters by means of remote correspondence is accessible just in a couple of nations. Remote medicinal services framework is useful and invaluable to the patients and territories where the execution of these frameworks will spare patient's healing facility costs, holding up time, and manage traffics at the doctor's facility [1]. Our research aims to develop a low-cost healthcare system which is affordable for people of developing and under developed countries [2].

2 Materials and Methods

2.1 Measuring the Patient's Body Temperature Using LM35

An age-old rudimentary indicator of patient's health is his/her temperature. The body's temperature has the ability to generate heat. The ordinary human body temperature depends on the level of action, time, and place of the body where assessment is made [3]. For measuring patient's temperature, LM35 temperature sensor is utilized. LM35 identifies temperatures in the range (−55 to +150 °C). The yield voltage of LM35 is directly corresponding to temperature in Celsius [4]. The formula utilized for voltage–temperature change of LM35 is given demonstrated as follows,

$$T\,^{\circ}C = (V_{out}(mV))/10 \tag{1}$$

A contrasting option to LM35 is thermistor which is a nonlinear gadget, and because of its good accuracy, high efficiency, low cost, and stability, it is used in most of temperature measuring instruments [4]. Mostly, bead-type thermistors are used. Equation for resistance measurement is,

$$R_T = R_{T0} * \exp\{\beta(T_0 - T)/(TT_0)\} \tag{2}$$

2.2 Measurement of Heartbeat Pulse

Heartbeat pulse is one of the deciding factors of the patient's health. The ECG signal is divided into many intervals i.e. P, PQ, QRS, ST, and U intervals. A small variation in any one of the intervals represents a specific heart disease. One of the simple ways to check is through the BPM, also known as, beats per minute. BPM is derived with the help of R-R interval. Figure 1 shows the Arduino connected with temperature sensor LM35.

$$\text{Heart Rate(HR)} = 60/(\text{R-R Interval})\text{bpm} \tag{3}$$

The normal heart rate of a human being is 72 bpm, and if the heart rate goes below 60 bpm, it will be called bradycardia, and if it goes above 100 bpm, it is called tachycardia. Therefore, to find the heartbeat, the pulse sensor which is depicted in Fig. 2 is used. Pulse sensor, using IR led and phototransistor, detects the sudden flow in blood during the heartbeat.

The above values were displayed on software named Processing. Processing is a flexible software sketchbook and a language for learning how to code within the context of the visual arts [5].

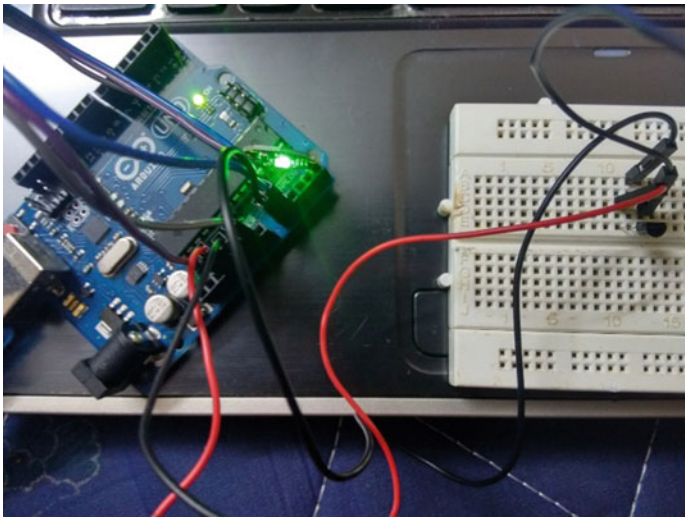

Fig. 1 Arduino connected with temperature sensor LM35

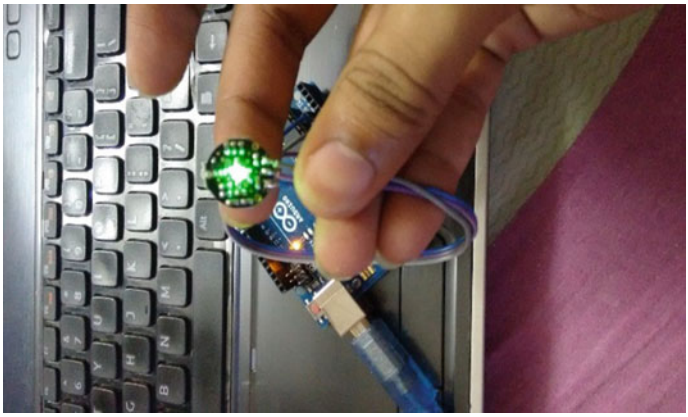

Fig. 2 Pulse sensor connection

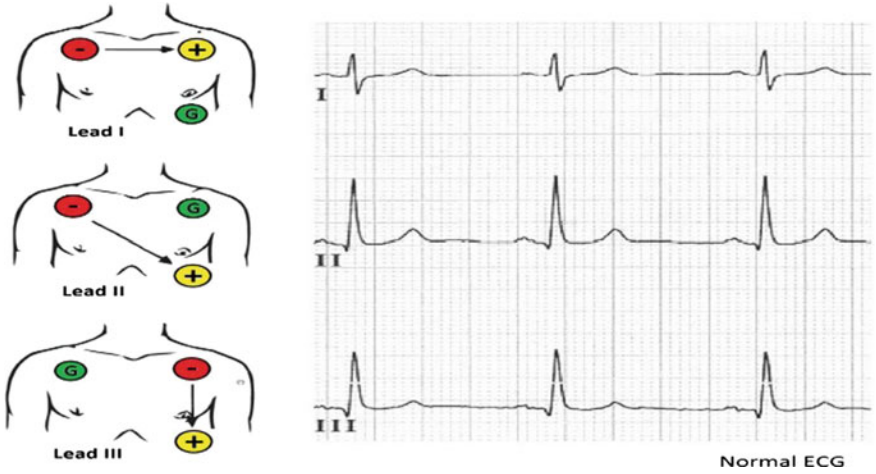

Fig. 3 3 Lead ECG placement configurations

2.3 ECG Signal Acquisition and Filtering

ECG signal is extracted from a patient's body using 3 lead electrodes (Fig. 3).

Configuration 2 was followed. From this arrangement, two of the terminals are connected to the inverting and non-inverting terminals of Instrumentation Amplifier INA128. Output from INA128 is passed through a notch filter which eliminates the 50 Hz AC supply noise. After eliminating the noise, it is passed through low-pass filter with cut-off frequency of 150 Hz. This gives the filtered ECG signal. It is further passed into an Op-Amp 741 which amplifies the signal. The amplified signal is sent through Arduino for further processing.

Arduino/Genuino Uno is a printed circuit board integrated with a multi-purpose microcontroller Atmega328, designed for the incorporation of various sensors and modules for effective data acquisition. The Arduino Integrated Development Environment (IDE) is an embedded system application written in Java programming language and can be combined with Processing IDE and other wiring projects. It has 14 digital I/O pins of which 6 pins can be used PWM purpose, 6 analog inputs, a 16 MHz external quartz crystal oscillator, a type B USB connection, a 12 V power jack, an In-Circuit Serial Programming (ICSP) header, and an inbuilt reset button.

In our system, we connect it to a laptop with a USB type A cable or power it with an 12 V adapter to get started. In most research applications, use of Arduino for data acquisition and data analyzing is quite easy and cost-effective (Figs. 4 and 5).

A power supply pf 9 V is given through a voltage regulator of 5 V. The electrodes' input is given to Vin^- and Vin^+ of the Instrumentation Amplifier INA128. Output from Instrumentation Amplifier is passed through a notch filter to eliminate 50 Hz noise from the AC supply. It is then passed through low-pass filter of cut-off frequency of 150 Hz. Filter output is passed through IC 741 to amplify the output. This is then passed to Arduino.

2.4 Sending Data Through Wi-fi to a Server

Wi-fi is run in almost every electronic device. In this twenty-first century, we can connect almost anything through Internet of Things. Data can be sent to a local server, data can extracted from a remote server, data logging can be done,

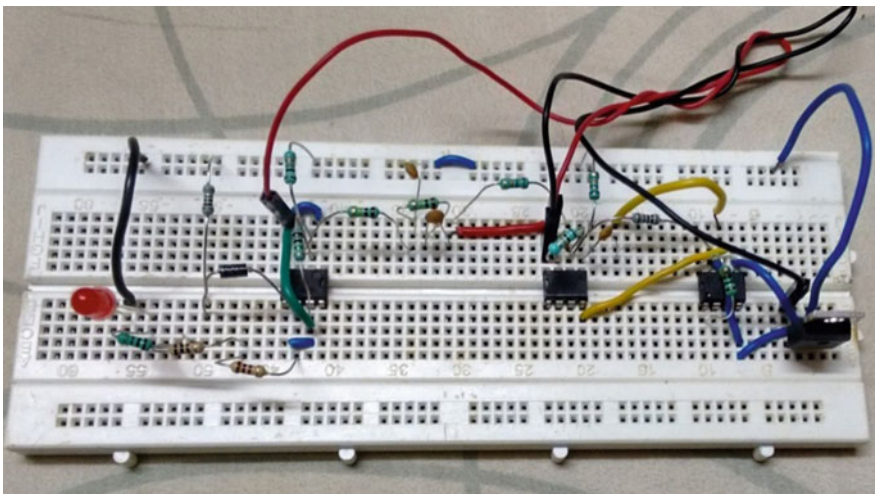

Fig. 4 ECG signal amplification and filtering circuit

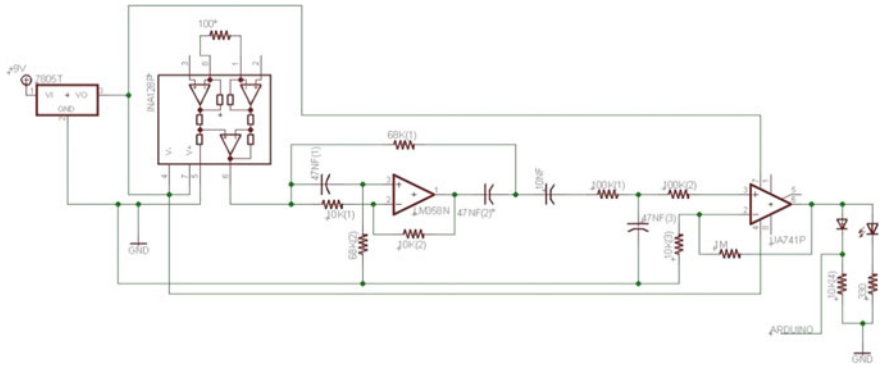

Fig. 5 Eagle schematic of ECG signal amplification and filtering circuit

and therefore, online visualization of data is possible. Therefore, these advantages were used and Wi-fi module ESP8266 was chosen over other communication modules such as Bluetooth, GSM, and Xbee. The ESP8266 ESP-01 is a low-cost Wi-fi module with full TCP/IP stack and microcontroller capability. It uses IEEE 802.11 communication protocol. It works on 3.3 V and consists of two GPIO pins, Rx and Tx, CH_PD, Reset, Power and ground Pin. ESP8266 can be configured to send data in two versions i.e. Standalone version and other version being with Arduino. The latter version was used and Wi-fi module's Rx and Tx will be connected to Tx and Rx of Arduino. The pulse sensor and temperature sensor were connected to the Analog ports of Arduino. There are a number of ways to send data to server. AT commands is the one of the ways, and this was used to transmit the data. These commands were used for their simplified version of coding. The values from pulse and temperature sensor are sent using AT commands using ThingSpeak. ThingSpeak is an open source Internet of Things (IoT) stage that empowers you to gather, store, investigate, imagine, and follow up on information from sensors or actuators, for example, Arduino, Raspberry Pi, Beagle Bone Black, and other equipment. ThingSpeak empowers the production of sensor logging applications, area following applications, and social networking with status updates.

A channel was created with two parameters i.e. Temperature and pulse rate sensor. Using the Wi-fi module, data was sent to the website using a unique API key. The values on ThingSpeak are updated every 15 s.

Therefore, uploading on a webpage will help not only the patient but also the remote doctors to assess or monitor the patient's health. Doctors can anytime login to their account and go to the channel which is made unique to each patient. This lowers the overall Medicare cost (Fig. 6).

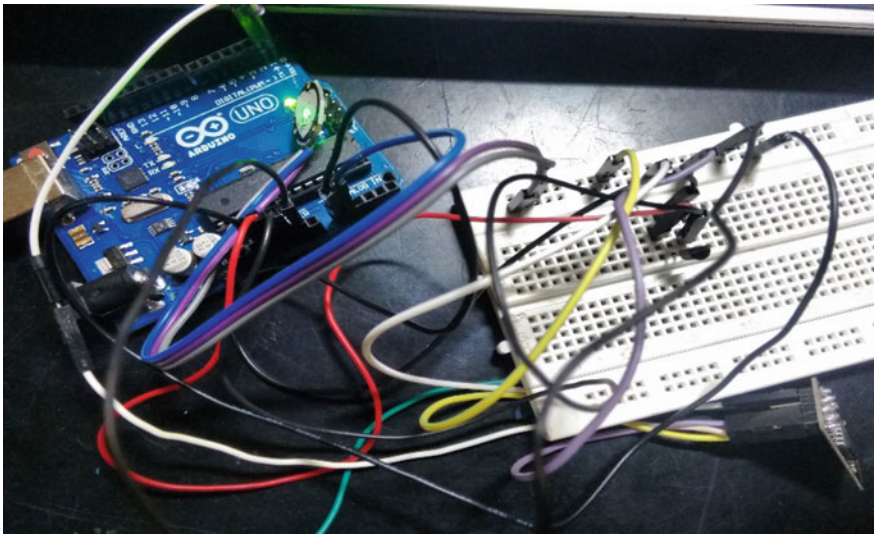

Fig. 6 Final circuitry containing pulse sensor, temperature sensor LM35 on breadboard, and ESP8266 ESP-01 Wi-fi module at bottom corner

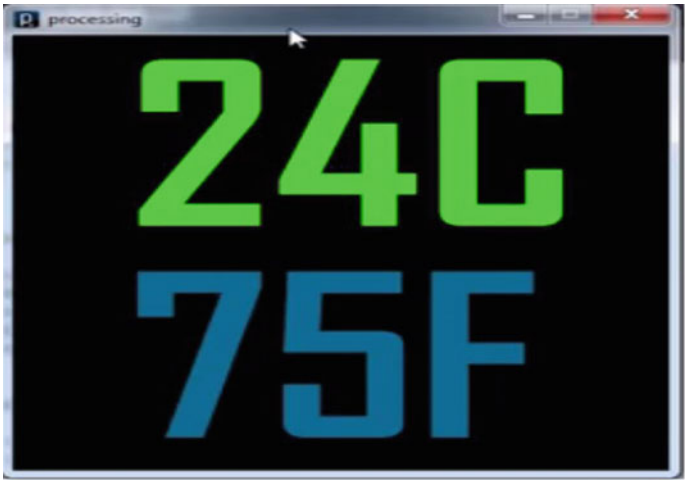

Fig. 7 Processing software displaying temperature

3 Results and Discussion

The Fig. 7 displays the temperature using Processing software. The temperature is measured using LM35 sensor. Low-yield impedance, direct yield, and exact interior adjustment of the LM35 sensor make it less demanding to interface.

Fig. 8 Processing software displaying the heart rate

Fig. 9 Filtered heartbeat display using serial monitor

The above Fig. 8 shows the output of the pulse sensor. The pulse sensor is quite accurate to get the raw values. The raw values are converted to beats per minute using an Arduino algorithm and displayed using Processing software. The Processing software is therefore best suited for testing purposes.

The Fig. 9 displays the filtered heartbeat connected to the serial monitor of Arduino. Using serial plotter in Arduino, we are able to get the heartbeat display. Though some noise has been eliminated, while getting the output through Arduino had some delay while displaying its output. This can be reduced by using a more efficient data acquisition system than the Arduino and therefore get more spontaneous result (Fig. 10).

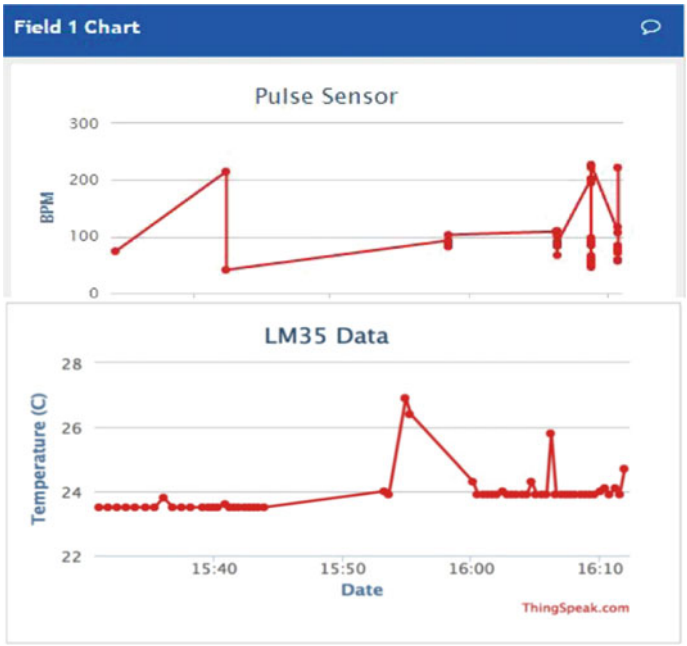

Fig. 10 Output on ThingSpeak

The above figure shows the output of the pulse sensor and temperature sensor data on ThingSpeak. Through ESP8266 Wi-fi module, the data is transmitted through AT commands. In the algorithm, there is an option for defining the refresh rate for sending the data to the server which the user can change it accordingly.

4 Conclusion

In this paper, new cheaper ways of obtaining medicare results such as ECG signal, beats per minute and the patient's temperature have been implemented. Using Processing software, displaying the values is easier. Also, using remote server tools such as ThingSpeak is used which allows storing and analyzing of data in a much easier way. This all corresponds to the main objective of making low-cost medicare system. However, there is no limit to the evolution of technology in any field. This project can further be taken to new heights such as sending email or message to the doctor in case of emergency. Also, doctors far away from the testing location can also feed the inputs to improve the patient's health.

References

1. Agham, N.D., Thool, V.R., Thool, R.C.: Mobile and web based monitoring of patient's physiological parameters using LABView. IEEE India Conference (INDICON) (2014)
2. Ahamed, M.A., Ahad, M.A.U., Sohag, M.H.A., Ahmad, M.: Development of low cost wireless bio-signal acquisition system for ECG EMG and EOG. In: 2nd International Conference Electrical Information and Communication Technology (EICT) (2015)
3. Mansor, H., Shukor, M., Meskam, S., Rusli, N., Zamery, N.: Body temperature measurement for remote health monitoring system. In: Smart Instrumentation Measurement and Applications (ICSIMA) (2013)
4. Agham, N., Thool, V.: Labview based physiological parameters monitoring system for patient health-care. Int. J. Eng. Res. Technol. **3** (2014)
5. Datta, R.P., Gupta, D.: Electrocardiogram using piezo-electric sensor. Int. J. Eng. Res. Technol. **4** (2015)
6. Alves, A.P., Silva, H., Lourenco, A., Fred, A.L.N.: BITtalino: a bio-signal acquisition system based on the arduino
7. LM35 Datasheet (Online): http://www.ti.com/lit/ds/symlink/lm35.pdf
8. INA129 Datasheet (Online): http://www.ti.com/lit/ds/symlink/ina129.pdf

Modelling of UPFC (Unified Power Flow Control) to Improve Stability of Power System by Real and Reactive Power Control of Transmission Line

Rakhi Kumari, Prerna and Chitrangada Roy

Abstract Power systems are very complicated, and it needs careful fabrication of recent equipment considering the already existing devices. Flexible AC transmission system (FACTS) devices are introduced to improve the controllability and to raise the power transfer capacity of electric power systems. In this paper, unified power flow controller (UPFC) is opted among various FACTS devices to improve real and reactive power flow in the transmission line. When UPFC is not connected to the system, real and reactive power through transmission line cannot be controlled. In this paper, a UPFC model has been designed and implemented using MATLAB/Simulink. The simulation results obtained from the model show the improvement of power quality and voltage stability in transmission line.

Keywords Flexible AC transmission systems (FACTS)
Unified power flow controller (UPFC)
State space vector pulse width modulation (SVPWM)
Hysteresis current-controlled PWM

1 Introduction

With the increased electrical power demands, complexity of power systems is increasing day by day. Due to inadequate sources of energy, extension of power generation and transmission has been critically affected. As a result, the stressed power systems face stability problems due to disturbances [1]. Therefore, it is

Rakhi Kumari · Prerna · Chitrangada Roy (✉)
Department of Electrical & Electronics Engineering, Sikkim Manipal Institute of Technology, Majitar, Sikkim, India
e-mail: roychitrangada@gmail.com

Rakhi Kumari
e-mail: newsrakhi17@gmail.com

Prerna
e-mail: prerna.singh1592@gmail.com

A. Konkani et al. (eds.), *Advances in Systems, Control and Automation*,
Lecture Notes in Electrical Engineering 442, https://doi.org/10.1007/978-981-10-4762-6_62

essential to improve the power transfer capacity of the current transmission systems. FACTS devices are used in order to make the system fast and flexible and to increase the controlling capability. FACTS technology is basically a collection of controllers which works individually or collectively with other devices to achieve better system performance [2].

Among various FACTS devices, UPFC has been used due to its various advantages over other FACTS device. It consists of shunt compensator as Static Synchronous Compensator (i.e. STATCOM) and series compensator as Static Synchronous Series Compensator (i.e. SSSC). These two converters are connected one after another with the help of a DC link. It can simultaneously or selectively control all the parameters such as voltage, phase angle, and impedance, which affects flow of power through the transmission. UPFC inserts voltage in the transmission line; thus, it controls the flow of real and reactive power through transmission line independently [3]. Voltage regulation and transient stability of power system are improved with the help of UPFC. In order to suppress oscillations of power system, UPFC effectively controls damping [4].

In this paper, the capability of UPFC on controlling real and reactive power flow in transmission line to improve stability of the power system is investigated. The simulation results are obtained using MATLAB/Simulink software to analyse the capability of UPFC.

2 Operating Principle of UPFC

Unified power flow controller is a speculated synchronous voltage source (SVC). It is expressed at the fundamental frequency by voltage phasor (V) with adjustable magnitude ($0 \leq V \leq V_{\max}$) and angle α ($0 \leq \alpha \leq 2\pi$). The UPFC consists of two voltage source inverters VSC1 and VSC2 as shown in Fig. 1. These converters are connected back-to-back through a capacitor.

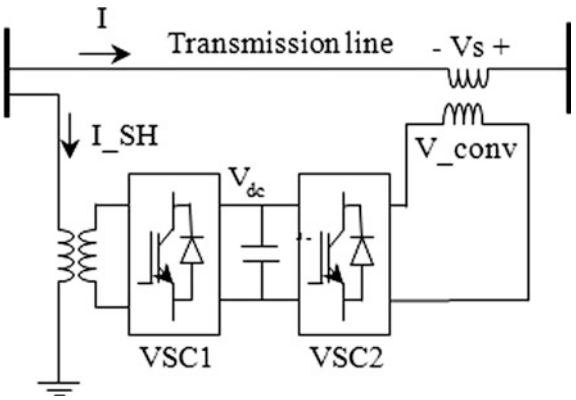

Fig. 1 Block diagram of UPFC connected to transmission line

The VSC2 injects a voltage to the transmission line through a coupling transformer, which is connected in series with the transmission line as shown in Fig. 1. The transmission line current I travels through this voltage source to provide real and reactive power interchange between UPFC and the transmission system. The VSC1 consumes or delivers active power as per the requirement of VSC2 at the DC link. The output voltage of VSC1 is delivered to the transmission line through a coupling transformer which is connected in parallel with the transmission line.

3 UPFC Controller Design

The equation of series controller is given as below. It injects the voltage V_{sr} in series with transmission line:

$$V_{sr} - V_{sr1} = R_{sr} I_{sr1} + I_{sr} \frac{d}{dt} I_{sr1} \tag{1}$$

$$\begin{bmatrix} P_0 \\ Q_0 \end{bmatrix} = \begin{bmatrix} V_{od} & V_{oq} \\ -V_{oq} & V_{od} \end{bmatrix} \begin{bmatrix} I_{srd} \\ I_{srq} \end{bmatrix} \tag{2}$$

$$\begin{bmatrix} V_{srd} \\ V_{srq} \end{bmatrix} = \begin{bmatrix} \frac{V_{od} - V_{id}}{N_{sr}} + R_{sr} I_{sr} I_d + L_{sr} \frac{d}{dt} I_{sr} I_d - w L_{sr} I_{sr} I_d \\ \frac{V_{oq} - V_{iq}}{N_{sr}} + R_{sr} I_{sr} I_q + L_{sr} \frac{d}{dt} I_{sr} I_q - w L_{sr} I_{sr} I_q \end{bmatrix} \tag{3}$$

$$\begin{bmatrix} I_{sr} I_d^* \\ I_{sr} I_q^* \end{bmatrix} = \frac{2}{3} \frac{1}{N_{sr}} \frac{1}{\left(V_{od}^2 + V_{oq}^2 \right)} \begin{bmatrix} V_{od} & V_{oq} \\ V_{oq} & V_{od} \end{bmatrix} \begin{bmatrix} P_0^* \\ Q_0^* \end{bmatrix} \tag{4}$$

where V_{sr} and I_{sr} are the series voltage and series current, respectively; L_{sr} is series inductance and N_{sr} is no. of turns of series transformer; w is the angular speed, and P_0 and Q_0 are the active power and reactive power, respectively.

The model of series converter using MATLAB/Simulink is shown in Fig. 2. In series converter, we generate the pulses with the help of Space Vector Pulse Width Modulation (SVPWM) technique [5], and these generated pulses are used to drive the voltage source series converter.

The blocks represent the shunt converter using MATLAB/Simulink as shown in Fig. 3. In case of shunt converter, pulses are generated with the help of Hysteresis Current Control PWM technique [6], and these generated pulses are used to drive the voltage source converter.

Equations (5)–(9) of shunt controller are given as follows:

$$P_{sh} = \frac{2}{3} \left(V_{id} I_{shd} + V_{iq} I_{shq} \right) \tag{5}$$

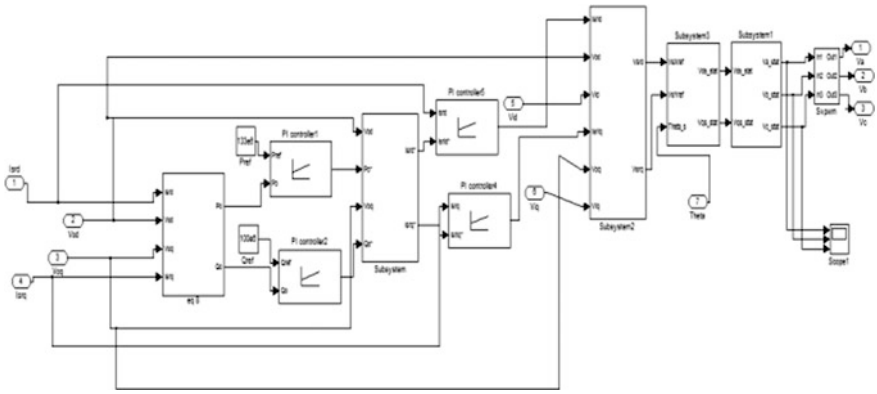

Fig. 2 Series converter using MATLAB/Simulink

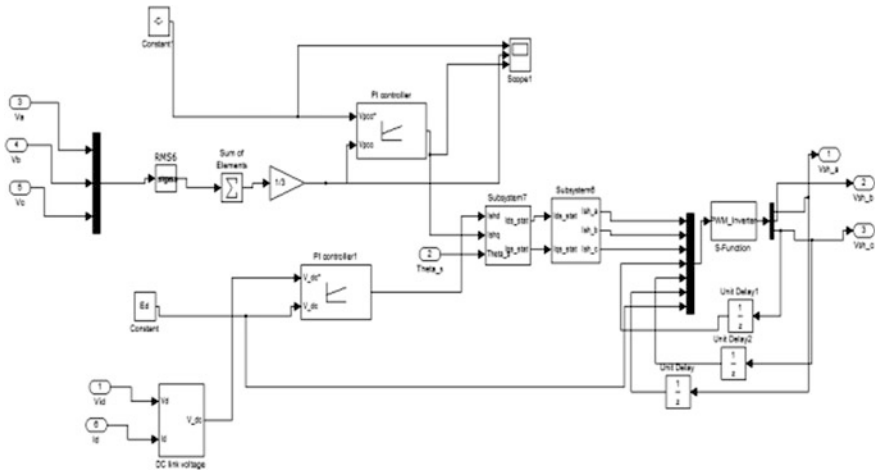

Fig. 3 Simulink model of shunt converter

$$Q_{\text{sh}} = \frac{2}{3}\left(V_{id}I_{\text{sh}q} - V_{iq}I_{\text{sh}d}\right) \tag{6}$$

$$\begin{bmatrix} I_{\text{sh}d} \\ I_{\text{sr}q} \end{bmatrix} = \frac{2}{3}\frac{1}{N_{\text{sh}}}\frac{1}{\left(V_{od}^2 + V_{oq}^2\right)}\begin{bmatrix} V_{id} & -V_{iq} \\ V_{iq} & V_{id} \end{bmatrix}\begin{bmatrix} P_{\text{sh}} \\ Q_{\text{sh}} \end{bmatrix} \tag{7}$$

$$V_{\text{dc\_actual}} = \frac{3}{2}\int \frac{1}{c}\frac{V_d I_d}{V_{\text{dc}}} \tag{8}$$

$$P_{\text{loss}} = \frac{V_{\text{dc}}^2}{R_c} + 3R_{\text{sh}}I_{\text{sh}}^2 + R_{\text{sr}}I_{\text{sh}}^2 \tag{9}$$

where V_{sh} and I_{sh} are the shunt voltage and shunt current, N_{sh} represents the no. of turns of shunt transformer, P_{loss} is the power loss in transmission line, and V_{dc} represents the DC link voltage.

4 Test System Modelling

The three-phase test system has been shown in Fig. 4. The generation voltage is 66 kV at 50 Hz. The length of three-phase 500 kV pi-section line is 60 km. In the receiving end, a RL load of 100 MW at 0.8 power factor lagging is connected.

5 Results and Discussion

In this thesis, active and reactive power control for a UPFC has been discussed. The principle control approach is such that the shunt controller of a UPFC controls the bus voltage and DC link capacitor voltage. The series controller of UPFC regulates the active and reactive power transfer of transmission line. The contribution to the work has been encapsulated as follows.

Figures 5 and 6 show the sending end rms voltage and receiving end rms voltage without UPFC. Sending end rms voltage is 352 kV and receiving end voltage is 347 kV. There is a difference in voltage between sending and receiving end rms voltage due to the losses in the transmission line.

Figures 7 and 8 show the improved sending end rms voltage and receiving end rms voltage in the presence of UPFC. Sending end rms voltage is slightly increased to 352.3 kV, and receiving end voltage is increased to 350 kV. It is observed here that the voltage regulation is improved when UPFC is installed in the transmission line.

Figure 9 shows the active power through the line without UPFC. Here, active power at the sending side is 28.11 MW and receiving end active power is

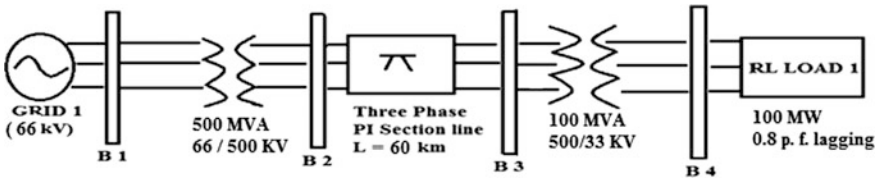

Fig. 4 Block diagram representation of the three-phase test system

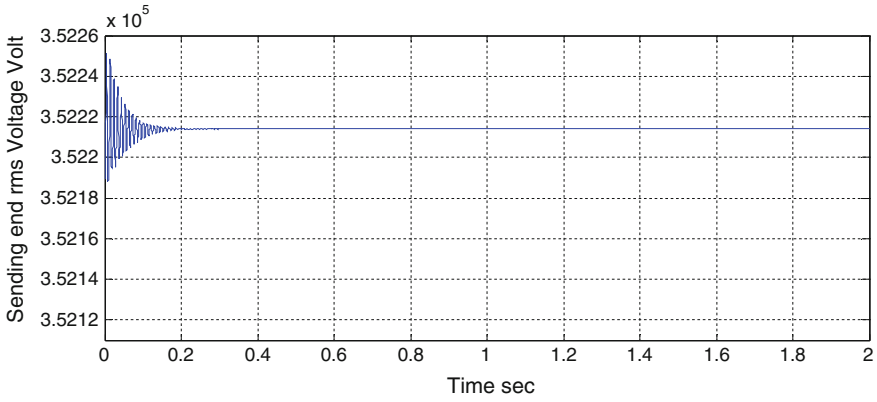

Fig. 5 Sending end rms voltage without UPFC

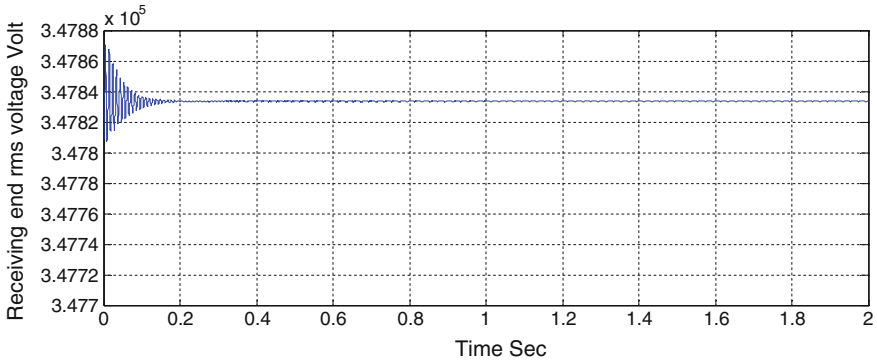

Fig. 6 Receiving end rms voltage without UPFC

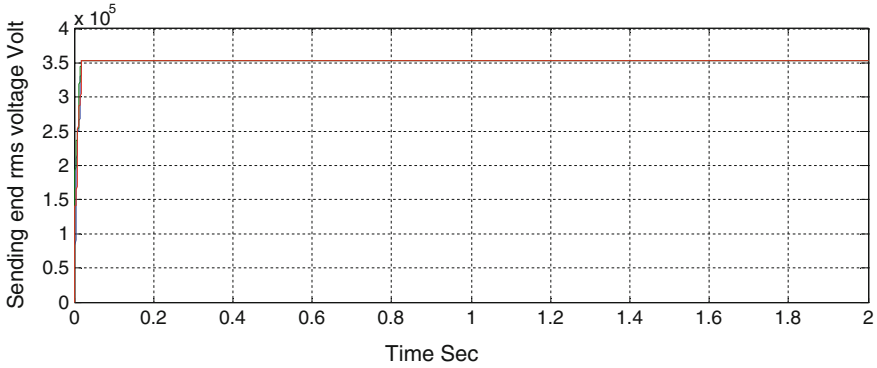

Fig. 7 Sending end rms voltage with UPFC

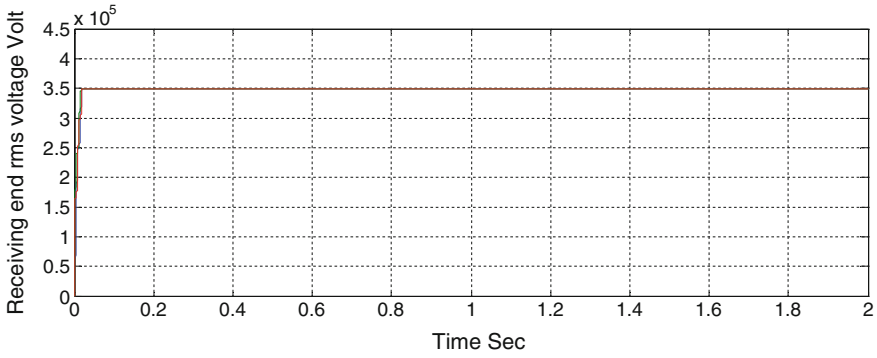

Fig. 8 Receiving end rms voltage with UPFC

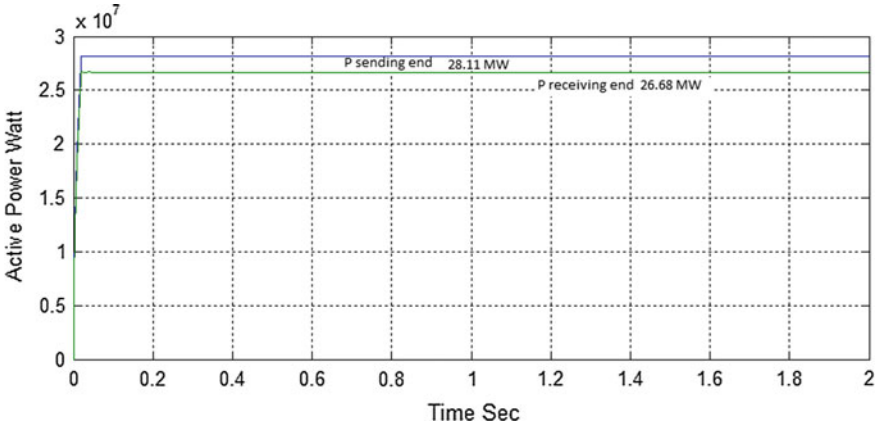

Fig. 9 Active power without UPFC

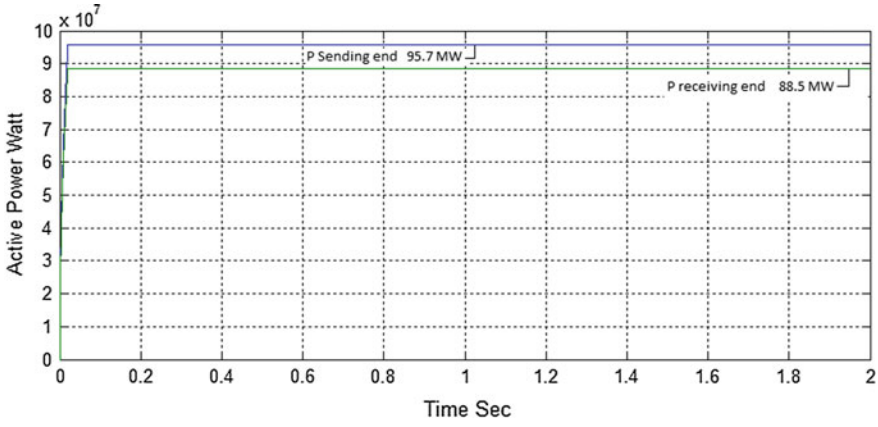

Fig. 10 Active power with UPFC

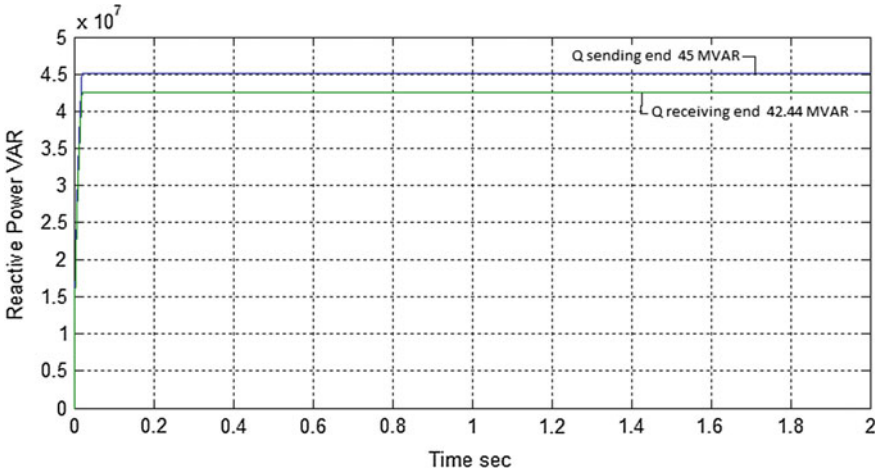

Fig. 11 Reactive power without UPFC

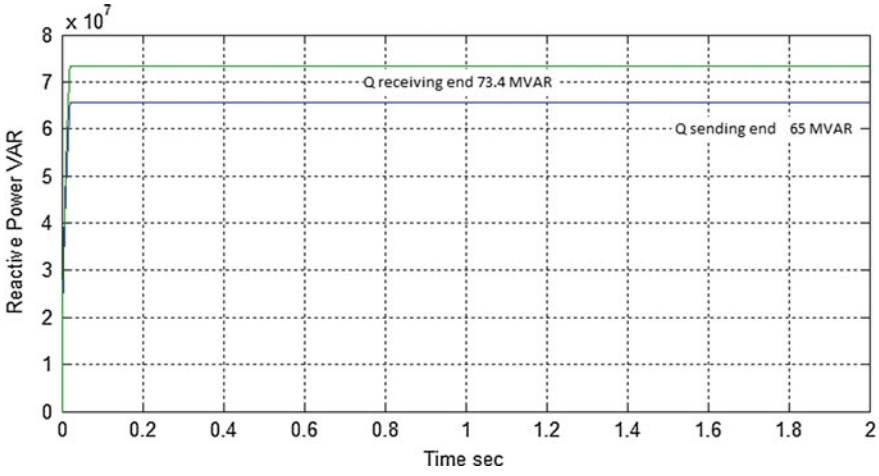

Fig. 12 Reactive power with UPFC

26.68 MW. When the transmission line is without UPFC, the real and reactive power flow cannot be regulated.

Figure 10 shows the active power flow through line in the presence of UPFC. Here, real power at the sending end side is increased to 95.7 MW (with UPFC) from 28.11 MW (without UPFC) and receiving end active power is improved to 88.5 MW (with UPFC) from 26.68 MW (without UPFC). It is observed that the transmission capacity of the existing transmission line is highly upgraded with the help of UPFC controller.

In the presence of UPFC, the difference between the sending end real power and receiving end real power is high in the transmission line. As a result of increased transmission line losses, it counts losses in the both converters.

The waveform for reactive power at sending and receiving ends without UPFC is shown in Fig. 11; in this case, sending end reactive power (45 MVAR) is greater than the receiving end reactive power (44.44 MVAR). When the transmission line is connected with the UPFC as shown in Fig. 12, the reactive power of receiving end is increased to 73.4 MVAR and the reactive power of sending end is increased to 65 MVAR. So here, it is observed that power quality of the transmission line gets improved in the presence of UPFC.

6 Conclusion

This paper clearly shows that UPFC used in this case has improved the real and reactive power flow and voltage stability in transmission line. The simulation results show that real power and reactive power at both sides, i.e. at receiving end and at sending end, are improved when UPFC is introduced in the transmission line. Voltage regulation is also improved when UPFC is placed in the transmission line. Thus, these results illustrate the performance of UPFC to improve stability of power system effectively.

References

1. Tiwari, S., Naresh, R., Jha, R.: Neur network predictive control predictive control of UPFC for improving transient stability performance of power system. Appl. Soft Comput. **11**(8), 4581–4590. ISSN 1568-4946 (2011)
2. Hingorani, N.G., Gyugyi, L.: Understanding FACTS: Concepts and Technology of Flexible AC Transmission Systems. IEEE Press, NewYork (2000)
3. Fujita, H., Akagi, H., Watanabe, Y.: Dynamic performance of a unified power flow controller for stabilizing AC transmission systems. In: IEEE 33rd Annual Conference on Power Electronics Specialists Conference, 2002 (pesc 02), vol. 1. IEEE (2002)
4. Benachaiba, C., Haidar, A.M., Doumbia, M.L.: Robust and Intelligent Control Methods to Improve the Performance of a Unified Power Flow Controller (2011)
5. Norouzizadeh, R., et al.: Design and simulation of unified power flow controllers using matrix converters. In: 2010 IEEE International Symposium on Industrial Electronics. IEEE (2010)
6. Suul, J.A., et al.: Synchronous reference frame hysteresis current control for grid converter applications. IEEE Trans. Ind. Appl. **47.5**, 2183–2194 (2011)

Autonomous Navigation Robot Based on Real-Time Image Processing

Bijay Rai, Pratik Pradhan and Roshan Pradhan

Abstract The project discusses the design and operation of a simple robot vehicle guided by the track and navigation system made capable by 2D image processing in MATLAB software. The system uses a robust and simple design to automatically track a robot toward a specified path. It does not use GPS or other position sensor system to track vehicle along the path but rather uses visual information run by a software program. The program takes real-time pictures of the vehicle, understanding its direction of projection, and guides to path set by the user. Its contribution can be used for unmanned autodriving/autopiloting of a vehicle in a given path through a monitoring camera or satellite imagery. Its implication consumes least resources of technology as only the imagery monitor system and simple control signal transmission apart from the complex dependency of resources of GPS technology or multiplexed sensor systems. The only requirement being the visibility of the robot from a static camera device, its approach is similar to the functionality of navigation through biological visual based guidance system of humans, so it is a direct, experienced, and simple robust approach.

Keywords Image processing · Automatic navigation · Automatic robot
Path follower

B. Rai (✉) · P. Pradhan (✉) · R. Pradhan (✉)
Department of Electrical and Electronics Engineering, Sikkim Manipal Institute of Technology, Majitar 737136, Sikkim, India
e-mail: bijay.rai1@gmail.com

P. Pradhan
e-mail: pratik.pradhan88@gmail.com

R. Pradhan
e-mail: roshanpradhan.rp@gmail.com

A. Konkani et al. (eds.), *Advances in Systems, Control and Automation*,
Lecture Notes in Electrical Engineering 442, https://doi.org/10.1007/978-981-10-4762-6_63

1 Introduction

The project setup required a moving robot, USB Web camera 5MP and MATLAB 7.11 running on desktop having CPU 3.2 GHz Intel i3 processor. The robot was a small DC motor-driven car capable of making left/right turns and forward movement. It was controlled wirelessly through a RF transmitter 2.4 GHz connected to the USB of the desktop. The robot car had the RF receiver and an 8-bit microcontroller to decode instruction given by transmitter to drive the car into its directed motion. The USB camera captures images of the robot and its surroundings on which the user can set a predetermined path. The image frames were fed to the program in MATLAB to process for information of the robot and its path. The frames were then processed in real time to understand the position and alignment of the robot comparatively with the path points to be followed. Image segmentation and geometrical calculations are computed for understanding and directing the position of the robot to its path. It generated the instruction of next movement to be executed by the robot. The system is a really efficient approach for automatic navigation of robots rather than the widely used triangulation method through complex machines such as radio towers and satellites [1]. GPS often is not perfect for autonomous control on navigation as it does not give an accurate idea of orientation of movement. It is assisted with other IMU (inertial measurement unit) to improve accuracy of movement direction sensors [2]. Image processing technology is an inexpensive technique possible and suitable for autonavigation in plain uniform terrain platform. The least resource requiring capability of the system can be applied in industrial and military applications [3].

2 IMAGE Acquisition and Object Recognition

A single image of the robot and its coverage area was taken through the USB camera. Image taken by camera was in HSV format which is an easier and better color segmentation method for image processing the color component is very immune to darkness and intensity level change [4]. First, the robot vehicle was to be marked with a target coordinate, by the user to identify the color of the object. It was done by using the mouse to click at the proximate midpoint of the robot in the picture. This needed to be done only once for the initialization of the robot identification. The hue (color) and value (brightness) of the target coordinates $h(x_t, y_t), v(x_t, y_t)$, respectively, are taken and stored for reference of object later. The robot body was given a definite shape and color so as to understand its position and alignment in the 2D plane. Here, an isosceles triangle blue-colored object was placed on top of the car to serve the purpose. It was then followed by user clicking path coordinate points to be covered by the robot. The coordinates were stored as $t(x_1, y_1), t(x_2, y_2), t(x_3, y_3) \ldots t(x_n, y_n)$ where n is the number of path points to be covered. Then, the program took continuous shot of the robot and its coverage area for automatic navigation through

image processing as shown in Fig. 2. Frame size of the continuous shot was taken at a low value as 150 × 150 pixels for fast efficient processing as imposed less dimensional matrix calculations. Segmentation of the image frame was carried out to create objects of the color matching to that of the target coordinate. Normalized Hue color and brightness value $h(x_i, y_j), v(x_i, y_j)$ of all coordinates (i.e., i, j = 1, 2, 3… 150) were run in a loop and compared with $h(x_t, y_t), v(x_t, y_t)$, respectively. By matching the color region, the target body is segmented and created into regions. This is an efficient and easy process of segmentation for identification and processing of the objects [5]. All values lying within a threshold of 0.02 hue and 0.2 value are segmented to form regional white image objects in black background. The saturation threshold value was taken higher to consider the effects of different lighting intensity effects. These objects are then applied with empty holes fill-up and Gaussian filter. This helps remove noises and black pixel gaps on the object created by irregular surface of body or lighting condition on the robot [6]. Following was the code written to recognize the object color using hue and saturation value limitation.

```
bw1 = hsv1(:,:,1)<(hue+hue_thres) & hsv1(:,:,1)>(hue-hue_thres) &
hsv1(:,:,2)>(sat-sat_thres) & hsv1(:,:,2)<(sat+sat_thres);
bw2 = imfill(bw1, 'holes');
h = fspecial('gaussian',[2 2],8);
bw = imfilter(bw2,h);
```

Gaussian filter formula is applied as

$$g(i,j) = c.e^{\frac{i^2+j^2}{2\sigma^2}}$$

where σ is defined by the user, and i, j are pixel coordinates controlled by the m-, n-dimensional matrix set by the user.

The object closest to the reference coordinate was taken as the robot object hence recognizing the robot and its position. The centroid of the object (x_c, y_c) was considered as the position of the robot in the 2D plane. It may be obvious that similar blue-colored objects may be lying around the robot. But they are neglected as the blue-colored object only to the nearest of the target coordinate $t(x_k, y_k)$ is considered. This is possible taking into consideration that the object lays distinctively close to the targeted body.

This closest reference point for progressive frame was considered as centroid (x_c, y_c) of the chosen object of robot in previous frame. There is a small time gap between each frame of around 100–200 ms so having a highest probability that the centroid of robot object in past frame will be closest to centroid of same object in next frame. This also makes identification of the robot immune, as program has a least chance that other similar objects in surroundings are misidentified as robot object under guidance. The head and centroid method is superior for orientation calculation of moving objects which is mostly impossible simple GPS-based systems. GPS often requires progressive reading of movement coordinates to understand the orientation of movement of a body [7].

3 Geometrical Measurements and Calculations

The crucial step in processing of every frame of the image becomes to understand the shape and movement projection of the object robot. A robot could be understood of its position and movement trajectory from the image frames processed with geometrical computation at high speeds [8]. Shape of the robot is designed as blue-colored isosceles triangle, making it asymmetrical between the upper and lower parts of the triangle. This helps in unique recognition of the tail and the head of the object. Distances from the centroid of triangle object to the extreme points of the objects are measured. The vertex in the furthermost distance (tip point of the triangle) is taken as the head of the object, while the centroid is taken as the bottom end of the object as shown in Fig. 1. This helps in clearly understanding the alignment of the robot in a 2D plane hence giving information of its movement projection angle on the plane. Angle in between head point coordinate (x_h, y_h), the tail point coordinate (x_c, y_c), and the horizontal axis passing through the tail point was measured to be taken as car angle α using formula

$$\theta_1 = \cos^{-1}\left[\left(\rho_{1,2}^2 + \rho_{1,3}^2 - \rho_{2,3}^2\right)/\left(2.\rho_{1,2} \cdot \rho_{1,3}\right)\right]$$

where $\rho_{1,2}$ the distance between two vertexes 1 and 2 (similar for $\rho_{1,3}$ and $\rho_{2,3}$), θ_1 is the angle at vertex 1 (Fig. 2).

Figure 3 represents the alignment of the car in the 2D plane. Angle between the target path coordinate $t(x_1, y_1)$, head point, and the tail point was taken as the path angle β. The path and car angles were compared to align the car straight toward target coordinate $\eta = \beta - \alpha$.

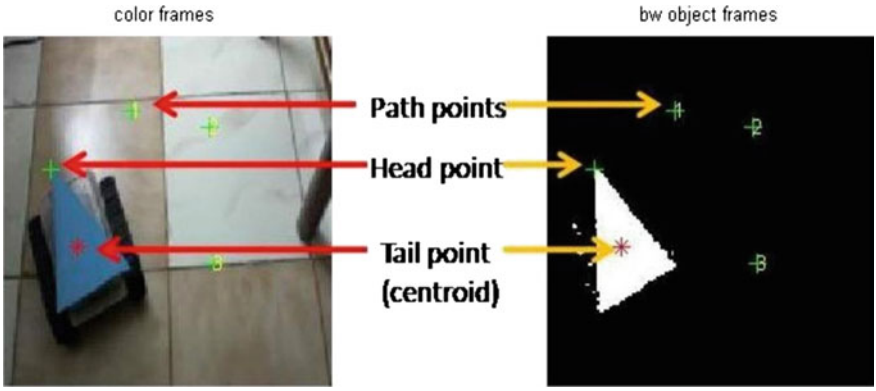

Fig. 1 Color image and recognized segmented object of the robot. Detailed head, tail, and path coordinates of the robot object

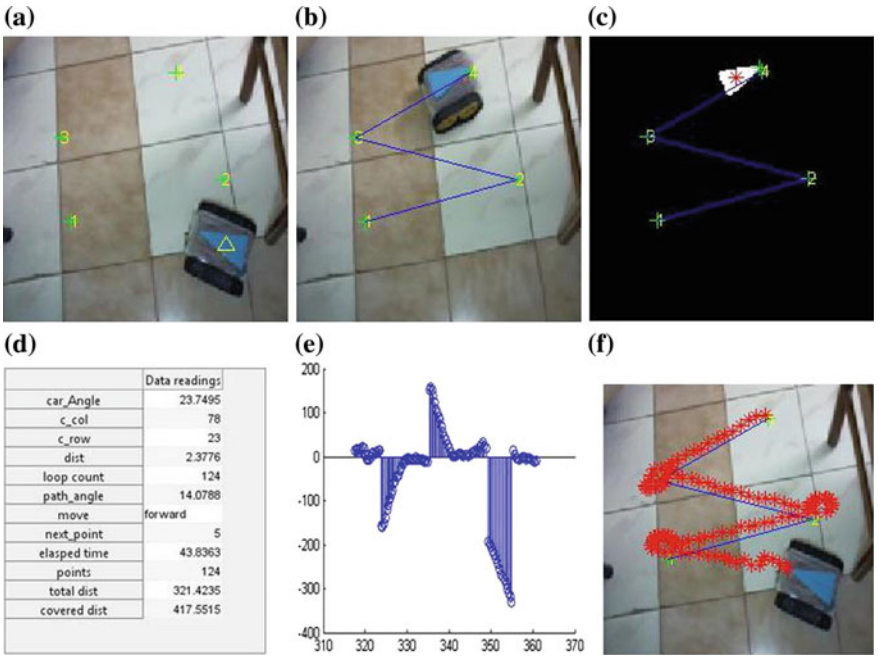

Fig. 2 GUI windows plot. **a** Click and set path points and robot. **b** Color frames stream of robot along path. **c** Filtered and segmented black and white image frame of robot object along the path set. **d** Progress real-time data interface table for user. **e** Plot of oscillation angle versus time. **f** Plotted movement of robot along path

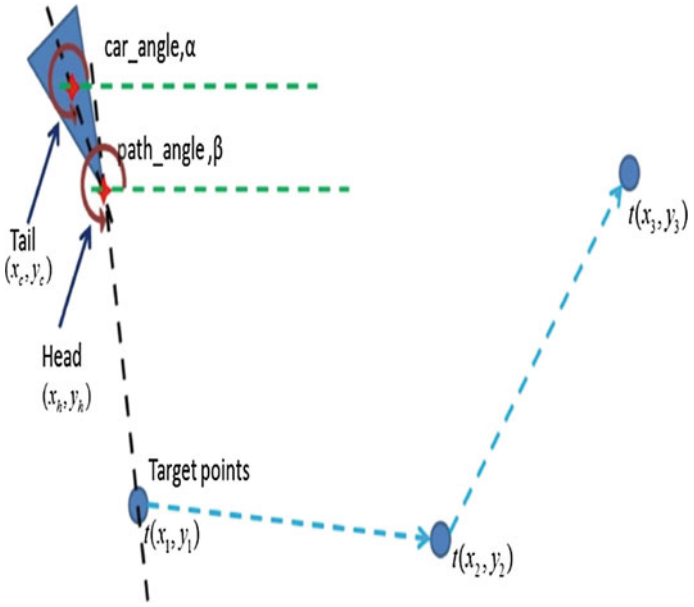

Fig. 3 Coordinates of path coordinates, head, tail, and car angle and path angle

4 Methodology Used for Movement of Robot

When car and path angles are almost equal to each other within a threshold angle, η_{thres} (set by user) the car was moved forward. In the case, $|\eta| < \eta_{\text{thres}}$, the robot has to rotate left or right as explained by the flowchart in Figs. 4 and 5 given.

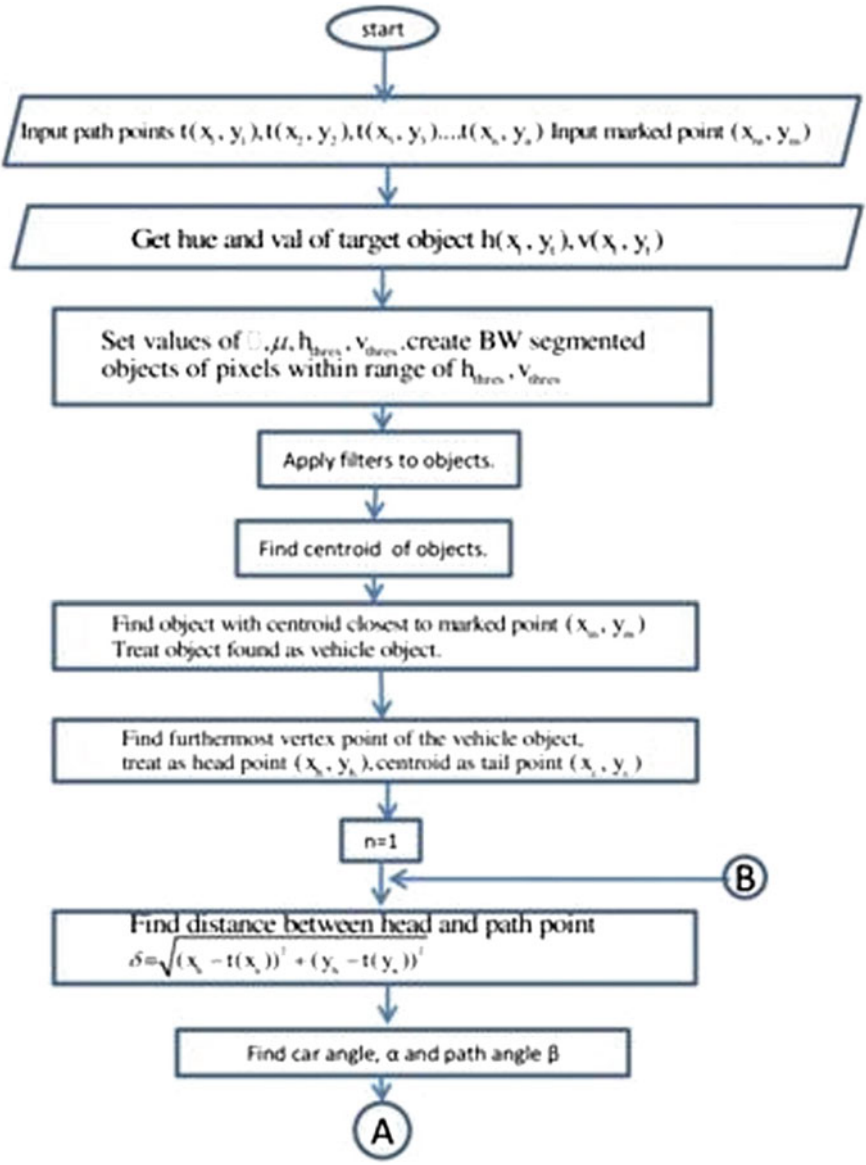

Fig. 4 Flowchart part 1

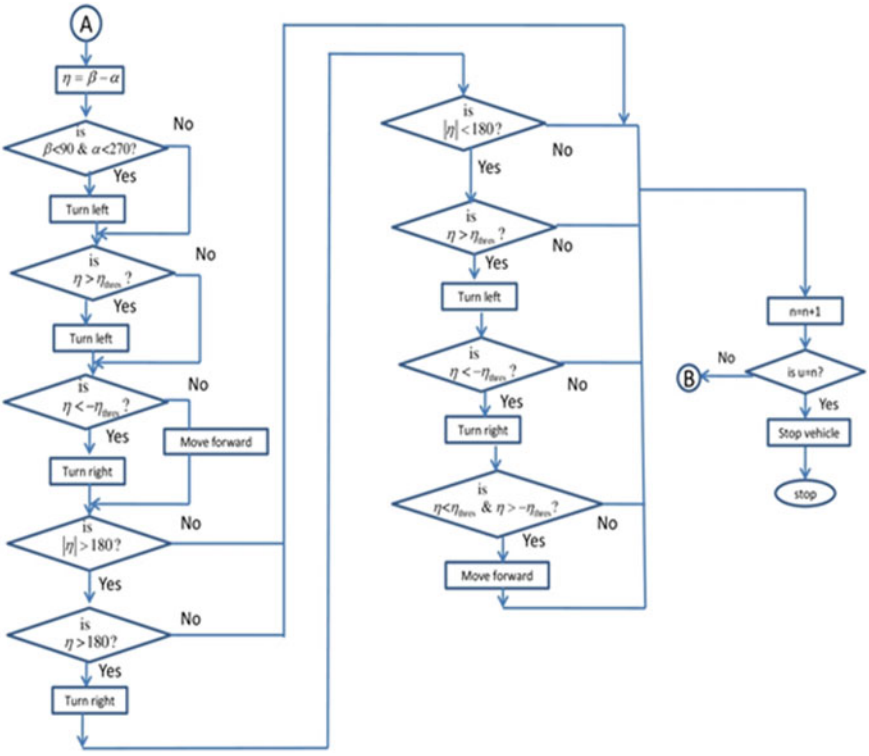

Fig. 5 Flowchart part 2

All angles were measured with the bottom edge of the figure as x-axis and left edge of the figure as y-axis. This way the car reaches to the target coordinate $t(x_1, y_1)$. The reach to the point was decided by measuring distance between centroid (x_c, y_c) of robot object and the next target point coordinate represented as δ, $\delta = \sqrt{(x_h - t(x_k))^2 + (y_h - t(y_k))^2}$. δ_{thres} is the threshold distance set by the user. When $|\delta| < \delta_{\text{thres}}$, the program automatically updates and guides the robot to the next target point $t(x_2, y_2)$, also incrementing the points covered at the same time. Any misalignment of the robot on its progression is corrected by the same method until $|\delta| < \delta_{\text{thres}}$. The process is carried out until the count for all the desired coordinates was reached. The detailed flow of processing is described as given by the flowchart in Figs. 4 and 5.

5 Observations on Performance

The project had been trialed with several different types of settings for different results of performance. The threshold angle and the speed of the robot played critical important role in performance. Figure 6 displays the plots and images for

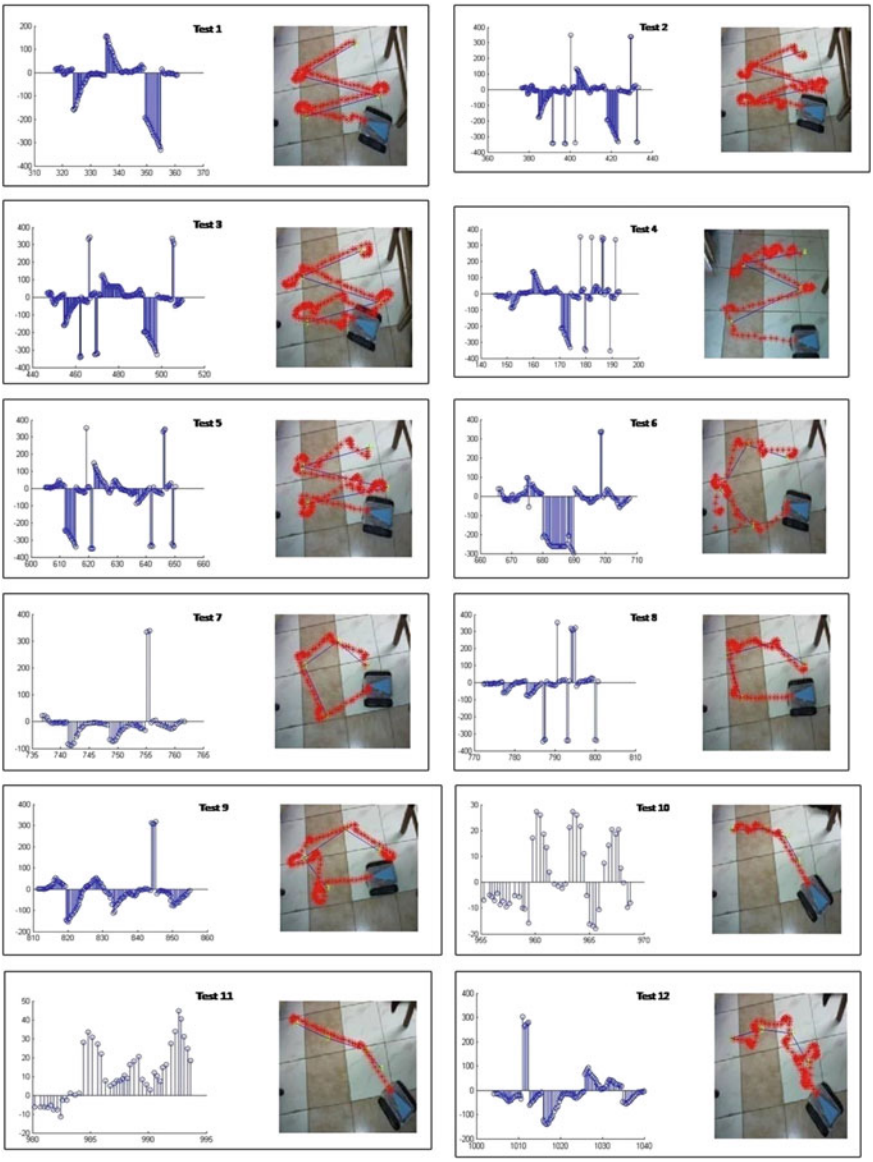

Fig. 6 Plot graph (oscillation angle vs. time) and plotted movement of robot along path for Test 1, Test 2… Test 12

output observations in real time. It plotted the track of the vehicle movement in real time, measuring the distance covered by the robot and total time taken to complete the desired track. The angle difference of path and car angles was also plotted in real-time graph. The robot could be set to different speeds of operation during forward movement **(f-spd)** and rotation **(t-spd)**. Three settings of speed possible are low speed-3, medium speed-4, and high speed-5. μ was set to various values to judge the performance.

Tests were operated at various conditions of paths and various speed settings of robot. The rotation turn speed and forward run speed were set at different speeds as required by the task. The MATLAB program with its multiple figures/plots/images and real-time capture and process tasks could only give frame speed around 3–4 frames per second. However, a reliable performance at low frame rate indicates that the system would certainly perform at higher frame rates with better hardware GPU and software like Open CV [9].

The distance covered by the vehicle is calculated in number of pixels. Total time taken by the robot is calculated in seconds, hence also giving the average speed of travel by the robot at pixels/s. High value of the distance error indicated the quantity of how much the robot had moved out of the desired path. The robot was tried under different shapes of path, i.e., zigzag, quadrilateral, and low-curved paths. The most difficult and time-taking path for robot remained the zigzag path as it had too large shift in path angle. The medium value of $\eta_{\text{thres}} = 20$ gave the best performance causing least oscillation of angle difference for the robot. Making the angle low produced too many oscillations on the path, high value of $\mu = 25$ caused the robot to move much out of the desired path causing elongated for more distance error. Setting low threshold angle is always better for perfect trajectory control of the vehicle on path but requires higher frame rate computing software and hardware. In all of the cases, the turning speed is always taken lesser than the forward speed as turning requires proper alignment of the robot to the path; however, the forward speed is an after process from when the path is already found. Test results are shown in Fig. 6 for different path and speed settings.

In Test 4, the both turning and forward were kept on the higher level. We saw the distance error increased but, however, did bring improvement in the speed of the vehicle.

In Test 5, we decreased the turning speed and increased the forward speed which further increased overall speed of the robot but caused significant distance error.

Tests 6–9 were based on quadrilateral path with corner turn point on the path. With same speed as in Test 5, the distance error increased most abruptly, causing the most inaccurate movements and time-consuming execution. Decreased forward speed in Test 7 produced much higher performance with least error and highest speed in quadrilateral path. Decreasing threshold angle in Test 8 has little change of effect on the performance. Increasing threshold angle in Test 9, however, reduces the performance to least, with lowest speed of all tests.

The last set of test was operated on low-curved almost straight paths. These paths gave best performances at low threshold angles and medium forward speed setting as shown on Tests 10 and 11.

Increasing the speed of the robot to the next level decreased performance as observed in Test 12.

It can therefore be concluded that system operates differently on different conditions. Zigzag path result gave best on medium $\eta_{\text{thres}} = 20^{\circ}$, performing at the higher average speed on high-level speed settings t-spd = 4, f-spd = 5 but with some loss in accuracy of path. It, however, gave a better accurate and faster performance at same threshold angle with speed t-spd = 3, f-spd = 4. Observation table of all experiments result is given in Table 1. Supporting graph of error and vehicle average speed is given in Figs. 7 and 8.

For quadrilateral type, path least distance error was possible with low $\eta_{\text{thres}} = 15^{\circ}-20^{\circ}$. The result was best and accurate at $\eta_{\text{thres}} = 20^{\circ}$ and speed setting t-spd = 3, f-spd = 4. Decreasing the angle caused oscillations, hence taking more time to reach destination and decreasing the speed of the car.

Less curve path was covered without much problem at low angle settings. It gave the best performance against distance error and for high-speed movement of vehicle.

Therefore, the test results can be tabulated as follows.

Table 1 Reading and observation data

Test No.	Actual distance (pixels)	Distance covered (pixels)	No. of frames	Time taken (s)	Turn speed	Forward speed	Threshold angle	Path description	Distance error %	Speed = pixel/s
1	321	417	124	43.8	3	4	20	Zigzag	29.9	7.3
2	311	473	154	57.1	3	4	15	Zigzag	52.1	5.4
3	311	512	169	63.1	3	4	25	Zigzag	64.6	4.9
4	336	424	129	47.6	4	5	20	Zigzag	56.0	7.1
5	347	471	126	45.6	3	5	20	Zigzag	35.7	7.6
6	222	501	118	42.2	3	5	20	Quad	125.7	5.3
7	219	258	75	25.1	3	4	20	Quad	17.8	8.7
8	224	268	84	28.8	3	4	15	Quad	19.6	7.8
9	213	384	125	43.8	3	4	25	Quad	80.3	4.9
10	144	147	43	13.9	3	4	15	Straight	2.1	10.4
11	150	165	44	13.8	3	4	25	Straight	10.0	10.9
12	161	324	105	36.2	3	5	25	Straight	101.2	4.4

Fig. 7 Distance error versus Test No.

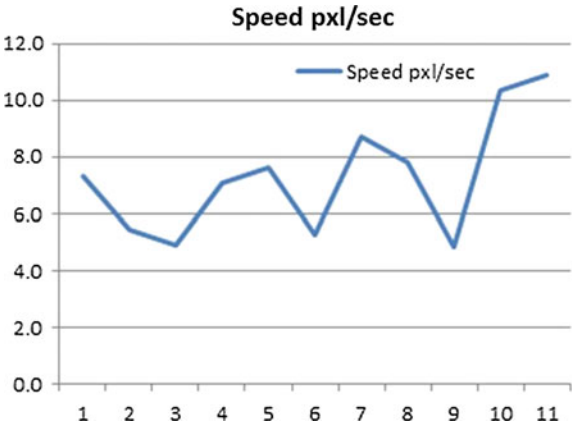

Fig. 8 Speed (pixels covered/s) versus Test No.

6 Conclusion

The successful execution of experiment on robot navigation system implies is an economical and reliable system and easy approach. It performs well in low frames for low-speed robot operations, hence promising of performance in high frame rate with better software and hardware integration. The project used MATLAB software, which has issues regarding memory access and management during real-time video processing. Higher frame rates could be achieved using more specific software like open CV. Such image processing technique can also be used in closed circuit industrial application for automatic navigation of free robots. It can even be applied for routing of machine tools in CNC machines, medical surgical operation, and UAV guidance system. It can be integrated with artificial algorithm to understand and be adaptive to complex new situations and detections of movements and its operation. The project can be further improved with better object

classification algorithm such as Hough transform. The robot can be equipped with more advanced tools and sensors for it to work in real scenarios for the idea of terrain depth to be perceived through a 2D image [10].

References

1. Sukkarieh, S., Nebot, E.M., Durrant-Whyte, H.F.: A High integrity IMU/GPS navigation loop for autonomous land vehicle applications. IEEE Trans. Robot. Autom. **15**(3), 572–578 (1999)
2. Chen, W., Shi, Y.Q., Xuan, G.: Identifying computer graphics using HSV color model and statistical moments of characteristic functions. In: IEEE International Conference on Multimedia and Expo, 2007, pp. 1123–1126, 2–5 July 2007
3. Salazar, D., Sanchez, R., Salazar, L.: Pipelined image and data processing for robot motion planning and navigation. In: 2006 IEEE International Symposium on Industrial Electronics, Montreal, Que, pp. 608–613, 9–13 July 2006
4. Ganesan, P., Rajini, V.: Value based semi automatic segmentation of satellite images using HSV color space, histogram equalization and modified FCM clustering algorithm. In: 2013 International Conference on Green Computing, Communication and Conservation of Energy (ICGCE), pp. 77–82, 12–14 Dec 2013
5. Gumbau, J., Sbert, M., Szirmay-Kalos, L., Chover, M., González, C.: Smooth shadow boundaries with exponentially warped Gaussian filtering. Comput. Graphics **37**(3), 214–224 (2013)
6. Bechman, G.S., Bowen, R.I.: Apparatus and method of determining an orientation of a GPS receiver. Patent US 6359585 B1 (2002)
7. Svasta, P.M., Hapenciuc, I.A.: Numerical processing of stereo optical images for autonomous navigation. In: Electronics System-Integration Technology Conference, 2008 (ESTC 2008), 2nd edn., pp. 639–644, 1–4 Sept 2008
8. Jianjun, Z., Man, Z., Min'gang, C., Su, L., Bin, L.: Automatic navigation system for electric power vehicles with EPS. Vehicle Power and Propulsion Conference, 2008 (VPPC'08). IEEE, Harbin, pp. 1–3, 3–5 Sept 2008
9. Matuska, S., Hudec, R., Benco, M.: The comparison of CPU time consumption for image processing algorithm in Matlab and Open CV. In: ELEKTRO Conference, Rajeck Teplice, pp. 75–78, 21–22 May 2012
10. Canhoto, A., Shiguemori, E.H., Domiciano, M.A.P.: Image sequence processing applied to autonomous aerial navigation. In: 2009 IEEE International Conference on Signal and Image Processing Applications (ICSIPA), Kuala Lumpur, pp. 496–499, 18–19 Nov 2009

The Performance Enhancement of Statistically Significant Bicluster Using Analysis of Variance

K. Vengatesan, S.B. Mahajan, P. Sanjeevikumar and Sana Moin

Abstract In this article, the performance enhancement of statistically significant bicluster using analysis of variance is articulated. Various statistical methods are used to analyze the gene expression level. It is found that analysis of variance is one of the efficient methods for aggregation between a pair of genes. It computes the values by comparing the mean value of each group, and results are tested using the hypothesis to calculate the *p*-value. Various tests are conducted to increase the performance of the gene pair. Various clustering techniques are functional to investigate the gene expression information for both homogeneous and heterogeneous. Statistical approaches are used to identify the relevant information from the subset of genes. Various testing methods were conducted to enhance the performance of correlated genes. When compared with the biclustering methods such as the paired *t*-test, two-sample tests, the ANOVAs One sample test produces better result.

Keywords ANOVAs · Bicluster · Correlation · Gene clustering Statistical approaches and variance

K. Vengatesan (✉)
Department of Computer Engineering, Sri Satya Sai University of Technology and Medical Science, Sehore, India
e-mail: vengicse2005@gmail.com

S.B. Mahajan
Department of Electrical and Electronics Engineering, Marathwada Institute of Technology (MIT), Aurangabad, India
e-mail: sagar25.mahajan@gmail.com

P. Sanjeevikumar
Department of Electrical and Electronics Engineering, University of Johannesburg, Auckland Park, Johannesburg, South Africa
e-mail: sanjeevi_12@yahoo.co.in

S. Moin
Department of Computer Science and Engineering, Manipal Institute of Technology, Manipal, India
e-mail: sana.moin.star@gmail.com

A. Konkani et al. (eds.), *Advances in Systems, Control and Automation*,
Lecture Notes in Electrical Engineering 442, https://doi.org/10.1007/978-981-10-4762-6_64

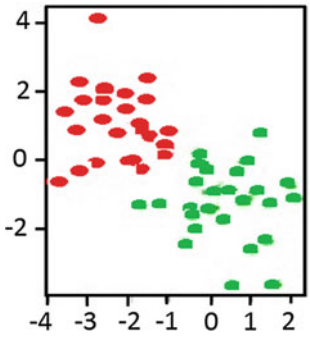

Fig. 1 Similarity group

1 Introduction

Clustering is a group of objects which are similar to one another, that can be separated by a region or by a surface, with different geometrical objects such as circle, rectangle, and triangle. Figure 1 shows that green and red color data points which are generated from different distributions such as probability distribution, binomial, Poisson, normal, and uniform distributions [1]. The gene expression or samples are represented in a row and column of a gene expression matrix. The clustering may be applied to gene or experimental conditions to form the required group [2, 3]. Identifying the group of possible co-regulated gene from the sequence of data are used in various mathematical techniques to identify the correlation between the pair of gene such as scatter or dot diagram, Karl Pearson's coefficient correlation, Spearman rank correlation, two-way frequency, and concurrent deviation method [4]. The statistical test is used to check whether samples are grouped supervised or unsupervised approach [5]. Generally, the cluster investigation depends upon on cluster algorithm and distance measure, from which distance measure is quantification of similarity or dissimilarity between the two objects and cluster algorithms procedure to group the objects within small cluster distance [6, 7]. In general for the distance measures, a variety of geometric formula are used to estimate the match of the pair of gene dataset such as average intercluster distance, average intracluster distance, centroid Manhattan distance, centroid Euclidean distance, ratio of merging two clusters, and intercluster distance [8].

2 Biclustering

A biclustering is a subset of gene, which is derived from various experimental conditions and discovers a desired pattern [9]. There are several existing methods to find significant bicluster in huge expression data. The classic clustering methods like K-mean, hierarchical clustering, self-organizing maps are pertinent when the genes are with the similar behaviors and in the same cluster over all conditions.

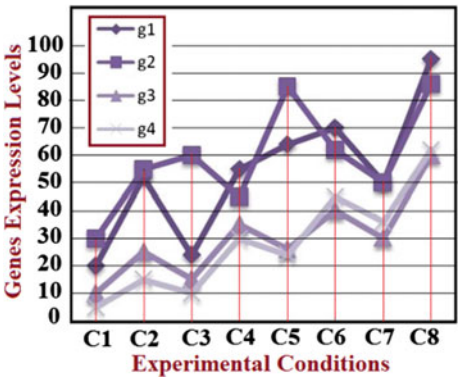

Fig. 2 Four genes with eight conditions

For example, in a cellular process, the set of gene is energetic barely in a certain split of environment or obscure in numerous pathways that either active or co-active under a subset of circumstances [10]. The classic clustering method could not be used to find the significant relevant group of gene in different experimental conditions, so the biclustering method is an efficient method for finding the relevant group of gene in different experimental conditions. The linear transformation of aggregation between different expression levels is measured by using a pattern-based model which is mainly used for positive correlated genes. When gene correlation is negative pattern, the existing work is then not applicable either tendency-based algorithm or pattern-based model.

Figure 2 represents four genes (g1, g2, g3, and g4) under various experimental conditions, from which g1 and g3 have similar characters and g2 and g4 are another set of genes that have analogous characters and consider various microarray of dataset for experimental purpose to form the clusters [11]. Bicluster is a uniform submatrix, uses the algorithm called greedy, in which every stage the best optimal value is chosen from the list of feasible solutions. The novel-based approach used in biclustering combines statistical consideration and graph theoretic to find similar expression pattern over a subset of conditions, and the gene is significantly changed based on the subset of values [12]. The observed bicluster is calculated using probability functions, which calculates tight upper bound value. The weighting schemes are used to find the significant bicluster in expression data and form bipartite graph. The drawback of the system is computationally hard and need degree restriction on the graph. It also limits the gene vertices degree and edges a fixed constant value C. The gene participation for weighted problem uses polynomial algorithm and maximum edge biclique, which are NP-complete problem. There are different patterns of biclusters available such as constant-value bicluster, a fixed-row bicluster, a fixed-column bicluster, successive addition of bicluster, and successive product of bicluster. Patterns of bicluster are depicted in Tables 1, 2, 3, 4, and 5. In a successive product of bicluster, set of rows and columns can be calculated by multiplying one column or row through a static assessment [8]. In a perfect bicluster successive model, $B_{I,J}$ can be expressed as follows

Table 1 Constant bicluster

	C1	C2	C3
R1	1.7	1.7	1.7
R2	1.7	1.7	1.7
R3	1.7	1.7	1.7

Table 2 Constant row

	C1	C2	C3
R1	1.6	1.6	1.6
R2	2.2	2.2	2.2
R3	4.3	4.3	4.3

Table 3 Constant column

	C1	C2	C3
R1	1.6	2.2	4.3
R2	1.6	2.2	4.3
R3	1.6	2.2	4.3

Table 4 Addition model (C1 = C2 + 1)

	C1	C2	C3
R1	4.5	3.5	4.0
R2	2.6	1.6	2.9
R3	1.7	0.7	3.4

Table 5 Successive multiplication (R2 = R1 × 2)

	C1	C2	C3
R1	4	2	9
R2	8	4	18
R3	2.6	7.4	2.7

$B_{I,J,} = \mu * G_r * G_c$; for all $i\varepsilon I$, $j\varepsilon J$, μ is a static value, G_r is the row value, and G_c is the column value. A successive addition of bicluster be capable of be obtained by each horizontal or vertical by adding some constant rate. A perfect bicluster with successive addition mode can be denoted by $B_{I,J}$ that can be written as $B_{I,J,} = \mu + G_r + G_c$; for all $i\varepsilon I$, $j\varepsilon J$, μ is a static value, G_r is the row value, and G_c is the column value. Similarly, a fixed row and fixed column of biclusters can be expressed as follows $B_{I,J} = \mu + G_r$ for all $i\varepsilon I$, $j\varepsilon J$; $B_{I,J} = \mu + G_c$ for all $i\varepsilon I$, $j\varepsilon J$, where μ is a constant value, G_r is gene row, and G_c is a column in the subset of values [11, 13]. A constant-value bicluster consists of constant value for each row and column in the expression matrix. A perfect constant bicluster can be written as $B_{I,J} = \mu$.

Figure 3 shows the operational block diagram of the entire proposed algorithm. With the gene expression data, primary microarray of the gene is obtained, and then

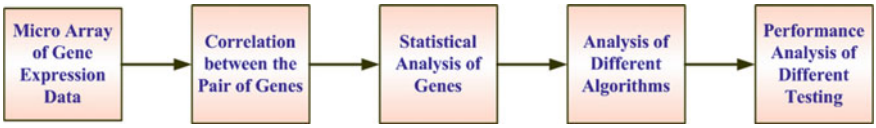

Fig. 3 The block diagram of the proposed system

Table 6 Statistical processes of six genes

Different algorithms	Gene 1	Gene 2	Gene 3	Gene 4	Gene 5	Gene 6
Bicluster BiMax	1.27	2.61	2.44	2.27	2.84	1.99
Bicluster CC	−0.88	−0.625	−1.402	0.201	0.049	−1.74
Bicluster ISA	0.071	0.047	1.749	2.73	−0.067	1.181
Bicluster OPSM	0.149	−0.45	0.961	1.105	1.44	1.686
Clustering HCL	−1.97	−0.386	−1.195	−0.807	−0.105	−0.092
Cluster K-mean	−1.973	0.107	−0.386	−1.195	−0.807	−0.105

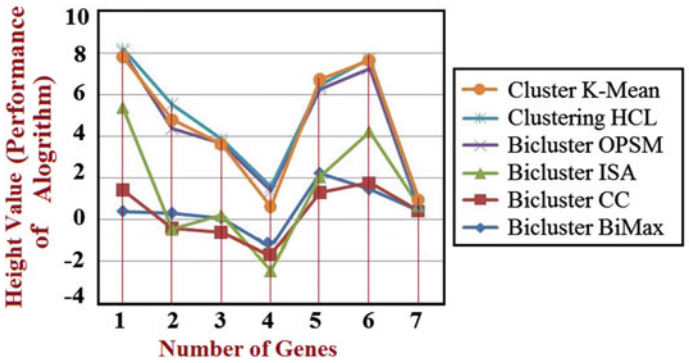

Fig. 4 Analysis of different algorithm

the correlation between each pair of genes is calculated by using correlation methods, in which each session output will be followed by the next part of the algorithm. BICAT tool is used for analysis the different existing algorithms for six sample genes [9], and the statistical process of six different gene analysis is provided in Table 6.

Figure 4 shows the number of algorithms of different data value. These data values have been extracted from the different gene datasets, i.e., from G1 to G6 [14]. It clearly states that there has been significant increase in the particular algorithm while there is a slight growth in other data values. One-way analysis of variation has been injected with these algorithms to analyze the variation in the graph. As a result, the hypotheses have clearly described that the cluster K-mean and clustering HCL made a huge difference when comparing to previous existing

two-sample *t*-test and paired *t*-test. Other algorithms such as bicluster Bimax, bicluster CC, and bicluster ISA are slightly growing in respective manner. Separate graph has been added for algorithm such as bicluster K-mean, bicluster HCL, bicluster OPSM, bicluster ISA, bicluster CC, and bicluster Bimax [8]. The correlation between the two variables X and Y has calculated by using Karl Pearson's mathematical formula that measuring the magnitude of the linear correlation coefficient between pair of variables. If X and Y are two variables, the correlation coefficient $\rho(X, Y)$ between them is written as

$$\rho(X,Y) = \frac{\sum_{i=1}^{n}(x_i - \bar{x})(y - \bar{y})}{\sqrt{\left\{\sum_{i=1}^{n}(x_i - \bar{x})^2\right\}\left\{\sum_{i=1}^{n}(y_i - \bar{y})^2\right\}}} \tag{1}$$

In above equation, $\bar{x}$ is mean of X and $\bar{y}$ mean of Y. Another direct method used to measure the correlation between X and Y can be written as

$$\rho(x,y) = \frac{\sum \mathrm{d}x * \mathrm{d}y}{\sqrt{\sum \mathrm{d}x^2 * \sum \mathrm{d}y^2}} \tag{2}$$

where $\mathrm{d}x = x_i - \bar{x}$, $\mathrm{d}x = x_i - \bar{x}$, $\bar{x}, \bar{y}$ are mean of X and Y.

Table 7 is sample microarray data consider for processing. Table 6 gives a detail about statistical processing of gene from Table 7. Comparing the gene pair G1 & G2, the correlation coefficient is 0.53, mean value is 96.25, covariance is 371.09, and a standard deviation value is 40.32; for each pair of sample, different types of test are applied to measure the performance such as two-sample *t*-test value is −1.79, paired *t*-test value is −2.08 and ANOVA One way value is 3.19, when the same test is to be applied for another pair of gene G1 & G3, the values are 0.64, 0.68, and 0.41. When compared G1 & G2, the ANOVA One way gives less value. But the overall statistical calculation shows that ANOVA One Way methods produce best result when compared to other methods.

In Table 8, the statistical expression of gene has been measured. It compares every gene to each other to find the variations. For example, comparison between genes pairs G1 and G2 to G6 results significant value for extracting datasets. Many analytical methods are being tested (e.g. standard deviation, covariance, mean, and

Table 7 Sample microarray data matrix

Gene	C1	C2	C3	C4	C5	C6	C7	C8
G1	42	47	145	42	40	181.5	45	83.5
G2	103	135	125.5	105	100	130.5	115	100
G3	75	65	52	92	−50	68	73	117.5
G4	85	−30	108	132	130	160	40	44
G4	30	40	37	20	−23	48	23	−2.2
G6	7.7	7	−84.6	8	7.5	−96.2	−13	28.8

Table 8 Statistical processing of testing methods

Gene pairs	Correlation coefficient (r)	Mean	Covariance	Standard deviation	Two-sample t-test	Paired t-test	ANOVA (one way)
G1 & G2	0.53	96.25	371.1	40.32	−1.79	−2.08	3.19
G1 & G3	−0.15	69.91	313.7	52.29	0.64	0.68	0.41
G1 & G4	0.46	80.94	1342	58.93	−0.18	−0.24	0.03
G1 & G5	0.49	49.92	2665	42.44	2.67	3.32	3.32
G1 & G6	0.99	30.70	30.70	51.19	3.72	2.71	13.81
G2 & G3	−0.44	87.91	180.1	36.25	2.91	2.98	8.45
G2 & G4	−0.03	98.94	180.1	45.31	1.35	1.83	8.45
G2 & G5	0.81	67.92	235.1	19.54	9.48	17.43	89.96
G2 & G6	0.53	48.70	382.2	34.65	7.57	6.48	57.27
G3 & G4	−0.37	72.59	2120	56.23	−0.78	−0.69	0.62
G3 & G5	−0.22	41.58	477	38.60	2.07	2.60	4.29
G3 & G6	0.08	22.36	2120	48.05	3.26	3.39	10.65
G4 & G5	0.16	52.61	119	47.21	2.63	2.55	6.90
G4 & G6	0.47	33.39	3413	55.21	3.64	3.00	13.25
G5 & G6	0.49	2.38	487.9	37.10	2.07	1.70	4.30

correlation coefficient are the basic methods in valuating gene expression). In this process, ANOVA (generally analysis of variation) has been used to find a reliable gene expression by comparing gene datasets. Hence ANOVA has been considered as the best approach for gene expression and uses several tools to view the result as hypotheses that need to be validated.

3 Conclusion

The performance enhancement of statistically significant bicluster using analysis of variance is presented. There are several clustering methods available to group the pair of genes, based on the similarity, the clustering can be applicable for different areas, of these gene cluster is a popular one, in which different ideas are followed to group pair of genes, it is NP Hard problem, different clustering methods for different problems. A microarray consists of the thousands of gene expression level and process the high number of genes, the ANOVA one way model is more suitable and produces effective result when compared to other testing methods such as two-sample t-test, paired t-test. Also the various common parameters are considered such as mean, covariance, standard deviation for each pair of genes, and various algorithms are tested by using bicluster analysis tool. Considering the pair of gene G1 & G6, the two-sample t-test produces 3.72 related with each other, the paired t-test produces 2.71 each other, and ANOVA one way produced 13.81 statistical results. It clearly shows that the analysis of variance with one sample test produces best result for huge amount of gene expression data.

References

1. Busygin, S., Prokopyev, O., Paradalos, P.: Biclustering in data mining. Comput. Oper. Res. **35**(9), 2964–2687 (2000)
2. Ji, J., Pang, W., Zhou, C., Han, X., Wang, Z.: A fuzzy k-prototype clustering algorithm for mixed numeric and categorical data. Knowl.-Based Syst. **30**, 129–135 (2012)
3. Rajkumar, P., Vennila, I., Nirmalakumari, K.: A novel hybrid method for gene selection in microarray based cancer classification. IJEST **5** (2013)
4. Hanczer, B., Nadif, M.: Using the bagging approach for biclustering of gene expression data. Neuro-Comput. **74**, 568–584 (2011)
5. Mederia, S., Oliveira, A.: Biclustering algorithm for biological data analysis: a survey. IEEE Trans. Comput. Biol. Bioinf. **1**(1), 24–45 (2004)
6. Dai, D., Yan, H.: Matrix decomposition for feature generation from high dimensional data. Pattern Recogn. Theor. Appl. **48**, 194–205 (2007)
7. Reiss, D., Beliga, N., Bonneau, R.: Integrated biclustering of heterogeneous genome-wide data set for the inference of global regulatory networks. BMC Bioinf. **7** (2006)
8. Yang, W., Dai, D.: Finding correlated biclusters from gene expression data. IEEE Trans. Knowl. Data Eng. **23**, 568–584 (2011)
9. Belacel, N., Wang, Q.: Cuperlovic culf, clustering methods for microarray gene expression data. OMICS **1**, 507–531 (2006)
10. Ayadi, W., Elloumi, M., Hao, J.: BiMNine+: An efficient algorithm for discovering relevant biclusters of DNA microarray data. Knowl. Based Syst. (KDS) **35**, 224–234 (2012)
11. Deng, Z., Choi, K., Chiung, F., Wang, S.: EEW-SC enhanced entropy-weighting subspace clustering for high dimensional gene expression data cluster analysis. Appl. Soft Comput. **41**, 1041–1050 (2011)
12. Dueck, D., Morris, Q., Frey, B.: Multi way clustering of microarray data using probabilistic sparse matrix factorization. Bioinformatics **21**, 1144–1151 (2005)
13. Liu, J., Yang, J., Wang, W.: Op-cluster: clustering by tendency in high dimensional space. In: IEEE International Conference on Data Mining (2003)
14. Han, L., Yan, H.: Hybrid method for the analysis of time series gene expression data. Knowl.-Based Syst. (KBS) **35**, 14–20 (2012)

Multimodal Classification of Arrhythmia and Ischemia Using QRS-ST Analysis

Akash Kumar Bhoi, Karma Sonam Sherpa and Bidita Khandelwal

Abstract Probabilistic classification approaches have been presented for arrhythmic and ischemic data using QRS-ST evaluation. The proposed methodology is segregated into two major parts, i.e., (a) detection of QRS complex and ST segments by improvised Pan-Tompkins and difference operation method, respectively, and (b) classification of healthy, arrhythmic, and ischemic classes using linear discriminant analysis (LDA), decision tree (DT), and artificial neural network (ANN), respectively. Two correlative classification features (frequency and time domain) of QRS-ST, i.e., (1) ratio of power spectrum (PS) and power spectral density (PSD) and (2) area under the curve (AUC), are introduced to these classifiers. The algorithm is evaluated and validated with standard databases such as FANTASIA (healthy), MIT-BIH Arrhythmia (arrhythmic), and long-term ST database (ischemic), respectively. For uniform probability classification, ECG episodes with 100% sensitivity (Se) and the specificity (Sp) are included in this analytical modeling. As the experimentation is performed to validate the possibility of these features for classification, the percentage of classification certainly could be improved by considering other vital features. We conclude that correlative analysis of QRS-ST may be evoked as significant marker for arrhythmia and ischemia.

Keywords Electrocardiography · Medical signal detection
Linear discriminant analysis · Decision trees · Artificial neural networks

A.K. Bhoi (✉) · K.S. Sherpa
Department of Electrical & Electronics Engineering, Sikkim Manipal Institute of Technology (SMIT), Sikkim Manipal University, Majitar, India
e-mail: akash730@gmail.com

K.S. Sherpa
e-mail: karmasherpa23@gmail.com

B. Khandelwal
Department General Medicine, Central Referral Hospital and SMIMS, Sikkim Manipal University, Gangtok, India
e-mail: drbidita@gmail.com

A. Konkani et al. (eds.), *Advances in Systems, Control and Automation*,
Lecture Notes in Electrical Engineering 442, https://doi.org/10.1007/978-981-10-4762-6_65

1 Introduction

Ventricular tachycardia (VT) is responsible for increasing the oxygen demand in heart muscle and also results in possible myocardial infarction [1]. Myocardial ischemia is responsible for morphological changes in ST-T wave. This will lead to bundle branch blocks and prolongation of QRS complex [2]. In addition to QRS slope particulars, the conventional ST segment analysis is an efficient method to monitor myocardial ischemia [3]. Various methods have been proposed, and with recent studies, it is found that (150–250 Hz) high-frequency content of the QRS complex is a better identification tool for ischemia than the traditional ST analysis [4–6]. Candil et al. discussed in their article that cute and transient myocardial ischemia detection may be initiated with QT interval analysis [7]. Xu et al. have presented an algorithm for QRS complex detection using slope vector waveform (SVW), and also, this method performed very well in case of noisy signals [8]. Arzeno et al. proposed a unique technique for discriminating various classes of ECG anomalies by comparing detection techniques for QRS complex and delineating its failure instances [9]. Li et al. have proposed the wavelet transform (WT) with multiscale features; among *P* and *T* waves, noise, and baseline drift, the QRS complex is distinguished properly [10]. There are several special digital filters (e.g., Hilbert transform, ANN, nonlinear high-pass filter, neural networks, wavelet transform, filter banks, and geometrical matching approach) which were implemented for detection, analysis, and classification of ECG signal both in time or in frequency domain [11–17]. Slimane et al. have presented an algorithm for QRS complex detection using empirical mode decomposition (EMD) which is integrated with high-pass filter, nonlinear transform, integration, and low-pass filter [18]. The performance is found to be better than "Christov's" detection method [19]. Romero et al. concluded that the evaluation of depolarization changes during ischemia could be analyzed robustly by QRS slopes [20]. Karimipour et al. have implemented a real-time P-QRS-T wave's detection algorithm using discrete wavelet transform (DWT), derivative (first-order), and adaptive thresholding techniques [21]. Other traditional methods developed before 1990, the Pan-Tompkins algorithm, has been the most efficient method for QRS complex detection (real-time) [22].

Yeh et al. proposed a computational free QRS complex detection method termed as the difference operation method (DOM) [23]. Here, this approached has been modified for T onset detection, whereas Pan–Tompkins method (PT method) was adopted for QRS detection. So the improvised combination of PT method and DOM segmented and localized the QRS complex and ST segments, respectively. The classification work has been performed with the extracted features from the mean of QRS-ST.

2 ECG Databases

The healthy, arrhythmic, and ischemic ECG signals are selected from three different databases, i.e., FANTASIA [24], MIT-BIH Arrhythmia [25], and long-term ST [26], respectively. All the ECG signals are with duration of 1 h which is selected from the 24 h recorded data. The 1 h recording from each episode (out of 24 h recorded data) is selected in such a way that the false-negative (FN) and false-positive (FP) beats are found to be 0 after detection of QRS complex and ST segment by improvised PT method and DOM, respectively. 36 recordings from each databases (i.e., total 108 ECG recordings) are selected which are satisfying 100% accuracy in QRS complex and ST segment detection.

3 QRS-ST Detection Methodologies

"The desirable passband to maximize the QRS energy is approximately 5–15 Hz [27, 28]." Cascaded low-pass and high-pass filters are implemented to decrease the noise produced by muscle, 60 Hz power-line interference, baseline drift, and T wave interference and also achieved a 3 dB passband using 5–12 Hz. After filtering, the QRS complex detection procedure is followed by derivative filter, squaring function, moving-window integration, thresholding, and adjusting RR interval Fig. 1. The difference equation operation is implemented to detect the $T_{\max}$ points, and the ST segment (i.e., S or J points and T_{onset}) is localized with search interval operation. The QRS complex detection operation is basically PAN-TOMPKINS method [29, 30], and the improvisation of difference operation method (DOM) is implemented for QRS Complex detection (Fig. 2).

3.1 Difference Equation Operation ($T_{\max}$ Detection)

The Pan–Tompkins' algorithm precisely detected the QRS complex and localized the Q, R and S or J point s in Fig. 3. Difference equation operation and search interval operation were performed after S or J point for the detection of T_{onset}.

Step 1: $T_{\max}$ threshold (T_{THD}) duration is calculated as follows

$$T_{\text{THD}} = \left| \frac{\text{length of ECG}}{\text{length of ECG/sampling frequency}} \right| \times 0.1 \tag{1}$$

Step 2: The final Tmax $(\hat{y}_{\text{ST}})$ is calculated as per the Eq. (4) with considering threshold values T_1 and T_2.

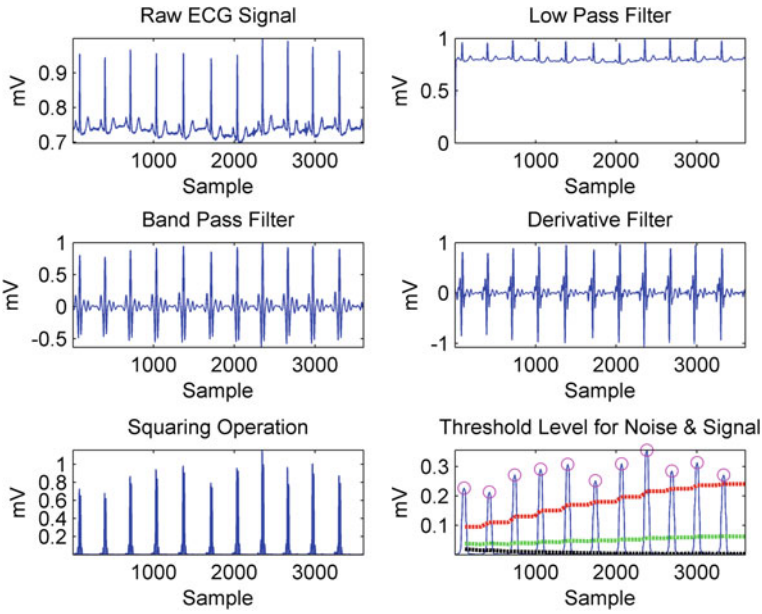

Fig. 1 Implementation of filters on ECG signals for QRS-ST detection

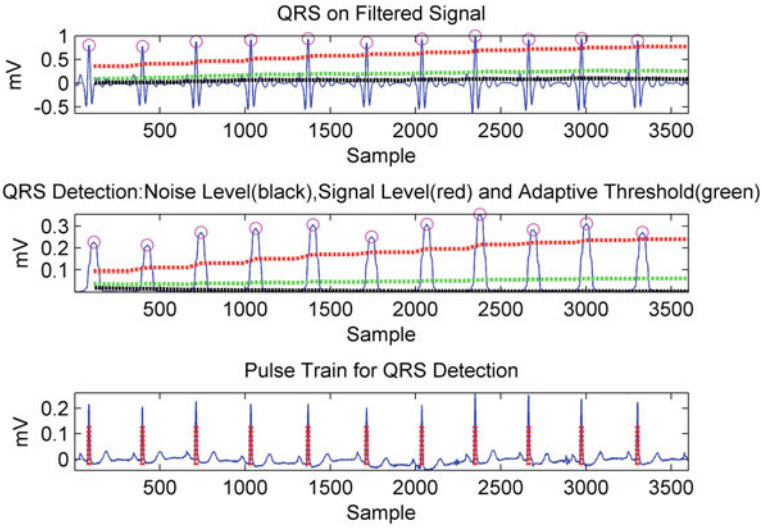

Fig. 2 QRS complex localization

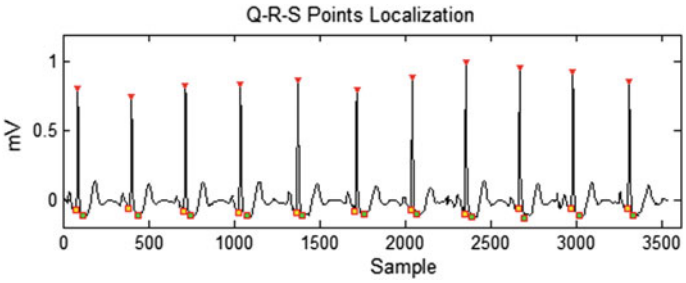

Fig. 3 Localization of QRS inflection points

$$\hat{y}_{\mathrm{ST}} = \begin{cases} 0 & \text{if } 0 < y_{\mathrm{ST}} < T_1, \quad \text{or} \quad T_2 < y_{\mathrm{ST}} < 0 \\ y_{\mathrm{ST}} & \text{if } y_{\mathrm{ST}} \geq T_1, \quad \text{or} \quad y_{\mathrm{ST}} \leq T_2 \end{cases} \tag{2}$$

where y_{ST} = Input ECG signal $T_1 = 2\mathrm{MV}_p$, and $T_2 = 2\mathrm{MV}_n$.
MV_p = mean values of all positive waveform amplitudes, and MV_n = mean values of all negative waveform amplitudes.

Step 3: The signal $\hat{y}_{\mathrm{ST}}$ is then dissected into positive part $\hat{y}_{\mathrm{ST}}^{+}$ and negative $\hat{y}_{\mathrm{ST}}^{-}$ part, respectively.

Step 4: Search operation is performed to find out the extreme value points for each interval of 200 samples from S point toward the direction of T wave. Nonzero extreme value in an interval of $\hat{y}_{\mathrm{ST}}^{+}$ and $\hat{y}_{\mathrm{ST}}^{-}$ are stored, and other values are discarded.

Step 5: This follows two substeps for selecting the correct extreme values.

Step 5.1: The time difference between $\hat{y}_{\mathrm{ST}}^{+}$ and $\hat{y}_{\mathrm{ST}}^{-}$ of two adjacent nonzero positive extreme values is measured.
Condition 1: The larger positive most extreme value is considered when time difference is $\leq$ interval duration.
Condition 2: Both positive extreme values are stored when time difference is > interval duration.

Step 5.2: Time difference between $\hat{y}_{\mathrm{ST}}^{+}$ and $\hat{y}_{\mathrm{ST}}^{-}$ of the two adjacent selected most extreme values are measured.
Condition 1: The selected two most extreme values are chosen as the correct pair when time difference is $\leq$ interval duration.
Condition 2: The chosen correct pair needs to be deleted (don't represent the actual pair), when the time difference is > interval duration.

Step 6: Check whether two consecutive selected peaks are within the threshold duration. If not, delete it.

Step 7: If the locations of these extreme points are matched to the input ECG signal, then the maximum positive value of the interval is $T_{\max}$ point, as shown in Fig. 4.

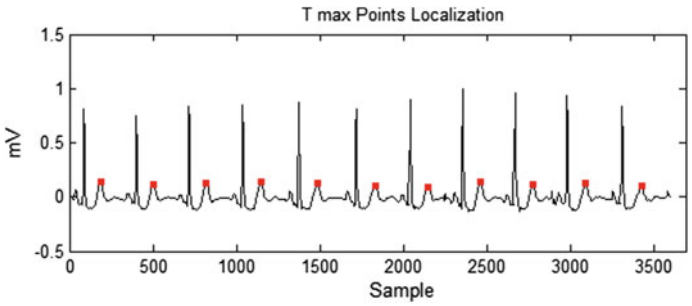

Fig. 4 Detection of T_{max} point

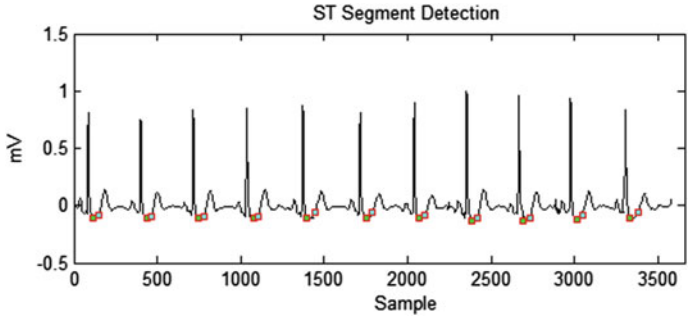

Fig. 5 Localization of S/J and T_{onset} points for ST detection

3.2 Search Interval Operation (T_{onset} Detection)

Step 13: Search interval-1 is defined which locates 20 sampling points before T_{max} point. The minimum value before T_{max} point is marked as point T_1.

Step 14: Search interval-2 is defined such that 40 sampling points before T_{max} point. The least point before T_{max} is T_2.

Step 15: Check the location and amplitude of T_1 and T_2 to confirm the location of T_{onset}. If their position is different and amplitude of T_1 is greater than T_2, then the position of T_1 is the position of T_{onset} or vice versa.

Figure 5 shows the ST segment, and Fig. 6 shows the complete segmented QRS-ST segments. Equations 4 and 5 are formulated by [23]:

$$\text{Se} = 1 - \frac{\text{FN}}{\text{TP} + \text{FN}} = \frac{\text{TP}}{\text{TP} + \text{FN}} \tag{3}$$

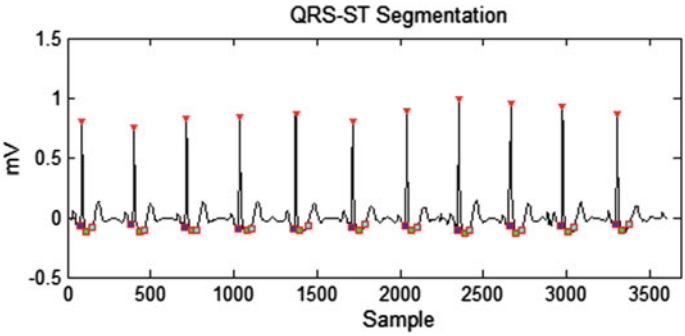

Fig. 6 Complete detection of QRS-ST segment

$$\mathrm{Sp} = 1 - \frac{\mathrm{FP}}{\mathrm{TP} + \mathrm{FP}} = \frac{\mathrm{TP}}{\mathrm{TP} + \mathrm{FP}} \tag{4}$$

Here, the beats are categorically under false positive (FP) = 0, false negative (FN) = 0, and true positive (TP) = 100%. Kindly note that quotes has been removed from the equations. Please check and confirm.‟ –>Therefore, Se and Sp are found to be 100% for the selected 108 recordings of three standard databases. The MITDB data #105, #108, #203, #222 are not included due to higher detection failure rate. Further, the features are extracted from the segmented *mean QRS complexes* and *mean ST segments* of 1-h recorded ECG signals.

4 Feature Extraction

The mean QRS complexes and mean ST segments are accumulated from all the detected QRS-ST segments, and the following features are also extracted from these *mean QRS-ST segments* for further classification parameters.

4.1 Ratio$_{PS\&PSD}$

Power spectrum, expressed as V_{rms}^2, is as follows:

$$\mathrm{PS}_{\mathrm{rms}}(f_m = m \cdot f_{\mathrm{res}}) = \frac{2 \cdot |y_m|^2}{S_1^2} \tag{5}$$

Power spectral density (PSD) is expressed in V^2/Hz;

$$\mathrm{PSD}_{\mathrm{rms}}(f_m = m \cdot f_{\mathrm{res}}) = \frac{\mathrm{PS}_{\mathrm{rms}}(f_m)}{\mathrm{ENBW}} = \frac{2 \cdot |y_m|^2}{f_s \cdot S_2} \tag{6}$$

where $m = 0...N/2$, f_{res} = frequency resolution, $S_1 = \sum_{j=0}^{N-1} w_j$, and $S_2 = \sum_{j=0}^{N-1} w_j^2$; w_j = window function, $j = 0...N-1$.

The ratio of power spectrum (PS) and power spectral density (PSD) has been considered as one of the features for classification, which is given as:

$$\mathrm{Ratio}_{\mathrm{PS\&PSD}} = \mathrm{PS}_{\mathrm{rms}}/\mathrm{PSD}_{\mathrm{rms}} \tag{7}$$

4.2 Area Under a Curve (AUC) of QRS-ST

The area under the curve of QRS complex and ST segment along the *x*-axis can be calculated by the trapezoidal rule, as shown in Fig. 7.

$$\mathrm{Area} = \int_a^b f(x)\mathrm{d}x \tag{8}$$

This may lead to both positive and negative results, based on the position of graph upon *x*-axis. The AUC of both QRS and ST segments is also considered as one of the classification features.

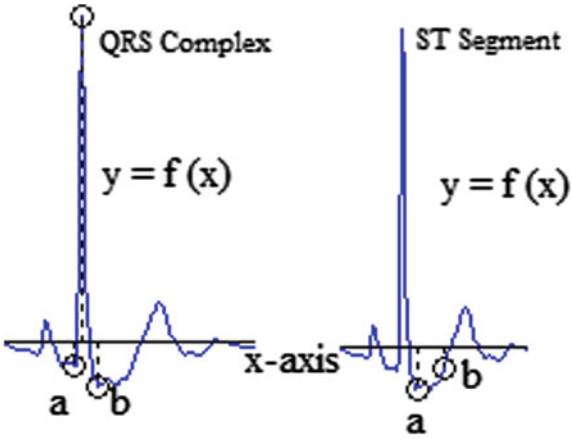

Fig. 7 Area estimation

5 Classification Techniques

The extracted features (i.e., $\text{Ratio}_{\text{PS\&PSD}}$ and AUC of QRS-ST) are introduced as classification attributes for following classifiers, and the classification results are shown in the subsections.

5.1 Linear Discriminant Analysis (LDA)

See Fig. 8.

5.2 Decision Tree

See Fig. 9.

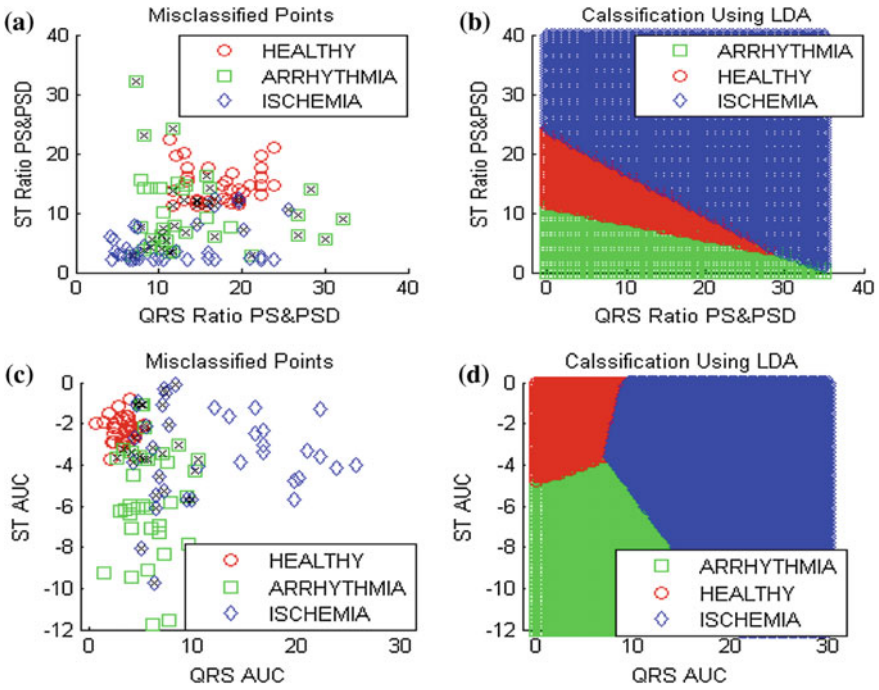

Fig. 8 **a**, **c** Misclassifications and **b**, **d** classification results using LDA

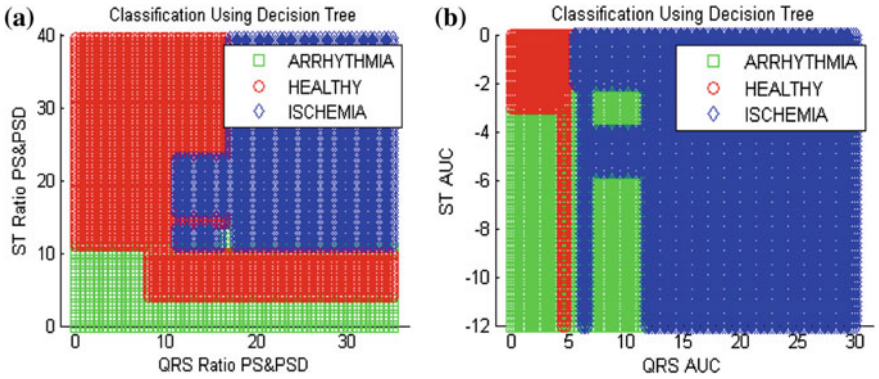

Fig. 9 **a**, **b** Classifications using decision tree

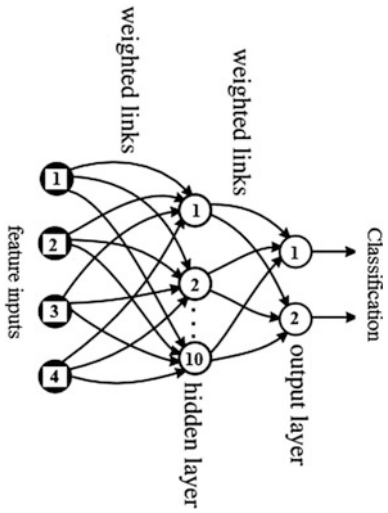

Fig. 10 Proposed two-layer feed-forward neural network

5.3 Feed-Forward Neural Networks

Figure 10 shows a two-layer feed-forward network. There are four feature inputs (i.e., $\text{Ratio}_{\text{PS\&PSD}}$ and AUC of QRS-ST) for classification, as shown in Figs. 11 and 12. "This first layer of functional nodes is sometimes referred to as a hidden layer, since we are not supposed to inspect or control the output values on these nodes during the process of setting the network weights, that is, during training or learning." The outputs of the 10 hidden layers are subsequently processed by an output layer which is used to read out the category in which the input pattern is placed.

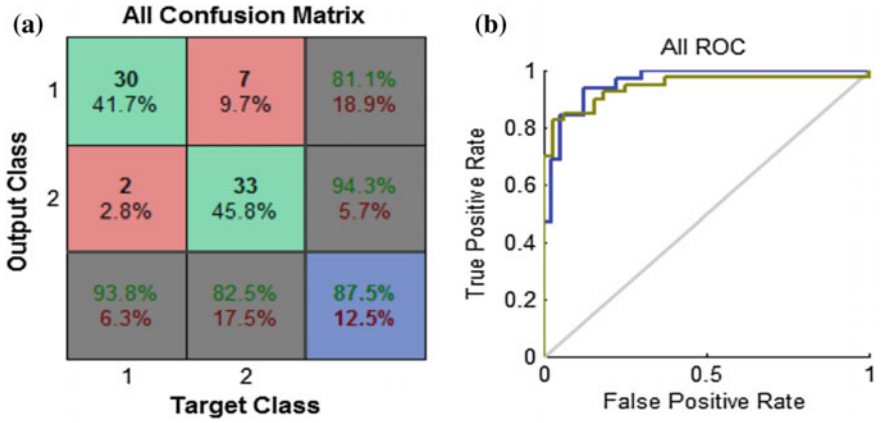

Fig. 11 Classification result of arrhythmia and healthy classification using ANN **a** all confusion matrix **b** all ROC

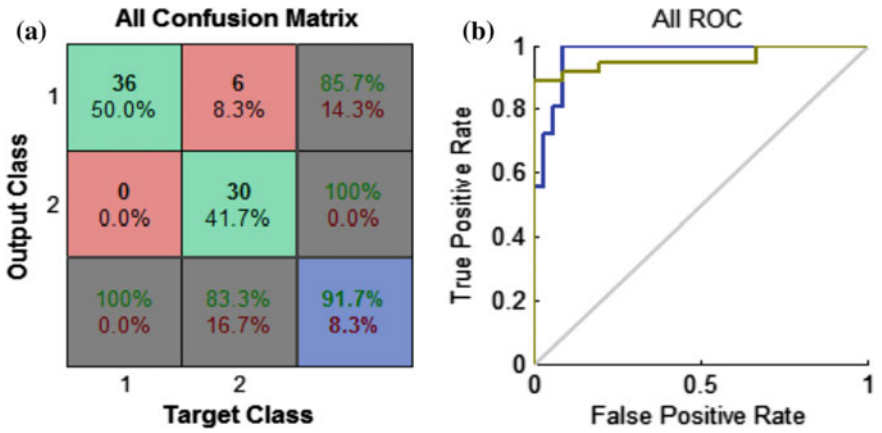

Fig. 12 Classification result of ischemia and healthy classification using ANN **a** all confusion matrix **b** all ROC

Here, the training was performed with the scaled conjugate gradient algorithm (SCG), developed by Moller [31]. SCG was designed to avoid the line search time-consuming operation.

6 Discussion

The proposed model is correlatively analyzed and classified using QRS-ST features; this further may be a marker for arrhythmogenic ventricular myocardial ischemia. We have already implemented an approach for analyzing classification probability for myocardial ischemia and cardiac arrhythmias using the frequency domain features [32]. The QRS-ST detection and classification algorithms are implemented and evaluated in MATLAB R2013a platform. ST segment detection by improvised DOM is implemented because it is easy to perform and computational free approach. Yeha et al. proposed method, DOM, has only 0.19% failure rate in MIT-BIH Arrhythmia database, which is significantly a better result as compared to earlier popular methods [23]. The Pan–Tompkins has also high accuracy of 99.3% in QRS complex detection [30]. But in this scenario, the focus is more on the probability classifications for the possible features, so the selected ECG signals from all the databases have 100% accuracy in inflection point detection. Implementing LDA classifier, the calculated resubstitution error is 37.96% and misclassification error of QDA is 30.56% across QRS $\text{Ratio}_{\text{PS\&PSD}}$ and ST $\text{Ratio}_{\text{PS\&PSD}}$. In case of decision tree, it is of only 7.41%. Resubstitution error of LDA across QRS AUC and ST AUC found to be 29.63%, whereas in case of decision tree, it is of 10.19%. Considering the same features, the classification work has been performed using ANN, and for arrhythmia and healthy, the result found to be 87.5% with 12.5% misclassification. In case of ischemia and healthy, the ANN classifiers show improvement in result with 91.7% accurate classification and 8.3% misclassification.

7 Conclusion

The important information related to onset of arrhythmia and ischemia can be studied statistically by analyzing the morphological changes in QRS complex and ST segments. The automated detection and analysis techniques help in improvising these findings. The proposed approach precisely detects the inflection points of QRS-ST and also explores the possibility of classification of ischemia and arrhythmia. This study also foregrounds on the salient features of QRS-ST correlation subjected to cardiovascular abnormality classification. Further comprehensive research involves with larger subjects for better feasibility of the applied techniques.

References

1. Ghuran, A.V., Camm, A.J.: Ischaemic heart disease presenting as arrhythmias. Br. Med Bull. **59**, 193–210 (2001)
2. Channer, K., Morris, F.: ABC of clinical electrocardiography myocardial ischemia. BMJ. **324**, 1023–1026 (2002)
3. Pueyo, E., Sörnmo, L., Laguna, P.: QRS Slopes for detection and characterization of myocardial ischemia. IEEE Trans. Biomed. Eng. **55**(2) (2008)
4. Pettersson, J., Pahlm, O., Cairo, E., Edenbrandt, L., Ringborn, M., Sörnmo, L., Warren, S.G., Wagner,G.S.: Changes in high-frequency QRS components are more sensitive than ST-segment deviation for detecting acute coronary artery occlusion. J. Amer. Coll. Cardiol. **36**, 1827–1834 (2000)
5. Abboud, S., Cohen, R.J., Selwyn, A., Ganz, P., Sadeh, D., Friedman, P.L.: Detection of transient myocardial ischemia by computer analysis of standard and signal-averaged high frequency electrocardiograms in patients undergoing percutaneous transluminal coronary angioplasty. Circulation **76**(3), 585–596 (1987)
6. Beker, A., Pinchas, A., Erel, J., Abboud, S.: Analysis of high frequency QRS potential during exercise testing in patients with coronary artery disease and in healthy subjects. Pacing Clin. Electrophysiol. **19**(12), 2040–2050 (1996)
7. Candil, J.J., Luengo, C.M.: QT interval and acute myocardial ischemia: past promises. New Evidences Rev. Esp. Cardiol. **61**(6), 561–563 (2008)
8. Xu, X., Liu, Y.: ECG QRS Complex Detection Using Slope Vector Waveform (SVW) algorithm. In: Proceedings of the 26th Annual International Conference of the IEEE EMBS San Francisco, CA, USA (2004)
9. Arzeno, N.M., Deng, Z.D., Poon, C.S.: Analysis of first-derivative based QRS detection algorithms. IEEE Trans. Biomed. Eng. **55**(2) (2008)
10. Li, C.W., Zheng, C.X., Tai, C.F.: Detection of ECG characteristic points using wavelet transforms. IEEE Trans. Biomed. Eng. **42**(1), 21–28 (1995)
11. Benitez, D., Gaydecki, P.A., Zaidi, A., Fitzpatrick, A.P.: The use of the Hilbert transform in ECG signal analysis. Comput. Biol. Med. **31**, 399–406 (2001)
12. Vijaya, G., Kumar, V., Verma, H.K.: ANN-based QRS-complex analysis of ECG. J. Med. Eng. Technol. **22**(4), 160–167 (1998)
13. Keselbrener, L., Keselbrener, M., Akselrod, S.: Nonlinear high pass filter for R-wave detection in ECG signal. Med. Eng. Phys. **19**(5), 481–484 (1997)
14. Dokur, Z., Olmez, T., Yazgan, E., Ersoy, O.K.: Detection of ECG waveforms by neural networks. Med. Eng. Phys. **19**(8), 738–741 (1997)
15. Kadambe, S., Murray, R., Boundreaux-Bartels, G.F.: Wavelet transform-based QRS complex detector. IEEE Trans. Biomed. Eng. **46**(7), 838–848 (1999)
16. Afonso, V.X., Tomkins, W.J., Nguyen, T.Q., Luo, S.: ECG beat detection using filter banks. IEEE Trans. Biomed. Eng. **46**(2), 192–202 (1999)
17. Suarez, K.V., Silva, J.C., Berthoumieu, Y., Gomis, P., Najim, M.: ECG beat detection using a geometrical matching approach. IEEE Trans. Biomed. Eng. **54**(4), 641–650 (2007)
18. Slimane, Z.E.H., Ali, A.N.: QRS complex detection using empirical mode decomposition. Digit. Sig. Proc. (2009). doi:10.1016/j.dsp.2009.10.017
19. Christov, I.I.: Real time electrocardiogram QRS detection using combined adaptive threshold. BioMed. Eng. Online. **3**, 28 (2004). http://www.biomedical-engineering-online.com/content/3/1/28
20. Romero, D., Ringborn, M., Laguna, P., Pahlm, O., Pueyo, E.: Depolarization changes during acute myocardial ischemia by evaluation of QRS slopes: standard lead and vectorial approach. IEEE Trans. Biomed. Eng. **58**(1) (2011)
21. Karimipour, A., Homaeinezhad, M.R.: Real-time electrocardiogram P-QRS-T detection–delineation algorithm based on quality-supported analysis of characteristic templates. Comput. Biol. Med. **52**, 153–165 (2014)

22. Portet, F., Hernandez, A.I., Carrault, G.: Evaluation of real-time QRS detection algorithms in variable contexts. Med. Biol. Eng. Comput. **43**(3), 379–385 (2005)
23. Yeha, Y.C., Wang, W.J.: QRS complexes detection for ECG signal: the difference operation method. Comput. Meth. Programs Biomed. **91**, 245–254 (2008)
24. Iyengar, N., Peng, C.K., Morin, R., Goldberger, A.L., Lipsitz, L.A.: Age-related alterations in the fractal scaling of cardiac inter beat interval dynamics. Am. J. Physiol. **271**, 1078–1084 (1996)
25. Goldberger, A.L., Amaral, A.L., Glass, L., Hausdorff, J.M., Ivanov, P.C., Mark, R.G., Mietus, J.E., Moody, G.B., Peng, C.K., Stanley, H.E.: PhysioBank physiotoolkit, and physionet: components of a new research resource for complex physiologic signals. Circulation **101**(23), e215–e220 (2000)
26. Jager, F., Taddei, A., Moody, G.B., Emdin, M., Antolic, G., Dorn, R., Smrdel, A., Marchesi, C., Mark, R.G.: Long-term ST database: a reference for the development and evaluation of automated ischaemia detectors and for the study of the dynamics of myocardial ischaemia. Med. Biolog. Eng. Comput. **41**(2), 172–183 (2003)
27. Goovaerts, H.G., Ros, H.H., vanden Akker, T.J., Schneider, H.: A digital QRS detector based on the principle of contour limiting. IEEE Trans. Biomed. Eng BME. **23**, 154 (1976)
28. Thakor, N.V., Webster, J.G., Tompkins, W.J.: Optimal QRS detector. Med. BioL Eng. Comput. **21**, 343–350 (1983)
29. Sedghamiz, H.: Complete Implementation of pan tompkins [Online] (2014). Available: http://in.mathworks.com/matlabcentral/fileexchange/45840-complete-pan-tompkins-implementation-ecg-qrs-detector
30. Pan, J., Tompkins, W.J.: A real-time QRS detection algorithm. IEEE Trans. Biomed. Eng. BME **32**(3) (1985)
31. Moller, M.F.: A scaled conjugate gradient algorithm for fast supervised learning. Neural Netw. **6**, 525–533 (1993)
32. Bhoi, A.K., Sherpa, K.S., Khandelwal, B.: Classification probability analysis for arrhythmia and ischemia using frequency domain features of QRS complex. Int. J. Bioautom. **19**(4), 531–542 (2015)

Electromyogram (EMG) Signal Categorization in Parkinson's Disease Tremor Detection by Applying MLP (Multilayer Perceptron) Technique: A Review

Rijhi Dey, Ardhendu Ghoshal and Bipan Tudu

Abstract In recent years, there has been extensive interest in the revelation of different technologies for artificial neural network (ANN) application in various classification of biomedical signals. Several publications have focused on diverse applications of ANN techniques for biomedical signals classification, detection, and processing. This review work gives an overview on the multilayer perceptron (MLP) technique of ANN and how this technology is useful for the classification of EMG signal. This paper will be interesting for those researchers who are studying the classification EMG signal for tremor detection in Parkinson's disease. Many researchers have worked and also working on Parkinson's disease tremor by using EMG signal and classifying its feature using ANN. Among those various techniques, MLP technique is highlighted in this work for the classification of EMG signal. The core center of this paper is to review the evolution and research works related to the topic mentioned above.

Keywords Electromyogram · ANN (artificial neural network)
MLP (multilayer perceptron) · Parkinson's tremor

R. Dey (✉)
Department of Electronics and Communication Engineering,
Sikkim Manipal Institute of Technology, Majitar, Sikkim, India
e-mail: rijhi.dey88@gmail.com

A. Ghoshal · B. Tudu
Department of Instrumentation and Electronics Engineering, Jadavpur University,
Kolkata, India
e-mail: ag@iee.jusl.ac.in

B. Tudu
e-mail: bt@iee.jusl.ac.in

A. Konkani et al. (eds.), *Advances in Systems, Control and Automation*,
Lecture Notes in Electrical Engineering 442, https://doi.org/10.1007/978-981-10-4762-6_66

1 Introduction

Biomedical signal is a term which is derived from a combined electrical signal extracted from any biological structure that portraits a physical variable of information [1]. These signals are generally taken as a function of time which is described in terms of its amplitude, frequency, and phase [2].

Among those biomedical signals, the electromyogram (EMG) is a signal that evaluates the electrical current generated in muscles during contraction which represents the neuromuscular activities [3]. EMG signals are regarded as most convenient as electrophysiological signals in both medical and engineering fields. Electromyography is mainly an examination which is done to record the electrical activities of muscles. It helps to detect various diseases and conditions muscles, including muscular dystrophy, pinched nerves, and myasthenia gravis. [4].

The technology, for recording the information from EMG signal, is relatively new [1]. There were few limitations in the processing of nonlinearity in the surface electromyography [5]. Recent studies and progress in technologies have made it possible for the development for advanced EMG detection and analysis techniques. In recent studies, neural network has become one of the effective methods to analyze and categorize the biomedical signals, due to its good capability, adaptability, and nonlinearity in its network [6]. The ANN technique is most acceptable for nonlinear data modeling and can cover divergence among different conditions [7]. The essential conditions for designing an ANN for a given application include:

(i) To determine the system construction
(ii) To define the actual number of layers, the number of hidden units in the middle layers, and number of units in the input and output layers
(iii) To have the training algorithm which is used during the learning phase [8].

Parkinson's disease (PD) has been identified as the commonest neurodegenerative disease that gradually deteriorates the central nervous system [9]. As reported by World Health Organization (WHO), it was evaluated that the world is having seven to 10 million PD patients [10, 11]. With the prevailing and ongoing progress development in microelectronics, it has expanded the interest in using computerized methods for detecting early symptoms or tremor detection on more objective basis. EMG signal analysis has been chosen as one of the technique for this reason.

MLP neural network, one of the commonly used ANN techniques, has been applied in many examples of a similar nature [12–14]. In fact, it had also been successfully developed as a test case to predict the tremor onset of PD [15]. The major advantage of using MLP network is that the initial results showed that it can act as an extremely effective predictor for the classification of EMG signal.

2 Related Research Works

Pan et al. (2007) has worked with ANN to anticipate the onset of Parkinson's disease tremor on human body [15]. In their work, it was shown how ANN can identify the pattern of the onset tremor from real-time recordings. Here, ANN was used for pattern recognition of EMG signal. Among various types of ANN techniques, MLP was chosen for this work due to its well-known properties. The MLP network is a responsible training network. This network was prepared using back propagation with the LFP signal that prevailed after sixty seconds, which provided the tremor training data for the network. During their experiment, they found that the total number of network inputs has an immense impact on the network training presentation. The tuned neural network was able to indicate properly when the tremor was taking place and also gave an indication when the tremor was likely to happen. Moreover, it was clearly depicted that neural network was able to detect the information correctly. Therefore, this work provided a better understanding of Parkinson's brain function.

In 2013, Gharehchopogh et al. studied the two techniques of ANN, MLP and radial basis function (RBF), which were used effectively for the classification of EMG signal for the diagnosis of Parkinson's disease [16]. In this work, the Parkinson's disease dataset was obtained from UCI machine learning database. It was observed from their study that MLP was one of the appropriate methods for the classification with 93.22% accuracy for the dataset.

According to their study, MLP technique is originally based on Rosenblatt's single perceptron [17]. But they had used conventional 3-layer MLP network to classify the EMG signal. The MLP network which was used contained an input layer, a hidden layer, and an output layer. Overall, 22 input nodes, 5 hidden nodes, and 1 output node were used. The inclusive computation of the MLP network was given by Eq. (1):

$$y = g\left(\sum_{j=1}^{m} w_j^2 g\left(\sum_{i=1}^{d} w_{ij}^2 x_i + b_j^1\right) + b^2\right) \tag{1}$$

Therefore, in their case study, the result was presented for $d = 22$ and $m = 5$. All the 22 input neurons used were totally connected to the hidden layer. The single output neuron was fully connected with the 5 hidden neurons, each one being evaluated by Eq. (1). For the Parkinson's disease detection, the MLP was compulsory to be 1 and 0 for healthy people. The algorithm which was applied for this network was Levenberg–Marquardt back-propagation optimization. An accuracy of 96.32% was achieved for the training set with MLP method. The structure for MLP method was shown in Fig. 1.

Nanda et al. (2015) has worked to find the basic difference between essential tremor and Parkinson's tremor, as both the tremors are alike and are very difficult to distinguish neurologically [18]. Before this work, mathematically the analysis of tremor was done successfully using non-invasive recording techniques. But the

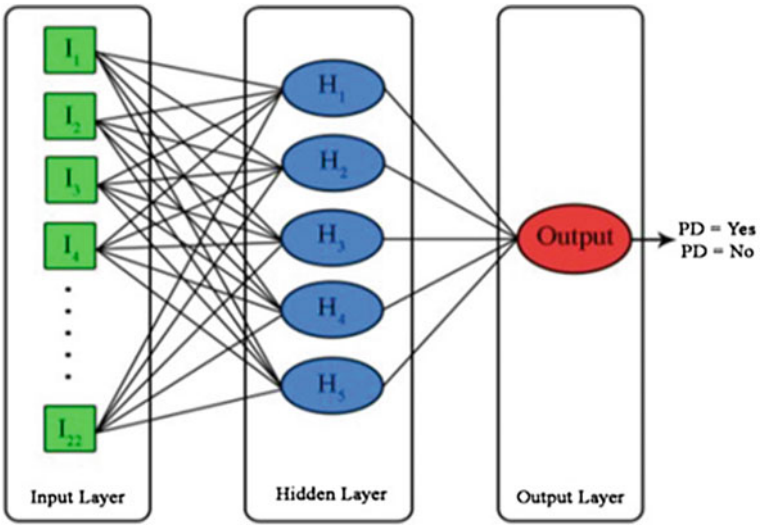

Fig. 1 MLP structure

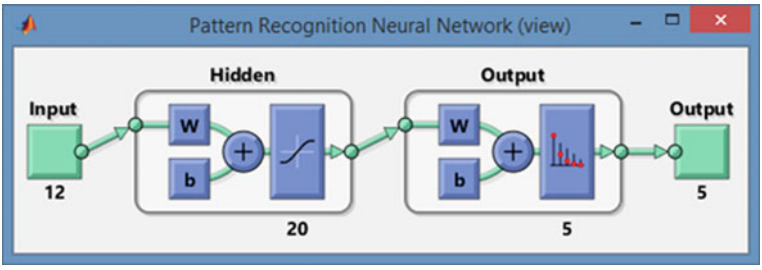

Fig. 2 Neural network architecture

classification of tremor signal from EMG has not been done accurately because of some problems like overlapping of frequencies. Therefore, to minimize this discrepancy, in this work, the neural network technique has classified the tremor sEMG signals with 91.66% accuracy. This suggested classification algorithm added intensity to the non-invasive signal detection methods at reduced cost and higher sensitivity.

In 2016, Shijiya et al. worked for automated analysis of EMG signals for different diseases due to muscular disorders [19]. This technique has useful for automated feature extraction and classification of EMG signals for diseases like Parkinson's disease and myopathy. In this work, 35 signals out of 75 signals were taken classified properly. The architecture which was used in their work is shown in Fig. 2.

As a result, from the EMG signal of selected signal length, the spectral and temporal features were extracted properly. By using those extracted features, the PD's tremor can be detected properly.

Challa et al. in 2016 has performed a comparative study among different machine learning models like MLP and random forest [20]. By this comparative study, it was concluded which model will be superior for the early prediction of Parkinson's disease. According to the study, the MLP technique is a feed-forward method. The basic theory of MLP network was that it takes input and maps it to a nonlinear space and then it tries to predict those corresponding outputs. The back-propagation algorithm is the main technique which governs this training model of MLP network.

3 Discussion

This study reports the significance for classification of EMG signals by MLP network technique, which is very essential for detecting several muscular and neuromuscular disorders. As EMG signal is very prone to noise interference, therefore the researchers tend to focus on the accurate classification of EMG signal. There are various techniques used for nonlinear classification of EMG signals using ANN; among those techniques MLP was used initially as it was found better than other techniques. But as work progressed, many new techniques of ANN were invented and also implemented for EMG classification for better result.

Though there are few demerits of using MLP technique nowadays, the advantages of MLP network have been focused in this review work. As it can represent multiple set of functions unlike generalized linear network, each layer has a set of adaptive weights, layers that are neither input nor output are considered as hidden and they are also included to give the total output. Therefore, the total output calculated by MLP techniques gives satisfactory result.

4 Conclusion

This review work contributes a general summary on how EMG signal systems are outlined, also how the MLP technology is being used to classify those signals. The growth and innovations of the researchers over years have resulted on several techniques for the nonlinear classification of EMG signal using various methods for the detecting the tremor in Parkinson's patients [21–24]. Current advancement in the study of EMG signal has accumulated and investigated mainly the classification of EMG signal for PD's tremor detection. From those researches that were made, a deduction can be drawn that repeated efforts are required to make EMG signals more accessible, and the technology of MLP should be improved more to classify the EMG signal with total precision and accuracy.

References

1. Reaz, M.B.I., Hussain, M.S., Mohd-Yasin, F.: Techniques of EMG signal analysis: detection, processing, classification and applications. Biolog. Proc. Onlin. **8**(1), 11–35 (2006)
2. Kleissen, R.F.M., Buurke, J.H., Harlaar, J., Zilvold, G.: Electromyography in the biomechanical analysis of human movement and its clinical application. Gait Posture **8**(2), 143–158 (1998)
3. Konrad, P.: The ABC of EMG. A Practical Introduction to Kinesiological Electromyography, vol. 1, pp. 30-35 (2005)
4. Tamil, E.M., Bashar, N.S., Idris, M.Y.I., Tamil, A.M.: A Review on feature extraction & classification techniques for bio-signal processing (part III: electromyogram). In: 4th Kuala Lumpur International Conference on Biomedical Engineering 2008, pp. 117–121. Springer, Berlin (2008)
5. Criswell, E.: Cram's Introduction to Surface Electromyography. Jones & Bartlett Publishers (2010)
6. Hiraiwa, A., Shimohara, K., Tokunaga, Y.: EMG pattern analysis and classification by neural network. In: IEEE International Conference Proceedings on Systems, Man and Cybernetics, 1989, IEEE, pp. 1113–1115 (1989)
7. Chowdhury, R.H., Reaz, M.B., Ali, M.A.B.M., Bakar, A.A., Chellappan, K., Chang, T.G.: Surface electromyography signal processing and classification techniques. Sensors **13**(9), 12431–12466 (2013)
8. Badri, L.: Development of neural networks for noise reduction. Int. Arab J. Inf. Technol. **7**(3), 289–294 (2010)
9. Oung, Q.W., Muthusamy, H., Lee, H.L., Basah, S.N., Yaacob, S., Sarillee, M., Lee, C.H.: Technologies for assessment of motor disorders in Parkinson's disease: a review. Sensors **15** (9), 21710–21745 (2015)
10. Parkinson Centre-Malaysian Parkinson Disease Association. Why is a Parkinson Centre Needed? Available online: http://www.mpda.org.my/helpparkinsonclub.php. Accessed on 5 May 2015
11. World Health Organization.: Neurological Disorders: Public Health Challenges. World Health Organization (2006)
12. Abbasi, B.: A neural network applied to estimate process capability of non-normal processes. Expert Syst. Appl. **36**(2), 3093–3100 (2009)
13. İşeri, A., Karlık, B.: An artificial neural networks approach on automobile pricing. Expert Syst. Appl. **36**(2), 2155–2160 (2009)
14. Takeda, F., Shiraishi, Y., Sanechika, T.: Alarm sound classification system of oxygen concentrator by using neural network. Int J Innovative Comput. Inform. Control (Special Issue on Innovative Computing Methods in Management Engineering) **3**(1), 211–222 (2007)
15. Pan, S., Warwick, K., Stein, J., Gasson, M.N., Wang, S.Y., Aziz, T.Z., Burgess, J.: Prediction of Parkinson's disease tremor onset using artificial neural networks. In: Proceedings of the fifth IASTED International Conference: Biomedical Engineering, ACTA Press, pp. 341–345) (2007)
16. Gharehchopogh, F.S., Mohammadi, P.: A case study of Parkinson's disease diagnosis using artificial neural networks. Int. J. Comput. Appl. **73**(19) (2013)
17. Rosenblatt, F.: The perceptron: a probabilistic model for information storage and organization in the brain. Psychol. Rev. **65**(6), 386 (1958)
18. Nanda, S.K., Lin, W.Y., Lee, M.Y., Chen, R.S.: A quantitative classification of essential and Parkinson's tremor using wavelet transform and artificial neural network on sEMG and accelerometer signals. In: 2015 IEEE 12th International Conference on Networking, Sensing and Control (ICNSC), IEEE, pp. 399–404 (2015)
19. Shijiya, S., Thomas, P: An improved method to detect common muscular disorders from EMG signals using artificial neural network and fuzzy logic. IJATES **4**(07) (2016)

20. Challa, K.N.R., Pagolu, V.S., Panda, G., Majhi, B.: An improved approach for prediction of Parkinson's disease using machine learning Techniques. arXiv preprint: arXiv:1610.08250 (2016)
21. Meigal, A.I., Rissanen, S., Tarvainen, M.P., Karjalainen, P.A., Iudina-Vassel, I.A., Airaksinen, O., Kankaanpää, M.: Novel parameters of surface EMG in patients with Parkinson's disease and healthy young and old controls. J. Electromyogr. Kinesiol. **19**(3), e206–e213 (2009)
22. Ruonala, V., Meigal, A., Rissanen, S. M., Airaksinen, O., Kankaanpää, M., Karjalainen, P.A.: EMG Signal Morphology in Essential Tremor and Parkinson (2013)
23. De Michele, G., Sello, S., Carboncini, M.C., Rossi, B., Strambi, S.K.: Cross-correlation time-frequency analysis for multiple EMG signals in Parkinson's disease: a wavelet approach. Med. Eng. Phys. **25**(5), 361–369 (2003)
24. Sturman, M.M., Vaillancourt, D.E., Metman, L.V., Bakay, R.A., Corcos, D.M.: Effects of subthalamic nucleus stimulation and medication on resting and postural tremor in Parkinson's disease. Brain **127**(9), 2131–2143 (2004)

Performance Analysis of Gene Expression Data Using Mann–Whitney *U* Test

K. Vengatesan, S.B. Mahajan, P. Sanjeevikumar, R. Mangrule, V. Kala and Pragadeeswaran

Abstract In this article, performance of gene expression data is analyzed using statistical method resembling Mann–Whitney *U* test. Biological field investigation of gene expression data is one of the budding domains, in which lot of research work is projected. The finding of the most correlated genes into a group is one of the challenging tasks that will be measured using some of the statistical methods like parametric or nonparametric methods. The microarray is taken as input from the gene expression data that is applied into different methods such as two-sample tests, one-way ANOVA, paired t-test, and Mann–Whitney *U* test. Scientifically evaluating the recital of each scheme based on virtual and natural information

K. Vengatesan (✉) · R. Mangrule
Department of Computer Engineering, Marathwada Institute of Technology, Aurangabad, India
e-mail: vengicse2005@gmail.com

R. Mangrule
e-mail: mangrule@gmail.com

S.B. Mahajan
Department of Electrical and Electronics Engineering, Marathwada Institute of Technology, Aurangabad, India
e-mail: sagar25.mahajan@gmail.com

P. Sanjeevikumar
Department of Electrical and Electronics Engineering, University of Johannesburg, Auckland Park, Johannesburg, South Africa
e-mail: sanjeevi_12@yahoo.co.in

V. Kala
Department of Computer Science and Engineering, Maharashtra Institute of Technology, Aurangabad, India
e-mail: mrskala@gmail.com

Pragadeeswaran
Department of Computer Science and Engineering, Muthayammal Engineering College, Rasipuram, Tamil Nadu, India
e-mail: pragadees.net@gmail.com

A. Konkani et al. (eds.), *Advances in Systems, Control and Automation*,
Lecture Notes in Electrical Engineering 442, https://doi.org/10.1007/978-981-10-4762-6_67

beneath conditions the result shows that clearly the Mann–Whitney *U* test will produce better result of correlated result and form as cluster group.

Keywords Microarray · Similarity measure · Statistics method
Correlation · Mann–Whitney *U* test

1 Introduction

In modern living, the gene expression information has been widely analyzed by both theoretic and experiment ways. The analysis of bacteria on cell is straightforward to do this analysis of sequence of data [1]. A noise present in the gene expression data very critical process in the living system and toughness to blast is supposed one of the foremost devise moralities of the connected gene rigid networks [2]. Basically, the images are converted into microarray information, which has to be distorted into gene expression matrix in which horizontal line stands for genes, vertical line stands for various samples like tissues or investigation situation, and information in every cell exemplify the appearance point of scrupulous gene in the exacting taster. Newly gene appearance profiles are additional favored structure of disease classification scheme than morphology [3]. In which classifies model based on the gene data samples for different predefined diseases. Existing system used various statistical techniques like naive Bayes approach, logistic regression, least square, discrimination methods, nearest neighbor for generate classifier model [4]. These statistical approaches frequently effect in an unbendable taxonomy scheme that is powerless to organize a sample, if the expressions of genes are to some extent sundry beginning the predefined summary. Machine learning approaches resembling support vector machine and artificial neural networks have been effectively functional to categorize microarray data [5]. Classifying microarray data using support vector machine and machine learning algorithms like artificial neural networks has been effectively applied. Still, these approaches fabricate high-quality categorization accurateness; the results formed through them are inflexible to interpret. The rule-based classifier model is one of the classifier models used to construct decision tree; however, the rules formed by them include in nature significant requisites, and it is a perceptive kind of classifier. Diminutive conflicts in the exercise model show the technique to bulky difference in the hierarchy formation [6]. A new figurative machine learning to move toward is planned to extort human being sensible convention commencing resolution trees. The appearance of DNA microarray technologies in excess of the earlier episode decade has efficient the progress in the direction of biological investigate in such a method that scientists be capable of calculate the expression levels of thousands of genes concurrently [7]. This high-throughput investigations information have permitted for modern explore to discover complex communications linking genes. Gene regulatory network (GRN) refers to a collection of molecular machinery, together with genes, proteins, and further molecules, as well as the connections among these

molecules that cooperatively take away a cellular task. The essential thought at the rear GRN examination is to take out prominent gene dogmatic facial appearance by probing gene appearance pattern [8]. Our conventional move toward to categorize gene despotic affairs is the triumph research, in which the expression levels of an exacting gene are decreased even as all further situations are reserved invariable. This approach is suitable for small number of genes, but this approach cannot be scaled up to study rigid networks consisting of hundreds of genes appropriate to the absolute quantity of investigation manipulations required to expose an entire regulatory network.

2 Related Work

DNA microarray is one such expertise which enables the researchers to explore and deal with recent problems which were once interest to be no perceptible. In clinical care to identify the relevance disease like prompt and methodical way to in gene expression data. Three model approaches are used statically to identify the similarity such as nonparametric t-test, Pearson's correlation, and Mann–Whitney or rank sum test; these model biologically similar genes are measured under certain noise-level value. In particular, the molecular biology field various researches involved for development of similarities in large number of gene using conventional methods [9]. DNA microarray expertise has empowered the precise society to recognize the elementary aspects underlining the enlargement and progress of life as glowing as to explore the heritable causes of issues stirring in the execution of the human being body.

Distance measure between the pair of genes, a choice of geometric formula are second-hand to estimate the connection of the brace of gene dataset like variance increase distance, Manhattan distance, Euclidean distance, average intracluster distance, and average intercluster distance. Generally, the cluster investigation is based on the two ingredients such as distance measure cluster algorithm and, from which distance measure is quantification of similarity or dissimilarity between the two objects and cluster algorithms procedure to group the objects within small cluster distance [10]. The probability model is another method used to express relationship between different experimental conditions and also to form a set of disjoint bicluster in a supervised manner. The novel-based approach used in biclustering combines statistical consideration and graph theoretic to find similar expression pattern over a subset of conditions, and the gene is significantly changed based on the subset of values.

$$\text{Euclidean distance}, d_E(x, y) = \sqrt{\sum_{i=1}^{n} (x_i - y_i)^2} \tag{1}$$

$$\text{Manhattan distance, } d_M(x,y) = \sum_{i=1}^{n} |x_i - y_i| \tag{2}$$

$$\text{Correlation distance, } d_C(x,y) = 1 - \frac{\sum_{i=1}(x_i - \bar{x})(y_i - \bar{y})}{\sqrt{\sum_{i=1}(x_i - \bar{x})^2 \sum_{i=1}(y_i - \bar{y})^2}} \tag{3}$$

$$\text{Average inters cluster distance, } D_2 = \sqrt{\frac{\sum_{pi \subset ci} \sum_{pj \subset cj} |p_i - p_j|^2}{|c_i||c_j|}} \tag{4}$$

$$\text{Average intra cluster distance, } D_3 = \sqrt{\frac{\sum_{pi,pj \subset ci \cup cj} |p_i - p_j|^2}{(|c_i| + |c_j|(|c_i| + |c_j|) - 1)}} \tag{5}$$

The coefficient of rank correlation is based on the various values of the variants and is denoted by R. The coefficient of rank correlation is given Eq. (6). Where D^2 the square of the difference of corresponding ranks, and n is the number of pairs of observations.

$$R = 1 - \frac{6\sum D^2}{n(n^2 - 1)} \tag{6}$$

Figure 1 shows the preparation DNA microarray in experimental way, in which normal or tumor sequence of data is processed with combine equal amount, then it passed into hybridize probe to microarray, after applied to scanning produce original microarray. Every group of DNA is inserted into some chip for hybridization or bind into the synthetic DNA, in which the sequence of process performed for individual genes.

2.1 Gene Expression Arrays

Gene expression arrays present a inclusive vision of gene movement in natural samples. Universal uses of gene expression arrays contain genome-wide degree of difference appearance studies, ailment classification, corridor analysis, expression-based quantitative trait loci (eQTL) mapping. Researchers might carry out gene expression scrutiny at a quantity of one of quite a lot of varied levels at which gene expression is keeping pace: post-translational protein modification, translational, post-transcriptional, and transcriptional.

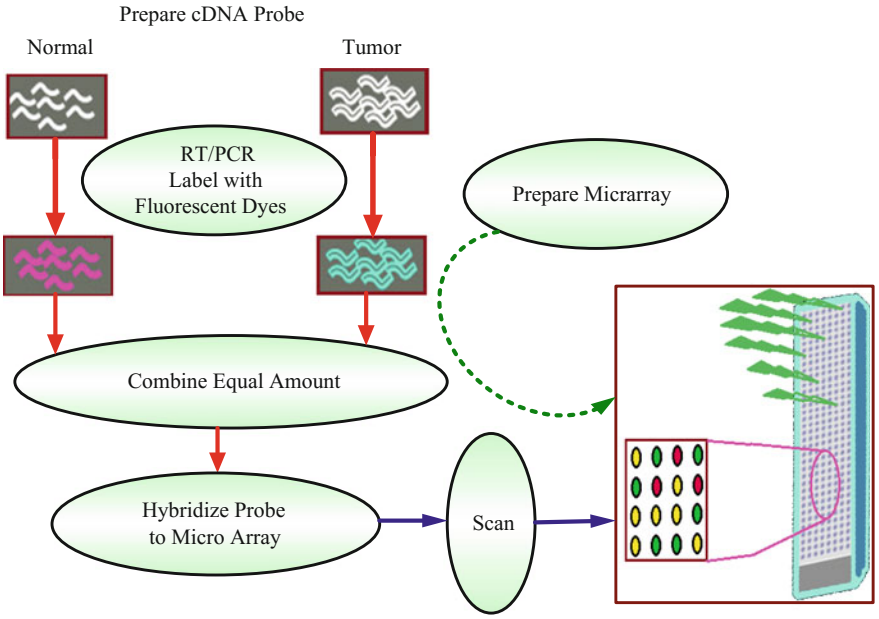

Fig. 1 DNA microarray work

3 Results and Discussion

Testing the significance of values was made by either parametric or nonparametric. Generally, the parametric tests are suitable when the sample size is very large and nonparametric are suitable, when the gene size is small [11]. As per the statistical method even the size of data is either large or small, it can analyze only the part of data according to hypothesis. The parametric test has following methods like Z-test and t-test that are based on the assumption that the random samples are selected from a normal population. The nonparametric test is also called as distribution free method, in which single mathematical equation used for calculating distribution under certain conditions. The proposed method has gene expression data with set of row and column that is called as microarray, in which Mann–Whitney *U* test is applied to measure the significance of genes. Nonparametric test has following advantages such as test generally simple to understand, quicker, and easier to apply when sample sizes are small. It will assume the part of data so does not need lengthily calculation. Mann–Whitney *U* test is a nonparametric test; therefore, it does not presuppose some assumptions associated to the delivery. On the other hand, a quantity of assumptions that are tacit one is the taster drawn from the populace is arbitrary and subsequent is self-determination surrounded by the samples and reciprocated sovereignty is implicit, and third is ordinal extent scale is understood.

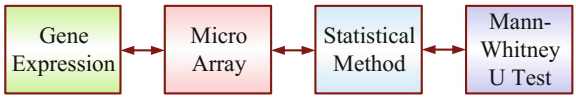

Fig. 2 Workflow of proposed work

Figure 2 shows the flow diagram of the systematic model of proposed method, and it will obtain the biological gene expression data, in which the data cannot be processed analysis because, has huge volume of data in different format, it will be converted into microarray. A micro array is $n * n$ matrix of set of genes. The microarray will be analysis suitable statistical methods like parametric and non-parametric. In which proposed method based on different statistical tests like Mann-Whitney U test for poles apart parameters.

3.1 Algorithm

Step 1: Assume Alternative hypothesis H_1 and null hypothesis H_0.

$$H_0 : \mu_1 = \mu_2$$
$$H_1 : \mu_1 \neq \mu_2$$

Step 2: Combine all sample values in an array from smallest to largest, and assign ranks, to all these values.

Step 3: First calculate the sum of the ranks for every of the samples that are denoting R_1 and R_2, similarly n_1, n_2 are their particular model sizes.

Step 4: Calculation of U to test the difference between the rank sums.

Step 5: Level of Significance assume $\alpha = 0.05$

$$\text{U-Statistic} = n_1 n_2 + \frac{n_1(n_1+1)}{t_1} - R_1, [\text{Corresponding the gene sample 1}] \quad (7)$$

$$\text{U-Statistic} = n_1 n_2 + \frac{n_2(n_2+1)}{t_1} - R_2, [\text{Corresponding the gene sample 2}] \quad (8)$$

$$\left.\begin{array}{l} \text{Mean}, \mu_u = \frac{n_1 n_2}{2} \\ \text{Variance}, \sigma_u^2 = \frac{n_1 n_2 (n_1+n_2+1)}{12} \end{array}\right\} \quad (9)$$

In Eqs. (7) and (8), sampling distribution of U is symmetrical and has a mean and variance given by Eq. (9). Where R_i = rank of the sample size n_1 = sample size one, n_2 = sample size two, and U = Mann–Whitney U test.

Table 1 Microarray gene expression data

Gene	c_1	c_2	c_3	c_4	c_5	c_6	c_7	c_8
G_1	42	47	145	42	40	181.5	45	83.5
G_2	103	135	125.5	105	100	130.5	115	100
G_3	75	65	52	92	−50	68	73	117.5
G_4	85	−30	108	132	130	160	40	44
G_5	30	40	37	20	−23	48	23	−2.2
G_6	7.7	7	−84.6	8	7.5	−96.2	−13	28.8

Table 2 Statistical comparisons of different methods

Gene	Two-sample test	Paired *t*-test	One-way ANOVA	Mann–Whitney *U* test
G_1&G_2	−1.79	−2.08	3.19	16
G_1&G_3	0.64	0.68	0.41	27
G_1&G_4	−0.18	−0.24	0.03	29.5
G_1&G_5	2.67	3.32	7.13	5.5
G_1&G_6	3.72	2.71	13.81	0
G_2&G_3	2.91	2.98	8.45	5
G_2&G_4	1.35	1.29	1.83	25
G_2&G_5	9.48	17.43	25	0
G_2&G_6	7.57	6.48	13.6	0
G_3&G_4	−0.78	−0.69	0.62	24
G_3&G_5	2.07	2.6	4.29	8
G_3&G_6	1.56	1.75	2.43	4
G_4&G_5	2.63	2.55	6.9	10.5
G_5&G_6	2.07	1.7	4.3	13

Table 1 consists of set of genes with different experimental conditions, from that columns c_1, c_2, c_3 …, c_8 are different experimental conditions and G_1, G_2, G_3 …, G_6 are different genes. The conversion of genes into microarray is a biological process that will be performed using different biological software or techniques are used. The microarray is commonly used in scientists to discover the particular diseases in human cells or organ and also that represents very large portion of the human genome. The microarray has various research problems in the recent days like microarrays that are used to learn the point to which convinced genes are twisted on or rotten in cells and tissues. In this case, as a replacement for of separating DNA from the samples, RNA (which is a transcript of the DNA) is isolated and calculated. Today, DNA microarrays are second-hand in medical analytical tests for a few diseases analysis. Occasionally, they are in addition worn to establish which drugs force survive best prearranged for meticulous folks, since genes decide how our bodies switch the chemistry interrelated to individuals drugs. Table 2 represents the statistical processed values pair of genes, in which every pair

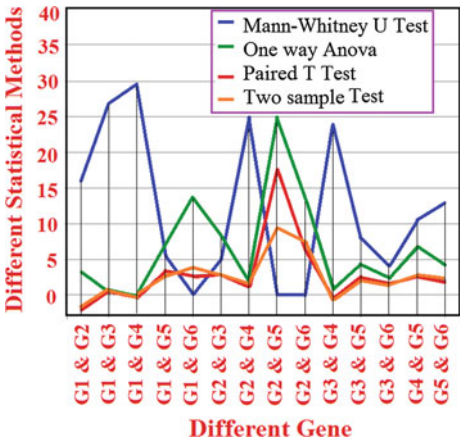

Fig. 3 Performance analysis

of gene was tested with one-way ANOVA, Mann–Whitney U test, two-sample test, and paired t-test, in which some are parametric test and remaining are nonparametric test, generally both test are suitable to analysis the set of values in different ways. It also considered some hypotheses to perform the various mathematical calculations to analysis the pair of genes. Consider the G_1&G_2 genes the processed values of two-sample tests is −1.79, paired t-test is −2.08, one-way ANOVA is 3.19, and Mann–Whitney U test is 16, similarly consider another pair G_1&G_3 two-sample test is 0.64, paired t-test is 0.68, one-way ANOVA is 0.41, and Mann–Whitney U test is 27. From the table clearly represents that the Mann–Whitney U test produced better results when compared to other statistical methods that is shown in Fig. 3, which is based on the following parameters such as N_1 is Sample size of G_1, N_2 is sample size of G_2 and R_1 is rank of the sample size.

4 Conclusion

The analysis of gene expression data has applied various statistical methods like parametric and nonparametric test. The verdict strappingly associated item set from operation database with sustain based Pearson's association coefficient correlated genes group is tough task together with the analysis various methods. Our proposed method Mann–Whitney was compared with two -sample tests, paired t-test, and ANOVA. Experimental results are presented in a direct appraisal of the Mann–Whitney U tests on a related microarray gene expression produced improved result.

References

1. Kumar, P.G., Victoire, T.A.A., Renukadevi, P., Devaraj, D.: Design of fuzzy expert system for microarray data classification using a novel genetic swarm algorithm. Expert Syst. Appl. **39**(2), 1811–1821 (2012)
2. Cano, C., Garcia, F., Lopez, F.J., Blanco, A.: Intelligent system for the analysis of microarray data using principal components and estimation of distribution algorithms. Expert Syst. Appl. **36**(3), 4654–4663 (2009)
3. Golub, T.R., Slonim, D.K., Tamayo, P., Huard, C., Gaasenbeek, M., Mesirov, J.P., Coller, H., Loh, M.L., Downing, J.R., Caligiuri, M.A., Bloomfield, C.D., Lander, E.S.: Molecular classification of cancer: class discovery and class prediction by gene expression monitoring. Science **286**, 531–537 (1999)
4. Terrence, F., Cristianini, N., Duffy, N., Bednarski, D., Schummer, M., Haussler, D.: Support vector machine classification and validation of cancer tissue samples using microarray expression data. Bioinformatics **16**, 906–914 (2000)
5. Ahmad, F.K., Deris, S., Othman, N.H.: The inference of breast cancer metastasis through gene regulatory networks. J. Biomed. Inform. **45**, 350–362 (2012)
6. Vengatesan, K., Selvarajan, S., Pragadeeswaran, S.: The performance analysis of microarray data using occurrence clustering. Int. J. Math. Sci. Eng. **3**(2), 69–75 (2014)
7. Jabado, O.J., Conlan, S., Quan, P., Hui, J., Palacios, G., Hornig, M., Briese, T., Lipkin, W.: Non parametric methods for the analysis of single-color pathogen microarrays. BMC Bioinform. **11**, 354 (2010)
8. Ankerst, M., Breunig, M.M., Kriegel, H., Sander, J.: OPTICS: Ordering Points to Identify the Clustering Structure. In: International Conference on Management of Data, *Sigmod*, Philadelphia (1999)
9. Ben-Dor, A., Shamir, R., Yakhini, Z.: Clustering gene expression patterns. J. Comput. Biol. **6** (34), 281–297 (1999)
10. Heyer, L.J., Kruglyak, S., Yoosepha, S.: Exploring expression data: identification and analysis of co-expressed genes. Genome Res. (1999). ISSN 1054-9803
11. Vengatesan, K., Selvarajan, S.: Maximize pair genes from microarray using the enhanced fuzzy clustering algorithm. J Pure Appl. Microbiol. **9**, 611–618 (2015)

Comparative Analysis of Membrane Potential of Bone Cell and Its Abnormalities

Saikat Chatterjee and Anjan Kumar Ray

Abstract Osteoblast bone cell is major part where different types of abnormalities are identified and analyzed. In these papers, electrical modeling of abnormal osteoblast cell is represented. Due to the presence of external field, the membrane potential as well as membrane current also varies. It is also observed that membrane potential of osteosarcoma cell increases compared to normal osteoblast cell. According to the value of membrane current or potential as well as nucleus membrane potential, different abnormalities can be identified.

Keywords Membrane potential · Osteoblast cell · Microelectrodes
Field intensity · Osteosarcoma

1 Introduction

Osteoblast cell is important part of bone cell. It consists of mainly two parts: the cell membrane and nucleus membrane, which are consider here as two spherical plate of the capacitor. The membrane potential of the osteoblast cell can varied according to the external field applied on it. Osteosarcoma, chondrosarcoma, Ewing's sarcoma, pleomorphic, and fibro sarcoma are the different examples of abnormalities of osteoblast cell where some abnormalities are also related to the cancer. Due to abnormal growth of osteoblast bone cell, it forms tumor (osteosarcoma). Due to the abnormalities in the osteoblast cell, there must be change in its internal operation as well as internal structure. The electrical modeling of ideal osteoblast cell is configured in this study for analyzing its abnormalities during different stages. Due to the effect of different electric field, the cell membrane potential and nucleus

S. Chatterjee (✉)
Sikkim Manipal Institute of Technology, Majitar, Sikkim, India
e-mail: Saikat.smit86@gmail.com

A.K. Ray
National Institute of Technology, Ravangla, Sikkim, India
e-mail: akray.nits@gmail.com

A. Konkani et al. (eds.), *Advances in Systems, Control and Automation*,
Lecture Notes in Electrical Engineering 442, https://doi.org/10.1007/978-981-10-4762-6_68

membrane potential will vary. Different abnormalities [1] of osteoblast cell were represented through electrical modeling, showing the effect of different electrodes (different shaped and thickness) through membrane potential and nucleus potential. The graphical output of every case will provide us a specific message.

2 Electrical Modeling of Human Cell

Human cell electrical modeling [2] is performed on the basis of variation of action potential. The action potential of human cell generates due to the generation of potential difference in cell membrane [1, 2]. Transfer of different ions (Na^+, Ca^{++}, K^+) from intercellular or intracellular level generates the potential difference in cell which is considered as action potential [3, 4]. Here, action potential represents the main role for the modeling (Fig. 1).

2.1 Electrical Modeling of Human Bone Cell (Osteoblast Cell)

Here, osteoblast cell modeling is performed in same manner (Fig. 2). The RC coupling part is related to the self-generated action potential due to external applied field. Here, C1 and R1 combinations are representing the self-generated circuit part which is affected by the external applied field. The internal parts (C2, R2, R3) represent the nucleus where R3 represents internal resistance of the osteoblast cell. C and R represent the total store charge and total resistance of the membrane potential.

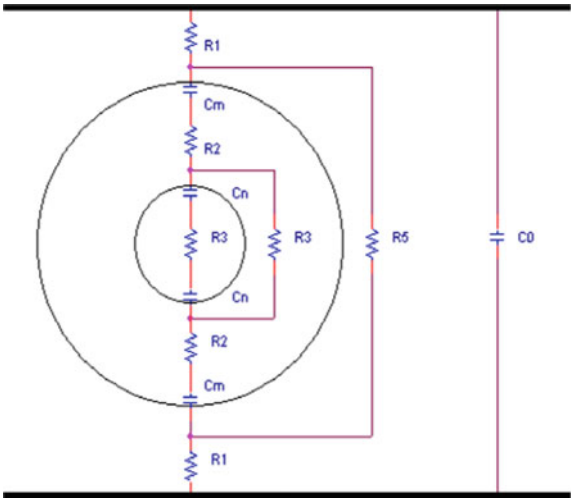

Fig. 1 Electrical equivalent circuit of a cell between electrodes

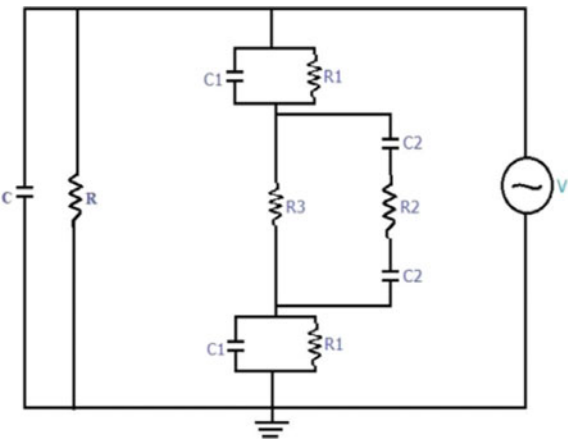

Fig. 2 Electrical model of osteoblast cell

3 Abnormalities of Osteoblast Cell

Osteoblast cell consists of specific part of the bone cell. If there any abnormality [3] occurs, then it will have effect on its function. There are different types of abnormalities that are identified. According to that, different diseases are diagnosis. The different abnormalities are:

- Osteosarcoma,
- Chondrosarcoma,
- Ewing's sarcoma.

3.1 Osteosarcoma

Osteoblast cell consists of osteoid tissue, and due to uncontrolled cell division, there will be generation of tumor from osteoid tissue. Mainly on knee and upper arm, this tumor occurs. Due to uncontrolled cell division, huge number of osteoblast cells generate, but the quantity of cytoplasm and nucleoplasm is reduced, which affect the main function of osteoblast cell. It may have effect on the average age of osteoblast cell. There is no swelling in bone, and it is not visible from outside. Osteosarcoma [3] is a cancerous tumor in a bone. It is most prevalent in children and young adults. Osteosarcomas tend to occur at the sites of bone growth, because proliferation makes osteoblast cells in this region prone to acquire mutations that could lead to transformation of cells.

3.2 Electrical Modeling of Osteosarcoma Cell

Figure 3 shows the electrical model of osteosarcoma bone cell [4]. Due to uncontrolled cell division, all new cells are not ideal and healthy condition.

The quantity of cytoplasm and nucleus is decreased compared to ideal one. Due to decrease in the quantity of nucleoplasm, the internal resistance of nucleoplasm increases and charge decreases. But in case of cytoplasm, internal resistance decreases and charge increases.

4 Microelectrode

Different microelectrodes [5] were applied to the osteoblast cell for observing the variation of membrane potential of nucleus and cytoplasm. Due to different shape and thickness of microelectrodes, the field intensity (Table 1) will vary to a certain range. In our study, the ranges of field intensity for different shaped electrodes were taken into consideration (Fig. 4). We are calculating the equivalent field voltage with implementing equivalent electrical modeling.

5 Result Analysis

When external field is applied across ideal osteoblast [6] cell for rectangular shaped electrodes and different thickness (1 μm), the resulting membrane potential is as follows. MULTISIM 10 software is used for the circuit configuration (Fig. 5).

Here, (Figs. 6 and 7) according to the plot, membrane current and membrane potential [7, 8] in presence of rectangular electrode (μA) remain unchanged to a

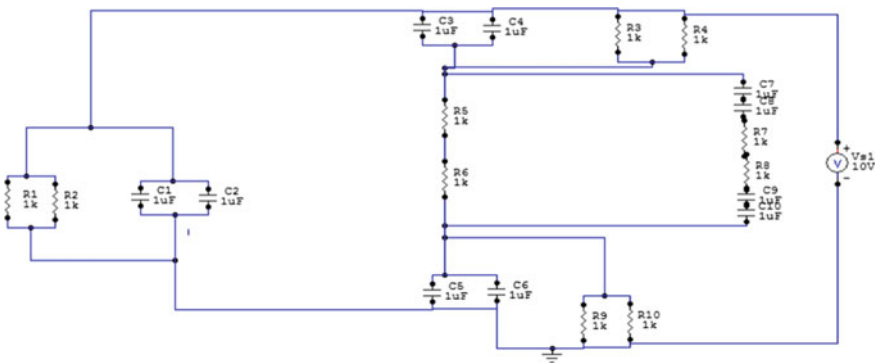

Fig. 3 Electrical model of osteosarcoma

Table 1 Range of field intensity [5]

Types of electrodes	Electric field intensity (10^{-4})
1. Rectangular	3.68–3.75
2. Semi circular	4.07–4.22
3. Saw tooth	3.61–8.87

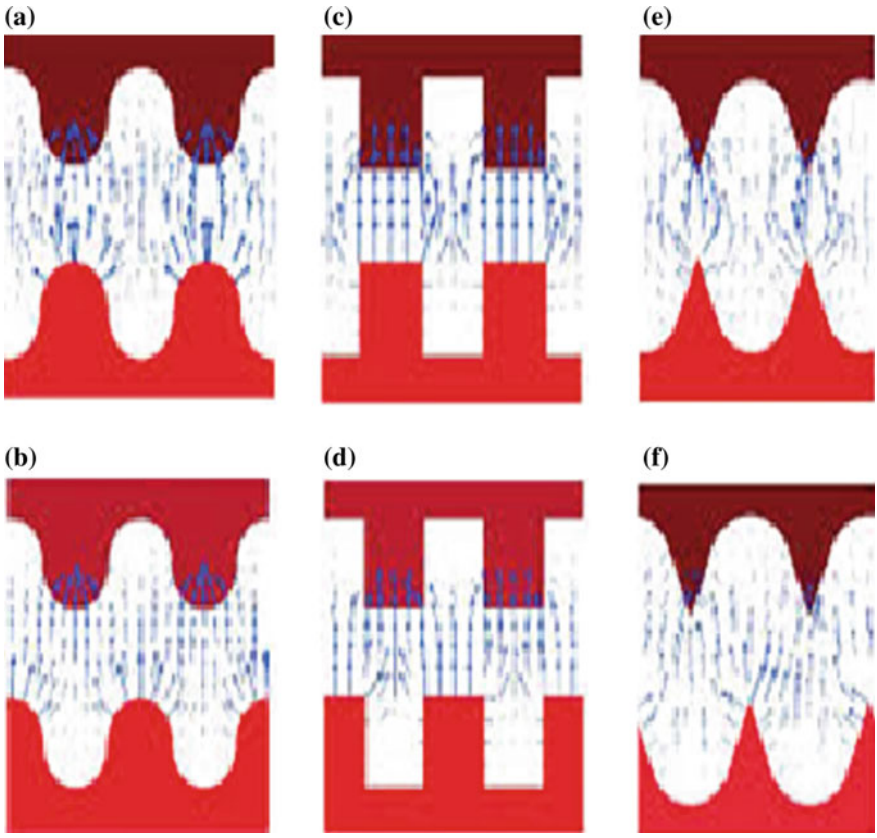

Fig. 4 Different shaped electrodes [5]

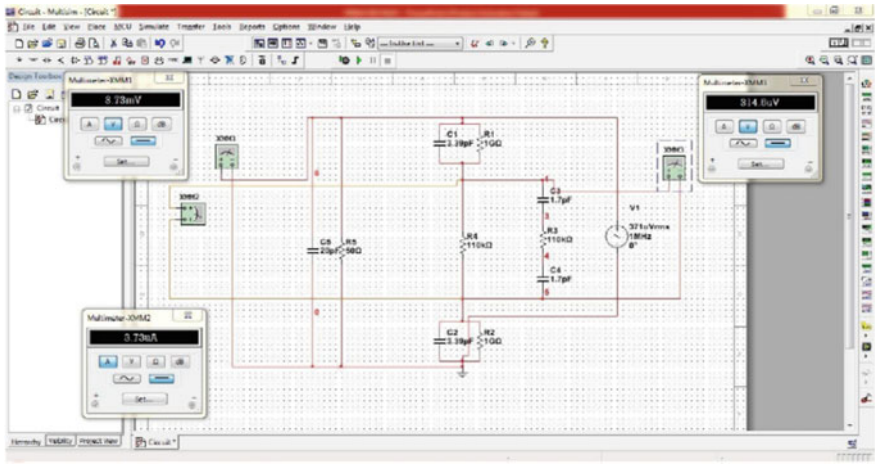

Fig. 5 Electrical modeling of osteoblast cell in MULTISIM

certain value and nucleus membrane potential decreases gradually with increase in field voltage.

Here, in Fig. 8 shown the electrical model of osteosarcoma bone cell using MULTISIM simulator software. In presence of rectangular electrode (d = 1 μm), osteosarcoma [9, 10] bone cell provides significant result (Fig. 9).

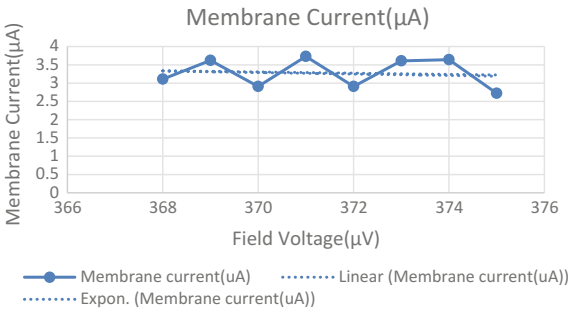

Fig. 6 Membrane current in the presence of rectangular electrode (d = 1 μm)

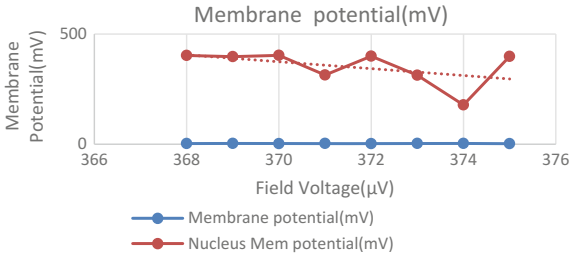

Fig. 7 Membrane and nucleus membrane potential

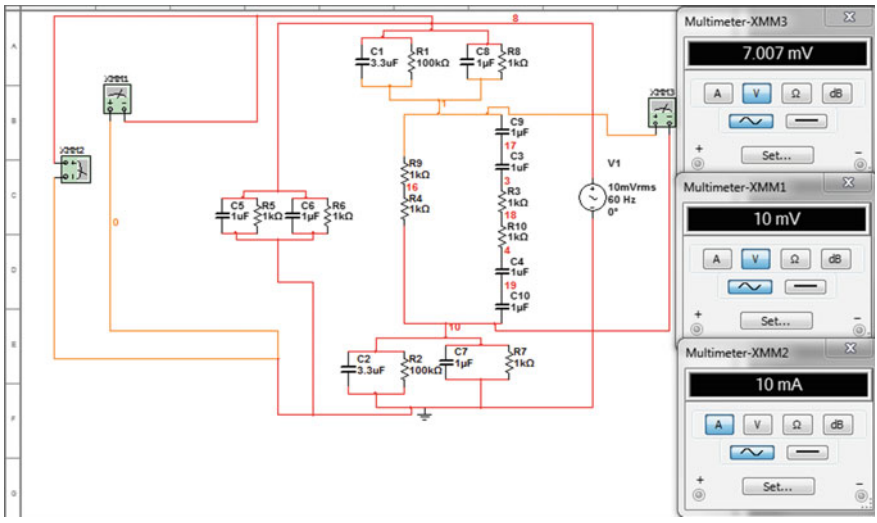

Fig. 8 Electrical modeling of osteosarcoma cell in MULTISIM

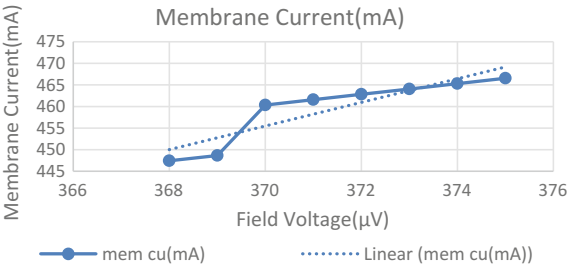

Fig. 9 Membrane current in the presence of rectangular electrode (d = 1 μm)

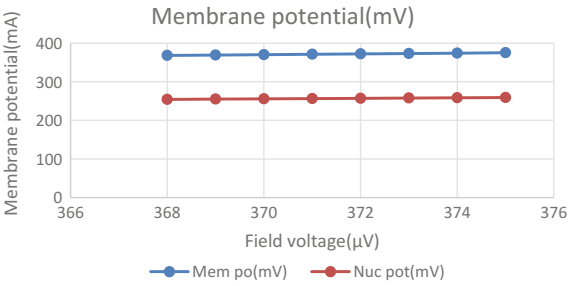

Fig. 10 Membrane potential in the presence of rectangular electrode (d = 1 μm)

6 Conclusion

From Figs. 8 and 10, it is found that transmembrane potential (nucleus membrane) of osteosarcoma (malignant cell) increases compared to osteoblast cell. It is also observed that its membrane potential reduces with increased field voltage and the membrane current also reduces with increased field voltage. With the analysis of the membrane potential and membrane current, different abnormalities of bone cell can be identified.

References

1. Sree, V.G., Udayakumar, K., Sundararajan, R.: Electric field-mediated inactivation of tumor cells (2009)
2. Pang, G.K., Qiao, D.: Skin impedance models for transdermal drug delivery. In: International Conference on Mechatronics and Automation, pp. 1784–1788 (2009)
3. Dev, S.B., et al.: Medical applications of electroporation. IEEE Trans. Plasma Sci. **28**(1), 206–223 (2000)
4. Dev, S.B., Rabussay, D.P., Widera, G., Hofmann, G.A.: Medical applications of electroporation. IEEE Trans. Plasma Sci. **28**(1), 206–223 (2000)
5. Sarkar, S., Mahapatra, R., Das, S., Bhoi, A.K.: Study the window effect of rectangular electrical pulse in membrane potential of dielectric model of osteoblast cell under different microelectrodes. Int. J. Eng. Res. Dev. **5**(9), 22–29 (2013)

6. Kirson, E.D., Gurvich, Z., Schneiderman, R., Dekel, E., Itzhaki, A., Wasserman, Y., Palti, Y.: Disruption of cancer cell replication by alternating electric fields. Can. Res. **64**(9), 3288–3295 (2004)
7. Bielack, S., Carrle, D., Casali, P.G.: ESMO Guidelines Working Group. ESMO Clinical recommendations for diagnosis, treatment and follow-up, Osteosarcoma, pp. 137–139 (2009)
8. Bielack, S., Carrle, D., Jost, L.: Osteosarcoma ESMO clinical recommendations for diagnosis, treatment and follow-up. Ann. Oncol. **19**, 94–96 (2008) (suppl 2)
9. Pang, G.K.H., Qiao, D.: Iontophoretic drug delivery models. In: 1st Middle East Conference on Biomedical Engineering, pp. 331–334. IEEE (2011)
10. Bielack, S.S., Carrle, D.: State-of-the-art approach in selective curable tumors: bone sarcoma. Ann. Oncol. **19**(Suppl 7), 155–160 (2008)

Dimensionality Reduction of Facial Features to Recognize Emotion State

Kiran P. Gaikwad, C.M. Sheela Rani, S.B. Mahajan and P. Sanjeevikumar

Abstract Lots of applications are based on facial emotion recognition such as action recognition in computer games, medical, and human–computer interaction. In past, number of approaches is proposed to recognize human emotions based on facial expressions by extracting facial features. As the number of facial features increases, the complexity level for recognizing expressions becomes high. Relatively, limited work is done on dimensionality reduction, which restricts the accuracy and robustness of the emotion. In this paper, work is done on dimensionality reduction of facial features and use of minimum number of facial features to represent emotion states.

Keywords Human–computer interaction (HCI) · Facial feature extraction Georgia technology face database · Accuracy and robustness · Emotions

K.P. Gaikwad (✉) · C.M. Sheela Rani
Department of Computer Science & Engineering, K.L. University, Green Fields, Vaddeswaram 522502, Andhra Pradesh, India
e-mail: kiran30march@gmail.com

C.M. Sheela Rani
e-mail: sheelarani_cse@kluniversity.in

S.B. Mahajan
Department of Electrical and Electronics Engineering, Marathwada Institute of Technology (MIT), Aurangabad, India
e-mail: sagar25.mahajan@gmail.com

P. Sanjeevikumar
Department of Electrical and Electronics Engineering, University of Johannesburg, Auckland Park, Johannesburg, South Africa
e-mail: sanjeevi_12@yahoo.co.in

A. Konkani et al. (eds.), *Advances in Systems, Control and Automation*, Lecture Notes in Electrical Engineering 442, https://doi.org/10.1007/978-981-10-4762-6_69

1 Introduction

Human–human communication includes spoken language. But in the absence of language, nonverbal information such as facial expressions, tone of the voice, and hand gestures is used. Human–computer interfaces evolved from conventional interfaces to modern advanced interfaces such as automatic speech recognition systems and special interfaces designed for handicapped people. Though these interfaces changed the way of human–computer interaction, it is not taking complete advantage of these valuable communicative abilities. It results often in a less than natural interaction. Information of an emotional state is usually extracted from facial expressions which are completely dependent on facial attribute. If computers could recognize these emotional inputs accurately, then it could give specific and appropriate help to users with the user's needs and preferences. Surprise, fear, disgust, anger, happiness, and sadness are the six different human emotions that are classified. Facial expressions and the tone of the speech play a major role in expressing these emotions. Previous study shows that the results to recognize emotion state with the use of facial expressions are more relevant than results obtained with tone of speech. Major part is played with facial expressions in the detection of emotions. As less work is carried out on emotion detection using facial expressions, scope is wide. Accuracy of emotion state recognition depends on the discriminant facial features extracted from facial expression. Lot of approaches has been suggested such as principle component analysis (PCA) and linear discriminant analysis (LDA) to extract the facial features. Recent techniques which are used to extract features are based on 2D discriminant analysis (2DDA) [1]. 2D LDA (2DLDA) and 2D PCA (2DPCA) are two representative methods which extract features from one direction. These techniques significantly reduce the feature extraction time than traditional PCA and LDA; Features are combined using row and column directions i.e. two-directional 2D LDA ((2D) 2LDA) and two-directional 2D PCA ((2D) 2 PCA) techniques used. These methods make more efficient representation than one-directional feature extraction approaches. Here, experimentation is carried out on facial expressions with two-dimensional maximum margin criteria and found reduction in facial feature vector size. This dimensionality reduction in feature vector has less space complexity and time complexity for recognizing emotion state.

2 Motivation and Related Work

Various works are carried out to recognize emotion state. Some of them used tone of speech, and others used facial expressions. Some emotions are better identified with audio and others with video. It is showed that these two modalities give complementary information, by arguing that the performance of the system increased when both modalities were considered together [2]. Several automatic emotion recognition systems have explored to locate human affective state by using

facial expressions or speech [3–5]. Very few efforts have focused on emotion recognition using both modalities. Variety of face expression analysis systems have been developed [6–9]. It is observed that the performance emotion recognition system based on facial expression is better than emotion recognition based on acoustic information. Image-based approaches process facial expressions based on 2D information, whereas geometric-based techniques share some common advantages such as explicit face structure. Dictionary-based approach for facial expression analysis is used [10]. This dictionary consists of AU-blocks. It has a structure; it is used to capture the high-level knowledge regarding AUs. Composition rules of AUs are extracted from FACS. To represent this knowledge in the sparse codes while designing the dictionaries, a two-layer approach for grouping the dictionary atoms is proposed. AU-layer is a lower layer which groups dictionary atoms corresponding to each AU. Expression layer is the top layer which uses the high-level knowledge to group different AUs that are composed to form an expression (e.g., sad, happy, and angry). This approach represents and characterizes a target facial expression with information extracted from a set of prototype models [11]. Initially, a set of prototype facial expression models are generated as a reference space of expressions. On this reference, space face images are projected which generates a set of registered face images. Facial expression appearance is characterized based on histograms of oriented gradients of each image. The obtained descriptors are then fed to the SVM for classification.

3 Emotion Recognition System

Proposed emotion recognition system consists of three modules. First is feature extraction module which extracts the discriminate facial features. Once the features are extracted, it is classified using second module, feature classification module. So, all the relevant features of respective emotions form a feature space. Then, finally using the third module, emotion states are recognized.

3.1 Feature Extraction Module

First step of emotion recognition system based on facial expression is feature extraction. Facial features are extracted using Two-Dimensional Maximum Margin Criteria (2D2MMC). Figure 1 depicts the block schematic of feature extraction module.

Initially, all the face images are aligned with cropping in one standard size 92×112. Images contain only facial expression. 2D2MMC extracts discriminant vectors from two directions and finds two optimal projectors in two directions as follows:

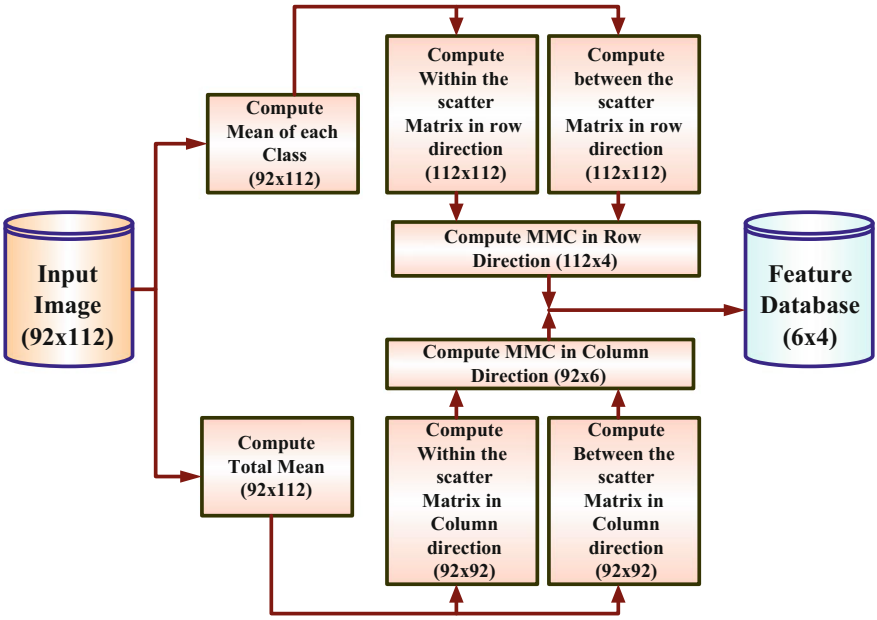

Fig. 1 Feature extraction module

Row projector $W_{\text{MMC\_R}}$:

$$\left.\begin{aligned} W_{\text{MMC\_R}} &= \arg\max \text{Tr}(W^t R_b W - W^t R_w W) \\ &= \left[w_1^r, w_2^r, \ldots, w_{nr}^r\right] \\ \text{where,} \quad & W \in R^{n \times nr}, W^t W = In_r \end{aligned}\right\} \tag{1}$$

Column projector $W_{\text{MMC\_C}}$:

$$\left.\begin{aligned} W_{\text{MMC\_C}} &= \arg\max \text{Tr}(W^t C_b W - W^t C_w W) \\ &= \left[w_1^c, w_2^c, \ldots, w_{nc}^c\right] \\ \text{where,} \quad & W \in R^{n \times nc}, W^t W = In_c \end{aligned}\right\} \tag{2}$$

3.2 *Dimensionality Reduction*

With the help of 2D2MMC, discriminative facial features are extracted. Like other 2D methods, the extracted features contain some redundant information. Selection of number of discriminant vectors is done with following approaches.

A direct and simple way is to screen out the eigenvectors corresponding to the negative eigenvalues:

$$\left.\begin{array}{l}(w_i^r)^t(R_b - R_w)w_i^r > 0, \quad i = 1, \ldots, n_r \\ (w_i^c)^t(C_b - C_w)w_i^c > 0, \quad i = 1, \ldots, n_c\end{array}\right\} \tag{3}$$

Eigenvectors corresponding to the eigenvalues are larger than the mean value of all eigenvalues:

$$\left.\begin{array}{ll}(w_i^r)^t(R_b - R_w)w_i^r > Tr(R_b - R_w) & i = 1, \ldots, n_r \\ (w_i^c)^t(C_b - C_w)w_i^c > Tr(C_b - C_w) & i = 1, \ldots, n_c\end{array}\right\} \tag{4}$$

A new feature selection criterion is defined in Eq. (5):

$$\left.\begin{array}{ll}(w_i^r)^t(R_b - R_w)w_i^r > \max(Tr(R_b - R_w)/n, 0) & i = 1, \ldots, n_r \\ (w_i^c)^t(C_b - C_w)w_i^c > \max(Tr(C_b - C_w)/m, 0) & i = 1, \ldots, n_c\end{array}\right\} \tag{5}$$

4 Experimental Result and Performance Analysis

Experiments are designed using standard Georgia Technology Face Database [12, 13]. This database contains 50 classes. All the images are resized to same size, and initially, feature extraction process is applied to the standard database. As more discriminant features are extracted, out of that only more distinguishing discriminant features are selected by feature selection criteria. As here, feature vector of size 4×6 is very less as compared to other feature vectors obtained. So, space complexity as well as time complexity of emotion state recognition is reduced. Classification of the emotion states such as neutral, smile, disgust, angry for the

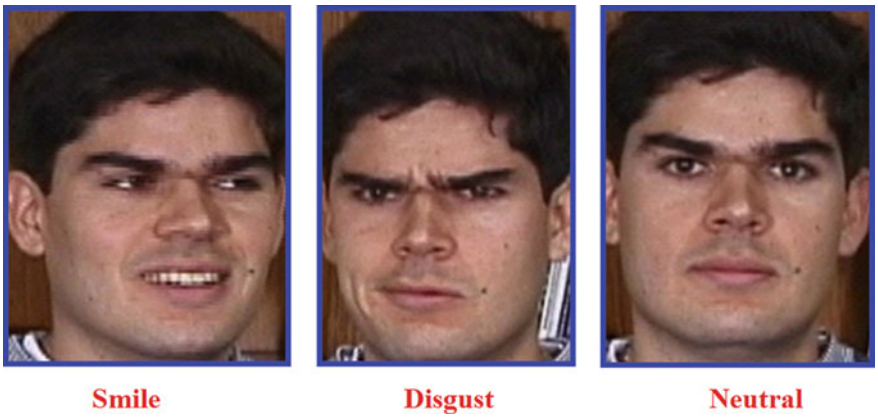

Fig. 2 Recognized emotion states of class-I

Fig. 3 Recognized emotion states of class-II

Table 1 Recognition rate for different emotion states

	Smile	Disgust	Neutral
Average recognition rate	98.75	98.6	98.56

database containing 110 person's expressions (with 10 varying experssion images for each person) is analyzed. Out of 10 images, four images which are expressing different emotion states are used for generating the emotion state database and others are used as test dataset. The recognition rate for the respective emotion state is 98.01%. Following are some classes on which experimentation is performed. The result of emotion state recognition is displayed in Fig. 2 (class-I) and Fig. 3 (class-II). The different emotion states are recognized with variation in facial expression. The recognition rate for different emotion states with given standard database is given in Table 1.

5 Conclusion

Though number of approaches is used to implement and recognize emotion state from facial expressions, the complexity level increases as extracted facial features are large in amount based on facial expressions. With the help of proper feature selection criteria, minimum discriminant invariant facial features are selected to decide the emotion state. With the experimental results, the minimum number of the feature vectors to represent the facial characteristics is 24, and size of feature vector is (6×4). This reduced dimensionality of feature space. And hence space complexity is reduced.

References

1. Wen Hui, Y., Dai, D.: Two-dimensional max. Margin feature extraction for face recognition. IEEE Trans. Syst. Man Cybern. **39**(4) (2009)
2. Daminic, W.M.: Illusions and issues in bimodal speech perception. In: Proceeding of Auditory Visual Speech Perception, vol. 98, pp. 21–26 (1998)
3. De Silva, L.C., Miyasato, T., Nakatsu, R.: Facial emotion recognition using multimodal information. In: IEEE International Conference on Information, Communications, and Signal Processing, Singapore (1997)
4. Chen, L.S., Huang, T.S., Miyasato, T., Nakatsu, R.: Multimodal human emotion/expression recognition. In: International Conference on Automatic Face and Gesture Recognition, Japan) (1998)
5. De Silva, L.C., Chi, N.P.: Bimodal emotion recognition. In: 4th IEEE International Conference on Automatic Face and Gesture Recognition (2000)
6. Black, M.J., Yacoob, Y.: Tracking and recognizing rigid and non-rigid facial motions using local parametric model of image motion. In: International Conference on Computer Vision, Cambridge (1995)
7. Essa, I.A., Pentland, A.P.: Coding, analysis, interpretation, and recognition of facial expressions. IEEE Trans. Pattern Anal. Mach. Intell. **19**(7), 757–763 (1997)
8. Kenji, M.: Recognition of facial expression from optical flow. IEICE Trans. Inf. Syst. **E74-D** (10), 3474–3483 (1991)
9. Tian, Y., Kanade, T., Cohn, J.: Recognizing lower face action units for facial expression analysis. In: 4th IEEE International Conference on Automatic Face and Gesture Recognition (2000)
10. Sima, T., Qiu, Q., Rama, C.: Structure-preserving sparse decomposition for facial expression analysis. IEEE Trans. Image Process. **23**(8) (2014)
11. Mohamed, D., Jean, M.: Prototype-based modeling for facial expression analysis. IEEE Trans. Multimedia **16**(6) (2014)
12. Gross, R.: Face databases. In: Stan, Z.L., Anil, K.J. (eds.) Handbook of Face Recognition. Springer, Berlin (2005)
13. Georgia Face database Link: http://www.face-rec.org/databases

Electro-Optically Tunable Switching Action Enhanced by Long-Range Surface Plasmon

Arijit Ghosh

Abstract By using analytical method, this paper depicts long-range surface plasmon-enabled electro-optically adjustable switching action by Goos–Hänchen shift for an alterable index of refraction of dielectric layer in Kretschmann–Reather geometry which is developed by a BK_7 prism, 5000 nm liquid crystal layer which may be considered as dielectric. This layer is sandwiched between 50 and 200 nm thin two gold layers. Here the phase difference varies from positive to negative with the incident angle of the fundamental light beam. This action can be achieved because of varying index of refraction of the dielectric layer with the applied external potential difference. In this scheme, Goos–Hänchen shift also plays a vital role for optical switching.

Keywords Optical switching · Long-range surface plasmon
Goos–Hänchen shift · Liquid crystal · Total internal reflection

1 Introduction

Surface plasmon is a phenomenon that occurs when the coherent electrons oscillate at the contact area within any two materials. The reason for this phenomenon is due to the changes of sign of real part of dielectric function throughout the junction (e.g., metal–dielectric or dielectric–metal interface). This phenomenon can be detected in some materials such as gold (Au), silver (Ag), copper (Cu), and sometimes in aluminum (Al) also for their low value of ionization potential [1, 2]. If a P-polarized highly directive laser beam incidents on a multilayered structure with an angle which is greater than the critical angle of the medium, an electromagnetic wave generates which is known as evanescent wave. This wave penetrates up to the last layer of that structure. Due to this wave, surface plasmon created among the

A. Ghosh (✉)
Department of Electrical & Electronics Engineering, Sikkim Manipal Institute of Technology, Sikkim Manipal University, Majitar 737136, Sikkim, India
e-mail: arijit0602@gmail.com

A. Konkani et al. (eds.), *Advances in Systems, Control and Automation*,
Lecture Notes in Electrical Engineering 442, https://doi.org/10.1007/978-981-10-4762-6_70

metal–dielectric interface. Otto and Kretschmann proposed configuration shows first time surface plasmon resonance (SPR) and Kretschmann–Reather geometry shows the phenomenon long-range surface plasmon (LRSP).

2 Proposed Scheme

In this proposed scheme first time designed and simulated enhanced by LRSP electro-optically adjustable switching using Goos–Hänchen shift (GH shift). In the suggested system, a liquid crystal layer of polyamide (p = 1.78, d_3 = 5 μm) which can be considered as dielectric layer [3] is placed between two thin metal layers of gold (p = 0.583 + 9.86i). The thicknesses of these two layers are 50 and 100 nm, respectively, at a wavelength of 1550 nm at a temperature of 25 °C [4]. Here the incident radiation is generated by an external laser cavity which is tuned at a wavelength of 1550 nm. The fundamental wavelength is developed by using gain-switched DFB laser which is functioning at a wavelength of 1550 nm, which can generate 30-ps pulses [5]. The laser radiation appears on the bottom surface of the prism with a specific angle which is more than critical angle of the medium [6]. When light appears at the lower edge of the prism, it will generate two surface plasmons at two metal–dielectric interfaces and coupled together at off-resonance condition which leads to LRSP condition. Later on that LRSP light is reflected back from the surface of the prism where the laser light has been incident. As the incident angle of the fundamental light beam is more than the critical angle of the surface then total internal reflection will occur. It is well known that during total internal reflection of light beam GH shift will be observed [7, 8]. This shift can be calculated with surface plasmon by the given equation

$$S = -\frac{1}{n}\frac{\mathrm{d}\beta}{\mathrm{d}\alpha} \tag{1}$$

In this equation, β is defined by phase difference between the incident light beam and reflected light beam, α can be defined as the angle of incident light beam, and n can be expressed as the wave vector in the medium of incidence. If for the surface plasmon the fundamental laser beam is TM-polarized then the coefficient of reflection of the multilayered proposed optical system can be depicted as [9],

$$r_{1234} = \frac{r_{12} + r_{12}r_{23}r_{34}\exp(2in_{3z}d_3) + [r_{23} + r_{34}\exp(2in_{3z}d_3)]\exp(2in_{2z}d_2)}{1 + r_{23}r_{34}\exp(2in_{3z}d_3) + r_{12}[r_{23} + r_{34}\exp(2in_{3z}d_3)]\exp(2in_{2z}d_2)} \tag{2}$$

The Fresnel coefficient of reflection r_{ij} for a TM-polarized light can be written as,

$$r_{ij} = \frac{n_{iz}/\varepsilon_i - n_{jz}/\varepsilon_j}{n_{iz}/\varepsilon_i + n_{jz}/\varepsilon_j} \tag{3}$$

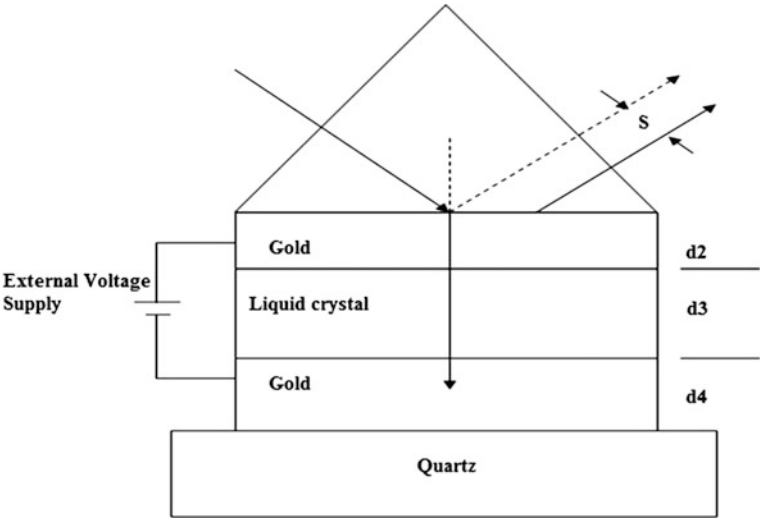

Fig. 1 Proposed structure for tunable optical switching with liquid crystal layer

where n_{iz} is the normal component of the wave vector quantity for individual medium, also $\varepsilon_i = p_i^2$ which is the constant of dielectric [10]. The subscripts $i, j = 1, 2, 3, 4$ signify the respective layers in the proposed configuration given in Fig. 1. Also

$$n_{iz} = (n_i^2 - n_y^2)^{\frac{1}{2}} \tag{4}$$

$$n_i = n\sqrt{\varepsilon_i} \tag{5}$$

$$n_y = n\sqrt{\varepsilon_1}\sin\theta_0 \tag{6}$$

$$n = \frac{2\pi}{\lambda} \tag{7}$$

where λ is the wavelength of incident laser beam. The phase difference β can be expressed as

$$\beta = \tan^{-1}\frac{\mathrm{Im}(X \times Y^*)}{\mathrm{Re}(X \times Y^*)} \tag{8}$$

where X and Y are the numerator and dominator of Eq. (2), respectively. With the help of equations above, the value of GH shift in the proposed multilayered LRSP configuration can be calculated. Here the index of refraction of the liquid crystal can vary from 1.5 to 1.85 with the applied potential difference as shown in Fig. 2. The incident angle versus phase difference graph is shown in Fig. 3.

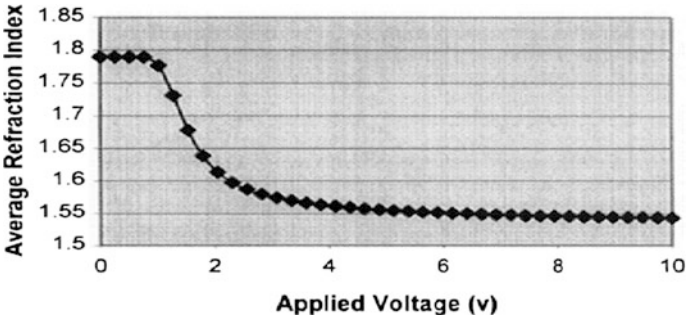

Fig. 2 Characteristic curve for the liquid crystal layer for change of index of refraction with applied potential difference

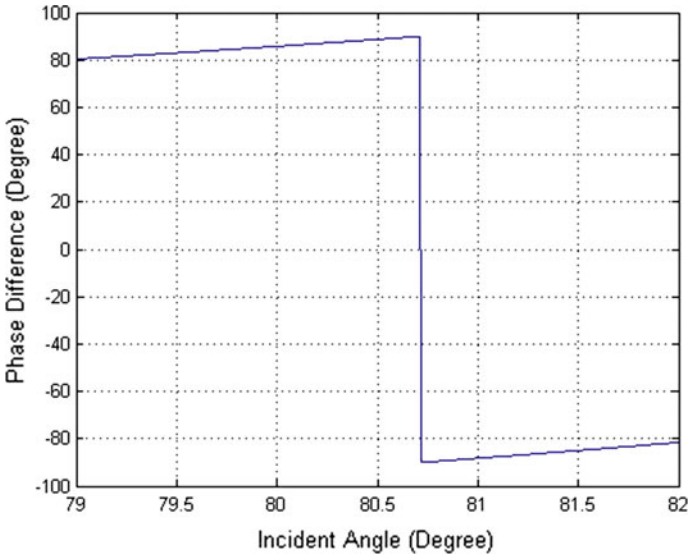

Fig. 3 Change in phase difference with varying incident angle of fundamental light

3 Conclusion

Simulated data clearly indicate that at 80.7° incident angle the phase difference changed drastically from positive to negative. This property can be used for the optical switching for any device. By using this proposed scheme and varying the external voltage applied on the dielectric layer (liquid crystal) tunable switching can be obtained. This structure can be used for any small application because all components which are used here are in micro-level structure.

References

1. Otto: Excitation of nonradiative surface plasma waves in silver by the method of frustrated total reflection. Zeitschrift für Physik **241**, 313–324 (1971)
2. Kretschmann, E.: The determination of the optical constants of metals by excitation of surface plasmons. Zeitschrift für Physik **216**, 398 (1968)
3. Zhang, H., Betremieux, Y., Noto, J., Kerr, R.: Novel tunable liquid crystal Fabry-Perot filters for fiber-optical system. In: Proceedings of SPIE **4583**, 64–72 (2001)
4. Rakić, A.D., Djurišic, A.B., Elazar, J.M., Majewski, M.L.: Optical properties of metallic films for vertical-cavity optoelectronic devices. Appl. Opt. **37**, 5271–5283 (1998)
5. Kim, S., Majewski, D.Y.: Generation of octave-spanning supercontinuum with 1550-nm amplified diode-laser pulses and a dispersion-shifted fiber. Opt. Expr. **14**(1), 270–278 (2006)
6. Sasagawa, K., Tsuchiya, M.: Highly efficient third harmonic generation in a periodically poled MgO: LiNbO3 disk resonator. Appl. Phys. Expr. **2**, 122401 (2009)
7. Goos, F., Hänchen, H.: Ein neuer und fundamentaler Versuch zur Totalreflexion. Anal. Phys. **6**, 333–346 (1947)
8. Artmann, K.: Calculation of the lateral shift of totally reflected beams. Anal. Phys. (Leipzig) **2**, 87–102 (1948)
9. Sui, G., Cheng, L., Chen, L.: Large positive and negative lateral optical beam shift due to long-range-surface plasmon resonance. Opt. Commun. **284**, 1553–1556 (2011)
10. Yang, X., Liu D., Xiet W.: High-sensitivity optical sensor based on surface plasmon resonance enhanced Goos-Hänchen shift. In: Proceedings of IEEE, Optoelectronic and Microelectronic Materials and Devices, pp. 74–77 (2006)

Dual Six-Phase Multilevel AC Drive with Single Carrier Optimized Five-Level PWM for Star-Winding Configuration

P. Sanjeevikumar, Mahajan Sagar Bhaskar, Frede Blaabjerg, Michael Pecht, Luigi Martirano and Matteo Manganelli

Abstract This article presents new multilevel modulation strategy based on single carrier-based pulse-width modulation for dual six-phase (twelve-phase) symmetrical/asymmetrical star-end winding converter. The four standard voltage source inverters with one bidirectional switch (MOSFET/IGBT) per phase constitute the power circuit. Further, through the two capacitor bi-directional switch link the neutral link. An algorithm-based single carrier zero-shifted five-level modulation (SCZSFM) modulates each two-level VSI as a five-level output multilevel inverter. The complete AC drive is numerically modelled in MATLAB/PLECS software and tested for predicting theoretical background.

Keywords Dual six-phase inverter · Multilevel inverters · Multiphase AC drives Space vector transformation · Split-phase space vector transformation

P. Sanjeevikumar (✉) · M.S. Bhaskar
Department of Electrical and Electronics Engineering, University of South Africa, Auckland Park, Johannesburg, South Africa
e-mail: sanjeevi_12@yahoo.co.in

M.S. Bhaskar
e-mail: sagar25.mahajan@gmail.com

P. Sanjeevikumar · M.S. Bhaskar
Research and Development (R & D), Ohm Technologies, Chennai, India

F. Blaabjerg
Department of Energy Technology, Center for Reliable Power Electronics (CORPE), Aalborg University, Aalborg, Denmark
e-mail: fbl@et.aau.dk

M. Pecht
Center for Advanced Life Cycle Engineering (CALCE), University of Maryland, College Park, MD, USA
e-mail: pecht@umd.edu

L. Martirano · M. Manganelli
Department of Electrical Engineering, University of Rome, Rome, Italy
e-mail: martirano@uniroma1.it

A. Konkani et al. (eds.), *Advances in Systems, Control and Automation*,
Lecture Notes in Electrical Engineering 442, https://doi.org/10.1007/978-981-10-4762-6_71

1 Introduction

AC drives based on multiphase (multiple stator winding >3) configuration are known for its high reliability, redundant structure, limited DC-link ripple, increased power density, fault tolerance, and low-voltage/high-current per phase inverter rating [1–5]. Multilevel inverters (MLIs) are renowned solution for high-voltage synthesis by multiple DC sources, limited total harmonic distortion (THD), and reduced dv/dt in the output voltages [6–12]. It has been proven that the combination of the multiphase and multilevel inverter is redundancy and fault tolerance AC drives [13–20]. But, failures are persistence multilevel inverters, (31–37.9%) by IGBT's mechanism. Other facts are discrete capacitors and current gate control techniques [1–5]. Still, the reliability of the standard two-level VSI is governed to frame multiphase and multilevel AC drives with redundant structures [1–20]. The isolated/non-isolated multilevel AC converter is reconfigured from quad-inverter configuration for star-winding loads. The dual three phases (twelve phases) are derived by two adjacent windings spatially shifted by 30° (symmetrical type) [15–22] or by 15° (asymmetrical) [15–22] as shown in Fig. 1. This article develops an optimal strategy based on single carrier zero-shifted five-level modulation (SCZSFM) dual six-phase asymmetrical/symmetrical converter as [15–22]. The proposed single carrier modulation algorithm (independent modulation) is used to regulate VSIs as a five-level standard multilevel inverters (MLIs) [15, 22]. Modular structure as four classical two-level VSIs. Further, each phase of VSIs as one bidirectional (IGBT) and switch linking the neutral with two capacitors. Features of the proposed class are that each VSI generates five-level line-to-line output with star-winding configuration. Confirming the total electric power quadrupling and are shared four isolated/non-isolated DC sources VSI's (H). Moreover, the reliability is governed under faulty conditions, i.e. one or two or three VSIs fail. Therefore, complete AC drive propagates with least one healthy VSI but with reduced power. Effectiveness to verify the proposed multilevel modulation, whole AC drive system is numerically modelled and executed with MATLAB/PLECS simulation softwares. Set of results which are observed are depicted in the paper under balanced conditions to show the proper five-level outputs modulation. It is always agreed with the results shown are close conformity by a performance with developed theoretical background

2 Split-Phase Decomposition SVT

The twelve-phase star-winding system is expressed by stationary space vectors (multiple) [22]. By expression (1) $\alpha = \exp(j2\pi/12)$ for the symmetrical and $\alpha = \exp(j\pi/12)$ for the symmetrical and asymmetrical converter as the spatial shift between windings [1, 2, 15–22]. The space vectors $\bar{x}_1, \bar{x}_5, \bar{x}_7, \bar{x}_{11}$ are multiple

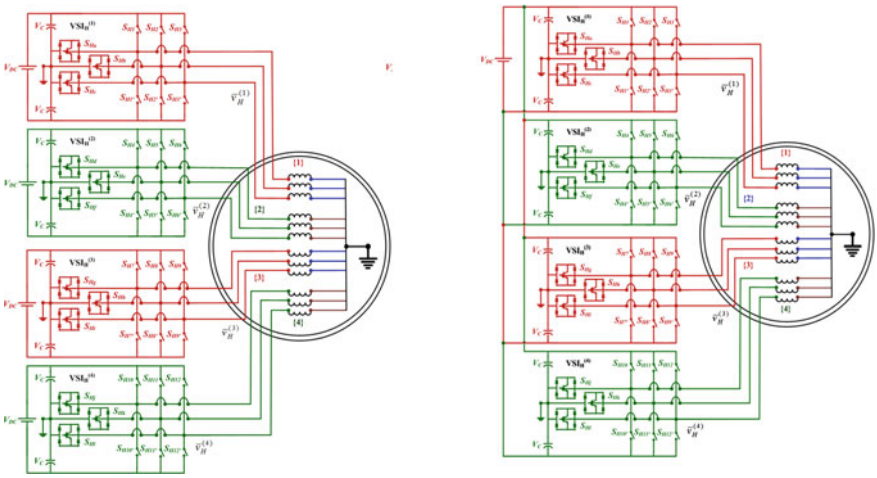

Fig. 1 Schematic circuit of dual six-phase star-winding multilevel converter. *Left* Isolated version. *Right* Non-isolated version (asymmetrical/symmetrical type)

components and rotating vectors, and $\bar{x}_3, \bar{x}_9$ are the zero-sequence (homo-polar) components available in sub-spaces of d_1-q_1, d_5-q_5, d_7-q_7, d_{11}-q_{11}, and d_3-q_3, d_9-q_9.

The AC drive can be split into four three-phase sub-systems {1}, {2}, {3}, {4} and tested for the performance [15–22]. The space (multiple) vectors, $\bar{x}^{(2)}$, $\bar{x}^{(3)}$, and $\bar{x}^{(4)}$ as well as the zero-sequence components $x_0^{(1)}$, $x_0^{(2)}$, $x_0^{(3)}$, $x_0^{(4)}$ are summarized below:

$$
\begin{aligned}
\bar{x}_1 &= \frac{1}{4}\left[\bar{x}^{(1)} + \alpha\,\bar{x}^{(2)} + \alpha^2\bar{x}^{(3)} + \alpha^3\,\bar{x}^{(4)}\right] \\
\bar{x}_5^* &= \frac{1}{4}\left[\bar{x}^{(1)} + \alpha^5\,\bar{x}^{(2)} + \alpha^{10}\bar{x}^{(3)} + \alpha^{15}\,\bar{x}^{(4)}\right] \\
\bar{x}_3 &= x_0^{(1)} + x_0^{(2)} + j\left(x_0^{(3)} + x_0^{(4)}\right) \\
\bar{x}_7 &= \frac{1}{4}\left[\bar{x}^{(1)} + \alpha^7\,\bar{x}^{(2)} + \alpha^{14}\bar{x}^{(3)} + \alpha^{21}\,\bar{x}^{(4)}\right] \\
\bar{x}_{11}^* &= \frac{1}{4}\left[\bar{x}^{(1)} + \alpha^{11}\,\bar{x}^{(2)} + \alpha^{22}\bar{x}^{(3)} + \alpha^{33}\,\bar{x}^{(4)}\right] \\
\bar{x}_9 &= x_0^{(3)} + x_0^{(4)} + j\left(x_0^{(1)} + x_0^{(2)}\right)
\end{aligned}
\tag{1}
$$

3 Five-Level Modulation Strategy

The total electric power, P, of the AC drive can be expressed as follows [15–22]:

$$P = \frac{3}{2}\bar{v}_H^{(1)} \cdot \bar{i}^{(1)} + \frac{3}{2}\bar{v}_H^{(2)} \cdot \bar{i}^{(2)} + \frac{3}{2}\bar{v}_H^{(3)} \cdot \bar{i}^{(3)} + \frac{3}{2}\bar{v}_H^{(4)} \cdot \bar{i}^{(4)} \tag{2}$$

Now, the bidirectional switches and two capacitors are neglected in Fig. 1, the resultant four standard two-level inverters with isolated/non-isolated DC source. Further, the modulations are carried out as two-level VSIs. Applying space vector theory, the $\bar{v}$ output voltage vector of twelve-phase AC drive is given by [15–22]:

$$\bar{v} = \bar{v}_H^{(1)} + \bar{v}_H^{(2)} + \bar{v}_H^{(3)} + \bar{v}_H^{(4)} \tag{3}$$

The modulating vectors of inverters $\text{VSI}_H^{(1)}$, $\text{VSI}_H^{(2)}$, $\text{VSI}_H^{(3)}$, and $\text{VSI}_H^{(4)}$ are now easily expressed by considering Eq. (2):

$$\bar{v}_H^{(1)} = \frac{1}{3} V_{\text{DC}} \left(S_{H1} + S_{H2} e^{j2\pi/3} + S_{H3} e^{j4\pi/3} \right) \tag{4}$$

$$\bar{v}_H^{(2)} = \frac{1}{3} V_{\text{DC}} \left(S_{H4}\alpha + S_{H5}\alpha e^{j2\pi/3} + S_{H6}\alpha e^{j4\pi/3} \right) \tag{5}$$

$$\bar{v}_H^{(3)} = \frac{1}{3} V_{\text{DC}} \left(S_{H7}\alpha^2 + S_{H8}\alpha^2 e^{j2\pi/3} + S_{H9}\alpha^2 e^{j4\pi/3} \right) \tag{6}$$

$$\bar{v}_H^{(4)} = \frac{1}{3} V_{\text{DC}} \left(S_{H10}\alpha^3 + S_{H11}\alpha^3 e^{j2\pi/3} + S_{H12}\alpha^2 e^{j4\pi/3} \right) \tag{7}$$

The SCZSFM algorithm for the dual six-phase converter is shown in Figs. 2 and 3 [15–22]. Against the single triangular carrier, the modulating reference signals (zero-shifted) are compared to utilize the maximum DC for proper five-level multilevel outputs. Figure 2a elaborates the single carrier zero-shifted five-level modulation algorithm of phase 'a' of $\text{VSI}_H^{(1)}$, and the same applies to other phases of the VSI [18, 19]. The detailed zero-shifted reference signal for switch S_{H1}, (red) and S'_{H1}, (blue). For phase 'a' $\text{VSI}_H^{(1)}$, the bidirectional switch S_{Ha} modulates entire fundamental period and generates an additional level to the inverter outputs swap {1, 0} always. The switch S_{H1} will modulate in the first half-cycle ON-state and the second half-cycle OFF-state always in the whole fundamental period. The switch S'_{H1} will modulate in vice versa to the device S_{H1}. Correspondingly, switching pattern for $\text{VSI}_H^{(1)}$ is depicted in Fig. 3 for modulation index 0.8 [22]. The same strategy is applied to all other leg phases (b, c, d, e, f, g, h, i, j, k, l) of VSIs ($\text{VSI}_H^{(2)}$, $\text{VSI}_H^{(3)}$, $\text{VSI}_H^{(4)}$), with the appropriate phase shifts between reference modulating signals ($\alpha = \exp(j2\pi/12)$ symmetrical or $\alpha = \exp(j\pi/12)$ asymmetrical). Figure 3 depicts the switch pattern for inverters $\text{VSI}_H^{(1)}$ with a modulation index of 0.8 [15–22].

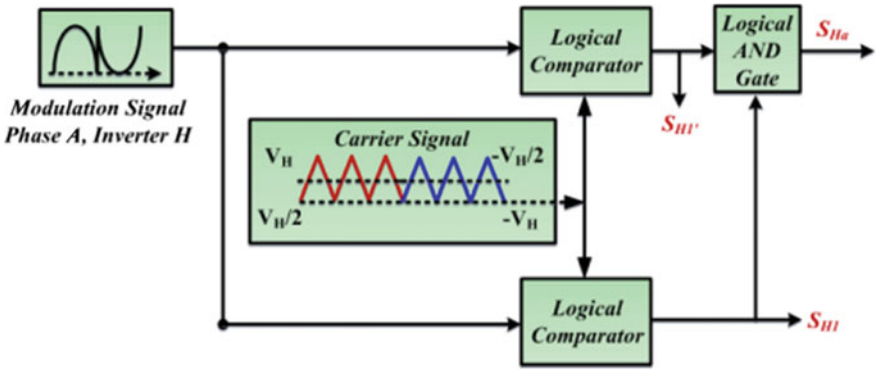

Fig. 2 Multilevel modulation scheme with one carrier for phase '*a*' of inverter $VSI_H^{(1)}$

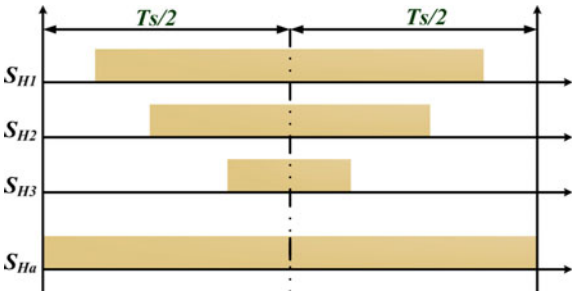

Fig. 3 PWM pattern for phase '*a*' of inverter $VSI_H^{(1)}$, modulation index = 0.8

4 Numerical Simulation Results and Discussion

The whole AC drive system is numerically developed in MATLAB/PLECS simulation software and tested for symmetrical, balanced operation with fixed modulation index 0.8. Parameters taken for investigation for the AC drive are given in Table 1. The complete behaviour of the proposed-AC multilevel converter system is elaborated in Fig. 4. By detail, Fig. 4a, b shows line-to-line voltages of the first-phase, fourth-phase windings of VSIs ($VSI_H^{(1)}$ and $VSI_H^{(2)}$) of the symmetrical isolated/non-isolated converter. Correspondingly, first the fundamental components are shown in the same figure and proven that amplitude is equal in magnitude. Second, it could be observed that the line-to-line voltages are spatially shifted by 30° as predicted. Third, each VSI is modulated to five levels of the developed single carrier zero-shifted five-level modulation (SCZFFM) algorithm [15–22]. Figure 4c, d shows the generated phase voltage of the first-phase ('*a*') {1}, fourth-phase ('*d*') {2} of the twelve-phase winding converter. Correspondingly first, phase voltages depicted with their fundamental components as time-averaged scale, proven that amplitude is equal in magnitude. Secondly, as predicted the voltage generated as seven-levels and in agreement with Eqs. (4)–(7). Third, the phase voltages are

Table 1 Main parameters of dual six-phase multilevel VSIs

DC Bus	V_{DC} = 400 V	Fundamental frequency	F = 50 Hz
Load resistances	R = 8 Ω	Switching frequency	F_S = 5 kHz
Load inductances	L = 10 mH	Capacitors	V_C = 2200 μF
Capacitors	V_C = 2200 μF		

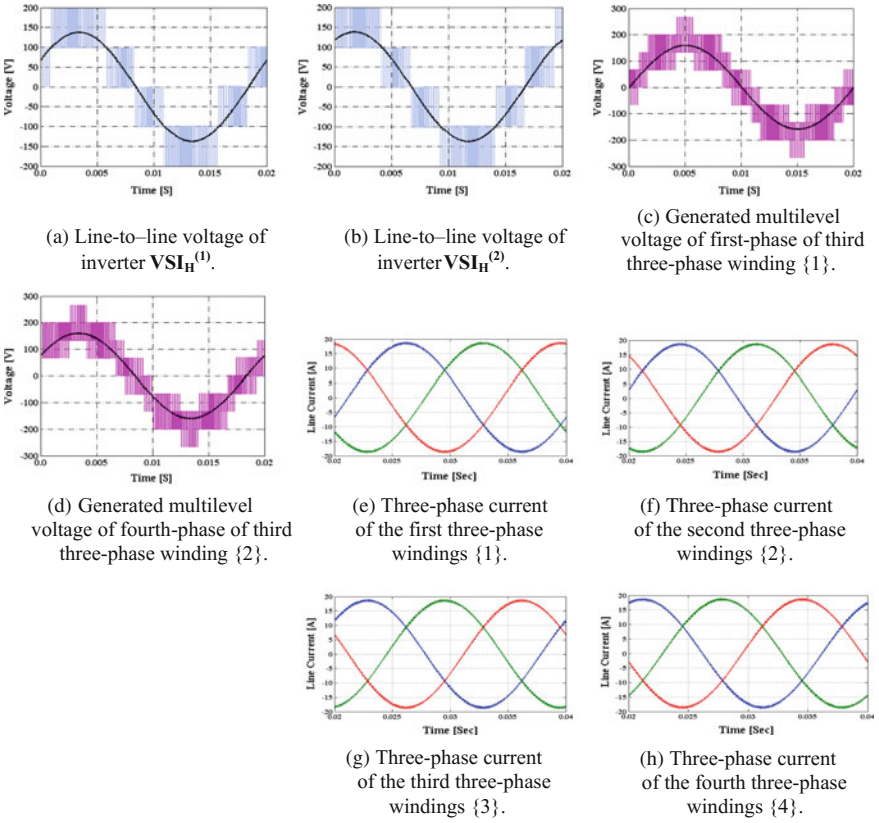

(a) Line-to–line voltage of inverter $\mathbf{VSI_H}^{(1)}$.

(b) Line-to–line voltage of inverter $\mathbf{VSI_H}^{(2)}$.

(c) Generated multilevel voltage of first-phase of third three-phase winding {1}.

(d) Generated multilevel voltage of fourth-phase of third three-phase winding {2}.

(e) Three-phase current of the first three-phase windings {1}.

(f) Three-phase current of the second three-phase windings {2}.

(g) Three-phase current of the third three-phase windings {3}.

(h) Three-phase current of the fourth three-phase windings {4}.

Fig. 4 Numerical simulation observed under the test behaviour of the proposed symmetrical ($\alpha = \exp(j2\pi/12)$) star-winding converter. Modulation index = 0.8, and for balanced condition maintained for operation. Voltages are depicted with its corresponding fundamental components with time-averaged scale

spatially shifted by 30° which is clearly noticed between voltages of star-windings {1} to {4}. Correspondingly, twelve-phase star-windings currents are shown in Fig. 4e, f, g, h, respectively. First, it is observed that twelve-phase currents are sinusoidal, balanced, equal in amplitude and spatial displacement of 30° between phases and smoothly propagated as predicted [15–22]. Observed results prove the set of developed theoretical background.

5 Conclusion

This paper investigated an isolated/non-isolated twelve-phase inverter configuration for optimal single carrier-based five-level modulation strategy. Developed pulse-width modulation behaves as five-level modulation and modulated the standard three-phase inverter as a multilevel converter. The numerical simulation software's modelling results are presented by developed theoretical developments. Pulse-width modulation algorithm can be easily implemented in any industry standard digital controller for realization with less computational burden. Investigation results suit for multiple batteries (isolated version) or fuel-cell-fed systems for (low-voltage–high-current) electrical vehicles, AC tractions, and 'more electric aircraft' (MEA) applications.

References

1. Sanjeevikumar, P., Grandi, G., Blaabjerg, F., Ojo, O., Wheeler, P.W.: Power sharing algorithm for vector controlled six-phase AC motor with four customary three-phase voltage source inverter drive. Eng. Sci. Technol. Int. J. **18**(3), 408–415 (2015)
2. Sanjeevikumar, P., Grandi, G., Blaabjerg, F., Wheeler, P.W., Ojo, O.: Analysis and implementation of power management and control strategy for six-phase multilevel ac drive system in fault condition. Eng. Sci. Technol. Int. J. **19**(1), 31–39 (2016)
3. Sanjeevikumar, P., Grandi, G., Ojo, O., Blaabjerg, F.: Direct vector controlled six-phase asymmetrical induction motor with power balanced space vector PWM multilevel operation. Int. J. Power Energy Convers. **7**(1), 57–83 (2016)
4. Grandi, G., Sanjeevikumar, P., Gritli, Y.: Transient analysis and control strategies for a quad-inverter multiphase multilevel motor drive in faulty conditions. J. Energy Power Eng. **7**, 1304–1315 (2013)
5. Oleschuk, V., Cernat, M., Pastor, M., Sanjeevikumar, P.: Synchronous PWM control of triple transformer-connected inverters for photovoltaic systems. In: Conference Proceedings. The 17th IEEE Power Electronics and Motion Control, IEEE-PEMC'16, Varna (Bulgaria) (2016)
6. Grandi, G., Sanjeevikumar, P., Gritli, Y., Filippetti, F.: Experimental investigation of fault-tolerant control strategies for quad-inverter converters. In: Conference Proceedings. IEEE International Conference on Electrical System for Aircraft, Railway and Ship Propulsion, IEEE-ESARS'12, Bologna (Italy), pp. 1–8 (2012)
7. Grandi, G., Sanjeevikumar, P., Gritli, Y., Filippetti, F.: Fault-tolerant control strategies for quad-inverter induction motor drives with one failed inverter. In: Conference Proceedings. IEEE 20th International Conference On Electrical Machines, IEEE-ICEM'12, Marseille (France), pp. 957–964 (2012)
8. Grandi, G., Sanjeevikumar, P., Casadei, D.: Preliminary hardware implementation of a six-phase quad-inverter induction motor drive. In: Conference Proceedings. The 14th IEEE European Power Electronics and Applications, IEEE-EPE'11, Birmingham (United Kingdom), pp. 1–9, 30 Aug–1 Sept 2011
9. Grandi, G., Sanjeevikumar, P., Ostojic, D., Rossi, C.: Quad-inverter configuration for multi-phase multi-level ac motor drives. In: Conference Proceedings. International Confetence on Computational Technologies in Electrical and Electronics Engineering, IEEE–SIBIRCON'10, Irkutsk Listvyanka (Russia), pp. 631–638 (2010)
10. Grandi, G., Tani, A., Sanjeevikumar, P.. Ostojic, D.: Multi-phase multi-level ac motor drive based on four three-phase two-level inverters. In: Conference Proceedings. IEEE Intl.

20th Symposium on Power Electron., Elect. Drives etc., IEEE-SPEEDAM'10, Pisa (Italy), pp. 1768–1775, (2010)
11. Sanjeevikumar, P., Pecht, M.: An isolated/non-isolated novel multilevel inverter configuration for dual three-phase symmetrical/asymmetrical converter. Eng. Sci. Technol. Int. J. **19**(4), 1763–1770 (2016)
12. Sanjeevikumar, P., Blaabjerg, F., Wheeler, P.W, Ojo, O.: Three-phase multilevel inverter configuration for open-winding high power application. In: Conference Proceedings. The 6th IEEE International Symposium on Power Electron. For Distributed Generation Systems, IEEE-PEDG'15, Aachen (Germany) (2015)
13. Sanjeevikumar, P., Wheeler, P.W., Blaabjerg, F., Ojo, O., Szcześniak, P.: Proposed novel multiphase-multilevel inverter configuration for open-end winding loads. In: Conference Proceedings. The 18th IEEE European Power Electronics and Applications Energy Conversion Congress and Expo, IEEE-EPE-ECCE'16, Karlsruhe (Germany) (2016)
14. Sanjeevikumar, P., Bhaskar, M.S., Pandav, K.M., Siano, P., Oleschuk, V.: Hexuple-inverter configuration for multilevel nine-phase symmetrical open-winding converter. In: Conference Proceedings. IEEE First International Conference on Power Electronics Intelligent Control and Energy System, IEEE-ICPEICES'16, pp. 1837–1844, Delhi (India) (2016)
15. Sanjeevikumar, P., Blaabjerg, F., Wheeler, P.W., Siano, P., Martirano, L., Szcześniak, P.: A novel multilevel quad-inverter configuration for quasi six-phase open-winding converter. In: Conference Proceedings. IEEE 6th International Conference on Power Engineering Energy and Electronics Drives 10th International Conference on Compatibility and Power Electronics, IEEE—CPE-POWERENG 16, Bydgoszcz (Poland), pp. 325–330 (2016)
16. Sanjeevikumar, P., Hontz, M., Khanna, R., Wheeler, P.W., Blaabjerg, F., Ojo, O.: Isolated/non-isolated quad-inverter configuration for multilevel symmetrical/asymmetrical dual six-phase star-winding converter. In: Conference Proceedings. 25th IEEE International Symposium on Industrial Electronics, IEEE-ISIE'16, Santa Clara, CA, (USA), pp. 498–503 (2016)
17. Sanjeevikumar, P., Blaabjerg, F., Wheeler, P.W., Khanna, R., Mahajan, S.B., Dwivedi, S.: optimized carrier based five-level generated modified dual three-phase open—winding inverter for medium power application. In: Conference Proceedings of IEEE International Transportation Electrification Conference and Expo, Asia-Pacific, (IEEE-ITEC'16), Busan (Korea), pp. 40–45 (2016)
18. Sanjeevikumar, P., Blaabjerg, F., Wheeler, P.W., Kyo-Beum, L., Mahajan, S.B., Dwivedi, S.: Five-phase five-level open-winding/star-winding inverter drive for low-voltage/high-current applications. In: Conference Proceedings of IEEE International Transportation Electrification Conference and Expo, Asia-Pacific, (IEEE-ITEC'16), Busan (Korea) (2016)
19. Sanjeevikumar, P., Blaabjerg, F., Wheeler, P.W., Ojo, O., Pandav, K.M.: A novel double quad-inverter configuration for multilevel twelve-phase open—winding converter. In: Conference Proceedings of 7th IEEE International Conference on Power System, IEEE-ICPS'16, Indian Institute of Technology, Delhi (India) (2016)
20. Sanjeevikumar, P., Bhaskar, M.B., Blaabjerg, F., Lars Norum, E., Sridhar, S., Hajizadeh, A.: Nine-phase hex-tuple inverter for five-level output based on double carrier pwm technique. In: 4th IET International Conference on Clean Energy and Technology, IET-CEAT'16, Kuala Lumpur (Malaysia) (2016)
21. Sanjeevikumar, P., Blaabjerg, F., Wheeler, P.W, Fedák, V., Duran, M.J., Siano, P.: A novel five-level optimized carrier multilevel pwm quad-inverter six-phase asymmetrical ac drive. In: Conference Proceedings of the 17th IEEE Power Electronics and Motion Control, IEEE-PEMC'16, Varna (Bulgaria) (2016)
22. Oleschuk, V., Sanjeevikumar, P., Cernat, M., Fedak, V.: Multiphase quad-inverter system with feedforward synchronous PWM and nonlinear voltage regulation. In: Conference Proceedings of the 17th IEEE Power Electronics and Motion Control, IEEE-PEMC'16, Varna (Bulgaria) (2016)